PROCEEDINGS OF THE

15th INTERNATIONAL CONFERENCE ON NUCLEAR REACTION MECHANISMS

Varenna (Italy), Villa Monastero
June 11–15, 2018

Edited by
F. Cerutti, A. Ferrari, T. Kawano, F. Salvat-Pujol, and P. Talou

CERN
Geneva
2019

Proceedings of the 15th International Conference on Nuclear Reaction Mechanisms

Varenna(Italy), Villa Monastero

June 11–15, 2018

Edited by

F. Cerutti, A. Ferrari. T. Kawano, F. Salvat-Pujol, and P. Talou

CERN, Geneva, 2019

CERN-Proceedings-2019-001
ISBN 978-92-9083-519-6 (paperback)
ISBN 978-92-9083-520-2 (PDF)
DOI: http://dx.doi.org/10.23727/CERN-Proceedings-2019-001

This volume is indexed in: CERN Document Server (CDS), INSPIRE and Scopus.
Available online at https://cds.cern.ch

This volume should be cited as:

Proceedings of the 15th International Conference on Nuclear Reaction Mechanisms, edited by F. Cerutti, A. Ferrari, T. Kawano, F. Salvat-Pujol, and P. Talou, CERN-Proceedings-2019-001 (CERN, Geneva, 2019).

A contribution in this volume should be cited as:

[Author name(s)], in Proceedings of the 15th International Conference on Nuclear Reaction Mechanisms, edited by F. Cerutti, A. Ferrari, T. Kawano, F. Salvat-Pujol, and P. Talou, CERN-Proceedings- 2019-001 (CERN, Geneva, 2019), pp. [first page]–[last page].

FOREWORD

It is a stimulating delight to observe that the fifteenth edition of the Varenna Conference Series on Nuclear Reaction Mechanisms (NRM), taking place 41 years after the first meeting initiated by Laura Colli Milazzo, demonstrated the vitality of this event, which through Ettore Gadioli's three-decade guidance has become a traditional appointment to review the advances in nuclear physics and its applications.

With about 90 participants and more than 70 oral contributions, ranging from nuclear structure and dynamics to hadrontherapy and facility survey, the attendance featured the usual fruitful mix of renowned experts and young researchers. An enriching novelty came from the successful initiative of an extended session on medical radioisotopes, whose contents, conclusions and propositions are presented at the end of this volume.

For the second time, as previously in 2012, the Conference was the occasion to celebrate two eminent scientists together. We are truly indebted to Anton Antonov and Pavel Oblozinsky, who were kindly available to join the last June meeting. Their prolific careers as well as respective tributes are found in the following pages.

Let us finally express all our deep and friendly gratitude to Mark Chadwick, who decided to leave the role of co-chairman he took in 2006. Since earlier times, Mark's lasting engagement and enthusiasm assured a very crucial support to this Conference Series. His close help will remain an essential ingredient for the continuation of the Varenna NRM experience, which we look forward to.

Francesco Cerutti Alfredo Ferrari Toshihiko Kawano Patrick Talou

DEDICATION

It is an honor for us to dedicate this 15th edition of the Varenna Conference on Nuclear Reaction Mechanisms to

Anton Antonov

and

Pavel Oblozinsky

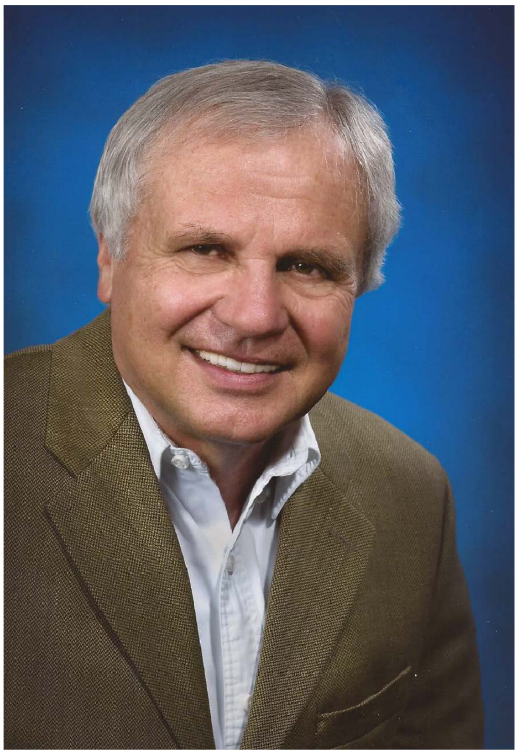

BIOGRAPHY OF ANTON N. ANTONOV

Prof. Anton N. Antonov completed his university studies at the Kharkov State University, in Ukraine, and succeeded the very selective examinations based on Minimum Landau in Theoretical Physics. He obtained his PhD with a thesis on High-Energy Electron and Proton Scattering by Nuclei in the Alpha-Particle Model under the supervision of Prof. E. V. Inopin. The original idea was to consider the scattering on pre-formed alpha particles in nuclei, highlighting the role of clusters. Back to Bulgaria, in 1973 he integrated the Institute of Nuclear Research and Nuclear Energy (INRNE), sharing his activity between Shumen and Sofia.

Prof. Antonov obtained the degree of Doctor of Science with a study on Nucleon-Nucleon Correlations and Characteristics of Nuclear Structure and Nuclear Reactions. He is 'the' expert of nucleon-nucleon correlations (short-range, tensor, long-range, ...) that play an important role in the structure of nuclei and the dynamics of nuclear reactions. He developed (with I. Z. Petkov and V. A. Nikolaev) the Coherent Density Fluctuation Model (CDFM), based on the delta-function approximation to the Generator Coordinate Method. The ansatz is that the One-body Density Matrix (ODM) of a finite nucleus can be expressed as an infinite superposition of ODM's of homogeneous pieces of nuclear matter, called «fluctons», of any size. The probability of each flucton is related to the density distribution of the nucleus. This model enters in several applications: spectral functions and density distributions in nuclei, including exotic and halo nuclei, form factors of light nuclei, description of the scattering of protons and neutrons on nuclei, and, more recently, electrons and (anti)neutrinos on nuclei, explaining the evidence for superscaling.

He established a longstanding collaboration with P. Hodgson. With him and I.Z. Petkov he wrote two monographs, well known by the students and researchers in the field.

He spent most of his career as Professor at the Laboratory of Theoretical Nuclear Physics, at INRNE, being extremely appreciated in his academic activity as lecturer and supervisor of PhD students, who are in turn well known physicists. Having a deep knowledge of west and east civilizations, he initiated and maintained collaborations with selected worldwide laboratories, from Russia to Spain, including France and Italy, Greece and Romania, as well as USA.

Prof. Antonov combines a rigorous and exigent attitude at work, together with a kind and human approach. Beyond physics, he has a passion for arts and history (transmitted to him by his mother, who is recognized for important archeological discoveries particularly in Shumen) as well as for musics (he plays the violin).

This unique background is probably the key for his successful academic and pedagogical career and leadership of his physics group.

LAUDATION OF ANTON N. ANTONOV

by Egle Tomasi-Gustafsson and Carlotta Giusti

at the 15th International Conference
on Nuclear Reaction Mechanisms
Varenna (Lake Como), Italy, 13 June 2018

Dear Anton,

It is a pleasure and an honor to highlight some aspects of your life, your achievements, and your career. The impressive quantity and quality of your scientific publications and of the well-known monographies (coauthored with P.E. Hodgson and I. Zh Petkov) witness your outstanding activity and contribution to Physics.

Prof. A.N. Antonov completed his university studies at the Kharkov State University, in Ukraine, and succeeded the very selective examinations based on 'Minimum Landau in Theoretical Physics'. He obtained his PhD, with a thesis on "High-Energy Electron and Proton Scattering by Nuclei in the Alpha-Particle Model" under the supervision of Prof. E. V. Inopin. The original idea was to consider the scattering on pre-formed alpha particles in nuclei, highlighting the role of clusters. Back to Bulgaria, in 1973, he integrated the Institute of Nuclear Research and Nuclear Energy (INRNE) of the Bulgarian Academy of Sciences (BAS), sharing his activity between Sofia and Shumen.

How to imagine today your travel from Sofia to Kharkov, in URSS times, what an interesting adventure for a young and clever boy! And, as we understand, you enjoyed the student times, even in specific conditions, but with huge enthusiasm and motivation for physics, cultivated by excellent Professors, such as Prof. M. P. Rekalo, your examinator, and Prof. Inopin, your supervisor... There you met good friends, 'friends for life'... and your wife Krasimira! How proud your children Vera and Todor, and your grandchildren must be!

Prof. A.N. Antonov obtained the degree of Doctor of Science with a study on «Nucleon-Nucleon Correlations and Characteristics of Nuclear Structure and Nuclear Reactions ». He is 'the' expert of nucleon-nucleon correlations (short-range, tensor, long-range) that play a very important role in the structure of nuclei and in the dynamics of nuclear reactions. Their importance is periodically 'rediscovered'. He developed (with I. Zh Petkov and V. A. Nikolaev) the Coherent Density Fluctuation Model (CDFM), based on the delta-function approximation to the Generator Coordinate Method. The ansatz is that the One-Body Density Matrix (OBDM) of a finite nucleus can be expressed as an infinite superposition of OBDM's of homogeneous pieces of nuclear matter, called «fluctons», of any size. The probability of each flucton is related to the density distribution of the nucleus. This model has been used in several applications, such as the calculation of the spectral function and of the density distribution of nuclei, including exotic and halo nuclei, the calculation of the form factors of light nuclei, the description of proton- and neutron-nucleus scattering and, more recently, of electron- and (anti)neutrino-nucleus scattering, explaining the evidence for superscaling.

Prof. Antonov established a longstanding collaboration with P.E. Hodgson. With him and I.Zh. Petkov he wrote two monographs, well- known by the students and researchers in the field: "Nucleon Momentum and Density Distribution in Nuclei" (Clarendon Press, Oxford, 1988) and "Nucleon Correlations in Nuclei" (Spinger-Verlag, Berlin-Heidelberg-New York, I993).

Prof. Antonov did most of his career as Professor at the Laboratory of Theoretical Nuclear Physics, INRNE, BAS, Sofia, and at the University of Shumen "Bishop Konstantin Preslavski". Teaching to

generations of students and supervising PhD students (who are, in their turn, well-known physicists), he is extremely appreciated in his academic, scientific, and pedagogical activity. He is the leader of his successful theory group in Sofia. Thanks to his deep knowledge of Western and Eastern civilizations, he initiated and maintained collaborations with selected worldwide laboratories, from Russia to Spain, including France and Italy, Greece and Romania, as well as USA. Moreover, he leads an 'international network' keeping ties among his collaborators from England, Spain, France, Italy, Japan, Kazakhstan, Dubna... thanks also to the Rila Workshop, that takes place every year in the enchanting scenery of the Rila mountains and where scientists from all over the world can gather together, discuss, carry out their collaborations, or establish new collaborations in a warm and friendly atmosphere.

Prof. Antonov combines a rigorous and exigent attitude at work together with a kind and human approach. Beyond physics, he has a passion for arts and history (transmitted to him by his mother, who was a famous archeologist, renowned for her important archeological discoveries, particularly in Shumen) as well as for music, playing himself violin, and transmitting his passion to Todor, his son, now a well-known violinist. The participants to this conference had the great opportunity to listen to him playing part of 'SONATA FOR SOLO VIOLINO OF BACH'.

This unique background is probably the key for his scientific and pedagogical achievements and for his successful career.

Dear Anton, it is a great pleasure to share with you this event, this Conference in your honor, where we have the chance to express our deep respect and gratitude for your contribution and dedication to Science!

BIOGRAPHY OF PAVEL OBLOZINSKY

Pavel Oblozinsky was born on the 16th of December 1943 in Bratislava, Slovakia. He studied nuclear physics at the Czech Technical University in Prague from 1961 to 1964 and then at the Moscow State University in 1965-1966. He obtained the Master of Science in nuclear physics from the Czech Technical University in 1967, graduating with red diploma (summa cum laude), and he received his PhD in 1973 from the Slovak Academy of Sciences.

There he spent twenty years, until 1993, as nuclear physicist, covering the role of Head of the Nuclear Physics Department from 1973 to 1980. His research activity spanned nuclear reaction mechanisms at low incident energies, neutron-induced reactions, reactions with 14 MeV neutrons, and the theory of preequilibrium decay. In fact, Pavel Oblozinsky is worldwide known for his numerous contributions to the exciton preequilibrium model of nuclear reactions.

In 1994 he integrated the Nuclear Data Section of the International Atomic Energy Agency (IAEA) in Vienna, where he became Deputy Section Head and coordinated several international research projects in nuclear reaction data. In particular, he developed the internationally recognized Reference Input Parameter Library for nuclear reaction calculations by nuclear model codes.

In 2000 he moved to the Brookhaven National Laboratory (BNL) in the US and joined the National Nuclear Data Center (NNDC), he led from 2002 to 2009. He chaired from 2001 to 2009 the Cross Section Evaluation Working Group and the US Nuclear Data Program. He supervised the release of the major upgrade of the US nuclear data evaluated library ENDF/B-VII.0 in 2006. He has been editor of Special Issues of the Nuclear Data Sheets since 2006 and he worked on the evaluation of neutron cross sections for fission products and neutron cross section covariances.

He got the Silver Medal for scientific achievements from the Slovak Academy of Sciences in 1993, the Merit Award for outstanding performance from the IAEA in 1998, and the Appreciation Award for outstanding leadership of the NNDC from the Department of Energy in 2009.

In March 2011 he retired from BNL and moved to Bratislava. Married to Ludmila since 1973, he has two sons and two grandsons.

LAUDATION OF PAVEL OBLOZINSKY

by Syed M. Qaim

at the 15th International Conference
on Nuclear Reaction Mechanisms
Varenna (Lake Como), Italy, 13 June 2018

Dear Pavel Oblozinsky,

You are being honoured by this international group of distinguished nuclear physicists, both experimentalists and theoreticians. Michal Herman will later highlight your scientific contributions and achievements. I am not a theoretician. I am an experimental nuclear chemist and more a technologist. Yet there are a few paths on which we have gone together for some parts of our lives, and a few common things bind us together. Among them are human relationship and international approach to science. So it is a great pleasure for me to say a few laudatory words on this auspicious occasion.

Dear Pavel,

We first met in May 1975 in Bratislava, i. e. exactly 43 years ago. You had just become the Head of the Nuclear Physics Department of the Institute of Research of the Slovakian Academy of Sciences in Bratislava, where studies with 14 MeV neutrons were going on. I was doing radiochemical work in that field at that time and had been invited for a talk on "Radiochemical Methods in the Determination of Nuclear Data for Fusion Reactor Technology" at a conference of the Czechoslovakian Chemical Society in Marianske Lázne. On my way from there to the Nuclear Data Section (NDS) of the IAEA in Vienna I visited your Institute. I exactly remember the words with which you introduced me: "We are grateful to Dr. Qaim for spending time and money to visit us in Bratislava." Those simple words really touched me, because they showed personal respect and depicted the reality of life in Eastern Europe at that time. From then onwards started our deeper contacts and mutual understanding. We met at several conferences, you visited Jülich and I visited Bratislava again. I realized more and more how difficult the circumstances were for you to be a free-thinking man, not following the exact party line. Anyway, you withstood the tide of time and, after the fall of the iron curtain, you could develop your independent thoughts. It is this steadfastness combined with your humility and human relationship which impressed me most.

A second phase of our cooperation and collaboration started in the 1990s when you joined the Nuclear Data Section of the IAEA. I was nominated by the German Government as a Member of the International Nuclear Data Committee (INDC), and we together could start work on "Nuclear Data for Medical Applications." It was a pioneering attempt because no other Data Centre was doing or willing to do this type of work. I was especially disappointed with the OECD-NEA and the Data Bank in Paris because of their lack of interest in this type of work. I had served as the Chairman of the NEA-NDC for several years and in 1995 had become a Vice-Chairman of the newly created Nuclear Science Committee. Yet I could not arouse the interest of NEA. The only thing it did was to install a "High Level Group on the Security of Supply of Medical Isotopes". Further activities were not possible due to the limited mandate of NEA to do only energy-related work.

I am happy today and grateful to you that you, as Head of the NDS of the IAEA, put all my thoughts and ideas into practice. By the time you left for USA, the first CRP on this topic was completed. Later came Roberto Capote Noy to the IAEA, and from 2004 onwards, he worked for the second CRP and brought it to a successful completion. It is satisfying to me that this activity, started by us together, has now become an integral part of the work of Nuclear Data Section of the IAEA.

Our third phase of cooperation started after 2002. You had emigrated to USA and were nominated as a US Member to the INDC, of which I had then become the Chairman. We worked closely on several aspects of internationalisation of science. Furthermore, based on a particular desire from USA, work on decay data was also initiated, thanks to the great competence and personal interest of Alan Nichols, the new Head of NDS. The work on data for ion-beam analysis was also started. Consideration was also given to data for applications in Astrophysics. Werner Burkart, the Deputy director General of the IAEA, supported us in those non-energy related activities. It is pleasing to me to see that the NDS of IAEA is now devoting considerable effort to non-energy related applications of nuclear data.

Today Pavel, as a retired scientist, you can look back at your achievements with great satisfaction. It has been a hard life for you but certainly full of rewards. You have been not only a successful theoretician but also a strong supporter of international science. I have always admired your civility, friendliness and soft-spoken character, yet having a courageous and dauntless approach to life. You are now getting a well-deserved award. My heartfelt felicitations to you on this great occasion, combined with the best wishes for you, your wife and other family members for the future.

CHAIRMEN OF THE CONFERENCE

A. Ferrari	CERN	**T. Kawano**	LANL

SCIENTIFIC SECRETARIES

F. Cerutti	CERN	**P. Talou**	LANL

ORGANIZING COMMITTEE

G. Battistoni	Milano	**A. Mairani**	Pavia & Heidelberg
F. Camera	Milano	**F. Salvat-Pujol**	CERN
F. Cerutti	CERN	**P. Talou**	LANL
M. B. Chadwick	LANL	**E. Tomasi**	Saclay
A. Ferrari	CERN	**A. Tsinganis**	CERN
T. Kawano	LANL		

INTERNATIONAL ADVISORY COMMITTEE

F. Ballarini	Pavia	**S. Goriely**	Brussels
E. Bauge	Bruyères-le-Châtel	**A. Guglielmetti**	Milano
A. Bonaccorso	Pisa	**M. Herman**	BNL
T. Borello Lewin	São Paulo	**H. Horiuchi**	Osaka
B. A. Brown	MSU East Lansing	**A. Koning**	IAEA
Z. Buthelezi	iThemba Labs	**S. Leray**	Saclay
L. Canton	Padova	**T. Motobayashi**	RIKEN
R. Capote	IAEA	**F. M. Nunes**	MSU
F. Cappuzzello	LNS Catania	**K. Parodi**	Munich
S. Chiba	Tokyo Inst. Tech.	**L. Pinsky**	Houston
N. Colonna	Bari	**A. Plompen**	Geel
L. Corradi	Legnaro	**L. Sajo Bohus**	Caracas
J. Escher	Livermore	**L. Sihver**	Vienna
S. Förtsch	iThemba Labs	**K. Tanaka**	KEK
E. Gadioli	Milano	**H. Toki**	Osaka

SECRETARY OFFICE

G. Aricò	CERN	**F. Meneghini**	Milano
D. Pifferetti	Milano		

ACKNOWLEDGEMENTS

This conference was supported by:

- Los Alamos National Laboratory, USA
- CERN, European Organization for Nuclear Research, Switzerland
- University of Milan, Italy
- DRF, IRFU, CEA, Saclay, France
- “Piero Caldirola” International Centre for the Promotion of Science, Italy

The organizing committee of the conference wishes to express its deepest appreciation and thanks to all these institutions.

15th International Conference on Nuclear Reaction Mechanisms

Varenna, June 11-15, 2018

Monday morning

8.50-11 [Chairperson**: H. Lenske]** ***Nuclear structure***

(10')

	OPENING

(25'+5')

A. Brown	Microscopic calculations of nuclear level densities with the Lanczos method
R. Broglia	Inverse kinematics and reaction mechanism at the drip line: probing virtual states and the nuclear vacuum
Y. Alhassid	The deformation dependence of level densities in the configuration-interaction shell model
G. Potel Aguilar	Probing nuclear structure with neutron transfer reactions

COFFEE BREAK

11.30-12.30 [Chairperson**: J.M. Quesada Molina]** ***Nuclear structure/reactions***

(15'+5')

G. Royer	Geometric shapes describing nuclear reaction mechanisms such as fusion, alpha emission and capture, binary and ternary fission, planar fragmentation and n-alpha nuclei
B. Tatischeff	Oscillation symmetry applied to: 1) hadronic and nuclei masses and widths, and used to suggest unknown spins, 2) astrophysics
J. Lopez	Symmetry energy in the liquid–gas mixture

Monday afternoon

15-17 [Chairperson**: P. Talou]** ***Fission***

(25'+5')

N. Schunck	Microscopic Description of Nuclear Fission: Progress and Perspectives
W. Younes	A basis for scission dynamics

(15'+5')

S. Okumura	Hauser-Feshbach Statistical Decay and Beta Decay Calculation for Primary Fission Fragments
C.-Y. Wu	Dependence of the prompt fission gamma-ray spectrum on the entrance channel of compound nucleus: spontaneous vs neutron-induced fission
P. Jaffke	Correlations between the fission fragment yields and the prompt fission gamma-ray spectrum

TEA BREAK

17.30-19 [Chairperson**: A. Andreyev]** ***Fission***

(25'+5')

Y. Iwata	Systematic TDDFT data for nuclear fission analysis

(15'+5')

I. Stetcu	Real-time description of fission
M. Verriere	First comparison between microscopic and macroscopic-microscopic potential energy surfaces for the description of fission
M. D. Usang	Effects of the temperature on nuclear deformation energy and the predictions of fission observables calculated within the Langevin approach

Tuesday morning

9-11 [Chairperson**: N. Schunck]** ***Fission***

(25'+5')

A. Tonchev	An Unexpected Energy Evolution of the Fission-Product Yields from Neutron-Induced Fission of 235U, 238U, and 239Pu
P. Talou	Correlated Prompt Fission Data in Transport Simulations

(15'+5')

M. Rapala	Gamma-ray cascade study in abundant fission fragments with the EXILL experiment and FIFRELIN simulation
L. Liu	Phenomenological study of fission yield for U233 induced by neutrons below 20 MeV
I. Tsekhanovich	Fission properties of nuclei in the 180Hg region

COFFEE BREAK

11.30-12.40 [Chairperson**: Y. Watanabe]** ***Fission***

(25'+5')

A. Andreyev	Fission studies using multi-nucleon transfer reactions at the JAEA tandem

(15'+5')

Y. Chen	Isoscaling study of binary fission yields
T. Yoshida	Aggregate Decay Behavior of Fission Products in Nuclear Reactors - Decay Heat, Reactor Antineutrino and the Pandemonium Problem -

Tuesday afternoon

14.45-16.45 [Chairperson**: R. Capote]** ***Nuclear reactions***

(25'+5')

H. Lenske	Probing Nuclear Beta-Decay by Heavy Ion Charge Exchange Reactions
M. Dupuis	Advances in microscopic modeling of (n,xn gamma) reactions for actinides

(15'+5')

M. Colonna	Heavy Ion charge exchange reactions and the link with beta decay processes
T. Borello-Lewin	Coulomb-nuclear interference and isospin characterization of the first 2+ and 3- transitions by inelastic scattering of alpha particles on 90,92Zr
A. Nasri	Towards a non-local microscopic description of scattering observables of nucleons on deformed nuclei

TEA BREAK

17.15-18.45 [Chairperson**: L. Pinsky]** ***Facilities***

(25'+5')

S. Foertsch	Novel Results from ALICE
K. Tanaka	Major accelerator facilities for nuclear physics in Asia Pacific
M. Pravikoff	Neutrinos, wine and fraudulent business practices

Tuesday evening

20.15 **Ettore Gadioli wine party** ***Villa Cipressi***

Wednesday morning

9-11 [Chairperson**: L. Canton]** ***Medical radioisotopes***
(25'+5')

S. Brandenburg	Future production of medical radioisotopes
S.M. Qaim	Nuclear data for production of novel medical radionuclides
Y. Nagai	Diagnostic 99Mo/99mTc and Therapeutic 67Cu Radioisotopes Produced by Neutrons from C,Be(d,n)
G. Pupillo	Cyclotron-based production of the theranostic radionuclides 67Cu and 47Sc

COFFEE BREAK

11.30-13.10 [Chairperson**: A. Plompen]** ***Medical radioisotopes***
(15'+5')

A. Fontana	Challenges in the modeling of nuclear reactions for theranostic applications
R. Capote	Nuclear data for the production of medical radionuclides
A. Guertin	Production of innovative radionuclides for therapy or diagnostic: nuclear data measurements and comparisons with the TALYS code
M. Sitarz	Production of medically interesting 97Ru via natMo(alpha,x) above 40 MeV at ARRONAX
all	General discussion

Wednesday evening

Session in honor of Anton Antonov and Pavel Oblozinsky

20.30 RECEPTION

21-23 [Chairperson**: C.H. Dasso]**

(15')

E. Tomasi

(30')

A. Antonov

(15')

T. Antonov Violin play

S.M. Qaim

M. Herman

(30')

P. Oblozinsky

Thursday morning

9-11 [Chairperson**: L. Sihver]** ***Hadrontherapy***

(25'+5')

J.I. Porras Sanchez	Perspectives in Neutron Capture Therapy of Cancer
M.P. Carante	A radiobiological database produced by the BIANCA model to predict the biological effectiveness of hadrontherapy beams

(15'+5')

A. Embriaco	MONET code: evaluation of the dose in Hadrontherapy
G. Aricò	Development of the nuclear reaction and fragmentation models for heavy ion collisions in the therapeutic energy range
M. Marafini	The FOOT (FragmentatiOn Of Target) experiment

COFFEE BREAK

11.30-12.50 [Chairperson**: T. Yoshida]** ***Radioactive waste, neutrino***

(15'+5')

H. Wang	Nuclear reaction study for high-level radioactive waste: Cross section measurements for proton- and deuteron-induced spallation reactions of long-lived fission products
R. Kimura	The demand for TRU nuclide cross-sections from the view point of TRU production and radiotoxicity
M. Ivanov	Charged-current quasielastic (anti)neutrino cross sections on 12C with realistic spectral functions including meson-exchange contributions
D. Torresi	Double charge exchange reactions for neutrino physics: recent results and future perspectives

Thursday afternoon

15-16.40 [Chairperson**: F. Cerutti]** ***Facilities***

(25'+5')

G. Tagliente	Recent results of n_TOF facility at CERN
F. Cavanna	Nuclear astrophysics at Gran Sasso Laboratory: the LUNA400 experiment

(15'+5')

M. Barbagallo	(n,cp) reactions study at the n_TOF facility at CERN: results for the Cosmological Lithium problem
D. Piatti	The Study of the 22Ne(alpha,gamma)26Mg at LUNA

TEA BREAK

17.15-18.45 [Chairperson**: J. Escher]** ***Potential, strangeness, pion***

(25'+5')

C. Giusti	Microscopic Optical Potential Derived from NN Chiral Potentials
J. Hirtz	Production of strange particles and hypernuclei in spallation reactions from the coupling of intranuclear cascade and de-excitation models
C. Hartnack	Isospin of pions - what do they tell us about the neutron skin of nuclei?

Friday morning

9-11 [Chairperson**: A. Ferrari]** ***Deuteron induced reactions***

(25'+5')

M. Avrigeanu	Comparative analysis of empirical parametrizations and microscopical studies of deuteron-induced reactions
F. Salvat Pujol	Towards inclusion of low-energy deuteron interactions with target nuclei in FLUKA

(15'+5')

E. Nigron	Production cross section of 197mHg induced by deuterons on natural gold target
Y. Watanabe	Isotopic production cross sections of residual nuclei in proton- and deuteron-induced reactions on 91,92Y, 92,93Zr, and 93,94Nb around 100 MeV/nucleon
X. Sun	Cross-section measurements in the reactions of 136Xe on proton, deuteron and carbon at 168 AMeV

COFFEE BREAK

11.30-13 [Chairperson**: M. Dupuis]** ***Nuclear reactions***

(25'+5')

H. Weidenmueller	Statistical-model description of gamma decay from compound-nucleus resonances

(15'+5')

E. Chimanski	Statistical multi-step direct reaction models and the RPA
B. Carlson	The role of nucleon knockout in pre-equilibrium reactions
S. Dimitrova	Proton induced pre-equilibrium reactions to the continuum as a test to the reaction mechanism

Friday afternoon

15-17.10 [Chairperson**: T. Kawano]** ***Nuclear reactions***

(25'+5')

J. Escher	Capture Cross Sections for Unstable Isotopes from Surrogate Reaction Data and Theory

(15'+5')

C. Oprea	Neutron Capture Cross Sections and Strength Functions on 147Sm Nucleus
P. Fanto	Neutron width statistics in a realistic resonance-reaction model
A. Georgiadou	Transfer reactions induced with 56Ni: np pairing and N=28 shell closure
F. Galtarossa	Multinucleon transfer processes in the 197Au+130Te system studied with a high-resolution kinematic coincidence
W. Richter	Shell-model studies of the astrophysical mirror rp-reactions 34S(p,gamma)35Cl and 34g,mCl(p,gamma)35Ar

TEA BREAK

LIST OF PARTICIPANTS

Yoram Alhassid
Yale University, United States

Andrei Andreyev
University of York, United Kingdom

Anton Antonov
Institute of Nuclear Research and Nuclear Energy of the Bulgarian Academy of Sciences, Bulgaria

Giulia Aricò
CERN, Switzerland

Marilena Avrigeanu
Horia Hulubei National Institute for Physics and Nuclear Engineering (IFIN-HH), Romania

Massimo Barbagallo
Università degli studi di Bari and INFN Bari, Italy

Thereza Borello-Lewin
Universidade de São Paulo, Brazil

Sytze Brandenburg
University of Groningen, Netherlands

Ricardo Broglia
University of Milan, Italy

Alex Brown
Michigan State University, United States

Simone Calzaferri
Università degli studi di Pavia and INFN Pavia, Italy

Luciano Canton
INFN - National Institute for Nuclear Physics, Italy

Roberto Capote Noy
IAEA, Austria

Mario Pietro Carante
INFN - National Institute for Nuclear Physics, Italy

Brett Carlson
Instituto Tecnológico de Aeronáutica, Brazil

Francesca Cavanna
INFN Genova, Italy

Francesco Cerutti
CERN, Switzerland

Yongjing Chen
China Institute of Atomic Energy, China

Emanuel Vicente Chimanski
Instituto Tecnológico de Aeronáutica, NAPC-Nuclear Data Section, Brazil

Maria Colonna
INFN - Laboratori Nazionali del Sud, Italy

Carlos H. Dasso
University of Seville, Spain

Sevdalina Dimitrova
Bulgarian Academy of Sciences, Bulgaria

Marc Dupuis
CEA, DAM, France

Alessia Embriaco
INFN - National Institute for Nuclear Physics, Italy

Jutta Escher
Lawrence Livermore National Laboratory, United States

Paul Fanto
Yale University, United States

Alfredo Ferrari
CERN, Switzerland

Siegfried Foertsch
iThemba LABS, National Research Foundation, South Africa

Andrea Fontana
Università degli studi di Pavia and INFN Pavia, Italy

Franco Galtarossa
INFN, Legnaro, Italy

Anastasia Georgiadou
Institut de Physique Nucléaire d'Orsay (IPN), France

Carlotta Giusti
Università degli Studi di Pavia and INFN Pavia, Italy

Arnaud Guertin
CNRS/IN2P3, France

Christoph Hartnack
IMT Atlantique, France

Mike Herman
Brookhaven National Laboratory, United States

Jason Hirtz
CEA - Saclay, France

Martin Ivanov
Institute for Nuclear Research and Nuclear Energy, Bulgarian Academy of Sciences, Bulgaria

Yoritaka Iwata
Tokyo Institute of Technology, Japan

Patrick Jaffke
Los Alamos National Laboratory, United States

Toshihiko Kawano
Los Alamos National Laboratory, United States

Rei Kimura
Toshiba Energy Systems & Solutions, Japan

Horst Lenske
Universität Giessen, Germany

Lile Liu
China Institute of Atomic Energy, China

Alex Long
Los Alamos National Laboratory, United States

Jorge Lopez
University of Texas at El Paso, United States

Michela Marafini
INFN Roma1 - Centro Fermi, Italy

Tohru Motobayashi
RIKEN Nishina Center, Japan

Liliana Mou
INFN - National Institute for Nuclear Physics, Italy

Matthew Mumpower
Los Alamos National Laboratory, United States

Yasuki Nagai
National Institute for Quantum & Radiological Science & Tecnology, Japan

Amine Nasri
Commissariat à l'Energie Atomique, France

Etienne Nigron
CNRS IN2P3 - Laboratoire Subatech, France

Pavel Oblozinsky
Slovakia

Shin Okumura
Tokyo Institute of Technology, Japan

Cristiana Oprea
JINR, Romania

Denise Piatti
Università degli Studi di Padova, Italy

Lawrence Pinsky
University of Houston (US), United States

Arjan Plompen
European Commission, Joint Research Centre, Belgium

Jose Ignacio Porras Sanchez
Universidad de Granada, Spain

Gregory Potel Aguilar
Michigan State University FRIB/NSCL, United States

Michael Pravikoff
CNRS/IN2P3, France

Gaia Pupillo
INFN - National Institute for Nuclear Physics, Italy

Syed M. Qaim
Forschungszentrum Jülich, Germany

Jose Manuel Quesada Molina
Universidad de Sevilla, Spain

Michal Rapala
CEA Saclay, France

Werner Richter
University of Stellenbosch, South Africa

Guy Royer
IN2P3/CNRS, France

Francesc Salvat Pujol
CERN, Switzerland

Nicolas Schunck
Lawrence Livermore National Laboratory, United States

Lembit Sihver
Technische Universität Wien, Austria

Mateusz Sitarz
GIP ARRONAX, France

Ionel Stetcu
Los Alamos National Laboratory, United States

Xiaohui Sun
RIKEN Nishina Center, Japan

Giuseppe Tagliente
Università degli studi di Bari and INFN Bari, Italy

Patrick Talou
Los Alamos National Laboratory, United States

Kazuhiro Tanaka
KEK, High Energy Accelerator Research Organization, Japan

Boris Tatischeff
CNRS IN2P3, France

Egle Tomasi
CEA saclay, France

Anton Tonchev
LLNL, United States

Domenico Torresi
INFN - LNS, Catania, Italy

Igor Tsekhanovich
CENBG/Bordeaux University, France

Andrea Tsinganis
CERN, Switzerland

Mark Dennis Usang
Tokyo Institute of Technology; Malaysia Nuclear Agency, Japan

Marc Verriere
Los Alamos National Laboratory, United States

He Wang
RIKEN Nishina Center, Japan

Yukinobu Watanabe
Kyushu University, Japan

Hans Weidenmueller
Max-Planck-Institut fur Kernphysik, Germany

Ching-Yen Wu
Lawrence Livermore Nat. Laboratory (US), United States

Tadashi Yoshida
Tokyo Institute of Technology, Japan

Walid Younes
Lawrence Livermore National Laboratory, United States

Table of Contents

One– and two– neutron halo at the dripline. From ^{11}Be to ^{11}Li and back: ^{10}Li and parity inversion.

R. A. Broglia[1,2], F. Barranco[3], G. Potel[4], and E. Vigezzi[5]

[1]Dipartimento di Fisica, Università degli Studi di Milano, Via Celoria 16, I-20133 Milano, Italy
[2]The Niels Bohr Institute, University of Copenhagen, DK-2100 Copenhagen, Denmark
[3]Departamento de Fìsica Aplicada III, Escuela Superior de Ingenieros, Universidad de Sevilla, Camino de los Descubrimientos, Sevilla, Spain
[4]National Superconducting Cyclotron Laboratory, Michigan State University, East Lansing, Michigan 48824, USA
[5]INFN Sezione di Milano, Italy

Abstract
The nuclei ^{11}Be and ^{11}Li provide paradigmatic examples of one–and two–neutron halo systems. Because the reaction ^{1}H(^{11}Li,^{9}Li)^{3}H is dominated by successive transfer, one can use the quantitative picture emerging from a nuclear field theory description of the structure and reaction mechanism of the above Cooper pair transfer process and of the ^{2}H(^{10}Be,^{11}Be)^{1}H and ^{1}H(^{11}Be, ^{10}Be)^{2}H reactions, to shed light on the structure of ^{10}Li. This analysis provides important support for a parity inverted scenario with a $1/2^+$ virtual state at about 0.2 MeV.

1 Introduction

Potential energy thrives on relative fixed positions of particles, fluctuations on delocalization. A quantitative measure of these two contrasting effects is provided in many–body systems, by the quantality parameter $q = \frac{\hbar^2}{ma^2}\frac{1}{|v_0|}$, where a and v_0 are the interaction range and strength, respectively. In the nuclear case $q \approx 0.5$ ($a = 0.9$ fm, $v_0 = -100$ MeV), testifying to a quantal–fluctuation–dominated regime and thus delocalization[1] which can be described at profit in terms of a mean field, shells, and magic numbers.

2 Neutron drip lines

If neutrons are progressively added to a light normal nucleus, Pauli principle forces the system, when the core becomes neutron saturated, to expel most of the wavefunction of the last neutrons outside to form a halo which, because of its large size, can have lower momentum. It is an open question how nature stabilizes such fragile objects and provides the glue to bind the halo neutrons to the core. Within this context, the fact that $^{9}_{3}$Li$_6$, $^{10}_{3}$Li$_7$, $^{11}_{3}$Li$_8$ are bound (closed shell (cs) in neutrons), unbound (one–neutron outside cs), barely bound (Cooper pair outside cs) nuclei respectively, provides evidence of a pairing mechanism resulting in a Cooper pair halo.

2.1 One-neutron halo

To elaborate on this issue, use is made of the bound ($T_{1/2} = 13.76$ s) one–neutron halo nucleus outside the $N = 6$ closed shell, ^{11}Be. To create a halo system one has to have an $s_{1/2}$–level (no centrifugal barrier) at threshold. But then, why not retain $N = 8$ as a magic number and eventually ^{13}Be as

[1]It is of notice that in the above reasoning no reference to the Pauli principle was made. The fact that $q \ll 1$ implies fixed positions while $q \approx 1$ delocalization, is essentially independent of the statistics obeyed by the particles.

one–neutron halo? Because one has to bring the $s_{1/2}$ down in energy to become weakly bound. And to do so one has essentially one possibility. To dress the bare $2s_{1/2}$ state ($\epsilon_{s_{1/2}} \approx 0.07$ MeV) with the quadrupole vibration of the core, a process which binds the dressed level by about 0.5 MeV. But equally inescapable is the weakening of the binding energy of the $p_{1/2}$ orbital ($\epsilon_{p_{1/2}} \approx -3.04$ MeV) to an essentially threshold situation ($\tilde{\epsilon}_{p_{1/2}} \approx -0.18$ MeV). This is a result of the fact that the amplitude of the main neutron component of the quadrupole vibration namely the $(p_{1/2}, p^{-1}_{3/2})_{2^+}$ is close to one. Pauli principle between the odd $p_{1/2}$ neutron and the same particle involved in the collective mode leads to almost 3 MeV repulsion (+2.86 MeV). In other words, to make the $2s$–state barely bound so as to produce a one–neutron halo, one is forced at the same time to weaken conspicuously the binding of the $p_{1/2}$ state [1]. While parity inversion is not a condition, what is inescapable is the melting away of the $N = 8$ magic number and the appearance of the $N = 6$ closed shell. Also of an $E1$–transition between the parity inverted levels carrying essentially one B_W (Weisskopf unit) (see App. B). A consequence of the very poor overlap existing between halo neutron and core nucleons which impedes the GDR to depopulate the low–energy $1/2^+ \rightarrow 1/2^-$ transition, being forced to leave about 10% of the TRK sum rule anchored to this low–lying $E1$–transition.

2.2 Two–neutron halo

While it will be natural, within the above scenario, to deal with the unbound system ^{10}Li, it is likely more useful to start with the bound ($T_{1/2} = 8.5$ ms) two–neutron halo nucleus ^{11}Li [2]. Simple estimates of such neutron halo Cooper pair can be made by assuming that the calculation scheme used in ^{11}Be [1], and based on the values of β_2, $\hbar\omega_2$ (core), $|E_{corr}| \approx S_{1n}$ and 10% TRK, is transferable to ^{11}Li and eventually through it, to the virtual system ^{10}Li (see Section A.3, App. A below). The physics at the basis of this ansatz is quite general and operative: a) poor overlap between halo neutrons and core nucleons (thus low–energy presence of a substantial fraction of the TRK sum rule); b) Lamb shift–like phenomena involving $2s_{1/2}$ and $1p_{1/2}$ orbitals, in particular Pauli principle between this last state and the same state found in the collective quadrupole vibration of the core; c) soft $E1$–mode and related induced pairing.

It could be argued that, in a similar way in which the quadrupole mode renormalize in a very conspicuous way the single–particle orbitals $2s_{1/2}$ and $1p_{1/2}$, it can induce pairing correlations in the $|s^2_{1/2}(0)\rangle$ $|p^2_{1/2}(0)\rangle$ configurations. However, the surface of ^{11}Li being a misty cloud formed by the halo neutrons, can hardly sustain multipole vibrations any better than the surface of hot nuclei does. Consequently, the only collective mode such a surface can participate in is a dipole mode, in which the negatively charged ($-Z/A\, e \approx -0.27\, e$) neutrons slosh back and forth with respect to the positively charged ($N/A\, e \approx 0.73\, e$) protons of the core. Namely, a soft dipole resonance [3] which we also refer to as dipole pygmy resonance (DPR).

In the QRPA calculation of the DPR in ^{11}Li, the single particle basis associated with ^{10}Li is worked out making use of a standard parametrized Saxon–Wood potential. The continuum states of this potential are calculated by solving the problem in a spherical box of radius equal to 40 fm, chosen to make the results associated to ^{10}Li and ^{11}Li stable. The states at threshold, in particular the parity inverted $s_{1/2}$ and $p_{1/2}$ levels are the renormalized states, and the amplitudes of the ^{11}Li ground state wavefunction are used as the U, V occupation factors. A separable dipole–dipole interaction ($H_D = -\kappa_1^0 \mathbf{D} \cdot \mathbf{D}$) is used with strength $\kappa_1^0 \approx -5V_1/A(R(^{11}\mathrm{Li}))^2$, close to the self–consistent value. Within this scenario one calculates self consistently the full $J^\pi = 1^-$ spectrum, including the GDR and DPR, fine tuning κ_1^0 so as to ensure a root at zero energy, which takes care of the elimination of the center of mass motion. The QRPA solutions fulfill the EWSR, the DPR carrying about 10% of it [2].

If the virtual $\widetilde{1/2^+}$ state of ^{10}Li were not at ≈ 0.15 MeV, but considerably higher in energy [4], ^{11}Li would not display the observed properties. But even more, neither the first excited 0^{+*} state of ^{12}Be ($E_x \approx 2.25$ MeV), neither the 2.71 MeV, 1^- state on top of it will. In fact, these states can be viewed as generated by the new neutron halo pair addition elementary mode of excitation, made out

of the symbiotic ($|\tilde{0}\rangle_\nu$, DPR) states of ^{11}Li, acting on $|^{10}\mathrm{Be}(gs)\rangle$. As it emerges from the Figure A5 of [5], such a level scheme is associated with the experimental quantities: $S_{2n}(^{11}\mathrm{Li}) = 396.6$ keV, $S_{2n}(^{12}\mathrm{Be}) = 3.672$ MeV, $S_{2n}(^{12}\mathrm{Be}) - E_x 0^{+*} = 1.422$ MeV, the 2.71 MeV state being likely only part of the dipole state based on $|^{12}\mathrm{Be}(0^{+*})\rangle$.

While one has dwelled only on the structure aspects of the one–and two–halo nuclei ^{11}Be, ^{10}Li, ^{11}Li and ^{12}Be, the associated one– and two–neutron transfer absolute differential cross sections can also be accurately described within the scenario discussed above, renormalization of single–particle wave-functions and associated formfactors, playing an important role in the quantitative description of the transfer processes [1, 5–7].

3 Conclusions

The picture of an $s_{1/2}$ state at threshold to create halo nuclei, involves parity inversion, a sizable fraction of the TRK sum rule in low energy $E1$ transitions and absolute value of one– and two– particle transfer cross sections of the same order of magnitude, in overall agreement with the experimental findings. At the basis of it one finds the renormalization of single particle motion due to the coupling of the quadrupole vibration of the core, and the pairing induced interaction due to the exchange of the soft $E1$–mode. The soundness of the theory does not stems from a single result, but from the comprehensive picture emerging from the variety of them, in comparison with the data. A single one of these features found incorrect, will set a question mark on the entire approach.

After the above physical arguments and associated estimates collected in the Appendices below had been written down and worked out, one got hold of the technical detail which likely explains the reason why the data of Cavallaro *et al.* [4] essentially do not contain any $s_{1/2}$ strength: the angular range in which measurements were carried out [8].

F. B. acknowledges funding from the Spanish Ministerio de Economía under Grant Agreement No. FIS2017-88410-P. This project has received funding from the European Union's Horizon 2020 research and innovation program under grant agreement No 654002.

Appendices

A

In this Appendix, analytic estimates of structure and reaction properties of the halo nuclei mentioned in the text are provided.

A.1 $^{11}_{4}\mathrm{Be}_7$, bound one–neutron halo system

In the calculation of the structure of ^{11}Be, four parameters defining the bare single–particle potential U –depth V, radius R, diffusivity a, and spin–orbit strength V_{ls}– were allowed to vary freely so that the single–particle states dressed through the coupling to the quadrupole vibration of the core ^{10}Be, best fitted the data[2] (ref. [1]). The bare single–particle energies $\epsilon_i (i = s_{1/2}, p_{1/2}, d_{5/2})$ are collected in Table A.1. Making use of the experimental values of $\hbar\omega_2$ and β_2 (energy and dynamical quadrupole deformation) of $|^{10}\mathrm{Be}(2^+_1)\rangle$, and the formfactor $R\partial U/\partial r$, the particle–vibration coupling vertices were calculated, and the single–particle states renormalized. The values of the self energies at convergence are shown in Fig. A.1, leading to dressed state energies,

$$\tilde{\epsilon}_{s_{1/2}} = (70 - 570)\ \mathrm{keV} = -0.5\ \mathrm{MeV}, \tag{A.1}$$

$$\tilde{\epsilon}_{p_{1/2}} = (-3.04 + 2.86)\ \mathrm{MeV} = -0.180\ \mathrm{MeV}, \tag{A.2}$$

$$\tilde{\epsilon}_{d_{1/2}} = (7.30 - 1.77 - 4.08)\ \mathrm{MeV} = 1.45\ \mathrm{MeV}. \tag{A.3}$$

[2]It is of notice that the resulting potential to be used with a k mass ($m_k = 0.7m$ (0.9) for $r = 0$ ($r = \infty$)), is quite similar to that obtained from SLy4 in the Hartree–Fock approximation.

As seen from Table A.1, theory provides an accurate account of the experimental findings. Furthermore, making use of the associated configuration space states

$$|\widetilde{1/2}^{+}\rangle = \sqrt{0.80}\,|s_{1/2}\rangle + \sqrt{0.20}\,|(d_{1/2}\otimes 2^{+})_{2^{+}}\rangle, \tag{A.4}$$

and

$$|\widetilde{1/2}^{-}\rangle = \sqrt{0.84}\,|p_{1/2}\rangle + \sqrt{0.16}\,|((p_{1/2},p_{3/2}^{-1})_{2^{+}}\otimes 2^{+})_{0^{+}},p_{1/2}\rangle, \tag{A.5}$$

one obtains, without free parameters

$$B(E1;1/2^{-}\rightarrow 1/2^{+}) = 0.11\,e^{2}\ \text{fm}, \tag{A.6}$$

to be compared with the experimental value

$$B(E1) = 0.102 \pm 0.002\,e^{2}\ \text{fm}, \tag{A.7}$$

the strongest known electric dipole transition between bound states in nuclei. Comparing this value to the ratio[3] $TRK/\hbar\omega_{GDR} \approx 1e^{2}$ fm^{2} one can conclude that the $1/2^{-}\rightarrow 1/2^{+}$ transition carries about 10% of the TRK (also known as the dipole energy weighted sum rule (EWSR)) and thus about one Weisskopf unit ($1\times B_{W}(E1)$; see App. B).

A.2 ^{11}Li bound two–neutron halo system

In this case we are in presence of a paradigmatic nuclear embodiment of the Cooper pair model. Extending BCS to the single–pair limit, one can estimate the correlation length through the standard relation

$$\xi = \frac{\hbar v_{F}}{\pi|E_{corr}|} \approx 20\ \text{fm}, \tag{A.8}$$

where use of[4] $(v_{F}/c)\approx 0.16$ and $E_{corr}\approx -0.5$ MeV was made. Dividing the density distribution of nucleons in ^{11}Li into a compact, normal closed shell $N=6$ core ^{9}Li of radius $R_{0}=1.2(9)^{1/3}$ fm≈ 2.5 fm, and a Cooper pair of correlation length (A.8), one can work out a simple estimate of the effective radius of ^{11}Li as,

$$R_{eff} = \left(\frac{9}{11}\times(2.5)^{2} + \frac{2}{11}\left(\frac{\xi}{2}\right)^{2}\right)^{1/2} \approx 4.8\ \text{fm}, \tag{A.9}$$

leading to $\langle r^{2}\rangle^{1/2} = \sqrt{\frac{3}{5}}R_{eff}\approx 3.7$ fm, to be compared with $\langle r^{2}\rangle^{1/2}_{exp} = 3.55\pm 0.1$ fm.

Let us now work out a simple estimate of E_{corr} used in (A.8). There is experimental evidence [9–12] of the presence in ^{10}Li, of a $1/2^{+}$ virtual state and of a low–lying $1/2^{-}$ resonant state[5]. In keeping with the analytic results of Sect. A.3 (see below), we assume these states to be $|\widetilde{1/2}^{+}\rangle = |s_{1/2};\widetilde{0.15\ \text{MeV}}\rangle$, and $|\widetilde{1/2}^{-}\rangle = |p_{1/2};\widetilde{0.60\ \text{MeV}}\rangle$. Again the scenario of a low–lying collective, soft $E1$–mode.

[3] Making use of the Thomas–Reiche–Kuhn (TRK) sum rule $TRK = \frac{9}{4\pi}\frac{\hbar^{2}e^{2}}{2m}\frac{NZ}{A}\approx 14.8\frac{NZ}{A}e^{2}$ fm^{2} MeV and of the energy parametrization of the giant dipole resonance (GDR), $\hbar\omega_{GDR}\approx 80$ MeV/$(11)^{1/3}\approx 36$ MeV, one obtains for ^{11}Be $TRK/\hbar\omega_{GDR}\approx 1e^{2}$ fm^{2}.

[4] Making use of the Thomas–Fermi model $k_{F} = (3\pi^{2}\times 8/(\frac{4\pi}{3}(4.58)^{3}))^{1/2}\ \text{fm}^{-1}\approx 0.8\ \text{fm}^{-1}$. Thus $(v_{F}/c) = (\hbar k_{F}/mc) = 0.2\times\ \text{fm}\ \times k_{F}\approx 0.16$.

[5] See also [4] and [8].

Making the ansatz of transferability from ^{11}Be, one can ascribe to this soft mode, a 10% of the TRK sum rule to solve the RPA dispersion relation

$$W(E) = \sum_{ki} \frac{2(\epsilon_k - \epsilon_i)|\langle i|F|k\rangle|^2}{(\epsilon_k - \epsilon_i)^2 - E^2} = \frac{1}{\kappa_1^0}. \tag{A.10}$$

In the schematic calculations carried out here, the full quasiparticle subspace discussed in Sect. 2.2 in connection with the QRPA calculation of the DPR is reduced to the $\tilde{s}_{1/2} \to \tilde{p}_{1/2}$ transition, and only the neutron halo degrees of freedom are considered. Degrees of freedom which constitute (2/11) of the total nucleonic space and feels an effective confining radius $\xi/2$. In other words, the factor $(1/R_{eff}^2)$ entering in κ_1^0 is to be replaced in the present estimates by $\frac{1}{\left(\frac{\xi}{2}\right)^2} \times \left(\frac{2}{11}\right)$. It leads to a dipole screened coupling constant of value $\kappa_1 = \frac{R_{eff}^2}{\left(\frac{\xi}{2}\right)^2}\kappa_1^0 \approx 0.04\kappa_1^0 \approx -0.021$ MeV fm^2, where

$$\kappa_1^0 = -\frac{5V_1}{AR_{eff}^2} \quad , \quad V_1 = 25 \text{ MeV}. \tag{A.11}$$

Replacing k and i by the renormalized states $|\widetilde{1/2}^-\rangle$ and $|\widetilde{1/2}^+\rangle$, and E by the energy of the dipole pygmy resonance (DPR) to be determined, one can write

$$(\tilde{\epsilon}_k - \tilde{\epsilon}_i)^2 - (\hbar\omega_{DPR})^2 = \kappa_1 \times 2 \times (0.1 \times TRK), \tag{A.12}$$

where[6]

$$TRK = \frac{3\hbar^2}{2m}\frac{NZ}{A} = 131 \text{ MeV fm}^2 \quad (^{11}_{3}\text{Li}_8). \tag{A.13}$$

Thus

$$\begin{aligned}\hbar\omega_{DPR} = ((0.6 - 0.15)^2 \text{ MeV}^2 - (-0.021 \text{ MeV fm}^{-2}) \\ \times 2 \times 0.1 \times 131 \text{ MeV fm}^2)^{1/2} \approx (0.45^2 + 0.74^2)^{1/2} \approx \text{ MeV},\end{aligned} \tag{A.14}$$

as compared to the centroid value of the resonance observed in $d(^{11}\text{Li}, d')$ experiment leading to 1.03 ± 0.03 MeV [3].

Let us now calculate the particle vibration coupling (PVC) strength Λ of this mode to the nucleons. Note the use in the following estimates of a dimensionless dipole single particle field $F' = F/R_{eff}(^{11}\text{Li})$. This is in keeping with the fact that one aims at obtaining a quantity with energy dimensions ($[\Lambda] = $ MeV), and κ_1^0 has been introduced in Eq. (A.10) as the self consistent value of the dipole–dipole separable interaction, normalized in terms of R_{eff}^2 (^{11}Li). An alternative way to obtain a similar result, is to work out the value of Λ without the $(1/R_{eff}^2)$, and multiply the result by $\overline{|\langle i|F|k\rangle|^2}$. It is expected that both results agree within 10-20% effects. One then obtains,

$$\begin{aligned}\Lambda^2 &= \left(\left(\frac{\partial W'(E)}{\partial E}\right)_{\hbar\omega_{DPR}}\right)^{-1} = \left\{2\hbar\omega_{DPR}\frac{2 \times 0.1 \times TRK/R_{eff}^2}{\left[(\tilde{\epsilon}_{p_{1/2}} - \tilde{\epsilon}_{s_{1/2}})^2 - (\hbar\omega_{DPR})^2)\right]^2}\right\}^{-1} \\ &= \left(\frac{2.3}{0.64 \text{ MeV}^2}\right)^{-1} \approx 0.28 \text{ MeV}^2 \quad (\Lambda = 0.53 \text{ MeV}).\end{aligned} \tag{A.15}$$

[6]Associated with the operator $F(r_k) = e\left[\frac{N-Z}{2A} - t_z(k)\right] r_k$ ($t_z(k) = \pm 1/2$), and thus no spherical harmonic.

The induced pairing interaction associated with the exchange of the DPR between the two halo neutrons leads to the matrix element

$$M_{ind} \approx -\frac{2\Lambda^2}{\hbar\omega_{DPR}} \approx -0.6 \text{ MeV}, \tag{A.16}$$

the factor of 2 being associated with the two possible time orderings (Fig. A.2). Let us now calculate the bare pairing interaction, taking into account the screening[7] due to the large radius of ^{11}Li. That is

$$(G)_{scr} = \frac{2}{8}\left(\frac{2.7}{4.8}\right)^3 G \approx 0.045 \times \frac{28}{A} \text{ MeV} \approx \frac{1.3 \text{ MeV}}{A} \approx 0.1 \text{ MeV}. \tag{A.17}$$

Consequently, the neutron halo Cooper pair binds the core ^{9}Li, with the correlation energy

$$E_{corr} = 2\tilde{\epsilon}_{s_{1/2}} - (G)_{scr} + M_{ind} = (0.3 - 0.1 - 0.6 \text{ MeV}) \approx -0.4 \text{ MeV}, \tag{A.18}$$

to be compared with the experimental value $(E_{corr})_{exp} = -380$ keV.

Furthermore, the absolute cross sections associated with the ^{1}H(^{11}Li, ^{9}Li(**f**)^{3}H reaction, requires two groups of components sharing about evenly the normalized value of the sum of the squared amplitudes. A many–body particle–hole–like one $\alpha|(p_{1/2}, s_{1/2})_{1^-} \otimes 1^-; 0^+\rangle + \beta|(s_{1/2}, d_{5/2})_{2^+} \otimes 2^+; 0^+\rangle$ ($\mathbf{f} = 1/2^-, 2.69$ MeV; $\alpha^2 + \beta^2 \approx 0.5, \alpha \gg \beta$), and another pairing–like $\gamma|s^2_{1/2}(0)\rangle + \delta|p^2_{1/2}(0)\rangle$ ($\mathbf{f} = gs, \gamma^2 + \delta^2 \approx 0.5, \gamma \approx \delta$). Thus, concerning this second one, one can write $|0\rangle = \sqrt{0.25}|s^2_{1/2}\rangle + \sqrt{0.25}|p^2_{1/2}\rangle$. If the first component was to be set equal to zero and thus, because of normalization $\sqrt{0.5}|p^2_{1/2}\rangle$, the absolute two–particle ground state cross section will be predicted a factor ≈ 7 smaller than that associated with $|0\rangle$, which reproduces the observed absolute differential cross section, within experimental errors [6, 7]. This in keeping with the fact that $\sigma(s^2_{1/2}(0)) \approx 15$ mb, while $\sigma(p^2_{1/2}(0)) \approx 2$ mb. Thus $\sigma(\sqrt{0.25}\sqrt{14} + \sqrt{0.25}\sqrt{2})^2$ mb ≈ 6.7 mb, while $(\sqrt{0.5} \times \sqrt{2})^2$ mb ≈ 1 mb.

A.3 ^{10}Li, unbound one–neutron halo system: structure and reactions in the continuum

In this case we use as input the value of $\hbar\omega_{2^+} \approx 3.3$ MeV and $\beta_2 = 0.8$ characterizing the low–lying quadrupole vibration of the core ^{9}Li, as well as $R_{eff}(^{11}\text{Li})$=4.8 fm worked out in the previous section.

As bare potential we use the standard WS potential $U(r) = Uf(r), f(r) = \left(1 + \exp\left(\frac{r-R_0}{a}\right)\right)^{-1}$, where $U = U_0 + 0.4E$, $U_0 = V_0 + 30(N-Z)/A$ MeV and $V_0 = -51$ MeV. The energy dependent term ($E = \hbar k^2/2m - \epsilon_F$) is taken care of by the k–mass $m_k = (1 + 0.4 \times \mathcal{O})^{-1}m \approx 0.93m$, where the overlap between halo and core single–particle wavefunctions is $\mathcal{O} = (2.7/4.8)^3 \approx 0.2$, as defined in Sect. A.2. Expressed differently, because of the large radius of the halo, the Pauli principle plays little role in the mean field, and $m_k \approx m$, m being the bare nucleon mass. Making use of the above potential and of the associated symmetry and spin–orbit terms, the bare single–particle energies $\epsilon_{p_{3/2}}, \epsilon_{p_{1/2}}, \epsilon_{s_{1/2}}$ and $\epsilon_{d_{5/2}}$ were calculated. They are displayed in Table A.2.

With the help of (-51+30$\frac{6-3}{9}$) MeV=-41 MeV, and of $\langle R_0 \partial U/\partial r\rangle \approx 1.44 \times U_0 \approx -60$ MeV ([13], App. D), one can calculate the PVC vertex associated with the quadrupole vibration of the core,

$$v = \langle H_c\rangle = \frac{\beta_2}{\sqrt{5}}\langle R_0 \frac{\partial U}{\partial r}\rangle \mathcal{O}\langle j||Y_2||1/2\rangle,$$

[7] The estimate $G \approx 28$ MeV$/A$ of the pairing strength is made with the help of a δ–force [13]. The corresponding matrix element in the configuration $j^2(0)$ can be expressed as $\langle j^2(0)|V_\delta|j^2(0)\rangle = -\frac{2j+1}{2}G$, with $G = V_0/R_0^3 \approx 28/A$ MeV($R_0 = 1.2A^{1/3}$ fm). Consequently in the case of ^{11}Li the strength G will be screened by the factor $(2/(2j+1))\mathcal{O}$ where $\mathcal{O} = \left(\frac{R_0(^{11}\text{Li})}{R_{eff}}\right)^3$ is the overlap between the core and the halo wavefunctions, and $j = k_F R_0 = 1.36$ fm$^{-1} \times 2.7$ fm ≈ 3.7 and $2j + 1 \approx 8$, while $2j + 1 = 2$ for both $s_{1/2}$ and $p_{1/2}$.

$$\langle j||Y_2||1/2\rangle = \sqrt{\frac{2j+1}{4\pi}} = \begin{cases} 0.7 & j = 5/2(d_{5/2}) \\ 0.6 & j = 3/2(p_{3/2}), \end{cases} \tag{A.19}$$

$$v \approx \frac{0.8}{\sqrt{5}}(-60 \text{ MeV}) \times 0.2 \times 0.7 \approx -3 \text{ MeV}. \tag{A.20}$$

In keeping with the fact that the $p_{1/2}$ is a bound state while $s_{1/2}$ is not, the corresponding wavefunction is more concentrated and, consequently, the corresponding matrix elements of H_c larger. We take the empirical ratio 26/20$\approx$ 1.3 between G_p and G_n as indicative ([13], p. 63). In what follows we shall thus use $v_{s_{1/2}} \approx -3.0$ MeV and $v_{p_{1/2}} \approx -3.9$ MeV. Let us now calculate the renormalization of the $s_{1/2}$ and $p_{1/2}$ states. The self–energy diagram (a) of Fig. A.1 gives, to second order of perturbation in v,

$$\Sigma_{s_{1/2}} = \frac{v^2}{\epsilon_{s_{1/2}} - (\epsilon_{d_{5/2}} + \hbar\omega_2)} = \frac{9 \text{ MeV}^2}{(1.5 - 6.8) \text{ MeV}} = -1.7 \text{ MeV}. \tag{A.21}$$

i	ϵ_i (MeV)	$\tilde{\epsilon}_i$ (MeV)	$(\epsilon_i)_{exp}$ (MeV)[b)]
$s_{1/2}$	0.07	-0.5	-0.5
$p_{1/2}$	-3.04	-0.18	-0.18
$d_{5/2}$	7.30	1.45	1.28[a)]

[a)] Centroid of resonance
[b)] [16] (see also [1] and references therein).

Table A.1: ^{11}Be: bare (ϵ_i), dressed ($\tilde{\epsilon}_i$), and experimental ϵ_{exp} single–particle energies of the lowest bound and resonant states.

i	ϵ_i (MeV)	$\tilde{\epsilon}_i$ (MeV)	$(\epsilon_i)_{exp}$ (MeV)[a),b)]
$d_{5/2}$	3.5		
$s_{1/2}$	1.2	0.15[c)]	0.1-0.25[a)]
$p_{1/2}$	-1.2	0.60[d)]	0.4-0.6[a),b)]
$p_{3/2}$	-4.7		

[a)] [10]
[b)] [4]
[c)] virtual
[d)] resonant

Table A.2: Same as Table A.1, but for ^{10}Li.

The renormalized energy $\tilde{\epsilon}_{s_{1/2}}$ at convergence is obtained by solving the secular equation

$$\begin{vmatrix} (E_a - E_i) & v \\ v & (E_\alpha - E_i) \end{vmatrix} = \begin{vmatrix} (1.5 - E_i) & -3.0 \\ -3.0 & (6.8 - E_i) \end{vmatrix} = 0. \tag{A.22}$$

That is

$$E_i^2 - 8.3E_i + 1.2 = 0, \tag{A.23}$$

where all the numbers in (A.22) and (A.23) are in MeV. The lowest root of (A.23) is $E_1 = \tilde{\epsilon}_{s_{1/2}} = 0.15$ MeV. It is of notice that in the present case, as well as in connection with the calculation of $\tilde{\epsilon}_{p_{1/2}}$ below, perturbation theory i.e. $\epsilon_{s_{1/2}} + \Sigma_{s_{1/2}} = (1.5 - 1.7)$ MeV =-0.2 MeV cannot be used, and the process displayed in Fig. A.1 (a) has to be summed to all orders of perturbation.

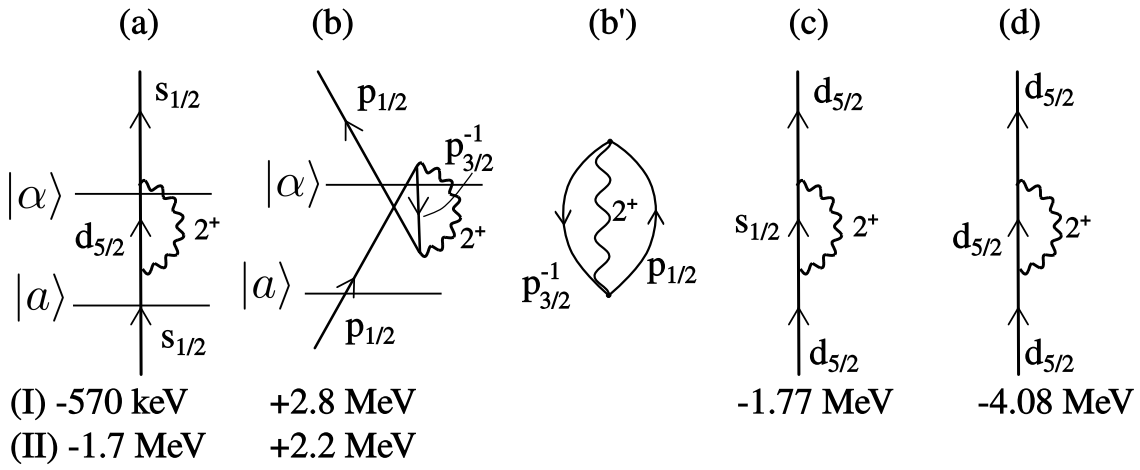

Fig. A.1: Self–energy associated with the lowest $s_{1/2}$ (**a**) $p_{1/2}$ (**b**) states and $d_{5/2}$ (**c**) and (**d**) resonance of ^{11}Be (line (**I**)) and of the $s_{1/2}$ virtual and $p_{1/2}$ resonant states of ^{11}Li (line (**II**).) The diagram (**b'**) describes the ZPF associated with the component $(p_{1/2}, p^{-1}_{3/2})_{2^+}$ of the quadrupole mode of the core ^{9}Li.. The label $|a\rangle$ stands for the state to be renormalized due to the coupling to the intermediate (virtual) state $|\alpha\rangle$. It is to be noted that the results displayed in (I) are at convergence, i.e. obtained by summing to all orders the corresponding process [1], while those shown in (II) are second order in the PVC vertex results (see A.21 and A.26).

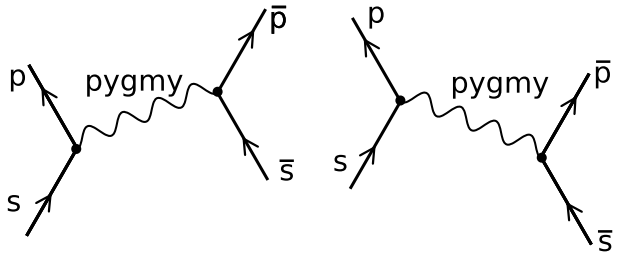

Fig. A.2: Induced pairing interaction between the halo neutrons resulting from the exchange of the DPR between the configurations $s^2(0)$ and $p^2(0)$. It is of notice that $|\bar{\nu}\rangle$ stands for the state time reversed to $|\nu\rangle$ ($\nu = s, p$).

The above provides a textbook example of the specificity with which one can single out, within the framework of NFT, the physical processes at the basis of a phenomenon under study, e.g. parity inversion in ^{10}Li, and the economy with which one can "exactly" treat them. But also only them, not being forced to waste resources, but most importantly, physical insight in keeping track at the same time of myriads of little relevant but somewhat connected processes.

Let us now work out the amplitudes of the $|\tilde{\epsilon}_{1/2}\rangle$ state. That is

$$c^2_{s_{1/2}}(1) = \left(1 + \frac{v^2}{(E_\alpha - E_1)^2}\right)^{-1} = \left(1 + \frac{9\ \text{MeV}^2}{(6.8 - 0.15)^2\ \text{MeV}^2}\right)^{-1}$$
$$= (1 + 0.2)^{-1} = 0.83. \tag{A.24}$$

Making use of normalization ($c^2_a(1) + c^2_\alpha = 1$) one can write

$$|\widetilde{1/2^+; 0.15}\rangle = 0.91|s_{1/2}\rangle + 0.41|(d_{5/2} \otimes 2^+); 1/2^+\rangle \tag{A.25}$$

From (A.24) one obtains that the mass enhancement factor is $\lambda = 0.2$ and thus the effective ω–mass $m_\omega = 1.2m$, while the discontinuity at the Fermi energy (single–particle content) is $Z_\omega = (m_\omega/m)^{-1} = 0.83$.

Let us now discuss the renormalization of the $p_{1/2}$ state. Following the same steps as before we find

$$\Sigma_{p_{1/2}} = \frac{(-1)^1(-3.9\text{ MeV})^2}{\epsilon_{p_{1/2}} - \Big[(2\epsilon_{p_{1/2}} - \epsilon_{p_{3/2}}) + \hbar\omega_2\Big]} = \frac{15.21\text{ MeV}^2}{\Big[\epsilon_{p_{1/2}} - (\epsilon_{p_{3/2}} - \hbar\omega_2)\Big]}$$
$$= \frac{15.21\text{ MeV}}{-1.2-(-4.7-3.3)} = \frac{15.21}{-1.2-(-8)} = \frac{15.21}{6.8} = 2.2\text{ MeV}, \tag{A.26}$$

where the phase $(-1)^n$ comes from the number of unavoidable crossing ($n = 1$) in diagram (b) of Fig. A.1. Thus, in second order perturbation theory, $\epsilon_{p_{1/2}} + \Sigma_{p_{1/2}} = -1.2$ MeV +2.2 MeV=1.0 MeV.

Let us now calculate the same process (a) Fig. A.1 to convergence. For this we need $E_a = \epsilon_{p_{1/2}} = -1.2$ MeV, $E_\alpha = \epsilon_{p_{3/2}} - \hbar\omega_{2^+} = (-4.7 - 3.3)$ MeV= -8 MeV. The associated secular equation being

$$\begin{vmatrix} (-1.2 - E_i) & -3.9 \\ -3.9 & (-8 - E_i) \end{vmatrix} = E_i^2 + 9.2E_i - 5.61 = 0, \tag{A.27}$$

again all numbers in MeV. We then obtain $E_1 = \tilde{\epsilon}_{p_{1/2}} = 0.6$ MeV, a result which again testifies to the inapplicability of perturbation theory. The square amplitude of the corresponding renormalized state is

$$c^2_{p_{1/2}} = \left(1 + \frac{(-3.9\text{ MeV})^2}{(0.6-(-8))^2}\right)^{-1} = (1 + 0.21)^{-1} = 0.83. \tag{A.28}$$

One then can write

$$|1/2^-; \widetilde{0.6\text{ MeV}}\rangle = 0.91|p_{1/2}\rangle + 0.41|((p_{1/2}, p^{-1}_{3/2})_{2^+} \otimes 2^+)_{0^+} p_{1/2}; 1/2^-\rangle, \tag{A.29}$$

the associated mass enhancement factor, ω–mass and Z_ω–factor being $\lambda = 0.21$, $m_\omega = 1.21m$ and $Z_\omega = 0.83$ respectively. The energy of the parity inverted states are compared in Table A.1 with the experimental findings.

In connection with the energy associated with the intermediate state $E_\alpha = \epsilon_{p_{3/2}} - \hbar\omega_{2^+} = (-4.7 - 3.3)$ MeV=-8 MeV in Eqs (A.27) and (A.28), we refer to the energy denominator of Eq. (A.26) for a mathematical explanation. The physics can be found in the Lamb shift–like effect described by diagram (b) of Fig. A.1, a phenomenon closely connected with Pauli principle and the ZPF process shown in diagram (b'). To allow the dressed $|\widetilde{p}_{1/2}\rangle$ state to acquire asymptotic waves, i.e. to be on shell, one has to annihilate simultaneously the quadrupole phonon and the $p^{-1}_{3/2}$ hole implying an overall energy change of -3.3 MeV-4.7 MeV=-8 MeV.

B $E1$–Weisskopf unit

The $E1$–unit, so called Weisskopf unit is defined[8] as $B_W(E1) = ((1.2)^2/4\pi)(3/4)^2 A^{2/3} e^2$ fm^2 $= \frac{0.81}{4\pi} A^{2/3} e^2$ fm^2 ([14] p. 389, Eq(3C-38)), which together with the comment at the end of p. 387 and starting of p. 388,

$$e \to (e)_{E1} = \begin{cases} \frac{N}{A}e = \frac{8}{11}e = 0.73e & \text{protons} \\ -\frac{Z}{A}e = -\frac{3}{11}e = -0.27e & \text{neutrons} \end{cases} \tag{B.1}$$

implies, for $^{11}_{3}\text{Li}_8$

$$B_W(E1) = 0.32(e)^2_{E1}\text{ fm}^2 = \begin{cases} 0.17e^2\text{ fm}^2 & \text{(p)} \\ 0.023e^2\text{ fm}^2 & \text{(n),} \end{cases} \tag{B.2}$$

[8]Both in the definition of B_W as well as of $S(E1)$ below (Eq. (A.26)) and at variance to TRK (Eq. (A.13), see also footnote 6), the corresponding dipole operator contains the spherical harmonics of multipolarity $\lambda = 1$.

and thus an average value

$$\overline{B_W(E1)} = \frac{0.17 + 0.023}{2} e^2 \text{ fm}^2 \approx 0.1 e^2 \text{ fm}^2 \tag{B.3}$$

Making now use of [15] p. 403 Eq. (6-176) for the case of ^{11}Li,

$$S(E1) = 14.8 \frac{NZ}{A} e^2 \text{ fm}^2 \text{ MeV} = 32.3 e^2 \text{ MeV fm}^2 \tag{B.4}$$

together with $\hbar\omega_{GDR} = 80 \text{ MeV}/A^{1/3}$ MeV$\approx$ 36 MeV gives

$$\frac{S(E1)}{\hbar\omega_{GDR}} \approx 0.9 e^2 \text{ fm}^2. \tag{B.5}$$

Assuming the DPR of ^{11}Li to carry $\approx$10% of $S(E1)$ one then obtains

$$10\% \left(\frac{S(E1)}{\hbar\omega_{GDR}} \right) \approx 0.09 e^2 \text{ fm}^2, \tag{B.6}$$

and thus a Weisskopf unit.

References

[1] F. Barranco, G. Potel, R. A. Broglia, and E. Vigezzi. Structure and reactions of ^{11}Be: many–body basis for single–neutron halo. *Phys. Rev. Lett.*, 119:082501, 2017.

[2] Barranco, F., P. F. Bortignon, R. A. Broglia, G. Colò, and E. Vigezzi. The halo of the exotic nucleus ^{11}Li: a single Cooper pair. *Europ. Phys. J. A*, 11:385, 2001.

[3] R. Kanungo, A. Sanetullaev, J. Tanaka, S. Ishimoto, G. Hagen, T. Myo, T. Suzuki, C. Andreoiu, P. Bender, A. A. Chen, B. Davids, J. Fallis, J. P. Fortin, N. Galinski, A. T. Gallant, P. E. Garrett, G. Hackman, B. Hadinia, G. Jansen, M. Keefe, R. Krücken, J. Lighthall, E. McNeice, D. Miller, T. Otsuka, J. Purcell, J. S. Randhawa, T. Roger, A. Rojas, H. Savajols, A. Shotter, I. Tanihata, I. J. Thompson, C. Unsworth, P. Voss, and Z. Wang. Evidence of soft dipole resonance in ^{11}Li with isoscalar character. *Phys. Rev. Lett.*, 114:192502, 2015.

[4] M. Cavallaro, M. De Napoli, F. Cappuzzello, S. E. A. Orrigo, C. Agodi, M. Bondí, D. Carbone, A. Cunsolo, B. Davids, T. Davinson, A. Foti, N. Galinski, R. Kanungo, H. Lenske, C. Ruiz, and A. Sanetullaev. Investigation of the ^{10}Li shell inversion by neutron continuum transfer reaction. *Phys. Rev. Lett.*, 118:012701, 2017.

[5] R. A. Broglia, P. F. Bortignon, F. Barranco, E. Vigezzi, A. Idini, and G. Potel. Unified description of structure and reactions: implementing the Nuclear Field Theory program. *Phys. Scr.*, 91:063012, 2016.

[6] G. Potel, F. Barranco, E. Vigezzi, and R. A. Broglia. Evidence for phonon mediated pairing interaction in the halo of the nucleus ^{11}Li. *Phys. Rev. Lett.*, 105:172502, 2010.

[7] Tanihata, I., M. Alcorta, D. Bandyopadhyay, R. Bieri, L. Buchmann, B. Davids, N. Galinski, D. Howell, W. Mills, S. Mythili, R. Openshaw, E. Padilla-Rodal, G. Ruprecht, G. Sheffer, A. C. Shotter, M. Trinczek, P. Walden, H. Savajols, T. Roger, M. Caamano, W. Mittig, P. Roussel-Chomaz, R. Kanungo, A. Gallant, M. Notani, G. Savard, and I. J. Thompson. Measurement of the two-halo neutron transfer reaction ^{1}H(^{11}Li,^{9}Li)^{3}H at 3A MeV. *Phys. Rev. Lett.*, 100:192502, 2008.

[8] F. Barranco, G. Potel, E. Vigezzi, and R. A. Broglia. $d(^9\text{Li},p)$, specific probe of ^{10}Li, paradigm of parity–inverted, soft–dipole isotones with one neutron outside the $N = 6$ closed shell. *To be published.*

[9] M. Thoennessen, S. Yokoyama, A. Azhari, T. Baumann, J. A. Brown, A. Galonsky, P. G. Hansen, J. H. Kelley, R. A. Kryger, E. Ramakrishnan, and P. Thirolf. Population of ^{10}Li by fragmentation. *Phys. Rev. C*, 59:111, 1999.

[10] M. Zinser, F. Humbert, T. Nilsson, W. Schwab, Th. Blaich, M. J. G. Borge, L. V. Chulkov, H. Eickhoff, Th. W. Elze, H. Emling, B. Franzke, H. Freiesleben, H. Geissel, K. Grimm, D. Guillemaud-Mueller, P. G. Hansen, R. Holzmann, H. Irnich, B. Jonson, J. G. Keller, O. Klepper, H. Klingler, J. V. Kratz, R. Kulessa, D. Lambrecht, Y. Leifels, and A. Magel. Study of the unstable nucleus ^{10}Li in stripping reactions of the radioactive projectiles ^{11}Be and ^{11}Li. *Phys. Rev. Lett.*, 75:1719, 1995.

[11] M Chartier, J.R Beene, B Blank, L Chen, A Galonsky, N Gan, K Govaert, P.G Hansen, J Kruse, V Maddalena, M Thoennessen, and R.L Varner. Identification of the ^{10}Li ground state. *Physics Letters B*, 510:24, 2001.

[12] H. Simon, M. Meister, T. Aumann, M.J.G. Borge, L.V. Chulkov, U. Datta Pramanik, Th.W. Elze, H. Emling, C. Forssén, H. Geissel, M. Hellström, B. Jonson, J.V. Kratz, R. Kulessa, Y. Leifels, K. Markenroth, G. Münzenberg, F. Nickel, T. Nilsson, G. Nyman, A. Richter, K. Riisager, C. Scheidenberger, G. Schrieder, O. Tengblad, and M.V. Zhukov. Systematic investigation of the drip–line nuclei ^{11}Li and ^{14}Be and their unbound subsystems ^{10}Li and ^{13}Be. *Nuclear Physics A*, 791:267, 2007.

[13] Brink, D. and R. A. Broglia. *Nuclear Superfluidity*. Cambridge University Press, Cambridge, 2005.

[14] A. Bohr and B. R. Mottelson. *Nuclear Structure, Vol.I*. Benjamin, New York, 1969.

[15] Bohr, A. and B. R. Mottelson. *Nuclear Structure, Vol.II*. Benjamin, New York, 1975.

[16] J.S. Winfield, S. Fortier, W.N. Catford, S. Pita, N.A. Orr, J. Van de Wiele, Y. Blumenfeld, R. Chapman, S.P.G. Chappell, N.M. Clarke, N. Curtis, M. Freer, S. Galès, H. Langevin-Joliot, H. Laurent, I. Lhenry, J.M. Maison, P. Roussel-Chomaz, M. Shawcross, K. Spohr, T. Suomijärvi, and A. de Vismes. Single-neutron transfer from ^{11}Be$_{gs}$ via the (p, d) reaction with a radioactive beam. *Nuclear Physics A*, 683:48, 2001.

The deformation dependence of level densities in the configuration-interaction shell model

Y. Alhassid,[1] *G.F. Bertsch*[2]*, C.N. Gilbreth,*[3] *and M.T. Mustonen*[1]
[1]Center for Theoretical Physics, Sloane Physics Laboratory, Yale University, New Haven, Connecticut 06520, USA
[2]Department of Physics and Institute for Nuclear Theory, Box 351560, University of Washington, Seattle, Washington 98195, USA
[3]Department of Physics, Central Washington University, Ellensburg, Washington 98926, USA

Abstract

The auxiliary-field quantum Monte Carlo (AFMC) method has enabled the microscopic calculation of nuclear level densities from the underlying Hamiltonian. However, AFMC is applied within the rotationally invariant framework of the configuration-interaction (CI) shell model, while deformation arises in the framework of a mean-field approximation that breaks rotational invariance. We review a recent method to study deformation in the CI shell model without invoking a mean-field approximation. Using a Landau-like expansion of the logarithm of the distribution of the quadrupole deformation tensor in the so-called quadrupole invariants, we determine the dependence of this distribution on intrinsic deformation. We can then calculate the dependence of nuclear state densities on intrinsic deformation. The method is demonstrated for a chain of even-mass samarium nuclei.

1 Introduction

The modeling of shape dynamics, e.g., fission, requires the knowledge of level densities as a function of deformation. The auxiliary-field quantum Monte Carlo (AFMC) method, known in nuclear physics as the shell model Monte Carlo (SMMC) [1–3], has enabled the calculation of state densities in model spaces that are many orders of magnitude larger than those that can be treated by conventional diagonalization methods [4–7]. However, it is a challenge to calculate level densities as a function of intrinsic deformation in the spherical configuration-interaction (CI) shell model approach.

Deformation originates in the context of mean-field approximations that break rotational invariance and can miss important correlations. Here we review a recent method we introduced to calculate the shape dependence of level densities in the rotationally invariant framework of the CI shell model without using a mean-field approximation [8]. The method is based on the AFMC calculation of the lab-frame distribution of the axial quadrupole deformation [9, 10], and on a Landau-like expansion which determines the distribution of the quadrupole deformation tensor in the intrinsic frame as a function of temperature. The deformation dependence of the state density is then calculated using the saddle-point approximation.

The outline of this article is as follows: in Sec. 2, we briefly review the AFMC method. In Sec. 3, we describe the calculation of the distribution of the axial quadrupole deofrmation in the laboratory frame. In Sec. 4, we discuss a Landau-like expansion to calculate the intrinsic-frame distribution of the quadrupole deformation. In Sec. 5, we use the saddle-point approximation to calculate the state density as a function of deformation and excitation energy. Finally, we conclude in Sec. 6. We demonstrate the various steps of our method for a chain of even-mass samarium isotopes $^{148-154}$Sm.

2 Auxiliary-field quantum Monte Carlo method for the CI shell model

The AFMC method is based on the Hubbard-Stratonovich transformation [11], in which Gibbs ensemble $e^{-\beta\hat{H}}$ for a system described by a Hamiltonian $\hat{H}$ at inverse temperature $\beta = 1/T$ is expressed as a functional integral over external auxiliary fields $\sigma(\tau)$ that depend on imaginary time τ ($0 \leq \tau \leq \beta$)

$$e^{-\beta\hat{H}} = \int \mathcal{D}[\sigma]\; G_\sigma \hat{U}_\sigma \; . \tag{1}$$

Here $\hat{U}_\sigma$ is a one-body ensemble of non-interacting particles moving in the external auxiliary fields $\sigma(\tau)$ and G_σ is a Gaussian weight. The thermal expectation value of an observable $\hat{O}$ is then given by

$$\langle\hat{O}\rangle = \frac{\mathrm{Tr}\,(\hat{O}e^{-\beta\hat{H}})}{\mathrm{Tr}\,(e^{-\beta\hat{H}})} = \frac{\int \mathcal{D}[\sigma] G_\sigma \langle\hat{O}\rangle_\sigma \mathrm{Tr}\,\hat{U}_\sigma}{\int \mathcal{D}[\sigma] G_\sigma \mathrm{Tr}\,\hat{U}_\sigma} \; , \tag{2}$$

where $\langle\hat{O}\rangle_\sigma \equiv \mathrm{Tr}\,(\hat{O}\hat{U}_\sigma)/\mathrm{Tr}\,\hat{U}_\sigma$ is the expectation value of $\hat{O}$ for non-interacting particles in a given configuration of the auxiliary fields.

We define a positive-definite weight function $W_\sigma = G_\sigma|\mathrm{Tr}\,\hat{U}_\sigma|$ and the W-weighted average of a quantity X_σ by

$$\langle X_\sigma\rangle_W \equiv \frac{\int D[\sigma] W_\sigma X_\sigma \Phi_\sigma}{\int D[\sigma] W_\sigma \Phi_\sigma} \; , \tag{3}$$

where $\Phi_\sigma \equiv \mathrm{Tr}\,\hat{U}_\sigma/|\mathrm{Tr}\,\hat{U}_\sigma|$ is the Monte Carlo sign function. We can then rewrite (2) in the form

$$\langle\hat{O}\rangle = \left\langle \frac{\mathrm{Tr}\,(\hat{O}\hat{U}_\sigma)}{\mathrm{Tr}\,\hat{U}_\sigma} \right\rangle_W \; . \tag{4}$$

The σ-dependent quantities in (4) are calculated by matrix algebra in the single-particle space, and the integration over the large number of auxiliary fields is carried out by sampling the fields according to W_σ using Monte Carlo methods.

3 Quadrupole distributions in the laboratory frame

The mass quadrupole operator is a second-rank tensor whose spherical components are given by

$$\hat{Q}_{2\mu} = \sqrt{\frac{16\pi}{5}} \int \mathrm{d}^3\mathbf{r}\hat{\rho}(\mathbf{r}) r^2 Y_{2\mu}(\theta,\varphi) \; , \tag{5}$$

where $\hat{\rho}(\mathbf{r}) = \sum_i \delta(\mathbf{r}_i - \mathbf{r})$ is the total single-particle density at point $\mathbf{r}$.

The probability $P(q)$ at inverse temperature $\beta = 1/T$ for the axial quadrupole operator $\hat{Q}_{20}$ to have a value q in the laboratory frame is given by

$$P(q) = \sum_n \delta(q - q_n) \sum_m \langle q_n|e_m\rangle^2 e^{-\beta e_m} \; , \tag{6}$$

where $|e_m\rangle$ and $|q_n\rangle$ are, respectively, the eigenstates of the Hamiltonian $\hat{H}$ and quadrupole operator $\hat{Q}_{20}$ with eigenvalues e_m and q_n. The distribution $P(q)$ can be written in the form

$$P(q) = \mathrm{Tr}\,[\delta(\hat{Q}_{20} - q)e^{-\beta\hat{H}}]/\mathrm{Tr}\,e^{-\beta\hat{H}} \; . \tag{7}$$

3.1 Projection on the axial quadrupole operator

Using the HS transformation (1) in Eq. (7) and the notation of (4), we can rewrite

$$P(q) = \left\langle \frac{\mathrm{Tr}\left[\delta(\hat{Q}_{20} - q)\hat{U}_\sigma\right]}{\mathrm{Tr}\,\hat{U}_\sigma} \right\rangle_W . \tag{8}$$

The projection on the axial quadrupole operator in Eq. (8) can be calculated with AFMC using a discrete Fourier transform of the Dirac delta function [9, 10]. Dividing a sufficiently large interval $[-q_{\max}, q_{\max}]$ into $2M+1$ intervals of equal length Δq, we have

$$\mathrm{Tr}\left[\delta(\hat{Q}_{20} - q_m)\hat{U}_\sigma\right] \approx \frac{1}{2q_{\max}} \sum_{k=-M}^{M} e^{-i\varphi_k q_m} \mathrm{Tr}\left(e^{i\varphi_k \hat{Q}_{20}}\hat{U}_\sigma\right) , \tag{9}$$

where $q_m = m\Delta q$ $(m = -M, \ldots, M)$ and $\varphi_k = \pi k/q_{\max}$ $(k = -M, \ldots, M)$. The grand-canonical trace on the r.h.s. of Eq. (9) can be written as a determinant in the single-particle space

$$\mathrm{Tr}\left(e^{i\varphi_k \hat{Q}_{20}}\hat{U}_\sigma\right) = \det\left(1 + e^{i\varphi_k \mathbf{Q}_{20}}\mathbf{U}_\sigma\right) , \tag{10}$$

where $\mathbf{Q}_{20}$ and $\mathbf{U}_\sigma$ are the matrices representing the operators $\hat{Q}_{20}$ and $\hat{U}_\sigma$ in the single-particle space. We also project on fixed numbers of protons and neutrons [5, 12].

3.2 Application to samarium isotopes

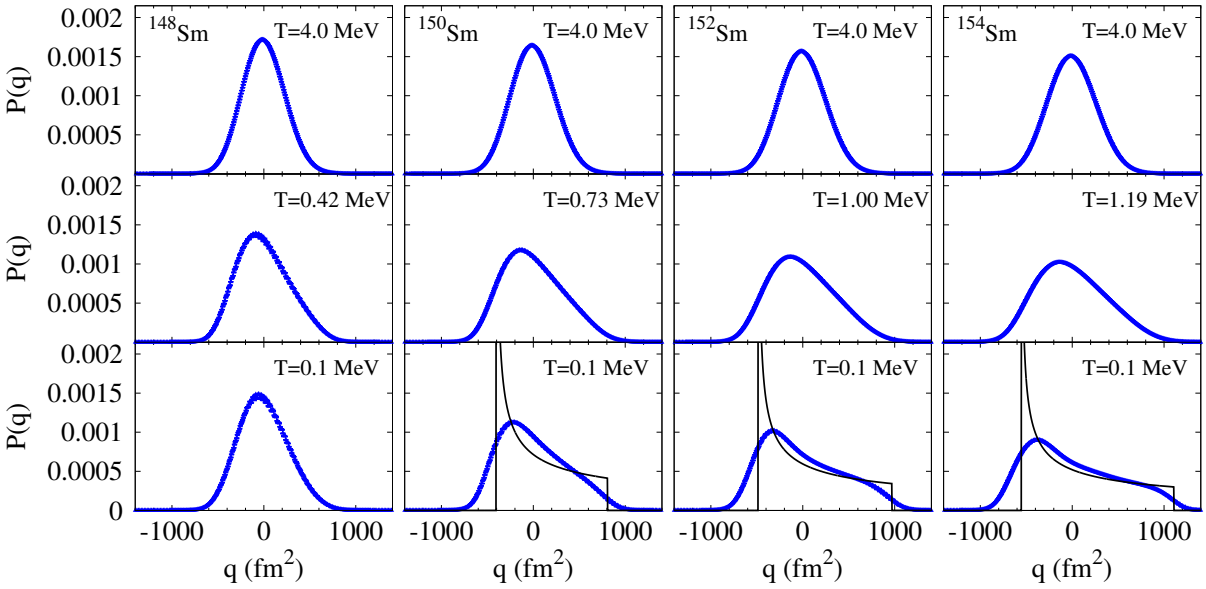

Fig. 1: Lab-frame distributions $P(q)$ of the axial quadrupole operator in a chain of samarium isotopes $^{148-154}$Sm. The solid lines are rigid-rotor distributions. Taken from Ref. [10].

We calculated the lab-frame quadrupole distributions $P(q)$ for a chain of even-mass samarium isotopes $^{148-154}$Sm at different temperatures [10]. We used the shell mode space and interaction discussed in Refs. [6, 7]. The results are shown in Fig. 1, where the bottom row corresponds to low temperature of $T = 0.1$ MeV (close to the ground state), the middle row are intermediate temperatures that are close to the shape transition temperatures in the Hartree-Fock-Bogoliubov (HFB) approximation [13, 14], and the top row corresponds the a high temperature of $T = 4$ MeV. We observe that in a nucleus whose mean-field ground state is deformed (i.e., in $^{150-154}$Sm), $P(q)$ is a skewed distribution at low temperatures

and it becomes close to a Gaussian at higher temperatures as the nucleus becomes spherical. The solid lines describe the lab-frame distributions of a rigid rotor whose intrinsic quadrupole moment is taken from the zero-temperature HFB approximation, and are in qualitative agreement with the exact AFMC distributions. We conclude that the lab-frame distribution $P(q)$ carries a model-independent signature of deformation.

4 Quadrupole distributions in the intrinsic frame

4.1 Intrinsic deformation

For a nucleus of mass number A, we define dimensionless quadruple deformation parameters $\alpha_{2\mu}$ through the liquid drop model relation

$$q_{2\mu} = \frac{3}{\sqrt{5\pi}} r_0^2 A^{5/3} \alpha_{2\mu} \ , \tag{11}$$

where $r_0 = 1.2$ fm. The intrinsic quadrupole deformation parameters $\tilde{\alpha}_{2\mu}$ are determined by a rotation with angles Ω to a frame in which $\tilde{\alpha}_{21} = \tilde{\alpha}_{2\,-1} = 0$ and $\tilde{\alpha}_{22} = \tilde{\alpha}_{2\,-2} =$ real. The intrinsic deformation parameters β, γ are then defined by the standard relations

$$\tilde{\alpha}_{20} = \beta \cos\gamma \ ; \quad \tilde{\alpha}_{22} = \tilde{\alpha}_{2,-2} = \frac{1}{\sqrt{2}} \beta \sin\gamma \ . \tag{12}$$

The volume element $\prod_\mu d\alpha_{2\mu}$ in the lab frame is given by

$$\prod_\mu d\alpha_{2\mu} = \frac{1}{2} \beta^4 |\sin(3\gamma)| \, d\beta \, d\gamma \, d\Omega \ . \tag{13}$$

Information on the intrinsic deformation can be obtained from the expectation values of rotationally invariant combinations of the quadrupole deformation tensor $\alpha_{2\mu}$, known as quadrupole invariants [15, 16]. For recent applications of quadrupole invariants in the framework of the CI shell model, see Refs. [17, 18]. There are three quadrupole invariants up to fourth order

$$\alpha \cdot \alpha = \beta^2 \ ; \quad [\alpha \times \alpha]_2 \cdot \alpha = -\sqrt{\frac{2}{7}} \beta^3 \cos(3\gamma) \ ; \quad (\alpha \cdot \alpha)^2 = \beta^4 \ . \tag{14}$$

4.2 Landau-like expansion

We denote by $P(T, \alpha_{2\mu})$ the distribution of the quadrupole deformation tensor $\alpha_{2\mu}$ at temperature T. This distribution is invariant under rotations and therefore depends only on the intrinsic variables β, γ. We expand the logarithm of $P(T, \beta, \gamma)$ in the quadrupole invariants up to fourth order to find

$$P(T, \beta, \gamma) = \mathcal{N}(T) e^{-a(T)\beta^2 - b(T)\beta^3 \cos(3\gamma) - c(T)\beta^4} \ , \tag{15}$$

where a, b, c are temperature-dependent coefficients and $\mathcal{N}$ is a normalization constant. Such a Landau expansion was used in Refs. [19, 20] for the free energy to describe nuclear shape transitions in the framework of a mean-field theory. Here we use a Landau-like expansion to describe the exact quadrupole shape distribution.

The coefficients a, b, c in Eq. (15) can be determined from the expectation values of the three quadrupole invariants in (14), which in turn are related to the corresponding moments of $\hat{Q}_{20}$ in the laboratory frame $\langle \hat{Q}_{20}^n \rangle = \int dq \, q^n P(q)$ [9, 10]. Using these relations we find

$$\chi^2 \langle \beta^2 \rangle_L = 5 \langle \hat{Q}_{20}^2 \rangle \ ; \quad \chi^3 \langle \beta^3 \cos(3\gamma) \rangle_L = \frac{35}{2} \langle \hat{Q}_{20}^3 \rangle \ ; \quad \chi^4 \langle \beta^4 \rangle_L = \frac{35}{3} \langle \hat{Q}_{20}^4 \rangle \ . \tag{16}$$

Here $\chi = \frac{3}{\sqrt{5\pi}} r_0^2 A^{5/3}$ [see Eq. (11)], and the expectation values $\langle f(\beta,\gamma)\rangle_L$ of a function f that depend on intrinsic deformation β, γ is defined by

$$\langle f(\beta,\gamma)\rangle_L \equiv 4\pi^2 \int d\beta\, d\gamma\, \beta^4 |\sin(3\gamma)| f(\beta,\gamma) P(T,\beta,\gamma)\ , \tag{17}$$

where we have used the metric (13), and $P(T,\beta,\gamma)$ is the distribution (15).

The lab-frame moments $\langle \hat{Q}_{20}^n \rangle$ are computed from the AFMC distribution $P(q)$, and Eqs. (16) are then used to determine the Landau parameters a, b, c as a function of temperature.

To validate the fourth-order Landau expansion, we express the quadrupole invariants in Eq. (15) in terms of the lab-frame $\alpha_{2\mu}$, and integrate over all $\alpha_{2\mu}$ with $\mu \neq 0$ to find the marginal distribution $P(T, \alpha_{20})$. The latter can be compared directly with the AFMC distribution $P(q)$, and we find these distributions to be indistinguishable on the scale of Fig. 1.

Figure 2 shows the distributions $P(T,\beta,\gamma)$ on a logarithmic scale for the chain of samarium isotopes $^{148-154}$Sm for the same temperatures as in Fig. 1. At the low temperature of $T = 0.1$ MeV (near the ground state), we observe that the maximum of $P(T,\beta,\gamma)$ describes a quantum phase transition from a spherical shape in ^{148}Sm to a prolate shape in ^{154}Sm. In the nuclei which are deformed in the ground state (i.e., $^{150-154}$Sm), we observe a thermal shape transition to a spherical shape as the temperature increases. Around the HFB transition temperature (middle panel), the shape distributions are rather soft. We note that the probability density to find a given shape β, γ is given by $4\pi^2\beta^4|\sin(3\gamma)|P(T,\beta,\gamma)$ [using the metric (13) and integrating over the spatial angles Ω].

To simplify the visualization of our results, we divide the $\beta - \gamma$ plane to three regions as shown in Fig. 3, which we call spherical, prolate and oblate. The probability to find the nucleus in a given region

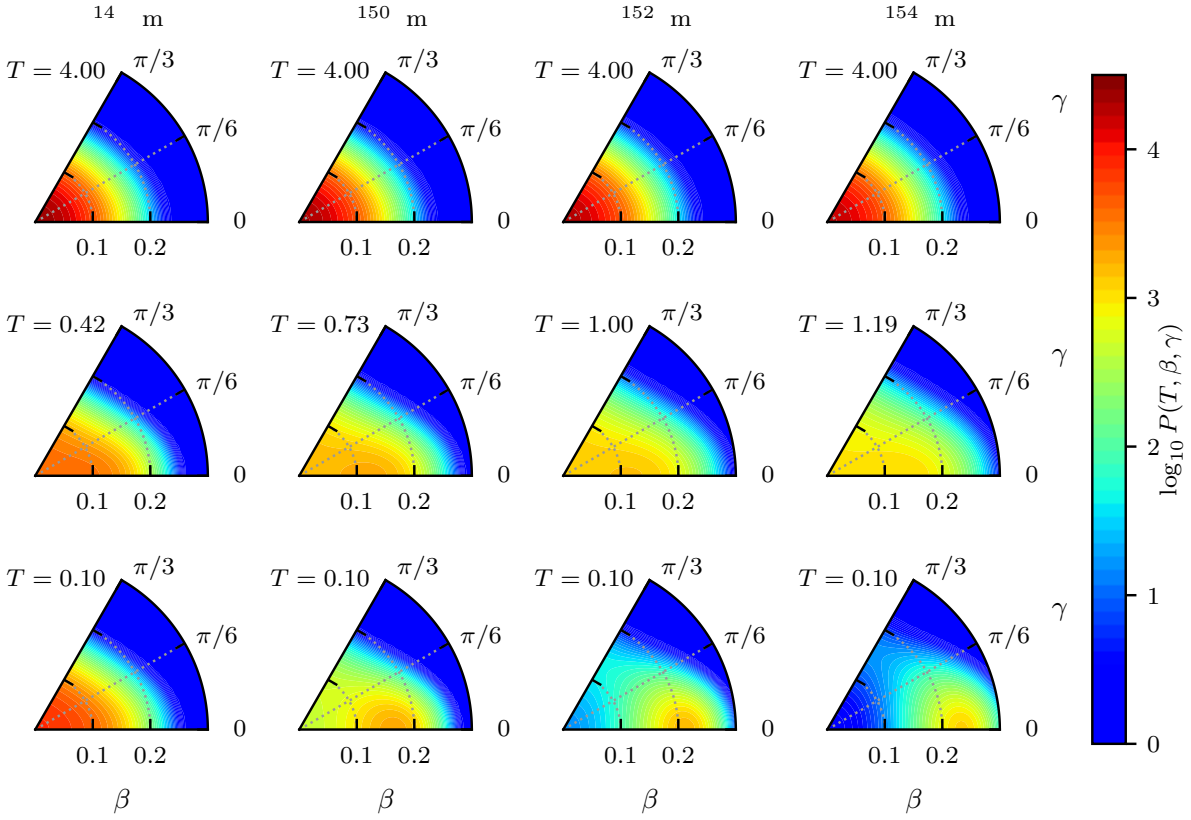

Fig. 2: Shape distributions in a chain of samarium isotopes $^{148-154}$Sm in the $\beta - \gamma$ plane. Adapted from Ref. [8].

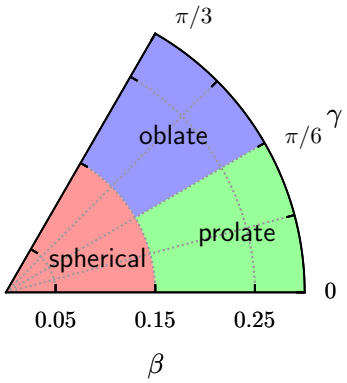

Fig. 3: Spherical, prolate and oblate shape regions in the β-γ plane. Taken from Ref. [8].

is

$$P_{\rm shape}(T) = 4\pi^2 \int_{\rm shape} d\beta\, d\gamma\, \beta^4 |\sin(3\gamma)| P(T,\beta,\gamma)\ . \tag{18}$$

In Fig. 4, we show (for the chain of samarium isotopes $^{148-154}$Sm) $P_{\rm shape}(T)$ as a function of temperature, where "shape" refers to each of the three regions in Fig. 3 (spherical, prolate and oblate) using $\beta_0 = 0.15$.

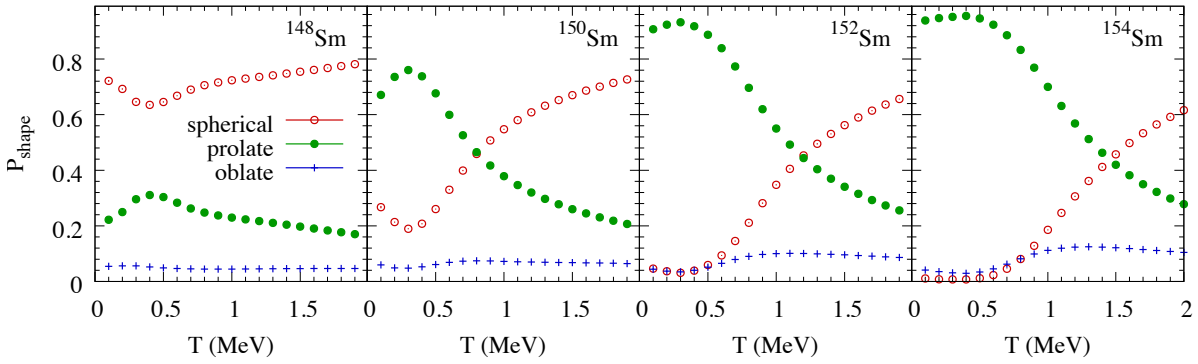

Fig. 4: Shape probabilities $P_{\rm shape}$ versus temperature T for the chain of samarium isotopes $^{148-154}$Sm for each of the three shape regions defined in Fig. 3 (spherical, prolate and oblate). Taken from Ref. [8].

5 State densities versus intrinsic deformation

The shape-dependent partition function $Z(T,\beta,\gamma)$ can be calculated from $P(T,\beta,\gamma)$ using $P(T,\beta,\gamma) = Z(T,\beta,\gamma)/Z(T)$, where $Z(T)$ is the total partition function (which is calculated from the thermal energy $E(T)$ [4]. The shape-dependent state density $\rho(E,\beta,\gamma)$ is the inverse Laplace transform of $Z(T,\beta,\gamma)$

$$\rho(E,\beta,\gamma) = \frac{1}{2\pi i}\int_{-i\infty}^{i\infty} d(1/T)\, e^{E/T} Z(T,\beta,\gamma)\ . \tag{19}$$

We calculate the average shape-dependent state density by evaluating the integral in (19) in the saddle-point approximation. We find

$$\rho(E,\beta,\gamma) \approx \frac{e^{S(T,\beta,\gamma)}}{\sqrt{2\pi T^2 C(T,\beta,\gamma)}}\ , \tag{20}$$

where $S(T,\beta,\gamma) = \ln Z(T,\beta,\gamma) + E/T$ and $C(T,\beta,\gamma) = T\partial S(T,\beta,\gamma)/\partial T$ are, respectively, the shape-dependent entropy and heat capacity. The temperature T in Eq. (20) is determined as a function

of energy E and β, γ using the saddle-point condition $E(T,\beta,\gamma) \equiv T^2 \partial \ln Z(T,\beta,\gamma)/\partial T = E$. The excitation energy is calculated from $E_x = E - E_0$, where E_0 is the ground-state energy.

The partition function $Z(T,\beta,\gamma)$ depends on the Landau parameters a, b, c of Eq. (15). Thus the entropy $S(T,\beta,\gamma)$ depends on the first derivatives of a, b, c with respect to T, while $C(T,\beta,\gamma)$ depends on both the first and second derivatives of a, b, c, with respect to T. In practice we fit cubic splines to describe the temperature dependence of the parameters a, b, c, and use these fits to calculate their derivatives.

In Fig. 5 we show the state densities as a function of excitation energy E_x for the three shape regions, determined by integrating $\rho(E_x,\beta,\gamma)$ over the corresponding shape region [as was done for the shape probability in Eq. (18)].

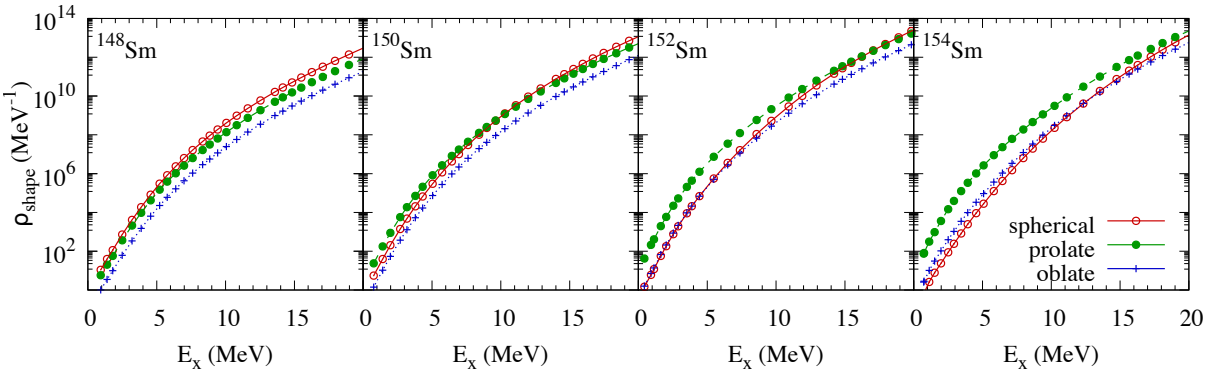

Fig. 5: State densities $\rho_{\rm shape}$ of the three shape regions as a function of E_x for the chain of samarium isotopes $^{148-154}$Sm.

In Fig. 6 we show the ratios $\rho_{\rm shape}(E_x)/\rho(E_x)$ of the shape-dependent density to the total state density for each of the three shape regions. The sum of these three ratios should be 1, a relation satisfied by our calculated shape-dependent densities within the statistical errors (solid lines in Fig. 6). In ^{148}Sm, the spherical shape makes the largest contribution to the total state density although the prolate region has a significant contribution at low energies. In $^{150-154}$Sm, the prolate region dominates at low energies, but as the excitation energy increases the contribution from the spherical region increases and becomes largest above a certain energy whose value is higher for the heavier isotopes in the chain. This is a signature of the thermal shape transition whose transition temperature increases with mass number in the chain of samarium isotopes.

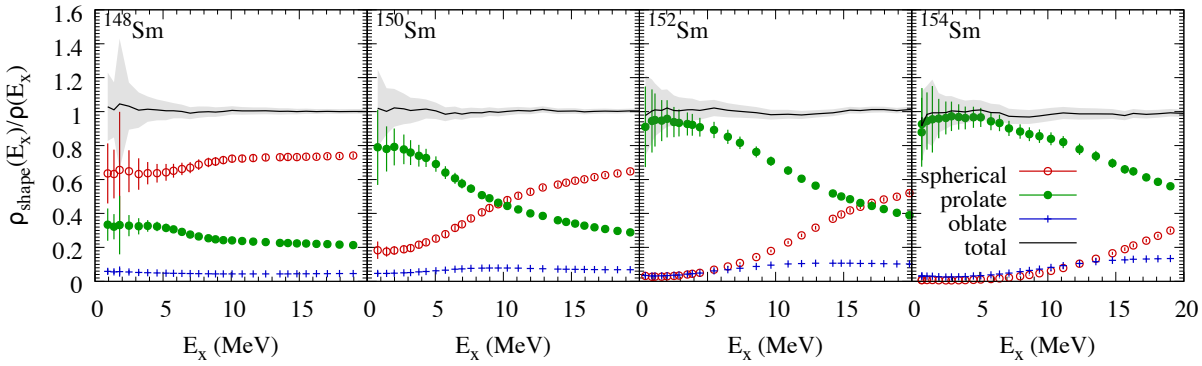

Fig. 6: State density ratios $\rho_{\rm shape}(E_x)/\rho(E_x)$ as a function of E_x for each of the three shape regions and for the chain of samarium isotopes $^{148-154}$Sm. The solid lines describe the sum of the three ratios. Taken from Ref. [8].

6 Conclusion and outlook

We reviewed a recent method we have introduced for calculating the deformation dependence of state densities in the rotationally invariant framework of the spherical CI shell model. The method uses a Landau-like expansion of the logarithm of the shape distribution in quadrupole invariants.

Our method can be generalized to finite-size systems that in the thermodynamic limit undergo a symmetry-breaking phase transition. We would like to determine the distribution of the order parameters that are associated with the phase transition in a framework that preserves the symmetry and without using a mean-field approximation. The main steps of the method consist of (i) calculating the marginal distribution of a subset of the order parameters; (ii) finding the expectation values of low-order combinations of the order parameters that preserve the symmetry; and (iii) expanding the logarithm of the distribution of the order parameters in the invariants constructed in (ii). In the example discussed here, the order parameters are the quadrupole deformation parameters $\alpha_{2\mu}$ which break rotational symmetry in the low-temperature phase.

6.1 Acknowledgements

This work was supported in part by the U.S. DOE grant Nos. DE-FG02-91ER40608 and DE-FG02-00ER411132. The research presented here used resources of the National Energy Research Scientific Computing Center, which is supported by the Office of Science of the U.S. Department of Energy under Contract No. DE-AC02-05CH11231. This work was also supported by the HPC facilities operated by, and the staff of, the Yale Center for Research Computing.

References

[1] G.H. Lang, C.W. Johnson, S.E. Koonin, and W.E. Ormand, Phys. Rev. C **48**, 1518 (1993).

[2] Y. Alhassid, D.J. Dean, S.E. Koonin, G. Lang, and W.E. Ormand, Phys. Rev. Lett. **72**, 613 (1994).

[3] For a recent review, see Y. Alhassid in *Emergent Phenomena in Atomic Nuclei from Large-Scale Modeling: a Symmetry-Guided Perspective*, edited by K. D. Launey (World Scientific, Singapore, 2017), pp. 267-298.

[4] H. Nakada and Y. Alhassid, Phys. Rev. Lett. **79**, 2939 (1997).

[5] Y. Alhassid, S. Liu, and H. Nakada, Phys. Rev. Lett. **83**, 4265 (1999).

[6] Y. Alhassid, L. Fang, and H. Nakada, Phys. Rev. Lett. **101**, 082501 (2008).

[7] C. Özen, Y. Alhassid, and H. Nakada, Phys. Rev. Lett. **110**, 042502 (2013).

[8] M.T. Mustonen, C.N. Gilbreth, Y. Alhassid, , and G.F. Bertsch, Phys. Rev. C **98**, 034317 (2018).

[9] Y. Alhassid, C.N. Gilbreth, and G.F. Bertsch, Phys. Rev. Lett. **113**, 262503 (2014).

[10] C.N. Gilbreth, Y. Alhassid, and G.F. Bertsch, Phys. Rev. C **97**, 014315 (2018).

[11] J. Hubbard, Phys. Rev. Lett. **3**, 77 (1959); R. L. Stratonovich, Dokl. Akad. Nauk SSSR [Sov. Phys. - Dokl.] **115**, 1097 (1957).

[12] W.E. Ormand, D.J. Dean, C.W. Johnson, G.H. Lang, and S.E. Koonin, Phys. Rev. C **49**, 1422 (1994).

[13] A.L. Goodman, Nucl. Phys. **A352**, 30 (1981).

[14] K. Tanabe, K. Sugawara-Tanabe, and H.J. Mang, Nucl. Phys. **A357** 20 (1981).

[15] K. Kumar, Phys. Rev. Lett. **28**, 249 (1972).

[16] D. Cline, Ann. Rev. Nucl. Part. Sci. **36**, 683 (1986).

[17] K. Hadyńska-Klek *et al.*, Phys. Rev. Lett. **117**, 062501 (2016).

[18] T. Schmidt, K. L. G. Heyde, A. Blazhev, and J. Jolie, Phys. Rev. C **96**, 014302 (2017).

[19] S. Levit and Y. Alhassid, Nucl. Phys. A **413**, 439 (1984).

[20] Y. Alhassid, S. Levit, and J. Zingman, Phys. Rev. Lett. **57**, 539 (1986).

Microscopic calculations of nuclear level densities with the Lanczos method

B. A. Brown[1] *and W. E. Ormand*[2]
[1] Department of Physics and the National Superconducting Cyclotron Laboratory,
Michigan State University, East Lansing, MI 42284-1321, USA
[2] Lawrence Livermore National Laboratory, P.O. Box 808, L-414, Livermore, California 94551, USA

Abstract

A new method for computing the density of states in nuclei using an extrapolated form for the tri-diagonal matrix obtained from the Lanczos method is presented. This can be applied to configuration-interaction calculations with fully realistic nuclear Hamiltonians that are known to provide an excellent description of the low-lying structure of nuclei. This extrapolated Lanczos matrix (ELM) approach provides an accurate computation of the density of states up to the neutron separation energy for states that lie within the configuration space. Comparisons between theory and experiment for the average level density for p-wave resonances for iron isotopes using the $1p-0f$-shell model space and realistic nuclear Hamiltonians are shown. Also we show results for J-dependence of the level density and the total level density for negative-parity states.

The density of states is a fundamental property of nuclear structure that plays an important role in nuclear reactions. Of particular importance is the radiative capture of neutrons on short-lived nuclei, which through the r-process [1] in supernovae and neutron-star mergers [2], are thought to be responsible for the synthesis of the elements heavier than iron. Ideally, these reactions can be measured or constrained by experiment. Unfortunately, in most cases, the target nuclei are so short lived that direct measurement is infeasible, and the only alternatives are to rely on theoretical calculations or on indirect measurements, such as surrogates [3], which themselves reliant on theoretical input. Theoretical modeling requires an in-depth, and accurate description of the reaction processes, and in particular the density of states at or near the neutron decay threshold.

We report on a new microscopic framework to provide an accurate estimate of the level density for a variety of nuclei using an extension of the configuration-interaction approach with fully realistic nuclear Hamiltonians that are known to provide an excellent description of the low-lying structure of nuclei. We will exploit a universal property of the Lanczos algorithm, which will allow us to extrapolate the tri-diagonal Lanczos matrix elements beyond what is computationally viable, to accurately estimate the density of states within the shell-model configuration space. We demonstrate that the information needed to perform the extrapolation can be extracted from just the lowest 100 Lanczos iterations, thus, leading to a computationally efficient way to compute the density of states.

The principal goal behind nuclear-structure models is to find energy eigenvalues and wave functions for the nuclear Hamiltonian within a well-defined Hilbert space. The nuclear shell model starts with a set of N many-body Slater determinants, $\mid \psi_i\rangle$, spanning the space to expand the full solution, i.e., $\mid \Psi\rangle = \sum_i c_i \mid \psi_i\rangle$. The coefficients c_i are found by computing the matrix element $H_{ji} = \langle \psi_j \mid H \mid \psi_i\rangle$ and diagonalizing the resulting symmetric matrix. One of the most effective methods to find the eigenvalues is the Lanczos algorithm [4], which starts with an arbitrary vector $\mid v_1\rangle$ in the Hilbert space, and through successive operations of $\hat{H}$, H_{ji} is reduced to tri-diagonal form with diagonal matrix elements, α, and symmetric off-diagonal matrix elements, β. The energies and observables do not depend on the signs of the β and they can be taken as positive.

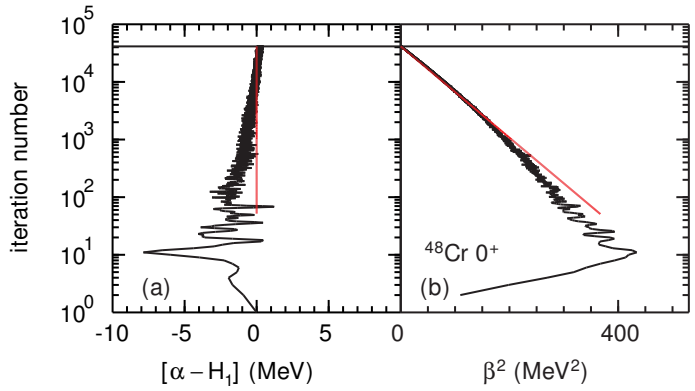

Fig. 1: TDME for ^{48}Cr, $J = 0^+$, is the pf model space. The black lines are the results of the exact calculation. The red lines correspond to the simplest approximation given by $\alpha_i = H_1$ and $\beta_i^2 = -(\sigma^2/2)z_i$.

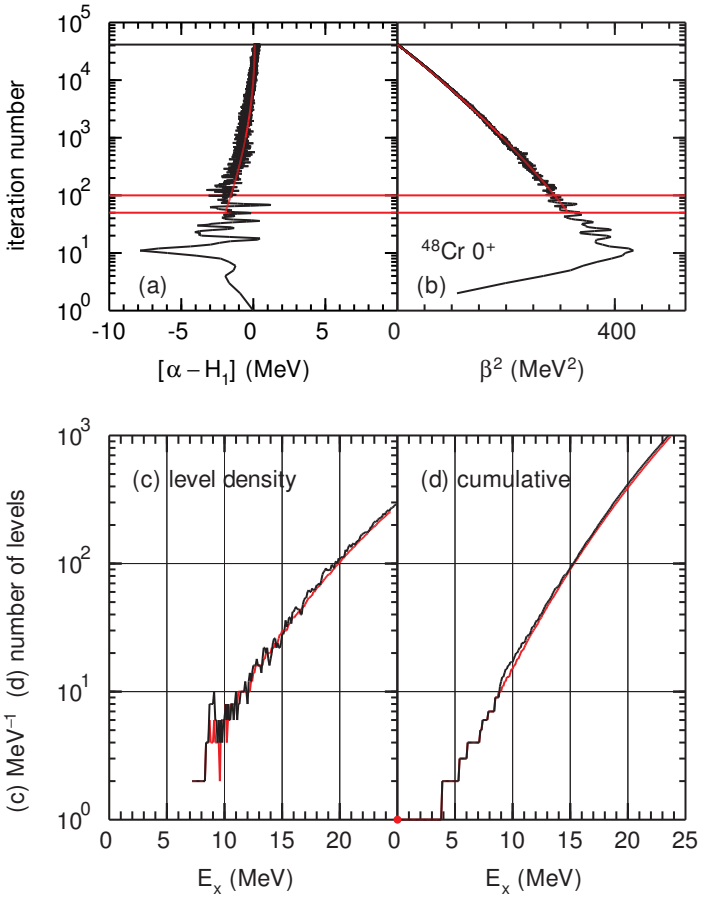

Fig. 2: (top) Tri-diagonal matrix elements (TDME) for ^{48}Cr, $J = 0^+$, in the pf model space. The black lines are the results of the exact calculations (same as in Fig. 1). The red lines are based on the ELM(100). (bottom) Level density with the exact calculation (black) compared to ELM(100) approximation (red).

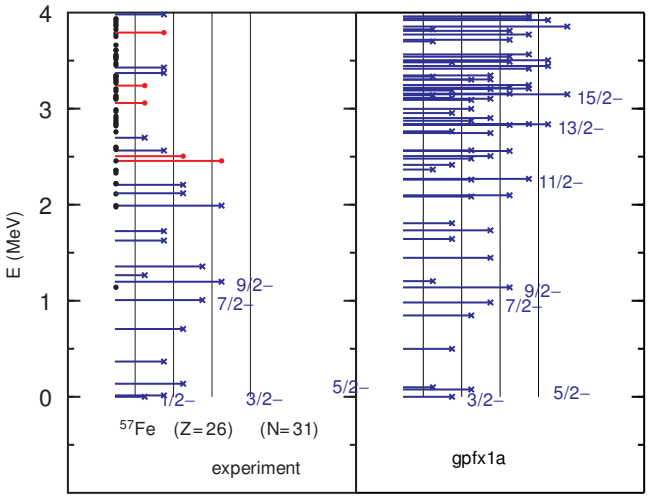

Fig. 3: Levels up to 3 MeV in excitation obtained with the GPFX1A Hamiltonian in the full pf model space are shown in the right-hand side. The length of each line indicates the J value. These are compared with the experimental energies from NNDC on the left-hand side. The blue lines are states with negative parity, and the red line are states with positive parity. If the spin-parity is uncertain it is shown as a black circle on the y axis.

Of particular interest is the behavior of the tri-diagonal matrix elements (TDME) with increasing iterations. The results for ^{48}Cr are shown in Fig. 1. After several iterations, the diagonal elements, α_i, are roughly constant and nearly equal to the first moment $H_1 = \mathrm{Tr}[\hat{H}] = (1/N_{dim}) \sum_i H_{ii}$, where N_{dim} is the matrix dimension. At the same time, the off-diagonal elements, β_i, generally decrease to zero as $i \rightarrow N_{dim}$, and exhibit a Gaussian-like behavior $\beta_i = \sqrt{-(\sigma^2/2)\ln(i/N_{dim})}$ [6]. We rewrite this as $\beta_i^2 = b_1 z_i$, where

$$z_i = \ln(i/N_{dim}) \tag{1}$$

and $b_1 = -(\sigma^2/2)$ and i is the iteration number. Thus, as in Fig. 1, when i is plotted on a log scale vs β_i^2 the results are close to a straight line for large i values.

At its core, the Lanczos algorithm is a moment method; efficiently computing $2n$ moments of $\hat{H}$ with respect to $\mid v_1\rangle$ after n iterations. With $\mid v_1\rangle = (1/\sqrt{N_{dim}}) \sum_i \phi_i \mid \psi_i\rangle$, where ϕ_i is a random phase, we have

$$\alpha_1 = \frac{1}{N_{dim}} \sum_i H_{ii} + \sum_{i \neq j} \frac{\phi_i \phi_j}{N_{dim}} H_{ji}. \tag{2}$$

Thus, moments of $\hat{H}$ can be computed stochastically by selecting several random initial pivots and averaging. We find that for most cases with large N_{dim}, the remainder in Eq. 1 is generally small and of the order 1 keV. Under this condition, good estimates for the first two moments of $\hat{H}$ can be extracted from just the first Lanczos iteration, namely

$$H_1 \approx \alpha_1 \quad \text{and} \quad M_2 = \sigma^2 \approx \beta_1^2 \tag{3}$$

As an example, we consider the exact results for ^{48}Cr, $J^\pi = 0^+$, obtained in the proton-neutron pf basis. The states contain all possible values of isospin T. The dimension is $N_{dim} = 41,355$. The calculations were carried with the NuShellX [7] code, and with GPFX1A Hamiltonian [8]. The results for the exact results for the TDME for are shown in Fig. 1. They are compared with extrapolations based on $\alpha_i = H_1$ and $\beta_i^2 = -2M_2 z_i$. They give an approximation to the exact results above about 1000 iterations.

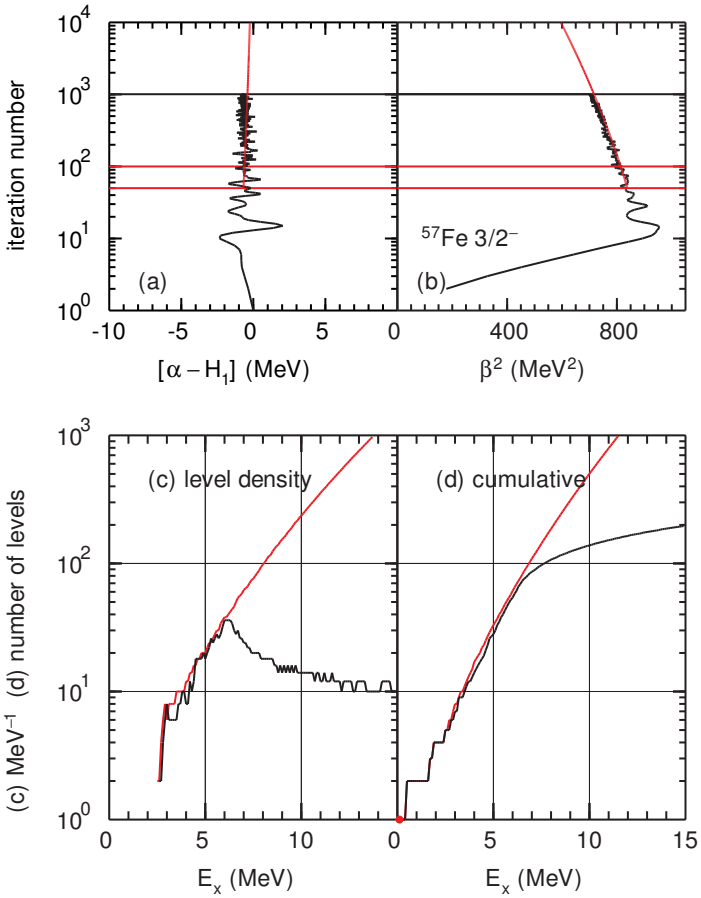

Fig. 4: (top) TDME for ^{57}Fe, $J^\pi = 3/2^-$ in the pf model space. The black lines are the results of the exact calculations. The red lines are based on the ELM(100). (bottom) Level density with the exact calculation (black) compared to ELM(100) approximation (red).

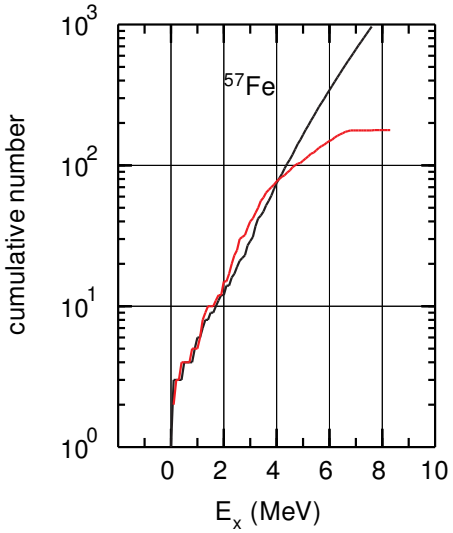

Fig. 5: The cumulative number of levels in ^{57}Fe. The theoretical results for negative-parity states are shown by the black line. The experimental data from NNDC for all levels (both parity) is shown by the red line.

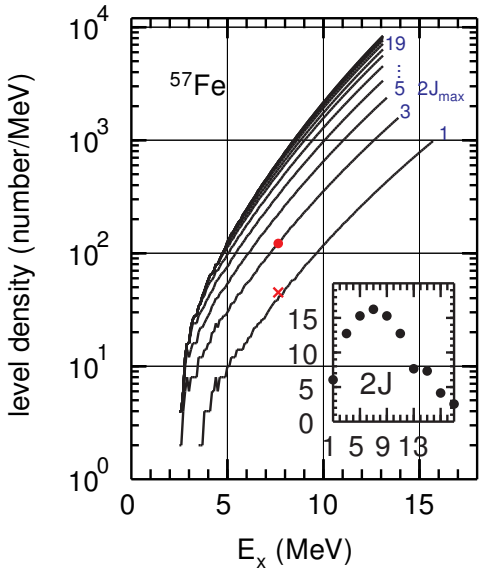

Fig. 6: Level density for negative parity states calculated for ^{57}Fe. The lines show the cumulative level density up to the value of $2J_{max}$ as indicated on the right-hand side. The red dot is the ℓ=1 experimental value for $J_{max} = 3/2^-$ at the neutron separation energy of $E_x = S_n = 7.65$ MeV [5]. The inset shows the percentage contribution to the total level density at S_n for each J. The red cross is the ℓ=0 experimental value for $J_{max} = 1/2^+$ [5].

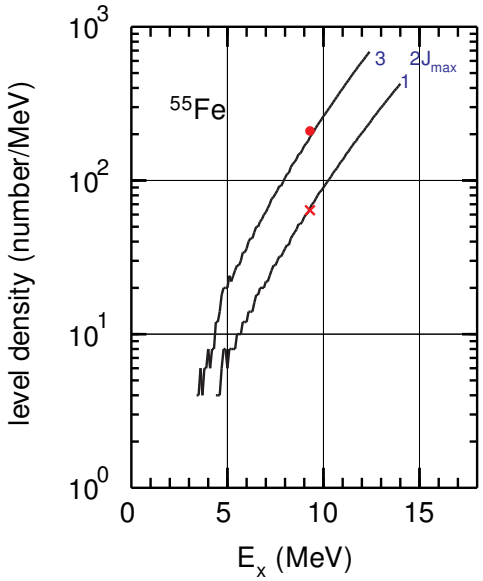

Fig. 7: Level density for negative parity states calculated for ^{55}Fe up to $J_{max} = 3/2^-$. The lines show the cumulative level density up to the value of $2J_{max}$ as indicated on the right-hand side. The red dot is the ℓ=1 experimental value [5] for $J_{max} = 3/2^-$ at the neutron separation energy. The red cross is the ℓ=0 experimental value [5] for $J_{max} = 1/2^+$.

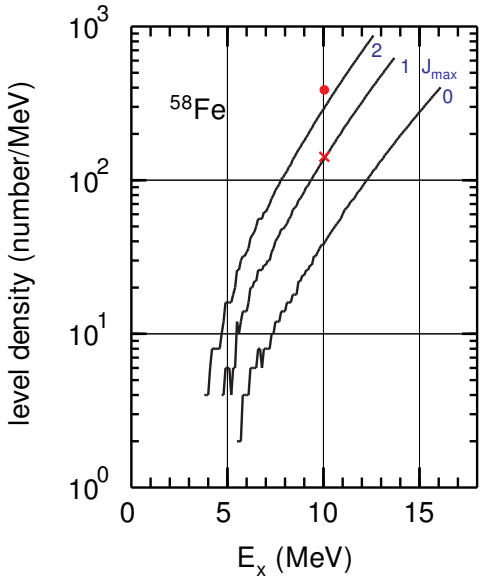

Fig. 8: Level density for positive parity states calculated for ^{58}Fe up to $J_{max} = 2$. The lines show the cumulative level density up to the value of J_{max} as indicated on the right-hand side. The red dot is the ℓ=1 experimental value [5] for $J_{max} = 2^+$ at the neutron separation energy. The red cross is the ℓ=0 experimental value [5] for $J_{max} = 1^-$.

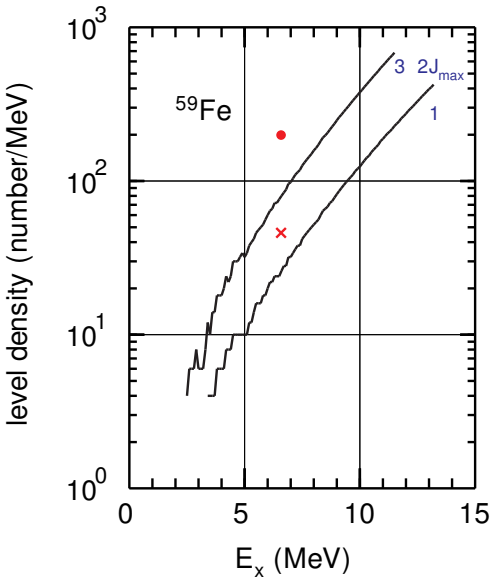

Fig. 9: Level density for negative parity states calculated for ^{57}Fe up to $2J_{max} = 3$. The lines show the cumulative level density up to the value of $2J_{max}$ as indicated on the right-hand side. The red dot is the ℓ=1 experimental value [5] for $J_{max} = 3/2^-$ at the neutron separation energy. The red cross is the ℓ=0 experimental value [5] for $J_{max} = 1/2^+$.

The next step is to improve the extrapolation by adding adding higher polynomials in z_i. There are several options for this, but based on the comparison to the exact calculations we propose

$$\alpha_i = a_0 + a_2\, z_i^2 \quad \text{and} \quad \beta_i^2 = b_1\, z_i + b_2\, z_i^2. \tag{4}$$

The first and second moments from these equations are

$$H_1 = a_0 + 2a_2 \quad \text{and} \quad M_2 = -2b_1 + 4b_2 \tag{5}$$

(the contribution of a_2 to M_2 can be neglected). From the exact results in Fig. 1 one observes that the coefficients of the two extra terms can be obtained from the exact calculation in the region around $i_f = 75$. We calculate the average $< \alpha >$ and $< \beta^2 >$ over the interval of iterations from 50 to 100. Then from the equations

$$\alpha_1 = a_0 + 2a_2 \quad \text{and} \quad < \alpha > = a_0 + a_2\, z_f^2, \tag{6}$$

we obtain a_0 and a_2. And from the equations

$$\beta_1^2 = -2b_1 + 4b_2 \quad \text{and} \quad < \beta^2 > = b_1\, z_f + b_2\, z_f^2, \tag{7}$$

we obtain b_1 and b_2. The results for ^{48}Cr are shown in Fig. 2. Our extrapolated Lanzcos matrix method, ELM(i_c), is to use the exact TDME up to some value i_c, and then to use the extrapolations based on the ELM above i_c. This large tri-diagonal matrix is then diagaonalized to obtain an approximation for the energies. For example, if we want 1000 energies in the approximation we need to diagonalize the ELM with a dimension of about dimension of about 15,000. The results for ELM(100) for the level density of ^{48}Cr are shown in the bottom of Fig. 2 and compared to the exact results. The agreement between the two is excellent.

Next we consider the case of ^{57}Fe. The NuShellX code is usually used with a Hamiltonian such as GPFX1A to study the low lying states. In full pf shell basis all states have negative parity and the M-scheme dimension is 455,078,656. In the proton-neutron basis of NuShellX this M-scheme dimension is divided among J-scheme dimensions for all possible J values. For the study of low-lying states one typically needs to have converged eigenvectors for the lowest 10 states and this requires about 150 Lanczos iterations for each J. The low-lying level scheme obtained from this calculation is compared to experiment in Fig. 3. There is a good agreement with theory with known negative parity states. The positive parity states start with the 9/2$^+$ at 2.46 MeV.

Our goal with the ELM method is to use the information obtained during the calculation for 10 converged low-lying states for each J value to make an extrapolation for the level density for up to several thousand states. We consider the case for $J^\pi = 3/2^-$ with a dimension of $N_{dim} = 25,743,302$. In order to compare the ELM method with a more complete calculation, we carried out about 1000 iterations. The results are shown in Fig. 4, where the TDME for the 1000 iterations (black) is compared to the ELM(100) approximation (red). The black line in the bottom panel shows the result of diagonalizing the TDME with a dimension of 1000. It shows the expected result that about 70 levels are converged in energy. Above that, the states no longer increase in density, but become equally spaced (the "picket-fence" type spacing). The ELM(100) level density follows the exact result up to about 70, but after that it continues to increase nearly exponentially.

We can compare the level density to experiment in two ways. First for the cumulative number of levels. The theoretical results are compared to experiment in Fig. 5. As expected, the theory and experiment agree well up to about 2 MeV. From 2-4 MeV there are more levels in experiment. That can be interpreted as the extra contribution of positive parity states. Above 6 MeV the experimental level information is incomplete and the data fall off compared to the theory.

The other type of information is from the level densities for resonances with ℓ=0 and ℓ=1 obtained from neutron scattering experiments for energies near the one-neutron separation energy. The experimental values for the level spacing D_0 (ℓ=0) and D_1 (ℓ=1) are given in [5]. These are used to obtain the

average level density, $\rho_\ell = 1/D_\ell$. For ^{55,57,59}Fe the neutron targets of ^{54,56,58}Fe have $J_i = 0^+$, and the ℓ=1 final states are 1/2$^-$ ($p_{1/2}$) and 3/2$^-$ ($p_{3/2}$). For ^{58}Fe the neutron target of ^{57}Fe has $J_i = 1/2^-$, and the ℓ=1 final states are (0,1,2)$^+$.

The level density in ^{57}Fe for all J^- states up to 19/2$^-$ is shown in Fig. 6. The contribution to the level density up to 15 MeV for higher J values is negligible. The calculation is in perfect agreement with the experimental value [5] for $J_{max} = 3/2^-$ at $E_x = S_n = 7.65$ MeV (red circle). The results for states reached by ℓ=1 are shown for ^{55}Fe (Fig. 7), ^{58}Fe (Fig. 8), and ^{59}Fe (Fig. 9). The comparison with experiment [5] for ℓ=1 resonances is excellent for ^{55,57,58}Fe. For ^{59}Fe the experimental level density for ℓ=1 at $S_n = 6.58$ MeV is about a factor of three larger than that calculated. If the experiment is correct, it indicates that model space must be expanded to include the the neutron $0g_{9/2}$ orbital. For all nuclei at higher excitation energy, the experimental level density for negative-parity states must become larger than that calculated due to the truncation to the pf model space.

For ^{57}Fe, experimental ℓ=0 level density for 1/2$^+$ states (red cross) [5] is close to the calculated level density value for the 1/2$^-$ states. This indicates that the parity ratio for the level density at this excitation energy is near unity at $E_x = 7.65$ MeV. This information together with that in Fig. 5 indicates that the positive to negative parity level density ratio increases from zero at low excitation energy to about one at $E_x = 7.65$ MeV.

The calculation for the 1/2$^+$ level density must take into account particle and hole excitations beyond the pf model space. For example, for ^{57}Fe we should consider the coupling of the $\nu(0g_{9/2})$ particle orbital to the calculated level density of (4,5)$^+$ states of ^{56}Fe, and the coupling of $\pi(0d_{3/2}, 1s_{1/2})$ hole orbitals to the calculated level density of (0,1,2,3)$^+$ states of ^{58}Co. This is a possible future extension.

Another extension of this work will be to consider the constraints on the polynomial expansion coefficients of Eq. 4 based upon higher moments from α_2, α_3, β_2 .... There will be many applications of this new method with regard to comparison with experimental data and other level density models. We can compare our result to those of the moments method [9] to constrain the eta parameter in that model.

Acknowledgments This work is partly supported by NSF grant PHY-1811855, and under the auspices of the U.S. Department of Energy by Lawrence Livermore National Laboratory under Contract DE-AC52-07NA27344

References

[1] M. Burbidge, G. Burbidge, W. Fowler, and F. Hoyle, Rev. Mod. Phys. 29, 547 (1957).

[2] D. Kasen, B. Metzger, J. Barnes, E. Quataert, and E. Ramirez-Ruiz, Nature Vol. **551**, 80 (2017).

[3] J. E. Escher, J. T. Burke, F. S. Dietrich, N. D. Scielzo, I. J. Thompson, W. Younes, Rev. Mod. Phys. **84**, 353 (2012).

[4] C. Lanczos, J. Res. Nat. Bur. Stand. **45**, 252 (1950); J. H. Wilkinson, *The Algebraic Eigenvalue Problem*, (Clarendon, Oxford, 1965).

[5] Atlas of Neutron Resonances Volume 1: Resonance Properties and Thermal Cross Sections Z= 1-60 by Said F. Mughabghab, Elsevier (2018) (doi.org/10.1016/B978-0-44-463769-7.00001-4).

[6] A.P. Zuker, L. Waha Ndeuna, F. Nowacki, and E. Caurier, Phys. Rev. C bf 64, 021394(R) (2001); E. Caurier, G. Martinez-Pinedo, F. Nowacki, A. Poves, A.P. Zuker, rev. Mod. Phys. **77**, 427 (2005).

[7] B. A. Brown and W. D. M. Rae, Nuclear Data Sheets **120**, 115 (2014).

[8] M. Honma, T. Otsuka, B.A. Brown and T. Mizusaki, Euro. Phys. Jour. A **25** Suppl. 1, 499 (2005).

[9] R. A. Sen'kov and M. Horoi, Phys. Rev. C **82**, 024304 (2010); R. A. Sen'kov, M. Horoi, and V. G. Zelivinsky, Comp. Phys. Comm. **184**, 215 (2013).

Analytical expression and neural network study of the symmetry energy

Jorge A. López and Jorge A. Muñoz
University of Texas at El Paso, El Paso, Texas, USA

Abstract
Motivated by classical molecular dynamics simulations of infinite nuclear systems with varying density, temperature and isospin content, an analytical expression that approximates the symmetry energy at subcritical densities is obtained. Similarly a neural network is used to evaluate E_{Sym} in the same temperature-density regime. The resulting expression and neural network can both be used to calculate the symmetry energy at a given density and temperature or, conversely, to extract the temperature of experimental data.

1 Introduction

The symmetry energy, E_{Sym}, relates the variation of the energy per nucleon to the proton-to-neutron ratio, and it is an important quantity in nuclear structure, reactions, equation of state, astrophysical processes, etc. [1, 2]. Although E_{Sym} has been studied mostly using mean-field approaches [1], it is known that at subsaturation densities its value is affected by the formation of clusters [3]. Some studies have introduced clusters into mean field theories through simplifying assumptions [4–6], or with thermal models [7], or other approaches [3], but none of these methods are fully satisfactory. In recent works [8,9] a model based on classical molecular dynamics (CMD) that is able to reproduce phase transitions, was used to study E_{Sym} in the low density regions where the liquid and gaseous phases coexist.

In such study, CMD data of the nuclear internal energy, $E(T, \rho, \alpha)$, were obtained from simulations of infinite nuclear systems at varying values of the density (ρ), temperatures (T) and isospin content ($\alpha = (N - Z)/(N + Z)$), and used to extract $E_{Sym}(T, \rho)$. At low densities the symmetry energy was found to have a good agreement with experimental observations [3, 10, 11] of $E_{sym} \approx 5$ to 10 MeV as $\rho \to 0$, corroborating the Natowitz conjecture [3] which argued against the mean field results [12] of $E_{sym} \to 0$ in such density region.

The present work uses the results of [8] to obtain an analytical expression and construct a neural network algorithm to evaluate $E_{Sym}(T, \rho)$ at subsaturation densities and warm temperatures.

2 Classical molecular dynamics

The present CMD has been used to study reactions, critical phenomena, neutron-rich nuclei (isoscaling and neutron star crusts) and, of course, phase changes, clusterization and symmetry energy [13], all without any adjustable parameters [14–21].

The CMD model treats nucleons as point particles interacting through two body potentials [22]. The resulting medium has a saturation density of $\rho_0 = 0.16$ fm^{-3}, binding energy $E(\rho_0) = -16$ MeV/A and compressibility of 250 MeV. To study "infinite" systems, 2000 nucleons were placed in a cubic cell under periodic boundary conditions, with isospin contents of $x = Z/A =$ 0.3, 0.4, and 0.5, densities from 0.01 to 0.2 fm^{-3}, and temperatures between $T =$1 and 5 MeV. For each set of values of $\{T, \rho, x\}$ the systems were thermalized, and the internal energy was averaged over 200 statistically independent times of a Markov chain. The CMD code used was developed at Los Alamos National Laboratory [23].

Fig. 1 shows the energy versus density at $T = 1$ and 5 MeV and $x =$0.3, 0.4 and 0.5. The liquid phase of the medium corresponds to the "$\cup$" shape, the saturation density is the minima of the energy curves, and the liquid-gas coexistence region is the lower density region where the points separate from the "$\cup$" curve (less noticeable at high temperatures). These points are the ones used to obtain the symmetry energy.

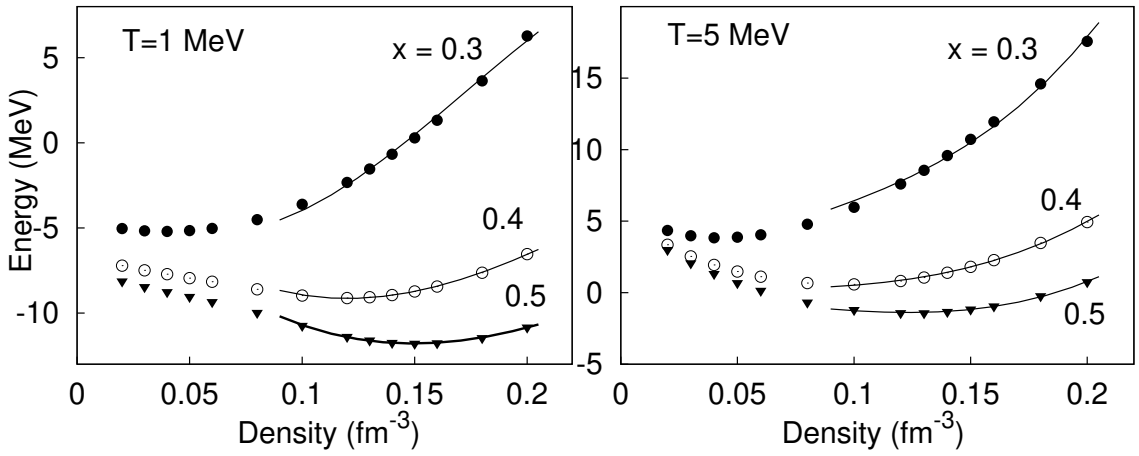

Fig. 1: Energy per nucleon versus density for systems with different isospin content at two temperatures. The lines pretend to delineate the ∪ curves that denote the liquid phase.

T (MeV)	E_{02}	E_{12}	E_{22}	E_{32}
1	28.2803	-349.243	6029.93	-13241.5
2	10.8479	-36.8188	4101.04	-9321.43
3	6.37652	88.9445	2966.63	-6241.85
4	2.92684	189.568	2040.28	-3654.5
5	2.73406	192.057	2055.3	-3875.61

Table 1: Symmetry energy coefficients.

3 Symmetry energy

The symmetry energy is the change of the binding energy as the ratio of protons and neutrons varies, it is defined as

$$E_{Sym}(\rho,T) = \frac{1}{2!}\left[\partial^2 E(\rho,T,\alpha)/\partial\alpha^2\right]_{\alpha=0}, \tag{1}$$

where, again, $\alpha = (N-Z)/(N+Z) = 1-2x$. As explained in [13], the procedure to obtain E_{Sym} from CMD data involves obtaining a fit of the internal energy of the type

$$E(T,\rho,\alpha) = E_0(T,\alpha) + E_1(T,\alpha)\rho + E_2(T,\alpha)\rho^2 + E_3(T,\alpha)\rho^3. \tag{2}$$

Figure 2 shows an example of such fit. The isospin dependence of the coefficients $E_0(T,\alpha)$, $E_1(T,\alpha)$, $E_2(T,\alpha)$, $E_3(T,\alpha)$ can be extracted from the CMD data assuming a functional dependence on α of the type

$$E_i(T,\alpha) = E_{i0}(T) + E_{i2}(T)\alpha^2 + E_{i4}(T)\alpha^4 \tag{3}$$

for $i = 0$, 1, 2 and 3 (notice that the odd terms in α are excluded to respect the isospin symmetry of the strong force). The behavior of these coefficients with respect to α was presented in Ref. [8], and the curves of $E_0(T,\alpha)$, $E_1(T,\alpha)$, $E_2(T,\alpha)$, $E_3(T,\alpha)$ are reproduced in Figures 3 for completeness.

Then, the symmetry energy is given by

$$E_{Sym}(T,\rho) = E_{02}(T) + E_{12}(T)\rho + E_{22}(T)\rho^2 + E_{32}(T)\rho^3, \tag{4}$$

with the coefficients $E_{02}(T)$, $E_{12}(T)$, $E_{22}(T)$, and $E_{32}(T)$ given in Table 1. Figure 4 shows the symmetry energy in the low density region and its comparison to experimental data [3, 10, 11].

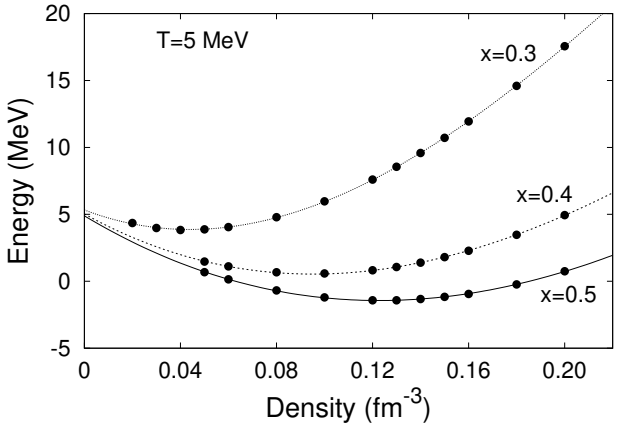

Fig. 2: Fits of the energy of the type of Eq. (2).

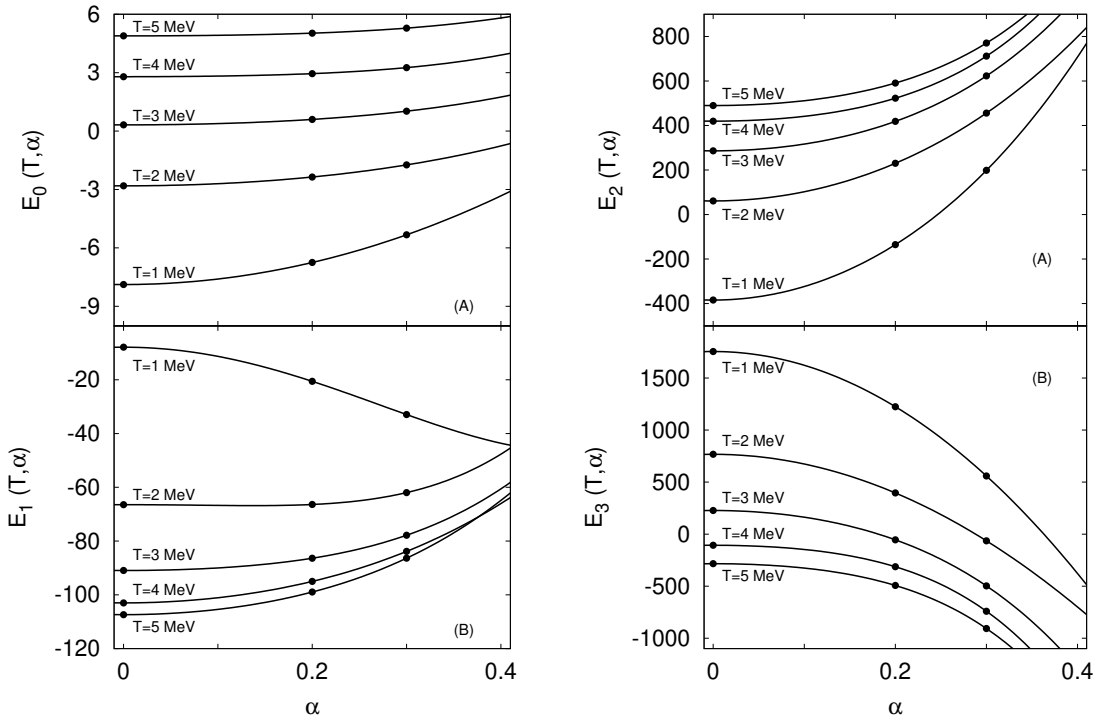

Fig. 3: Coefficients $E_0(T,\alpha)$, $E_1(T,\alpha)$, $E_2(T,\alpha)$ and $E_3(T,\alpha)$ as a function of α at various temperatures. The curves are the fits according to Eq. (3)

Notice that the experimental values of symmetry energy, which are known to correspond to temperatures between 3 and 11 MeV [3, 10, 11, 24], lie on the appropriate range of temperatures of the CMD results; these results corroborate the conjecture of Natowitz et al [3].

4 An analytical expression of E_{Sym}

A mathematical formula for $E_{Sym}(T,\rho)$ can be obtained from the previous results by finding fits of $E_{02}(T)$, $E_{12}(T)$, $E_{22}(T)$, and $E_{32}(T)$ to the coefficients of Table 1. Figure 5 shows the values of E_{02},

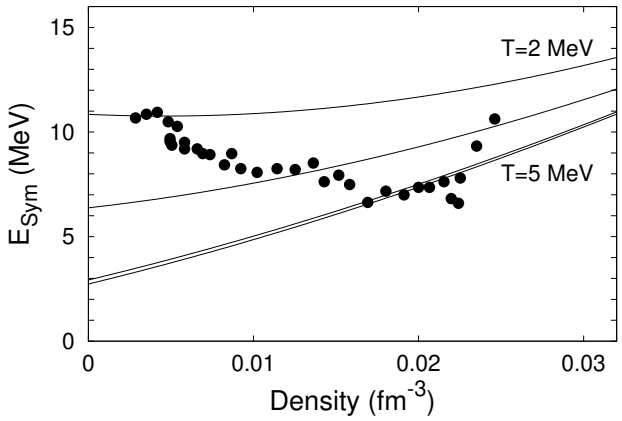

Fig. 4: Symmetry energy from CMD for $T = 2$, 3, 4 and 5 MeV and experimental data [3, 10, 11].

i	E_{i20}	E_{i21}	E_{i22}	E_{i23}
0	13.915	2.6602	- 2.842	0.3725
1	- 71.786	- 127.7	96.922	-12.166
2	4060.8	1523.1	- 995.93	122.22
3	- 7692.4	- 5726.8	3228.2	-386.04

Table 2: Coefficients of the temperature fit of Eq. (4) (cf. Fig. 5).

E_{12}, E_{22}, and E_{32} obtained from the CMD data for $T = 2$, 3, 4 and 5 MeV, and fits of the form

$$E_{i2}(T) = E_{i20} + E_{i21}T + E_{i22}T^2 + E_{i23}T^3, \tag{5}$$

where $i = 0$, 1, 2, and 3. Notice that the $T = 1$ MeV data was not included since the experimental data falls between the curves of $T = 2$ and 5 MeV. With such fits and the coefficients listed in Table 2, the analytical approximation to the symmetry energy at subsaturation densities and temperatures in the range $2\ MeV \leq T \leq 5\ MeV$ is

$$\begin{aligned} E_{Sym}(T,\rho) &= E_{020} + E_{021}T + E_{022}T^2 + E_{023}T^3 + (E_{120} + E_{121}T + E_{122}T^2 + E_{123}T^3)\rho \\ &+ (E_{220} + E_{221}T + E_{222}T^2 + E_{223}T^3)\rho^2 + (E_{320} + E_{321}T + E_{322}T^2 + E_{323}T^3)\rho^3, \end{aligned} \tag{6}$$

Furthermore, the symmetry energy parameters L, K_{Sym}, and Q_{Sym} [25] can also be calculated as

$$L = 3\rho_0(dE_{Sym}/d\rho)_{\rho_0} = 3\rho_0(E_{12} + 2E_{22}\rho_0 + 3E_{32}{\rho_0}^2) \tag{7}$$

$$K_{Sym} = 9{\rho_0}^2(d^2E_{Sym}/d\rho^2)_{\rho_0} = 9{\rho_0}^2(2E_{22} + 6E_{32}\rho_0) \tag{8}$$

$$Q_{Sym} = 27{\rho_0}^3(d^3E_{Sym}/d\rho^3)_{\rho_0} = 162{\rho_0}^3E_{32} \tag{9}$$

5 Neural networks analysis of E_{Sym}

Since the CMD data of $E(\rho, T, \alpha)$ needed to obtain E_{Sym} is computationally expensive to generate, a neural network was trained to perform a multivariate interpolation of E_{Sym}. Neural networks are not in general physically interpretable, but they can approximate any smooth function to arbitrary accuracy [26], and the size of the networks required to approximate multivariate polynomials is bounded by the complexity of the polynomial [27].

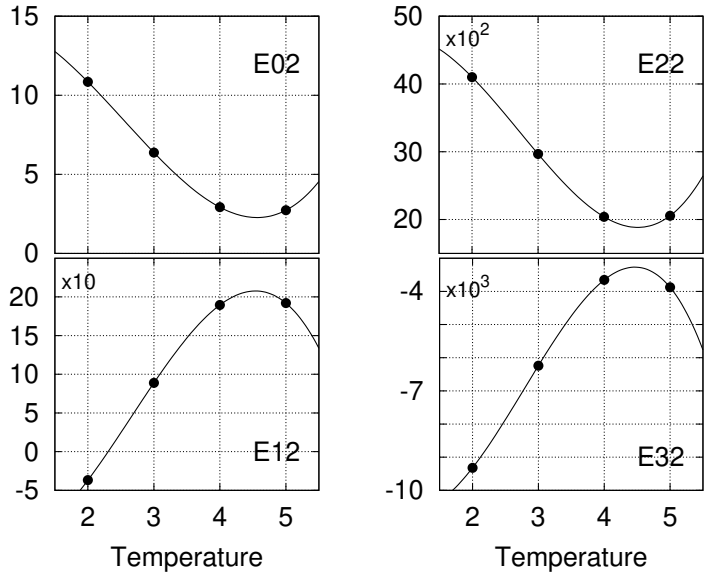

Fig. 5: Values of E_{02}, E_{12}, E_{22}, and E_{32} obtained from CMD data, and cubic fits of Eq. (5).

A dataset was generated using the coefficients in Table 1 for $T = 1$ to 5 MeV, and densities $0 \leq \rho \leq 0.16$ fm^{-3} in steps of 0.01 fm^{-3}, and was used to train a fully connected, feed-forward neural network with two hidden layers and 50 neurons in each hidden layer. The hyperbolic tangent was used as the activation function, and Monte Carlo cross-validation for model selection and parameter tuning, with 80% of the data randomly assigned to the train dataset and 20% to the test dataset. The architecture with two hidden layers resulted in better models than the one with one hidden layer, which is expected for nonlinear systems [28]. The package scikit-learn [29] was used for the regressor, which optimized the squared-loss using the limited-memory Broyden-Fletcher-Goldfarb-Shanno ("lbfgs") algorithm. Defaults were used for all other hyperparameters. Figure 6 shows the resulting $3D$ plot of E_{Sym}.

6 Concluding remarks

CMD data from simulations of infinite nuclear systems were used to extract analytical expressions of the symmetry energy. The range of validity of Eqs. (6) - (9) is at subcritical densities, $0 \leq \rho \leq 0.16\, fm^{-3}$, and warm temperatures, $2 \leq T \leq 5$ Mev. Conversely, expression (6) can also be used to infer the temperature achieved in a reaction from the values of density and E_{Sym}, task specially simple using the *Solve* command in *Mathematica*. Finally, a neural network was trained to approximate E_{Sym}, and its results show agreement with the CMD results, experimental data, and analytical expression Eq. (6).

References

[1] B.A. Li, L.W. Chen and C.M. Ko, Phys. Rep. **464**, 113 (2008).

[2] B.A. Li, A. Ramos, G. Verde, and I. Vidana, Eds., Eur. Phys. J. **A 50**, 39 (2014).

[3] K. Hagel, J.B. Natowitz and G. Röpke, Eur. Phys. J. **A 50**, 39 (2014)

[4] M. Hempel, et al., Nucl. Phys. **A837**, 210 (2010).

[5] C.J. Horowitz, A. Schwenk, Nucl. Phys. **A 776**, 55 (2006).

[6] M. Hempel, K. Hagel, J. Natowitz, G. Röpke, and S. Type, Phys. Rev. **C91**, 045805 (2015).

[7] B.K. Agrawal, J.N. De, S.K. Samaddar, M. Centelles, and X. Viñas, Eur. Phys. J. **A50**, 19 (2014).

[8] J.A. López and S. Terrazas Porras, Nuc. Phys. **A 957** 312 (2017).

[9] C. Dorso, G. Frank, and J. López, Nuc. Phys. **A 978**, 35 (2018).

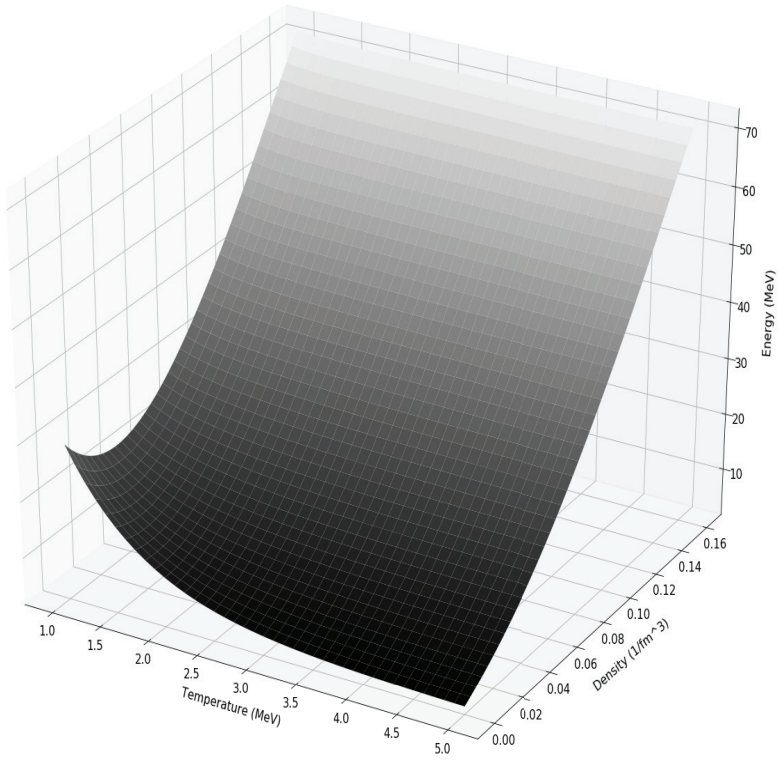

Fig. 6: E_{Sym} obtained from neural network.

[10] S. Kowalski, et al., Phys. Rev. **C 75**, 014601 (2007).

[11] R. Wada, et al., Phys. Rev. **C 85**, 064618 (2012).

[12] L.W. Chen, C.M. Ko and B.A. Li, Phys. Rev. **C76**, 054316 (2007).

[13] J.A. López, E. Ramírez-Homs, R. González, and R. Ravelo Phys. Rev. **C89**, 024611 (2014).

[14] P. A. Gimenez Molinelli, J.I. Nichols, J. A. López, and C.O. Dorso, Nucl. Phys. **A 923**, 31 (2014).

[15] C.O. Dorso, P.A. Gimenez M. and J.A. López, Phys. Rev. **C 86**, 055805 (2012).

[16] C.O. Dorso, P.A. Gimenez M. and J.A. López, J. Phys. G: Nucl. Part. Phys. **38**, 115101 (2011).

[17] A. Barranon, C.O. Dorso, and J.A. López, Nucl. Phys. **A 791**, 222 (2007).

[18] C.O. Dorso, C.R. Escudero, M. Ison, and J.A. López, Phys. Rev. **C 73**, 044601 (2006).

[19] A. Barranon, J. Escamilla Roa, and J.A. López, Phys. Rev. **C 69**, 014601 (2004).

[20] A. Chernomoretz, L. Gingras, Y. Larochelle, L. Beaulieu, R. Roy, C. St-Pierre, and C. O. Dorso, Phys. Rev. **C 65**, 054613 (2002).

[21] C. O. Dorso and J. A. López, Phys. Rev. **C 64**, 027602 (2001).

[22] A. Vicentini, G. Jacucci and V.R. Pandharipande, Phys. Rev. **C31**, 1783 (1985); R. J. Lenk and V. R. Pandharipande, Phys. Rev. **C34**, 177 (1986); R.J. Lenk, T.J. Schlagel and V. R. Pandharipande, Phys. Rev. **C42**,372 (1990).

[23] B.L. Holian, A.F. Voter and R. Ravelo, Phys. Rev. **E52**, 2338 (1995).

[24] J.B. Natowitz, et al., Phys. Rev. Lett. **104**, 202501 (2010).

[25] J.M. Lattimer and Y. Lim, Astrophys J, **771**, 51 (2013).

[26] G. Cybenko, Math. Control Signals Syst., **2**, 303 (1989).

[27] H. W. Lin, M. Tegmark, and D. Rolnick, J. Stat., Phys. **168**, 1223 (2017).

[28] E. Sontag, IEEE Trans. Neural Networks, **3**, 981 (1992).

[29] F. Pedregosa, et al., J. Mach. Learn. Res., **12**, 2825 (2011).

Oscillation symmetry applied to: 1) hadronic and nuclei masses and widths 2) astrophysics, and used to predict unknown data.

B. Tatischeff
PNO, CNRS/IN2P3, Université Paris-Sud, Universté Paris-Saclay, 91406 Orsay Cedex, France

Abstract
A systematic study of given spin hadronic and nuclear masses shows regular oscillations observed when the difference between adjacent masses of each family is plotted versus the corresponding mean masses. The width variations, when plotted versus the masses, show the same behaviour. The oscillatory behaviour is also observed for astronomical data. This oscillatory symmetry is used to tentatively predict some unknown nuclear spins, and different properties of two new hypothetical solar planets.

1 Introduction

A new property of hadronic and atomic masses was recently shown [1, 2], namely that they obey to regular oscillations, fitted by simple cosine functions. Such property appears legitimated afterwards, since these bodies result from different smaller bodies (quarks and nucleons) which are subject to at least two different interactions, one attractive and one repulsive.

This property was observed for mesons, baryons [1], and nuclei [2] masses and widths [3]. Since the hadronic and nuclei masses result from the Schrödinger equation, with a kinetic and a potentiel interactions, like pendulum in classical physics, such observation could be predicted. The widths however of all these states do not arise simply from the Schrödinger equation.

The oscillatory behaviour quoted above result from the existence of opposite forces. Different opposite interactions are often observed in the nature. They are observed when a body results from the existence of several smaller bodies, like quarks and gluons for hadrons, or like nucleons for nuclei. Indeed the existence of opposite forces prevents the "large" bodies disintegration or self destruction.

Since the astronomic bodies are also subject to opposite interactions: gravitation and centrifugal forces related to the kinetic energy, their characteristics should also exhibit oscillatory properties. They will be studied below.

The mass variations are studied using the following equation, after having been classified in increasing order:

$$m_{(n+1)} - m_n = f[(m_{(n+1)} + m_n)/2], \tag{1}$$

where $m_{(n+1)}$ corresponds to the (n+1) hadron mass value. Two successive mass differences are therefore plotted versus their corresponding mean masses.

The function used to the fits is:

$$\Delta M = \alpha_0 + \alpha_1 \cos((M - M_0)/M_1) \tag{2}$$

where M_0 /M_1 is defined within 2π. The oscillation periods, P = 2 πM_1 are studied. The amplitude of oscillations deserves theoretical studies which are outside the scope of the present work. The widths are plotted versus the corresponding masses.

The analysis requires the existence of several masses (at least five) having the same spin, without intermediate masses corresponding to particles with unknown spin. These restrictions limitate the appropriated data basis. Since many figures were shown in previous papers [2, 3], a selection is done to illustrate data not presented before, and particularly those allowing to predict some still unknown property of the considered particles.

2 Oscillations in hadronic masses and widths

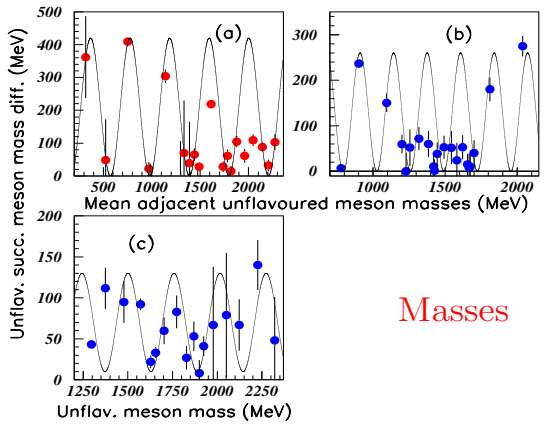

FIG. 1. Color on line. Unflavoured mesons. J=0, 1, and 2 for inserts (a), (b), and (c).

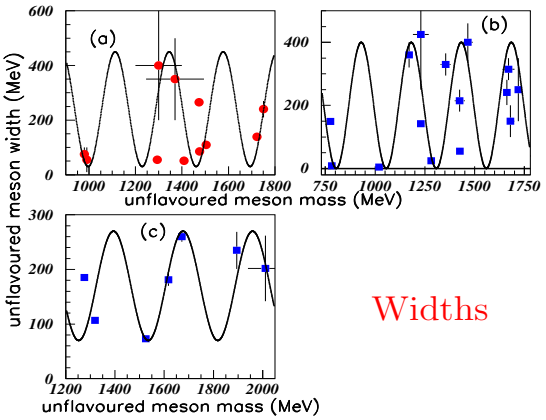

FIG. 2. Color on line. Unflavoured mesons. J=0, 1, and 2 for inserts (a), (b), and (c).

The data are read in the PDG tables [4]. Fig. 1 shows the successive mass differences of unflavoured mesons, plotted versus the mean corresponding masses. Inserts (a), (b), and (c) correspond respectively to spins J=0, 1, and 2. The mass periods decrease with increasing spins, from P=408 MeV to P=258 MeV. Fig. 2 shows the unflavoured meson widths plotted versus their masses. Here again, inserts (a), (b), and (c) correspond respectively to spins J=0, 1, and 2. The width periods increase with increasing spins, from P=232 MeV up to P=283 MeV. The oscillatory behaviour is clearly observed in all data.

Fig. 3 (Fig. 4) shows mass (width) data corresponding to strange mesons. Red full circles show the fitted data where masses, widths, and spins are known. There is a low mass strange meson with an unknown spin K(1630) I(J^P)=1/2(?$^?$). This mass is successively introduced in the known data figures for different spins. In Fig. 3 the two new data are shown by stars (blue on line) surrounded by squares and in the same time one point, localized between the two new data (red encircled by black on line) should be removed. We observe that this new mass is more compatible with spins J=1 and J=2, than with J=0 (see fig.3(a)). Fig. 5 shows the Δ masses M (insert (a) et (b) for J=1/2 and J=3/2) and width W (insert

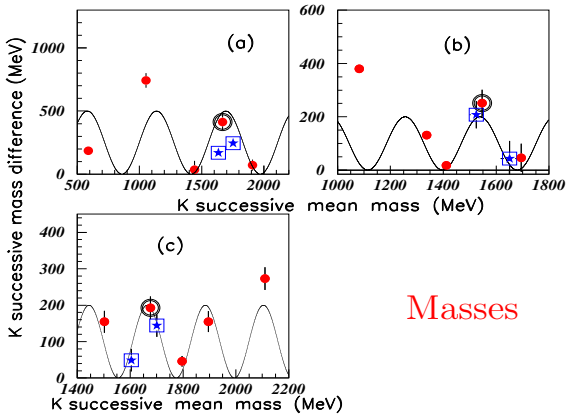

FIG. 3. Color on line. Strange mesons. J=0, 1, and 2 for inserts (a), (b), and (c).

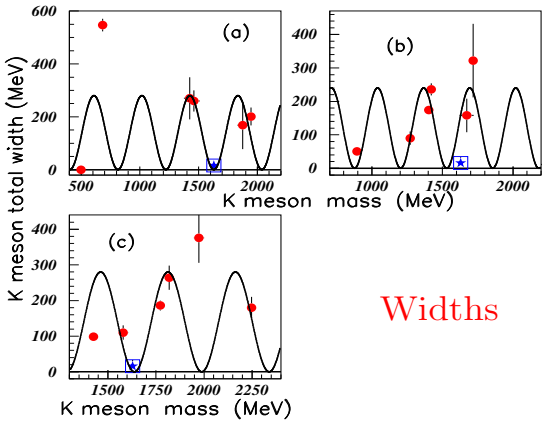

FIG. 4. Color on line. Strange mesons. J=0, 1, and 2 for inserts (a), (b), and (c).

(c) and (d) for J=1/2 and J=3/2 data. The data here are very well fitted.

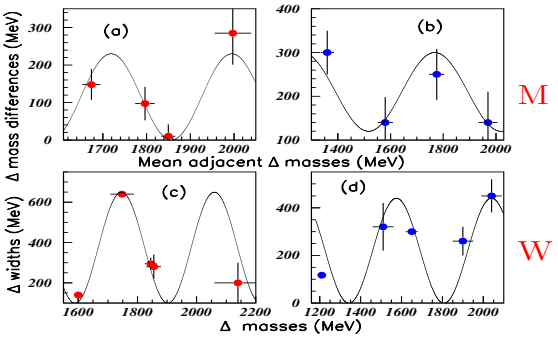

FIG. 5. Color on line. Δ baryons.
J=1/2 in inserts (a) and (c), 3/2 for (b) and (d).

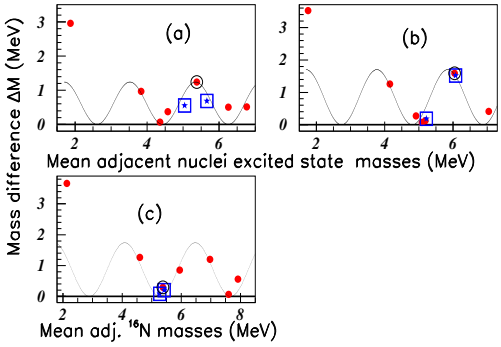

FIG. 6. Color on line. ^{16}N.
J=1 in (a), J=2 in (b), and J=3 in (c).

3 Oscillations in nuclei masses and widths

The very small widths of the first excited levels, which decay by weak or electromagnetic interactions, are omitted. This explains the large values of the first mass in the corresponding figures.

Fig. 6 shows the the mass differences of increasing ^{16}N excited level masses [5], plotted versus their mean values. Inserts (a), (b), and (c) correspond respectively to spins J=1, 2, and 3 respectively. Spin J=0 cannot be tested since their is only one J=0 state below M=5.318 MeV. The spin of the M=5.318 $\pm$0.03 MeV, Γ=260 keV is given to be $(0^+, 1^+)$ [5]. The masses in Fig. 6(a) and the corresponding widths show that this spin is compatible with J=1.

Fig. 7 illustrates the possible determination of the spin of the M=9.72 MeV level of ^{15}O $(1/2, 3/2)^+$. Its mass and width are M=9.72 $\pm$0.050 MeV, Γ=1185 $\pm$ 50 keV [6]. From the mass figure the spin J=1/2 appears favored. This mass level is included in insert (a).

Fig. 8 shows the attempt to suggest the spin of the M=9.928 MeV level of ^{15}N. When introduced in the data describing the levels with known spin, fig. 8 shows the agreement with J=1/2 in mass and width figs., when it shows a disagreement with J=3/2. We conclude that the favored spin of this level is J=1/2.

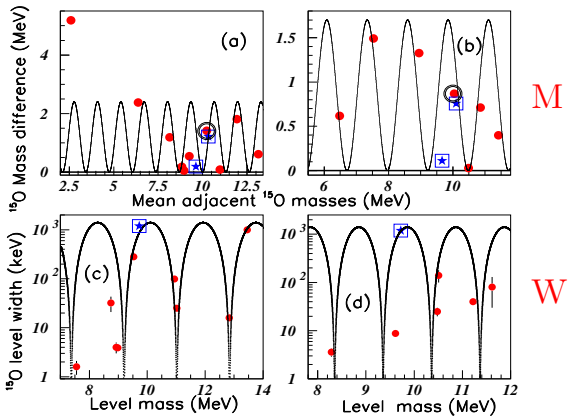

FIG. 7. Color on line. ^{15}O.
J=1/2 in inserts (a) and (c), J=3/2 for (b) and (d).

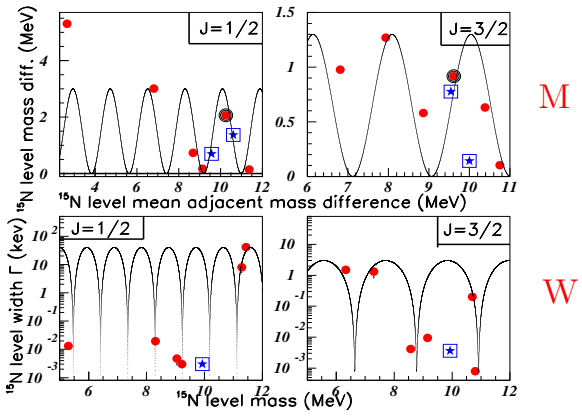

FIG. 8. Color on line. ^{15}N.
J=1/2 in (a) and (c), J=3/2 in (b) and (d).

4 Oscillations in astronomical bodies

The oscillatory symmetry was already used to predict the possible mass of the seventh planet around TRAPPIST-1 star observed in Ref. [7], namely that such mass should be M(7) $\approx 0.7 \pm 0.1$ earth mass [8].

We restrict here the discussion to tentatively predict the properties of the possible additional ninth

and tenth solar planets. Their existence was suggested in order to explain the strange behaviour of some bodies belonging to the Kuiper belt, to stabilize several orbits of transneptuniens bodies, and to explain the Kuiper cliff behaviour. The prediction of their masses is: ten earth mass (em) for the ninth planet [9] (on line drawn in blue in the following figures), and half (em) (drawn in green) for the tenth planet [10]. Fig. 9 shows the successive solar planet mass differences [11], after classification along increasing masses, plotted versus the corresponding mean masses. Insert (a) show the data without introduction of these two new possible masses. Insert (b) shows the data with the new masses plotted by blue and green squares, where one has to suppress the black data corresponding to the mass difference of the previous sequence. The masses of these new planets are well fitted with the oscillations obtained using the "classical planet" masses. This agreement can be considered as an argument in favour of the existence of these two new solar planets.

Fig. 10 shows several possible properties of the anticipated ninth and tenth solar planets.

Fig. 11 shows some solar planet moon data for Saturn, Jupiter, Uranus. Neptune data are not shown, due to the small number of associated moons. The following relation (Pd)*m$^{-1/3}$ $\approx$ 4.27(0.23) is observed for the four planets, where P is the period of the moon planet diameters plotted versus the moon distances from planet, d is the planet distance from the Sun (in astronomic units), and m the planet mass (in 10^{23} kg).

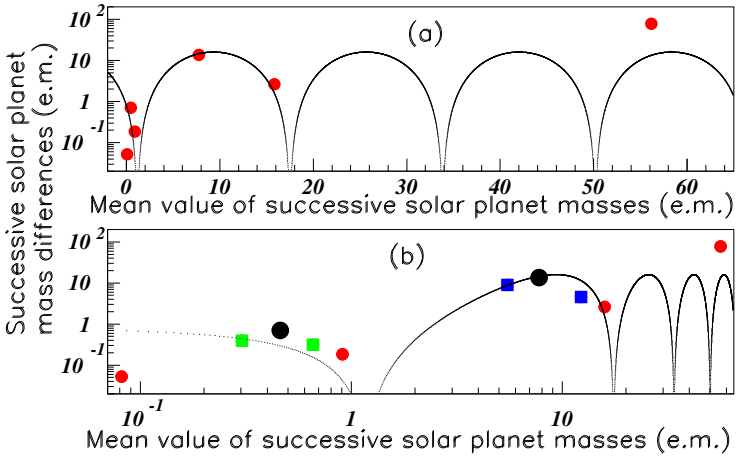

FIG. 9. Color on line. Mean value of successive solar planet masses (e.m.) plotted versus their mean value. See text.

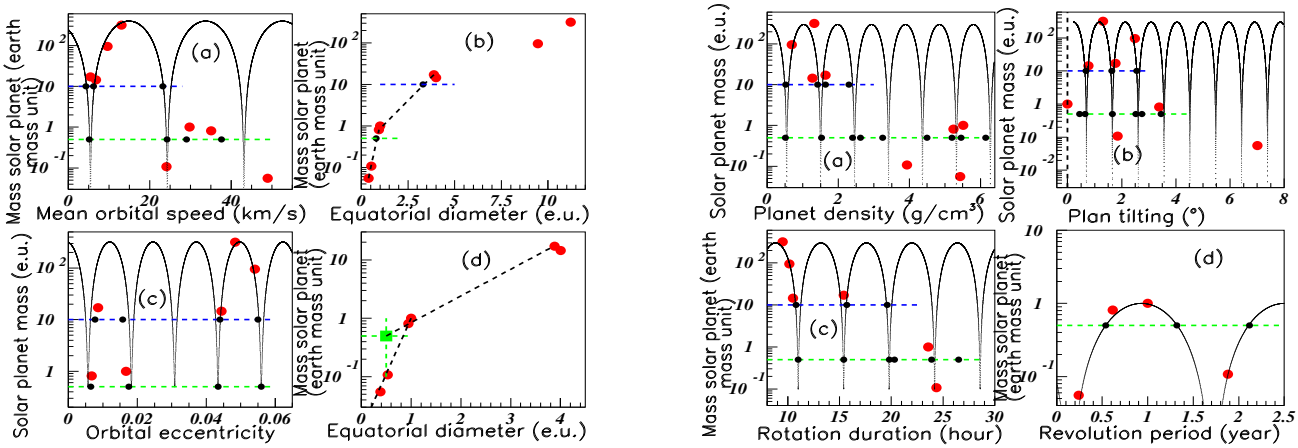

FIG. 10. Color on line. Different properties predicted for the two new possible solar planets 9 and 10.

Fig. 12 shows some solar planet ring data. The following relation P(ring)/r $\approx$ 0.234(0.014) (arbitrary units) is observed for the three planets, where P(ring) is the period of oscillations of the solar planet ring widths versus the planet ring radii, and r is the solar planet mean radius.

5 Conclusion

Regular oscillations are observed in masses and widths of particles, nuclei, and astrophysical bodies, although the forces acting in these different fields are very different. The existence of several data of the same family is a necessary condition for observing a regular behaviour.

The oscillations are fitted using cosine functions.

This oscillatory symmetry is verified in classical physics, quantum physics and astrophysics. Indeed the necessary condition is the existence of opposite interactions allowing the bodies to avoid their disintegration or fusion into a totally new object.

This symmetry can be used to predict still unknown properties.

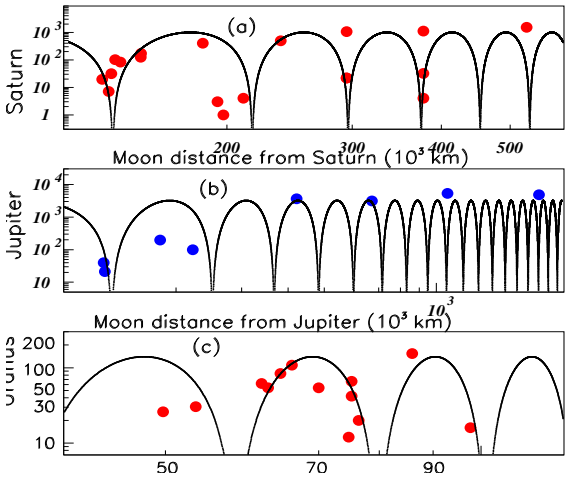

Fig. 11. Solar planet moon diameters plotted versus the moon distances from planet. Inserts (a), (b), and (c) correspond to Saturn, Jupiter, and Uranus data.

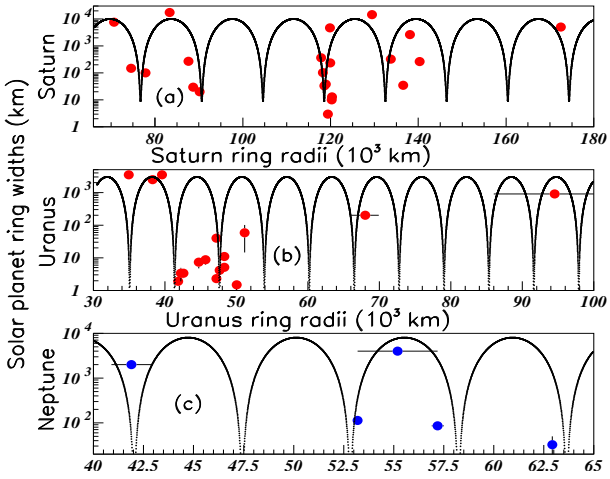

Fig. 12 Solar planet ring widths plotted versus the planet radii. Inserts (a), (b), and (c) correspond to Saturn, Uranus, and Neptune data.

References

[1] B. Tatischeff, 'Systematics of oscillatory behavior in hadronic masses and widths,' arXiv:1603.05505[hep-ph], 2016.

[2] B. Tatischeff, 'Variation of hadronic and nuclei mass level oscillation periods for different spins', Journal of Particle Physics, **1**, 13 (2017) DOI: 10.22606/jpp.2017.11002.

[3] B.Tatischeff, 'Oscillation symmetry applied to nuclear level widths and masses', Journal of Particle Physics, **2**, 5 (2018) DOI:1022606/jpp.2018.22001.

[4] C. Patrignani *et al.* (Particle Data Group), Chin. Phys. C, **40**, 100001 (2016) and 2017 update.

[5] D.R. Tilley, H.R. Weller, and C.M. Cheves, 'Energy levels of Light Nuclei A = 16', Nucl. Phys. **A564**, 1 (1993).

[6] F. Ajzenberg-Selove, 'Energy levels of Light Nuclei A = 13-15', Nucl. Phys. **A268**, 1 (1976).

[7] M. Gillon *et al.*, 'Seven temperate terrestrial planets around the bearby ultracooldwarf star TRAPPIST-1', Nature Letter, **542**, 456 (2017), *ibid* doi:10.1038/nature 21360.

[8] B. Tatischeff, 'May the oscillation symmetry be applied to TRAPPIST-1 terrestrial planets to predict the mass of the seventh's planet', Phys Astron Int J. 2(3), 193 (2018). DOI: 10.15406/paij.2018.02.00085.

[9] K. Batygin and M. Brown, 'Evidence for a distant giant planet in the solar system', The Astronomical Journal, 151:22, 2016. doi:10.3847/0004-6256/151/2/22.

[10] K. Volk and R. Malhotra, 'The curiously warped mean plane of the Kuiper belt', arXiv:1704.02444v3 [astro-ph.EP].

[11] https://en.wikipedia.org/wiki/Planetary-mass; [Mercury, Mars, Venus, Earth, Uranus, Neptune, Saturn, (and Jupiter)].

The Statistical Model of Nuclear Reactions: Open Problems

P. Fanto[1]*, Y. Alhassid*[1]*, and H. A. Weidenmüller*[2]
[1]Center for Theoretical Physics, Sloane Physics Laboratory, Yale University, New Haven, Connecticut 06520, USA
[2]Max-Planck-Institut für Kernphysik, D-69029 Heidelberg, Germany

Abstract
Several experiments [1–3] show significant deviations from predictions of the statistical model of nuclear reactions. We summarize unsuccessful recent theoretical efforts to account for such disagreement in terms of a violation of orthogonal invariance caused by the Thomas-Ehrman shift. We report on numerical simulations involving a large number of gamma decay channels that also give rise to violation of orthogonal invariance but likewise do not account for the discrepancies. We discuss the statistical model in the light of these results.

1 Motivation

In recent years, several predictions of the statistical model of nuclear reactions have been tested experimentally, with puzzling results. The statistical model predicts that the reduced partial neutron widths of isolated compound-nucleus resonances have a Porter-Thomas distribution (PTD), i.e., a χ^2 distribution in one degree of freedom. Moreover, the total gamma decay width of an isolated neutron resonance is the sum of a very large number of partial gamma decay widths. If the latter have a PTD, the distribution of total gamma decay widths should be very narrow. However, the data show strong deviations from these predictions:

(i) In the scattering of slow neutrons on the target nuclei ^{192}Pt and ^{194}Pt, 158 and 411 isolated resonances, respectively, were analysed. The data reject the validity of the PTD with 99.997% statistical significance [1].

(ii) A reanalysis of the nuclear data ensemble (NDE) rejects the validity of the PTD with 99.97% statistical significance [2].

(iii) The measured distributions of total gamma decay widths for isolated neutron resonances in the compound nucleus ^{96}Mo are much wider and are peaked at significantly larger values of the widths than predicted by the statistical model. The ground state of the nucleus ^{95}Mo has spin/parity $5/2^+$, hence s-wave and p-wave resonances in the compound nucleus ^{96}Mo have spin/parity values $2^+, 3^+$ and $1^-, 2^-, 3^-, 4^-$, respectively. For all these spin/parity values, Fig. 1 shows the measured cumulative width distributions (i.e., the fraction of widths larger than a given value) as dark lines with error bars and the values predicted by the statistical model as red lines [3].

Here we summarize previous attempts and present a new approach aimed at reconciling the statistical model with the data of Refs. [1–3]. To that end, we first recall in Sec. 2 the essential features of the statistical model.

2 Statistical Model

For states of fixed spin and parity, we consider a compound-nucleus (CN) reaction induced by slow neutrons (s-wave or p-wave) that leads either to elastic neutron scattering or to gamma decay of the CN. We neglect direct reactions. Denoting by $c = 1$ the neutron channel and $c = 2, 3, \ldots, \Lambda \gg 1$ the gamma channels, the scattering matrix is

$$S_{cc'}(E) = \delta_{cc'} - 2i\pi \sum_{\mu\nu} W_{c\mu}(E)[(E - H^{\rm eff})^{-1}]_{\mu\nu} W_{\nu c'}(E) \ . \tag{1}$$

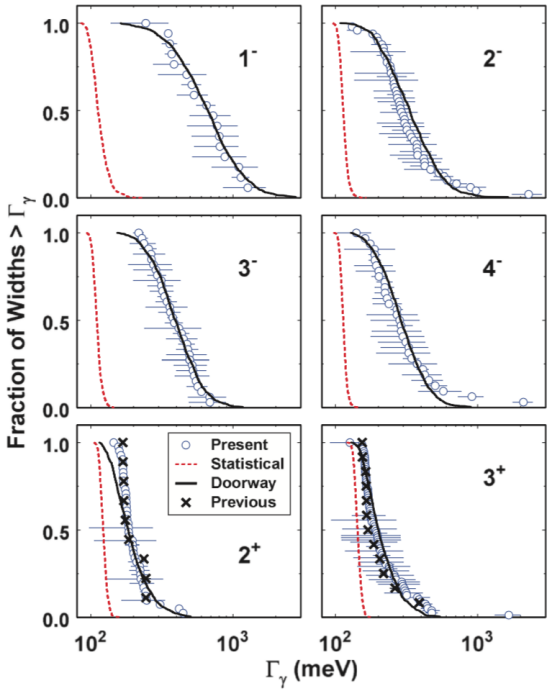

Fig. 1: Cumulative distributions of the total gamma decay widths for neutron resonances in ^{96}Mo as described in the text. Taken from Ref. [3].

Here E is the excitation energy of the CN, with $E = 0$ for the ground state. The threshold energy of channel c is denoted by E_c. The real matrix elements $W_{c\mu}(E) = W_{\mu c}(E)$ (defined for $E \geq E_c$) describe the coupling of channel c to the compound nucleus states, spanned by the states $\mu = 1, 2, \ldots, N \gg 1$. In the framework of the statistical model, the nuclear Hamiltonian is, within the space of compound states, replaced by $H^{\rm GOE}$, a matrix of dimension $N \gg 1$ drawn from the Gaussian orthogonal ensemble (GOE) of random matrices [4]. The effective Hamiltonian is given by

$$H^{\rm eff}_{\mu\nu} = H^{\rm GOE}_{\mu\nu} + \sum_c \mathcal{P} \int_{E_c}^{\infty} {\rm d}E' \, \frac{W_{\mu c}(E') W_{c\nu}(E')}{E - E'} - i\pi \sum_c W_{\mu c}(E) W_{c\nu}(E) \; , \qquad (2)$$

where $\mathcal{P}$ denotes the principal-value integral.

The derivation of the PTD rests on the fact that the GOE is invariant under orthogonal transformations in the space of compound states. Such invariance is violated by the last two terms on the right-hand side of Eq. (2), describing the coupling of the CN to the channels. In recent years, considerable theoretical effort has been devoted to the question whether the discrepancies listed in Sec. 1 can be attributed to these two terms.

We discuss these terms using simplifications that apply in the present case. (i) For the overwhelming majority of gamma channels ($c \geq 2$) the gamma decay energy E differs substantially from the threshold energy E_c. Then it is legitimate to neglect the principal-value integrals, and we do so for all gamma channels. (ii) For slow neutrons the energy dependence of the matrix elements that couple to the neutron channel is given by $W_{1\mu}(E) \approx (E - E_1)^{(2l+1)/4} W^{(0)}_{1\mu}$. Here $l = 0$ ($l = 1$) for s-wave (p-wave) neutrons, respectively, while $W^{(0)}_{1\mu}$ is independent of energy. With that approximation the two coupling terms in Eq. (2) are given by the product of $W^{(0)}_{\mu 1} W^{(0)}_{1\nu}$ and of a complex energy-dependent factor that is independent of μ, ν. (iii) The absence of direct reactions implies channel orthogonality in the form $\pi \sum_\mu W_{c\mu} W_{\mu c'} = \delta_{cc'} \lambda \kappa_c$. Here $\lambda = Nd/\pi$ is the standard GOE parameter and d is the mean GOE level spacing in the center of the spectrum. The dimensionless parameter κ_c measures the strength

of the coupling to channel c. Channel orthogonality allows us to diagonalize the matrices coupling the compound states to the channels, and we obtain

$$H_{\mu\nu}^{\rm eff} = H_{\mu\nu}^{\rm GOE} + \delta_{\mu\nu} V_\mu \ , \tag{3}$$

where

$$V_c = \begin{cases} \lambda\left(\frac{1}{\pi}\mathcal{P}\int_{E_1}^{\infty} {\rm d}E' \frac{\kappa_1(E')}{E-E'} - i\kappa_1(E)\right) & \text{for } c = 1 \ , \\ -i\lambda\kappa_c & \text{for } c = 2, \ldots, \Lambda \ , \\ 0 & \text{for } c > \Lambda \ . \end{cases} \tag{4}$$

The average S matrix is $\langle S_{cc'} \rangle = \delta_{cc'}(1-\kappa_c)/(1+\kappa_c)$, and the transmission coefficient in channel c is $T_c = 1 - |\langle S_{cc} \rangle|^2 = 4\kappa_c/(1+\kappa_c)^2$.

3 Nonstatistical Effects: Thomas-Ehrman Shift

In the platinum isotopes, the single-particle $4s$ state of the nuclear shell model is close to neutron threshold, causing a maximum of the s-wave neutron strength function in that mass region and, at the same time, an enhancement of the principal-value integral (the shift function) in V_1 of Eq. (4). In light nuclei the shift due to the principal-value integral is known as the Thomas-Ehrman shift. Several authors [5–7] have addressed the question whether that enhancement may be responsible for deviations of the distribution of partial neutron resonance widths from the PTD. In all these works, the gamma channels were neglected (except for a constant imaginary shift in the GOE energies).

For real values of V_1 that are consistent with the enhancement due to the $4s$ state but were taken to be independent of energy, the numerical results of Volya et al. [5] showed significant deviations of the distribution of reduced partial neutron widths from the PTD. Bogomolny [6] succeeded in diagonalizing the Hamiltonian (3) with an energy-independent real V_1 in the limit of large matrix dimension N. He showed that deviations from the PTD do arise but that locally the width distribution remains a PTD. The effect found in Ref. [5] is attributed to ignoring the secular variation of the average width with energy. Once the average width is divided out, the fluctuations of the reduced widths follow the PTD. Fanto et. al. [7] studied a model that includes a realistic description of the neutron channel in a Woods-Saxon potential, and effectively takes full account of the energy dependence of V_1. The resulting local distribution of partial neutron widths was found to be consistent with the PTD.

We note that a sufficiently large imaginary part of V_1 can lead to deviations from a PTD [8]. However, no such deviations are observed for realistic values of κ_1 [5, 7].

Therefore, the deviations from the PTD listed under (i) and (ii) in Sec. 1 cannot, for realistic values of the parameters, be accounted for by violations of orthogonal invariance due to the coupling to the neutron channel. In view of this result, we consider the shift function in the first of Eqs. (4) to be insignificant and we disregard it in what follows.

4 Nonstatistical Effects: Many Gamma Channels

In medium-mass and heavy nuclei, the number of gamma decay channels is huge (of the order of 10^6 or so) for each isolated neutron resonance. We ask: can that fact account for the deviations listed in Sec. 1 even though the coupling of each individual gamma channel to the CN is very weak? Prior to addressing that question we recall in Sec. 4.1 the calculation of the total gamma decay width in the statistical model.

4.1 Total Gamma Width

An isolated neutron resonance labelled μ with spin/parity J^π and resonance energy E_μ decays by emission of photons of multipolarity L and parity π (E1, M1, E2, M2, ..., jointly written as XL) to final states

f with spins/parities J_f^π. (The label f replaces the channel label c used in Eq. (3).) The corresponding partial decay widths are denoted by $\Gamma^{J^\pi}_{\mu\gamma J_f^\pi f XL}$. The total gamma decay width is

$$\Gamma^{J^\pi}_{\mu\gamma} = \sum_{XL} \sum_{J_f^\pi f} \Gamma^{J^\pi}_{\mu\gamma J_f^\pi f XL} \, . \tag{5}$$

In the statistical model, the partial width is written as a product,

$$\Gamma^{J^\pi}_{\mu\gamma I_f^\pi f XL} = x_f^2 \langle \Gamma^{J^\pi}_{\mu\gamma J_f^\pi f XL} \rangle \, . \tag{6}$$

The average value in Eq. (6) is expressed in terms of the gamma strength function $f_{XL}(E_\gamma)$ and the average spacing d_{J^π} of the resonances of spin J and parity π,

$$\langle \Gamma^{J^\pi}_{\mu\gamma I_f^\pi f XL} \rangle = d_{J^\pi} E_\gamma^{2L+1} f_{XL}(E_\gamma) = d_{J^\pi} \frac{2}{\pi} \kappa_f \, , \tag{7}$$

where the dimensionless parameters κ_f have the same physical meaning as the parameters κ_c in Eq. (4). The factors x_f^2 are uncorrelated random variables that each have mean value unity and follow the PTD. These account for fluctuations of the partial widths. The statistical model is implemented by choosing values for the strength function and for the average level density from which the actual values of the final energies E_f are drawn. The average total total gamma decay width is given by

$$\langle \Gamma^{J^\pi}_{\mu\gamma} \rangle = d_{J^\pi} \sum_{XL} \sum_{J_f^\pi} \int_0^{E_\mu} \mathrm{d}E_\gamma \, \rho(E_\mu - E_\gamma, J_f^\pi) E_\gamma^{2L+1} f_{XL}(E_\gamma) \, , \tag{8}$$

where $\rho(E_\mu - E_\gamma, J_f^\pi)$ is the average level density at energy $E_\mu - E_\gamma$ and spin/parity J_f^π of the final levels into which the compound nucleus decays.

4.2 Simulation of Gamma Decay of the ^{96}Mo Compound Nucleus

The influence of the coupling of many gamma channels on the statistical properties of the neutron resonances was simulated as follows. It is impractical to use in Eqs. (3) and (4) the totality of channels f resulting from the treatment in Section 4.1. Their number is simply too large. For each group of neutron resonances carrying spin-parity values $(2^+, 3^+)$ for s-wave neutrons and $(1^-, 2^-, 3^-, 4^-)$ for p-wave neutrons, a set of representative channels $c = 1, 2, \ldots, \Lambda - 1$ (distinguished in notation from the actual channels labelled f) was constructed instead. Below an excitation energy of 2.79 MeV, known measured discrete levels were used. Above that energy, representative channels labelled c were defined by coarse-graining: final states f close in energy and carrying identical quantum numbers were grouped together. The average density of final states c was taken proportional to the actual level density. For the latter, the back-shifted Fermi gas model with a spin distribution described by the spin cutoff model were used. States with opposite parity were assumed to have the same level density. Only E1 and M1 gamma transitions were considered as these contribute the bulk to the widths. For the E1 and M1 strength functions the parametrization of Ref. [9] was used. The effective coupling parameters κ_c are sums over the parameters κ_f for the states f in the group. The number of gamma channels so constructed was 400. The total number of channels was 401: one neutron channel, 200 E1 channels, and 200 M1 channels. Results shown below are taken from the middle of the GOE spectrum to avoid edge effects.

4.3 Results

The scheme described in Sec. 4.2 was used to check for deviations of neutron and gamma decay widths from the PTD. For a width Γ and its average $\langle \Gamma \rangle$ we define $x = \Gamma / \langle \Gamma \rangle$ and $y = \ln x$. For y the PTD takes the form $P(y) = \sqrt{x/(2\pi)} \exp(-x/2)$. For neutron resonances with spin/parity 2^+ that function

is shown in Fig. 2 for the partial widths in the neutron channel and in the most strongly coupled E1 channel. The solid black lines describe the PTD, and the histograms are the result of the simulations. They agree perfectly. We have found similar agreement for less strongly coupled gamma channels and for other spin/parity values. We conclude that a large number of gamma channels with realistic coupling strengths does not alter the PTD of partial widths in any channel (neutron or gamma).

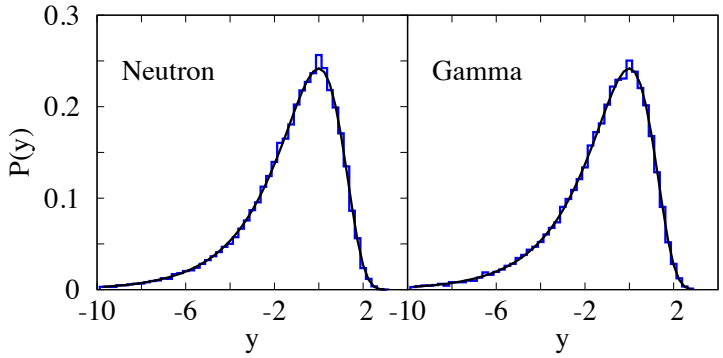

Fig. 2: Distribution of $y = \ln x$, where $x = \Gamma/\langle\Gamma\rangle$ is the reduced partial width. The left panel shows the result for the neutron channel, the right panel shows the result for the most strongly coupled gamma channel. Histograms are model calculations (see text), and the solid black lines are the PTD.

Total gamma decay widths were obtained from Eqs. (5), (6) and (7) with the adopted values for the level density and the strength function, and with a PTD for the variables x_f^2. To check for the sensitivity of our results to the form of the strength function we have used three different parametrizations of the E1 strength function displayed in Fig. 3. The blue solid line describes the standard parameterization of the E1 strength function, the red dotted-dashed line is found by taking twice the width of the giant dipole resonance in the E1 strength function, and the green dashed line corresponds to half the width of the giant dipole resonance. The resulting cumulative distributions of the total gamma decay width for the 2^+ neutron resonances (normalized to give the experimental total average gamma width) are shown in Fig. 4. These cumulative distributions virtually coincide. Also shown with error bars is the measured cumulative distribution of Ref. [3]. That distribution is clearly much wider than the simulated ones.

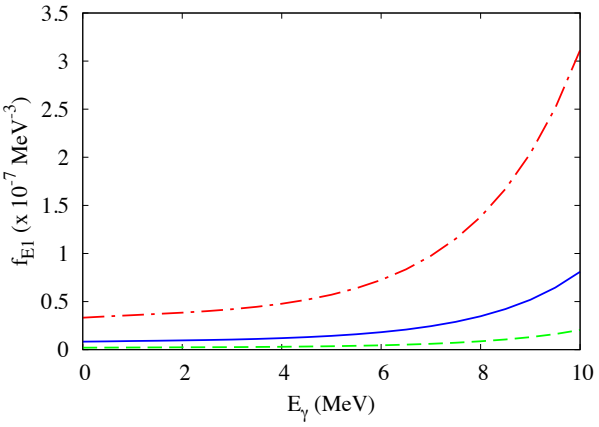

Fig. 3: Three different parametrizations of the E1 strength function as described in the text.

The disagreement of statistical-model predictions with the data of Ref. [3] extends to the maxima of the (un-normalized) total gamma decay width distributions. Table 1 shows that the locations of the peaks of the distributions (or more accurately, the average values) also differ markedly. The experimental average total widths have significantly larger values than the corresponding average withs predicted by

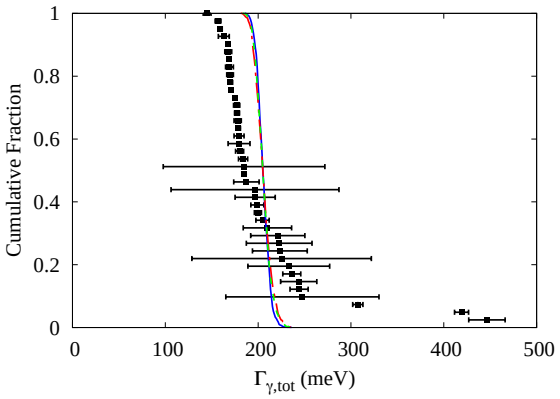

Fig. 4: The cumulative distribution of the total gamma decay width for the 2^+ resonances in ^{96}Mo. The black squares with error bars are data taken from Ref. [3]. The three colored lines correspond to simulations that use the three parametrizations of the E1 strength function shown in Fig. 3.

the statistical model. For the 1^- states the ratio is larger than three. Individual peak positions for given spin/parity can be fitted by an ad-hoc modification of the E1 strength function. It was not possible, however, to fit all peak positions simultaneously by such modification.

J^π	2^+	3^+	1^-	2^-	3^-	4^-
$\langle\Gamma_{\gamma,\mathrm{sim}}\rangle$ (meV)	165.5	157.5	191.2	172.8	169.2	153.8
$\langle\Gamma_{\gamma,\mathrm{exp}}\rangle$ (meV)	206 (31)	240 (58)	670 (225)	374 (115)	404 (100)	361 (106)

Table 1: Comparison of simulated average total gamma widths $\langle\Gamma_{\gamma,\mathrm{sim}}\rangle$ with the experimental results $\langle\Gamma_{\gamma,\mathrm{exp}}\rangle$.

The PTD for the partial gamma decay widths is corroborated by the results shown in Fig. 2. The disagreement of the simulated neutron partial width distribution (a PTD) with the data of Refs. [1,2] may cast doubt on the validity of that conclusion. That raises the question: Would a distribution of partial gamma widths different from the PTD yield better agreement of the predicted distribution of total gamma widths with the data of Ref. [3]? To generate such a distribution we have used a dynamical model with an unrealistically strong coupling of the GOE Hamiltonian to the neutron channel, $V_\mu = -i0.8\lambda\delta_{\mu 1}$ in Eq. (3). The resulting distributions of the partial widths are shown in Fig. 5 for the neutron channel (blue histograms) and for one gamma channel (green histograms). Both distributions differ markedly from the PTD (black). It is noteworthy that strong coupling to the neutron channel also modifies the width distribution in the gamma channels. However, Fig. 6 shows that use of the modified distribution for the gamma channels does not affect the disagreement with the data of Ref. [3]. The calculated cumulative distribution for the 2^+ resonances using the modified gamma channel distribution (dashed green line) is nearly indistinguishable from the one obtained using the PTD (black line). Even if we use for the partial gamma width distribution the blue distribution in Fig. 5 (i.e., assuming the gamma channels to be strongly coupled to the resonances), the resulting cumulative distribution (dashed-dotted blue line) is not much different. In comparison, the data for the 2^+ resonances (black squares with error bars) differ substantially from the theoretical curves.

The reason for the near coincidence of the simulated cumulative distributions is actually quite simple. According to the construction in Eqs. (5) to (6), the total gamma width is the sum of a very large number (K, say) of independently distributed random variables with similar or identical distributions (describing the partial gamma widths). The central limit theorem implies that the total width has a Gaussian distribution with a variance that is inversely proportional to K. The narrowness of the predicted total width distributions is, thus, independent of the actual form of the partial-width distribution and is a

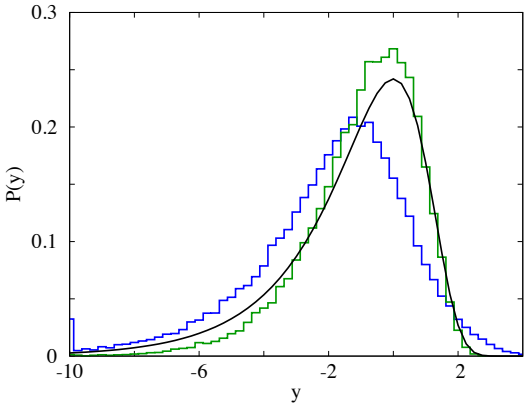

Fig. 5: Distribution of $y_i = \ln x_i$ for the model of Eq. (3) with $V_\mu = -i0.8\lambda\delta_{\mu 1}$, where $i = 1$ denotes the neutron channel (blue histogram) and $i = 2$ denotes one gamma channel (green histogram). The set $\{x_i\}$ equals the set $\{\Gamma_{i\mu}/\langle\Gamma_{i\mu}\rangle)\}$, and $y_i = \ln x_i$ as in Fig. 2. The solid black line is the PTD.

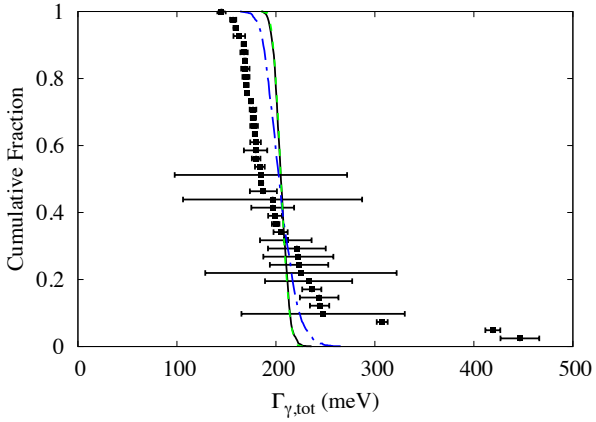

Fig. 6: Simulated cumulative total width distributions are compared with experimental data for resonances of spin-parity 2^+. The black solid line is obtained using the PTD for the partial widths. The green dashed line and blue dotted-dashed line are obtained using modified distributions for the partial gamma widths given, respectively, by the green and blue histograms in Fig. 5. The black squares with error bars show the experimental data of Ref. [3]. The simulated widths are normalized to match the experimental average total width.

universal feature resulting directly from the basic tenets of the statistical model.

5 Discussion

The distributions of reduced partial neutron widths reported in Refs. [1, 2] deviate significantly from the PTD. Within the framework of the statistical model, violation of orthogonal invariance is a possible culprit. Two mechanisms for such violation have been investigated. The Thomas-Ehrman shift, addressed by several authors, is ruled out. Simulations involving a large number of gamma channels yield perfect agreement with the PTD in all channels. That mechanism is, therefore, also ruled out. Furthermore, the measured distributions of total gamma decay widths in ^{96}Mo reported in Ref. [3] disagree with those obtained in simulations that follow the statistical model. These predicted distributions are too narrow, and the mean values of the total gamma widths are too small when compared with the experimental results.

In summary, the statistical model fails to account for the data in platinum isotopes, in the nuclear data ensemble, and in ^{96}Mo. Violation of orthogonal invariance due to channel coupling cannot be held responsible for these failures. The observed deviations suggest that at neutron threshold, the mixing

of CN states is less complete than implied in the statistical model by the use of a GOE Hamiltonian. The small mean values of the total gamma decay widths predicted by the statistical model show that gamma strength is missing in the model. That poses the question whether the Brink-Axel hypothesis actually applies to all gamma transitions that contribute significantly to the gamma decay of the neutron resonances. Such consequences are rather drastic. We feel that additional experimental tests of the statistical model are called for.

Given the experimental results, a small number of strong gamma transitions to low-lying final states might offer a way out of the dilemma [3]. These should have sufficient intensity to shift the simulated distribution of total gamma decay widths towards the experimental values. Their number should be sufficiently small to overcome the limits of the central-limit theorem and to broaden the distribution of total gamma decay widths. It is an open question whether a comparatively small number of such strongly coupled gamma decay channels could also cause a change of the PTD for the reduced neutron widths.

Acknowledgements

We thank M. Krtička and P. E. Koehler for useful discussions. We also thank P. E. Koehler for providing the experimental data used here. This work was supported in part by the U.S. DOE Grant No. DE-FG02-91ER40608 and by the U.S. DOE NNSA Stewardship Science Graduate Fellowship under cooperative agreement No. DE-NA0003864. The initial part of this work was performed at the Aspen Center for Physics, which is supported by a National Science Foundation Grant No. PHY-1607611.

References

[1] P. E. Koehler et al., Phys. Rev. Lett. 105, 072502 (2010).

[2] P. E. Koehler, Phys. Rev. C **84**, 034312 (2011).

[3] P. E. Koehler, Phys. Rev. C **88**, 041305(R) (2013).

[4] G. E. Mitchell, A. Richter, and H. A. Weidenmüller, Rev. Mod. Phys. **82**, 2845 (2010).

[5] A. Volya, H. A. Weidenmüller, and V. Zelevinsky, Phys. Rev. Lett. **115**, 052501 (2015).

[6] E. Bogomolny, Phys. Rev. Lett. **118**, 022501 (2017).

[7] P. Fanto, G. F. Bertsch, and Y. Alhassid, Phys. Rev. C **98**, 014604 (2018).

[8] G. L. Celardo, N. Auerbach, F. M. Izrailev, and V. G. Zelevinsky, Phys. Rev. Lett. **106**, 042501 (2011).

[9] S. A. Sheets, Phys. Rev. C **79**, 024301 (2009).

Theory of Heavy Ion Single and Double Charge Exchange Reactions

Horst Lenske[1,2]
[1]Institut für Theoretische Physik, Justus-Liebig-Universität Gießen, D-35392 Gießen
[2]NUMEN Collaboration, LNS Catania

Abstract
Peripheral heavy ion single and double charge reactions are described by fully quantum mechanical distorted wave methods. A special class of nuclear double charge exchange (DCE) reactions proceeding as a one-step reaction through a two-body process are shown to proceed by nuclear matrix elements of a diagrammatic structure as found also in $0\nu2\beta$ decay. These hadronic Majorana-type DCE reactions (MDCE) have to be distinguished from second order DCE reactions, given by double single charge exchange (DSCE) processes, resembling $2\nu2\beta$ decay. The theoretical concepts of MDCE are discussed. First results show that ion-ion DCE reactions are the ideal testing grounds for investigations of rare second order nuclear processes, giving insight into nuclear in-medium two-body correlation.

1 Introduction

To a large extent, nuclear phenomena are well explained by the mean-field dynamics of nucleons, competing with residual interactions of much smaller strength. Because of the central role played by the independent (quasi-)particle model of nuclei, it is tempting to search for processes by which the limits of the shell model are tested. Promising candidates are rare processes which are suppressed by selection rules or because they can proceed only through higher order correlations. Such processes may reveal details of nuclear dynamics which otherwise are hidden behind dominating leading order effects. Interestingly, already in the 1930ties Marie Goeppert-Mayer formulated such ideas in her work on atomic double-gamma and nuclear double-beta decay [1], in the latter case even before the discovery of the nuclear shell model. Nuclear double-beta decay is still an example of highest actuality. Of special interest is neutrino-less nuclear double beta-decay ($0\nu2\beta$), heavily searched for but still waiting to be detected. There is broad consensus that $0\nu2\beta$ decay will be a highly promising gateway to physics beyond the standard model of elementary particle physics. Once observed, it will give direct evidence on the Majorana-nature of neutrinos with far reaching implications for neutrino masses, neutrino-matter interactions and flavour mixing up to the question of the matter-antimatter asymmetry in the universe [2–6]. Such a signal has to be distinguished from the two-neutrino beta-decay ($2\nu2\beta$) [1, 7] which is fully compatible with the standard model. Although both decays correspond to second order nuclear processes, they are dynamically distinct. Double beta-decay with neutrino emission is a sequential decay process where the leptons are emitted subsequently in an uncorrelated manner. A few nuclei are known to decay by this already rather rare process, as discussed e.g. in Ref. [8, 9]. While the matrix elements are accessible by the observed $2\nu2\beta$ transitions such a check against data does not yet exist for $0\nu2\beta$ processes. Thus, estimates of life times and transition probabilities are relying on theoretical investigations, notoriously showing an uncomfortably large spread of values. Independent tests of the nuclear structure input under controllable dynamical conditions are highly necessary, allowing to evaluate and gauge the theoretical results by an independent process. The field will profit tremendously if a surrogate process could be identified which is technically and physically easily accessible. While single charge exchange (SCE) reactions with light and heavy ions have been studied intensively, including our own work [10–12], close to nothing is known about double charge exchange reactions. Only very recently, the NUMEN project has been initiated [13], using heavy ion reactions to explore that unknown territory, also aiming at establishing the relation to double beta decay. Clearly, to establish that connection requires additional efforts in our theoretical understanding of nuclear multi-step reactions. Hence, in section 2 we start with a brief introduction into the

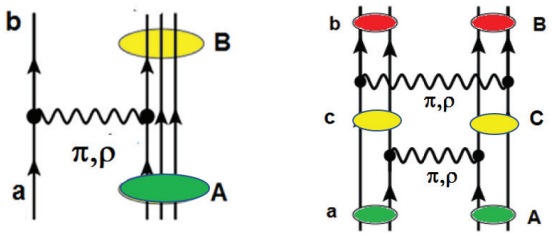

Fig. 1: Diagrammatic structure of nuclear charge exchange reactions by the exchange of $\pi^{\pm}$ and $\rho^{\pm}$ mesons. SCE reactions (left) can be studied by nucleon-induced and light and heavy ion reactions while the sequential DSCE process (right) requires interactions of two complex nuclei.

theoretical background for single and double single charge exchange reactions. In section 3 the physical concept of Majorana DCE reactions is briefly introduced. First results are discussed in section 4 and in section 5 an outlook will be given.

2 Single Charge Exchange and Double Single Charge Exchange Reactions

Single charge exchange reactions (SCE) have become a widely used tool for studying the spin-isospin response of nuclei. The discovery of the giant Gamow-Teller resonance (GTR) by the pioneering experiments at IUCF [14] initiated widespread experimental and theoretical research activities, continuing with even increasing intensity until today. Over the years, a wealth of data has been accumulated as reviewed e.g. in [15–19]. Beyond using nucleonic probes, light ion reactions as e.g. $(^3He, ^3H)$ have become another workhorse of the field, now reaching accuracies allowing to investigate subtle details of spectral distributions in both the τ_+ and the τ_- branches. Soon after the first light ion studies, also heavy ions were used in charge exchange studies as in [11, 20]. It was recognized that peripheral heavy ion collisions, leading to direct reactions, are as useful for spectral studies as light ion scattering. An especially appealing aspects is the broad range of projectile-target combinations which, for example, allow to project out selectively specific features, e.g. spin flip and non-spin flip transitions [10]. Nuclear spin-dynamics and the population of continuum states were central aspects of the $(^7Be, ^7Li)$ reactions considered in [21, 22]. In Fig, 1 the diagrams contributing to a SCE reaction is indicated. Also shown is the DSCE reactions, given by a two-step reaction of sequential SCE processes.

As discussed in detail in Ref. [23], the SCE reaction amplitudes are expressed as DWBA matrix elements of the nucleon-nucleon T-matrix with spin-isospin elements of tensorial rank 0 and form factors $V_{ST}^{(C)}$, and rank 2 with corresponding form factors $V_{ST}^{(Tn)}$. They are connecting the initial channel $\alpha = a + A$ and the final channel $\beta = b + B$. The SCE reaction kernel is given by products of nuclear form factors

$$\begin{aligned} K_{\alpha\beta}^{(ST)}(\mathbf{p}) &= (4\pi)^2 (V_{ST}^{(C)}(p^2) F_{ST}^{(ab)\dagger}(\mathbf{p}) \cdot F_{ST}^{(AB)}(\mathbf{p}) \\ &+ \delta_{S1} \sqrt{\frac{24\pi}{5}} V_{ST}^{(Tn)}(p^2) Y_2^*(\hat{\mathbf{p}}) \cdot \left[F_{ST}^{(ab)\dagger}(\mathbf{p}) \otimes F_{ST}^{(AB)}(\mathbf{p}) \right]_2) \end{aligned} \tag{1}$$

where the rank-2 tensorial coupling relates to the spin degrees of freedom only. Through the form factors $F_{ST}^{(ab),(AB)}$, the kernels contain the spectroscopic information on the nuclear transitions, and the dynamics by the interaction form factors $V_{ST}^{(C),(Tn)}$. In the central interaction part, the scalar product indicates the contraction of the projectile and target form factor with respect to the spin and isospin degrees of freedom. The isospin degrees of freedom are of course projected by the nuclear transitions to the proper combination of $\tau_{\pm}$ operators. In terms of the reaction kernels, the SCE transition potential is

found

$$\mathcal{U}_{\alpha\beta}(\mathbf{p}) = \sum_{ST} K^{(ST)}_{\alpha\beta}(\mathbf{p}). \tag{2}$$

A caveat of heavy ion scattering is the dominant role played by initial (ISI) and final (FSI) state ion-ion interactions. Hence, the question arises whether under such conditions it is still possible to deduce spectroscopic information from data. From our former work, we conclude that peripheral heavy ion reactions indeed show a clear correlation of cross sections and nuclear spectroscopy. However, in order to understand the subtleties of that connection a detailed study of the reaction mechanism will be helpful, as done recently for single charge exchange reactions in Ref. [23]. Here, we only indicate the approach allowing to separate formally reaction and nuclear structure effects.

The ISI/FSI effects contained in the distorted waves $\chi^{(\pm)}_{\alpha,\beta}$ are well described by optical potentials. The strategy is to factorize the reaction amplitude into a plane wave form factor part, i.e. the Fourier transform of the nuclear transition currents and densities, and an amplitude containing the elastic ion-ion interactions. As discussed in [23] a momentum space representation allows to perform such a separation. The one-step SCE reaction amplitude is obtained

$$M_{\alpha\beta}(\mathbf{k}_\alpha, \mathbf{k}_\beta) = \int d^3p N_{\alpha\beta}(\mathbf{p}) \mathcal{U}_{\alpha\beta}(\mathbf{p}). \tag{3}$$

Initial and final state interactions are now described by the distortion coefficient [23, 24]

$$N_{\alpha\beta}(\mathbf{p}) = \frac{1}{(2\pi)^3} \langle \chi^{(-)}_\beta | e^{-i\mathbf{p}\cdot\mathbf{r}} | \chi^{(+)}_\alpha \rangle. \tag{4}$$

As discussed in detail in [23], the distortion coefficient $N_{\alpha\beta}$ is closely related to the elastic scattering amplitude: For $p \to 0$ and $k_\beta \to k_\alpha$ the definition of the elastic S-matrix is indeed recovered. Thus, in leading order, the above equation corresponds to the folding of the nuclear transition form factors with the ion-ion elastic scattering amplitude. Becasue of the strong absorption, the distortion coefficient acts mainly as a scaling factor, typically reducing the forward cross section by several orders of magnitudes compared to the plane wave limit. Only at momentum transfers exceeding 100 MeV/c $N_{\alpha\beta}$ leads to modifications of the momentum structure of cross sections.

If we consider, on the other hand, the effective operator underlying the conventional double-SCE two-step reaction mechanism, we find

$$V^{(DSCE)}(\mathbf{13}, \mathbf{24}) \sim \sum_{cC} T_{NN}(\mathbf{3}, \mathbf{4}) \mathcal{G}_{cC}(\mathbf{2-4}, \mathbf{1-3}) T_{NN}(\mathbf{2}, \mathbf{1}) \tag{5}$$

where T_{NN} is the isovector nucleon-nucleon T-matrix and $\mathcal{G}_{cC}$ denotes the (full many-body) propagator of the intermediate nuclei reached in the first SCE reaction step. Using distorted waves, we find in momentum representation

$$\mathcal{G}_{cC}(\omega) = \int \frac{d^3k}{(2\pi)^3} \frac{|\chi^{(+)}_\gamma cC\rangle\langle cC\tilde{\chi}^{(+)}_\gamma|}{\omega - \omega_k - E_c - E_C - i0+} \tag{6}$$

where the biorthogonality of the optical waves has been taken into account by $\tilde{\chi}^{(+)}_\gamma$. Hence, the DSCE reaction amplitude is given effectively by a second order distorted wave expression

$$M^{(DSCE)} = \langle \chi^{(-)}_\beta bB | V^{(DSCE)} | aA\chi^{(+)}_\alpha \rangle. \tag{7}$$

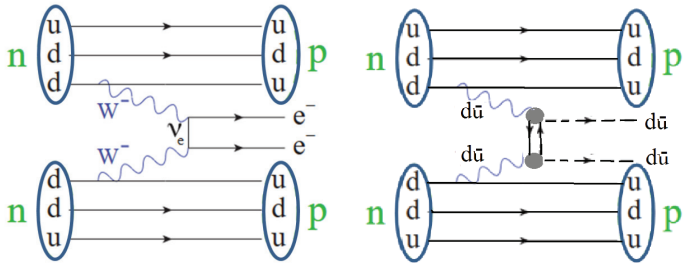

Fig. 2: The elementary weak interaction process mediating nuclear $0\nu2\beta$ decay (left) and a corresponding strong interaction process (right) are depicted schematically. The QCD counterpart is given by the simultaneous emission of two $[d\bar{u}]$ pairs in an isovector-vector, e.g. 1^-, configuration (wavy lines), decaying into a pionic $[d\bar{u}]$ configuration and a charge-neutral $q\bar{q}$ pair.

3 Majorana Double Charge Exchange Reactions

Second order quantal processes like heavy ion double charge exchange reactions are of genuine reaction theoretical interest. First of all, until now heavy ion DCE reactions have not been studied, neither experimentally nor theoretically. Some attempts were made on (π^+, π^-) reactions but the notoriously bad energy definition of the incoming pion beams is unfavorable for spectroscopic work. Thus, double charge exchange reactions with heavy ions are much better suited for explorations of weakly populated transitions. Here, we consider collisional charge exchange processes given by elementary interactions between target and projectile nucleons. In accordance with explicit calculations, the mean-field driven transfer contributions are neglected because they are at least of 4th order for DCE reactions considered here [25]. Thus, only processes with changes of the charge partitions but leaving the projectile-target mass partition unaltered will be discussed.

A central question is whether we can identify on the elementary level a correspondences between strong and weak interaction processes. The answer is yes, as illustrated in Fig. 2. Under nuclear structure aspects, the $0\nu2\beta$ decay of a nucleus is nothing but special class of two-body correlation, sustained by the exchange of a (pair of) Majorana neutrino(s) between two nucleons where the interaction vertices are given by the emission of virtual $W^{\pm}$ gauge bosons. The strong interaction counterpart is a two-nucleon correlation built up by the exchange of a virtual charge-neutral quark-antiquark ($q\bar{q}$) pair accompanied by the emission of a charged $q\bar{q}$ component, thus changing at the same time the nucleonic charges. Similar to the weak process, the strong vertices are originating from gauge bosons, here given by the initial emission of gluons which materialize into two $q\bar{q}$ pairs. At the end, the highly off-shell $q\bar{q}$ compounds will decay into mesons, preferentially into pions but also multi-pion configurations like the scalar and vector mesons.

Such interaction process may occur frequently in nuclei, both on the weak as well as on the strong interaction scale. They remain unobserved if the emitted electrons or charged mesons are reabsorbed by the same nucleon. This will lead to vertex and propagator correction and, as such, contributes to the nucleon in-medium mass operator of a, however, negligibly small strength. Nevertheless, it is worthwhile to keep in mind that we are dealing here with phenomena belonging to the large class of nuclear ground state correlations beyond the commonly studied mean-field sector [26–29]. Short-range correlations are known to modify nuclear momentum contributions on the level of up to 20%.

Both processes become of interest if they reveal their existence and nature in observable signals. In this respect, we encounter a fundamental difference between $0\nu2\beta$ decay and the hadronic process: Only the former may occur in an isolated nucleus while the latter one is inhibited by energy conservation. Thus, in order to observe the double-meson emission by a nucleon pair a partner nucleus is required which takes

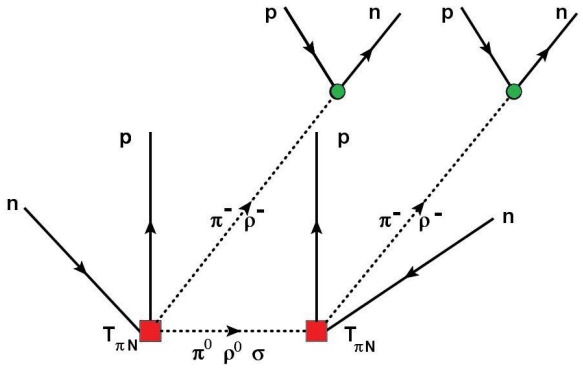

Fig. 3: Generic diagram illustrating the hadronic surrogate process for $0\nu2\beta$ decay. A virtual $nn \to pp\pi^-\pi^-$ scattering process, causing the $\Delta Z = +2$ target transition $A \to B$, is accompanied by $nnp^{-1}p^{-1}$ double-CC excitation in the projectile. Crossed diagrams are not displayed.

care of the virtuality of the process by absorbing the two charged virtual mesons. For that purpose, heavy ion double charge exchange reactions are the ideal tool. The diagrammatic structure of such a reaction is indicated in Fig. 3. The target undergoes a correlated double-meson pair decay $nn \to pp\pi^-\pi^-$ (in fact a $2p2n^{-1}$ 2p-2h transition with coherent emission of a pion pair) and the projectile absorbs the pions by the simultaneous excitation of two np^{-1} -type configurations. Other mesons will contribute as well.

The whole reaction will proceed as a one-step reaction via a special kind of two-body interaction generated by the correlation diagram. Denoting the (in-medium) pion-nucleon T-matrix by $T_{\pi N,\pi' N'}$, the target-part of the interaction is in a somewhat symbolic notation

$$V^{(MDCE)}(\mathbf{13},\mathbf{24}) \sim T_{\pi^- p,\pi^0 n}(\mathbf{1},\mathbf{3}) D_{\pi^0}(\mathbf{1}-\mathbf{2}) T_{\pi^0 n,\pi^- p}(\mathbf{2},\mathbf{4}) \tag{8}$$

where the $n \to p$ target transitions are denoted by $\mathbf{1}$ and $\mathbf{2}$, respectively. The coordinates $\mathbf{3}$ and $\mathbf{4}$ indicate the outgoing charged pions, inducing the complementary transitions in the projectile. The correlation built up by the neutral pion is described by the propagator D_{π^0}. A decomposition into irreducible tensors gives rise in particular to an effective rank-2 iso-tensor projectile-target interaction of operator structure $[\boldsymbol{\tau}_{1A} \otimes \boldsymbol{\tau}_{2A}]_2 \cdot [\boldsymbol{\tau}_{3a} \otimes \boldsymbol{\tau}_{4a}]_2$. We recognize immediately the similarity to the nuclear matrix element of $0\nu2\beta$ decay, justifying the name Majorana-DCE. At present, the strengths of the nucleon-nucleon and the pion-nucleon T-matrices are taken from data. More refined description will be scrutinized in future work by an effective field theoretical description [30] and by referring to the data base available for free space $nn \to pp\pi^-\pi^-$ reactions. Previously, the charge-conjugated reaction $pp \to nn\pi^+\pi^+$ reaction and other double-pion production channels were investigated at CELSIUS and COSY [31–35] and more recent also at HADES [36]. Theoretical studies of the on-shell reaction combining meson exchange and resonance excitation are found in [37, 38].

4 Heavy Ion DCE Reactions and Data

The full DCE reaction amplitude is given by the coherent sum of the MDCE and the DSCE amplitudes:

$$M_{\alpha\beta} \sim \langle \chi_\beta^{(-)\dagger}, bB | V^{(MDCE)} + V^{(DSCE)} | aA, \chi_\alpha^{(+)} \rangle = M_{\alpha\beta}^{(MDCE)} + M_{\alpha\beta}^{(DSCE)} \tag{9}$$

The results discussed below were obtained fully quantum mechanically by one-step DWBA calculations for the MDCE amplitudes and second order DWBA calculations for the DSCE amplitudes, respectively. Thus, ion-ion interactions are treated to all orders. As discussed in Ref. [23] the strong absorption

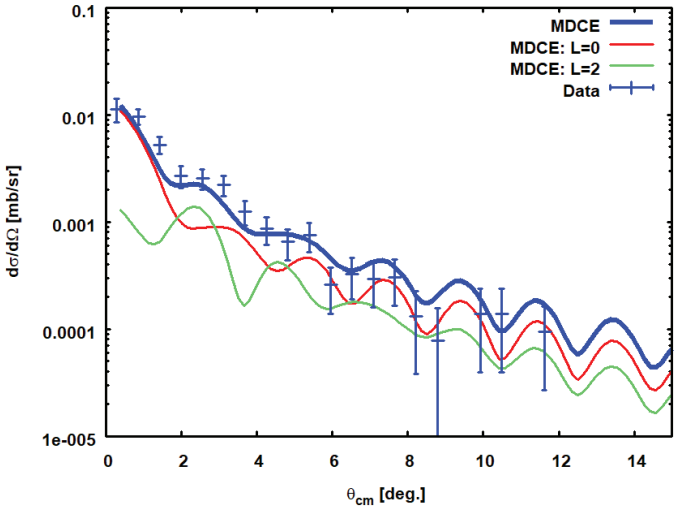

Fig. 4: Angular distribution of the DCE reaction $^{18}O + ^{40}Ca \rightarrow ^{18}Ne + ^{40}Ar$ at $T_{lab} = 270$ MeV. Theoretical MDCE results are compared to the data of Ref. [39]. In addition to the full MDCE cross section also the partial contributions with $L = 0, S = 1$ and $L = 2, S = 2$, respectively, are shown separately. The theoretical results have been normalized to the data at the smallest scattering angle.

in grazing ion-ion collisions allows to evaluate the distortion coefficient in black disk approximation. As mentioned before, under such conditions the ISI/FSI effects are resulting effectively in a scaling factor, allowing to relate at forward angles the cross sections to the corresponding plane wave cross sections. Thus, in principle spectroscopic information can be extracted from the data, provided the elastic interactions are known to the necessary precision. In the present calculations, double folding potentials have been used.

First results of a DCE calculation along the line discussed above are shown in Fig. 4 and compared to recent NUMEN data [39] for the reaction $^{18}O + ^{40}Ca \rightarrow ^{18}Ne + ^{40}Ar$ at $T_{lab} = 15$ AMeV. The reaction leads from the 0^+ ground states of the initial to the 0^+ ground states of the final nuclei, constraining the total angular momentum transfer to $J^P = 0^+$. The transition strengths are taken from QRPA calculations, see e.g. Ref. [23]. For these exploratory investigations MDCE form factors and interactions were treated schematically by approximating the complex off-shell momentum structure by the on-shell strength. Only the pionic contributions were included. This leaves open an overall scaling factor which was fixed by normalizing the MDCE cross section to the data point at the smallest scattering angle. The forward peak of the angular distribution is dominated, in fact, by the ($L = 0$, $S = 1$) MDCE component. However, as seen in Fig. 4, the ($L = 2$, $S = 2$) components are of comparable importance at the larger scattering angles. Moreover, they are essential for the description of the data. Overall, the shape of the measured angular distribution is described decently well in view of the exploratory character of the calculations.

A competing reaction mechanism is the two-step DSCE process. In Fig. 5, DSCE and MDCE cross sections are displayed and compared to data as a function of the momentum transfer. Remarkably, the measured angular range covers a momentum range of more than 400 MeV/c. The DSCE cross section was normalized to the large angle region because higher order reactions typically prevail at larger momentum transfers. That conjecture is confirmed by the DSCE angular distribution: Aside from the typical L=0 forward structure the main body of the angular distribution oscillates around a mean-value of a few times $10^{-4} mb/sr$. Cross sections of igher multipolarities are carrying less strengths and are of flatter shape. With all caution, we may conclude that the data are in favor of the one-step MDCE

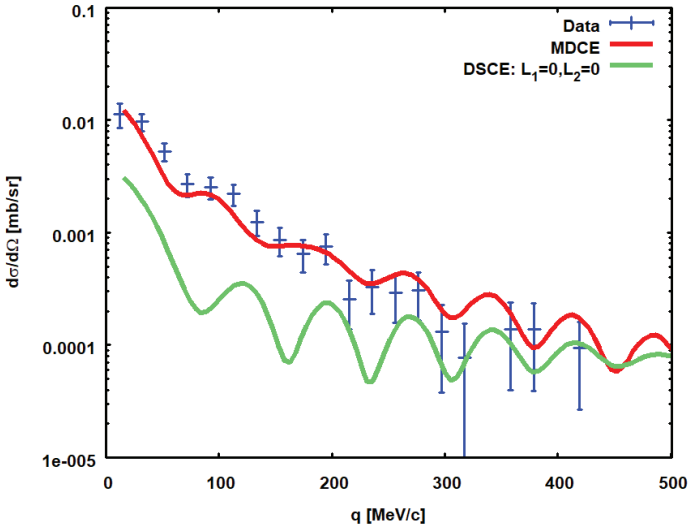

Fig. 5: Angular distribution of the DCE reaction $^{18}O + {}^{40}Ca \rightarrow {}^{18}Ne + {}^{40}Ar$ at $T_{lab} = 270$ MeV. The one-step MDCE and the two-step DSCE cross sections are shown separately in comparison to the data of Ref. [39].

angular distribution. Even if the DSCE cross section would be scaled to the measured forward angle cross section, its shape would not match the observed angular distribution, an observation giving further evidence to the dominance of the MDCE one-step reaction mechanism.

5 Outlook

A new theoretical scenario for heavy ion double charge exchange reactions was introduced. At the diagrammatic level, structures similar to $0\nu2\beta$ matrix elements have been identified. The hadronic Majorana-DCE process is accessible only by reactions of composite nuclei. We have discussed explicitly the case of a DCE reaction with medium mass ions at relatively low incident energy. ISI and FSI ion-ion interactions were taken into account and the quantum mechanical coherence of the MDCE and the DSCE reaction mechanism was treated properly. The strongly forward peaked measured angular distributions indicate a direct mechanism which indeed is confirmed by the calculations. These first results are very promising by indicating a new way of accessing second order nuclear matrix elements of charge changing interactions. Together with the much better studied SCE reactions and their established usefulness for spectroscopic work, heavy ion DCE reactions are opening a new window to high-precision spectroscopy. Although it will not be possible to insert the extracted matrix elements directly into a $0\nu2\beta$ analysis, DCE reactions provide an unique way to validate nuclear structure models under controllable laboratory conditions by comparison to data on processes of comparable physical content. New impact on theoretical investigations in both reaction and nuclear structure theory is demanded for a quantitative understanding of these special reactions. Although the present calculations do not yet include the full spectrum of contributions, they are establishing the hadronic Majorana-DCE reaction mechanism. The refinements may lead to changes in detail but will not alter the overall picture. An exciting and encouraging result is that the MDCE process is clearly visible, even dominating the cross section at extreme forward angles.

References

[1] Goeppert M 1935 *Phys. Rev.* **48** 512

[2] Haxton W C and Stephenson G J 1984 *Prog. Part. Nucl. Phys.* **12** 409

[3] Tomoda T 1991 *Rept. Prog. Phys.* **54** 53
[4] Suhonen J and Civitarese O 1998 *Phys. Rept.* **300** 123
[5] Vergados J D, Ejiri H and Šimkovic F 2012 *Rep. Prog. Phys.* **75** 106301
[6] Cremonesi O and Pavan M 2014 *Adv High Energy Phys.* 951432 (*Preprint* arXiv:1310.4692[physics.ins-det])
[7] Stefanik D, Simkovic F and Faessler A 2015 *Phys. Rev. C* **91** 064311 (*Preprint* arXiv:1506.00835[nucl-th])
[8] Grewe E W and Frekers D 2006 *Prog. Part. Nucl. Phys.* **57** 260
[9] Barabash A S 2015 *Nucl. Phys. A* **935** 52 (*Preprint* arXiv:1501.05133[nucl-ex])
[10] Lenske H, Wolter H H and Bohlen H G 1989 *Phys. Rev. Lett.* **62** 1457
[11] Brendel C, von Neumann-Cosel P, Richter A, Schrieder G, Lenske H, Wolter H H, Carter J and Schuell D 1988 *Nucl. Phys. A* **477** 162
[12] Bohlen H G, Lenske H *et al.* 1988 *Nucl. Phys. A* **488** 89
[13] Cappuzzello F *et al.* 2018 *Eur. Phys. J.* **A54** 72
[14] Goodman C D, Goulding C A, Greenfield M B, Rapaport J, Bainum D E, Foster C C, Love W G and Petrovich F 1980 *Phys. Rev. Lett.* **44** 1755–1759
[15] Ichimura M, Sakai H and Wakasa T 2006 *Prog. Part. Nucl. Phys.* **56** 446–531
[16] Thies J H *et al.* 2012 *Phys. Rev.* **C86** 044309
[17] Frekers D, Puppe P, Thies J H and Ejiri H 2013 *Nucl. Phys.* **A916** 219–240
[18] Frekers D *et al.* 2015 *Phys. Rev.* **C91** 034608
[19] Fujita Y, Rubio B and Gelletly W 2011 *Prog. Part. Nucl. Phys.* **66** 549–606
[20] Bérat C *et al.* 1989 *Phys. Lett.* **B218** 299–303
[21] Cappuzzello F *et al.* 2004 *Europhys. Lett.* **65** 766–772
[22] Cappuzzello F *et al.* 2001 *Phys. Lett.* **B516** 21–26
[23] Lenske H, Bellone J I, Colonna M and Lay J A 2018 *Phys. Rev. C* (*Preprint* 1803.06290)
[24] Lenske H 2018 *J. Phys. Conf. Ser.* **1056** 012030
[25] Lay J A, Burrello S, Bellone J I, Colonna M, Lenske H and Lenske (within the NUMEN project) 2018 *J. Phys. Conf. Ser.* **1056** 012029
[26] Froemel F, Lenske H and Mosel U 2003 *Nucl. Phys. A* **723** 544 (*Preprint* [nucl-th/0301038])
[27] Konrad P and Lenske H 2007 *Eur. Phys. J. A* **33** 291 (*Preprint* [nucl-th/0612078])
[28] Rocco N, Lovato A and Benhar O 2016 *Phys. Rev. Lett.* **116** 192501 (*Preprint* arXiv:1512.07426[nucl-th])
[29] Benhar O 2016 *Nucl. Phys. News* **26** 15
[30] Santopinto E and Lenske H 2018 *work in progress*
[31] Johanson J *et al.* 2002 *Nucl. Phys. A* **712** 75
[32] Clement H *et al.* 2005 *Int. J. Mod. Phys. A* **20** 1747
[33] El-Bary S A *et al.* 2008 *Eur. Phys. J. A* **37** 267
[34] Tsuboyama T, Sai F, Katayama N, Kishida T and Yamamoto S S 2000 *Phys. Rev. C* **62** 034001
[35] Sarantsev V V *et al.* 2007 *Phys. At. Nucl.* **70** 1885
[36] Agakishiev G *et al.* 2015 *Phys. Lett. B* **750** 184 (*Preprint* arXiv:1503.04013[nucl-ex])
[37] Alvarez-Ruso L, Oset E and Hernandez E 199 *Nucl. Phys. A* **633** 519
[38] Cao X, Zou B S and Xu H S 2010 *Phys. Rev. C* **81** 065201 (*Preprint* [arXiv:1004.0140[nucl-th]])
[39] Cappuzzello F *et al.* 2015 *Eur. Phys. J. A* **51** 145 (*Preprint* arXiv:1511.03858[nucl-ex])

Shell-model studies of the astrophysical mirror rp-reactions ^{34}S(p,γ)^{35}Cl and ^{34g,m}Cl(p,γ)^{35}Ar

W. A. Richter[1,2]*, B. Alex Brown*[3]*, R. Longland*[4]*, C. Wrede*[3] *and C. Fry* [3]
[1] University of Stellenbosch, South Africa, [2] iThemba LABS, Somerset West, South Africa, [3] Department of Physics and Astronomy and NSCL, Michigan State University, East Lansing, Michigan, USA, [4] Department of Physics and Astronomy, University of North Carolina, Chapel Hill, USA

Abstract

The two mirror rp-reactions ^{34}S(p,γ)^{35}Cl and ^{34g,m}Cl(p,γ)^{35}Ar were studied via a shell-model approach. At energies in the resonance region near the proton-emission threshold many negative-parity states appear. We present results of calculations in a full (0+1)$\hbar\omega$ model space which addresses this problem. Energies, spectroscopic factors and proton-decay widths are calculated for input into the reaction rates. Comparisons are also made with a recent experimental determination of the reaction rate for the first reaction. The thermonuclear ^{34g,m}Cl(p,γ)^{35}Ar reaction rates are unknown because of a lack of experimental data. The rates for transitions from the ground state of ^{34}Cl as well as from the isomeric first excited state of ^{34}Cl are explicitly calculated taking into account the relative populations of the two states.

1 Introduction

Our analysis is confined to typical novae temperatures, going up to 1 GK. In a recent experiment [1], [2] the ^{34}S(^{3}He,d)^{35}Cl reaction was studied and proton-transfer spectroscopic factors measured for 21 states in an energy region of about 1 MeV above the threshold energy ($S_p = 6.371$ MeV). As a result a new ^{34}S(p,γ)^{35}Cl reaction rate could be determined directly from the experimental data. The product $(2J+1)C^2S$ was measured so that it was not necessary to determine the J values of the resonances explicitly. We have done a theoretical calculation of the rate which takes into account contributions from positive and negative parity states in a full (0+1)$\hbar\omega$ model space based on the interaction sdpfmu [3]. The motivation is to correlate theory and experiment, to determine where differences exist and the reasons for these.

The thermonuclear ^{34g,m}Cl(p,γ)^{35}Ar reaction rates are unknown at nova temperature due to a lack of experimental nuclear physics data for the resonances up to about 800 keV above the ^{35}Ar proton separation energy [4]. Current nova models treat the ^{33}S(p,γ)^{34}Cl and ^{34}Cl(p,γ)^{35}Ar rates as single, total rates, without separately considering the ground state ^{34g}Cl and the isomeric first excited state ^{34m}Cl (Ex = 146.36(3) keV, $T_{1/2} = 2.5$ min). However, similar to the case of ^{26}Al, the ^{34}Cl ground state and its long-lived isomer are not necessarily in thermal equilibrium at nova temperatures and it is therefore necessary to calculate the reaction rates on both initial states, in order to represent their influence accurately in a nucleosynthesis calculation [5], [6]. In some cases capture on an excited state can dominate a thermonuclear reaction rate even when it is in thermal equilibrium with the ground state [7].

Estimates based on shell-model calculations are complicated by high level density and the presence of negative-parity states in the resonance region near the proton-emission threshold. We present results of calculations in a full (0+1)$\hbar\omega$ model space which addresses this problem using the interaction sdpfmu [3] and NuShellX [8]. The basis consists of a complete (0+1)$\hbar\omega$ basis made from all possible excitations of one nucleon from 1s-0d to 0p-1f. Such calculations were carried out recently for the first

time for the ^{30}P(p,γ)^{31}S reaction [9]. We explicitly calculate the rates for transitions from the ground state of ^{34}Cl as well as from the isomeric first excited state of ^{34}Cl.

In a study by Fry et al. seventeen [4] new ^{35}Ar levels have been found in the energy region $E_x = 5.9 - 6.7$ MeV and their excitation energies= have been determined, but not spins and parities. Because of the paucity of such information we are obliged to rely on shell-model calculations. We have calculated energies, spectroscopic factors and proton-decay widths for input into the reaction rate.

Uncertainty limits for the total calculated reaction rates have been included based on Monte Carlo techniques of estimating statistically meaningful reaction rates and their associated uncertainties [10] via Starlib (starlib.physics.unc.edu).

2 The ^{34}S(p,γ)^{35}Cl reaction

2.1 Results for the reaction rate

In Fig. 1 in the top panel we show the total rp reaction rate versus temperature T9 (GigaK) as well as the contributions from positive and negative parity states. In the lower panel the contributions of the various dominant resonances are shown. The details of these resonances are shown in Table 1.

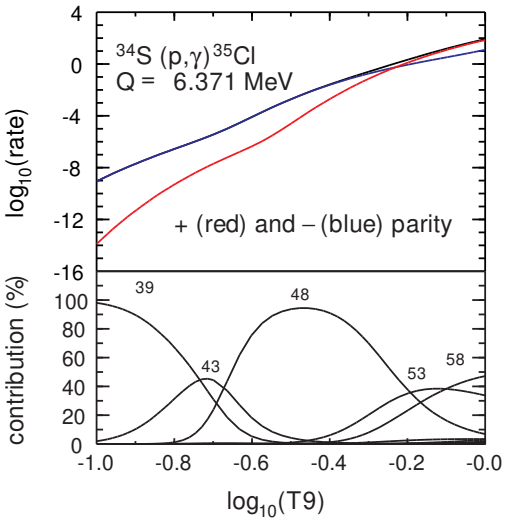

Fig. 1: The total rp reaction rate versus temperature T9 (GigaK) for positive and negative parity states for transitions from the ground state of ^{34}S(top panel) (solid line), and the contribution of each of the final states (lower panel) obtained with the data from Table 1.

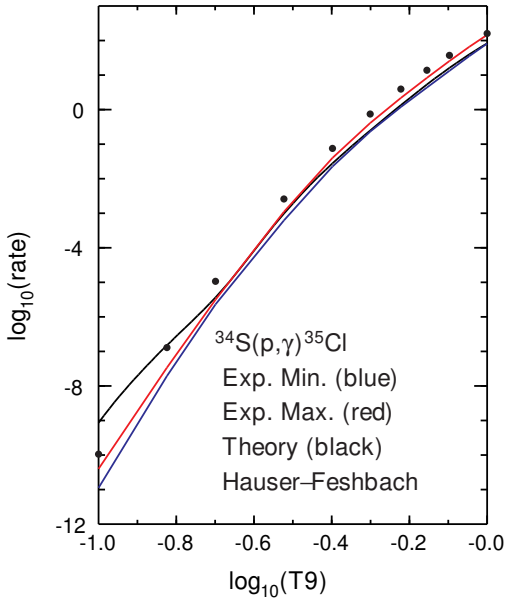

Fig. 2: The total rp reaction rate versus temperature T9 (GigaK) for transitions from the ground state of ^{34}S (dotted line), and the minimum and maximum rates from Ref. [2], as well as a Hauser-Feshbach rate [11].

In Fig. 2 we show a graph of the minimum and maximum rates from Ref. [2], Table 4.5 and our result. A statistical Hauser-Feshbach plot is also shown [11]. Evidently our result is larger in the low temperature region, otherwise the agreement is quite good. The three dominant contributions in the lower temperature region according to our calculations are from the negative parity states 1/2$^-$(2) (6.513 MeV), 3/2$^-$(4) (6.587 MeV) and 3/2$^-$(5) (6.762 MeV). The corresponding energies for Refs. [1], [2] are 6.545 MeV, 6.643 MeV and 6.671 MeV. The $\omega\gamma$ values for the three states correspond reasonably well with the maximum values of Gillespie et al., which correspond to $l = 1$ transfer and thus negative parity as in our calculation. In Ref. [1] it has been assumed that the contribution from Γ_γ is dominant, so that

Table 1: Properties of the rp-resonance states for transitions from the ground state of ^{34}S

n	J^π	k	$E_{\rm x}$(th)	E_{res}	C^2S+	C^2S+	Γ_γ	Γ_p	$\omega\gamma$
			(MeV)	(MeV)	$\ell=0(1)$	$\ell=2(3)$	(eV)	(eV)	(eV)
39	$1/2^-$	2	6.513	0.142	3.6×10^{-1}		2.4	2.4×10^{-9}	2.4×10^{-9}
43	$3/2^-$	4	6.587	0.216	1.5×10^{-2}		3.7×10^{-2}	1.2×10^{-7}	2.5×10^{-7}
48	$3/2^-$	5	6.761	0.390	4.1×10^{-2}		4.1×10^{-2}	1.7×10^{-3}	3.3×10^{-3}
53	$1/2^+$	4	7.006	0.635	6.3×10^{-3}		1.6	3.3×10^{-1}	2.8×10^{-1}
58	$1/2^+$	5	7.116	0.745	1.4×10^{-2}		2.5	3.1	1.4

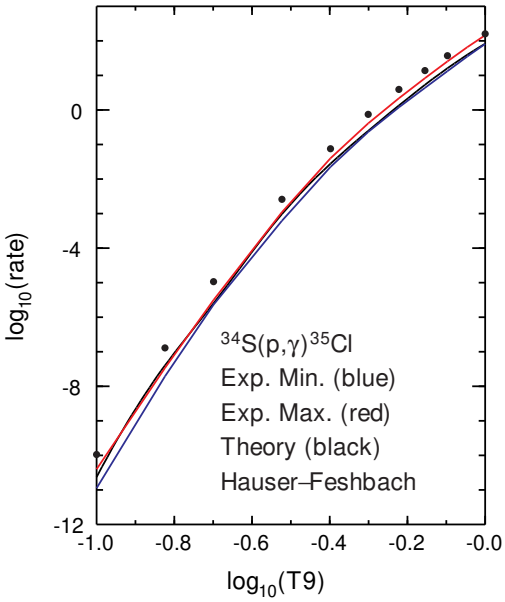

Fig. 3: The same as the previous figure but with the spectroscopic factor for the $1/2^-(2)$ state of Ref. [1] substituted (dotted line).

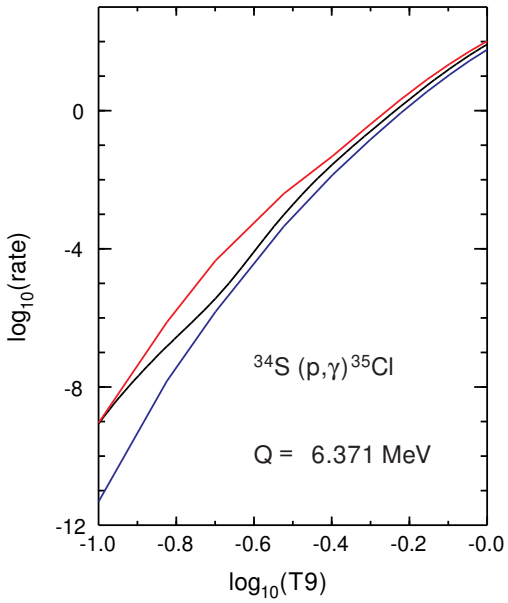

Fig. 4: The total rp reaction rate versus temperature T9 (GigaK) for transitions from the ground state of ^{34}S, and the high and low rates according to the Monte Carlo estimates indicated in red and blue respectively.

$\omega\gamma$ depends only on Γ_p. The main difference between experiment and theory resides in the contribution of the $1/2^-(2)$ state through the spectroscopic factor. The theory value $(2J+1)C^2S$ is 0.36 while the experimental value is 0.0028. When we substitute the spectroscopic factor of Gillespie et al. in our calculation the discrepancy at lower temperature is removed. (Fig. 3).

In Fig. 4 the total reaction rate is shown as well as a low rate and a high rate for each temperature, corresponding to the 0.16 and 0.84 quantiles of the cumulative reaction rate distribution [10].

3 The ^{34g,m}Cl(p,γ)^{35}Ar reaction

3.1 Results for the reaction rate

Fig. 5 shows the total rp reaction rate versus temperature T9 (GigaK) for positive and negative parity states for transitions from the ground state of ^{34}Cl(top panel) and the contribution of each of the final states(lower panel) obtained with the data from Table 2. It is evident that the negative parity states dominate the reaction rate by up to three orders of magnitude at the lower temperatures. The rate is

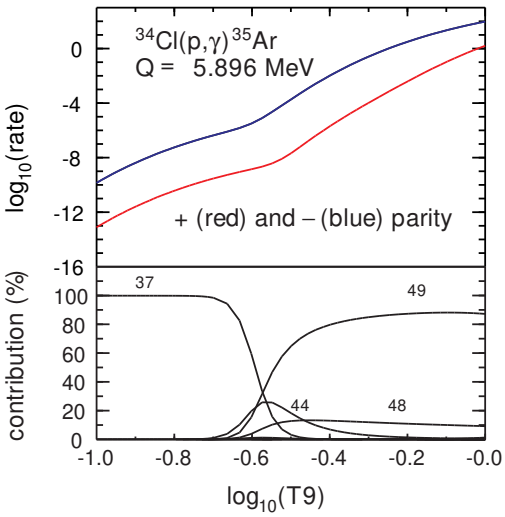

Fig. 5: The total rp reaction rate versus temperature T9 (GigaK) for positive and negative parity states for transitions from the ground state of ^{34}Cl(top panel) (solid line), and the contribution of each of the final states (lower panel) obtained with the data from Table 2.

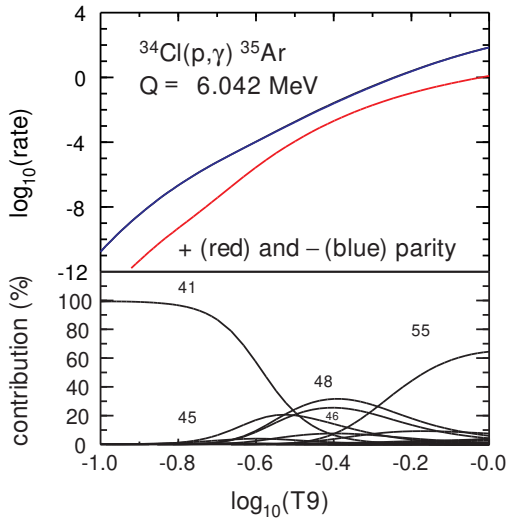

Fig. 6: The total rp reaction rate versus temperature T9 (GigaK) for positive and negative parity states for transitions from the first excited state of ^{34}Cl(top panel) (solid line), and the contribution of each of the final states (lower panel) obtained with the data from Table 3.

Table 2: Properties of the rp-resonance states for transitions from the ground state of ^{34}Cl

n	J^π	k	$E_{\rm x}$(th)	E_{res}	C^2S	C^2S	Γ_γ	Γ_p	$\omega\gamma$
			(MeV)	(MeV)	$\ell=0(1)$	$\ell=2(3)$	(eV)	(eV)	(eV)
37	3/2$^-$	3	6.052	0.156	3.7×10^{-1}		1.9×10^{-1}	1.0×10^{-9}	2.0×10^{-9}
44	3/2$^-$	4	6.345	0.449	3.5×10^{-3}		7.8×10^{-2}	2.7×10^{-4}	5.4×10^{-4}
46	5/2$^-$	6	6.469	0.573		1.6×10^{-2}	3.5×10^{-1}	2.6×10^{-5}	7.7×10^{-5}
48	3/2$^-$	5	6.476	0.580	2.6×10^{-2}		6.0×10^{-2}	3.7×10^{-2}	4.6×10^{-2}
49	1/2$^-$	2	6.501	0.605	2.2×10^{-1}		1.4	9.8×10^{-1}	5.8×10^{-1}

Table 3: Properties of the rp-resonance states for transitions from the first excited state of ^{34}Cl

n	J^π	k	$E_{\rm x}$(th)	E_{res}	C^2S	C^2S	Γ_γ	Γ_p	$\omega\gamma$
			(MeV)	(MeV)	$\ell=0(1)$	$\ell=2(3)$	(eV)	(eV)	(eV)
41	5/2$^-$	5	6.278	0.236	1.9×10^{-1}	6.0×10^{-2}	8.5×10^{-2}	6.1×10^{-6}	2.6×10^{-6}
45	7/2$^-$	7	6.395	0.353	2.6×10^{-2}	3.0×10^{-2}	7.8×10^{-2}	3.0×10^{-4}	1.7×10^{-4}
46	5/2$^-$	6	6.469	0.427	3.3×10^{-2}	1.0×10^{-3}	3.5×10^{-1}	6.4×10^{-3}	2.7×10^{-3}
48	3/2$^-$	5	6.476	0.434	5.3×10^{-2}	4.4×10^{-2}	6.0×10^{-2}	1.9×10^{-2}	4.1×10^{-3}
55	5/2$^-$	7	6.695	0.653	1.9×10^{-1}	7.1×10^{-2}	1.9	4.4	5.6×10^{-1}

mainly due to two resonances, the 3/2$^-$(3) and 1/2$^-$(2) states. Fig. 6 shows the same for positive and negative parity states for transitions from the first excited state of ^{34}Cl (top panel) using the data from Table 3. Again the negative parity states dominate the rate by up to two orders of magnitude, and the rate is mainy due to two resonances, the 5/2$^-$(5) and 5/2$^-$(7) states. Fig. 7 shows the total rate including positive and negative parity and transitions from both the ground and first excited state of ^{34}Cl. The

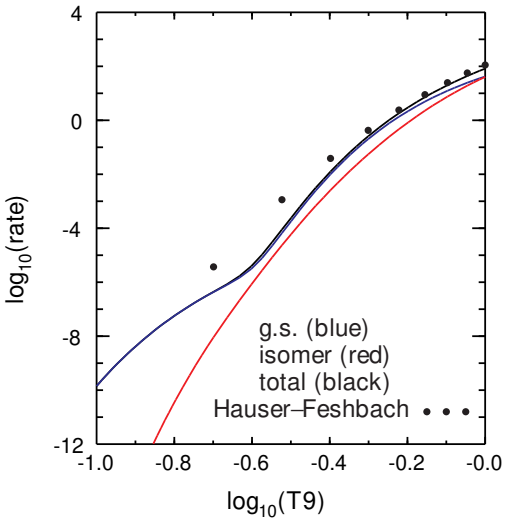

Fig. 7: The total rp reaction rate (which includes positive and negative parity with the relative populations of the ground and first excited isomeric states of ^{34}Cl taken into account) versus temperature T9 (GigaK). The contributions from the ground state and the isomeric state are also shown.

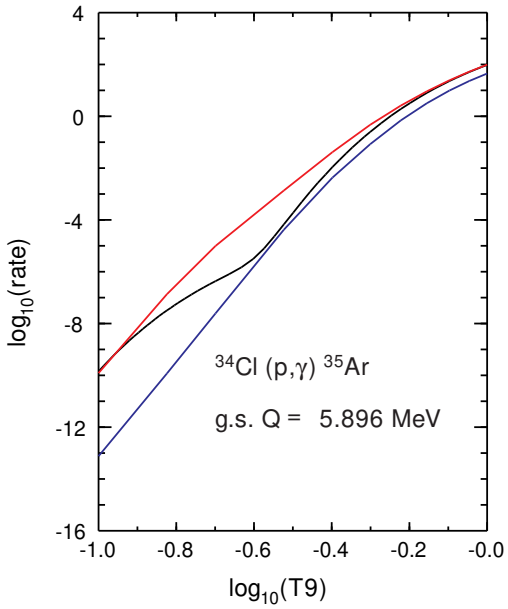

Fig. 8: The total rp reaction rate versus temperature T9 (GigaK) for transitions from the ground state of ^{34}Cl, and the high and low rates according to the Monte Carlo estimates indicated in red and blue respectively.

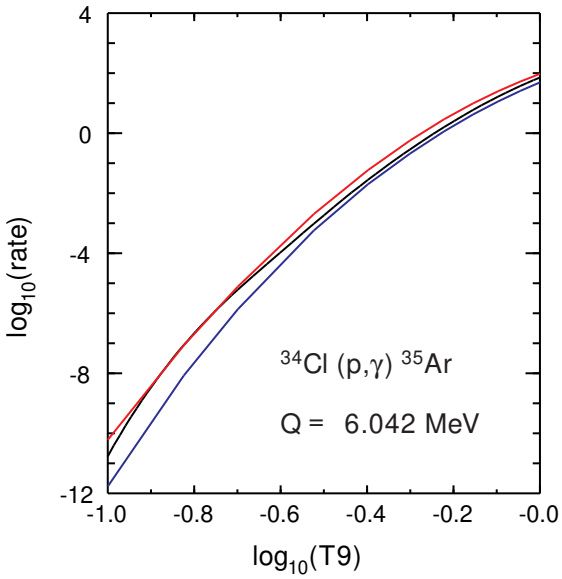

Fig. 9: The total rp reaction rate versus temperature T9 (GigaK) for transitions from the isomeric first excited state of ^{34}Cl, and the low and high rates according to the Monte Carlo estimates indicated in red and blue respectively.

relative populations of the two states have been taken into account through the stellar enhancement factor (SEF), which is the ratio of the stellar rate (including the isomeric state) and the rate from the ground state. It is evident that the rate from the ground state is dominant. In Figs. 8 and 9 the high and low rates based on a Monte Carlo analysis are shown for the ground state and isomeric state respectively.

4 Conclusions

In the comparison of our calculations for ^{34}S(p,γ)^{35}Cl with the recent experiment of Gillespie et al. on ^{34}S(^{3}He,d)^{35}Cl there is good agreement between the calculated total rate and the experimental rate up to 1 GK, except in the low-temperature region where the theory is up to an order of magnitude larger. The difference is due to the spectroscopic factor of the 1/2^{-}(2) state. Adopting the experimental value resolves the problem. However, given the large energy uncertainty at low energy in particular, the discrepancy could be due to an energy shift within this uncertainty.

The contribution from negative parity dominates except for a region near 1 GK. Our theoretical analysis shows that the ^{34g,m}Cl(p,γ)^{35}Ar reaction rates both for transitions from the ground state of ^{34}Cl and the first excited state are dominated by negative parity states by between two and three orders of magnitude. The contributions to the total rate from the isomeric first excited state of ^{34}Cl become important and dominant above about half of the temperature range considered. The statistical Hauser-Feshbach rate differs from our ground-state rate at lower temperatures by up to about a order of magnitude, but is close to our result for higher temperatures. The calculations also identify the most prominent resonances in the reaction rates, and the analysis should serve as a guide for experiments as the spin-parity assignments of the most prominent resonances are given.

Acknowledgments This work is partly supported by NSF Grant PHY-1811855, the Joint Institute for Nuclear Astrophysics NSF Grant PHY08-22648, and the National Research Foundation of South Africa Grant No. 105608.

References

[1] S. A. Gillespie, A. Parikh, C. J. Barton, T. Faestermann, J. Jose, R Hertenberger, H.-F. Wirth, N. de Sereville, J. E. Riley, and M. Williams Phys. Rev. C 96, 025801 (2017)

[2] S. A. Gillespie, Ph.D thesis, University of York (2016).

[3] Y. Utsuno, T. Otsuka, B. A. Brown, M. Honma, T. Mizusaki, and N. Shimizu, Phys. Rev. C 86, 051301 (2012)

[4] C. Fry, C. Wrede, S. Bishop, B. A. Brown, A. A. Chen, T. Faestermann, R. Hertenberger, A. Parikh, D. Pérez-Loureiro, H.-F. Wirth, A. García, and R. Ortez, Phys. Rev. C 91, 015803 (2015)

[5] M. Coc, M. Porquet and F. Nowacki, Phys. Rev. C 61, 015801 (1999)

[6] P. Banerjee, G. Wendell Misch, S. K. Ghorui and Yang Sun2, Phys. Rev. C 97, 065807 (2018)

[7] H. Schatz, C. A. Bertulani, B. A. Brown, R. R. C. Clement, A. A. Sakharuk, and B. M. Sherrill, Phys. Rev. C 72, 065804 (2005).

[8] B. A. Brown and W. D. M. Rae, Nuclear Data Sheets 120, 115 (2014).

[9] B. A. Brown, W. A. Richter, and C. Wrede, Phys. Rev. C 89, 062801(R) (2014)

[10] R. Longland, C. Iliadis, A. E. Champagne, J. R. Newton, C. Ugalde, A. Cocc, and R. Fitzgerald, Nucl. Phys. A 841, 1 (2010)

[11] C. Iliades, J. M. D'Auria, S. Starfield, W. J. Thompson, and M. Wiescher, Astrophys. J. Suppl.134,151 (2001).

[12] A. Graue, L. H. Herland, J. R. Lien, G. E. Sandvik, E. R. Cosman and W. H. Moore, Nucl. Phys. A 136, 577 (1969)

The role of nucleon knockout in pre-equilibrium reactions

E.V. Chimanski[1,2], *B.V. Carlson*[1], *R. Capote*[2], *A.J. Koning*[2]
[1]Aeronautics Institute of Technology, São José dos Campos, Brazil
[2]NAPC-Nuclear Data Section, International Atomic Energy Agency, Vienna, Austria

Abstract
Nucleon-induced pre-equilibrium reactions are predominantly direct reactions. At low incident energies, excitation of all but the lowest energy collective states can be well described in terms of one-step reactions that produce particle-hole pairs. As the incident energy increases, the probability of exciting a nucleon to the continuum rather than to a bound particle state also increases. These knockout nucleons can escape the nucleus or induce secondary collisions that create still other continuum or bound particle-hole pairs. We discuss their role in precompound nuclear reactions here.

1 Introduction

Above an incident energy of about 20 MeV, nucleon-induced pre-equilibrium reactions are dominated by direct reactions. Excitation of all but the lowest energy collective states can be well described in terms of one-step reactions that produce particle-hole pairs for smaller incident energies in this range. As the incident energy is increased, more complex excitations involving two or more particle-hole pairs become accessible through multi-step reactions. Quantum mechanical models of such multi-step direct reactions were developed many years ago [1–3] and have been studied and improved many times over since then [4–7]. In these models, a leading continuum particle initiates the reaction and remains in the continuum as it scatters repeatedly from the nucleus to produce successive particle-hole pairs. However, as the incident energy increases, the probability of exciting a nucleon to the continuum rather than to a bound particle state also increases [8]. These knockout nucleons can escape the nucleus or induce secondary collisions that create still other continuum or bound particle-hole pairs. They are not taken into account in the MSD models developed until now.

The calculation of knockout to the continuum is a relatively straightforward extension of actual MSD calculations. However, here we would like to obtain a more general idea of the importance of this mechanism in pre-equilibrium reactions. This would require an extension of the existing MSD models codes to an arbitrary number of interactions leading to both bound and continuum configurations. As this is unfeasible, we will make use of the semiclassical DDHMS pre-equilibrium simulation model of Blann and Chadwick [9, 10]. As well as being the most conceptually sound semiclassical model, it is also the closest in correspondence to the quantum mechanical MSD models.

2 Method

An important characteristic of nucleon-induced pre-equilibrium reactions is that their early stages are dominated by collisions that increase the number of particle-hole pairs [3, 11]. This implies that the equal occupation of states with the same particle-hole number, assumed in the semiclassical exciton and hybrid models, is not justified. This limits their applicability to low energies, for which configurations above the two particle - one hole one are not extremely important.

As an alternative, Blann proposed the "hybrid Monte Carlo simulation" (HMS) model [9], in which a sequence of independent particle-hole pairs is excited during a reaction. Each excited particle and hole is considered an independent degree of freedom. Particles can be emitted and particles and holes with sufficient energy can create subsequent particle-hole pairs. Emission occurs in accord with the particle emission widths and excitation in accord with the particle and hole damping widths. At each step of the

Monte Carlo simulation, an emission or particle-hole excitation is chosen based on the relative weight of the widths. The process continues until no particle or hole possesses sufficient energy to be emitted or to excite another particle-hole pair. Blann and Chadwick later extended the model to the DDHMS one, which calculates angular distributions as well as spectra [10].

While the equal occupation assumption of the exciton and hybrid models requires a strong residual interaction between states with the same particle-hole number, the independent particle and hole modes of the HMS model require that there be no residual interaction at all. Comparisons with complete simulations performed using an interaction consistent with the shell model show the HMS model to provide excellent agreement with the more complete calulations while the exciton model does not [12].

Since all active particles and holes can be followed in an HMS calculation, we can tag them according to the number of collisions that have occured. Collision 1 is induced by the incident particle and initially labels this particle as well as the particle-hole pair it produces. Collision 2 is induced by one of these three and labels it as well as the particle-hole pair produced. The labelling continues for higher collison numbers.

The average number of collisons before formation of a residual compound nucleus is quite small on the average, as can be seen in Fig. 1, where, for a proton incident on ^{58}Ni, it increases from a value of about two at 10 MeV to about four at 200 MeV. The standard deviation also grows slowly, from a value of about one at 10 MeV to about three at 200 MeV. Interestingly, the difference between the average value and the standard deviation appears to be fixed at a value of one at all energies. In contrast, the maximum number of collisions before compound nucleus formation grows approximately linearly with the energy and reaches a value close to 50 at 200 MeV.

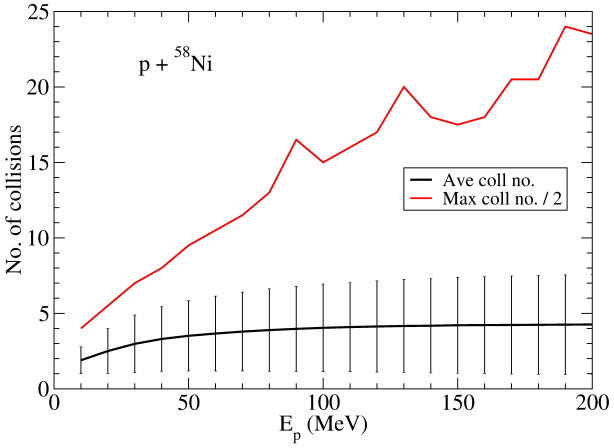

Fig. 1: Average and total number of collisions before compound nucleus formation for the collision $p + {}^{58}$Ni

We label the emited particles according to their collision numbers as follows:

- **inel** - particles emitted after one collision in which the second particle is in a bound state;
- **ko** - particles emitted after one collision in which the second particle is also emitted;
- **1** - particles emitted after on collision independently of hat happens to the collision partner;
- **2** - particles emitted after two collisions (although the second collision might be the emitted particles first collision) independently of what happens to the collision partner;
- **all** - particles emitted after any number of collisions.

The particles labelled **inel** correspond most closely to the leading particle of a usual one-step MSD reaction. In all cases, the residual nucleus might still emit other particles.

3 Results

To relate our calculations to experimental data, we compare our inclusive proton and neutron emission spectra for 90 MeV proton-induced reactions with the data of Refs. [13] and [14]. Our calculations were obtained using the HMS module in the EMPIRE-3 neutron reaction code [15]. All pre-equilibrium and compound nucleus emission has been taken into account. The quasi-elastic peak has not been included.

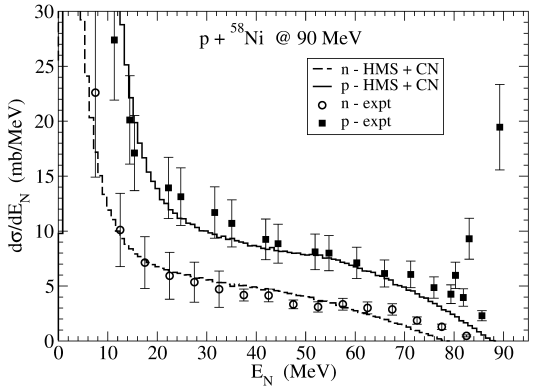

Fig. 2: Calculated inclusive neutron and proton emission spectra compared with the experimental data of Refs. [13] and [14] for the collision $p + {}^{58}$Ni.

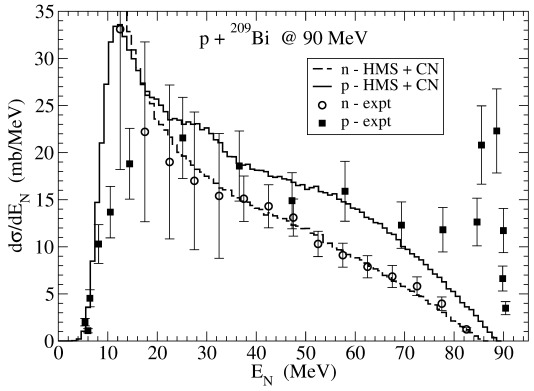

Fig. 3: Calculated inclusive neutron and proton emission spectra compared with the experimental data of Refs. [13] and [14] for the collision $p + {}^{209}$Bi.

In Figs. 2 and 3, we display the calculated inclusive emission spectra for ^{58}Ni and ^{209}Bi together with the experimental data. The agreement between the two is quite good, except for the lower energy proton emission from ^{209}Bi, which is overestimated by the calculations.

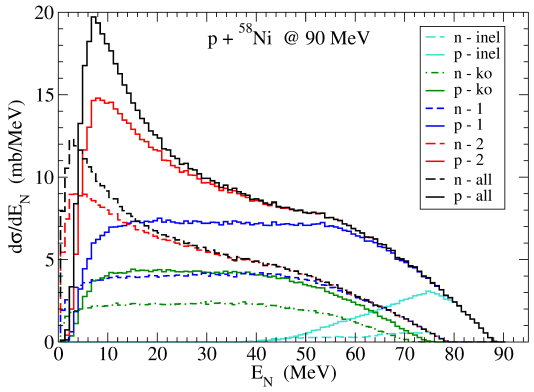

Fig. 4: Contributions to the inclusive nucleon emisson cross sections from the collision $p + {}^{56}$Ni.

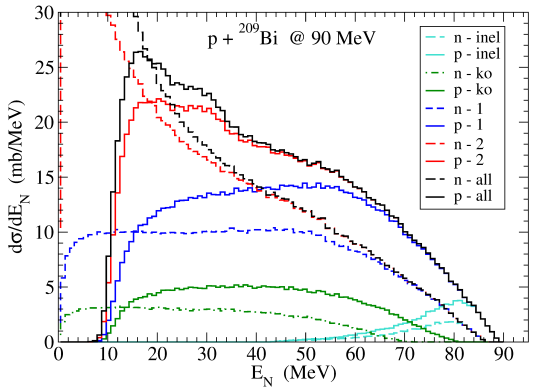

Fig. 5: Contributions to the inclusive nucleon emisson cross sections from the collision $p + {}^{209}$Bi.

In Figs. 4 and 5, we show the decomposition of the inclusive emission cross spectra for ^{58}Ni and ^{209}Bi into their inelastic (inel), knockout (ko), first collision (1) and second collision (2) components. We observe that the emissions resulting in inelastic excitation exhaust the emission spectra for only a small range of about 10 MeV of the most energetic emissions. They then fall slowly, reaching zero at an energy corresponding to an excitation of the residual nucleus of about 50 MeV. Each of the first emission spectra minus the corresponding inelastic spectrum increases roughly in parallel with the corresponding knockout spectrum as the emission energy is reduced from its maximum value. The first emission and knockout spectra saturate at an energy corresponding to an excitation of the residual nucleus of about 25 to 30 MeV and remain flat until decreasing to zero at the Coulomb barrier for protons and at zero energy for neutrons. Finally, we observe that the particles emitted after at most two collisons (2) exhaust

the spectra except at very low excitation energies. As we have seen in Fig. 1, the average number of collisons at 90 Mev is between three and four. We can thus conclude, to a good approximation, that the collisions beyond the first two lead on the average to the formation and subsequent decay of a compound nucleus.

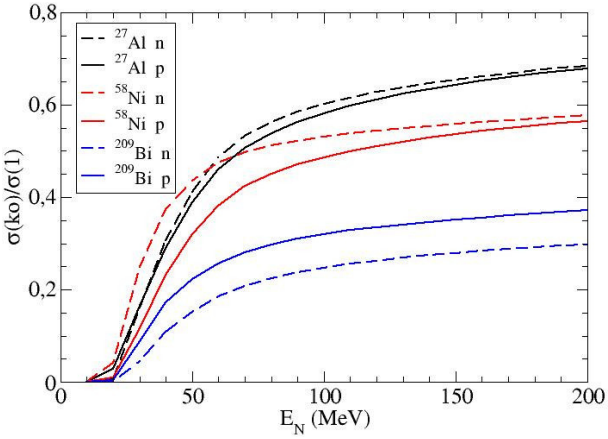

Fig. 6: Ratio of knockout to one interaction neutron and proton emission cross sections for p + ^{27}Al, ^{58}Ni and ^{209}Bi.

The similar behavior of the knockout and first emission spectra as a function of energy suggests a simple relation between the two. The definitions of the two types of emissions also suggest such a relation: in knockout, both nucleons leave the nucleus after only one collision, while in first collison emission, the emitted nucleon suffers only one collision. The difference betwen the two thus refers to the first collisions in which the second nucleon suffers a second collison (or more) before escaping. Since the number of collisions a nucleon participates in is roughly proportional to the nuclear matter through which it passes, we can associate knockout emission with superficial collisions with the target and the remaining first emission nucleons with more central collisions. The simplest estimate we might make is that the knockout cross section should be restricted to an outer ring of width ΔR of the total first emission cross section πR^2. We would then have for the ratio

$$\sigma(ko)/\sigma(1) = (\pi R^2 - \pi(R - \Delta R)^2)/\pi R^2 = 1 - (1 - \Delta R/R)^2.$$

We plot the ratio of the two cross sections as a function of the incident energy for three nuclei: ^{27}Al, ^{58}Ni and ^{209}Bi in Fig. 6. We observe that the ratios for neutron and proton knockout are very similar for each nucleus. The ratios increase fairly rapidly below about 50 MeV, in the region of excitation energy in which inelastic excitation still contributes, and much more slowly above. The ratios decrease with increasing mass of the target nucleus as would be expected from the discussion above.

Table 1: Average ratio of knockout to first emission cross sections at 200 MeV and the corresponding effective surface thickness ΔR for the given nuclei.

Nucleus	Ratio	ΔR (fm)
^{27}Al	0.7	1.7
^{58}Ni	0.55	1.6
^{209}Bi	0.35	1.4

In the table, we give an estimate of the cross section ratio at an incident energy of 200 MeV and of the ring thickness ΔR in which knockout dominates. We observe that the value of ΔR is not constant

but decreases slowly as the mass number of the nucleus increases. We argue that this does not invalidate the interpretation but simply reflects the increasing thickness of the matter that must be traversed as the mass number increases.

4 Conclusions

Nucleon-induced pre-equilibrium reactions are dominated by direct reactions. Quantum mechanical multi-step direct models of these reactions have treated them as being exclusively inelastic excitations. Using the semiclassical HMS model, we have shown here that nucleon knockout - direct excitation to the continuum - makes an important contribution to the emission cross section at incident energies above about 20 to 30 MeV. We are currently working to extend the quantum mechanical MSD model to explicitly include these reactions.

Acknowledgements

EVC acknowledges financial support from grants 2016/07398-8 and 2017/13693-5 of the São Paulo Research Foundation (FAPESP). BVC acknowledges financial support from grant 2017/05660-0 of the São Paulo Research Foundation (FAPESP) and grant 306433/2017-6 of CNPq. EVC and BVC acknowledge support from the INCT-FNA project 464898/2014-5.

References

[1] H. Feshbach, A. Kerman, S. Koonin, Ann. Phys (N.Y.). 125 (1980) 429.

[2] T. Tamura, T. Udagawa, H. Lenske, Phys. Rev. C 26 (1982) 379.

[3] H. Nishioka, H. A. Weidenmüller, S. Yoshida, Ann. Phys. (N.Y.) 183 (1988) 166.

[4] A. Koning, M. Chadwick, Phys. Rev. C 56 (1997) 970.

[5] T. Kawano, S. Yoshida, Phys. Rev. C 64 (2001) 024603.

[6] M. Dupuis, T. Kawano, J. P Delaroche, E. Bauge, Phys. Rev. C 83 (2011) 014602.

[7] M. Dupuis, E. Bauge, S. Hilaire, S. F. Lechaftois, S. Péru, N. Pillet, C. Robin, Eur. Phys. J. A 51 (2015) 168.

[8] B. V. Carlson, J. E. Escher, M. S. Hussein, 41 (2014) 094003.

[9] M. Blann, Phys. Rev. C 54 (1996) 1341.

[10] M. Blann, M. Chadwick, Phys. Rev. C 57 (1998) 233.

[11] J. Bisplinghoff, Phys. Rev. C 33 (1986) 1569.

[12] C. A. Pompeia, B.V. Carlson, Phys. Rev. C 74 (2006) 054609.

[13] J. R. Wu, C. C. Chang, H. D. Holmgren, Phys. Rev. C 19 (1973) 698.

[14] A. M. Kalend, B. D. Anderson, A. R. Baldwin, R. Madey, J. W. Watson, C. C. Chang, H. D. Holmgren, R. W. Koontz, J. R. Wu, and H. Machner, Phys. Rev. C 28 (1983) 105.

[15] M. Herman, R. Capote, B. V. Carlson, P. Oblozinský, M. Sin, A. Trkov, H. Wienke, V. Zerkin, Nuclear Data Sheets 108 (2007) 2655.

Neutron width statistics using a realistic description of the neutron channel

P. Fanto[1]*, G. F. Bertsch*[2]*, and Y. Alhassid*[1]
[1]Center for Theoretical Physics, Sloane Physics Laboratory, Yale University, New Haven, Connecticut 06520, USA
[2]Department of Physics and Institute for Nuclear Theory, Box 351560, University of Washington, Seattle, Washington 98195, USA

Abstract
A basic prediction of the statistical model of compound nucleus reactions is that the partial widths for decay into any open channel channel fluctuate according to the Porter-Thomas distribution (PTD). A recent experiment on s- and p-wave neutron scattering from platinum isotopes found that the experimental s-wave partial neutron width distributions deviated substantially from the PTD. Several explanations for this finding have been proposed within the statistical model, but none has resolved this issue. Here, we review the application of a realistic resonance-reaction model to s-wave neutron scattering from ^{194}Pt. Our main conclusion is that the PTD provides an excellent description of the partial neutron width distribution, provided that the secular energy dependence of the average neutron width is correctly described. Within a realistic range of model parameters, there can be a near-threshold bound or virtual state of the neutron channel that changes this secular dependence from the usual $\sqrt{E}$ dependence, as proposed by Weidenmüller [1]. In this case, the use of the $\sqrt{E}$ dependence to analyze the data will lead to apparent deviations from the PTD. We discuss the limited parameter range where such a near threshold state can have a significant effect.

1 Introduction

Compound nucleus (CN) reactions are important in basic nuclear science, nuclear astrophysics, and nuclear technology applications. The statistical model of CN reactions [2] provides the theoretical framework for understanding this class of nuclear reactions. The basic assumption of the statistical model is that the CN can be described by a random matrix drawn from the Gaussian orthogonal ensemble (GOE) [2, 3]. Energy-averaged cross sections and resonance parameters are calculated as averages over the ensemble. The statistical model modifies the traditional Hauser-Feshbach theory of CN reactions [4] through the so-called width fluctuation correction (WFC) [5]. The Hauser-Feshbach plus WFC approach is used in statistical reaction codes [6].

A basic prediction of the statistical model is that, for isolated resonances, the partial widths for any reaction channel fluctuate according to the Porter-Thomas distribution (PTD) [2, 7]. However, a relatively recent experiment [8] found that the distributions of partial neutron widths in s-wave scattering of neutrons off ^{192,194,196}Pt were significantly broader than the PTD. A number of theoretical studies attempted to explain these deviations from PTD within the statistical model framework. These studies proposed the following explanations:

(i). In the experiment of Ref. [8], the resonance energies and partial widths were extracted using an R-matrix fit to measured data. To obtain the partial width fluctuations, the partial widths must be divided by the secular dependence of the average neutron width on the resonance energy. This energy dependence is expected to be proportional to $\sqrt{E}$ for s-wave neutrons. Weidenmüller proposed [1] that,

for the Pt isotopes, a near threshold bound or virtual state of the s-wave neutron channel[1] changes this secular energy dependence. Thus, the use of the $\sqrt{E}$ form in the experimental analysis might have caused the observed PTD violation in Ref. [8].

(ii). Coupling to the reaction channels induces non-statistical interactions among the CN resonances. These interactions consist of a purely imaginary term due to on-shell coupling to the channels, and a real term called the Thomas-Ehrman shift due to off-shell processes [2]. In the regime of isolated resonances, these interactions are expected to be negligibly weak. However, the experimental finding of Ref. [8] motivated closer studies of the effect of these interactions on the fluctuations of the partial widths. It was shown numerically [9] and analytically [10] that even a relatively weak imaginary term could cause the partial width fluctuations to deviate from the PTD. However, it is unclear if the coupling for isolated resonances is strong enough to cause this effect. In Ref. [11], it was proposed that the Thomas-Ehrman shift could be quite strong near the neutron threshold for the Pt isotopes and cause deviations from the PTD. However, Bogomolny subsequently proved that the only effect of an energy-independent real shift is to modify the secular variation of the average partial neutron width with energy [12]. The numerical results of Ref. [11] were obtained using the entire resonance spectrum without dividing out this secular variation.

However, explanations (i) and (ii) have not been studied within a model that describes fully the coupling between the entrance neutron channel and the CN states. Specifically, near threshold, the non-statistical interactions vary significantly with energy, and this variation has been neglected in the above studies.

Here, we review a recent study [13] of s-wave neutron scattering from ^{194}Pt within a model that combines a realistic description of the entrance neutron channel with the usual GOE description of the internal CN states. This model enables the calculation of cross sections and resonance energies and widths within the same framework. We used a baseline set of the model parameters from the published literature. We then varied these parameters to investigate explanations (i) and (ii) above. Our main conclusion is that the PTD provides an excellent description of the partial neutron width distribution, provided that the secular dependence of the average width on energy is correctly described. Within our parameter range, there can be a near-threshold bound or virtual state of the neutron channel that modifies the usual $\sqrt{E}$ secular variation of the average neutron width. In this case, use of the $\sqrt{E}$ form to analyze the width fluctuations yields apparent PTD violation. We find that this effect is significant only within a limited range of the model parameters.

2 Resonance-reaction model

We describe the s-wave neutron channel on a spatial mesh with spacing Δr and N_n radial sites $r_i = i\Delta r$ $(i = 1, ..., N_n)$. The neutron channel Hamiltonian matrix is obtained by discretizing the usual radial Schrödinger equation

$$\mathbf{H_n}_{,ij} = [2t + V(r_i)]\delta_{ij} - t\delta_{i,j+1} - t\delta_{i,j-1}\,, \qquad i,j = 1, ..., N_n\,, \tag{1}$$

where $t = \hbar^2/(2\mu\Delta r^2)$ (μ is the reduced mass) and $V(r)$ is the neutron channel potential. The neutron channel potential has a Woods-Saxon form $V(r) = -V_0[1 + \exp((r-R)/a)]^{-1}$ where $R = r_0 A^{1/3}$ for mass number A of the target nucleus. The model includes N_c internal CN states, taken from the middle third of the spectrum of a GOE matrix. To account for gamma decay of the resonances, we add to each energy a constant imaginary term that corresponds to the total gamma decay width Γ_γ. This gives the CN Hamiltonian matrix

$$\mathbf{H_c}_{,\mu\nu} = \delta_{\mu\nu}\left(\epsilon_\mu - \frac{i}{2}\Gamma_\gamma\right)\,, \qquad \mu,\nu = 1, ..., N_c\,, \tag{2}$$

[1] A bound state of the s-wave neutron channel corresponds to a pole of the S-matrix on the positive imaginary axis in the complex wavenumber k space. As the potential is made less attractive, this pole crosses onto the negative imaginary axis and becomes a virtual state with negative energy and zero width. See Ref. [16] for details.

The neutron channel is coupled to the internal states at one spatial site $r_{\rm ent} = i_{\rm ent}\Delta r$ by the coupling matrix

$$\mathbf{V}_{i\mu} = \delta_{i,i_{\rm ent}} v_0 s_\mu (\Delta r)^{-1/2} \ . \tag{3}$$

In Eq. (3), v_0 is a model parameter, s_μ is a normally distributed random variable accounting for the fluctuations of the GOE internal states, and the explicit Δr dependence allows the results to be consistent in the continuum limit $\Delta r \to 0$. The full Hamiltonian matrix $\mathbf{H}$ of dimension $(N_n + N_c) \times (N_n + N_c)$ is obtained by combining Eqs. (1-3).

For a pole of the S-matrix, the wavefunction is asymptotically purely outgoing with a complex wavenumber k, i.e, $u(r) \to B(k)e^{ikr}$ for large r. This form implies that, at the edge of the mesh,

$$u(N_{n+1}) = u(N_n)e^{ik\Delta r} \ . \tag{4}$$

The Schrödinger equation consequently yields

$$\left(\mathbf{H} - te^{ik\Delta r}\mathbf{C} - \frac{\hbar^2 k^2}{2\mu} \right) \vec{u} = 0 \ , \tag{5}$$

where $\mathbf{C}_{ij} = \delta_{ij}\delta_{iN_n}$ and $\vec{u}$ is an $(N_n + N_c)$-component vector that represents the wavefunction in the model space. We solve Eq. (5) iteratively to obtain the complex resonance wavenumbers k_r. The resonance energies and total widths are then determined from $E_r - (i/2)\Gamma_r = \hbar^2 k_r^2/2\mu$, and the partial neutron widths are found from $\Gamma_{n,r} = \Gamma_r - \Gamma_\gamma$. All calculations shown here used $(\Delta r, N_n, N_c) = (0.01 \text{ fm}, 1500, 360)$. More details can be found in the Supplemental Material of Ref. [13].

To calculate cross sections, one uses instead the asymptotic boundary condition $u(r) \to e^{-ikr} - S_{nn}(k)e^{ikr}$, where $S_{nn}(k)$ is the elastic neutron scattering amplitude (see Supplemental Material of Ref. [13]). The model discussed here was introduced by G. F. Bertsch in his computer code Mazama [14].

3 Results

3.1 Model parameter sets

The model described above has the following physical parameters: the parameters (V_0, r_0, a) of the Woods-Saxon neutron channel potential, the average resonance spacing D and their total gamma decay width Γ_γ, and the channel-CN coupling parameter v_0. For the n+^{194}Pt reaction, we used $(r_0, a) = (1.27, 0.67)$ fm from Ref. [15], and $D = 82$ eV, $\Gamma_\gamma = 72$ meV from the RIPL-3 database [17].

In Table 1, we list the parameter sets (V_0, v_0) used in our calculations. The baseline set corresponds to $V_0 = -44.54$ MeV taken from Ref. [15] and v_0 tuned to reproduce the RIPL-3 neutron strength function parameter $S_0 = 2 \times 10^{-4}$ eV$^{-1/2}$ at 8 keV of neutron energy (which is in the middle of the experimental range of Ref. [8]). In sets M2 and M3, we take v_0 to be, respectively, half and twice its value for the baseline set. In sets M4–M6 with $V_0 = -41.15$ MeV, a near-threshold bound state with energy $E_0 \approx -2$ keV exists in the neutron channel. In M4 v_0 is tuned to reproduce the RIPL-3 neutron strength function parameter, while M5 and M6 correspond, respectively, to half and twice the value of v_0 for the M4 set.

3.2 Cross sections

In Fig. 1, we show the cross sections for the baseline model, compared with evaluated data from the JEFF-3.2 database [18] and experimental data from Ref. [19]. For the model calculations, the cross sections were averaged over 10 realizations of the GOE and over energy bins of 1 keV. The agreement between our model calculations and the available data is reasonably good.

In Fig. 2, we compare the average cross sections of the baseline parameter set and of the set M4 (see Table 1). The presence of a near-threshold bound or virtual state in the neutron channel enhances significantly the elastic scattering cross section, but does not affect much the capture cross section. As is seen in Table 1, the cross sections are not very sensitive to the coupling parameter v_0.

Model	Baseline	M2	M3	M4	M5	M6
V_0 (MeV)	-44.54	-44.54	-44.54	-41.15	-41.15	-41.15
v_0 (keV-fm$^{1/2}$)	11.0	5.5	22.0	1.6	0.8	3.2
$\overline{\sigma}_{\rm el}$ (b)	30.	19.0	23.	279.	288.	249.
$\overline{\sigma}_{\rm cap}$ (b)	0.44	0.32	0.50	0.47	0.39	0.53
χ^2_r A	0.9	1.0	1.1	0.9	1.0	1.4
χ^2_r B	1.0	1.0	1.3	5.8	6.0	6.1

Table 1: Various parameter sets used to study the n+^{194}Pt reaction. The average elastic scattering cross section $\overline{\sigma}_{\rm el}$ was evaluated at $E = 8$ keV, and the average neutron capture cross section $\overline{\sigma}_{\rm cap}$ was evaluated over the interval 5-7.5 keV. The experimental value for $\overline{\sigma}_{\rm cap}$ over this interval from Ref. [19] is 0.6 b. χ^2_r is the reduced χ-squared parameter from comparing the reduced partial neutron width distributions with the PTD. Reductions A and B are discussed in the text. Adapted from Table 1 of Ref. [13].

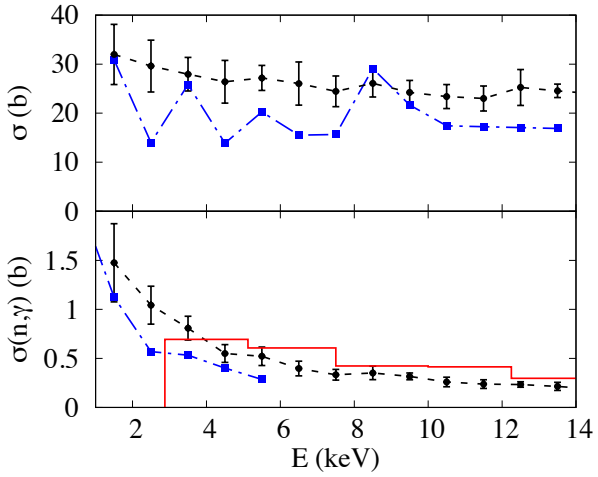

Fig. 1: Elastic (top panel) and capture (bottom panel) cross sections. Baseline model calculations (black circles connected by dashed lines) are compared with evaluated data from the JEFF-3.2 library (blue squares connected by dashed-dotted lines). Error bars represent standard deviations from the 10 GOE realizations. The red histogram is experimental data from Ref. [19]. Taken from Fig. 1 of Ref. [13].

3.3 Partial neutron width fluctuations

For each parameter set in Table 1, we calculated a set of resonance energies and partial neutron widths from 100 GOE realizations, taking from each realization 160 resonances whose real energies are at the center of the resonance spectrum. This restriction to the center is necessary to avoid edge effects due to the finite number of resonances in the model. In Fig. 3, we show the average partial neutron width $\langle\Gamma_n\rangle$ as a function of the neutron energy for the baseline and M4 sets. We compare with the $\sqrt{E}$ dependence, as well as with the squared neutron wavefunction at the entrance point $u^2_E(r_{\rm ent})$. This latter quantity is expected to describe the energy dependence of the average width within the statistical theory. In the right-hand panel, we also compare the formula derived by Weidenmüller [1]

$$\langle\Gamma_n\rangle(E) \propto \frac{\sqrt{E}}{E + |E_0|} \,, \tag{6}$$

where E_0 is the energy of the near-threshold bound or virtual state. This formula is in excellent agreement with our model calculations using $E_0 \approx -2$ keV. We find similar results to those shown in the left and right panels of Fig. 3 for other parameter sets of Table 1 with $V_0 = -44.54$ MeV and $V_0 = -41.15$ MeV, respectively.

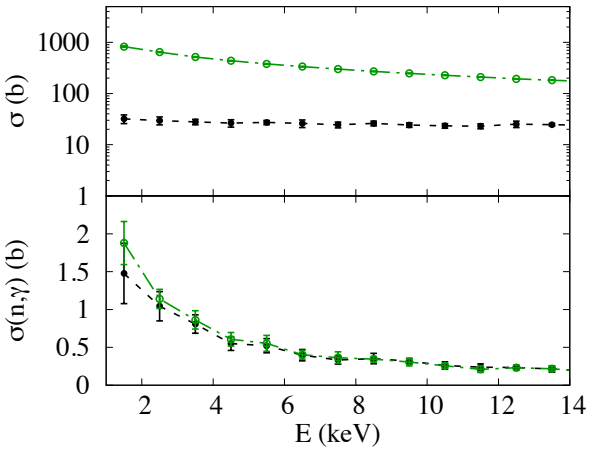

Fig. 2: Elastic (top panel) and capture (bottom panel) cross sections. Baseline model calculations (black solid circles connected by dashed lines) are compared with calculations based on parameter set M4 of Table 1 (green open circles connected by dashed-dotted lines). The error bars represent standard deviations using 10 GOE realizations (see text).

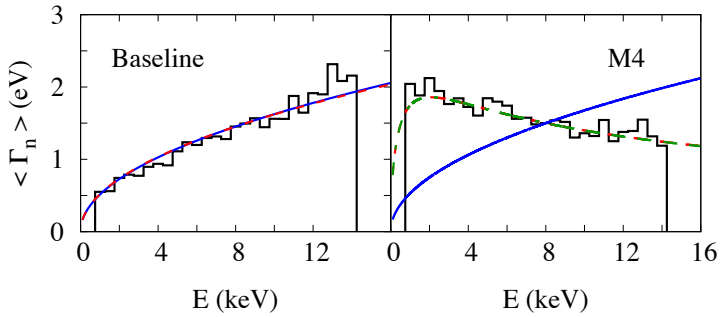

Fig. 3: Average neutron widths $\langle\Gamma_n\rangle$ as a function of neutron energy E. The black solid histograms are the model calculations, the blue solid lines are proprotional to $\sqrt{E}$, and the red dashed lines are the squared neutron wavefunction $u^2_E(r_{\rm ent})$. The green dashed-dotted line describes Eq. (6) with $E_0 \approx -2$ keV. See text for further details.

The reduced partial neutron width for each resonance r is defined as

$$\hat{\Gamma}_{n,r} = \Gamma_{n,r}/\langle\Gamma_n\rangle(E_r)\ . \tag{7}$$

According to the statistical theory, the fluctuations of the normalized reduced width $x = \hat{\Gamma}_n/\langle\hat{\Gamma}_n\rangle$ should follow the PTD. We consider the distribution $P(y)$ of $y = \ln x$. The PTD for y is given by

$$\mathcal{P}_{\rm PTD}(y) = \sqrt{\frac{x}{2\pi}}e^{-x/2}\ . \tag{8}$$

We extracted the reduced widths (7) in two ways. In reduction A, we used the average widths calculated in the model as shown in Fig. 3, while in reduction B, we used the ansatz $\langle\Gamma_n\rangle(E) \propto \sqrt{E}$. In Fig. 4, we compare the distributions obtained using these two reductions with the PTD for various parameter sets. For the baseline case, excellent agreement is obtained in both reductions A and B. For set M4, in which there is a near-threshold state in the neutron channel, the reduced width distribution obtained with reduction B is broader than the PTD. For a goodness-of-fit test, we calculated the reduced χ-squared value χ^2_r [20], using $\chi^2_r \approx 1$ as the metric for a good fit. The results in Fig. 4 are consistent with the

χ^2_r values shown in Table 1. For set M4, we also show a best-fit χ-squared distribution in ν degrees of freedom. The PTD corresponds to $\nu = 1$. For set M4 in reduction B, we find $\nu_{\rm fit} = 0.92$, and the fitted distribution differs noticeably from the model results. Similar results were found for different values of the coupling parameter v_0. This parameter controls the strength of the non-statistical interactions among the resonances. Thus, within our parameter range, these interactions do not significantly affect the partial neutron width fluctuations.

Eq. (6) indicates that the deviation between the correct average width energy dependence and the $\sqrt{E}$ form will be largest for $E_0 \approx 0$. In our model, this occurs for $V_0 = -41$ MeV. The bottom panel of Fig. 4 shows results from the parameter set $(V_0, v_0) = (-41\ \text{MeV}, 1.4\ \text{keV-fm}^{1/2})$. The reduced width distribution obtained with reduction B is noticeably broader than in set M4.

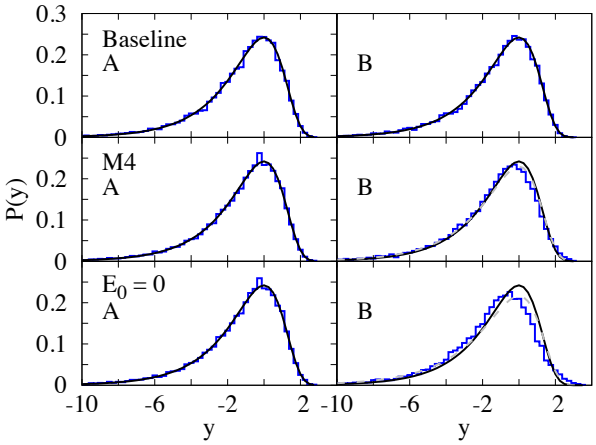

Fig. 4: Reduced partial neutron width distributions calculated from the model (blue histograms) are compared with the PTD (black solid lines) for various parameter sets. The grey dashed lines are fits of a χ-squared distribution in ν degrees of freedom to the model results. Shown are results for reductions A (left panels) and B (right panels). These reductions are discussed in the text.

4 Conclusions

We have studied the partial neutron width statistics for the n+^{194}Pt reaction within a model that combines a realistic description of the neutron channel with the GOE description of the CN. Our main conclusion is that the PTD describes the reduced width distributions for a reasonably large range of physical model parameters, provided the energy dependence of the average width is correctly described. Thus, explanation (ii) of Sec. 1 is ruled out. Within our parameter space, there can be a near-threshold bound or virtual state of the neutron channel that modifies the energy dependence of the average neutron width from the $\sqrt{E}$ dependence used in the experimental data analysis, as proposed by Weidenmüller [1]. If the $\sqrt{E}$ dependence is used to extract the reduced widths in such a case, broader distributions than the PTD are obtained.

In order to explain the findings of Ref. [8], the bound or virtual state must have an energy of only a few keV from threshold in all three platinum isotopes studied. The experimentalists found that using Eq. (6) in their analysis did not improve the agreement between their data and the PTD [21]. However, they note that their data fitting might break down in the presence of such a state. As shown in Fig. 2, the existence of this state enhances significantly the elastic scattering cross section. A measurement of this cross section could thus shed light on the possible existence of a near threshold bound or virtual state.

Acknowledgements

This work was supported in part by the U.S. DOE grant Nos. DE-FG02-00ER411132 and DE-FG02-91ER40608, and by the DOE NNSA Stewardship Science Graduate Fellowship under cooperative agreement No. DE-NA0003864. We would like to thank H. A. Weidenmüller for useful discussions. PF and YA acknowledge the hospitality of the Institute for Nuclear Theory at the University of Washington, where part of this work was completed during the program INT-17-1a, "Toward Predictive Theories of Nuclear Reactions Across the Isotopic Chart." This work was supported by the HPC facilities operated by, and the staff of, the Yale Center for Research Computing.

References

[1] H. A. Weidenmüller, Phys. Rev. Lett. **105**, 232501 (2010).

[2] G. E. Mitchell, A. Richter, and H. A. Weidenmüller, Rev. Mod. Phys. **82**, 2845 (2010).

[3] Y. Alhassid, Rev. Mod. Phys. **72**, 895 (2000).

[4] W. Hauser and H. Feshbach, Phys. Rev. **87**, 366 (1952).

[5] T. Kawano, P. Talou, and H. A. Weidenmüller, Phys. Rev. C **92**, 044617 (2015).

[6] A. J. Koning and D. Rochman, Nucl. Data Sheets **113**, 2841 (2012).

[7] C. E. Porter and R. G. Thomas, Phys. Rev. **104**, 483 (1956).

[8] P. E. Koehler, F. Bečvář, M. Krtička, J. A. Harvey, and K. H. Guber, Phys. Rev. Lett. **105**, 072502 (2010).

[9] G. L. Celardo, N. Auerbach, F. M. Izrailev, and V. G. Zelevinsky, Phys. Rev. Lett. **106**, 042501 (2011).

[10] Y. V. Fyodorov and D. V. Savin, Euro. Phys. Lett. **110**, 40006 (2015).

[11] A. Volya, H. A. Weidenmüller, and V. Zelevinsky, Phys. Rev. Lett. **115**, 052501 (2015).

[12] E. Bogomolny, Phys. Rev. Lett. **118**, 022501 (2017).

[13] P. Fanto, G. F. Bertsch, and Y. Alhassid, Phys. Rev. C **98**, 014604 (2018).

[14] G. F. Bertsch, D. Brown, and E. D. Davis, Phys. Rev. C **98**, 014611 (2018).

[15] A. Bohr and B. R. Mottelson, *Nuclear Structure* Vol. I (W. A. Benjamin, New York, 1975).

[16] J.R. Taylor, *Scattering Theory: the Quantum Theory of Nonrelativistic Collisions* (Wiley, New York, 1972).

[17] R. Capote *et. al.* , Nucl. Data Sheets **110**, 3107 (2009).

[18] OECD/NEA Data Bank, "The JEFF-3.2 Nuclear Data Library" (2014).

[19] P.E. Koehler and K.H. Guber, Phys. Rev. C **88**, 035802 (2013).

[20] P.R. Bevington and D.K. Robinson, *Data Reduction and Error Analysis for the Physical Sciences* (McGraw-Hill, New York, 2003).

[21] P. E. Koehler, F. Bečvář, M. Krtička, J. A. Harvey, and K. H. Guber, arXiv:1101.4533 (2011).

Heavy ion charge exchange reactions and the link with β decay processes

M.Colonna[1,5]*, J.I.Bellone*[1,2,5]*, S.Burrello*[1,5]*, José-Antonio Lay*[3,1,5]*, H.Lenske*[4,5]
[1]INFN-LNS, I-95123 Catania, Italy
[2]Dipartimento di Fisica e Astronomia, Universitá degli studi di Catania, Italy
[3]Departamento de FAMN, Universidad de Sevilla, Apartado 1065, E-41080 Sevilla, Spain
[4]Institut für Theoretische Physik, Justus-Liebig-Universität Giessen, D-35392 Giessen, Germany
[5]NUMEN collaboration, LNS Catania

Abstract
Within the DWBA framework, we develop a theoretical description of single and double heavy ion charge exchange (CE) reactions. We show that absorption effects are particularly important for heavy ion reactions, leading to a noticeable reduction of the CE cross sections. At low momentum transfer, the single CE cross section can be factorised, thus allowing to evaluate corresponding distortion factors and access β decay strengths. Applications are shown for a system of experimental interest. Preliminary results are discussed also for double CE reactions, modeled as a two-step mechanims, i.e. a sequence of two charge-changing processes.

1 Introduction

Nuclear charge exchange reactions offer the possibility to explore the nuclear interaction in the spin-isospin channel, being related to excitations inducing isospin flip (with possibly also spin flip), such as the Gamow-Teller resonance (GTR). Over the years, a wealth of data has been accumulated as reviewed e.g. in [1–5]. Beyond using nucleonic probes, light ion reactions as e.g. $(^3He, ^3H)$ have become another workhorse of the field, now reaching accuracies allowing to investigate subtle details of spectral distributions in both the τ_+ and the τ_- branches. Soon after the first light ion studies, also heavy ions were used in charge exchange studies, as in [6, 7].

While the past experiments have been focused on single charge exchange (SCE) reactions, new territory was entered by the pilot experiment of Cappuzzello et al. [8], studying for the first time a nuclear double charge exchange (DCE) reaction. The reaction $^{18}O + ^{40}Ca \rightarrow ^{18}Ne + ^{40}Ar$ gave strong evidence for a direct reaction mechanism even for double charge exchange processes. Quite recently, the NUMEN project at LNS Catania was initiated, dedicated to investigations of SCE and DCE heavy ion reactions, elucidating and optimizing their potential for spectroscopic studies [9], also in the perspective of probing the single/double β-like nuclear response. DCE experiments have been recently performed also with different goals: search for exotic systems (such as the tetra-neutron (4n) system in $^4He(^8He,^8Be)4n$ reactions); search for the Double GT resonance for quantitative information about the corresponding sum-rule (for example in $(^{12}C,^{12}Be)$ reactions) [10, 11].

A thorough theoretical investigation of the dynamics of heavy-ion CE reactions, concerning in particular the possibility of extracting the nuclear structure information out of the total reaction cross section, is still missing, though some progress has been made over the past year [12]. This is especially important for DCE reactions, that necessarily involve heavier projectiles than the light ones traditionally employed in CE reactions. The possibility to single out the relevant structure information is an essential point if one wishes to exploit the measured cross sections as stringent benchmarks to constrain the theoretical structure models and the predicted transition matrix elements. This would allow to shed light on yet unknown aspects of charge-exchange transitions and of the underlying nuclear effective interaction. Moreover, owing to the analogies between strong and weak charge exchange processes, DCE studies can provide useful information to improve the accuracy of the calculations of the nuclear matrix elements responsible for neutrinoless double-beta decay, a quite hot subject of investigation nowadays.

In this contribution, we briefly review some aspects of the theory for heavy ion charge exchange reactions. In particular, we discuss the possibility to single out the structure information from the reaction cross section. Illustrative results are shown for systems recently investigated by the NUMEN collaboration.

2 Theory of Heavy Ion Charge Exchange Reactions

Charge changing reactions require two reaction partners, which are acting mutually as the source or sink, respectively, of the charge-changing virtual meson fields. Let us start considering ion-ion SCE reactions according to

$$ {}^{a}_{z}a + {}^{A}_{Z}A \rightarrow {}^{a}_{z\pm1}b + {}^{A}_{Z\mp1}B \tag{1}$$

which change the charge partition by a balanced redistribution of protons and neutrons.

The differential SCE cross section for a reaction connecting the channels α and β is defined as

$$ d^2\sigma_{\alpha\beta} = \frac{m_\alpha m_\beta}{(2\pi\hbar^2)^2}\frac{k_\beta}{k_\alpha}\frac{1}{(2J_a+1)(2J_A+1)} \times \sum_{M_a,M_A\in\alpha;M_b,M_B\in\beta} |M_{\alpha\beta}(\mathbf{k}_\alpha,\mathbf{k}_\beta)|^2 d\Omega, \tag{2}$$

where $\mathbf{k}_\alpha$ ($\mathbf{k}_\beta$) and m_α (m_β) denote the relative 3-momentum and reduced mass in the entrance (exit) channel $\alpha = \{a, A\}$ ($\beta = \{b, B\}$). $\{J_aM_a, J_AM_A\cdots\}$ and $\{J_bM_b, J_BM_B\cdots\}$ account for the full set of (intrinsic) quantum numbers specifying the initial and final channel states, respectively.

In distorted wave approximation, the direct charge exchange reaction amplitude is given by the expression

$$ M_{\alpha\beta}(\mathbf{k}_\beta,\mathbf{k}_\alpha) = \langle \chi^{(-)}_\beta, bB|T_{NN}|aA,\chi^{(+)}_\alpha\rangle. \tag{3}$$

The distorted waves, denoted by $\chi^{(\pm)}_{\alpha,\beta}$ for asymptotically outgoing and incoming spherical waves, respectively, depend on the respective channel momenta $\mathbf{k}_{\alpha,\beta}$ and the optical potentials, thus accounting for initial state and final state interactions.

The charge-changing process is described by the nucleon-nucleon (NN) T-matrix T_{NN}. The anti-symmetrized T-matrix is given in non-relativistic momentum representation by

$$ T_{NN}(\mathbf{p}) = \sum_{S,T}\left\{V^{(C)}_{ST}(p^2)O_{ST}(1)\cdot O_{ST}(2) + \delta_{S1}V^{(Tn)}_{T}(p^2)\sqrt{\frac{24\pi}{5}}Y^*_2(\hat{\mathbf{p}})\cdot[O_{ST}(1)\otimes O_{ST}(2)]_2\right\}, \tag{4}$$

including isoscalar and isovector central spin-independent ($S = 0$) and spin-dependent ($S = 1$) interactions with form factors $V^{(C)}_{ST}(p^2)$, respectively, and rank-2 tensor interactions with form factors $V^{(Tn)}_{T}(p^2)$. O_{ST} denotes the spin-isospin operators $O_{ST}(i) = (\boldsymbol{\sigma}_i)^S(\boldsymbol{\tau}_i)^T$.

In Eq.(4) scalar products are indicated as a dot-product and the rank-2 tensorial coupling affects only the spin degrees of freedom. The subset of isovector operators, corresponding to Fermi-type $S = 0, T = 1$ and Gamow-Teller-type $S = 1$, $T = 1$ operators contributes to the charge-changing reaction amplitudes.

The matrix element of a single charge exchange reaction, Eq.(3), can be written in slightly different form as:

$$ M_{\alpha\beta}(\mathbf{k}_\alpha,\mathbf{k}_\beta) = \langle \chi^{(-)}_\beta|\mathcal{U}_{\alpha\beta}|\chi^{(+)}_\alpha\rangle. \tag{5}$$

Then the nuclear structure information on multipolarities, transition strength and interactions are contained in the (anti-symmetrized) transition potential $\mathcal{U}_{\alpha\beta}$, depending on the channel coordinates $\mathbf{r}_{\alpha,\beta}$.

In the momentum representation, the full reaction amplitude can be rewritten as:

$$ M_{\alpha\beta}(\mathbf{k}_\alpha,\mathbf{k}_\beta) = \int d^3p\mathcal{U}_{\alpha\beta}(\mathbf{p})N_{\alpha\beta}(\mathbf{k}_\alpha,\mathbf{k}_\beta,\mathbf{p}), \tag{6}$$

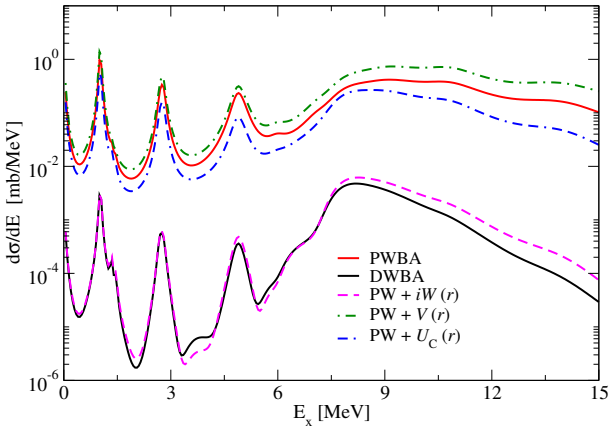

Fig. 1: (Color online) Cross sections as a function of the target excitation energy, E_x, for the $J^P = 1^+$ transition, for the SCE reaction $^{40}Ca\left(^{18}O,^{18}F\right)^{40}K$ reaction at $T_{lab} = 270\,MeV$, integrated over the full angular range. The different curves show the effect of Coulomb potential ($U_C(r)$), of real ($V(r)$) and imaginary ($W(r)$) components of the optical potential and of the full potential (DWBA), with respect to PWBA calculations.

where the distortion coefficient

$$N_{\alpha\beta}(\mathbf{k}_\alpha, \mathbf{k}_\beta, \mathbf{p}) = \frac{1}{(2\pi)^3}\langle\chi_\beta^{(-)}|e^{-i\mathbf{p}\cdot\mathbf{r}}|\chi_\alpha^{(+)}\rangle, \tag{7}$$

has been introduced, showing the dressing of the nuclear transition potential by initial and final state ion-ion interactions.

The reaction kernel is given by a product of form factors:

$$\begin{aligned} U_{\alpha\beta}^{(ST)}(\mathbf{p}) &= (4\pi)^2 (V_{ST}^{(C)}(p^2) F_{ST}^{(ab)\dagger}(\mathbf{p}) \cdot F_{ST}^{(AB)}(\mathbf{p}) \\ &+ \delta_{S1}\sqrt{\frac{24\pi}{5}} V_{ST}^{(Tn)}(p^2) Y_2^*(\hat{\mathbf{p}}) \cdot \left[F_{ST}^{(ab)\dagger}(\mathbf{p}) \otimes F_{ST}^{(AB)}(\mathbf{p})\right]_2), \end{aligned} \tag{8}$$

where $F_{ST}(\mathbf{p})$ represents the Fourier transform of the (projectile or target) transition density.

A possible extension of the formalism to DCE reactions is based on second order perturbation theory, thus double charge exchange is depicted as a two-step process, i.e. a sequence of two single charge exchange transitions. This implies a summation over (virtual) intermediate states, and the treatment of the relative distortion effects in the intermediate channel.

3 Results for single CE

As stressed above, our guiding principle to describe charge exchange reactions is direct nuclear reaction theory, based on the Distorted Wave Born Approximation (DWBA). Initial and final state ion-ion interactions are described by optical potentials. Microscopic optical potentials are used, obtained in the impulse approximation, by folding projectile and target Hartree-Fock-Bogoliubov (HFB) ground state densities with free space nucleon-nucleon T-matrices. QRPA calculations are performed for nuclear SCE transition densities and response functions, employing a G-Matrix interaction (see Ref. [12] and Refs. therein). For the sake of consistency, the same iteraction is considered for the evaluation of the reaction kernel, Eq.(8). More details can be found in Ref. [12].

As a case of physical interest, we consider throughout the SCE reaction $^{18}O + ^{40}Ca \rightarrow ^{18}F + ^{40}K$ at $T_{lab} = 15$ AMeV. In particular, we consider transitions leading to the ^{18}F g.s., that is a 1^+ state, and to $J^P = 1^+$ states for the target. Fig.1 represents the SCE cross section, integrated over the full angular range, as a function of the target excitation energy, as obtained with the HIDEX code [13]. One can

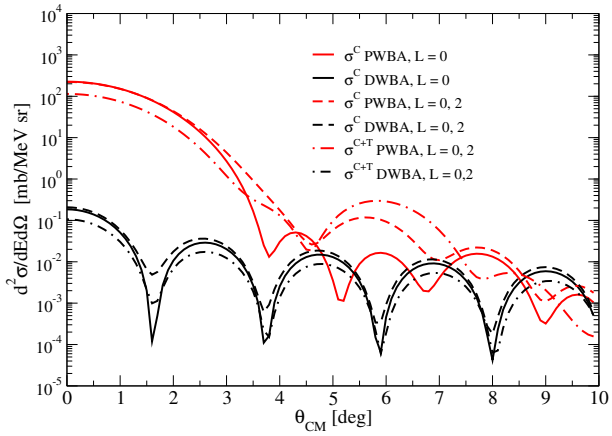

Fig. 2: (Color online) Angular distribution for the target state at E_x = 0. The plot shows the effects related to central and tensor components of the nuclear interaction, for the two multipolarities allowed by $J^\pi = 1^+$ transitions: $L = 0, 2$. The system is the same as in the previous figure.

identify several peaks, associated with corresponding excited states. For comparison, calculations are performed also in the Born approximation (PWBA), and isolating the effect of the different parts of the optical potential. One can notice that the DWBA cross section is quite suppressed with respect to PWBA results, pointing to strong absorption effects. Indeed results very close to the full DWBA calculations are obtained by simply considering the imaginary part of the optical potential. We notice that strong absorption effects are peculiar of heavy ion reactions. Fig.2 displays the angular distribution obtained for the 1^+ target state at the lowest excitation energy. The contribution of the two allowed multipolarities, as well as the effect of central and tensor components of the nuclear interaction, are shown on the figure. Also in this case PWBA and DWBA results are compared, allowing one to appreciate how the diffraction pattern is affected by the distortion effects. One can also observe that at small angles L = 0 transitions dominate and that the effects of the tensor component of the nuclear interaction are rather small.

4 Cross section factorization

Explicit simplified expressions can be derived for forward angle cross sections, owing to the small momentum transfer $\mathbf{q}_{\alpha\beta}$. Indeed, in this case the reaction kernel in Eq.(8) can be factorized into the product of its on-shell value, $\mathcal{U}(\mathbf{q}_{\alpha\beta})$, and a coefficient, $h(\mathbf{q})$, depending on the off-shell momentum $\mathbf{q} = \mathbf{p} - \mathbf{q}_{\alpha\beta}$. Then, after the integration is performed, Eq.(6) can be written as $M_{\alpha\beta} = \mathcal{U}(\mathbf{q}_{\alpha\beta})(1 - n_{\alpha\beta})$, leading to the distortion factor $f_{\alpha\beta} = |1 - n_{\alpha\beta}|^2$ in the cross section.

Analytical calculations can be performed in the black disk (BD) approximation and considering a Gaussian fit of the transition form factors. Results for the distortion factor are displayed in Fig.3 (left panel), as a function of the BD radius R_{abs}. For the reaction considered in our study, $R_{abs} \approx 8$ fm, as it can be extracted from the absorption cross section. Correspondingly, the suppression factor is found to be 8.14 10^{-4}, in good agreement with the numerical DWBA/PWBA result, $f_{BD}(numerical)|_{Ex=0} =$ 8.35 10^{-4}, as it can be extracted from the ratio between DWBA and PWBA calculations at zero angle (see Fig.2). Fig.3 (right panel) shows the distortion factor obtained for the reaction considered so far and for the system $^{18}O + ^{116}Sn$, as a function of the beam energy. Larger distortion effects are observed for the heavier system.

Thanks to the factorization of the distortion effects, it is possible to isolate the form factor, containing projectile and target transition densities, from the reaction cross section. It should be noticed that for L = 0 transitions, the latter are directly connected to β decay strengths. Thus heavy ion SCE reactions are indeed providing access to nuclear matrix elements relevant also for β-decay. The results derived in this section are of special importance since they are showing explicitly the potential of heavy ion SCE

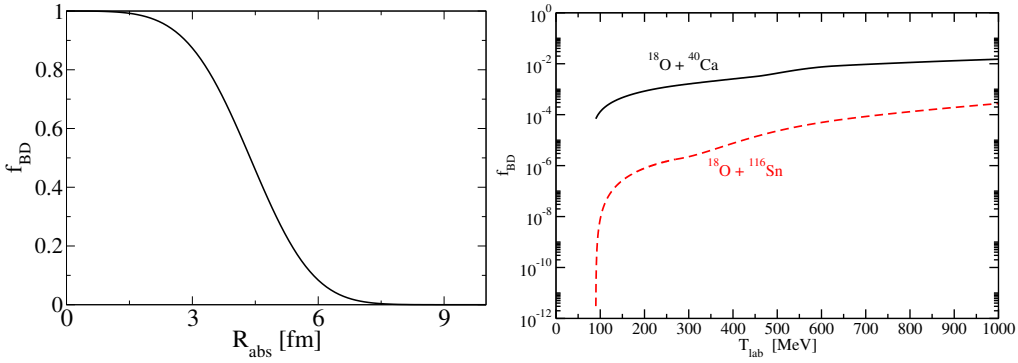

Fig. 3: (Color online) Left panel: Distortion factor as a function of R_{abs}, for the same system as in the previous figures. Right panel: The distortion factor f_{BD} is displayed as a function of the beam energy for two reaction systems: $^{18}O + ^{40}Ca$ and $^{18}O + ^{116}Sn$. The results were obtained numerically by the ratio of the quantum mechanical DWBA and PWBA forward angle cross sections.

reactions for spectral investigations, including the deduction of nuclear matrix elements for β-decay.

5 Results for DCE cross sections

Within the hypothesis of a two-step process, calculations have been performed for the double charge exchange reaction $^{18}O + ^{40}Ca \rightarrow ^{18}\ Ne + ^{40}Ar$ considering just one intermediate state (a 1+ state for both projectile and target). Results have been obtained using the FRESCO code [14] or by combining the results given by HIDEX for the two single SCE steps. The same form factors are employed in the two cases. Calculations have been performed in PWBA and DWBA approximations, as shown in Fig.4. The two methods (HIDEX double step and FRESCO) are in excellent agreement at the PWBA level. As far as DWBA calculations are concerned, two approximations are employed in the HIDEX case to deal with the distortion effects in the intermediate channel: i) plane waves are considered; ii) distorted waves associated with the full (absorptive) optical potential are employed. By comparing with the FRESCO results, one observes that the ii) option gives the right diffraction pattern, though the cross section is underestimated by a factor $f_{p.w.} \approx 10$. This indicates that distortion effects mainly act only in the entrance and exit channels and should not affect much the virtual intermediate states. On the other hand, the option i) reproduces the correct cross section order of magnitude (as given by FRESCO), though the angular pattern is not well described. A quite good agreement with FRESCO is obtained by scaling the results of ii) by the factor $f_{p.w.}$. The conditions allowing to factorize the DCE cross section described above, that would enable to access nuclear matrix elements of similar structure as (two neutrino) double β decay, are presently under investigations [15, 16].

6 Conclusions

In this contribution we discuss new results for heavy ion SCE and DCE reactions. As a general feature, heavy ion reactions are characterized by quite large absorption effects, justifying the use of the black disk approximation to account for initial and final state interactions. Then predictions are derived for the behavior of the distortion factor as a function of beam energy and projectile/target combinations.

We show that at forward angles the SCE cross section can be factorised, allowing one to isolate the CE transition matrix element. Preliminary results are shown also for DCE reactions, depicted as a sequence of two single CE steps. The cross section is further reduced for DCE reactions, with respect to SCE processes, as one can realize by comparing DWBA to PWBA calculations in each case.

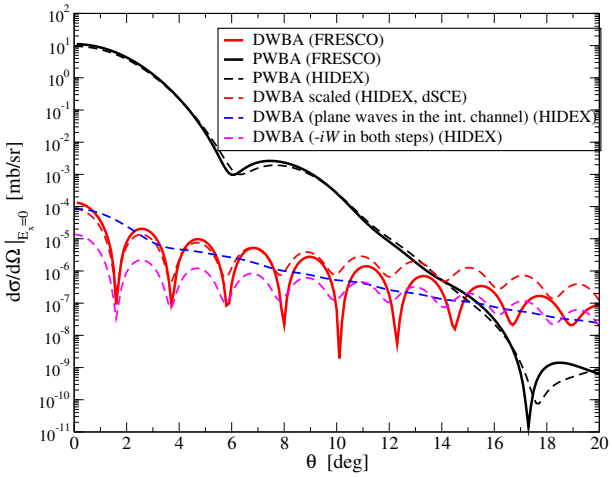

Fig. 4: (Color online) Angular distribution for the DCE reaction $^{18}O + ^{40}Ca \rightarrow ^{18}\ Ne + ^{40}Ar$ at 15 AMeV, as obtained with FRESCO and with double-step Hidex simulations (with two approximations for the intermediate channel, see text), in PWBA and in DWBA.

Acknowledgements

This project has received funding from the European Union's Horizon 2020 research and innovation programme under grant agreement N. 654002, and from the Spanish Ministerio de Economia y Competitividad and FEDER funds under Project FIS2017-88410-P.

References

[1] M. Ichimura, H. Sakai and T. Wakasa, *Prog. Part. Nucl. Phys.* **56** (2006) 446.

[2] J. H. Thies *et al.*, *Phys. Rev. C* **86** (2012) 044309.

[3] D. Frekers, P. Puppe, J. H. Thies and H. Ejiri, *Nucl. Phys. A* **916** (2013) 219.

[4] D. Frekers *et al.*, *Phys. Rev. C* **91** (2015) 034608.

[5] Y. Fujita, B. Rubio, and W. Gelletly, *Prog. Part. Nucl. Phys.* **66**, (2011) 549.

[6] C. Brendel, P. von Neumann-Cosel, A. Richter, G. Schrieder, H. Lenske, H. H. Wolter, J. Carter and D. Schüll, *Nucl. Phys. A* **477** (1988) 162.

[7] C. Bérat *et al.*, *Phys. Lett. B* **218** (1989) 299.

[8] F. Cappuzzello, M. Cavallaro, C. Agodi, M. Bondi, D. Carbone, A. Cunsolo and A. Foti, *Eur. Phys. J. A* **51** (2015) 145.

[9] F. Cappuzzello *et al.*, *Eur. Phys. J. A* **54** (2018) 72.

[10] K. Kisamori *et al.*, *Phys. Rev. Lett.* **116** (2016) 052501.

[11] M. Takaki *et al.*, CNS Ann. Rep. 94 (2014) 9.

[12] H. Lenske, J.I. Bellone, M. Colonna, J-A. Lay, Theory of Single Charge Exchange Heavy Ion Reactions, arXiv:1804.04827, accepted for publication in *Phys. Rev. C*.

[13] F. Cappuzzello *et al.*, *Nucl. Phys. A* **739** (2004) 30.

[14] I. Thompson, *Comp. Phys. Rep.* **7** (1988) 167.

[15] H. Lenske, *J. Phys. Conf. Ser.* **1056** (2018) 012030; J.I. Bellone, M. Colonna, H. lenske, J-A. Lay, *J. Phys. Conf. Ser.* **1056** (2018) 012004.

[16] E. Santopinto, H. García-Tecocoatzi, R. I. Magana-Vsevolodovna, J. Ferretti, Heavy-ion double-charge-exchange and its relation to neutrinoless double-beta decay, arXiv:1806.03069.

Proton induced pre–equilibrium reactions to the continuum as a test to the reaction mechanism

S. S. Dimitrova[1]*, A. Cowley*[2]*, E. V. Zemlyanaya*[3] *and K. V. Lukyanov*[3]
[1]Institute of Nuclear Research and Nuclear Energy, Bulgarian Academy of Sciences, 1784 Sofia, Bulgaria,
[2]Department of Physics, Stellenbosch University, Private Bag X1, Matieland, 7602, South Africa,
[3] Joint Institute for Nuclear Research, 141980 Dubna, Russia

Abstract
Pre-equilibrium proton induced emissions of light complex nuclei with energies in the continuum have been studied comprehensively for many years. The process is considered as an intra-nuclear nucleon-nucleon multistep statistical reaction with typical double-differential cross sections and especially analyzing power distributions. The final stage of the reaction may be a result of a direct pickup or knockout of the ejectile. The discussion on this subject continues to be a hot topic for theoretical and experimental investigations. Here we will discuss the interplay between the knockout and pickup mechanisms as final step of the pre-equilibrium reaction and its dependence on the energy of the projectile.

1 Introduction

Pre–equilibrium nuclear reactions have been studied extensively over many years. In the early nineties E. Gadioli and P.E. Hodgson collected all valuable experimental and theoretical results in a book [1] concluding that for a deeper insight into the reaction mechanism of this type of reaction a systematic study of their characteristics is needed. A comprehensive program for investigating the properties of the proton induced pre–equilibrium reactions to the continuum has been conducted in iThemba LABS in Faure, South Africa. The earliest results about the double differential cross–section of the ^{90}Zr(p,p') reaction [2] showed that the features of the experimental angular distributions can be reproduced very good by the statistical multistep direct theory of Feshbach, Kerman and Koonin (FKK) [3] (see Fig.1). First the classical exciton model of Griffin [4] exploits the idea that the projectile undergoes several intra-nuclear collisions before the final stage of the reaction. Quantum mechanical theories based on the same assumption were suggested also by Tamura, Udagawa and Lenske [5], Nishioka, Weidenmüller and Yoshida [6]. Later Koning and Akkermans [7] studied critically the models mentioned above and came to the conclusion that the calculated angular distribution of the ^{90}Zr(p,p') reaction at 80 MeV incident energy do not differ very strongly. Thus they recommended the simplest multistep direct method (the FKK model) as most adequate for the analysis of experimental data.

As part of the systematic studies [8–10] of proton induced pre–equilibrium reactions we have compare experimental data obtained in iThemba LABS with results from theoretical FKK calculations of (p,α) reactions to the continuum recognizing that the emission of composite particles follows the same multistep mechanism as the nucleon emission. In this contribution we will sketch briefly the method we use to study double–differential cross–section and analyzing power and discuss few examples which demonstrate the importance of the reaction mechanism as a crucial ingredient of the calculations.

2 The theoretical method

We assume that pre-equilibrium $(\vec{p},\alpha)$ reactions occur in a series of nucleon–nucleon scattering events within the target, followed by a final process in which the α–particle is emitted. The single step direct reaction can be a knockout of an α–cluster or a pickup of a triton.

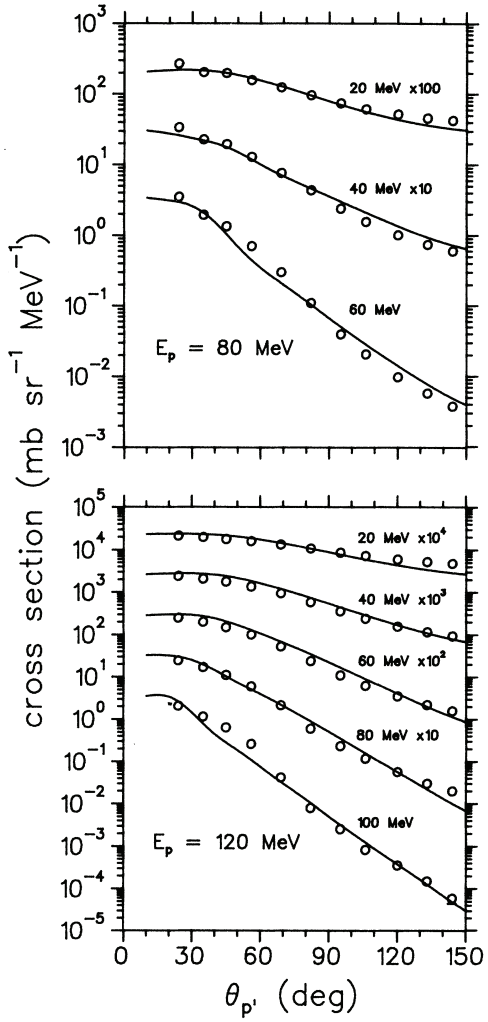

Fig. 1: Laboratory angle distribution for the reaction $^{90}\mathrm{Zr}(p,p')$ at selected ejectile energies as adopted from Cowley et al. [2].

For the theoretical description of the $(\vec{p},\alpha)$ reaction we implement the FKK multistep direct theory [3], where the double differential cross section is a sum of terms related to one-, two- and so on steps.

$$\frac{d^2\sigma}{d\Omega dE} = \left(\frac{d^2\sigma}{d\Omega dE}\right)^{1-\mathrm{step}} + \left(\frac{d^2\sigma}{d\Omega dE}\right)^{2-\mathrm{step}} + \cdots . \tag{1}$$

The first-step cross section is calculated in terms of the DWBA method:

$$\left(\frac{d^2\sigma}{d\Omega dE}\right)^{1-\mathrm{step}}_{(p,\alpha)} = \sum_{N,L,J} \frac{(2J+1)}{\Delta E}\frac{d\sigma^{\mathrm{DW}}}{d\Omega}(\theta,N,L,J,E)\ , \tag{2}$$

where the differential cross sections $d\sigma^{\mathrm{DW}}/d\Omega$ to particular final (N,L,J) states are calculated using the computational code DWUCK4 [11].

The distorted waves in the incident and outgoing channels are calculated within the hybrid nucleus-nucleus optical potential [12] for the volume part and standard spin-orbit potential, both ingredients of the optical potential being complex. The volume part generally depends on the radius–vector **r** connecting

the centers of the target and projectile.

$$U(\mathbf{r}) \;=\; N^R V^{DF}(\mathbf{r}) \;+\; iN^I W^{DF}(\mathbf{r})\;. \tag{3}$$

The parameters N^R and N^I correct the strength of the microscopically calculated real V^{DF} and imaginary W^{DF} constituents of the whole potential.

The spin–orbit parts of the optical potentials can be chosen among the phenomenological potentials available in the literature, as we have done in [9, 10]. Another possibility is to use the standard form of the spin–orbit potential as defined in DWUCK4, but the depth and the geometrical parameters of the Woods–Saxon potential are those which fit best the double folding potential eq.3. This procedure reduces the number of the phenomenological parameters and derives all parts of the optical potentials in a consistent way.

When the emission energy decreases the multi–step contribution to the calculated observables have to be taken into account. Using the FKK theory [3] the two–step cross section is calculated as a convolution of the (p,p') cross section and the direct (p,α) cross section:

$$\left(\frac{d^2\sigma}{d\Omega dE}\right) \;=\; \int \frac{d\mathbf{k}}{(2\pi)^3}\left(\frac{d^2\sigma(\mathbf{k}_i,\mathbf{k})}{d\Omega_i dE_i}\right)_{(p,p')}\left(\frac{d^2\sigma(\mathbf{k},\mathbf{k}_f)}{d\Omega_f dE_f}\right)^{1-step}_{(p,\alpha)}\;, \tag{4}$$

where $\mathbf{k}_i,\ \mathbf{k}$ and $\mathbf{k}_f$ are the momenta of the initial, intermediate and final steps. The three-step double differential cross-section can be calculated analogously.

The theoretical (p,p') and (p,p',p'') double-differential cross section distributions which are required for the calculation of the two– and three–step contributions were derived from Refs. [8,13]. These cross section distributions which were extracted by means of a FKK theory, reproduce experimental inclusive (p,p') quantities [13]. Interpolations and extrapolations in incident energy and target mass were introduced to match the specific requirements accurately.

The extension of the FKK theory from cross–sections to analyzing power is formulated by Bonetti *et al.* [14]. The multistep expression for the analyzing power becomes

$$A_{\rm multistep} = \frac{A_1\left(\frac{d^2\sigma}{d\Omega dE}\right)^{1-\rm step} + A_2\left(\frac{d^2\sigma}{d\Omega dE}\right)^{2-\rm step} + \cdots}{\left(\frac{d^2\sigma}{d\Omega dE}\right)^{1-\rm step} + \left(\frac{d^2\sigma}{d\Omega dE}\right)^{2-\rm step} + \cdots}, \tag{5}$$

with A_i, $\{i = 1, 2, \ldots\}$ referring to analyzing powers for the successive multisteps.

One should emphasize the role of the analyzing power in the study of the reaction mechanism. The main advantage of the experiments with polarized proton beams is namely the possibility to measure this observable. The shape of the analyzing power as a function of the scattered angle is much more sensitive to the reaction mechanism then the differential cross–section. Moreover as the analyzing power is a ratio of cross–sections, it is independent of the absolute cross section of the reaction. For small difference between the incident and the outgoing energy, where the first step dominates, the analyzing power has a distinctive shape. When the higher steps take place, they affect significantly the shape and the magnitude of the analyzing power and it tents towards zero for low emission energies. Figs.3 and 2 illustrate this statement.

3 Energy dependence of the reaction mechanism

The mechanism of the direct $(\vec{p},\alpha)$ reaction has been discussed intensively over the years, but a decisive conclusions has not been made. For example in Ref. [15] it was shown that calculations assuming pickup of a triton and knockout of an α–particle equally well fit the angular distribution and the analyzing power of the ^{90,92}Zr$(\vec{p},\alpha)$ reactions to the ground state and the first few excited states, while the knockout

mechanism is preferred for describing transitions to the continuum [16]. To address this problem for pre–equilibrium processes we studied proton induced reactions on ^{59}Co and ^{93}Nb at incident energies from 160 MeV to 65 MeV (see Ref. [17] and references there). We performed DWBA calculations assuming both reaction mechanisms and compared the theoretical results with the experimental data for the double differential cross–section and the analyzing power for a small difference between the incoming and outgoing energies, where the first–step process dominates. Numerically the difference between both types of calculations lies in the form factor, and the incoming and the outgoing distorted waves are calculated using the same optical model potentials for protons and α–particles, respectively.

In Ref. [9] was shown that at 160 MeV incident energy the experimental data for the characteristics of the ^{93}Nb(p,α) reaction are reasonably well described assuming that the ejectile originates from an α–cluster knockout in the final stage.

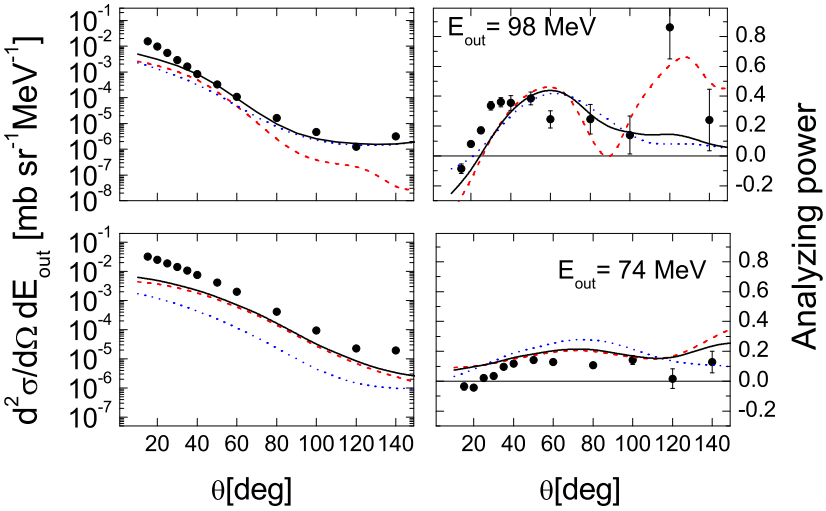

Fig. 2: Double-differential cross sections (left panels) and analyzing power (right panels) as a function of scattering angle θ for the ^{93}Nb$(\vec{p},\alpha)$ reaction at an incident energy of 100 MeV and two α- particle emission energies E_{out} as indicated. Theoretical cross-section and analyzing power calculations for pickup (red dashed lines) and knockout (blue dashed-dotted lines) are shown, with the sums of both reaction mechanisms plotted as black solid lines.

In. Fig. 2 double-differential cross sections and analyzing power as a function of scattering angle for the ^{93}Nb$(\vec{p},\alpha)$ reaction at an incident energy of 100 MeV and two α–particle emission energies E_{out} are shown. At the highest outgoing energy of 98 MeV where the first step contribution dominates the results for both reaction mechanisms, knockout and pickup, are shown. It is seen that for forward scattering angles the pickup differential cross–section is closer to the experimental points, while for the backwards angles the knockout process dominates. Looking at the analyzing power, the pickup is the reaction mechanism which describes best the main features of the shape and magnitude of the analyzing power. For the lower emission energies the knockout differential cross–section decreases faster then the pickup one. In this case we conclude that both reaction mechanisms should be taken into account although the importance of the pickup prevails.

To extend the study of the ^{93}Nb$(\vec{p},\alpha)$ reaction for lower incident energies we re-examine the experimental data for 65 MeV proton incident energy by Sakai et al. [18]. We use the same procedure mentioned before. The double-differential cross–section and the analyzing power for the highest outgoing energy of 53 MeV are described reasonably well by the knockout mechanism and no other combination of pickup and knockout achieves better agreement with the experimental data. Once fitted at this emission energy the magnitudes of the differential cross section and the analyzing power are in very good agreement with the experimental data at lower emission energies as well.

The reason for the energy dependence of the reaction mechanism is in detail discussed in our

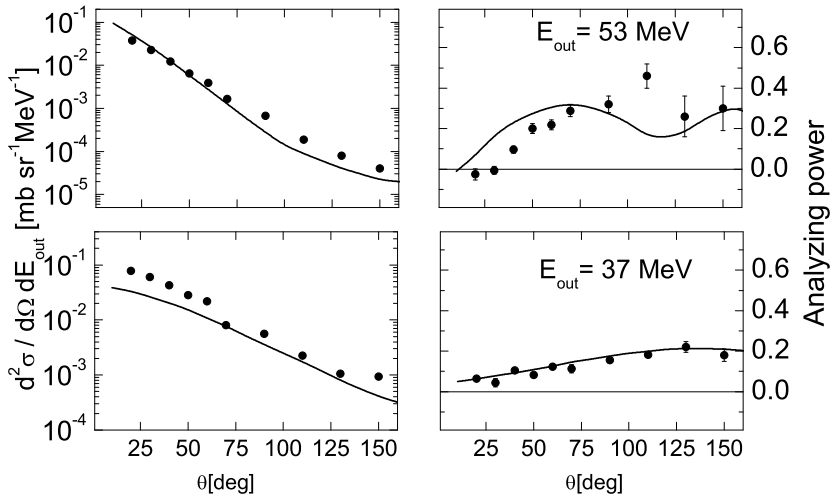

Fig. 3: Double-differential cross sections (left panels) and analyzing power (right panels) as a function of scattering angle θ for the ^{93}Nb$(\vec{p},\alpha)$ reaction at an incident energy of 65 MeV and two α- particle emission energies E_{out} as indicated. Theoretical calculations for a knockout reaction mechanism (solid line) are compared with the experimental data by Sakai et al. [18]

previous papers [17, 19]. The differential cross–section for either knockout or pickup depends on the difference between the angular momentum in the incident and exit channel, the so called momentum mismatch. Knockout is characterized by a low angular momentum relative to the core, because the α–particle is a fully paired system. Pickup in a (p,α) reaction involves a system of two neutrons and a proton and this composite system can have a large angular momentum in respect to the core. The momentum mismatch depends on the energy of the projectile, thus reaction mechanism is influenced strongly by the incident energy.

4 Conclusion

Based on the investigation of the pre–equilibrium ^{93}Nb$(\vec{p},\alpha)$ reaction we offer an explanation about the energy dependence of the reaction mechanism at the final step of the process. We have shown that both mechanisms - knockout and pickup are important and the angular momentum of the transferd composite particle to the rest of the system has a far-reaching consequence for the cross–section trends as a function of incident energy.

Acknowledgments

This work is partly supported by the DFNI-T02/19 and DNTS/Russia 01/3 grants of the Bulgarian Science Foundation and by the Russian Foundation for Basic Research grand No. 17-52-18057-bolg-A. This financial support is gratefully acknowledged. AAC thanks the South African National Research Foundation (NRF) (Grant Numbers 115020).

References

[1] Gadioli E and Hodgson P E 1991, *Pre-Equilibrium Nuclear Reactions* (Oxford University Press, New York)

[2] Cowley A A et al., 1991 *Phys. Rev.* **C 43** 678

[3] Feshbach H, Kerman A, and Koonin S 1980 *Ann. Phys. (N. Y.)* **125** 429

[4] Griffin J J 1966 *Phys. Rev. Lett.* **17** 478

[5] Tamura T, Udagawa T and Lenske H 1982 *Phys. Rev.* **C 26** 379

[6] Nishioka H, Weidenmüller H A and Yoshida S 1988 *Ann. Phys. (NY)* **183** 166

[7] Koning A J and Akkermans J M 1993 *Phys. Rev.* **C 47** 724

[8] Cowley A A, Arendse G J, Koen J W, Richter W A, Stander J A, Steyn G F, Demetriou P, Hodgson P E and Watanabe Y 1996 *Phys. Rev.* **C 54** 778

[9] Dimitrova S S, Cowley A A, van Zyl J J, Zemlyanaya E V and Lukyanov K V 2014 *Phys. Rev.* **C 89** 034616

[10] Dimitrova S S, Cowley A A, van Zyl J J, Zemlyanaya E V and Lukyanov K V 2014 *Phys. Rev.* **C 90** 054604

[11] Kunz P D and E. Rost E, in *Computational Nuclear Physics* 1993, ed. Langanke K *et al*. Springer-Verlag, Berlin Vol. 2, Chap. 5

[12] Lukyanov V K, Zemlyanaya E V and Lukyanov K V 2006 *Phys. At. Nucl.* **69** 240

[13] Richter W A, Cowley A A, Hillhouse G C, Stander J A, Koen J W, Steyn S W, Lindsay R, Julies R E, Lawrie J J, J., Pilcher V and Hodgson P E, 1994 *Phys. Rev.* **C 49** 1001

[14] Bonetti R, Colli Milazzo L, Doda I and Hodgson P E 1982 *Phys. Rev.* **C 26** 2417

[15] Gadioli E, Gadioli–Erba E, Guazzoni P, Hodgson P E and Zetta L 1984 *Z. Phys.* **A 318** 147

[16] Bonetti R, Crespi F, and Kubo K I 1989 *Nucl. Phys.* **A 499** 381

[17] Cowley A A, Dimitrova S S, Zemlyanaya E V, Lukyanov K V and van Zyl J J 2016 *Phys. Rev.* **C 93** 034624

[18] Sakai H, Hosono K, Matsuoka N, Nagamachi S, Okada K, Maeda K and Shimizu H 1980 *Nucl. Phys.* **A 344** 41

[19] Cowley A A, Dimitrova S S, Zemlyanaya E V, Lukyanov K V and van Zyl J J 2016 *EPJ Web of Conf.* **107** 08004

Multinucleon transfer processes in the ^{197}Au+^{130}Te reaction studied with a high-resolution kinematic coincidence

F. Galtarossa[1,2], L. Corradi[1] and S. Szilner[3], E. Fioretto[1], G. Pollarolo[4], T. Mijatović[3], D. Montanari[5], D. Ackermann[6], D. Bourgin[7], S. Courtin[7], G. Fruet[7], A. Goasduff[1], J. Grebosz[8], F. Haas[7], D. Jelavić Malenica[3], S. C. Jeong[9], H. M. Jia[10], P. R. John[5], D. Mengoni[5], M. Milin[11], G. Montagnoli[5], F. Scarlassara[5], N. Skukan[3], N. Soić[3], A. M. Stefanini[1], E. Strano[5], V. Tokić[3], C. A. Ur[12], J. J. Valiente-Dobón[1], Y. X. Watanabe[9]

[1]Istituto Nazionale di Fisica Nucleare, Laboratori Nazionali di Legnaro, Legnaro, Italy
[2]Dipartimento di Fisica e Scienze della Terra, Università di Ferrara, Ferrara, Italy
[3]Ruđer Bošković Institute Zagreb, Croatia
[4]Dipartimento di Fisica, Università di Torino, and Istituto Nazionale di Fisica Nucleare, Torino, Italy
[5]Dipartimento di Fisica, Università di Padova, and Istituto Nazionale di Fisica Nucleare, Padova, Italy
[6]GANIL, CEA/DSM-CNRS/IN2P3, Boulevard Henri Becquerel, Caen, France
[7]Institut Pluridisciplinaire Hubert Curien, CNRS-IN2P3, Université de Strasbourg, Strasbourg, France
[8]The Henryk Niewodniczanski Institute of Nuclear Physics, Krakow, Poland
[9]Institute of Particle and Nuclear Studies, High Energy Accelerator Research Organization (KEK), Tsukuba, Ibaraki, Japan
[10]China Institute of Atomic Energy, Bejing, China
[11]Department of Physics, Faculty of Science, University of Zagreb, Zagreb, Croatia
[12] Horia Hulubei National Institute of Physics and Nuclear Engineering, Bucharest, Romania

Abstract

Multinucleon transfer processes in the ^{197}Au+^{130}Te at E_{lab}=1.07 GeV system were studied with the PRISMA magnetic spectrometer in coincidence with an ancillary particle detector. For neutron transfer channels we extracted total cross sections and compared them with calculations performed with the GRAZING code. We associated to each light fragment identified in PRISMA the corresponding mass distribution of the heavy partner and, through the comparison with Monte Carlo simulations, we could infer about the role of neutron evaporation in multinucleon transfer for the population of neutron-rich heavy nuclei.

1 Introduction

The production of neutron-rich nuclei close to the N = 126 shell closure is fundamental to investigate different physical scenarios, ranging from shape coexistence phenomena in neutron-rich Pt-Os isotopes [1] to the path chosen by the r-process to synthesize the heaviest elements [2]. Accessing this region is not an easy task due to the lack of suitable beam-target combinations. Fusion reactions with stable beams and fission yield quite low cross sections and the beam intensities from radioactive beam facilities are not sufficient to perform detailed nuclear structure studies.

Nuclear reaction models [3,4] predict large primary cross sections employing multinucleon transfer (MNT) reactions. One has to keep in mind that at energies close to the Coulomb barrier, multinucleon transfer reactions are mainly governed by optimum Q-value considerations and nuclear form factors [5,6]. For this reason with stable projectiles and targets the main open channels are neutron pick-up and proton stripping from the light partner, while the inverse path can be accessed if neutron-rich projectile and targets are employed, as was recently shown in [7].

Recent experiments have shown that MNT reactions are in fact a suitable and complementary mechanism to fragmentation reactions at relativistic energies for the production of neutron-rich nuclei in the Pb region. In Ref. [8] the products of the fragmentation of ^{208}Pb at 1 A GeV on a Be target were identified in charge Z and mass A with good resolution, due to their high energy. The production cross sections decrease rapidly moving to the neutron-rich side but the reaction products are strongly forward focused and considerable yields can be obtained. In Ref. [9] MNT reactions in the ^{136}Xe+^{198}Pt system at $E_{lab} \sim 8$ A MeV were studied with the magnetic spectrometer VAMOS++ coupled to the EXOGAM γ array. In this case the direct identification in Z and A of the heavy partner was extremely challenging and the production cross sections for the Pt-like ions could only be reconstructed in a complex iterative way from the measured yields and total kinetic energy loss (TKEL) distributions of the primary fragments. These cross sections turned out to be higher compared to those obtained in the fragmentation case, but the authors stressed that neutron-rich heavy nuclei are populated in transfer reactions involving low excitation energies, thus increasing the probability for the primary heavy partner to survive the effect of secondary processes, like nucleon evaporation or fission.

To better understand the effect of such competitive processes we performed an experiment at the INFN Laboratori Nazionali of Legnaro (LNL) to study MNT reactions at near-barrier energies in the ^{197}Au+^{130}Te (E_{lab} = 1.07 GeV). We chose the most neutron-rich Te stable isotope as a target to open the proton and neutron transfer channels leading to neutron-rich heavy partners. We employed a novel experimental method which aims at the simultaneous detection of light and heavy transfer products where one of the reaction partners (the light one) is identified with high A and Z resolution. This allows to correlate the masses of the two reaction partners and follow the behaviour of the heavy partner after the transfer process. The choice of the inverse kinematics allows to have enough kinetic energy of the recoils for their detection though maintaining a low bombarding energy.

2 The experiment and the analysis

For the experiment we used a 1.5-pnA ^{197}Au beam delivered by the PIAVE positive-ion injector followed by the ALPI post accelerator of LNL, impinging onto a 200 μg/cm^2 (2-mm strip) ^{130}Te target with a purity of 99.6%. The layout of the experimental set-up is depicted in Figure 1.

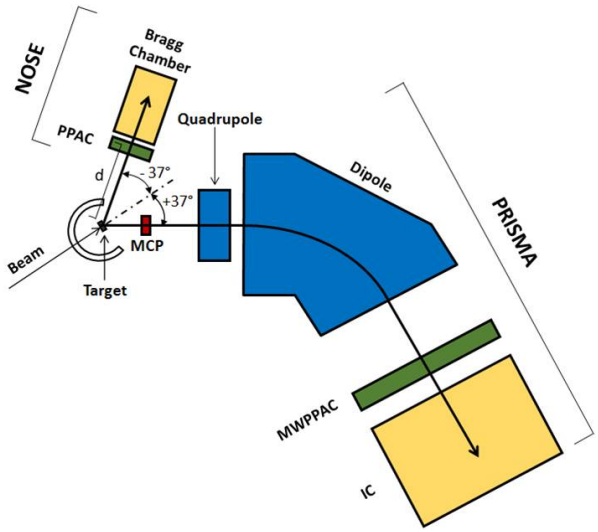

Fig. 1: Layout of the set-up used in the study of the ^{197}Au+^{130}Te reaction, with the PRISMA spectrometer set in coincidence with the NOSE detector. Bragg chamber: axial field ionization chamber; PPAC: multiwire parallel-plate avalanche counter of NOSE; MCP: micro-channel plate detector; MWPPAC: parallel-plate detector of multiwire type; IC: ionization chamber of PRISMA.

The PRISMA magnetic spectrometer [10] was employed for the detection of Te-like ions. The heavy partner was identified in NOSE [11], the ancillary detector coupled to PRISMA, composed of a MWPPAC followed by an axial ionization chamber (Bragg chamber). PRISMA and NOSE were placed at the symmetric angles of $\pm$ 37° for kinematic reasons.

Figure 2 shows the quality of the Z identification in the ionization chambers of the two detectors. In PRISMA (left) the nuclear charge is measured with the E-ΔE technique. The inset shows that the Z resolution (ΔZ/Z $\sim$ 1/65) allows to distinguish several proton transfer channels. The cross sections for these channels are about one order of magnitude less than for neutron transfer, due to the chosen low bombarding energy. For this reason in this work we will focus on pure neutron transfer channels. In NOSE the nuclear charge is measured according to the principle of Bragg Curve Spectroscopy [12]. In this case it is not possible to distinguish proton transfer channels for the heavy partner but a clear separation between Te-like and Au-like events is visible.

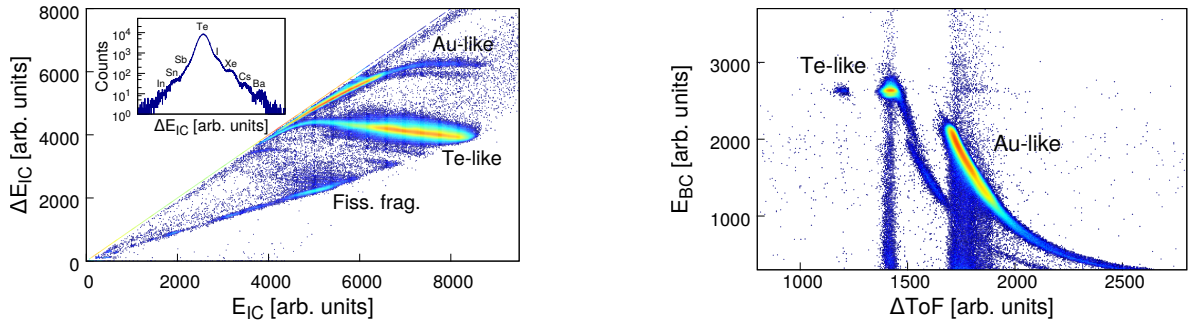

Fig. 2: (Left) Matrix of ΔE_{IC} versus energy E_{IC} of the PRISMA ionization chamber for the ^{197}Au+^{130}Te reaction at E_{lab}=1.07 GeV and θ_{lab}=37°. Besides the Te-like and Au-like ions, those corresponding to fission events, which are not stopped in the IC, are labeled. Inset: Z distributions of the reaction products in the Te region. (Right) Two-dimensional matrix of total energy measured with the Bragg chamber (E_{BC}) vs the time-of-flight between the MCP of PRISMA and the PPAC of NOSE (ΔToF). The clearly separated Te-like and Au-like events are labeled.

In PRISMA the mass identification is performed on an event-by-event basis through the reconstruction of the ions trajectory inside the magnetic elements of the spectrometer, from the measurement of the entrance and exit position of the ions on a MCP detector and a MWPPAC detector, respectively. Figure 3 (left) shows the resulting mass spectrum for Te ions. The mass resolution is ΔA/A $\sim$ 1/240. Transfer channels down to the stripping of 6 neutrons are visible. These are the channels that lead to the population of neutron-rich Au ions.

The experimental yields could be compared with theoretical calculations performed with the GRAZING code [13, 14] that implements a model of the collision that is predominantly binary. The model calculates the evolution of the reaction by taking into account, besides the relative motion variables, the intrinsic degrees of freedom of projectile and target. These are the surface degrees of freedom and the one-nucleon transfer channels. The relative motion of the system is calculated in a nuclear plus Coulomb field. The exchange of many nucleons proceeds via a multi-step mechanism of single nucleons.

To compare calculations and experimental data we normalized the measured yields to the ^{129}Te, keeping the same normalization constant for all the other transfer channels. This is made possible by the fact that for neutron transfer the angular distributions have similar shapes and the acceptance of PRISMA selects the same fraction of events for the different transfer channels. The comparison clearly shows that neutron evaporation must be taken into account to reproduce the experimental cross sections.

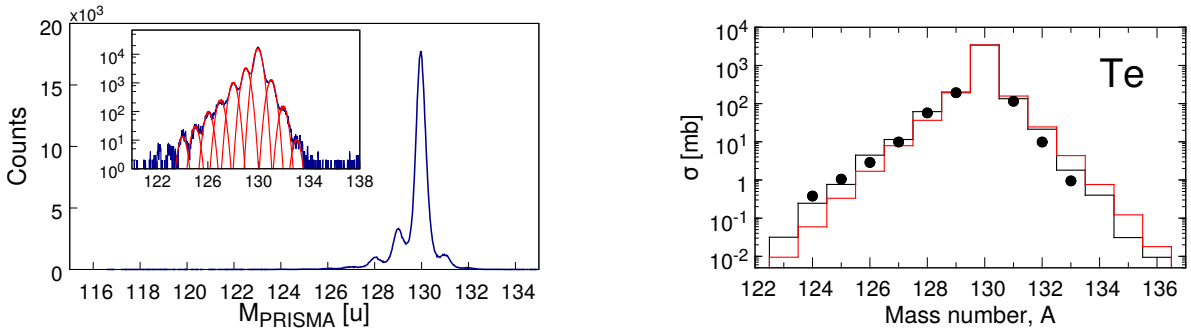

Fig. 3: (Left) Mass distribution for the Te isotopes obtained after ion trajectory reconstruction in PRISMA. The inset shows the distribution in logarithmic scale with the multigaussian fit used to evaluate the yields of neutron transfer channels. (Right) Total experimental cross sections of Te isotopes (points) and GRAZING calculations with (black histogram) and without (red histogram) taking into account the effect of evaporation. Errors are only statistical and are within symbols.

2.1 Mass-mass correlation and Monte Carlo simulations

Indicating the collision as $A + a \rightarrow B + b$ the mass M_B of the heavy partner can be determined from the measured scattering angles, θ_b in PRISMA and θ_B in NOSE, and of the time-of-flight τ_B taken by the heavy partner to cover the distance d $\sim$ 90 cm from the target to the PPAC of NOSE. We call p_A the momentum of the beam in the laboratory frame, we assume a binary character of the reaction and impose momentum conservation, finally obtaining:

$$M_B = \frac{p_A}{d} \frac{sin\theta_b}{sin(\theta_b + \theta_B)} \tau_B \tag{1}$$

The mass resolution strongly depends on the resolution on τ_B and is only slightly affected by the angular resolution. The obtained value is ΔA/A $\sim$ 1/40, which means $\sim$ 5 mass units for the Au-like mass distribution. The kinematic coincidence allows to construct a mass-mass correlation matrix, as shown in Fig. 4, where the total mass distribution of the heavy partner results to be divided in well-separated bands in correspondence of the coincident light fragment identified in PRISMA.

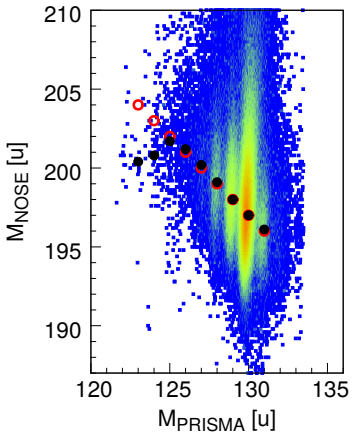

Fig. 4: Mass-mass correlation matrix of Te isotopes detected in PRISMA and the heavy partner detected in coincidence with NOSE. The red circles indicate the centroids of the correlated masses of the primary neutron transfer channels, the black dots indicate the experimental centroids as derived from the fits of their projections.

One can notice that after the transfer of $\sim$ 3-4 neutrons the centroids of the experimental distributions (full black circles) begin to deviate from the expected trend of the primary centroids (empty red circles). The shift between primary and secondary centroids is an effect of the onset of neutron evaporation.

More quantitative information can be extracted by comparing the mass distributions of the heavy partner associated to each Te isotope, which can be obtained by projecting the mass-mass correlation matrix on the y axis for each transfer channel, with Monte Carlo (MC) simulations. The inputs to the MC simulation are the relevant experimental observables (measured cross sections, TKEL distributions, experimental resolution). Then, starting from a given event as recorded by PRISMA and assuming a binary character of the reaction, we can follow the behavior of the heavy partner after the reaction. From the measured TKEL ditributions we can assign an excitation energy to the heavy partner assuming, in first approximation, an equal sharing of the energy between the two fragments. More details can be found in Ref. [15].

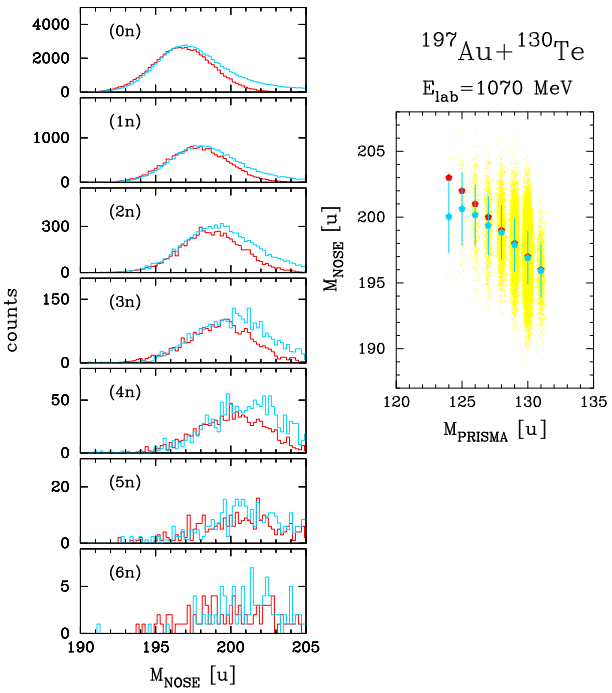

Fig. 5: (Right) Simulated mass-mass correlation matrix. The points are the centroids of the primary (red) and actual (blue) Au isotope distributions. The blue bars represent the standard deviations. (Left) Comparison between the simulated (red) and experimental (blue) mass distributions obtained from the projection of the corresponding mass-mass matrix. The label in each frame indicates the number of neutrons stripped from ^{130}Te.

The comparison between simulated and experimental Au mass distributions is shown in Fig. 5. Neutron evaporation, besides shifting the secondary centroids with respect to the primary ones, shows up as an increase of the width of the mass distributions as more neutrons are transferred.

3 Conclusions

In this contribution we presented our method to measure the effect of neutron evaporation on the heavy partner in the multinucleon transfer reaction ^{197}Au+^{130}Te at E_{lab} = 1.07 GeV, focusing on pure neutron transfer channels. We identified the light partner in A, Z and Q value in PRISMA and determined the mass of the heavy partner in NOSE from momentum conservation in a binary collision. We compared the extracted cross sections for the light partner with the predictions of GRAZING and obtained an

overall good agreement. We constructed a mass-mass correlation matrix and, through the comparison with Monte Carlo simulation, we could evidence the role of evaporation in multinucleon transfer.

References

[1] P. R. John, *et al.*, Phys. Rev. C **90**, 021301(R) (2014); Phys. Rev. C **95** 064321 (2017).

[2] H. Grawe, *et al.*, Rep. Prog. Phys. **70**, 1525 (2007),

[3] C. H. Dasso, G. Pollarolo, and A. Winther, Phys. Rev. Lett. **73**, 1907 (1994).

[4] V. Zagrebaev and W. Greiner, Phys. Rev. Lett. **101**, 122701 (2008).

[5] R. A. Broglia and A. Winther, *Heavy Ion Reactions* (Addison- Wesley, Redwood City CA, 1991).

[6] L. Corradi, G. Pollarolo, and S. Szilner, J. Phys. G: Nucl. Part. Phys. **36**, 113101 (2009).

[7] T. Mijatović, *et al.*, Phys. Rev. C **94**, 064616 (2016).

[8] T. Kurtukian-Nieto, *et al.*, Phys. Rev. C **89**, 024616 (2014).

[9] Y. X. Watanabe, *et al.*, Phys. Rev. Lett. **115**, 172503 (2015).

[10] S. Szilner, *et al.*, Phys. Rev. C **76**, 024604 (2007).

[11] E. Fioretto, *et al.*, Nucl. Instr. and Meth. in Phys. Res. A **899** (2018) 73-79.

[12] C. Gruhn, *et al.*, Nucl. Instr. and Meth. in Phys. Res. **196** (1982).

[13] A. Winther, Nucl. Phys. A **572**, 191 (1994); Nucl. Phys. A **594**, 203 (1995).

[14] Program GRAZING [http:/www.to.infn.it/∼nanni/grazing]

[15] F. Galtarossa, *et al.*, Phys. Rev. C **97**, 054606 (2018).

Transfer reactions induced with ^{56}Ni: shell gaps and np pairing

A. Georgiadou[1], M. Assié[1], Y. Blumenfeld[1], B. Le Crom[1], J. Guillot[1], F. Flavigny[1],L. Achouri[2], M. Aouadi[2], B. Bastin[3], A. Benitez[4], R. Borcea[5], W. Catford[6], E. Clement[3], A. Corsi[7], G. Defrance[3], M-C. Delattre[1], F. Delaunay[2], N. De Séréville[1], Q. Deshayes[2], B. Fernandez[8], M. Fisichella[9], S. Franchoo[1], J. Gibelin[2], A. Gillibert[7], F. Hammache[1], O. Kamalou[3], A. Knapton[6], V. Lapoux[7], S. Leblond[2], M. Marques[2], A. Matta[6], P. Morfouace[1], N. Orr[2], J. Pancin[3], X. Pereira[2,8], L. Perrot[1], E. Pollacco[6], D. Ramos[7], T. Roger[3], F. Rotaru[5], J-A. Scarpaci[10], M. Sénoville[7], O. Sorlin[3], M. Stanoiu[5], I. Stefan[1], D. Suzuki[1], J-C. Thomas[3], M. Vandebrouck[3], G. Verde[1]

[1]Institut de Physique Nucléaire d'Orsay, Université Paris-Sud-CNRS/IN2P3, 91406 Orsay, France
[2]Laboratoire de Physique Corpusculaire de Caen, ENSICAEN-CNRS/IN2P3, 14050 Caen, France
[3]Grand Accélérateur National d'Ions Lourds, CEA/DSM-CNRS/IN2P3, 14076 Caen, France
[4]Centro de Física Nuclear da Universidade de Lisboa, 1649-003 Lisboa, Portugal
[5]Horia Hulubei National Institute of Physics and Nuclear Engineering, Magurele, Romania
[6]Department of Physics, University of Surrey, Guildford GU2 5XH, United Kingdom
[7]Service de Physique Nucléaire, CEA-Saclay/IRFU, 91191 Gif-sur-Yvette, France
[8]Universidade de Santiago de Compostela, E-15782 Santiago de Compostela, Spain
[9]Laboratori Nazionali del Sud, Instituto Nazionale di Fisica Nucleare, Catania, Italy
[10]Centre de Sciences Nucléaires et Sciences de la Matiére, Université Paris-Sud-CNRS/IN2P3, 91406 Orsay, France

Abstract

The structure of the unstable doubly magic nucleus ^{56}Ni has been investigated by measuring one- and two-nucleon transfer reactions. The radioactive beam of ^{56}Ni was produced at GANIL-Caen, France at 30 MeV/u by means of the LISE spectrometer. The experimental set-up used consists of the TIARA-MUST2-EXOGAM combination which provides an almost 4π coverage and the ability to perform particle-γ coincidences. To probe the N=28 gap, we studied the spectroscopy of ^{55}Ni through one-nucleon transfer reactions on ^{56}Ni. The excitation energy spectrum is deduced by measuring the light ejectiles only, while particle-γ coincidences are used to improve the resolution of the populated states and select the main ones. Comparison between the extracted angular distributions and DWBA calculations allows the extraction of the spectroscopic strength of the hole- and particle- states populated by these one neutron pick-up reactions.

1 Introduction

Historically, nuclear reactions were performed, by using light ion beams on the target consisting of the nuclei of interest. As to be able to study short-lived nuclei far from stability one has to inverse the problem. That led to the use of the inverse kinematics where the target consist of the light ion and the beam is produced by the short-lived unstable nuclei or else the radioactive exotic beam.

The last three decades inverse kinematics have been used to reveal the properties of the radioactive nuclei in exotic regions of the nuclear chart, such as the drip-lines, and initialized the ability to study the shell evolution far from stability [1].

In this work with the use of one- and two-nucleon transfer reactions we study two different physical aspects. The doubly magic nucleus ^{56}Ni, with $N = Z = 28$ [2,3], makes an excellent probe for studying the $N = 28$ shell closure next to stability as well as the neutron-proton (np) pairing correlations.

The Ni isotopic chain provides a variety of doubly magic nuclei. From the proton drip-line and ^{48}Ni lying in the edge of the particle-stability and being the mirror nucleus of ^{48}Ca, to the $N = Z$ ^{56}Ni

and finally ^{78}Ni lying in the neutron-drip line. The shell evolution of the $N = Z = 28$ has been of great interest the recent years. With new experimental results on the neutron drip line, the $Z = 28$ magic shell reveals a resistive strength making ^{78}Ni the most neutron rich doubly magic nucleus [4]. Although as one moves to the edges of the nuclear chart the $N = 28$ shell closure becomes questionable and a quenching of the single-particle states is expected to take place.

One-nucleon transfer reactions such as (d,p), (p,d) and (d,t) are one of the most direct ways to test the single particle configuration of the magic nucleus ^{56}Ni. Measuring the occupancy and vacancy of neutron orbits will provide information on the robustness of the $N = 28$ magic number through the N=27 and N=29 isotones.

The structural evolution studied with N=27 isotones for ^{48}Ca is described in detail in the review paper of O.Sorlin and M-G. Porquet [5]. It is noted specifically that about 90% of the ground state configuration of the spherical ^{47}Ca nucleus corresponds to a neutron hole inside the $f_{7/2}$ shell (0p1h configuration) and a closed proton core (0p0h configuration). They presented a possible development of collectivity in the N = 27 isotones, by comparing the characteristics of their first states.

The first excited state with $J^{\pi} = 3/2^{-}$ is expected to involve the promotion of one neutron in the upper $p_{3/2}$ shell with two neutron holes coupled in the $f_{7/2}$ shell (1p2h). This agrees with theoretical calculation showing that the strength lies mainly in the pure excitation of one neutron and less from three neutrons [6, 7]. This state, with closed proton configuration, would be found well above the ground state of all the N=27 isotones, except if the N=28 shell gap is reduced and there is domination by the correlations. As it is shown in the same study it is the case for the N=27 isotones in the sd shell.

Experimentally, the measurement of the cross sections for one-nucleon transfer have to be compared with theoretical calculations to compare the experimental ones. The ratio in between the two values give the Spectroscopic factor of the single particle state of interest that can later be used to reveal the neutron occupancy.

2 Experimental Case

The experiment was performed in 2014 in Grand Accélérateur National d'Ions Lourds (GANIL), Caen. The radioactive beam of ^{56}Ni at 30 MeV/u was produced by fragmentation of a primary beam of ^{58}Ni and purified by means of the LISE3 separator [8]. Measurements were performed in inverse kinematics on CH_2 and CD_2 targets. Two beam tracking multiwire proportional chambers (CATS) were placed upstream of the reaction target and yielded event by event the position and angle of the incoming beam particles [9].

The experiment included close to 4π coverage for the light charged ejectiles. The two components of the double sided silicon strip detector (DSSSD) TIARA, Barrel and Hyball, were placed at central and backward angles [10], while four telescopes of the DSSSD MUST2 covered the forward angles [11]. Tiara and MUST2 provided the necessary parameters for extracting excitation energy and angular distribution.

Around the target 4 germanium clovers of EXOGAM were used for particle-γ coincidences in order to identify the populated state of the residue and disentangle the excited states [12]. At the end of the beam line the Si-Si-CsI telescope CHARISSA was placed to detect heavy residues (although it was not used in the current analysis). The energy loss, residual energy, angle and time of flight were measured in order to perform particle identification.

3 One-nucleon transfer reactions

3.1 Reaction Kinematics

The kinematic lines are unique for any two-body reaction. They give the identification of light ejectiles which consequently add to the identification of the populated levels of the residue nucleus. Hereby,

we present the kinematics obtained for the one nucleon transfer reactions (d,t) and (p,d) at 30 MeV per nucleon on a 7 mg/cm^2 CD_2 and 6.8 mg/cm^2 CH_2 target respectively (see Figure 1). The experimental kinematic lines of the one nucleon transfer reactions show the population of the ground state, as well as the first excited states and also allow us to compare the two different reactions populating the same nucleus ^{55}Ni. In the experimental spectra, with red and green we identify the ground state and one of the excited states, the 3.185 MeV, respectively.

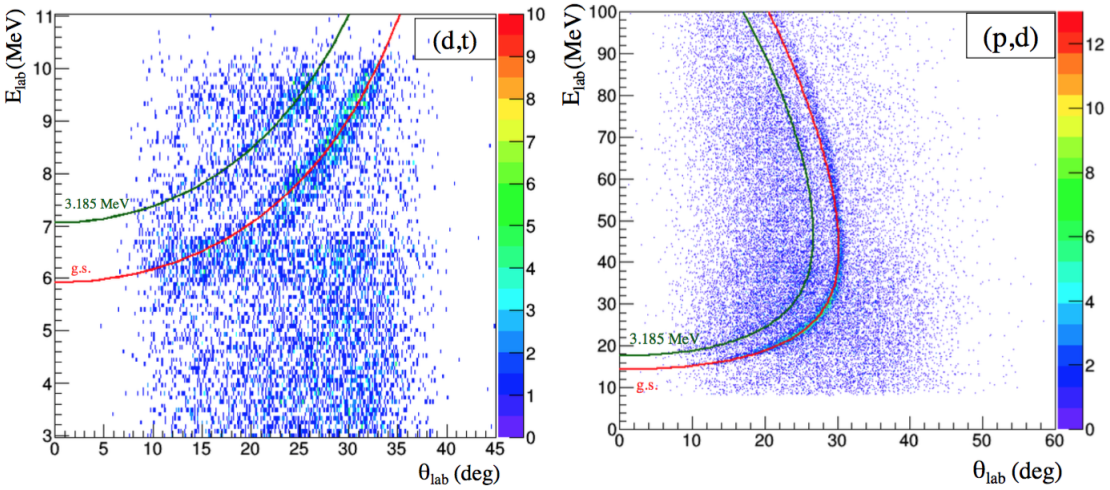

Fig. 1: Kinematic lines of one-nucleon transfer reactions.Left: for the (d,t). Right: of the (p,d) reactions. Red line is the theoretical expected kinematic line for the ground state while with green the excited state of 3.185 MeV is being depicted.

3.2 Excitation Energy

For the (d,t) reaction the excitation energy spectrum is shown in the left of Figure 2. The separation in between the ground state and the excited states is clear with the ground state peak resolution being 1.8 MeV (FWHM) and in a relatively good agreement with the simulation if we consider the uncertainty on the beam energy resolution in the simulations. The CD_2 target has a thickness of 7 mg/cm^2, this adds the effect of straggling of the light ejectile in the target and that is why the energy resolution is not the one expected for MUST2 detector.

For the (p,d) reaction the excitation energy spectrum from Figure 2 (right) shows the ground state separated from the excited states as well, with the energy resolution of the ground state of 910 keV (FWHM).

The resolution of the energy peaks as well as the sparse knowledge of the level scheme of ^{55}Ni do not allow a clear picture of the population of the excited states by looking only in the particle energy spectra. In this work in addition to the particle information we were able to perform particle-γ coincidences that allow the disentanglement of the excited state which are populated by these reactions.

3.3 Particle-γ coincidences

By gating on excitation energy for the energy range 1.5 MeV to 4.5 MeV, we can identify the γ-ray corresponding to each energy level transition that each of these reactions populates in the particle-γ coincidence spectrum. Some of the γ-rays resulting from transitions between excited states of ^{55}Ni (see Figure 3) were well identified on the spectrum with a resolution of 80 keV. We identify 3 clear separated γ-rays, the 735, 1100 and 2100 keV that correspond to the levels of interest. The blue numbers in Figure 3

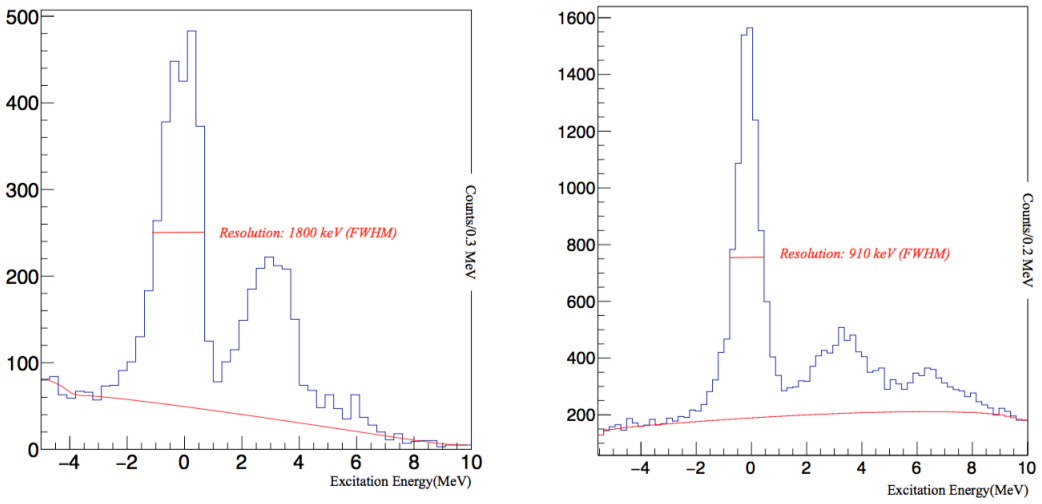

Fig. 2: The excitation energy plots for both one nucleon transfer. Left: Excitation energy spectrum for the (d,t) reaction. Right: Excitation energy spectrum for the (p,d) reaction. With red, the carbon background contribution is indicated and at the FWHM the resolution of each ground state.

corresponds to new measurements that we add in the level scheme of ^{55}Ni. The γ yields are obtained by a Gaussian fit which gives the number of counts that are used to calculate the relative population for each level.

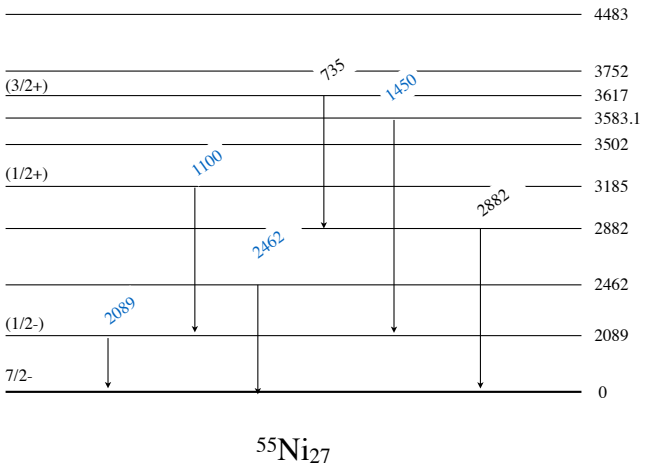

Fig. 3: Levels and γ-rays observed in this experiment. The new ones are indicated with blue and the ones already known with black (Based on ENSDF).

For the fit of each state in both reactions, we use the additional information given from the particle-γ coincidences to identify each excited state. In the case of the (p,d) reaction, we use the information provided by the relative population of the γ-rays to adjust the limits of the maximum and minimum expected yields for each excited state in the particle spectra due to better statistics and larger angular coverage of this reaction channel.

3.4 Angular Distributions

We measure the differential cross section for $N_{^{56}Ni}$ incoming beam particles hitting a target with N_{target} protons or deuterons per cm^2 in different angular ranges.

The angular distributions for the (d,t) and (p,d) reactions are shown in Figure 4. The measured angular distributions were compared with Distorted Wave Born Approximation calculations and the spectroscopic factors obtained can be shown in Table 1.

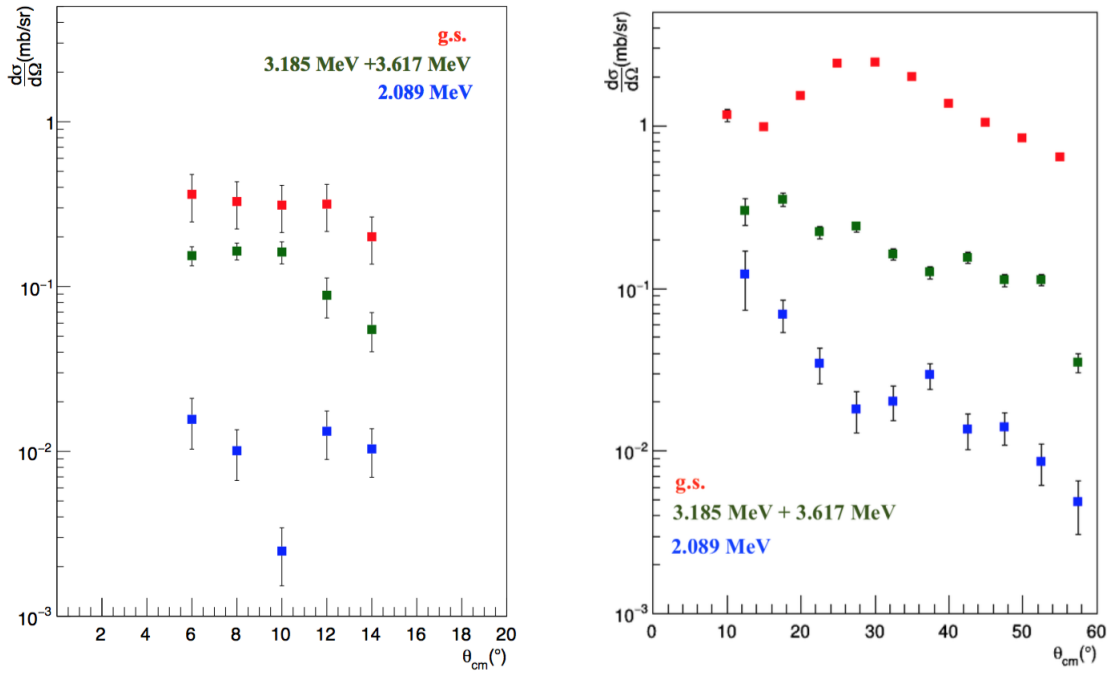

Fig. 4: Angular distributions for the one nucleon transfer reactions, for the ground state $f_{7/2}$, 2.09 $2p_{3/2}$, 3.185 $2s_{1/2}$ together with the 3.6 $d_{3/2}$

State	E_{exp}(MeV)	E (MeV) [13]	$E^{\star}_{SM1}$ (MeV)	$SF^{(p,d)}_{exp}$	$SF^{(d,t)}_{exp}$	SF [13]	SF_{SM1}
$1f_{7/2}$	0.0	0.0	0.0	5.4±1.0	5.8±1.2	6.7±0.7	6.75
$2p_{3/2}$	2.1	2.09	1.89	0.10±0.02	0.020±0.004	0.19±0.03	0.13
$2s_{1/2}$	3.2	3.18	3.039	2.0±0.4	0.20±0.04	1.0±0.2	1.57
$1d_{3/2}$	3.617	(3.752)	3.309	1.8±0.4	1.07±0.21	-	2.88

Table 1: Experimental and calculated information on the $f_{7/2}$, $2p_{3/2}$, $2s_{1/2}$ and $d_{3/2}$ states.Where E_{exp}(MeV) and SF_{exp} indicated the results of this work.

The results obtained by this work for the ground state and the 2.089 MeV state, were compared with the ones obtained by A. Sanetullaev *et al.* [13]. In addition, new information about the single particle states below the N=20 gap were obtained that will allow us to study the evolution of the N=28 shell gap [14].

4 Conclusions

With the one-nucleon transfer reaction we obtained the spectroscopic factors for the ground state and the three excited states corresponding to the removal of a neutron in the $1f_{7/2}$, $2p_{3/2}$, $2s_{1/2}$ and $1d_{3/2}$ via the

(d,t) and (p,d) reactions. The combined information from particle-γ coincidences, allowed us to enrich the level scheme of 55Ni and disentangle the different energy levels. We are able now to investigated the evolution of the N=28 shell gap by comparing spectroscopic factors obtained by previous measurements all along the *fp* shell for the N=27 isotones with Z=20 until Z=28.

5 Perspectives

^{56}Ni, as an N=Z nucleus with fully closed shell, is a key nucleus to investigate neutron-proton pairing in the largest shell accessible experimentally, the fp shell. Neutron-proton pairing can occur both in the isoscalar (T=0) and in the isovector (T=1) channels. The relative intensity of both channels reveals the collective nature of the states. However angular distribution for the state J=0^+,T=1 and J=1^+,T=0 states are highly desirable to disentangle the reaction mechanism [15]. We have previously measured the two-nucleon transfer reaction ^{56}Ni(p, ^{3}He)^{54}Co [16] and anew analysed the ^{56}Ni(d,α)^{54}Co. In the (p,^{3}He) reaction, the ratio of the population of the T=0 and T=1 states indicates a predominance of T=1 isovector pairing weakening of the strength in the T=0 channel. The selectivity in ΔT=0 of the (d,α) reaction enables further investigation of the isoscalar channel contribution. The results for the transfer reaction ^{56}Ni(d,α)^{54}Co will complete the information about the strength of the isoscalar neutron-proton pairing and will are expected to show that the cross-sections are low in the fp shell .

References

[1] A. Obertelli, *Eur. Phys. J. Plus* (2016) 131: 319

[2] M. Mayer, *Phys. Rev.*, 74:235-239 (1948)

[3] M. Mayer, *Phys. Rev.*, 75:1969-1970 (1949)

[4] L. Olivier *et al.*, *Phys. Rev. Lett.* 119, 192501

[5] O. Sorlin and M. -G. Porquet, *Phys. Scripta*, Vol. T152 (2013)

[6] F. Nowacki and A. Poves, *Phys. Rev. C*, 79 014310 (2009)

[7] L. Gaudefroy *et al.*, *Phys. Rev. C*, 78 034307(2008)

[8] R. Anne *et al.*, *NIM A*, 257(2):2150-232, (1987)

[9] S. Ottini-Hustache *et al. NIM A*, 431:476-484, (1999)

[10] M. Labiche *et al.*, *NIM B*, 614:439-448, (2010)

[11] E. Pollacco *et al.*, *Eur. Phys. J.*, 25(10.1140/epjad/i2005-06-162-5):287-288, (2005).

[12] F. Azaiez, *Nuclear Physics A*, 654 (1999) 1003c-1008c

[13] A. Sanetullaev *et al.*, *Physics Letters B* 736 (2014) 137-141

[14] A.Georgiadou, PhD thesis, Université Paris-Saclay, Institut de Physique Nucléaire, CNRS/IN2P3/Université Paris-Sud XI, 91406 Orsay Cedex, (2018)

[15] G.Potel *et al. Reports on Progress in Physics*, 76(10):106301, (2013)

[16] B. Le Crom, PhD thesis, Université Paris-Saclay, Institut de Physique Nucléaire, CNRS/IN2P3/Université Paris-Sud XI, 91406 Orsay Cedex, (2016)

Microscopic description of the two-step direct pre-equilibrium process with non-local potentials and collective states

Amine Nasri[1]*, Marc Dupuis*[1] *Guillaume Blanchon*[1]*, Hugo F. Arellano*[2]*, Eric Bauge*[1]
1 CEA, DAM, DIF, 91297 Arpajon, France
2 Department of Physics - FCFM, University of Chile, Av. Blanco Encalada 2008, Santiago, Chile

Abstract
We present our calculation of contributions to the pre-equilibrium emission cross section coming from two-step direct processes, using a fully microscopic approach based on the nuclear matter method, and treating explicitly the non locality in the potentials. Collective states are included using the Random Phase Approximation (RPA) nuclear structure model. Collective excitations enhanced the two-step cross section when compared to a calculation performed with uncorrelated particle-hole excitations. This results, as well as possible improvements of our modeling, are discussed.

1 Introduction

The preequilibrium stage of a nucleon induced nuclear reaction corresponds to the situation in which the projectile shares enough of its kinetic energy and angular momentum with a few nucleons of the target, and excitation lying in the continuum can be reached. This stage can be observed in the experimental energy spectrum of particles emitted, that present a continuous behavior. A quantum-mechanical treatment of the first part of the preequilibrium nuclear reactions, that are associated with Multistep Direct processes (MSD) is a complicated task that requires an accurate description of the target's excited states even in the continuum, along with an appropriate effective interaction. Moreover, in order to reach a usable form of the transition amplitude for practical calculations, a number of approximations have to be made. The three well-known statistical MSD theories are form Tamura-Udagawa-Lenske (TUL) [1], Nishioka-Weidenmüller-Yoshida (NWY) [2] and Feshbach-Kerman-Koonin (FKK) [3]. A review and thorough comparison of the assumptions and approximations in each of these models is given in [4] and references therein and in [5].

There has been some practical calculations made with MSD models [6,7], which use uncorrelated particle-hole (p-h) excitations for the target. Recently, Dupuis achieved a microscopic calculation of the contribution coming from one-step processes [8] using RPA states for the target (implemented with the Gogny D1S force [9]) and the Melbourne G matrix [10] as effective interaction between the nucleon projectile and the target nucleons. In this calculation, non-natural parity transition are taken into account explicitly and the knock-out exchange term is also accounted for without any localization procedure. The results of this study show a good agreement with experimental data where one-step processes are believed to contribute the most, namely at low excitation energy and forward angles; but the analysis of the calculated preequilibrium angular distribution and energy spectrum of the emitted particle shows that at backward emission angles and for excitation energies above approximately 20 MeV, contributions are missing.

The present work is to be seen as a first stage towards the inclusion of two-step direct processes using the same ingredients as in [8], namely an RPA description of the target's states corresponding to two-step processes, the Melbourne G matrix as effective interaction and a modified version of the NWY model. We compare calculations using RPA states, represented by phonons, to calculations with uncorrelated p-h states and investigate interference effects. In section 2, we briefly remind the approximations we use in our MSD model and we present the microscopic ingredients we use for this calculation. In section 3 we display our results and give some comments, and we draw a conclusion and give some perspectives in section 4.

2 MSD model and microscopic ingredients

2.1 Hypotheses for the MSD calculation

The quantum mechanics description of the MSD process starts from the Born expansion of the transition amplitude for an inelastic process leading to the excitation of a target in its ground state (GS) ψ_i to a final target states $|\psi_f\rangle$, namely

$$T^{i\to f} = \langle \chi^{-}_{\overrightarrow{k_f}}, \psi_f |\; V \;+\; VGV \;+\; VGVGV \;+\; \cdots \;| \chi^{+}_{\overrightarrow{k_i}}, \psi_i \rangle \;, \tag{1}$$

where V is a residual interaction acting between the the nucleon projectile and the target nucleons. The state $\chi^{+}_{\overrightarrow{k_i}}/\chi^{-}_{\overrightarrow{k_f}}$ is the distorted wave in the entrance/exit channel, k_i/k_f and E_{k_i}/E_{k_f} are the associated wave number and kinetic energy. The system Hamiltonian reads $H = H_A + t + V$, where H_A is the target Hamiltonian, t is the kinetic energy operator for the relative motion. The distorted waves in eq. (1) are solution of the Schrödinger equation $(t + U - E_k)\,\chi^{\pm}_{\overrightarrow{k}} = 0$, where U is the optical potential defined as $U = \langle \psi_i | V | \psi_i \rangle$. The many-body propagator G in eq. (1) is $G = \frac{1}{E_{k_i} - U - t - H_A + i\epsilon}$, and its spectral decomposition on eigenstates of H_A and $t + U$ or $t + U^\dagger$ reads

$$G = \sum_N \int \frac{d\overrightarrow{k}}{(2\pi)^{\frac{3}{2}}} \frac{|\tilde{\chi}^{+}_{k}, \psi_N\rangle\langle \chi^{+}_{k}, \psi_N|}{E_{k_i} - E_k - E^*_N + i\epsilon} \;, \tag{2}$$

where E^*_N is the target excitation energy, namely $H_A|\psi_N\rangle = (E_0 + E^*_N)|\psi_N\rangle$ if E_0 is the GS energy, and $\tilde{\chi}^{+}_{k}$ solves $\left(U^\dagger + t - E_k\right)\tilde{\chi}^{+}_{k} = 0$.

The doubly differential cross section for a nucleon emitted at given outgoing angle and energy is:

$$\frac{d^2\sigma(\overrightarrow{k_i}, \overrightarrow{k_f})}{d\Omega_f dE_{k_f}} = \frac{\mu^2}{(2\pi\hbar^2)^2}\frac{k_f}{k_i}\sum_f \delta(E_{k_i} - E_{k_f} - E^*_f)|T^{i\to f}|^2 \;. \tag{3}$$

The n-step direct process corresponds to the n$^{\text{th}}$ order of the series (1). Second order involves the excitation of two particle-hole (2p-2h) states, or two phonon states. Such a process is schematically described on Fig. 1. Since we use the Melbourne g-matrix to represent the effective interaction V, contributions to elastic scattering that comes from the coupling of excited states to the GS are already accounted for in the effective interaction, so in our calculation we must not keep them. We also apply the never-come-back approximation, which assumes that at each step of the reaction the process leading to the creation of a new pair p-h is dominant over the processes of scattering and annihilation. Consequently, the coupling terms that are not included in our calculation are displayed in Fig. 1 by dash, thin arrows while the terms we explicitly calculate are embodied by full thick arrows. Considering these assumptions, one-step and two-step processes lead to distinct final states, thus interferences between the first and the second order of the transition amplitude (1) vanish when the cross section is calculated.

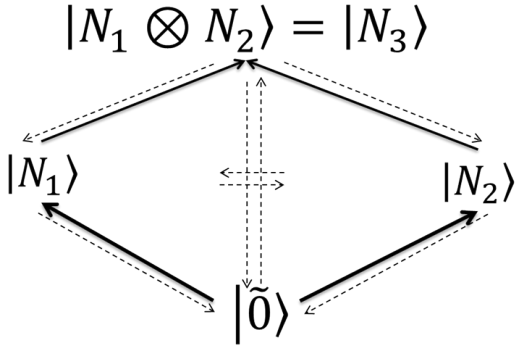

Fig. 1: Schematic representation of the coupling potentials involved in the calculation of a 2-step process. The GS is labeled $|\widetilde{0}\rangle$, target states excited after one-step processes are labeled $|N_1\rangle$ and $|N_2\rangle$, and $|N_3\rangle$ is the target state excited after the second step. Here, we describe the situation where the final state is a 2p-2h (or two-phonon) states made of the N_1 and N_2 1p-1h (or 1-phonon) components. The arrows are defined in the text body.

In our modeling, we consider the two cases in which the target's real states $|\psi_N\rangle$ are a linear combination of either p-h states or RPA states. Moreover, we make use of the sudden approximation used in the NWY model that assumes that configuration mixing is slower than the projectile-target interaction processes. In our approach, this implies that the real intermediate states N_1 and N_2 are shrunk from a linear combination of 1p-1h, 2p-2h, ... (resp. 1-phonon, 2-phonons, ...) states to simply 1p-1h (resp. 1-phonon) states. Consequently of this assumption associated to our use of a 2-body interaction is that the only matrix elements connecting the intermediate state to 2p-2h (reps. 2-phonon) component of the final state remain. Note that we account for the finite life time of the target final states. This leads to replace the delta functions in eq. (3) by the Lorentz distribution $\rho_N(E) = \frac{1}{\pi} \frac{\Gamma_N}{(E-E_N)^2+\left(\frac{\Gamma_N}{2}\right)^2}$ where Γ_N represents the sum of the escape and damping widths. In the present work, we make use of the on-shell approximation which means that we neglect the principal part in eq. (2). Finally, the second order double differential cross section we calculate reads:

$$\frac{d^2\sigma(\overrightarrow{k_i},\overrightarrow{k_f})}{d\Omega_f dE_{k_f}} = \frac{\pi^2\mu^2}{(2\pi\hbar^2)^2}\frac{k_f}{k_i}\sum_f \rho_f(E_{k_i}-E_{k_f})\left|\sum_\beta \langle \chi^-_{\overrightarrow{k_f}}, \psi_f|V|\tilde{\chi}^+_{\overrightarrow{k}}, \psi_\beta\rangle\langle\chi^+_{\overrightarrow{k}}, \psi_\beta|V|\chi^+_{\overrightarrow{k_i}}, \psi_i\rangle\right|^2 . \quad (4)$$

Final states f are 2p-2h (resp. 2-phonon) states, β labels 1p-1h (resp. 1-phonon) states, and ρ_f is the density of 2p-2h (resp. 2-phonon) states. This formula includes interference terms between various intermediate β states. The effect of these interferences is shown in section 3.

2.2 Microscopic ingredients

In our calculation, the use the Melbourne G matrix as residual two-body interaction, which is the solution of Bruckner-Bethe-Goldstone equation in all spin and isospin channels for a mapping of nuclear matter densities ρ. The Melbourne G matrix is a local finite range interaction parameterized as a sum of Yukawa form factors:

$$G(\overrightarrow{r}, \overrightarrow{r}', \rho, E) = \sum_j G_j(\rho, E)\frac{e^{-\frac{|\overrightarrow{r}-\overrightarrow{r}'|}{\mu_j}}}{|\overrightarrow{r}-\overrightarrow{r}'|} , \quad (5)$$

with μ_j denoting the range of the interaction, and where the energy and density dependent amplitudes $G_j(\rho, E)$ are complex. This interaction is made of a central, a spin-orbit and a tensor terms. Since the Melbourne G matrix is calculated in infinite nuclear matter, we use a local density approximation to make calculations in finite nuclei, following the prescription used in the DWBA98 code [11]. As we earlier mentioned, the potentials obtained from the nuclear matter approach and with a finite-range 2-body effective interaction are non local in the space coordinate basis.

As for the nuclear structure input of our calculation, we first describe uncorrelated states. A 1-body potential between an initial state i and a final state f can be written:

$$U^{i\to f} = \langle f|V|i\rangle = \sum_{\alpha,\beta,k,k'} \langle k', \alpha|V|\widetilde{k,\beta}\rangle \rho^{i\to f}_{\alpha,\beta} a^\dagger_{k'} a_k , \quad (6)$$

with α labeling single particle states, and $|\widetilde{k,\beta}\rangle = |k,\beta\rangle - |\beta,k\rangle$. The term $-|\beta,k\rangle$ generates the knock-out exchange potential which is non-local if V has a finite range. The quantity $\rho^{i\to f}_{\alpha,\beta}$ is a one-body transition density matrix element between initial and final state defined by:

$$\rho^{i\to f}_{\alpha,\beta} = \langle f|a^\dagger_\alpha a_\beta|i\rangle \quad (7)$$

In our study, we calculate the target's GS with the Hartree-Fock (HF) theory implemented with the Gogny D1S force. Details on this implementation can be found in [12]. In the HF theory, the GS is a Slater

determinant written as:

$$|\psi_{HF}\rangle = \prod_{h=1}^{h_{Fermi}} a_h^\dagger |-\rangle \ , \tag{8}$$

with h_{Fermi} labeling the Fermi level and $|-\rangle$ the void of particles. A 1p-1h excited state can be built on this GS using the angular momentum coupled creation and annihilation operator:

$$|1p1h\rangle = \left[a_p^\dagger \otimes a_{\widetilde{h}}\right]_M^J |\psi_{HF}\rangle = \sum_{m_p m_h} (-)^{j_h - m_h} \langle j_p m_p j_h - m_h | JM\rangle \, a_p^\dagger a_h |\psi_{HF}\rangle \ , \tag{9}$$

with $a_{\widetilde{h}}$ the time reversed annihilation operator of a hole state, J the total spin of the excitation and M its projection on the quantization axis, and j_i the intrinsic total angular momentum of the particle i. A 2p-2h state is built by coupling two 1p-1h states to the correct total spin and parity (of the 2p-2h state):

$$|N_3\rangle = n|N_2 \otimes N_1\rangle = n \left[\left[a_{p_2}^\dagger \otimes a_{\widetilde{h_2}}\right]^{J_2} \otimes \left[a_{p_1}^\dagger \otimes a_{\widetilde{h_1}}\right]^{J_1}\right]_{M_3}^{J_3} |\psi_{HF}\rangle \tag{10}$$

with N_3 the 2p-2h state, N_2 and N_1 the two 1p-1h states, n a normalization factor. We can use similar definitions for the RPA cases, considering first the definition of a 1-phonon creation and annihilation operators. Let $|\psi_{\widetilde{0}}\rangle$ denote the void of phonon, describing the GS of the nucleus. We define $\Theta_N^\dagger$ the operator that creates a phonon labeled $|\psi_N\rangle$. We associate to the creation operator its adjoint operator Θ_N that annihilates the vibrational mode N. Formally, these definitions read:

$$|\psi_N\rangle = \Theta_N^\dagger |\psi_{\widetilde{0}}\rangle \quad , \quad \langle\psi_N|\Theta_N = \langle\psi_{\widetilde{0}}| \quad , \quad \langle\psi_{\widetilde{0}}|\Theta_N^\dagger = 0 \quad , \quad \Theta_N|\psi_{\widetilde{0}}\rangle = 0 \tag{11}$$

We use the same definition for the angular momentum coupled operators that we introduced for uncorrelated p-h states, and also for 2-phonon states which reads:

$$|\psi_{N_3}\rangle = n \left[\Theta_{N2}^\dagger \otimes \Theta_{N1}^\dagger\right]_{M_3}^{J_3} |\psi_{\widetilde{0}}\rangle \ , \tag{12}$$

with n a normalization factor.

2.3 The ECANOL and MINOLOP codes

From the definitions previously given, we have written a code called MINOLOP that computes the non local coupling potentials using the Melbourne G matrix and nuclear structure input. In the present work, our practical applications were done using only the central part of these potentials, for the spin-orbit and tensor parts still require some validations. Furthermore, we developed the ECANOL code that solves coupled-channel equations with non local potentials. This code uses a numerical method developed by Arellano and successfully applied to the description of charge exchange reactions [13]. We extended this method to take into account other excitations and be able to make calculations for inelastic scattering, and use the results in our preequilibrium calculations.

3 Results

In equation (4), we mentioned that interference effects are expected to occur. In order to evaluate the effect of these interferences, we made the calculation in the same spirit of that made by Kawano *et al.* [6] of a few random cases with and without interferences. We display on the left panel of Fig. 3 the results for the following case: the GS of ^{90}Zr is 0^+, the states corresponding to one-step processes are a 3^- and a 5^-, and we display the results for the 2^+ and 4^+ 2-phonon states. On the right panel, we display a similar calculation but in the case of uncorrelated p-h excitations, and only in for the 2^+ final state.

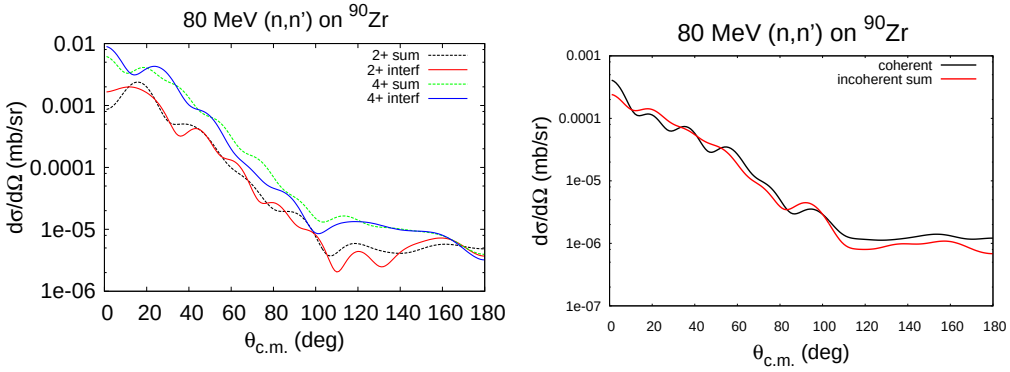

Fig. 2: Angular distribution to 2-phonon (left) and 2p-2h (right) states built by coupling the first, 1-phonon (left) and 1p-1h (right) 3^- and 5^- states in ^{90}Zr for an incident neutron.

We notice that interferences modify the shape of the angular distribution but not the magnitude, and the positions of the relative minima and maxima between coherent and incoherent calculation present a random nature. Also, the relative difference of the integrated cross section is below 10%. This calculation indicates that interference effects should average out provided we include in the preequilibrium calculation a very large number of states. In ^{90}Zr, there are about 10,000 2-phonon states with an excitation energy below 22 MeV, and such a number should be significant enough so that we can make a calculation without interferences (the situation is similar in the case of p-h excitations).

So, we have made a calculation of the contribution to the preequilibrium cross section that comes from 2-step processes, considering a incident neutron with 80 MeV of kinetic energy on ^{90}Zr. We have done two separate calculations: one in which we consider uncorrelated p-h excitations of the target, and one in which we use RPA states. We have included all states with an excitation energy below 16 MeV. As the excitation energy increases, the number of states that correspond to 2-step processes becomes larger and larger than the number of states for one-step processes. Therefore, we expect that the tendencies we observe in the excitation energy range of our calculation will be more pronounced at higher excitation energies. The results are displayed on Fig. 3.

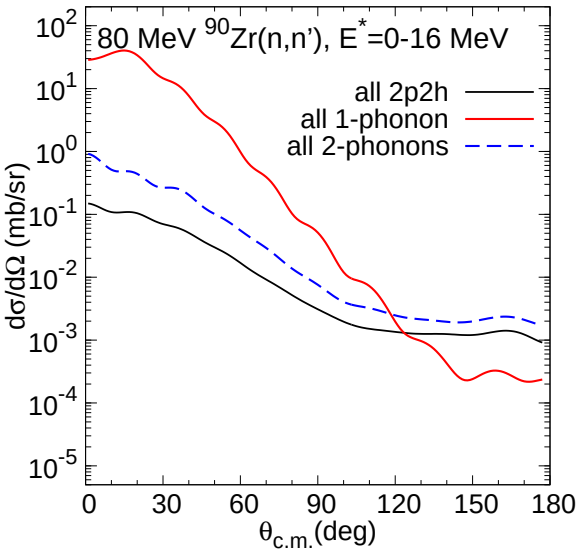

Fig. 3: Comparison between the angular distribution obtained with RPA states for 1 (red curve) and 2-phonon states (blue curve), and with uncorrelated 2p-2h (black curve) state. The excitation energies considered in this calculation range from 0 to 16 MeV.

The contribution that comes from 2-step processes is bigger than the contribution of one-step processes for emission angles above approximately 100°. This can be understood by the larger transfer

of angular momentum in the case of 2-step processes, which leads to emitted particles at higher angles. The contribution that comes from 2-phonon states is bigger than the contribution from 2p-2h states. Two reasons explain this difference: 2-phonon states are collective states, and here the impact of this collectivity is to increase the cross section. The other reason is that in our RPA calculations, we used the Quasi-Boson Approximation (QBA)which can cause a strong violation of the Pauli principle and may artificially enhance the cross section. In the present calculation, it is not possible to distinguish the separate contributions of collectivity and of the QBA.

4 Conclusion

This work is a first step towards the extension of the microscopic calculation of MSD emissions carried out by Dupuis [8] to 2-step processes. Our results indicate that with the present modified version of the NWY model, interference effects should average out with a sufficient number of states. Also, our calculations show the enhancement of the angular distribution at backward emission angles when 2-step processes are accounted for, even at low excitation energies. Finally, we observe the effect due to both collectivity and the use of the QBA in RPA calculations. Possible improvements for this work are the inclusion of all components of the effective interaction so that states with non-natural parity can also be included, lifting the on-shell approximation and check if our observations on interferences are modified, and make a larger calculation that includes states with a higher excitation energy. With the MINOLOP and ECANOL codes that we have developed, such study should be feasible in the near future.

References

[1] T. Tamura, T. Udagawa, and H. Lenske. Multistep direct reaction analysis of continuum spectra in reactions induced by light ions. *Phys. Rev. C*, 26:379–404, Aug 1982.

[2] H. Nishioka, H.A Weidenmüller, and S. Yoshida. Statistical theory of precompound reactions: The multistep direct process. *Annals of Physics*, 183(1):166 – 187, 1988.

[3] H. Feshbach, A. Kerman, and S. Koonin. The statistical theory of multi-step compound and direct reactions. *Annals of Physics*, 125(2):429 – 476, 1980.

[4] A. J. Koning and J. M. Akkermans. Intercomparison of multi-step direct reaction models. In Syed M. Qaim, editor, *Nuclear Data for Science and Technology*, pages 891–893, Berlin, Heidelberg, 1992. Springer Berlin Heidelberg.

[5] M. Dupuis. *Modèles de réactions directes et de pré-équilibre quantique pour la diffusion de nucléons sur des noyaux sphériques,*. PhD thesis, University Of Bordeaux, 2006.

[6] T. Kawano and S. Yoshida. Interference effect in the scattering amplitudes for nucleon-induced two-step direct process using the sudden approximation. *Phys. Rev. C*, 64:024603, Jun 2001.

[7] H. Lenske, H. H. Wolter, M. Herman, and G. Reffo. *Proceeding of the International conference on nuclear data for science and technology*.

[8] M. Dupuis. Microscopic description of elastic and direct inelastic nucleon scattering off spherical nuclei. *The European Physical Journal A*, 53(5):111, May 2017.

[9] J.F. Berger, M. Girod, and D. Gogny. Time-dependent quantum collective dynamics applied to nuclear fission. *Computer Physics Communications*, 63(1):365 – 374, 1991.

[10] K. Amos, P. J. Dortmans, H. V. Von Geramb, S. Karataglidis, and J. Raynal. Nucleon-nucleus scattering, a microscopic nonrelativistic approach. *Adv. Nucl. Phys.*, 25:275–540, 2000.

[11] Raynal Jacques. computer code dwba98. *NEA*, 1999.

[12] J.P. Blaizot and D. Gogny. Theory of elementary excitations in closed shell nuclei. *Nuclear Physics A*, 284(3):429 – 460, 1977.

[13] H. F. Arellano and W. G. Love. In-medium full-folding model approach to quasielastic (p, n) charge-exchange reactions. *Phys. Rev. C*, 76:014616, Jul 2007.

Geometric shapes describing nuclear reaction mechanisms such as fusion, alpha emission and capture, binary and ternary fission, planar fragmentation and n-alpha nuclei

G. Royer, J. Jahan and N. Mokus
Subatech laboratory, UMR : IN2P3/CNRS-University-IMT, Nantes, France

Abstract
Different shape sequences useful to describe simply the fusion, alpha emission or capture, binary and ternary fission, planar and three dimensional fragmentation and n-alpha nuclei are gathered together. Their geometric characteristics allowing to determine the total energy and the dynamics of a nuclear system are provided, mainly the volume, the surface, the Coulomb function, the moments of inertia, the quadrupole moment and the rms radius.

1 Introduction

To describe macroscopically nuclear reaction mechanisms such as fusion [1], alpha emission and capture [2], binary and ternary fission [3], fragmentation [4] and n-alpha nuclei [5, 6] one simulates the nuclear system by geometric shapes [7, 8] and determines the main geometric characteristics such as volume, surface, Coulomb function, moments of inertia, quadrupole moment and rms radius. In this work, the following shapes will be investigated: elliptic and hyperbolic lemniscatoids, prolate compact ternary shapes, tori and bubbles.
Other multibody shapes such as linear chain, triangle, square, tetrahedron, pentagon, trigonal bipyramid, square pyramid, hexagon, octahedron, octagon and cube used to describe some light nuclei as alpha molecules have been used recently [5, 6].

2 Elliptic lemniscatoids and pumpkin-like shapes

The fusion, alpha and cluster radioactivities and fission through compact shapes lead, in first approximation, from one sphere to two tangent spheres or vice-versa. Such a deformation valley can be simulated using two halves of different elliptic lemniscatoids. An elliptic lemniscatoid is the inverse of an oblate ellipsoid. One elliptic lemniscate is defined, in polar coordinates, by

$$R(\theta)^2 = a^2 \sin^2\theta + c^2 \cos^2\theta, \tag{1}$$

and the equation of the elliptic lemniscatoid is

$$a^2x^2 + a^2y^2 + c^2z^2 = (x^2 + y^2 + z^2)^2, \tag{2}$$

where the z axis is the axis of revolution. Assuming volume conservation, the ratio $s = a/c$ of the neck radius to the half-elongation of the system defines completely the shape. When s decreases from 1 to 0 the lemniscatoid varies continuously from a sphere to two tangent equal spheres. When the perpendicular x axis is taken as axis of revolution the elliptic lemniscates generate pumpkin-like configurations (see Fig. 1). For the elliptic lemniscatoid the volume and surface are given by

$$Vol = \frac{4}{3}\pi {R_0}^3 = \frac{\pi}{12}c^3 \left[4 + 6s^2 + \frac{3s^4}{\sqrt{1-s^2}} \sinh^{-1}\left(\frac{2}{s^2}\sqrt{1-s^2}\right)\right], \tag{3}$$

$$S = 4\pi {R_0}^2 B_s = 2\pi c^2 \left[1 + \frac{s^4}{\sqrt{1-s^4}} \sinh^{-1}\left(\frac{1}{s^2}\sqrt{1-s^4}\right)\right], \tag{4}$$

Fig. 1: Evolution of the elliptic lemniscatoids generates by a revolution of the lemniscates around the horizontal axis and of the pumpkin-like shapes generates by a revolution around the vertical axis.

R_0 being the radius of the initial or final sphere and B_s the dimensionless surface function.
r, the distance between the mass centres of the right and left parts of the object, is given by

$$r = \pi c^4 \frac{1 + s^2 + s^4}{3V}. \tag{5}$$

The dimensionless perpendicular and parallel moments of inertia (relatively to the moment of inertia of the equivalent sphere $\frac{2}{5} m {R_0}^2$) are expressed as

$$I_{\perp,rel} = \frac{c^5 s^2}{512(1-s^2){R_0}^5}\left[\frac{112}{s^2} + 8 + 30s^2 - 135s^4 + \frac{120s^4 - 135s^6}{\sqrt{1-s^2}} \sinh^{-1}\left(\sqrt{\frac{1-s^2}{s^2}}\right)\right]. \tag{6}$$

$$I_{\parallel,rel} = \frac{c^5 s^2}{512(1-s^2){R_0}^5}\left[\frac{32}{s^2} + 48 + 100s^2 - 210s^4 + \frac{240s^4 - 210s^6}{\sqrt{1-s^2}} \sinh^{-1}\left(\sqrt{\frac{1-s^2}{s^2}}\right)\right]. \tag{7}$$

The dimensionless quadrupole moment is

$$Q = \frac{\pi c^5 s^2}{96(1-s^2){R_0}^5}\left[\frac{16}{s^2} - 8 - 14s^2 + 15s^4 - \frac{24s^4 - 15s^6}{\sqrt{1-s^2}} \sinh^{-1}\left(\sqrt{\frac{1-s^2}{s^2}}\right)\right]. \tag{8}$$

Similar formulas are available for the pumpkin-like shapes [7].

To generalize the elliptic lemniscatoid shape sequence to asymmetric but axially symmetric shapes it is sufficient to join two halves of different elliptic lemniscatoids assuming the same transverse distance a (see Fig. 2 and [1, 7]) and two different c_1 and c_2 half elongations and two different ratios $s_1 = a/c_1$ and $s_2 = a/c_2$.

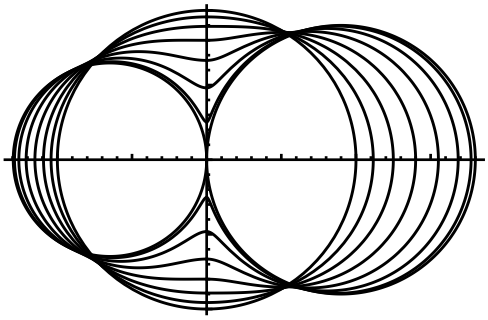

Fig. 2: Two parameter shape sequence varying from two touching unequal spheres to one sphere or vice versa.

3 Hyperbolic lemniscatoids

The most commonly admitted fission path corresponds to elongated shapes with shallow necks. It can be simulated, in first approximation, by hyperbolic lemniscatoids.
For the one-body configurations the hyperbolic lemniscatoids are defined by

$$x^2 = -z^2 + 0.5c^2(s^2 - 1) + 0.5c\sqrt{8(1 - s^2)z^2 + c^2(1 + s^2)^2}. \tag{9}$$

For the two-body shapes the separated ovals are given by

$$x^2 = -z^2 - 0.5c^2(s^2 + 1) + 0.5c\sqrt{8(1 + s^2)z^2 + c^2(1 - s^2)^2}. \tag{10}$$

Assuming the volume conservation, these shapes are one-parameter dependent. The ratio of the minor and major axes $s = a/c$ can be used for the one-body shapes. When the ovals are separated, the opposite s of the ratio of the distance between the tips of the fragments and the system elongation can be retained (see Fig. 3). When s varies from 1 to -1 the shapes evolves from one sphere to two infinitely separated spheres. The volume of the system is, respectively for the one-body and two-body shapes:

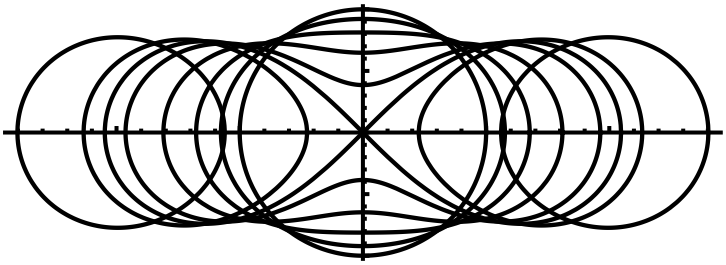

Fig. 3: Hyperbolic lemniscatoid shape sequence. At the scission point, the configuration is the Bernoulli lemniscate.

$$Vol = \frac{\pi c^3}{12}\left[-2 + 6s^2 + 3\frac{(1 + s^2)^2}{\sqrt{2(1 - s^2)}}\sinh^{-1}\left(\frac{2\sqrt{2(1 - s^2)}}{1 + s^2}\right)\right], \tag{11}$$

$$Vol = \frac{\pi c^3}{12}\left[-2(1 + s)^3 + 3\frac{(1 - s^2)^2}{\sqrt{2(1 + s^2)}}\sinh^{-1}\left(\frac{2(1 + s)\sqrt{2(1 + s^2)}}{(1 - s)^2}\right)\right]. \tag{12}$$

For the one-body shapes, the relative surface function reads

$$B_s = \frac{c^2}{4{R_0}^2} \times \left[4(1 + s^2) + 2\sqrt{\frac{2(1 + s^2)}{1 - s^2}}s^2 F\left(\sin^{-1}\sqrt{1 - s^2}, \frac{1}{\sqrt{1 + s^2}}\right)\right. \tag{13}$$
$$\left. - 2(1 + s^2)\sqrt{\frac{2(1 + s^2)}{1 - s^2}}E\left(\sin^{-1}\sqrt{1 - s^2}, \frac{1}{\sqrt{1 + s^2}}\right)\right].$$

E and F are incomplete elliptic integrals [7]. B_s is calculated numerically for the two-body configuration. The distance r between the centres of the right and left parts is for the one and two-body shapes

$$r = \frac{c^4}{8{R_0}^3} \times (1 + 4s^2 + s^4) \tag{14}$$

$$r = \frac{c^4}{8{R_0}^3} \times \frac{(1 - s^2)^3}{1 + s^2}. \tag{15}$$

For the one-body shapes the parallel and perpendicular moments of inertia and the quadrupole moment are given by

$$I_{\parallel} = \frac{c^5}{512(1-s^2){R_0}^5} \times \Big[147 - 27s^2 - 15s^4 - 225s^6 - \frac{15(1+s^2)^2(15-34s^2+15s^4)}{2\sqrt{2(1-s^2)}} \sinh^{-1}\left(\frac{2\sqrt{2(1-s^2)}}{1+s^2}\right)\Big], \tag{16}$$

$$I_{\perp} = \frac{c^5}{1024(1-s^2){R_0}^5} \times \Big[269 + 251s^2 - 145s^4 - 255s^6 - \frac{15(1+s^2)^2(17-30s^2+17s^4)}{2\sqrt{2(1-s^2)}} \sinh^{-1}\left(\frac{2\sqrt{2(1-s^2)}}{1+s^2}\right)\Big], \tag{17}$$

$$Q = \frac{\pi c^5}{192(1-s^2){R_0}^5} \times \Big[-5 + 61s^2 - 23s^4 + 39s^6 + \frac{3(1+s^2)^2(13-38s^2+13s^4)}{2\sqrt{2(1-s^2)}} \sinh^{-1}\left(\frac{2\sqrt{2(1-s^2)}}{1+s^2}\right)\Big]. \tag{18}$$

For the two-body shapes these quantities are expressed as

$$I_{\parallel} = \frac{c^5}{512(1+s^2){R_0}^5} \times \Big[147 + 225s + 27s^2 - 15s^3 - 15s^4 + 27s^5 + 225s^6 + 147s^7 - \frac{15(1-s^2)^2(15+34s^2+15s^4)}{2\sqrt{2(1+s^2)}} \sinh^{-1}\left(\frac{2(1+s)\sqrt{2(1+s^2)}}{(1-s)^2}\right)\Big], \tag{19}$$

$$I_{\perp} = \frac{c^5}{1024(1+s^2){R_0}^5} \times \Big[269 + 255s - 251s^2 - 145s^3 - 145s^4 - 251s^5 + 255s^6 + 269s^7 - \frac{15(1-s^2)^2(17+30s^2+17s^4)}{2\sqrt{2(1+s^2)}} \sinh^{-1}\left(\frac{2(1+s)\sqrt{2(1+s^2)}}{(1-s)^2}\right)\Big], \tag{20}$$

$$Q = \frac{\pi c^5}{192(1-s^2){R_0}^5} \times \Big[-5 - 39s - 61s^2 - 23s^3 - 23s^4 - 61s^5 - 39s^6 - 5s^7 + \frac{3(1-s^2)^2(13+38s^2+13s^4)}{2\sqrt{2(1+s^2)}} \sinh^{-1}\left(\frac{2(1+s)\sqrt{2(1+s^2)}}{(1-s)^2}\right)\Big]. \tag{21}$$

4 Comparison between the elliptic lemniscatoid and hyperbolic lemniscatoid shape valleys

In nuclear physics the question of reversibility of the fission and fusion mechanisms was a focus of discussions already in 1939 between Fermi and Bohr. The different possible shapes taken by a fissioning nucleus were firstly explore using a development of the radius in terms of Legendre polynomials, thinking that the fission process is only governed by the balance between the repulsive Coulomb forces and the attractive surface tension forces. This method leads naturally to smooth elongated one-body configurations resembling to hyperbolic lemniscatoids. This development cannot simulate strongly distorted shapes and the rupture into compact fragments or the alpha decay or capture and cluster radioactivity.

Furthermore, within liquid drop models, to reproduce the fusion data and the alpha and cluster radioactivities one must introduce an additional term, the so-called proximity energy, to take into account the strong nuclear interaction between nucleons of the surfaces in regard between almost spherical nuclei or in a deep crevice in one-body shapes. This proximity energy is evidently very small for elongated shapes with shallow necks and, then, it is often neglected but this term is important in fusion or fission through compact and creviced shapes. It exists a degeneracy in energy between these two deformation valleys. The main available experimental data are the moments of inertia and quadrupole moments and it has been shown that they are similar in the two paths [9].

5 Prolate ternary shapes

One of the hypotheses to explain the nucleosynthesis in stars is the ternary fusion of three alpha particles to form the ^{12}C nucleus. In the decay channels the ternary fission has been observed even though its probability is much lower than the one of the binary fission. From the asymmetric binary shapes one may generate prolate ternary shapes (see Fig. 4) in cutting the smallest fragment along its maximal transverse distance by a symmetry plane. The shape is still only two-parameter dependent. For s_1=s_2=1 the shape corresponds to the initial or final sphere and for s_1=s_2=0 two spheres of radius R_1 are aligned with a central smaller sphere of radius R_2.

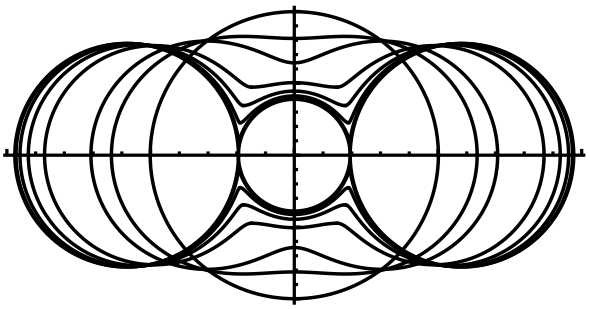

Fig. 4: Evolution of the shape from a sphere to two equal spheres aligned with a smaller sphere between them.

6 Tori and bubbles

Beyond the pumpkin like shapes, ring torus may appear to finally desintegrate into n fragments emitted roughly in the same plane (see Fig. 5). The dimensionless parameter s_t allows to follow this evolution

$$s_t = (r_t - r_s)/2r_s, \tag{22}$$

where r_s and r_t are the sausage and torus radii.
The different geometric characteristics are given by

$$Vol = \frac{4\pi {R_0}^3}{3} = 2\pi^2 r_t {r_s}^2 = \frac{\pi^2 {c_t}^3}{4}(1+2s_t), \tag{23}$$

$$I_{\perp,rel} = \frac{35}{32}(1+3s_t+3{s_t}^2)\left(\frac{16}{3\pi(1+2s_t)}\right)^{2/3}, \tag{24}$$

$$\langle r^2\rangle_{rel} = \frac{5}{6}(1+2s_t+2{s_t}^2)\left(\frac{16}{3\pi(1+2s_t)}\right)^{2/3}, \tag{25}$$

$$B_s = \frac{4\pi^2 r_s r_t}{4\pi {R_0}^2} = \frac{\pi {c_t}^2}{4{R_0}^2}(1+2s_t), \tag{26}$$

$$r_s = R_0 \left(\frac{2}{3\pi(1+2s)}\right)^{1/3}. \tag{27}$$

Bubbles of thick skin are often formed within violent reactions where the out of equilibrium effects play an essential role. Calculations within bubbles of constant density can give a first rough approach of the more complex reality [7]. Assuming volume conservation, the bubble characteristics can be calculated from the ratio $p = r_1/r_2$ of the inner and outer radii.

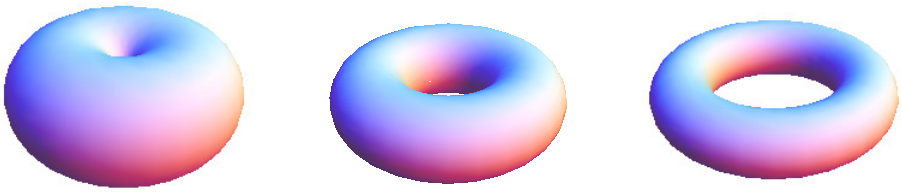

Fig. 5: Evolution of the torus configuration.

7 n-alpha nuclei

Within an α-particle model the energy of the ^{12}C, ^{16}O, ^{20}Ne, ^{24}Mg and ^{32}S nuclei has been determined assuming different α-molecule configurations: linear chain, triangle, square, tetrahedron, pentagon, trigonal bipyramid, square pyramid, hexagon, octahedron, octagon, and cube [6].

8 Conclusion

Different shape sequences are proposed to describe simply the alpha emission or absorption, cluster radioactivity, fusion, fission, fragmentation and n-alpha nuclei. Their geometric definitions and properties are provided, mainly, the volume, the surface, the Coulomb function, the moments of inertia, the quadrupole moment and the rms radius. Within a liquid drop model approach, the total energy of a nuclear system, the dynamics of the processes and the angular distribution of the fragments may be determined.

References

[1] G. Royer and B. Remaud, *Nucl. Phys. A* **444** (1985) 477.

[2] G. Royer, *J. Phys. G: Nucl. Part. Phys.* **26** (2000) 1149.

[3] G. Royer, M. Jaffré, and D. Moreau, *Phys. Rev. C* **86** (2012) 044326.

[4] C. Fauchard and G. Royer, *Nucl. Phys. A* **598** (1996) 125.

[5] G. Royer, A. Escudie, and B. Sublard, *Phys. Rev. C* **90** (2014) 024607.

[6] G. Royer, G. Ramasamy, and P. Eudes, *Phys. Rev. C* **92** (2015) 054308.

[7] G. Royer, N. Mokus, and J. Jahan, *Phys. Rev. C* **95** (2017) 054610.

[8] R. W. Hasse and W. D. Myers, Geometrical Relationships of Macroscopic Nuclear Physics, 1988 (Springer verlag, Berlin).

[9] J. Mignen, G. Royer, and F. Sebille, *Nucl. Phys. A* **489** (1988) 461.

Statistical multi-step direct reaction models and the eikonal approximation

E.V. Chimanski[1,2]*, R. Capote*[2]*, B.V. Carlson*[1]*, A.J. Koning*[2]
[1]Aeronautics Institute of Technology, São José dos Campos, Brazil
[2]NAPC-Nuclear Data Section, International Atomic Energy Agency, Vienna, Austria

Abstract
Nucleon-induced pre-equilibrium reactions are now recognized as consisting almost exclusively of direct reactions in which incident nucleons induce excitations over a wide range of energy in the target nuclei. At low energies, one step reactions dominate with more steps becoming important as the incident energy increases. The characterization of this multistep scattering process in terms of eikonal waves and an optical interaction potential could furnish an important simplification of the description of the collision process. In this preliminary work we perform an analysis of elastic angular distributions for different target nuclei and incident projectile energies, using the eikonal approximation and a $t\rho$ interaction potential.

1 Introduction

Nuclear reactions are of interest in a wide range of areas, from basic science to nuclear and atomic technological applications. Their measured cross sections are energy-dependent quantities, which allows the study of a variety of processes using different theories accordingly to the energy scales and experimental set up involved. Pre-equilibrium emissions are events that occur on an intermediate time scale when compared to the slower process of evaporation (CN compound nucleus) and the fast single interaction of a direct nuclear reaction. A pre-equlibrium particle is emitted after one or more collisions with the nucleons of the target nucleons, but leaves the target nucleus before the statistical equilibrium of the compound system is reached. The relevance of these reactions goes beyond fundamental studies, playing a key role in technical applications in applied areas, e.g., fast nuclear reactors and accelerator-driven system (ADS), radiation beam therapy and medical radioisotope production.

The quantum formalism describing the pre-equilibrium component relies on the multi-step reaction theory framework. The first model was proposed by Agassi, Weindenmüller and Mantzouranis [5], being more rigously deduced later [4], and denominated the multi-step compound theory. The direct (continuum) version of the theory were pioneered by Feshbach, Kerman and Koonin [1]; Tamura, Udagawa and Lenske [3] followed by Nishioka, Weindenmüller and Yoshida [2]. The multi-step direct models describe a collision in terms of a leading incident particle that interacts with the nucleons on its way throw the target nucleus. This processes can generate different particle hole excitations with energy values varying from a few to tens of MeVs. The number of projectile-target interactions is associated with number of steps in the multi-step formalism context. This is also directly related to the energy transferred in the reaction, where the one step is predominant for lower excitation energy events, while more and more steps are expected for reactions with higher energy transfer.

The transition matrix elements for each particle-hole excitations requires the description of the incoming and outgoing projectile waves. These functions represent scattering waves solutions and are usually taken as an expansion of distorted plane waves in the DWBA (distorted wave Born approximation). A sum of several terms representing waves with different angular momenta is required. For high energy scattering, the contribution of larger angular momenta are expected to be relevant, slowing down the convergence of this expansion. For these cases, the angular momentum sum can be conveniently substituted by an integral over the impact parameter. This is a semi-classical approximation, often called

the Glauber approximation in a nuclear scattering context, but more often known as the eikonal approximation, since it was firstly applied in optics. The phase shift of the scattered particle is obtained by an integral of the optical potential along a straight line trajectory. The projectile-target interaction is taken as complex function to account for absorption of particles from the incident beam. For charged projectiles, the Coulomb part of the interaction is usually treated separately [6].

In this work we report our preliminary results on the description of elastic nucleon-induced reactions in which we use the eikonal distorted wave representation of the wave functions and the $t\rho$ approximation to the optical potential. This work is intended to be a test of both the eikonal approximation and the optical potential that we plan to use in the future in a description of multi-step reactions.

We organize the present work as follows. An introduction to the main concepts regarding the eikonal and the optical interactions used in this work are given in Sec. 2. In Section 3 we present the elastic cross sections computed for proton induced reactions on two different targets ^{90}Zr and ^{208}Pb. We summarize our results in Sec. 4. Sec. 4.1 contains the expression we plan to use to obtain the inelastic cross section corresponding to a particle-hole excitation in the first step of a reaction.

2 Formalism and Interaction

Particle scattering wave functions are usually taken as free plane-waves in the first order Born approximation to the scattering amplitude. A better representation, for higher energy particles, is to assume a straight line trajectory for the incident particle and to add a phase correction taking into account the effects of the potential on the scattered wave. This can be considered a semi-classical approximation due to its connection to the more generic WKB (Wentzel-Kramers-Brillouin) approach. The eikonal distorted wave in cylindrical coordinate system is given by [6]

$$\psi_k^{(+)}(z,\,\mathbf{b}) = \exp\left[i\mathbf{k}\cdot(\mathbf{b}+z\hat{\mathbf{z}}) - \frac{i}{\hbar v}\int_{-\infty}^{z} U\left(z',\,\mathbf{b}\right)dz'\right], \tag{1}$$

where b is the cylindrical radius variable. For an interaction potential U centered at the origin, the distance b can be interpreted as the classic impact parameter.
With this wave function, the elastic scattering amplitude becomes

$$\begin{aligned} f_{el}(\mathbf{k}_f,\,\mathbf{k}_i) &= -\frac{1}{4\pi}\int d^3r\, e^{-i\mathbf{k}_f\cdot\mathbf{r}}\,\frac{2\mu}{\hbar^2}U(z,\,\mathbf{b})\,\psi_{k_i}^{(+)}(z,\,\mathbf{b}) \\ &= \frac{k}{i}\int bdb\,J_0(qb)\left(e^{2i\delta(b)}-1\right) \end{aligned}$$

where the eikonal phase shift is defined as

$$\delta(b) = -\frac{1}{\hbar v}\int_0^{\infty} U(z,\,\mathbf{b})\,dz\,. \tag{2}$$

For the transferred momentum $\mathbf{q}=\mathbf{k}_i-\mathbf{k}_f$, since $|\mathbf{k}_f|=|\mathbf{k}_i|=k$, we take

$$q = |\mathbf{k}_i-\mathbf{k}_f| = 2k\sin(\theta/2)\ ,$$

where θ is the scattering angle.
The differential elastic cross section is given by the squared absolute value of the scattering amplitude as

$$\frac{d\sigma_{el}}{d\Omega} = |f_{el}(k,\,\theta)|^2\ .$$

Here, we approximate the projectile-target optical interaction present in the eikonal phase (2), using the $t\rho$ approximation [7, 8]. The forward-angle nucleon-nucleon t-matrix is often parameterized as

$$t_{n_1n_2}(\mathbf{q}=0) = -\frac{2\pi\hbar^2}{\mu}f_{n_1n_2}(\mathbf{q}=0) = -\frac{\hbar v}{2}\sigma_{n_1n_2}^{T}(\alpha_{n_1n_2}+i)$$

where $f_{n_1 n_2}$ is the $n_1 - n_2$ scattering amplitude ($n_{1,2} = n,\, p$) and $\sigma_{pp}^T = \sigma_{nn}^T$ and σ_{pn}^T are the proton-proton, neutron-neutron and proton-neutron total cross sections. The quantity $\alpha_{n_1 n_2}$ represents the ratio between the imaginary and the real part of the proton-nucleon scattering amplitude. We take for the proton-target optical potential

$$U(\mathbf{r}) = -\frac{\hbar v}{2}\left[\sigma_{pp}^T (i + \alpha_{pp})\, \rho_p(\mathbf{r}) + \sigma_{pn}^T (i + \alpha_{pn})\, \rho_n(\mathbf{r})\right],$$

where the total cross sections $\sigma_{n_1 n_2}^T$ as well as the factors $\alpha_{n_1 n_2}$ are energy dependent. We take both parameters from [7,9] and interpolate between the point given there when necessary. We assume that the cross sections and $\alpha_{n_1 n_2}$ factors used in the optical potential also contain the effects of Pauli blocking in the nuclear medium. The position dependent quantities $\rho_p(\mathbf{r})$ and $\rho_n(\mathbf{r})$ are the target proton and neutron densities. These are often approximated as Z/A and N/A times the total nucleon density, $\rho_m(\mathbf{r})$, where Z and N are the proton and neutron number of the nucleus of mass number $A = Z + N$.

The proton elastic scattering phase shift in the $t\rho$ approximation is then given by

$$\begin{aligned}
\delta(b) &= \frac{1}{2}\sigma_{pp}^T (i + \alpha_{pp}) \int_0^\infty \rho_p(z,\, b)\, dz + \frac{1}{2}\sigma_{pn}^T (i + \alpha_{pn}) \int_0^\infty \rho_n\left(\sqrt{z^2 + b^2}\right) dz \\
&\approx \frac{1}{2}\left[\sigma_{pp}^T (i + \alpha_{pp})\frac{Z}{A} + \sigma_{pn}^T (i + \alpha_{pn})\frac{N}{A}\right] \int_0^\infty \rho\left(\sqrt{z^2 + b^2}\right) dz\,,
\end{aligned}$$

where ρ is the nucleon density. For proton-induced reactions, we peform the usual separation into a pure Coulomb amplitude and a Coulomb-mdoified nuclear amplitude [6]. We also take into consideration the nuclear recoil correction [10].

In the next section we present the results obtained for proton induced reactions considering two different target nuclei, ^{90}Zr and ^{208}Pb. We performed this analysis for a large range of incident energy beams. Non-relativistic kinematics were employed. The experimental data sets used to compare with our calculations are given in Table 1.

Table 1: Data sets for the proton elastic cross sections.

Reaction	Proton Incident Energy E (MeV)
^{90}Zr(p,p)	61.4 [11], 80, 135, 160 [12], 156 [13], 185 [14], 400 [15]
^{208}Pb(p,p)	30.3 [16], 200, 400 [15], 318, 800 [17]

3 Results

We show in Figure 1 the normalized (to Rutherford) elastic proton angular distribution as a function of the scattering angle. We performed the calculations of p+^{90}Zr elastic scattering for several different incident energies. The theoretical calculations are in good agreement with the data, especially for higher energies and small angle deflections, as would be expected. At energies below 160 MeV, we overestimate the distribution at backward angles $\theta > 50°$. For lower incident energies, 80 and 61.4 MeV, the calculated distributions are slightly shifted in angle when compared to the experimental data. This is an effect caused by the geometry of the target nucleus and can be adjusted with the use of a more precise target radius.

Fig. 2 presents the cross section dependence on two different quantities for the same ^{208}Pb(p,p) reaction at different incident proton energies. In the left panel, the angular distribution is compared to data for three cases, two higher and one lower incident energies. The results for theses cases, just as in the previous figure, also follow the experimental data more closely for forward angular deflections. For

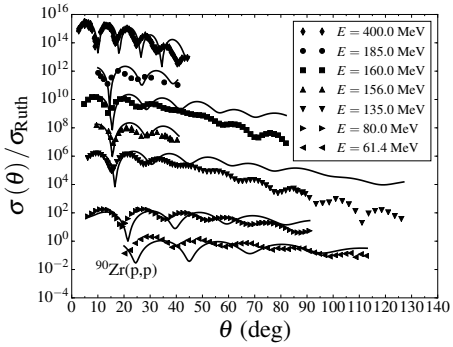

Fig. 1: Differential proton elastic scattering angular distribution (normalized to Rutherford) ^{90}Zr(p,p) for different incident projectile energies. Black solid curves are obtained with the eikonal and $t\rho$ approximations. The experimental data are shown as symbols (see Table 1). The cross sections are numerically shifted starting from the bottom.

the most extreme case at 30.3 MeV of incident energy, the oscillations in the calculation become very different from the experimental ones at the backward scattering angles, although the magnitude of the distribution is reproduced. In the right panel of Fig. 2, the dependence of the angular distribution on the transferred momentum is given. The curves at both 318 and 800 MeV show excellent agreement with the data. Small differences are seen for larger transferred momenta, corresponding to particle emission at backward angles. The results above are also aimed to test both the eikonal and $t\rho$ approaches close to

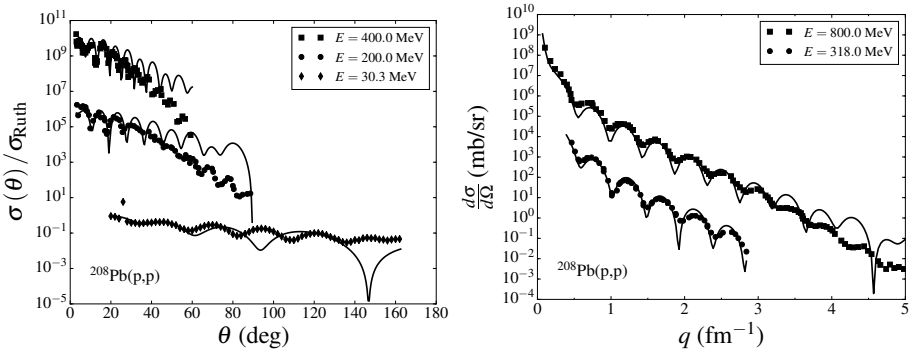

Fig. 2: Normalized differential proton elastic scattering cross sections is shown in the left panel for different incident proton energies. The dependence of the angular distribution on the transferred momentum is presented in the right panel. For these cases the ^{208}Pb(p,p) reaction is studied. Black solid curves are obtained with the eikonal and $t\rho$ approximations. The experimental data are shown as symbols (see Table 1). The cross sections are numerically shifted starting from the bottom.

their limits of validity. The $t\rho$ optical potential is expected to work for higher energy processes, where the medium effects present at lower energies can be neglected. The straight-line trajectory assumption of the eikonal scattering is also questionable in the low energy region. These are the main reasons for the observed discrepancy at lower energies and larger deflection angles. Apart from these limiting cases, our results are in fairly good agreement with the data for proton-induced reactions.

4 Conclusions

Calculations of elastic angular distributions for proton-induced reaction were performed at different incident energies for different targets. The eikonal distorted wave approximation together with a $t\rho$ approximation to the optical potential form the basis of the description we used to compare the theoretical cross sections to the experimental data. The results for ^{90}Zr and ^{208}Pb provided a good description of the experimental angular distributions. The agreement with the data is rather good for small angles and small transferred momenta, i.e. in the forward part of the angular distributions.

Although the eikonal approach was developed for high-energy processes, we have shown that the model can still provide accurate results for incoming particle energies of around 60 MeV. More extreme cases, such as at 30 MeV, can also be studied in this formalism with some restriction. The application of the present model for inelastic scattering is now in progress. Our objective is to represent emitted particles in the eikonal plus $t\rho$ approximation. The simplified picture of this approach provides important guidance for a better description of the inelastic scattering present in the multi-step direct formalism. Below we give the expression for a particle-hole excitation resulting from a collision between the incident particle and the nucleons in the target.

4.1 Perspectives

Here we consider the extension of the use of eikonal waves to represent the distorted waves of the DWBA. The integral over impact parameter reduces the complicated angular momentum coupling drastically and provides a simpler formula for implementations. The one-step DWBA amplitude of a nucleon-induced reaction has the general form

$$T_{DWBA} = \int d^3r\, \psi_{k_f}^{(-)*}(\mathbf{r}) \left\langle B \left| \sum_{j=1}^{A} V(\mathbf{r} - \mathbf{r}_j) \right| A \right\rangle \psi_{k_i}^{(+)}(\mathbf{r}) \ ,$$

where we have written the nucleon-nucleus interaction as a sum of nucleon-nucleon interactions $V(\mathbf{r} - \mathbf{r}')$. Any individual interaction can be written as

$$\langle \mathbf{k}_f;\, ph\,|T|\,\mathbf{k}_i\rangle = \int d^3r\, d^3r'\, \psi_{k_f}^{(-)*}(\mathbf{r})\ \psi_p^*(\mathbf{r}')\ V(\mathbf{r} - \mathbf{r}')\ \psi_h(\mathbf{r}')\ \psi_{k_i}^{(+)}(\mathbf{r}) \ ,$$

where ψ_h is an occupied orbital in the initial nucleus (a hole state after the collision) and $\psi_p$is an unoccupied orbital or continuum state of the initial nucleus.

Acknowledgements

EVC acknowledges financial support from grants 2016/07398-8 and 2017/13693-5 of the São Paulo Research Foundation (FAPESP). BVC acknowledges financial support from grant 2017/05660-0 of the São Paulo Research Foundation (FAPESP) and grant 306433/2017-6 of the CNPq. EVC and BVC acknowledge support from the INCT-FNA project 464898/2014-5.

References

[1] H. Feshbach, A. Kerman, S. Koonin, *Ann. Phys.* **125** (1980) 429.

[2] H. Nishioka, H.A. Weidenmüller, S. Yoshida, *Ann. Phys.* **183** (1988) 166.

[3] T. Tamura, T. Udagawa and H. Lenske, *Phys. Rev. C* **26** (1982) 379.

[4] H. Nishioka, J.J.M. Verbaarschot, H.A. Weidenmüller, S. Yoshida, *Ann. Phys.* **172** (1986) 67.

[5] D. Agassi, H.A. Weidenmüller, G.Mantzouranis, *Phys. Rep.* **22** (1975) 145.

[6] R. J. Glauber, in *Lecture in Theoretical Physics*, edited by W. E. Brittin and L. G. Dunham (Interscience, New York), **1** (1959) 315.

[7] L. Ray, *Phys. Rev. C* **20** (1979) 1857.
[8] M.S. Hussein, R.A. Rego, C.A. Bertulani, *Phys. Rep.* **5** (1991) 279.
[9] S. M. Lenzi, A. Vitturi, and F. Zardi, *Phys. Rev. C* **38** (1988) 2086.
[10] C.A. Bertulani, C.M. Campbell, T. Glasmacher, *Comp. Phys. Commun.* **152** (2003) 317.
[11] C. B. Fulmer, J. B. Ball, A. Scott, and M. L. Whiten, *Phys. Rev.* **181** (1969) 1565.
[12] A. Nadasen *et al.*, *Phys. Rev. C* **23** (1981) 1023.
[13] V. Comparat, R. Frascaria, N. Marty, M. Morlet, A. Willis, *Nucl. Phys. A* (1974) 403.
[14] E. Hagberg, A. Ingemarsson and B. Sundqvist, *Phys. Scripta* **3** (1971) 245.
[15] L. Lee *et al.*, *Phys. Lett. B* **205** (1988) 219.
[16] R.C. Barrett, A.D. Hill, P.E. Hodgson, *Nucl. Phys.* **62** (1965) 133.
[17] Norton M. Hintz *et al.*, *Phys. Rev. C* **37** (1988) 692.

Coulomb-nuclear interference and isospin characterization of the first 2^+ and 3^- transitions by inelastic scattering of alpha particles on ^{90,92}Zr

L. B. Horodynski-Matsushigue, T.Borello-Lewin, M. R. D. Rodrigues, C. L. Rodrigues, H.Miyake

Instituto de Física, Universidade de São Paulo, São Paulo, Brasil

Abstract

Angular distributions for inelastic scattering of 21 MeV alpha particles, exciting the first 2^+ and 3^- states of ^{90,92}Zr, were measured using the São Paulo Pelletron-Enge-Spectrograph facility. Coulomb-nuclear interference analysis was applied and values of $C_L=\delta_L{}^C/\delta_L{}^N$, the ratios of charge to isoscalar deformation lengths for L=2(3) and of $\delta_L{}^N$ were extracted, through comparison of experimental cross sections to DWBA-DOMP predictions. A relative accuracy of ~5% was achieved for C_L. The ratio of reduced charge to isoscalar transition probability, B(EL) to B(ISL), is, for each L, related to the square of the parameter C_L. A homogeneous collective excitation was revealed by C_2=1.057(50) for the first ^{90}Zr quadrupole transition, in sharp contrast with the C_2=0.587(20) value extracted for ^{92}Zr. No such difference was detected for the octupole excitations, since values of 0.865(47) and 0.870(37) C_3 were determined for ^{90}Zr and ^{92}Zr, respectively. A strong ^{92}Zr GS configuration mixing is suggested.

1 Introduction

The Zirconium isotopic chain, where rather abrupt changes in nuclear properties are experimentally observed, in special along the region of N from 50 to 60, has attracted renewed interest in recent years. In particular, a group of authors of the University of Tokyo [1], after performing large-scale Monte Carlo shell model calculations, claims that a "Quantum Phase Transition" is observed in the systematics of the excitation energies of low-lying states in Zr isotopes. Shape coexistence has consistently been invoked as a cause of some of the experimentally observed aspects and the work of Heyde and Wood [2] may be taken as an example. However, from an experimental point of view, several unexpected results continue to intrigue researchers, resulting in an effort to find causes for differences in the outcomes of inelastic scattering by different probes, either in the data themselves or in their analyses.

Some years ago, a great investment was made in the attempt of reconciling results of a (^{6}Li,^{6}Li') work on Zr isotopes obtained by the Yale group [3] with other data, particularly with findings of a former (α, α') experiment on $^{90\text{-}96}$Zr, performed in Heidelberg by Rychel et al. [4]. With this purpose, a very careful reproduction of the Heidelberg alpha scattering experiment was undertaken by Lund et al. [5], at the Yale facility, with the same incident energy of 35.4 MeV. No disagreement with the German data or their analysis was found. In fact, a clear explanation of the observed results is still lacking.

In this scenario, it is the purpose of the present work to put forward some interesting aspects of experimental studies which examine differences between ^{90}Zr and its neighbours, as part of a study program aiming at collective properties in the Zr-Mo-Ru region, using light T=0 projectiles at the São Paulo Pelletron-Enge-Spectrograph facility. The unpublished data for ^{90,92}Zr (α, α') [6], are being analysed in more detail, in view of recent interpretations. Coulomb-nuclear interference (CNI) effects are much enhanced at the lower incident energy of 21 MeV chosen in this experiment, which favours the isospin characterization of the transitions to the first 2^+ and 3^- states.

2 Experimental Setup

The São Paulo Pelletron-Enge-Spectrograph system has been employed in several high resolution studies of isotopic chains in the A~100 region, due to its excellent energy resolution. Special care was taken in the present work to optimize resolution and accuracy of the Zr data. Two kinds of targets were produced in the Target Laboratory at the S. Paulo Pelletron facility in order to optimize experimental conditions. Being essential for good forward-angles measurements, rectangular spot targets were fabricated for both Zr isotopes (A=90,92) to guarantee an adequate object for the spectrograph while avoiding scattering on defining slits, which could be maintained wide open. Furthermore, as an important factor to obtain good quality spectra at intermediate scattering angles, self-supported thin targets of the same isotopes were also produced. These were employed to increase substantially the Zr to C and O rates, allowing those light contaminants, which are associated with wide unfocused peaks on the detection plane, to be better separated from the peaks of interest.

The emerging ions of the reaction, admitted and momentum analysed by the field of the spectrograph, were detected on the focal surface either by nuclear emulsion plates (Fuji G6B 50 micron thick, covering 25cm) or by a position sensitive 38cm gas detector [7]. The detector was basically a combination of a drift chamber and a proportional counter with a cylindrical delay line providing the position information. More than forty spectra were measured at carefully chosen scattering angles in a range of $14^{o} \leq \theta_{Lab} \leq 80^{o,}$ in order to characterize CNI in the angular distributions corresponding to the first quadrupole and octupole excitations in both nuclei. An overall energy resolution between 17 and 22 keV was achieved using a spectrograph entrance solid angle of 2.68 msr. Relative normalization of the data for the various scattering angles was obtained through simultaneous measurements of elastic scattering, while, for absolute normalization, optical model predictions to experimental elastic data, on the same target and under similar conditions, were considered. The absolute uncertainty of the experiment is estimated to be 20%.

3 Data analysis and Results

To extract relative transition probabilities between the ground state and the excited levels of interest, the distorted wave Born approximation (DWBA) prediction employing the deformed optical potential model (DOMP) approach was applied to the experimental angular distributions. The effective transition potential responsible for nuclear excitation is associated with non-sphericities of the optical potential, whether these are of dynamic or static origin. An adequate parametrization of the intensity of macroscopic effects is thus provided. In the present work, the same geometry and deformation lengths for the real and imaginary parts of the standard Woods-Saxon optical potential employed by Rychel et al. [4], for α particles of 35.4 MeV, were taken. Incident energy corrections of the corresponding well depths, following Put and Paans in their extensive work on an optical model for alpha particles [8], were applied. The total transition potential is the sum of Coulomb and nuclear transition potentials. The corresponding Coulomb transition potential for radii (r) equal or larger than R_C determines the reduced electric transition probability B(EL) [5]. In the present work, for r smaller than R_C the Coulomb transition potential is taken to be zero without harm, since the reaction occurs peripherically.

The values of the ratio, C_L, between the charge, δ_L^C, and mass, δ_L^N, deformation lengths for L=2(3) were obtained from the best fits to the shapes of the angular distributions associated, respectively, with the 2^+ and 3^- excitations in both nuclei. The square of the corresponding mass deformation lengths, $(\delta_L^N)^2$ was also extracted, as a scale factor. The procedure applied for the χ^2 minimization was the iterative method of Gauss, extracting the correlated parameters δ_L^N and C_L. The ratio $B(EL)/[B(ISL)e^2]$, considering the definition of B(ISL) scaled by Z, as proposed by Bernstein et al. [9], is expressed by the product of the squares of C_L and $(r_o^c/ r_o^m)^{L-1}$ and is also obtained. In the present work, the values of r_o^c =1.22 fm and r_o^m=1.16 fm for, respectively, the charge and the mass reduced nuclear radii sharp cut-off distributions were used.

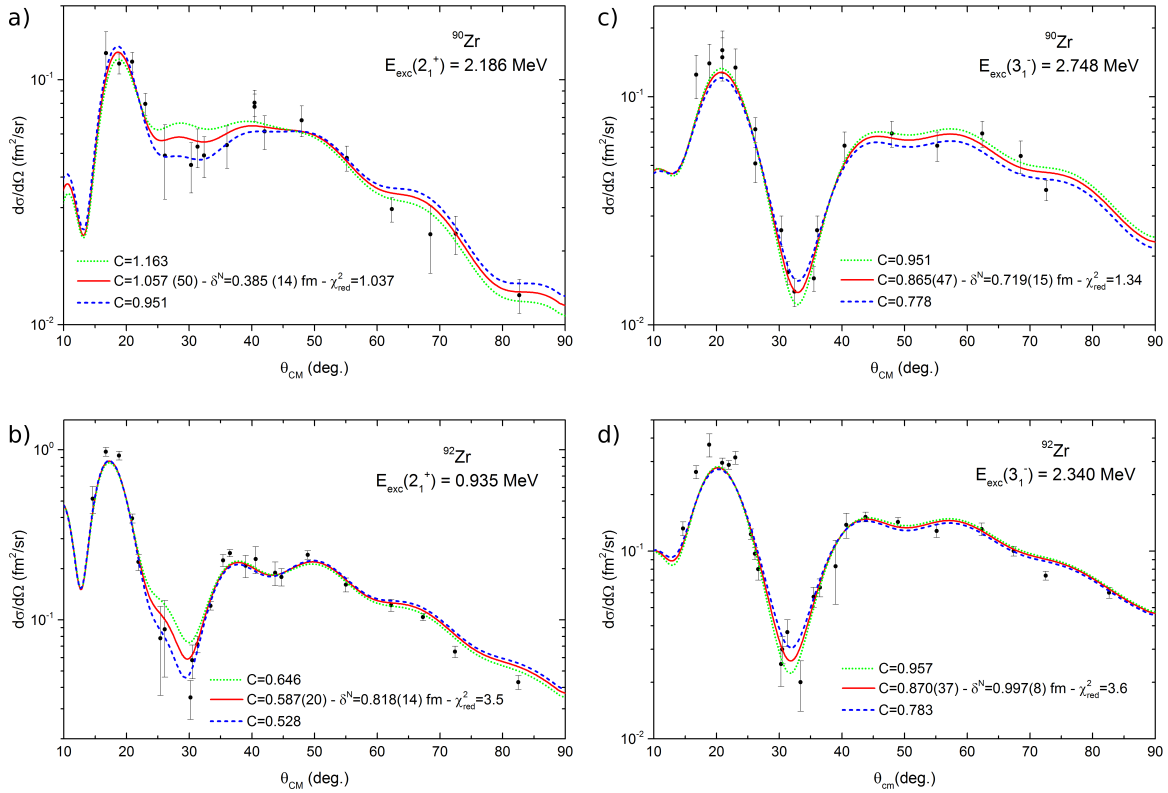

Fig. 1: Comparison of experimental angular distributions with DWBA-DOMP predictions for inelastic alpha scattering on ^{90,92}Zr, exciting the first quadrupole and octupole levels. Full lines represent the best fit and correspond to indicated values of the correlated parameters (C and delta), while respectively, dotted(interrupted) ones represent fits with values of the C parameter increased(decreased) by two (or, exceptionally, three) times the attributed uncertainties.

.

Figures 1(a)-(d) illustrate the results obtained from the best fit of the experimental angular distributions for ^{90,92}Zr (α, α') ^{90,92}Zr in the excitation of the first quadrupole (L=2) and octupole (L=3) excited states, when compared to DWBA-DOMP predictions, in each nucleus. The error bars represent the relative uncertainties composed by the statistical uncertainties and the contribution from the background and contaminant subtraction. The results obtained in this data analysis for the two correlated parameters of interest, the corresponding random uncertainties and reduced χ^2, are also indicated. It is to be noted, however, that the absolute scale uncertainty was incorporated in the final results. For ^{90}Zr, the best fits for, respectively, L=2 and L=3, are shown in Figs. 1(a) and (c), while the fits corresponding to ^{92}Zr are presented in Figs. 1(b) and (d). The values extracted for C and δ^N are given in each of the respective figures. In order to illustrate the sensibility of the method, the predicted angular distributions associated with values of C corresponding, respectively, to that of the best fit (continuous curve) and this value increased (dotted curve) and decreased (interrupted curve), by about two times the calculated random uncertainty, are also presented, in each figure.

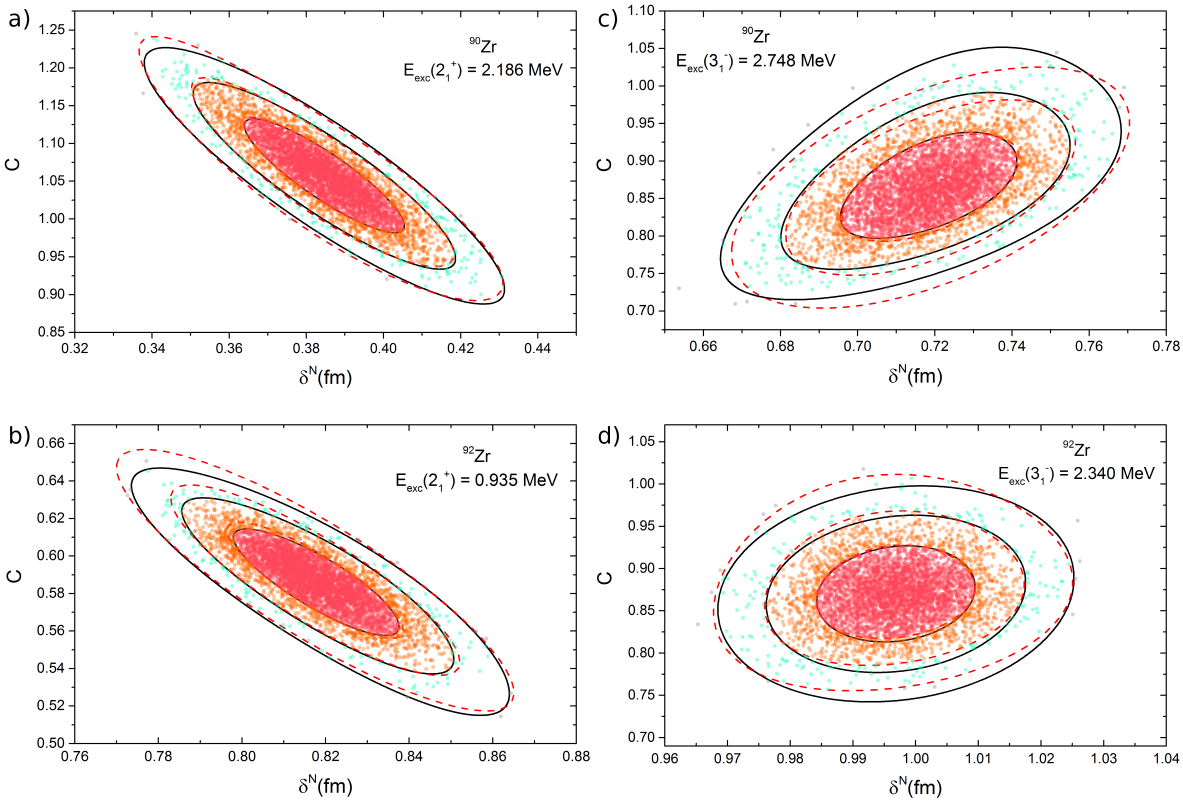

Fig. 2: Results from Monte Carlo simulations for the first quadrupole and octupole excitations in ^{90,92}Zr. Also shown are the contour lines CL (full lines) and Gauss ellipses GE (interrupted lines), respectively, associated with usual 68.3%, 95.5% and 99.7% confidence levels. The adequacy of the attributed uncertainties in the extracted parameters may, thus, be appreciated.

A Monte Carlo (MC) simulation of 5000 angular distributions, each one generated by randomly choosing values from a Gaussian distribution with the given standard deviation around each experimental point, was used to illustrate the adequacy of the attributed uncertainties. In fact, almost elliptical χ^2 contour lines (CL) associated with usual confidence levels (68.3%, 95.5% and 99.7%) were obtained. Figures 2(a) and (b) show the MC results for the ^{90,92}Zr 2^+_1 excitations, respectively, and the CL associated with the indicated confidence levels (full lines). For comparison, the Gauss approximation ellipses (GE) (interrupted lines), corresponding to the same confidence levels, are also presented. Figs. 2(c) and (d) show the results for the ^{90,92}Zr 3^-_1 excitations. For the first quadrupole excitations, in both nuclei, the resulting contour lines (CL) agree very well with the Gauss ellipses (GE).The corresponding results for octupole excitations reveal CL which also follow the GE, but with slightly higher deviations.

The final results obtained in this work are: C_L, δ_L^N and B(EL)/[B(ISL)e^2], associated with the first quadrupole (L=2) and octupole (L=3) excitations for ^{90}Zr and ^{92}Zr, as shown in Table1.

It is to be noted that the ratios B(EL)/[B(ISL)e^2] here determined were not previously reported and to be stressed that these ratios are not affected by the scale uncertainty.

Table 1: Results for first quadrupole and octupole excitations by inelastic alpha scattering on ^{90,92}Zr

A	C_2	δ_2^N (fm)	B(E2)/B(IS2) (e^2)	C_3	δ_3^N (fm)	B(E3)/B(IS3) (e^2)
90	1.057(50)	0.385(42)	1.24(12)	0.865(47)	0.719(72)	0.91(10)
92	0.587(20)	0.817(82)	0.381(27)	0.870(37)	0.997(99)	0.93(8)

Table 1 shows a strongly depressed C_2 value for the first quadrupole excitation in ^{92}Zr, in comparison with the almost homogeneous excitation in ^{90}Zr. Due to the cancellation of scale uncertainties in this ratio, the experimental values of B(E2)/[B(IS2)e^2], here presented for the first time, were obtained with a relative accuracy of 10% and 7%, for ^{90}Zr and ^{92}Zr, respectively.

In contrast, the present investigation points to very similar values for the first octupole collective excitations in both, ^{90,92}Zr, these being practically homogeneous, since only a very slight predominance of the neutrons relative to the protons has been detected. The experimental ratios B(E3)/[B(IS3)e^2] which also had not been previously reported, were extracted with a relative accuracy of 11% and 9%, for ^{90,92}Zr, respectively.

The very complete work of Lund et al. [5], presenting much more detailed data than did Rychel et al. [4] could not define the CNI region as well as the present experiment, since performed at the higher incident alpha particles energy of 35.4MeV. The $\delta_L{}^N$ values, here extracted agree with the values of the DOMP analysis reported in Ref. [5], for both states, 2^+ and 3^-, in ^{90,92} Zr.

It is to be noted that inelastic scattering, even if there is configuration mixing in the ground state, would excite only the configuration that connects the ground and the 2^+_1 states of each isotope. In this context, the C_2 value extracted for ^{92}Zr suggests a strong ground state configuration mixing involving not only the neutron degree of freedom, but also probably other configurations associated with subshell closures. These configurations, in the neighbourhood, are possibly an alpha or (2p+2n) plus a core of ^{88}Sr (Z=38, N=50) [10] and (2n) plus ^{90}Zr (Z=40, N=50).

The C_2 values extracted in this CNI study for the first quadrupole excitations in ^{90,92}Zr reveal a clear difference in the contribution of protons relative to the neutrons in those neighbouring isotopes. In ^{92}Zr the neutron role is strongly enhanced to an extent not formerly observed in other nuclei and represents an abrupt change in comparison with ^{90}Zr, for which the measured value indicates a homogeneous excitation.

Acknowledgements

T.B.L, M.R.D.R. and H.M. are members of INCT-FNA, Brazil

References

[1] T. Togashi, Y. Tsunoda, T. Otsuka and N. Shimizu, *Phys. Rev. Lett.***117**, 172502 (2016).
[2] K. Heyde and J. L. Wood, *Rev. Mod. Phys.* **83**(2011) 1467.
[3] D. J. Horen et al., *Phys. Rev. C***47**(1993) 629.
[4] D. Rychel et al., *Z. Phys. A***326**(1987) 455.
[5] B. J. Lund et al., *Phys. Rev. C***51**(1995) 635.
[6] L. B. Horodynski-Matsushigue, T. Borello-Lewin and J. L. M. Duarte, *Int. Nucl. Phys. Conf.,* São Paulo Brasil 1989, Proceedings **I**, 307.
[7] K. Koide et al., *Nucl. Instrum. and Meth.***215** (1983) 177.
[8] L. W. Put and A. M. J. Paans, *Nucl. Phys. A***291**(1977) 93.
[9] A. M. Bernstein, V. R. Brown and V. A. Matser, *Phys. Lett. B***71**(1977) 48, B**103** (1981) 255.
[10] M. A. Souza, H. Miyake, *Phys.Rev. C***91**, 034320 (2015).

Neutron capture cross sections and strength functions on ^{147}Sm

C. Oprea[1,2], A. Mihul[2,3], A. Oprea[1]
[1]Joint Institute for Nuclear Research, Frank Laboratory of Neutron Physics, 6 Joliot-Curie, 141980 Dubna, Russian Federation
[2]Romanian National Agency for Scientific Research, 21-25 Mendeleev, 010362 Bucharest, Romania
[3]CERN, CMS, CH-1211, 23 Geneva, Switzerland

Abstract
Cross sections and strength functions in neutron induced reactions on ^{147}Sm nucleus from slow neutrons up to 15 - 20 MeV's were evaluated. The neutron resonance parameters, transmission coefficients and the Hauser – Feshbach formalism were included in the calculations. In the MeV's region theoretical evaluations are performed by using Talys free software and author's computer programs. The obtained cross sections and strength functions are compared with experimental data in order to explain possible non-statistical effects reported previously by some authors on the alpha widths distributions.

1 Introduction

Cross sections, asymmetry effects and strength functions at the EG-5 and IREN basic facilities of FLNP - JINR by using a double gridded ionization chamber were regularly measured in the last decade. By recent measurements cross sections for 5 and 6 MeV of ^{147}Sm (n,α) reaction were obtained. Because the values of the cross sections are very low (hundreds of microbarns) their measurements are very difficult. The cross sections experimental data are very well described by the theoretical model evaluations performed in this study [1,2].

Capture processes of neutrons with emission of charged particles, starting from thermal region up to 14 MeV, on ^{147}Sm, were analyzed. Cross sections for (n,α) reactions, from slow neutrons up to some MeV's, in the frame of Hauser – Feshbach formalism (HFF), were evaluated using computer codes realized by authors [3]. The main element of HFF is represented by the transmission coefficients for incident and emergent channels. Transmission coefficients were calculated by applying a quantum-mechanical approach based on reflection factor [3,4].

Starting from 0.5 MeV up to 14 MeV, a separation in the contribution of different nuclear reaction mechanisms related to discrete and continuum states were realized with the help of Talys computer codes. It was demonstrated that the main contribution to the cross sections is given by compound nucleus processes followed by direct processes. Also, nuclear data as parameters of optical potential, nuclear states densities and other were extracted.

The computed cross sections and strength functions are compared with experimental data in order to explain possible nonstatistical effects reported previously by some authors on the distributions of alpha widths.

2 Theory and codes

Compound processes can be described in the frame of the statistical model of nuclear reactions. Main assumptions of statistical approach are: a) by interaction of incident particle with target nucleus a compound nucleus (CN) is formed; b) CN time of life is much larger than the time necessary to incident particle to pass the target nucleus; c) CN decays on one possible channels and "forget" how it was formed (Bohr hypothesis); d) CN and residual nucleus are characterized by a great number of

states; e) nuclear potential acts in a finite range and is zero outside. These assumptions lead to the following consequences: 1) no interference terms in the cross section; 2) differential cross section is symmetrical relative to 90^0 in the center mass system [5,6]. In this case, for a binary nuclear reaction, A(a,b)B, according to Hauser – Feshbach approach the cross section has the [7]:

$$\sigma_{ab} = g\pi \lambda\!\!\!^{-2}_{a} T_a T_b W_{ab} [\sum_c T_c]^{-1}, \quad (1)$$

where: g= statistical factor; $\lambda\!\!\!^{-}$= reduced wave length; T= transmission coefficient; W_{ab}= width fluctuation correction factor.

Transmission coefficients are defined as the probability of a particle to pass a potential barrier. This parameter can be calculated using the Gamow factor or applying a quantum mechanical approach based on the reflection factor [4].

Widths fluctuation correction factor, W_{ab}, represents the correlation between incident and emergent channels. When Bohr hypothesis is working, W_{ab}=1 and is slowly decreasing with the increasing energy of incident particle. There are a few ways to calculate $W_{ab,}$ but for evaluations, the authors have chosen the Moldauer expression [8].

For the evaluation of compound processes contribution to the cross section a computer code was created based on the Hauser – Feshbach formalism and quantum mechanical approach for transmission coefficients calculations. Previous results on (n,α) reactions are in [1,3].

The contributions of direct and pre-equilibrium processes to the cross sections, considering continuum and discrete states of residual nuclei, were evaluated with Talys, which is a dedicated software to nuclear reactions and structure of atomic nuclei calculations [9]. For strength function evaluation (S), the definitions from reference [2] are used. Then the strength function is:

$$S = \langle \Gamma \rangle / D = T/2\pi, \quad (2)$$

where: <Γ>= averaged width; D= average level spacing.

Expression (2) demonstrated the relation between strength function and transmission coefficients. Furthermore, strength functions describe how widths are distributed in the nucleus.

Spectra of emitted alpha particles in ^{147}Sm(n,α)^{144}Nd reaction from a target with a given thickness have been realized by Monte Carlo modeling. Angular correlation is simulated by using the direct method. Solving the following integral equation the current polar angle θ_c is extracted:

$$\frac{\int_0^{\theta c<\pi} [p_0 + p_1 \cos\theta + p_2 (\cos\theta)^2] \sin\theta d\theta}{\int_0^{\pi} [p_0 + p_1 \cos\theta + p_2 (\cos\theta)^2] \sin\theta d\theta} = r \in [0,1), \quad (3)$$

where: p_1, p_2, p_3= coefficients; θ= polar angle; θ_c= current polar angle; r= random number.

Stopping power of alpha particles in the Samarium target was determined using SRIM & TRIM free software [10].

3 Results and discussion

Nuclear reaction ^{147}Sm(n,α)^{144}Nd (Q=10.128 MeV) induced by incident neutrons with energy starting from 0.5 keV up to 20 MeV had been analyzed. Using the soft created by authors the (n,α) cross sections, from 0.5 keV up to 0.5 MeV were calculated. Results are shown in the Fig. 1 and are compared with experimental data [11]. In the calculations, a nuclear potential, U = V + iW, with real and imaginary parts, is considered. Spin and parity of target and compound nucleus are: for ^{147}Sm - $(7/2)^+$ and for ^{148}Sm - 3^-, 4^-, respectively. Ten discrete levels of residual nucleus were taken into account. In the mentioned incident neutrons energy interval the compound nucleus mechanism was considered.

Real and imaginary parts of nuclear potential in the incident and emergent channels have the following values: V_n= 65 MeV, W_n= 0.15 MeV, V_α= 225 MeV, W_α= 0.15 MeV. The results are not very sensible to the imaginary part for neutrons and alphas. The real part of potential, V_α, is increasing with about 15% from 0.5 up to 500 keV neutron energies.

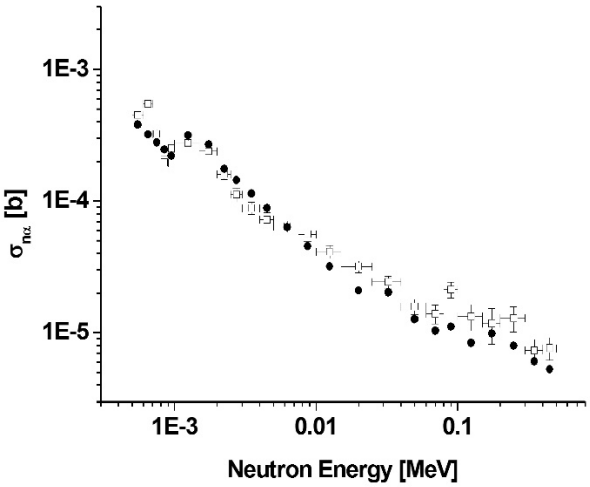

Fig. 1. ^{147}Sm(n,α)^{144}Nd cross section. □- Experiment. ●- Theory

For energies higher than 0.5 keV the cross sections were calculated with Talys because for fast neutrons the contributions of direct and pre-equilibrium processes become significant. In Fig. 2a a separation between nuclear reaction mechanisms correlated with discrete and continuum states of the residual nuclei was realized. They are compared with experimental data from Fig. 2b and a good agreement can be observed between them. In Table 1 the results for experimental data at 5, 6 MeV are shown [12].

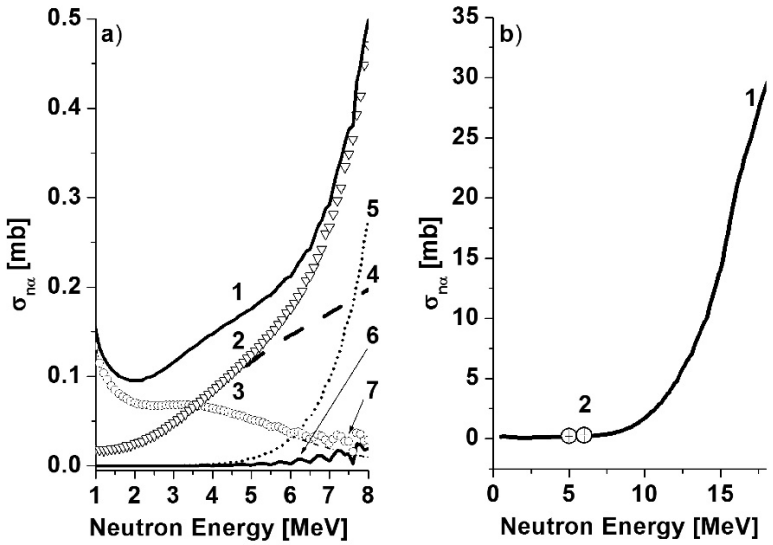

Fig. 2. ^{147}Sm(n,α)^{144}Nd cross section. Talys calculations: a) Separation between mechanisms related to discrete and continuum states. 1- All contributions from 2 to 7; 2- Continuum states & Direct + Compound processes; 3- Discrete states & Direct +Compound; 4- Continuum & Compound; 5- Continuum & Direct; 6- Discrete & Compound; 7- Discrete & Direct. b) 1- Talys evaluation; 2- Experimental data

Table 1. Contribution of reaction mechanisms and states of residual nucleus

E_n [MeV]	Direct [mb]		Compound [mb]		$\sigma_{n\alpha}$ [mb]	$(\sigma_{n\alpha})_{exp}$ [mb]
	Discrete	Continuum	Discrete	Continuum		
5±0.16	0.00097	0.00787	0.05023	0.11627	0.1754	0.23±0.023
6±0.12	0.00248	0.02951	0.03379	0.14606	0.2118	0.28±0.028
15	0.04970	1.57825	0.00156	0.26330	1.89201	-

From Table 1 and Fig. 2b it is shown that up to 8 - 10 MeV the compound processes are dominant, but higher than 10 MeV the direct mechanism becomes important. With the increasing of incident energy, the contribution to the cross section of the continuum states is also increasing in comparison with discrete ones. For 15 MeV there are no experimental data and it can be observed that direct processes and continuum states give the main contribution to the cross section.

The experimental data for $^{147}Sm(n,\alpha)^{144}Nd$ fast neutron process are poor because: a) cross section values are very small; b) low intensity of incident deuterons beam with energy of about 2 - 4 MeV, necessary to produce fast neutrons in $^{2}H(d,n)^{3}He$ reaction; c) high background due to the presence of open channels involving alphas in $^{147}Sm(n,\alpha)^{144}Nd$ reaction [12].

Differential cross sections in the fast neutron energy range were evaluated by Talys. In the Figs. 3a - c the contributions of direct and compound mechanisms for 5, 6, and 15 MeV are shown. In [12] a forward – backward asymmetry effect was measured. This effect was defined as the ratio between the number of forward and backward events. In the case of a point target the ratio is:

$$A_{FB} = N_F/N_B = \int_0^{\pi/2} \sigma(\theta) \sin\theta \, d\theta \Big/ \int_{\pi/2}^{\pi} \sigma(\theta) \sin\theta \, d\theta, \quad (4)$$

where: $N_{F,B}$ = events in forward and backward directions; $\sigma(\theta)$= differential cross section.

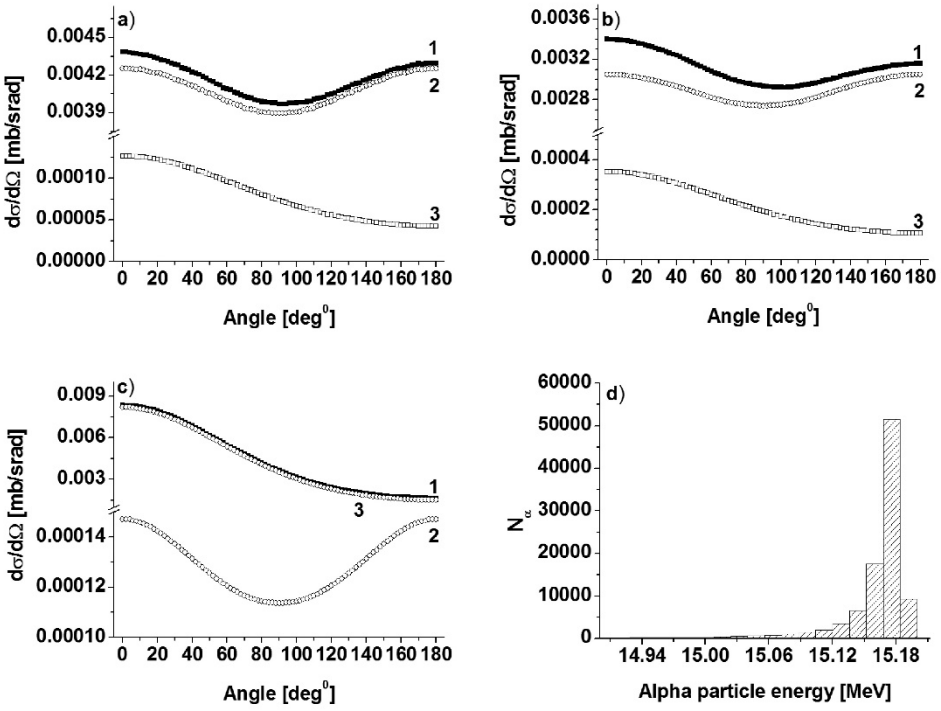

Fig. 3. Differential cross section a) 5 MeV; b) 6 MeV; c) 15 MeV d) alpha spectra for E_n = 5 MeV, 100000 events, 5 mg/cm^2 target thickness. Curves: 1 - sum of compound and direct processes; 2 - compound processes; 3 - direct processes

Using the obtained results on cross sections and angular distribution, considering a 5 mg/cm^2 thickness target and alpha particles stopping power, the forward – backward effect was calculated by two methods. In the first way, Talys results and relation (4) was applied. The alpha particles lose in the

target was neglected. In the second way, a direct Monte Carlo simulation was realized, based on relation (3) and a finite dimensions target. Both theoretical results and experimental measurements on forward – backward effect are presented in Table 2 for 5, 6 and 15 MeV, respectively.

From Figs. 3a - c at 5 and 6 MeV, compound processes are dominant in comparison with the 15 MeV case. It is expected that the asymmetry generated by the direct component is small for 5 and 6 MeV and significant at 15 MeV.

Table 2. Forward – backward effect: 1) Talys; 2) Simulation; 3) Experimental

E_n[MeV]	$(A_{FB})_{Talys}$	$(A_{FB})_{MC}$	$(A_{FB})_{exp}$
5	1.0122 ± 0.0096	1.02 ± 0.007	1.65 ± 0.165
6	1.0436 ± 0.0127	1.04 ± 0.009	2.54 ± 0.254
15	2.342 ± 0.008	2.31 ± 0.017	-

Experimental data on asymmetry from Table 3 are much higher than the theoretical evaluations. At 15 MeV there are not experimental data on forward – backward effect. The authors from [12] tried to explain such an unexpected high asymmetry effect by the presence of the so-called non-statistical effects. Taking into account the present theoretical evaluations, the experimental results from Table 2 can be explained by the presence of other emergent channels involving alpha particles. Very low value of (n,α) cross section in fast neutrons energy range makes difficult the separation of "α+^{144}Nd" channel in the measurements.

Theoretical results evaluated with Talys were obtained in the frame of the constant temperature Fermi gas model for nuclear states density and optical potentials with real and imaginary parts (volume-central (V), surface-central (D), spin-orbit (SO)) for incident (n) and emergent (α) channels [9]. In Table 3 the nuclear potential parameters are shown.

Table 3. Parameters of optical potential. Parameters of surface-central potential are not shown

	Volume central			**Volume central**			**Spin orbit**			**Spin orbit**		
	Real			**Imaginary**			**Real**			**Imaginary**		
	V [MeV]	**r_v [fm]**	**a_v [fm^{-1}]**	**W [MeV]**	**r_W [fm]**	**a_w [fm^{-1}]**	**V_{so} [MeV]**	**r_{vso} [fm]**	**a_{vso} [fm^{-1}]**	**W_{so} [MeV]**	**r_{wso} [fm]**	**a_{wso} [fm^{-1}]**
n	49.81	1.227	0.656	0.11	1.227	0.656	6.18	1.063	0.59	-0.01	1.063	0.59
α	226.25	1.227	0.657	0.38	1.227	0.657	0	1.071	0.59	0	1.071	0.59

In reference [2] strength functions ratio (S_3/S_4) in ^{147}Sm(n,α)^{144}Nd reaction for incident neutrons from 3 eV up to 700 eV were measured. In the process the compound nucleus ^{148}Sm is formed characterized by spin and parity $J^{\Pi}=3^-,4^-$, respectively. Experimental results from [2] and calculations realized by our program are presented in Fig. 4.

It is expected that strength functions have to be constant with energy [2]. At 300 eV an evident decreasing is observed (Fig. 4). The authors of [2] tried to explain the results of measurements like in [12], by the presence of non-statistical effects.

Using the relation (3), quantum mechanical approach for the calculation of transmission coefficients, optical potential U = V+iW, and radius channel $R = R_0A^{1/3}$ [fm] (R_0 = 1.45 fm, A = atomic mass number), we have described the experimental data, by increasing the alpha radius channel with about 20% higher 300 eV. The optical potential for alpha channel was U = (225+I 0.45) MeV. Other explanations for the above results could be the following: a) large errors in alpha strength functions ratio; b) the presence of alpha particles from other channels; c) compound nucleus ^{148}Sm is an even-even nucleus and therefore it is of interest to search emission of complex particles larger than alpha.

4 Conclusions

Cross sections, forward-backward effects, alpha spectra and strength functions were obtained using own codes and Talys software in $^{147}Sm(n,\alpha)^{144}Nd$ reaction. Cross section experimental and theoretical data are in good agreement. The concurrence of reaction mechanisms related to residual nucleus states is reflected. For the forward - backward and strength functions ratios experimental data, new explanations were proposed. Further data (cross sections, angular distributions), in a wide energy range are necessary. Improvements of computer simulations, strength functions evaluations correlated with nuclear reaction mechanism analysis are planned. Present results on $^{147}Sm(n,\alpha)$ process were realized in the frame of FLNP JINR Dubna thematic plan and are proposals for future measurements at FLNP basic facilities.

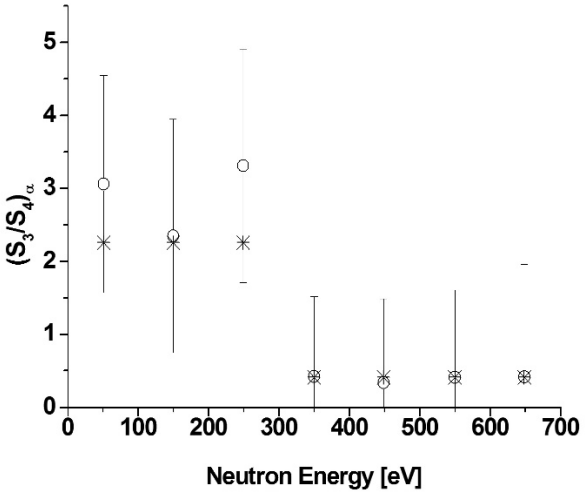

Fig. 4. Alpha strength functions ratio: Circle – measurements; Star – theoretical evaluations

References

[1] Y.M. Gledenov, M.V. Sedysheva, P.V. Sedyshev, *et all*, *Nucl. Sci. Techn.*, **Suppl. 2**, (2002) 342.

[2] P.E. Koehler, Yu.M. Gledenov, T. Rauscher, E. Frohlich, *Phys Rev* **C 69** (2004) 015803.

[3] A.I. Oprea, C. Oprea, C. Pirvutoiu, D. Vladoiu, *Rom. Rep. Phys.* 63 **1** (2011) 107.

[4] A. Foderaro, The Elements of Neutron Interaction Theory, The MIT Press (1971).

[5] J.B. Marion, J.L. Fowlers, Fast Neutron Physics, **1**, New York, Interscience Publishers Inc (1960).

[6] T. G. Krieger, *Annals of Physics* **31** (1965) 88.

[7] W. Hauser, H. Feshbach, *Phys. Rev*. 87 **2**, (1952) 366.

[8] P.A. Moldauer, *Nucl. Phys.* **A 344** (1980) 185.

[9] A.J. Koning, S. Hilaire and M.C. Duijvestijn, TALYS-1.0. Proceedings of the International Conference on Nuclear Data for Science and Technology, April 22-27, 2007, Nice, France, editors O.BERSILLON, F.GUNSING, E.BAUGE, R.JACQMIN, S.LERAY, EDP Sciences, p. 211 (2008).

[10] J.F. Ziegler, SRIM & TRIM Software – http://www.srim.org.

[11] Y.M. Gledenov, P.E. Koehler, J. Andrzejewsky et all, *Phys. Rev*. **C 62** (2000) 042801(R).

[12] Yu. M. Gledenov, M. V. Sedysheva, V. A. Stolupin et all, *Phys. Rev.* **C 80** (2009) 044602.

Comparative analysis of empirical parametrization and microscopical studies of deuteron-induced reactions

M. Avrigeanu and V. Avrigeanu
Horia Hulubei National Institute for Physics and Nuclear Engineering, P.O. Box MG-6, 077125 Bucharest-Magurele, Romania

Abstract
An extended analysis of the deuteron–induced reactions is carried out paying due consideration to both the reaction cross-section parametrization procedure and theoretical models associated to the deuteron interaction process. The key role of direct interactions, i.e., breakup, stripping and pick-up processes is stressed out by the comparison of data with theoretical and evaluation predictions.

1 Introduction

So far the Hauser-Feshbach statistical model has mainly been involved as the main tool to calculate the deuteron reaction cross sections at low and medium incident energies, the compound-nucleus (CN) mechanism being considered to be dominant within this energy range. However, the specific non-compound processes direct interactions (DI), namely breakup, stripping and pick-up, make substantially different the deuteron-induced reactions than the case of other incident particles. Therefore, neglected peculiarity of the deuteron interaction process is evidenced by the apparent discrepancies between the data and either theoretical or evaluated predictions. The specific reaction mechanism among the deuteron DI is the breakup (BU), particularly important due to the large variety of reactions initiated by the breakup nucleons along the whole incident-energy range [1]. Moreover, the role of the deuteron BU increases with the target-nucleus mass and charge, so that it becomes dominant for heavy target nuclei at deuteron incident energies particularly around the Coulomb barrier [2]. Otherwise, the deuteron interaction with low- and medium-mass target nuclei below and around the Coulomb barrier proceeds largely through stripping and pick-up direct reactions (DR) mechanisms, while pre-equilibrium emission (PE) and evaporation from fully equilibrated CN become important at higher energies [1, 3–5].

However, while the associated models for DR, PE, and CN mechanisms are already settled, an increased attention should be paid to the theoretical description of the BU-mechanism two components, namely the elastic breakup (EB), with no interaction target nucleus–breakup nucleons, and inelastic BU or breakup fusion (BF), where one of these constituents interacts non-elastically with the target nucleus. This is why a comparative assessment of measured data and results of BU microscopic description [6, 7] as well as current parametrization [9] already involved within recent systematic studies [1–5] are equally useful to basic studies and improved nuclear data evaluations.

Obviously an update of the theoretical analysis of deuteron-nuclei interaction within a consistent account of the related reaction mechanisms is highly requested not only by the strategic research programs as the International Thermonuclear Experimental Reactor (ITER) [10], the International Fusion Material Irradiation Facility (IFMIF) [11], in connection with the ITER program, and the Neutron For Science (NFS) project at SPIRAL-2 facility [12], but also by use of deuteron surrogate reactions for (n, γ) and (n, f) cross sections [2], of interest for breeder reactors studies, as well as by medical investigations using accelerated deuterons [13].

2 reaction cross-section parametrization vs model analysis

The reaction cross-section parametrization within the analysis of the most important deuteron induced reactions, the deuteron monitor reactions, has been recommended by Hermanne *et al.* [13] in a recent

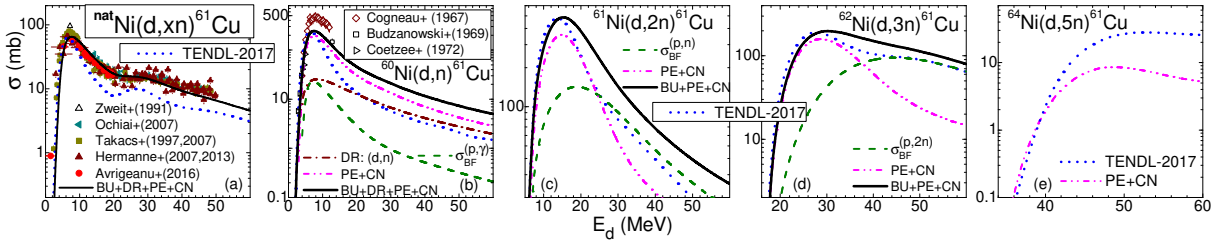

Fig. 1: (Color online) Comparison of measurements [14], TENDL-2017 [15] evaluation (dotted curves), and model calculation (solid curves) of ^{nat}Ni$(d,xn)^{61}$Cu, ^{60}Ni$(d,n)^{61}$Cu, ^{61}Ni$(d,2n)^{61}$Cu, ^{62}Ni$(d,3n)^{61}$Cu, and ^{64}Ni$(d,5n)^{61}$Cu reaction cross sections, along with BF enhancement (dashed curves), stripping (d,n) reaction (dash-dotted curve), and PE+CN components (dash-dot-dotted curves) corrected for DI deuteron flux leakage [4].

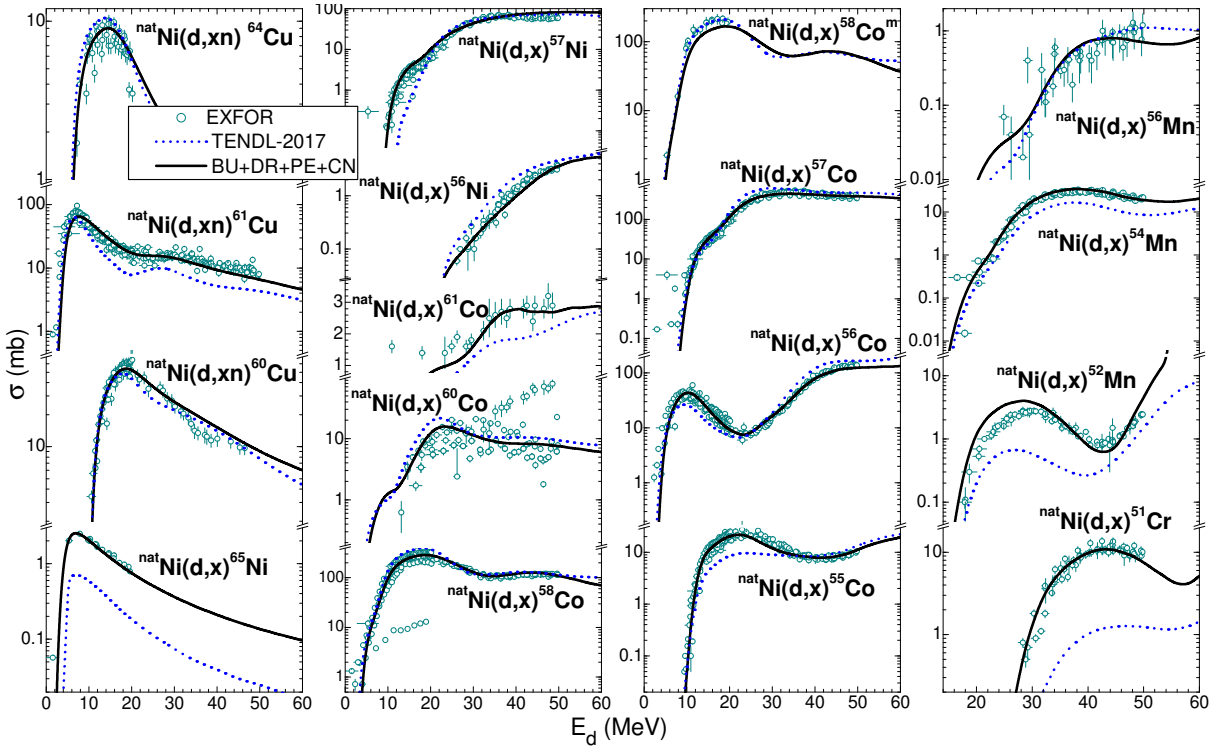

Fig. 2: Comparison of measurements (solid circles) [14], TENDL-2017 [15] evaluation (short-dotted curves), and model calculations (solid curves) of excitation functions for deuteron-induced reactions on ^{nat}Ni [4].

paper published in a Special Issue on Nuclear Reaction Data. Thus, for the comparative analysis of both experimental data and theoretical predictions and the final evaluation, the authors replaced the theory by Padé fit, with so low predictive power and apart from nuclear modeling advance.

A consistent and unitary nuclear reaction mechanisms analysis, considering all contributing Ni isotopes, is interposed to their Padé fit of the experimental ^{nat}Ni$(d,xn)^{61}$Cu excitation function (Fig. 20 (b) of Ref. [13]). The corresponding results are shown in Fig. 1 [4] including also the TENDL-2017 evaluation predictions [15]. The most complete picture of the involved mechanisms for the population of ^{61}Cu residual nucleus is shown in Fig. 1(b). The consequent model calculations including the contributions from the breakup process through the (p,γ) reaction initiated by breakup protons, the (d,n) stripping reaction, as well as statistical pre-equilibrium and compound nucleus mechanisms, describe the experimental ^{60}Ni$(d,n)^{61}$Cu excitation function [14], except the oldest Cogneau *et al.* data [14], totally discrepant with those reported for natural Ni target too. Important contribution to the population

of ^{61}Cu residual nucleus comes also from ^{61}Ni$(d,2n)$ and ^{62}Ni$(d,3n)$ processes, Fig. 1(c,d), where the competition between the deuteron-induced PE+CN and the inelastic breakup through ^{61}Ni(p,n) and respectively ^{62}Ni$(p,2n)$ processes changes toward breakup mechanism for the incident energies of $\sim$ 25 MeV and 35 MeV, respectively. Thus, the breakup contributions make slower the decrease of the (d,xn) excitation function, comparing with their steep increase above the threshold. The disregard of the breakup and the stripping mechanisms contributions leads to the underestimation of both ^{nat}Ni$(d,x)^{61}$Cu [14] and ^{60}Ni$(d,n)^{61}$Cu [14] experimental excitation functions, e.g., TENDL–2017 evaluations (dotted curves), [15] shown in Fig. 1(a,b).

Actually almost all deuteron-induced monitor reactions described with Padé fit by Hermanne *et al.* [13] have already been analyzed in the frame of breakup, stripping, pick-up, pre-equilibrium emission and compound nucleus reaction mechanisms models [3–5]. These analyzes covered the whole experimental systematics of the deuteron induced reactions on the natural element of interest, e.g., updated Fig. 2 from Ref. [4] by considering the TENDL-2017 evaluation predictions [15]. There are included among them the specific monitor reactions ^{nat}Ni$(d,x)^{56}$Co, ^{nat}Ni$(d,x)^{58}$Co, and ^{nat}Ni$(d,xn)^{61}$Cu. Moreover, as long as there exist both available dedicated codes for nuclear reactions calculations and the powerful computers, the complexity of deuteron interactions can not motivate the use of Padé approximations [13] for the analysis of measured deuteron–reaction cross sections.

3 Breakup

Our analyzes of the deuteron breakup mechanism are based on the parametrization [8, 9] of both the total breakup (EB+BF) and EB data, assuming that the inelastic-breakup cross section for neutron emission σ^{n}_{BF} is the same as that for the proton emission σ^{p}_{BF} (e.g., Ref. [16]), so that the total breakup cross sections σ_{BU} is given by the sum σ_{EB}+2$\sigma^{n/p}_{BF}$. The parametrization has concerned the total BU nucleon-emission and EB fractions, i.e. $f^{n/p}_{BU} = \sigma^{n/p}_{BU}/\sigma_R$ and f_{EB}=σ_{EB}/σ_R, respectively, where σ_R is the deuteron total-reaction cross section. The dependence of these fractions on the deuteron incident energy E and the target-nucleus atomic Z and mass A numbers was obtained [9] through analysis of the experimental systematics of deuteron-induced reactions on target nuclei from ^{27}Al to ^{232}Th and incident energies up to 80 MeV for the former [17], but within a more restricted energy range up to 30 MeV [16, 17] for the latter. Because of that, the correctness of the extrapolation of elastic breakup parametrization has been checked [18] by comparison with results of the microscopic continuum-discretized coupled-channels (CDCC) method [19]. Thus, a normalization factor has been introduced for the extrapolation of f_{EB} at energies beyond the available data, in agreement with the behavior of f^{p}_{BU} and the CDCC calculation results [9]. Nevertheless, the empirical parametrization should be confirmed by further data measurements and also advanced theoretical modeling.

The comparison of the measured total BU proton-emission cross sections σ^{p}_{BU} at 15, 25.5, 56, 70 and 80 MeV deuteron energies and for target nuclei from ^{12}C to ^{232}Th [17], with the above-described parametrization and the microscopic cross sections obtained in the frame of the CDCC extension of the eikonal reaction theory (ERT), using microscopic optical potentials by Neoh *et al.* [6] and those of Carlson *et al.* [7] obtained in the frame of distorted wave Born approximation (DWBA) method with post form interaction and zero–range approach is shown in Fig. 3 (a-d). Since the absolute cross sections may depend on the model ingredients of reaction mechanisms involved within the experimental data analysis, e.g., optical-potential and PE model parameters, a similar comparative analysis concerns at the same time in Fig. 3 (e-h) the corresponding total BU proton-emission fractions f^{p}_{BU}. On the other hand, the f^{p}_{BU} values may illustrate the importance of the breakup process among the other reaction mechanisms related to the deuteron interactions. Moreover, the same scale has been used for σ^{p}_{BU} as well as f^{p}_{BU} values at all incident energies of the available experimental data, in order to make also possible an assessment of their energy dependence.

There are several features which are pointed out by this comparative analysis. First, the increase

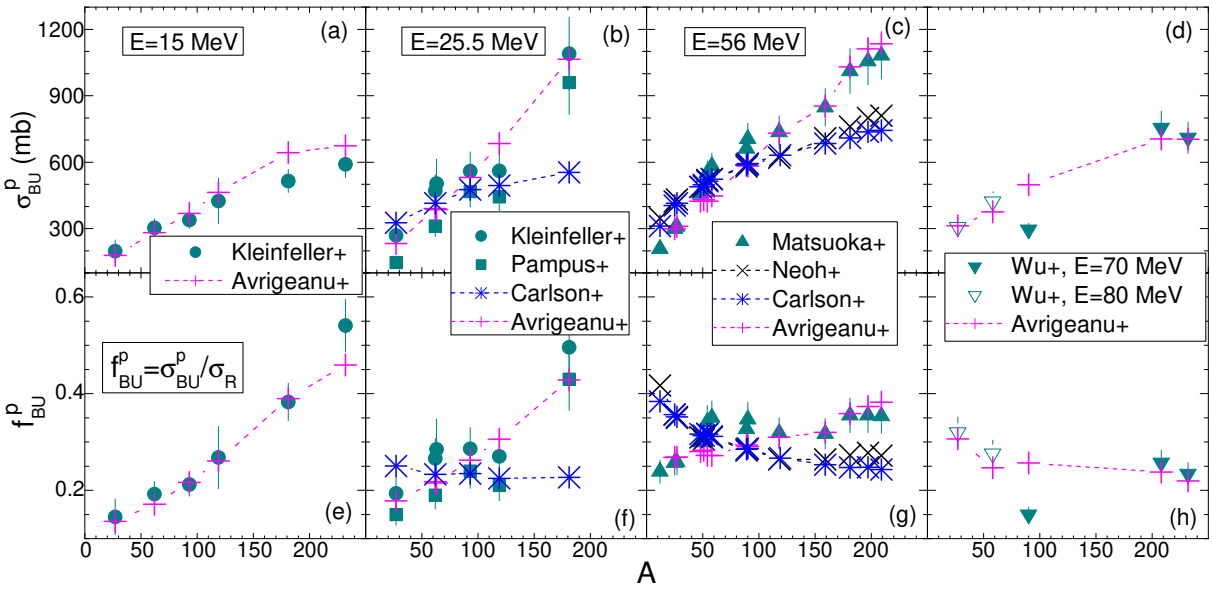

Fig. 3: (Color online) Comparison of the mass dependence of measured (solid circle, ■, ▲, ▼, ▽) [17] total BU proton-emission cross sections (top) and fractions (bottom) with the predictions of the microscopic eikonal model [6] (×), DWBA formalism [7] (∗), and of the empirical parametrization (+), connected by dashed lines for eye guiding, for target nuclei from ^{12}C up to ^{209}Bi, at the incident energies of 15, 25.5, 56, 70, and 80 MeV.

of σ^p_{BU} with the target-nucleus mass is well described by the empirical parametrization for all deuteron energies from 15 to 80 MeV. There is a similar trend of the microscopic results for medium-mass nuclei with $40<A<120$, while it is apparent an overestimation of the measured data for light nuclei ($A<40$) at both 25 and 56 MeV incident energies, as well as an underestimation for heavier ones ($A>120$). Second, the importance of the BU mechanism, shown by f^p_{BU}, is increasing with the target-nucleus mass, from ^{27}Al up to ^{232}Th, at the lower incident energies of 15 and 25.5 MeV. This increase is less significant at the energy of 56 MeV, and even reversed at 70-80 MeV. Actually it seems that the fraction f^p_{BU} has reached its maximum at 56 MeV, for the target nuclei with $A>120$, while for $40<A<120$ this maximum moves at energies over 56 MeV but lower than 70-80 MeV. Moreover, the f^p_{BU} values are still increasing with the incident energy even at 80 MeV for the deuteron interaction with light target nuclei ($A<40$). These energy dependencies of the measured f^p_{BU} are satisfactorily described by the empirical parametrization. The microscopic results at 25 MeV [7] show almost constant f^p_{BU} for the whole A interval analyzed, while at 56 MeV [6, 7] show a steep decrease for target nuclei from A=12 up to $A\sim120$, apart from the data, while for $A>120$ their underestimated values describe however the target-nucleus mass dependence.

Overall, there are actually two opposite effects of the deuteron breakup on the deuteron activation cross sections that should be considered. Firstly, the total-reaction cross section, that is shared among different outgoing channels, is reduced by the value of the total breakup cross section σ_{BU}. On the other hand, the BF component brings contributions to different reaction channels [1–5]. Thus, the absorbed proton or neutron following the deuteron breakup contributes to the enhancement of the corresponding (d, xn) or (d, xp) reaction cross sections, respectively. The compound nuclei in reactions induced by the BF nucleons differ by one unit of the atomic mass and maybe of also the atomic number than in deuteron-induced reactions, the partition of the BF cross section among various residual-nuclei population being triggered by the energy spectra of the breakup nucleons and the excitation functions of the reactions induced by these nucleons on the target nuclei [1–5]. In order to calculate the BF enhancement of, e.g., the (d, xn) reaction cross sections, the BF proton-emission cross section σ^p_{BF} should be (i) multiplied by the ratios $\sigma_{(p,x)}/\sigma^p_R$, corresponding to the enhancing reaction, (ii) convoluted with the Gaussian line shape

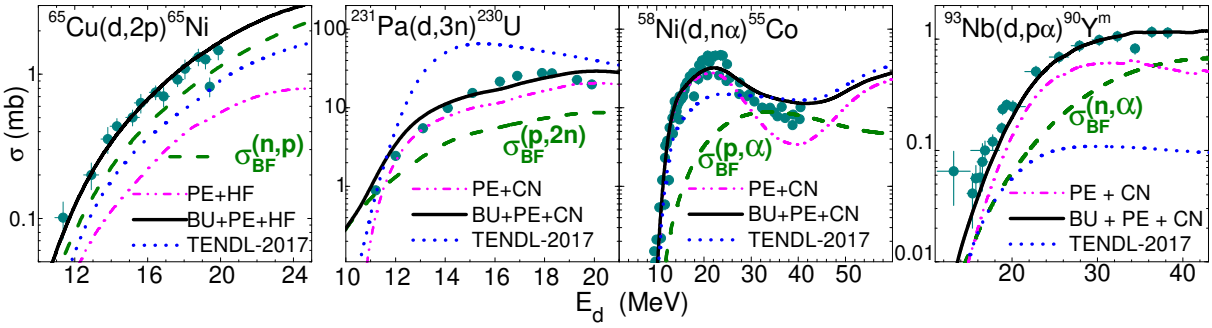

Fig. 4: (Color online) Comparison of measured deuteron activation cross sections [14], complete analysis results (thick solid curves) [2–4] taking into account the BF enhancement (dashed curves) and PE+CN contributions (dash-dot-dotted curves), and the TENDL-2017 evaluations (dotted curves) [15].

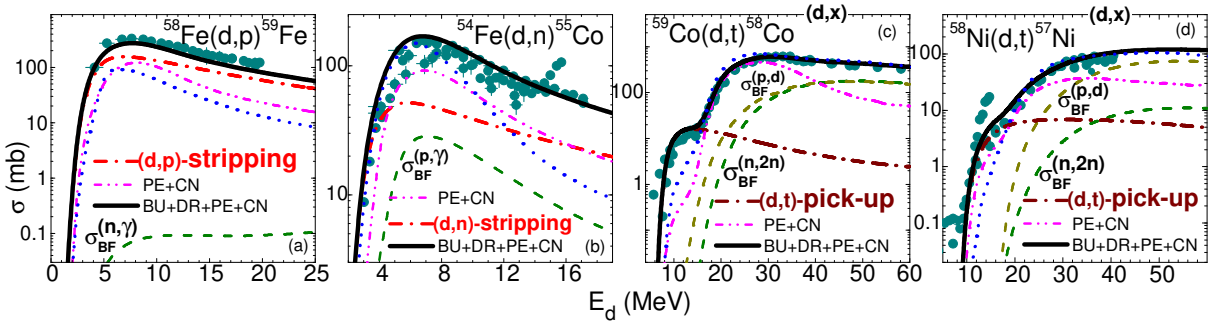

Fig. 5: (Color online) Comparison of measured deuteron activation cross sections [14], the TENDL-2017 evaluations (dotted curves) [15], and the analysis results (thick solid curves) [3,4] taking into account the BF enhancement (dashed curves), DR (dot-dashed curves), and PE+CN contributions (dash-dot-dotted curves).

distribution of the BF–proton energy E_p for a given deuteron incident energy E_d, and (iii) integrated over the BF proton energy. Consequently, the BF–enhancement cross section has the form [4]:

$$\sigma^{p,x}_{BF}(E_d) = \sigma^{p}_{BF}(E_d) \int_0^{E_d - B_d} dE_p \; \frac{\sigma_{(p,x)}(E_p)}{\sigma^{p}_{R}(E_p)} \frac{1}{(2\pi)^{\frac{1}{2}} w} exp[-\frac{(E_p - E^0_p)^2}{2w^2}] \; , \qquad (1)$$

where B_d is the deuteron binding energy, σ^p_R is the proton total reaction cross section, x stands for various γ, n, d, or α outgoing channels, while the Gaussian distribution parameters w and E^0_p are given by Kalbach [20].

The BF enhancements brought by the breakup neutron and proton interactions with various target nuclei from ^{54}Fe up to ^{231}Pa shown by dashed curves in Figs. 4 and 5 are important mainly for describing the excitation functions for second and third chance emitted-particle channels [2–4].

4 Direct reactions

The assessment of transfer reaction cross sections in addition to that of BU mechanism is mandatory for the final correct estimation of even the PE+CN contribution to population of various residual nuclei, in spite of poor attention given so far in deuteron activation analysis. However, a suitable estimation of DR cross sections is subject of available experimental spectroscopic factors, outgoing particle angular distributions, or at least the differential cross-section maximum values. The calculation of DR cross sections has been performed using the DWBA formalism within the FRESCO code [21]. The post/prior form distorted-wave transition amplitudes for the stripping and pick-up reactions, respectively, and the finite-range interaction have been considered. The n-p effective interaction in deuteron [22] as well as

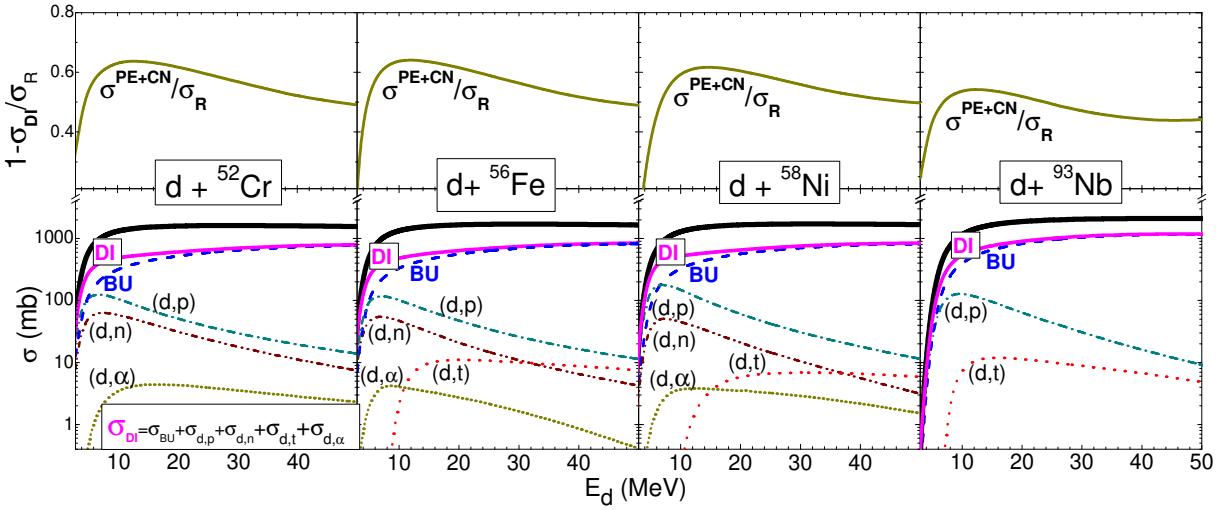

Fig. 6: (Color online) (Bottom) Total-reaction (solid curves), BU (dashed curves), stripping (d, n) (dash-dot-dotted curves) and (d, p) (dash-dotted curves), and pick-up (d, t) (dotted curves) and (d, α) (short-dotted curves) reaction cross sections for deuterons on ^{52}Cr, ^{56}Fe, ^{58}Ni, and ^{93}Nb [3–5]; (Top) the corresponding reduction factors of the deuteron flux going towards statistical processes (solid curves).

d-n effective interaction in triton [23] were assumed to have a Gaussian shape, at the same time with a Woods-Saxon shape [24] of the d-d effective interaction within the α particle. The transferred nucleon and deuteron bound states were generated in a Woods-Saxon real potential [3–5, 8]. The populated discrete levels and the corresponding spectroscopic factors which have been available within the ENSDF library [25] were used as the starting input for the DWBA calculations.

The significant effects of the stripping (d, p), (d, n), and pick-up (d, t) reactions for the deuteron interaction with ^{58}Fe, ^{54}Fe, and respectively with ^{59}Co and ^{58}Ni target nuclei have been reassessed in Fig. 5. It is thus proved that the direct reactions are quite important for the first-chance particle emission, the (d, p) stripping mechanism being the dominant mechanism for the (d,p) reactions [3–5], as can be seen from Fig. 5 (a). A particular note should also concern the pick–up essential contribution to the total (d, t) activation cross section at the energies between its threshold and those for the (d, nd) and $(d, 2np)$ reactions that lead to the same residual nucleus, see Fig. 5 (c,d).

Finally, we have taken into account the deuteron total-reaction cross section that remains available for the PE+CN mechanisms, following the correction for the incident flux leakage through direct interactions of the breakup, stripping and pick-up processes, given by a reduction factor:

$$1 - \frac{\sigma_{BU} + \sigma_{(d,n)} + \sigma_{(d,p)} + \sigma_{(d,t)} + \sigma_{(d,\alpha)}}{\sigma_R} = 1 - \frac{\sigma_{DI}}{\sigma_R}. \quad (2)$$

The energy dependence of the above mentioned reduction factor is shown for deuteron interaction with ^{52}Cr, ^{56}Fe, ^{58}Ni, ^{93}Nb target nuclei at the top of Fig. 6 while at the bottom of the same figure the excitation functions of the DI and its components, BU, stripping and pick-up reactions are shown. Firstly, one may note a steep increases with energy of the reduction factor since the major BU but also and especially the DR components increase with energy. Most significant in this respect is the maximum of the (d, p) and (d, n) stripping excitation functions around 6-8 MeV, which provides the fastest slope of this factor. Finally, the reduction factor reaches its own maximum around deuteron energies of 15–20 MeV, and continues with a slow decrease due to the continuous increase of BU with the incident energy. The reduction factor values are close to around half of σ_R [3–5] at the deuteron incident energy of 50 MeV, pointing out the important DI role of the direct interactions.

5 Statistical particle emission

The statistical PE+CN reaction mechanisms which complete the deuteron interaction analysis along an enlarged nuclear-interaction time scale, become important with the increase of the incident energy above the Coulomb barrier. The corresponding reaction cross sections have been calculated using various versions of TALYS code [26], taking into account also the above-discussed BU, stripping, and pick–up results through the reduction factor of the optical model potential (OMP) total-reaction cross section. Another particular point of these calculations is the use of the same model parameters to account for different reaction mechanisms as, e.g., the same OMP parameters for calculation of the distorted waves in the ingoing/outgoing channels in direct reactions, of the PE transition rates, as well as of the transmission coefficients of various CN channels.

Additional PE+CN calculations have been carried out with the code STAPRE-H [27] for more detailed analysis involving particular options of various input parameters, e.g. for gamma-ray strength functions or initial p-h configurations.

The due consideration of all BU+DR+PE+CN is proved by the description of all measured data corresponding to deuteron interaction with a specific natural element target [2–5], e.g., activation excitation functions for d+^{nat}Ni interaction process shown in Fig. 2 [4].

The mark BU, rather than BF, for the sum of various contributions to an activation cross section in Figs. 1, 2, 4, and 5 underlines the consideration of both breakup effects, i.e., the overall decrease of σ_R, as well as the BF enhancement. On the other hand, the apparent discrepancies between the experimental data and corresponding TENDL-2017 [15] evaluation, shown in Figs. 1, 2, 4, and 5 stress out the effects of disregarding the direct processes within TENDL evaluation.

6 Conclusions

The present work has concerned a deeper analysis of the key role of DI, particularly of the breakup mechanism, in deuteron-induced reactions. The overall agreement between the measured data and model calculations supports the description of nuclear mechanisms taken into account for the deuteron-nucleus interaction, emphasizing the effects of direct interactions so far ignored in the evaluation procedures.

However, while the associated theoretical models for stripping, pick-up, PE and CN are already settled, an increased attention should be paid to the theoretical description of the breakup mechanism, including its inelastic component. The recently increased interest on the theoretical analysis of the breakup components [6, 7, 28, 29] may lead eventually to the refinement of the deuteron breakup empirical parametrization and increased accuracy of the deuteron activation cross section calculations, well beyond reaction cross sections recommended most recently for high-priority elements still using data fit by various-order Padé approximations [13].

On the other hand, the improvement of the deuteron breakup description requires, beyond the increase of its own data basis, also complementary measurements of (d, px) and (n, x), as well as (d, nx) and (p, x) reaction cross sections for the same target nucleus, within corresponding incident-energy ranges.

Acknowledgments

This work was partly supported by Autoritatea Nationala pentru Cercetare Stiintifica (Project PN-16420102), within the framework of the EUROfusion Consortium and has received funding from the Euratom research and training programme 2014-2018 under grant agreement No 633053. The views and opinions expressed herein do not necessarily reflect those of the European Commission.

References

[1] M. Avrigeanu and V. Avrigeanu, Phys. Rev. C **92** (2015) 021601(R).

[2] M. Avrigeanu, V. Avrigeanu, and A. J. Koning, *Phys. Rev.* C **85** (2012) 034603. M. Avrigeanu and V. avrigeanu, *Proceedings of the 14th International Conference on Nuclear Reaction Mechanisms Varenna, Italy, 2015*, edited by F. Cerutti *et al.*, CERN-Proceedings-2015-001 (CERN, Geneva, 2015), pp. 203 – 208; *J. Phys: Conf. Ser.* **724** (2016) 012003; *J. Phys: Conf. Ser.* **1023** (2018) 012009; M. Avrigeanu, V. Avrigeanu, and C. Costache *EPJ Web of Conferences* **146** (2017) 012020.

[3] P. Bém *et al.*, Phys. Rev. C **79** (2009) 044610; E. Šimečková *et al.*, Phys. Rev. C **84** (2011) 014605; M. Avrigeanu *et al.*, Phys. Rev. C **88** (2013) 014612; M. Avrigeanu and V. Avrigeanu, Nucl. Data Sheets **118** (2014) 301; M. Avrigeanu *et al.*, Phys. Rev. C **89** (2014) 044613.

[4] M. Avrigeanu *et al.*, Phys. Rev. C **94** (2016) 014606.

[5] E. Šimečková *et al.*, Phys. Rev. C **98** (2018) 034606.

[6] Yuen Sim Neoh, Kazuki Yoshida, Kosho Minomo, and Kazuyuki Ogata, Phys. Rev. C **94** (2016) 044619.

[7] B. V. Carlson, R. Capote, and M. Sin, Few-Body Syst. **57** (2016) 307.

[8] M. Avrigeanu *et al.*, Fusion Eng. Design **84** (2009) 418.

[9] M. Avrigeanu and V. Avrigeanu, Phys. Rev. C **95** (2017) 024607.

[10] http://www.iter.org/proj

[11] http://www.ifmif.org/b/

[12] http://pro.ganil-spiral2.eu/spiral2/instrumentation/nfs

[13] A. Hermanne *et al.*, Nucl. Data Sheets **148** (2018) 338.

[14] Experimental Nuclear Reaction Data (EXFOR), www-nds.iaea.or.at/exfor

[15] A. J. Koning and D. Rochman, 'TENDL-2017: TALYS-based evaluated nuclear data library', Dec. 30, 2017.

[16] M. G. Mustafa, T. Tamura, and T. Udagawa, Phys. Rev. C **35** (1987) 2077.

[17] J. Pampus *et al.*, Nucl. Phys. **A311** (1978) 141; J. R. Wu, C. C. Chang, and H. D. Holmgren, Phys. Rev. C **19** (1979) 370; N. Matsuoka *et al.*, Nucl. Phys. A**345** (1980) 1; J. Kleinfeller *et al.*,Nucl. Phys. A **370** (1981) 205.

[18] M. Avrigeanu and A. M. Moro, Phys. Rev. C **82** (2010) 037601.

[19] M. Kamimura *et al.*, Prog. Theor. Phys. **89**, Suppl. 1, (1986) 1; N. Austern *et al.*, Phys. Rep. **154** (1987) 125; A. Deltuva, A. M. Moro, E. Cravo, F. M. Nunes, and A. C. Fonseca, Phys. Rev. C **76** (2007 064602); K. Ogata and K. Yoshida, Phys. Rev. C **94** (2016) 051603(R).

[20] C. Kalbach Walker, "Deuteron Breakup and ^{21}Na Production", in *Triangle University Nuclear Laboratory Progress Report* **XLII (2002-2003)**; www.tunl.duke.edu/publications/tunlprogress/2003/.

[21] I. J. Thompson, Comput. Phys. Rep. **7** (1988) 167; v. FRES 2.9 (2011).

[22] I. Iseri, M. Yahiro, and M. Kamimura, Prog. Theor. Phys. Suppl. **89** (1986) 84.

[23] P. Guazzoni *et al.*,Phys. Rev. C **83** (2011) 044614.

[24] R. M. DelVecchio, Phys. Rev. C **7** (1973) 677.

[25] Evaluated Nuclear Structure Data File (ENSDF), http://www.nndc.bnl.gov/ensdf/

[26] A. J. Koning, S. Hilaire, and S. Goriely, v. TALYS-1.9, 2017, http://www.talys.eu

[27] M. Avrigeanu and V. Avrigeanu 1995 *IPNE Report* NP-86-1995, Bucharest, and Refs. therein; http://www.oecdnea.org/tools/abstract/detail/iaea0971/; M. Avrigeanu and V. Avrigeanu, Comp. Phys. Comm. **112** (1998) 191; A.Harangozo, I.Stetcu, M.Avrigeanu, and V.Avrigeanu, Phys. Rev. C **58** (1998) 295.

[28] Jin Lei and A. M. Moro, Phys. Rev. C **97** (2018) 011601; *ibid.* **92** (2015) 061602.

[29] G. Potel *et al.*, Eur. Phys. J. A. **53** (2017) 178.

Isotopic production cross sections of residual nuclei in proton- and deuteron-induced reactions on ^{91,92}Y, ^{92,93}Zr, and ^{93,94}Nb around 100 MeV/nucleon

Yu. Watanabe[a], J. Suwa[a,b], K. Nakano[a,b], S. Kawase[a], H. Wang[b], H. Otsu[b], H. Sakurai[b], D.S. Ahn[b], M. Aikawa[c], T. Ando[d], S.Araki[a,b], S. Chen[b], N. Chiga[b], P. Doornenbal[b], N. Fukuda[b], T. Isobe[b], S. Kawakami[f,b], T. Kin[a],Y. Kondo[e], S. Koyama[d], S. Kubono[b], Y. Maeda[f], A. Makinaga[g,h], M. Matsushita[i], T. Matsuzaki[b], S. Michimasa[i], S. Momiyama[d], S. Nagamine[d], T. Nakamura[e], M. Niikura[d], T. Ozaki[e], A. Saito[e], T. Saito[d], Y. Shiga[j,b], M. Shikata[e], Y. Shimizu[b], S. Shimoura[i], T. Sumikama[b], P.A. Soderstrom[b], H. Suzuki[b], H. Takeda[b], S. Takeuchi[e], R. Taniuchi[d], Y. Togano[e], J. Tsubota[e], M. Uesaka[b], Ya. Watanabe[b], K. Wimmer[d,i,b],T. Yamamoto[f,b], and K. Yoshida[b]

[a] Department ofAdvanced Energy Engineering Sciences,Kyushu University, Kasuga, Japan, [b] RIKEN Nishina Center,Wako, Japan, [c] Faculty of Science, Hokkaido University, Sapporo, Japan, [d] University of Tokyo, Tokyo, Japan, [e] Tokyo Institute of Technology,Tokyo, Japan, [f] University of Miyazaki, Miyazaki, Miyazaki, Japan, [g] JEin Institute for Fundamental Science, NPO Einstein, Kyoto, Japan, [h] Graduate School of Medicine, Hokkaido University, Sapporo, Japan, [i] Center for Nuclear Study, University of Tokyo,Wako, Saitama, Japan, [j] Department of Physics, Rikkyo University, Tokyo, Japan

Abstract

Production cross sections of residual nuclei via proton- and deuteron-induced spallation reactions on ^{91,92}Y, ^{92,93}Zr, and ^{93,94}Nb at projectile energies around 100 MeV/nucleon were measured in inverse kinematics at the RIKEN Radioactive Isotope Beam Factory. Noticeable jumps in the measured cross sections of isotone production appear between the neutron numbers N=51 and 50 for target nuclei with the initial neutron number N_{init}=53 (^{92}Y, ^{93}Zr, and ^{94}Nb), while such jump is not clearly seen for target nuclei with N_{init}=52 (^{91}Y, ^{92}Zr, and ^{93}Nb). The measured isotopic production cross sections are compared with PHITS calculations considering both the intranuclear cascade and evaporation processes in order to benchmark the reaction models.

1 Introduction

In recent years, a new research project has started for cross-section measurement of residues produced in p- and d-induced spallation reactions on long-lived fission products (LLFPs) (*e.g.*, ^{79}Se, ^{93}Zr [1], ^{107}Pd [2], ^{126}Sn, ^{135}Cs) using the inverse kinematics technique at RIKEN RI Beam Factory (RIBF) in order to accumulate basic data necessary for nuclear waste transmutation. In the isotopic distribution of the measured cross sections for ^{93}Zr [1] at 105 MeV/nucleon, noticeable jumps at the neutron magic number N = 50 were observed in the produced Zr and Y isotopes. In the ^{93}Zr experiment, the secondary beams containing ^{91,92}Y, ^{92,93}Zr, and ^{93,94}Nb at kinetic energies around 100 MeV/nucleon were produced by in-flight fission of ^{238}U at 345 MeV/nucleon on a beryllium target. Therefore, it is possible to extract isotopic-production cross sections of p- and d-induced spallation reactions on these nuclei except ^{93}Zr by identifying the particles in the secondary beams in off-line data analysis.

In the present work, further data analysis of the ^{93}Zr experiment has been performed and the cross sections for p- and d-induced spallation reactions on five nuclei adjacent to ^{93}Zr (*i.e.*, ^{91,92}Y, ^{92}Zr, and ^{93,94}Nb) have been obtained. Based on the systematic data, the behaviour of isotopic distribution of the measured cross sections is investigated with particular attention to the effect of neutron shell closure with N=50 on the p- and d-induced spallation reactions. Moreover, the measured data are compared with model calculations using the Particle and Heavy Ion Transport code System (PHITS) [3] in order to benchmark the reaction models used in PHITS, namely, the Liège Intranuclear Cascade model (INCL) [4] and the generalized evaporation model (GEM) [5].

2 Experiment

The experiment was performed at RIBF. The details of the experimental procedure have been reported in Refs. [1, 2]. The secondary beam containing ^{91,92}Y, ^{92,93}Zr, and ^{93,94}Nb at kinetic energies around 100 MeV/nucleon was produced by in-flight fission of ^{238}U at 345 MeV/nucleon on a 3 mm thick beryllium target in the first stage of the BigRIPS separator [6]. In the second stage of BigRIPS, the beam particles were selected and identified event-by-event using the Bρ-TOF-ΔE method [7]. Fig. 1 depicts the correlation plot of the mass-to-charge ratio A/Q and the proton number Z for the secondary beam.

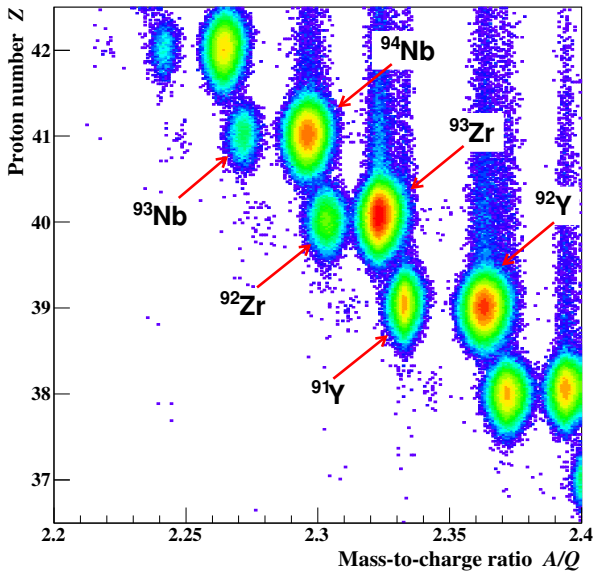

Fig. 1: Correlation plot of the proton number Z and the mass-to-charge ratio A/Q in BigRIPS.

Then, the beam particles bombarded the secondary targets, CH_2, CD_2, and natural C placed at the entrance of the ZeroDegree Spectrometer (ZDS). The target thicknesses were 179.2, 218.2, and 226.0 mg/cm^2, respectively. The residual nuclei produced by nuclear reactions in the second targets were analysed and identified event-by-event using the ZDS. Since the momentum acceptance of the ZDS is limited to $\sim \pm 3\%$, the experiment was carried out by using five different momentum settings (Δ(Bρ)/Bρ = -9%, -6%, -3%, 0%, and +3%) for each target so as to accept the produced isotopes with a wide range of A/Q. Fig. 2 shows a correlation plot of A/Q and Z for the Δ(Bρ)/Bρ = -6% run in the ZDS used for particle identification after ^{91}Y was selected in Fig. 1.

3 Results and Discussion

3.1 Experimental results

Figure 3 shows the measured isotopic production cross sections via the ^{91}Y spallation reactions on proton and deuteron as an example. The black and red symbols denote proton-induced cross sections (σ_p) and deuteron-induced cross sections (σ_d), respectively. They were obtained from the measurements using the CH_2 and CD_2 targets, respectively, after the subtraction of contributions from carbon (using data from the C target run) and beam-line materials (using data from the empty-target run). The error bars include only the statistical uncertainties. The systematic uncertainties were estimated in accordance with Ref. [1]: the target thickness ($\leq$2%) and the charge state distributions in ZDS (5%).

In Fig. 3, σ_p is found to be approximately twice as large as σ_d for Zr isotopes produced by charge-

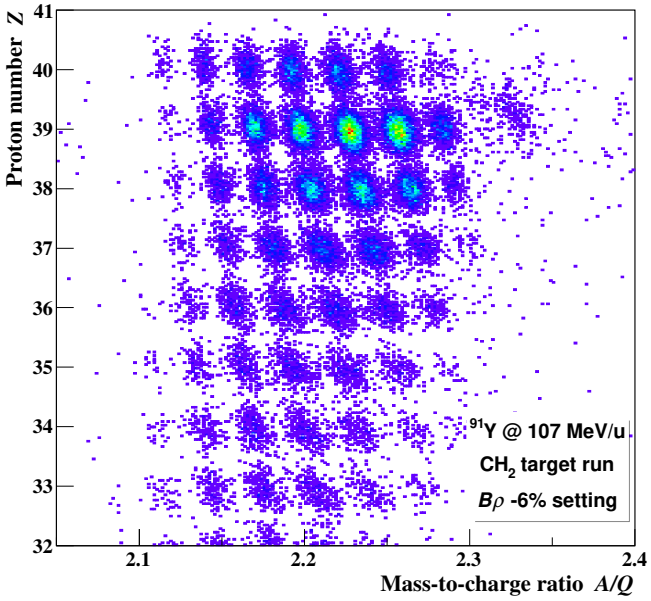

Fig. 2: Correlation plot of the proton number Z and the mass-to-charge ratio A/Q in ZDS.

increasing reactions, and σ_p and σ_d are almost identical for Y isotopes produced by charge-unchanging reactions. Meanwhile, σ_d becomes large compared to σ_p as the atomic number decreases from Sr to Br. The observed trends are the same as in the results of ^{93}Zr [1] and ^{107}Pd [2]. In the case of ^{93}Zr [1], characteristic jump structure near N=50 was observed in the isotopic distribution for the elements corresponding to charge-unchanging (ΔZ = 0) and one-proton-removal (ΔZ = -1). However, no discontinuous change in the cross section is observed in Y isotopes produced in the reactions ^{91}Y + p and d as shown in Fig. 3, while a jump is seen in the production of isotopic chains between ^{88}Sr and ^{89}Sr in the ^{91}Y + p reaction.

To investigate the effect of neutron shell closure with N = 50, we have obtained the isotone production cross sections, namely, the production cross sections of residual nuclei with the same neutron number N. The isotone production cross sections are plotted as a function of N for six nuclei in Fig. 4. The six nuclei are divided into the two groups according to the initial neutron number N_{init}. The upper panel presents the results of nuclei with N_{init}=52 (*i.e.*, ^{91}Y, ^{92}Zr, and ^{93}Nb), and the lower panel corresponds to the result of nuclei with N_{init}=53 (*i.e.*, ^{92}Y, ^{93}Zr, and ^{94}Nb). In the lower panel, the distributions looks very similar among the three nuclei with N_{init}=53. The measured cross sections have characteristic shoulders at N=52 and relatively large jumps are seen between N=51 and 50, which is considered as a signature of the effect of neutron shell closure with N = 50. On the other hand, the cross sections show a monotonic decrease with change in the neutron number from 50 to 52 in the upper panel, and such jumps as observed in the lower panel are not clearly seen between N=51 and 50. The similar behaviour of isotone production was observed in d-induced reactions as well. Further consideration accompanied with theoretical model analyses will be necessary to clarify why the distributions of measured isotone production cross sections are different between N_{init}=52 and 53.

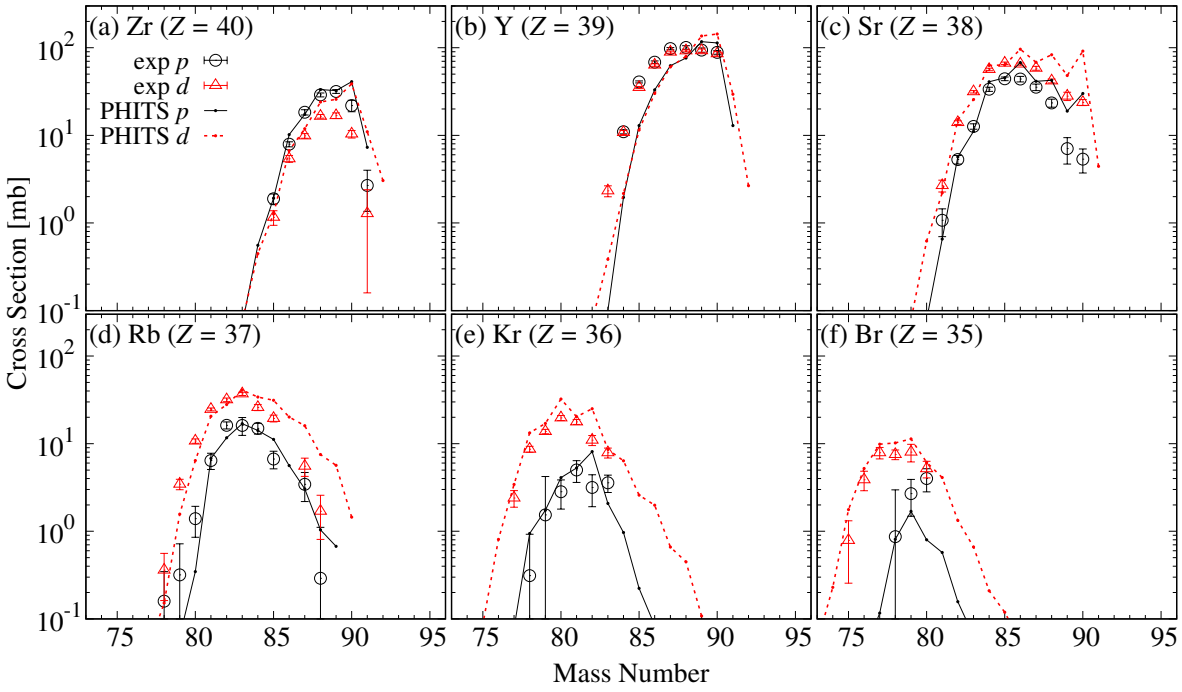

Fig. 3: Isotopic production cross section for the spallation reactions ^{91}Y + p and d as a function of mass number for each isotope in the experimental acceptance: (a) Zr, (b) Y, (c) Sr, (d) Rb, (e) Kr, and (f) Br.

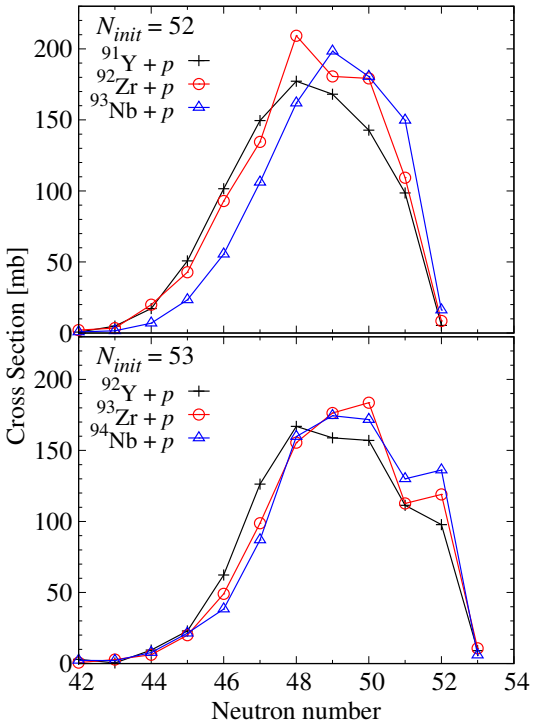

Fig. 4: Experimental cross sections of isotone production as a function of neutron number N for ^{91}Y, ^{92}Zr, and ^{93}Nb (upper panel) and ^{92}Y, ^{93}Zr, and ^{94}Nb (lower panel).

3.2 Comparison with theoretical model calculation

The spallation reactions have been well described as a two-step process, namely, the formation of pre-fragments via the intranuclear cascade process and the de-excitation process of the pre-fragments by evaporation of light particles. As in our previous works [1,2], we have used INCL 4.6 [4] and GEM [5] for the cascade and evaporation processes, respectively, in the present work. These models are implemented in PHITS [3].

The lines in Fig. 3 denote the cross sections calculated with PHITS. The black solid line and the red dashed line correspond to the p- and d-induced production cross sections(σ_p and σ_d), respectively. The overall behaviour of the cross section is well reproduced by the PHITS calculation. However, there are some discrepancies between the measured and calculated cross sections. For Zr-isotope, the calculation cannot explain the twofold difference between σ_p and σ_d. The calculated σ_p and σ_d for Y-isotopes underestimate the measured ones substantially in the neutron deficient region. The PHITS calculation overestimates the measured σ_p and σ_d in the neutron rich region for Zr, Y, and Sr isotopes. As discussed in Ref. [1], this overestimation is partly due to inappropriate treatment of the intranuclear cascade process in the peripheral region in INCL. In addition, the even-odd staggering seen in the calculated cross sections is exaggerated in Rb and Kr isotopes. Similar discrepancies were seen in the benchmark test of PHITS for p- and d-induced spallation reactions on ^{93}Zr [1] and ^{107}Pd [2]. Thus, further study will be required toward improvement of the INCL and GEM models.

4 Summary and Conclusions

We have measured systematically the production cross sections of residual nuclei in proton- and deuteron-induced reactions on ^{91,92}Y, ^{92,93}Zr, and ^{93,94}Nb at projectile energies around 100 MeV/nucleon. Noticeable jumps in the measured cross sections of isotone production were observed between N=51 and 50 for target nuclei with the initial neutron number N_{init}=53 (^{92}Y, ^{93}Zr, and ^{94}Nb), while the similar jumps were not clearly seen for target nuclei with N_{init}=52 (^{91}Y, ^{92}Zr, and ^{93}Nb). The measured isotopic production cross sections for ^{91}Y were compared with the PHITS calculations with INCL 4.6 for the intranuclear cascade process and GEM for the evaporation process. Although the PHITS calculations were in overall good agreement with the measured cross sections, some discrepancies to be improved were found: *e.g.*, overestimation in neutron-rich side, exaggerated even-odd staggering, and so on. We will continue to investigate the effect of neutron shell closure on p- and d-induced spallation reactions along with further improvement of the reaction models.

Acknowledgements

We are grateful to the accelerator staff of the RIKEN Nishina Center for providing a high-quality ^{238}U beam. This work was funded by ImPACT Program of Council for Science, Technology and Innovation (Cabinet Office, Government of Japan).

References

[1] S. Kawase *et al.*, *Prog. Theor. Exp. Phys.* **2017** (2017) 093D03.
[2] H. Wang *et al.*, *Prog. Theor. Exp. Phys.* **2016** (2016) 021D01.
[3] T. Sato *et al.*, *J. Nucl. Sci. Technol.,* **50** (2013) 913.
[4] A. Boudard *et al.*, *Phys. Rev. C* **87** (2013) 014606.
[5] S. Furihata, *Nucl. Instrum. Meth. B* **171** (2000) 251.
[6] T. Kubo *et al.*, *Prog. Theor. Exp. Phys.* **2012** (2012) 03C003.
[7] N. Fukuda *et al.*, *Nucl. Instrum. Meth. B.* **317** (2012) 323.

Towards an effective model for low-energy deuteron interactions in FLUKA

F. Salvat-Pujol on behalf of the FLUKA Collaboration
CERN, Geneva, Switzerland

Abstract
An overview is presented on recent efforts towards inclusion of low-energy ($\lesssim 200$ MeV) deuteron interactions in FLUKA, a general-purpose Monte Carlo code for the simulation of radiation transport. Differential cross sections for elastic deuteron break-up have been calculated within the distorted wave Born approximation (DWBA), obtaining reasonable agreement with experimental data at various energies and scattering geometries at the 4-differential level. An attempt has been made to put the various partially integrated distributions in as convenient a form as reasonably possible for sampling.

1 Introduction

Deuteron interactions are interesting not only from a fundamental point of view as a benchmark for both reaction and structure theories: they are also useful from an eminently practical point of view as high-intensity neutron sources for deuteron lab kinetic energies below ~ 200 MeV. Applications range from the production and study of fissionable material [1], to material-damage studies under intense neutron fluxes [2] and the production of medical radioisotopes [3], to name but a few.

In this contribution we discuss our recent efforts towards inclusion of low-energy ($\lesssim 200$ MeV) deuteron interactions in FLUKA, where no dedicated model exists yet. We restrict ourselves here to the description of elastic break-up, a process where the deuteron splits into its constituent neutron and proton in the Coulomb and nuclear field of a target nucleus with mass and atomic number A and Z, respectively, assumed in the ground state and at rest in the lab frame. By definition, the elastic break-up mechanism leaves the recoiling nucleus in the ground state. A schematic representation of the process is displayed in Fig. 1.

In view of processes like material damage, one needs to keep track of the final momentum not only of the emitted neutron and proton, but also of the recoiling target nucleus; for this it is essential to keep a reasonably strict control on the kinematics[1]. The model has to be flexible enough to return cross sections data for arbitrary deuteron lab kinetic energies (in the domain from threshold up to ~ 200 MeV), as well as for any target A and Z that a Monte Carlo simulation may encounter. Unfortunately, due to finite memory resources, we cannot afford to keep differential cross sections tabulated on a dense grid of abscissas: we have to resort effective parametrized expressions. We will briefly discuss the approach to calculate the differential cross section within the distorted-wave Born approximation (DWBA) and how we have prepared the aforementioned cross sections for sampling in FLUKA.

2 A condensed overview of the formalism

We have based our description of the deuteron elastic break-up process on the distorted-wave Born approximation (DWBA), given its conceptual simplicity and the availability of state-of-the-art numerical tools for the solution of the radial Schrödinger equation [4], with which one can readily build distorted waves and readily evaluate cross sections. The development of the DWBA formalism for the deuteron elastic break-up problem was pioneered in the 1970s and 1980s in a series of distinctly clear references, initially considering the break-up in the Coulomb field of the nucleus [5–10] and later including also the

[1] For other deuteron interaction mechanisms like nucleon-transfer reactions, where one of the constituent nucleons is transferred to a bound state of the target nucleus, it is also essential to keep track of the quantum state of the resulting nucleus (ground state, 1st excited state, 2nd excited state, etc.).

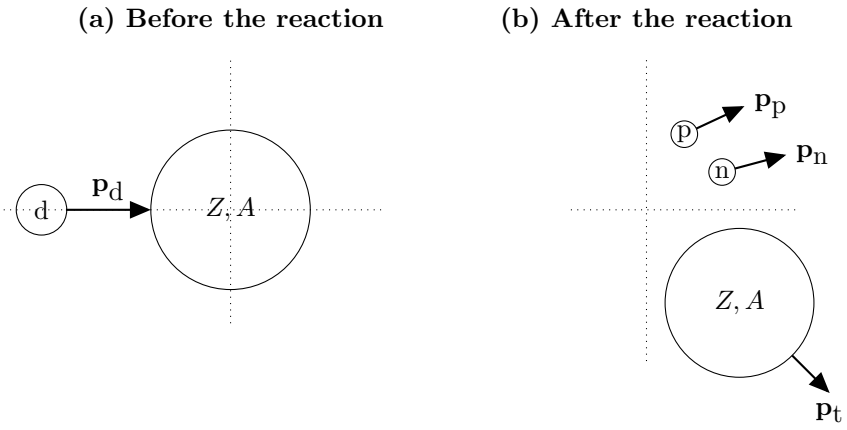

Fig. 1: Schematic representation of the deuteron elastic break-up reaction. A deuteron with momentum $\boldsymbol{p}_d$ impinges on a target nucleus with mass and atomic numbers A and Z, respectively (a). A proton and a neutron are emitted, leaving the recoiling target nucleus in the ground state (b).

nuclear field with effective optical-potential models [11, 12]. Application to a series of measurements confirmed the overall reasonable adequacy of the distorted wave calculations [13] (we show examples below). More elaborate continuum-discretized coupled-channels calculations (CDCC) are able to attain further refined agreement [14–17], but are left here as a future step: for an initial Monte Carlo model, and in particular given the imperative necessity to parametrize cross sections (thereby sacrificing a bit of detail anyway), comparatively simple DWBA calculations suffice. In this section we give a minimalistic overview of the various steps of the calculation needed to obtain a differential cross section for the elastic break-up of the deuteron.

Within the zero-range post-form DWBA approximation, the $\mathcal{T}$-matrix element is given by [12]

$$\mathcal{T} = D_0 \langle \chi_\mathrm{p}^{(-)} \chi_\mathrm{n}^{(-)} | \chi_\mathrm{d}^{(-)} \rangle, \tag{1}$$

where $\chi_\mathrm{p}^{(-)}$ and $\chi_\mathrm{n}^{(-)}$ represent the distorted wave of the *outgoing* proton and neutron in the nuclear and Coulomb field of the recoiling target nucleus, with *incoming* boundary condition [18]. Conversely, $\chi_\mathrm{d}^{(+)}$ represents the distorted wave of the *incoming* deuteron in the Coulomb and nuclear field of the nucleus with *outgoing* boundary condition. The quantity D_0 is the zero-range constant [5]. The reaction has four degrees of freedom, which we take as the proton kinetic energy E_p, the proton emission polar angle θ_p, the neutron emission polar angle θ_n, and the neutron emission azimuthal angle φ_n. Values of these four variables allow one to close the kinematics and build the momentum of the neutron, the proton, and the recoiling nucleus. There remains an overall rotational symmetry around the direction of incidence with homogeneously distributed angle so as to conserve the azimuthal symmetry present in the entry-channel state.

The cross section is given by

$$\frac{\mathrm{d}\sigma}{\mathrm{d}E_\mathrm{p}\mathrm{d}\Omega_\mathrm{p}\mathrm{d}\Omega_\mathrm{n}} = \frac{2\pi}{\hbar^2 k_\mathrm{dA}} \rho(E_\mathrm{n}, \Omega_\mathrm{n}, \Omega_\mathrm{p}) \left|\mathcal{T}\right|^2, \tag{2}$$

where E_n is the neutron kinetic energy, and Ω_n and Ω_p are condensed notation for the emission polar and azimuthal angles of the neutron and the proton, respectively[2]; k_dA is the relative deuteron-target momentum, and $\rho(E_\mathrm{n}, \Omega_\mathrm{n}, \Omega_\mathrm{p})$ is the phase-space volume element [19].

[2]We set $\varphi_\mathrm{p} = 0$.

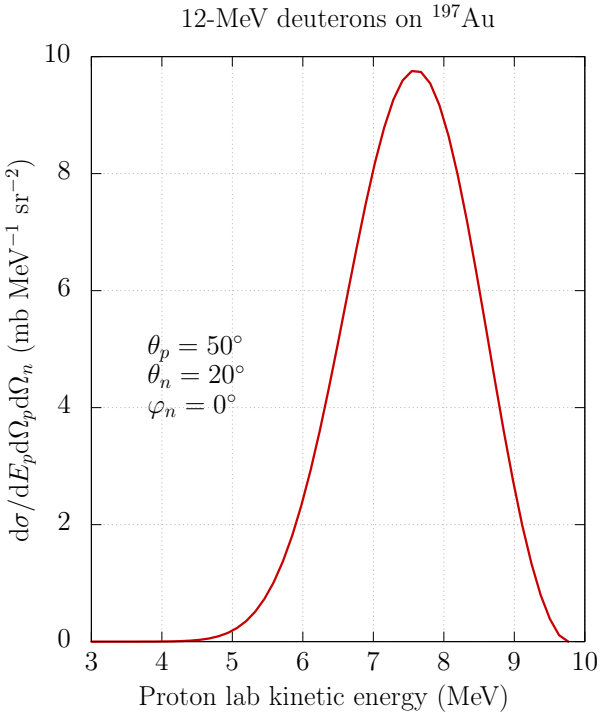

Fig. 2: Differential cross section for the break-up of a 12-MeV deuteron on ^{197}Au leading to the emission of a proton with $\theta_p = 50°$ and a neutron with $\theta_n = 20°$ and $\varphi_n = 0°$.

3 Break-up in the Coulomb field of the nucleus

Before considering the full Coulomb and nuclear interaction, it is interesting to examine first the case of interaction in the bare Coulomb potential of the target nucleus, *i. e.*, disregarding for the time being the contribution of the strong nuclear force. In this scenario, the proton and the deuteron feel the Coulomb potential of the target nucleus (their wavefunctions are Coulomb waves), whereas the neutron experiences no potential as it has no charge (its wavefunction is a plane wave). This simple case has the advantage that the wavefunctions are analytic and, surprisingly, so is the transition amplitude [5, 6, 22]. Although one would assume that this potential would be suitable for energies well below the Coulomb barrier, it turns out that experimental data at higher energy and for scattering geometries near the forward emission direction are reasonably described by the Coulomb break-up model [7, 8]. Even for the more realistic case of break-up in the Coulomb and nuclear field of the target nucleus, having the Coulomb break-up amplitude under control is essential: subtraction of the Coulomb amplitude from the partial-wave series and addition in analytical form is of enormous help in taming the otherwise impracticably slow convergence of the full partial-wave series.

As an example, Fig. 2 displays the differential cross section for the Coulomb break-up of a 12-MeV deuteron in the electrostatic field of a ^{197}Au nucleus, resulting in a proton emitted at 50° off the direction of incidence, and a neutron emitted with $\theta_n = 20°$ and $\varphi_n = 0°$, resolved as a function of the proton kinetic energy. This differential cross section exhibits a peak towards the high-energy end of the spectrum: as the deuteron climbs the Coulomb potential, it is decelerated and breaks up. The resulting neutron carries on with little energy whereas the proton picks up energy while climbing down the Coulomb potential as it moves away from the nucleus. The calculated cross section reproduces Baur *et al.*'s Coulomb calculation in Fig. (5) of [5].

Similarly, Fig. 3 displays the differential cross section for the Coulomb break-up of 140-MeV deuterons on the electrostatic field of a ^{12}C nucleus, for forward emission of the neutron and the proton being emitted at $\theta_p = 0°, 1°, 2°$, reproducing the analysis of Tostevin *et al.* [8], represented in the figure

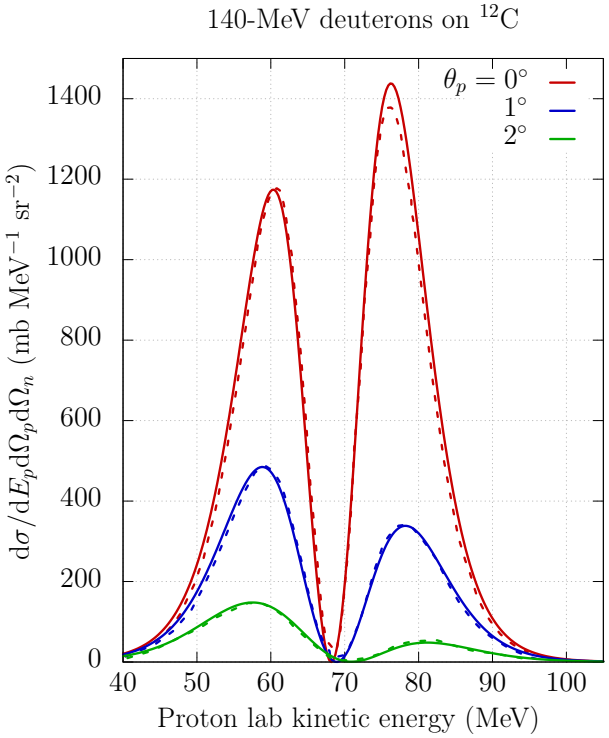

Fig. 3: Differential cross section for the Coulomb break-up of 140-MeV deuterons on ^{12}C, for forward emission of the neutron and for the indicated proton polar angles θ_p. The dashed curves are from [8].

in a dashed trace. An effective explanation for the presence of the drop at roughly half the deuteron energy is provided by Okamura *et al.* [7] in terms of the prior-form DWBA matrix element in the dipole approximation,

$$\mathcal{T}_{\text{prior,dipole}} \sim \left\langle \chi_{\text{dA}} \left| \frac{\boldsymbol{k}_{\text{np}} \boldsymbol{k}_{\text{dA}}}{r_{\text{dA}}^3} \right| \chi_{\text{dA}} \right\rangle , \tag{3}$$

where χ_{dA} is the distorted wave describing the relative motion of the deuteron and the nucleus, and $\boldsymbol{k}_{np}$ and $\boldsymbol{k}_{dA}$ are, respectively, the relative neutron-proton and deuteron-target momenta. At forward emission, and for $E_n \approx E_p \approx E_d/2$ the relative neutron-proton momentum vanishes, and a dip is expected in the cross section, as we indeed observe.

4 Break-up in the Coulomb and nuclear field of the nucleus

The deuteron, neutron, and proton feel not only the Coulomb field but also the nuclear force as they move interact with the target nucleus. We have employed Koning and Delaroche's optical-model parametrization to describe the potential experienced by the neutron and proton [20]; for the deuteron we have used Han's parametrization [21]. Since the optical potential models above are central potentials, we may expand the distorted waves in a partial-wave series:

$$\chi_k^{(\pm)}(\boldsymbol{r}) = \frac{4\pi}{kr} \sum_{\ell=0}^{\infty} \mathrm{i}^{\ell} \mathrm{e}^{\pm \mathrm{i}\delta_\ell} P_E(r) \sum_{m=-\ell}^{\ell} Y_{\ell m}^*(\hat{\boldsymbol{r}}) Y_{\ell m}(\hat{\boldsymbol{k}}), \tag{4}$$

where $Y_{\ell m}(\hat{\Omega})$ are the spherical harmonics, and the phase shifts δ_ℓ and the radial function $P_E(r)$ follow from the numerical solution of the radial Schrödinger equation

$$\left[-\frac{\hbar^2}{2\mu} \frac{\mathrm{d}^2}{\mathrm{d}r^2} + U(r) + \frac{\hbar^2}{2\mu} \frac{\ell(\ell+1)}{r^2} \right] P_E(r) = E P_E(r), \tag{5}$$

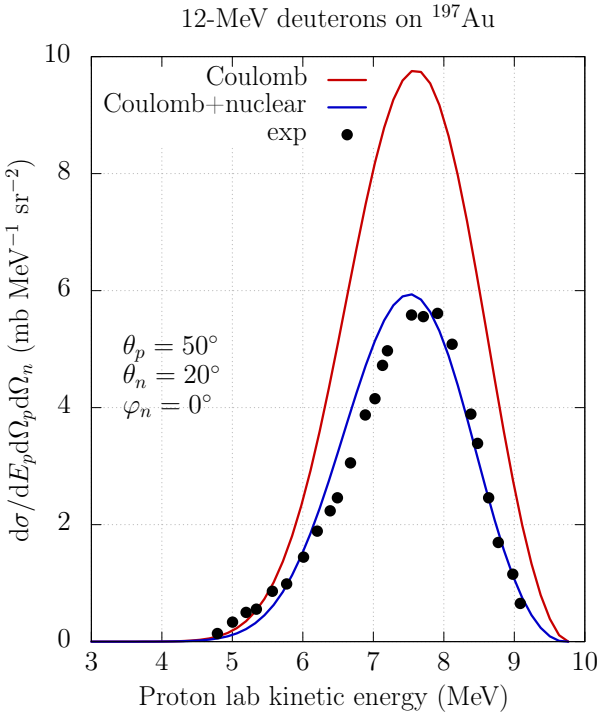

Fig. 4: Red curve: Same as Fig. 2. Blue curve: idem, but with the inclusion of the nuclear field of the target nucleus. Dots: experimental data [12].

where $U(r)$ is the interaction potential and μ the reduced mass of the two interacting particles. We have used the state-of-the-art numerical subroutine package `RADIAL` [4] to obtain $P_E(r)$, as well as the phase shifts δ_ℓ. Inclusion of a series expansion (4) for each distorted wave in Eq. (1) leads to a few technical complications. First, the resulting radial integral is highly oscillatory to infinity; we have resorted to a complex-plane integration scheme [23, 24]. The other noteworthy technical issue concerns the slow convergence of the resulting partial-wave series due to the long range of the Coulomb potential (partial waves with increasing ℓ keep contributing). We have opted for the subtraction (in partial-wave form) of the Coulomb amplitude from the partial-wave series and the addition in closed (summed over) form which we used in the previous section. This makes the convergence of the partial-wave series possible [7].

In Fig. 4 we recover the case considered in the previous section, that is, the differential cross section for the elastic break-up of 12-MeV deuterons on ^{197}Au with the proton emitted at $50°$ and the neutron at $20°$ off the incidence direction. Whereas the red curve is the Coulomb break-up curve displayed before, the blue curve is the result of the calculation outlined above for the elastic break-up in the Coulomb and nuclear field of the target nucleus. The agreement with experimental data is greatly improved, thus suggesting the need to take the full Coulomb and nuclear potential into account.

We perform a numerical integration of the differential cross section so as to obtain the various partially integrated cross sections needed for the subsequent Monte Carlo simulation. In Fig. 5 a preliminary comparison is shown between our cross sections (integrated over all kinematically allowed proton energies, directions, and neutron directions) and similar quantities available in the literature. The agreement is within 10%-20% of more elaborate CDCC calculations [17].

Encouraged by the reasonable agreement of the DWBA calculation with both experimental data at the 4-differential level and with similar calculations, we proceeded to fit a series of parametrized expressions to the various n-differential distributions, so as to ease the sampling of deuteron elastic break-up events in a Monte Carlo simulation. Work is currently underway to refine these fits.

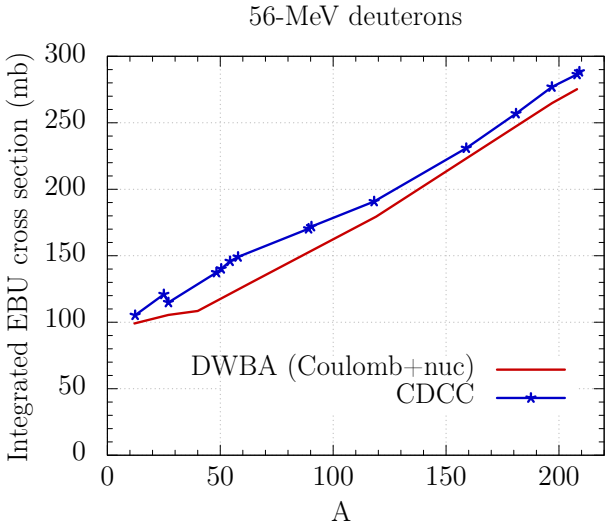

Fig. 5: Preliminary comparison between our numerical integration of elastic break-up cross and a similar calculation based on CDCC [17] for 56-MeV deuterons on targets with various A.

5 Conclusions

Advancing towards overcoming the lack of a dedicated model in `FLUKA` for low-energy deuteron interactions, a model based on the DWBA formalism has been developed and implemented to describe the elastic break-up of deuterons in the Coulomb and nuclear field of target nuclei (assumed at rest and in the ground state). Reasonable agreement has been obtained when comparing our calculated cross sections with experimental data and with similar contemporary calculations. Although we have only presented our results for the elastic break-up channel, work is underway also to model deuteron stripping reactions involving the transfer of a nucleon to a bound state of the target nucleus, as well as stripping reactions to the continuum, thus accounting for the most relevant deuteron interactions in the low-energy domain ($\lesssim$ 200 MeV).

References

[1] IAEA Technical Reports Series No. 435, "Implications of Partitioning and Transmutation in Radioactive Waste Management" (2004).

[2] A. Moeslang *et al.*, *Fus. Eng. Des.* **81** 863–871 (2006).

[3] Y. Nagai *et al.*, *J. Phys. Soc. Jpn.* **82** 064201 (2013).

[4] F. Salvat *et al.*, `RADIAL` user manual (2017).

[5] G. Baur *et al.*, *Nucl. Phys. A* **191** 321–331 (1972).

[6] L. Jarczyk *et al.*, *Phys. Rev. C* **8** 1 68–74 (1973).

[7] H. Okamura *et al.*, *Phys. Rev. C* **58** 4 2180-2191 (1998).

[8] J. A. Tostevin *et al.*, *Phys. Rev. C* **57** 6 3225–3236 (1998).

[9] M. Zadro, *Phys. Rev. C* **66** 034603 (2002).

[10] M. Zadro, *Phys. Rev. C* **70** 044605 (2004).

[11] J. Lang *et al.*, *Nucl. Phys. A* **204** 97–109 (1973).

[12] G. Baur *et al.*, *Nucl. Phys. A* **265** 101–112 (1976).

[13] N. Matsuoka *et al.*, *Nucl. Phys. A* **391** 357–376 (1982).

[14] T. Ye *et al.*, *Phys. Rev. C* **80** 014604 (2009).

[15] M. Avrigeanu *et al.*, *Phys. Rev. C* **82** 037601 (2010).

[16] Y. S. Neoh *et al.*, *Phys. Rev. C* **94** 044619 (2016).
[17] M. Avrigeanu *et al.*, *Phys. Rev. C* **95** 024607 (2017).
[18] H. Bethe *et al.*, *Phys. Rev.* **91** 417-418 (1953).
[19] H. Fuchs, *Nucl. Instrum. Meth.* **200** 361–368 (1982).
[20] A. J. Koning *et al.*, *Nucl. Phys. A* **713** 231–310 (2003).
[21] Y. Han *et al.*, *Phys. Rev. C* **74** 044615 (2006).
[22] A. Nordsieck, *Phys. Rev.* **93** 4 785–787 (1954).
[23] C. M. Vincent *et al.*, *Phys. Rev. C* **2** 3 782–792 (1970).
[24] K. T. R. Davies *et al.*, *J. Phys. G Nucl. Phys.* **14** 961–972 (1988).

Cross section measurements in the reactions of ^{136}Xe on proton, deuteron and carbon at 168 MeV/u

X. Sun [a], H. Wang [a], H. Otsu [a], H. Sakurai [a], D.S. Ahn [a], M. Aikawa [a], P. Doornenbal [a], N. Fukuda [a], T. Isobe [a], S. Kawakami [c], S. Koyama [d], T. Kubo [a], S. Kubono [a], G. Lorusso [a], Y. Maeda [c], A. Makinaga [e], S. Momiyama [d], K. Nakano [f], M. Niikura [d], Y. Shiga [g, a], P.-A. Söderström [a], H. Suzuki [a], H. Takeda [a], S. Takeuchi [a], R. Taniuchi [d, a], Ya. Watanabe [a], Yu. Watanabe [f], H. Yamasaki [d], K. Yoshida [a]

[a] RIKEN Nishina Center, Wako, Japan, [b] Faculty of Science, Hokkaido University, Sapporo, Japan, [c] Department of Applied Physics, University of Miyazaki, Miyazaki, Japan [d] Department of Physics, University of Tokyo, Tokyo, Japan, [e] Graduate School of Medicine, Hokkaido University, Sapporo, Japan, [f] Department of Advanced Energy Engineering Science, Kyushu University, Fukuoka, Japan, [g] Department of Physics, Rikkyo University, Tokyo, Japan

Abstract

The isotopic distribution of the production cross sections of ^{136}Xe on proton and carbon at 168 MeV/u were obtained in inverse kinematics technique at RIKEN Radioactive Isotope Beam Factory. The target dependence at 168 MeV/u was investigated systematically. The cross sections measured in the present work are compared with the previous results obtained at different reaction energies to investigate the energy dependence for the reactions on proton. The experimental results on proton are compared with the PHITS calculations including both the cascade and evaporation processes for the model benchmarking.

1 Introduction

Spallation and/or fragmentation reaction is a promising method for the production of the radioactive ion beams in flight [1]. Many experiments have been performed to study the reaction mechanisms of the spallation. The cross sections of the reaction products are important for the investigation. The isotopic production cross sections of ^{238}U + p at 1 GeV/u [2], ^{197}Au + p at 800 MeV/u [3], ^{208}Pb + p at 500 MeV/u [4] and 1 GeV/u [5] have been measured. In particular, the reaction of ^{136}Xe is studied systematically. Because the stable nuclei ^{136}Xe is usually used as a primary beam to generate neutron-rich nuclei by fragmentation or spallation reaction. The investigation of the target dependence and energy dependence is of great importance to optimize the beam production. The reaction of ^{136}Xe induced by proton at 200 MeV/u [6], 500 MeV/u [7] and 1 GeV/u [8] has been measured and the energy dependence on proton has been investigated. As for the reactions induced by other targets, such as deuteron- and carbon-induced reaction, the study is scarce. Only the reactions of ^{136}Xe + d at 500 MeV/u [9] and ^{136}Xe + Be [10] at 1 GeV/u are available.

In order to have a comprehensive understanding of the reaction mechanisms, we measured the isotopic cross sections of ^{136}Xe + p, ^{136}Xe + d and ^{136}Xe + C at 168 MeV/u by using the inverse kinematics technique. These data are helpful for the target dependence investigation. Together with the previous data measured at other reaction energies, the energy dependence would be studied. The isotopic production cross sections obtained from the experiment are expected to be helpful to understand the spallation reaction mechanisms and to benchmark the model calculations.

2 Experiment

The experiment was performed at RIKEN RIBF using the BigRIPS separator and ZeroDegree Spectrometer [11], operated by RIKEN Nishina Center and the Center for Nuclear Study, University of Tokyo. The experimental setup is same as the one for ^{137}Cs [12]. The primary beam was ^{238}U at 345 MeV/u, with the

intensity of 12 pnA. The secondary beams were produced by the in-flight fission of ^{238}U on a beryllium target located at the entrance of the BigRIPS. The total intensity of the secondary beams is about 8.5 $\times$ 10^3 particles per second (pps). Particles can be identified in BigRIPS separator event by event by using the TOF-$B\rho$-ΔE method [13]. The intensity of ^{136}Xe is 2.1 $\times$ 10^3 pps, with the purity of 24%.

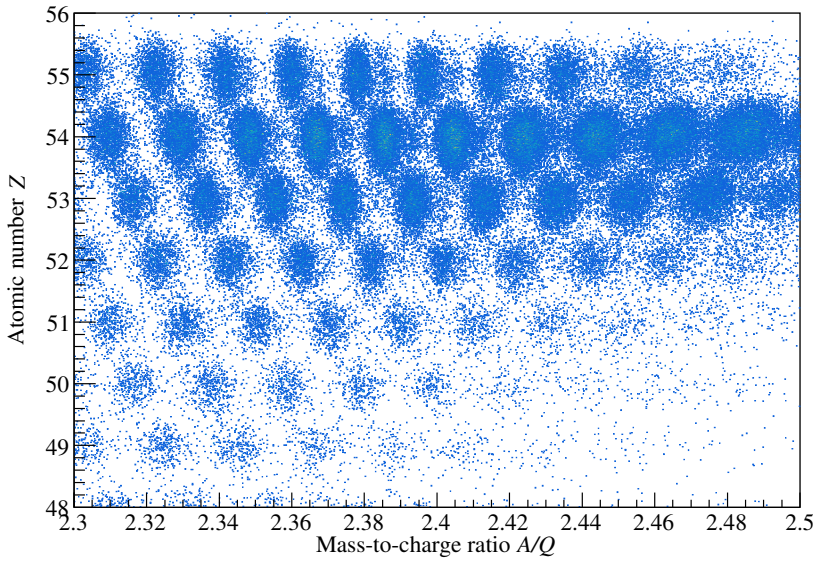

Fig. 1: Particle identification of Z versus A/Q analyzed by ZeroDegree Spectrometer for the reaction of ^{136}Xe on CH_2 target, with $B\rho$ -6% setting.

The inverse kinematics was adopted for the experiment. CH_2 (179.2 mg/cm^2), CD_2 (217.8 mg/cm^2) and carbon (226.0 mg/cm^2) targets were used to induce the secondary reactions. The energy of ^{136}Xe at the center of the secondary targets is 168 MeV/u. The data was also taken only use the target frame without target material (empty target run) in order to subtract the background contribution. The reaction products were measured and identified in the ZeroDegree Spectrometer unambiguously, using the similar method with BigRIPS. The time of flight (TOF) information was measured by the plastic scintillator. The magnetic rigidity ($B\rho$) was determined by the trajectory reconstruction using the position of particles measured by PPAC. The ionization chamber was used to measure the energy loss (ΔE). The atomic number Z and the mass-to-charge ratio A/Q were determined by the TOF-ΔE and $B\rho$-TOF correlations, respectively. The angular acceptance of the ZeroDegree Spectrometer is $\pm$45 mrad and $\pm$30 mrad in horizontal and vertical direction, respectively, and the momentum acceptance is $\pm$3%. In order to cover a wide range of the reaction products, 5 different $B\rho$ settings (+3%, 0%, -3%, -6%, -9%) were applied in the ZeroDegree Spectrometer. Fig. 1 shows the particle identification plot of the reaction products obtained from the ^{136}Xe beam on CH_2 target with $B\rho$ -6% setting. The typical A/Q and Z resolutions were 6.1 $\times 10^{-3}$ (FWHM) and 0.52 (FWHM), respectively. After the particles pass through the ZeroDegree Spectrometer, for the xenon isotopes, the ratio of the fully stripped ions ($Q = Z$) was about 67%.

3 Results and discussion

Fig. 2 shows the preliminary results of the isotopic production cross sections for ^{136}Xe on proton and carbon at 168 MeV/u. The statistical uncertainties were shown in the figure. The cross sections on carbon (σ_C) were obtained from the carbon target after subtracting the contribution from the beam-line material.

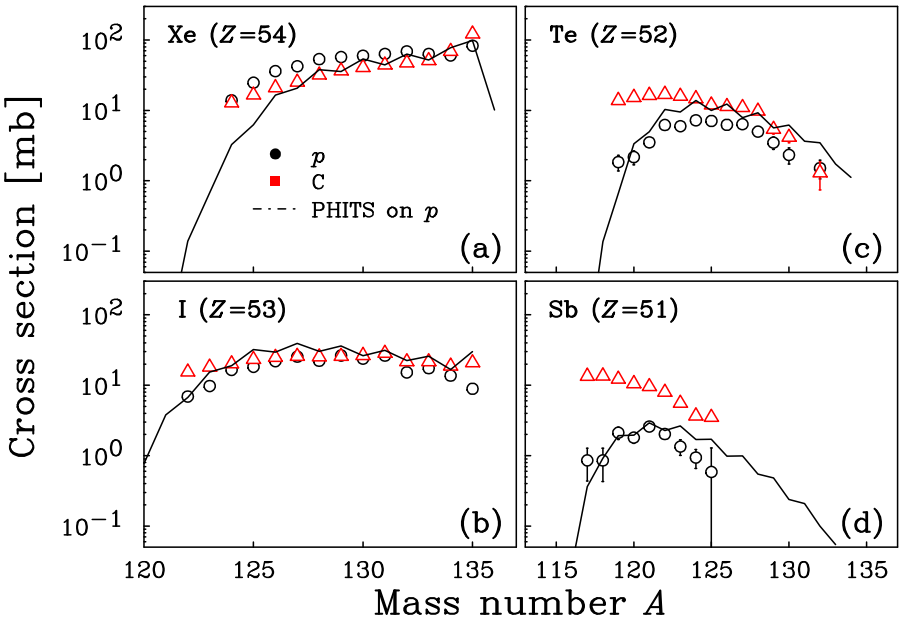

Fig. 2: Isotopic distribution of the cross sections for ^{136}Xe on proton (black dot) and carbon (red triangle) at 168 MeV/u. The black line represents the PHITS calculations on proton.

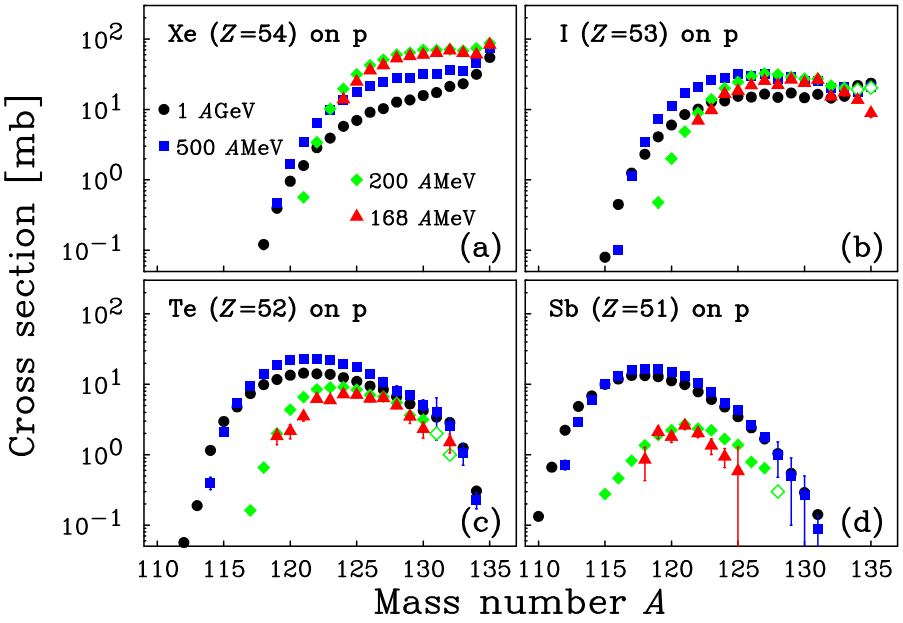

Fig. 3: Isotopic distribution of the production cross sections from element xenon ($Z = 54$) to antimony ($Z = 51$) for the reaction of ^{136}Xe + p at 168 MeV/u (red), 200 MeV/u (green), 500 MeV/u (blue) and 1 GeV/u (black). Empty diamonds at 200 MeV/u represent extrapolated value.

The cross sections on proton (σ_p) were obtained from CH_2 target after subtracting the contribution from carbon target and the beam-line material.

For the xenon and iodine isotopes in Fig. 2 (a) and (b), σ_p and σ_C looks similar, and the cross sections keep almost constant both on proton and carbon. For the tellurium and antimony isotopes, σ_C became larger than σ_p. These light products were produced by the central collision, the cross sections depend on the excitation energy of the pre-fragments. A relatively higher deposited energy of the pre-fragments in the carbon-induced reactions result in the higher cross sections.

The model calculations on proton target by Particle and Heavy Ion Transport system (PHITS) 2.76 [14] were shown in Fig. 2 to compare with the experimental results. The Intranuclear Cascade model of Liège (INCL) [15] and the generalized evaporation model (GEM) [16] were used for the cascade and evaporation processes, respectively. For the 4 elements shown in Fig. 2, PHITS calculations reproduce the overall tendency of the experimental results. While the overestimation in the neutron-rich side was observed. Such overestimation was also seen in the calculations of ^{93}Zr at 105 MeV/u [17] and ^{107}Pd at 118 MeV/u and 196 MeV/u [18]. Besides, the calculated cross sections by PHITS give a more obvious even-odd staggering than experimental results, which was also observed for the calculations of ^{137}Cs at 185 MeV/u [12] on proton.

The cross sections measured in the present work for the reaction of ^{136}Xe + p at 168 MeV/u were compared with the results obtained previously at different reaction energies in order to investigate the energy dependence. As shown in Fig. 3 for the comparison with the reactions at 200 MeV/u [6] (green) , 500 MeV/u [7] (blue), 1000 MeV/u [8] (black). For the xenon isotopes, the shape of the isotopic distribution is similar at different reaction energies, the value of the cross sections decrease as the reaction energy increase. For the tellurium and antimony isotopes, the cross sections at low reaction energies (168 MeV/u and 200 MeV/u) decreased rapidly, the cross sections at high reaction energy become larger, especially for the products in the neutron-deficient side. As discussed above, the cross sections of these light products depend on the excitation energy of the pre-fragment after the intranuclear cascade process, more energy deposited for the reaction at high reaction energy resulting in a larger cross sections.

4 Summary

The isotopic distribution of the cross sections for ^{136}Xe on proton and carbon at 168 MeV/u were obtained in inverse kinematics technique. The target dependence was investigated systematically. The cross sections of the light products are larger for the carbon-induced reaction because of the higher deposited energy. The cross sections on proton obtained in the present work were compared with the previous data measured at different reaction energies. It was found that for the xenon isotopes, the cross sections at low reaction energy are larger. The experimental results were compared with PHITS calculations, the overall tendency of the isotopic cross sections was reproduced. The overestimation in the neutron-rich side was observed. Such a comparison is expected to be helpful for the model benchmarking.

Acknowledgements

We express our gratitude to the accelerator staff of the RIKEN Nishina Center for providing the ^{238}U primary beam. This work was supported by the ImPACT Program of the Council for Science, Technology and Innovation (Cabinet Office, Government of Japan).

References

[1] H. Suzuki *et al.*, *Nucl. Instrum. Methods B* **317** (2013) 756.

[2] J. Taieb *et al.*, *Nucl. Phys. A* **724** (2003) 413.

[3] F. Rejmund *et al.*, *Nucl. Phys. A* **683** (2001) 540.

[4] L. Audouin *et al.*, *Nucl. Phys. A* **768** (2002) 1.
[5] W. Wlazło *et al.*, *Phys. Rev. Lett.* **84** (2000) 5736.
[6] C. Paradela *et al.*, *Phys. Rev. C.* **95** (2013) 044606.
[7] L. Giot *et al.*, *Nucl. Phys. A* **899** (2013) 116.
[8] P. Napolitani *et al.*, *Phys. Rev. C* **76** (2007) 064609.
[9] J. Alcántara-Núñez *et al.*, *Phys. Rev. C* **92** (2015) 024607.
[10] J. Benlliure *et al.*, *Phys. Rev. C* **78** (2008) 054605.
[11] T. Kubo *et al.*, *Prog. Theor. Exp. Phys.* **2012** (2017) 03C003.
[12] H. Wang *et al.*, *Phys. Lett. B.* **754** (2016) 104.
[13] N. Fukuda *et al.*, *Nucl. Instrum. Methods. B* **317** (2013) 323.
[14] T. Sato *et al.*, *J. Nucl. Sci. Technol.* **50** (2013) 913.
[15] A. Boudard *et al.*, *Phys. Rev. C.* **87** (2013) 014606.
[16] S. Furihata *et al.*, *Nucl. Instrum. Meth. B* **171** (2000) 251.
[17] S. Kawase *et al.*, *Prog. Theor. Exp. Phys.* **2017** (2017) 093D03.
[18] H. Wang *et al.*, *Prog. Theor. Exp. Phys.* **2016** (2016) 021D01.

Correlations between fission fragment yields and the prompt fission γ-ray spectrum

P. Jaffke[1]*, P. Talou*[1]*, T. Kawano*[1]*, I. Stetcu*[1]*, M. Devlin*[2]*, N. Fotiades*[2]*, C.-Y. Wu*[3]*, and A. Chyzh*[3]
[1] Theoretical Division, Los Alamos National Lab, Los Alamos, NM 87545, USA
[2] Physics Division, Los Alamos National Lab, Los Alamos, NM 87545, USA
[3] Lawrence Livermore National Lab, Livermore, CA 94550, USA

Abstract
We illustrate correlations between the prompt fission γ-ray spectrum (PFGS) and the input fission fragment yields $Y(A)$ with a Monte Carlo implementation of the statistical Hauser-Feshbach decay theory, the `CGMF` code. We find that the slope of the PFGS at high γ-ray energies is correlated to the yields near the closed-shell ^{132}Sn nucleus. Low-energy PFGS peaks from discrete transitions of particular post-neutron fission products result from a complex interplay between the yields, the nuclear level structure, and the spin of nearby nuclei. We demonstrate this complexity with ^{128}Sn and derive level correction factors, which can be used to relate fission product yields to discrete transition intensities, for several even-even nuclei.

1 Introduction

The prompt γ-ray emission following nuclear fission is a resurging area of interest in the nuclear community for both experiment [1–3] and theory [4–6], due to its importance across a variety of applications. The prompt γ-ray contribution to the reactor heating [7] has been identified as a high-priority subject by the Nuclear Energy Agency [8]. In addition, the production of γ rays from isomers can provide an indirect probe of the spin of fission fragments [9]. Finally, γ-ray spectroscopy has been used to connect the fission product yields to the intensities of discrete γ-ray transitions [10, 11].

We utilize the `CGMF` code [4], a Monte Carlo implementation of the statistical Hauser-Feshbach theory [12], to model the prompt γ-ray and neutron emissions after fission. The code is described in full elsewhere [13], so we merely summarize the method here. Calculations begin by determining the initial distribution of fragments in mass A, charge Z, spin and parity J^π, and - indirectly - the excitation energy U. From this distribution, a pair of fragments, along with their J^π and U, are sampled. Each fragment is then sequentially decayed by the following process. Transition probabilities for neutron and γ-ray emissions are calculated using the global optical potential [14], strength-function formalism [15] with parameters from the RIPL-3 [16] database, and level densities from the Gilbert-Cameron formalism [17] supplemented with discrete levels from RIPL-3 [16]. Transition probabilities are then used to sample a neutron or γ-ray emission with a given energy. The process repeats with the residual nucleus until it decays to a stable or long-lived state, resulting in a list of all prompt neutrons and γ rays emitted for each fission event.

From the above method, one can see that the prompt fission γ-ray spectrum (PFGS) is a complicated calculation. To simplify this picture, we attempt to find correlations between PFGS properties and the input mass yields $Y(A)$. In particular, we correlate the slope of the PFGS at high γ-ray energies with the yields near the closed-shell ^{132}Sn nucleus. In addition, we discuss the complexities of discrete γ-ray transitions and calculate level corrections to relate the transition intensity to fission product yields.

2 PFGS high-energy slope

First, we test the impact of simple changes in the $Y(A)$ distribution on the PFGS using ^{239}Pu$(n_{\rm th}, f)$ as a case study. The pre-neutron mass distribution $Y(A)$ is often parameterized with 5 Gaussians, three of

which are unique, as in Ref. [13]. On the left in Fig. 1, we display our fit to the experimental data [18–20] in red (solid), along with five other artificially shifted $Y(A)$. The fit captures the experimental trend

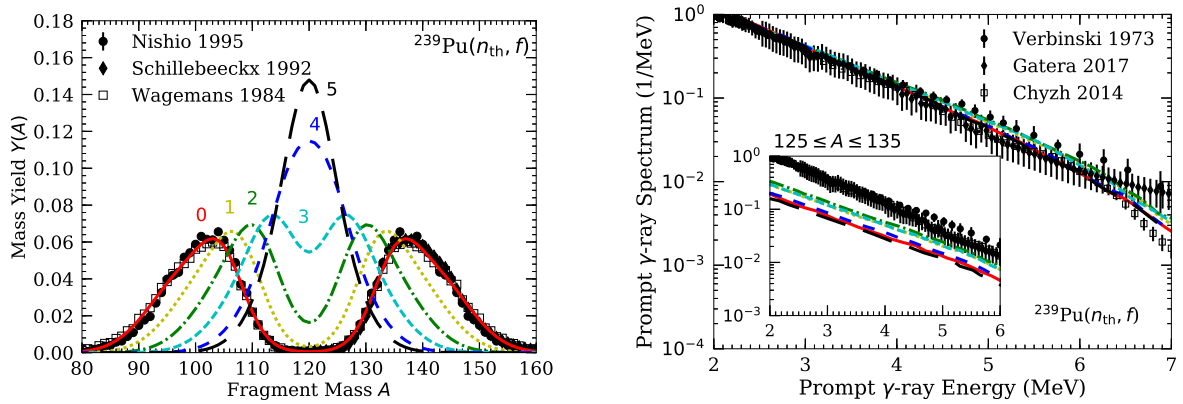

Fig. 1: Left: fitted pre-neutron mass yields $Y(A)$ from ^{239}Pu$(n_{\rm th}, f)$ to experimental data [18–20]. Exact fit is in solid red, with the other colors demonstrating an increasingly symmetric $Y(A)$. Right: resulting PFGS for the six input $Y(A)$ in 200 keV bins, alongside experimental data [1, 2, 21]. Insert shows the contribution from fission products with $125 \leq A \leq 135$, which drive the high-energy slope.

adequately and the shifts are determined by moving the Gaussian means towards symmetry. Thus, the red (solid) curve indicates the experimental result and the black (long dashed) is a fully symmetric yield, with the others in between.

Using the six different input $Y(A)$ shown on the left in Fig. 1, we perform six CGMF calculations, each with 500000 fission events. The resulting PFGS is plotted on the right in Fig. 1. We see that the slope of the PFGS is steeper for the red (solid), blue (medium dashed), and black (long dashed) calculations. This is because these $Y(A)$ had lower yields in the $125 \leq A \leq 135$ mass region, near doubly-magic ^{132}Sn. The level spacing of these products are known to be large [16], leading to higher energy γ-ray transitions. Thus, when a $Y(A)$ features these fragments more prominently, say in the yellow (dotted), green (dot-dashsed), and cyan (short dashed) cases, more high-energy γ rays are produced leading to a harder spectrum. The partial PFGS from the $125 \leq A \leq 135$ mass region is shown in the insert. The fitted slopes to the total PFGS are given in Tab. 1, where the slope changes by 9% between the $Y(A)$ following experimental ^{239}Pu$(n_{\rm th}, f)$ data to a fully symmetric $Y(A)$.

	$Y_0(A)$	$Y_1(A)$	$Y_2(A)$	$Y_3(A)$	$Y_4(A)$	$Y_5(A)$
Slope (1/MeV)	-0.243	-0.228	-0.222	-0.226	-0.236	-0.241
$125 \leq A \leq 135$ Contr.	18.7%	29.2%	33.8%	29.6%	21.0%	16.6%

Table 1: Fitted slopes to the $2-6$ MeV range of the PFGS for six input $Y(A)$ ranging from least to most symmetric (see text) and the PFGS contribution in this energy range from fission products with mass $125 \leq A \leq 135$.

3 Discrete transitions

Discrete transitions from fission products can manifest as low-energy peaks in the PFGS [2, 21]. The peak intensity depends on the direct production of the fission product, but also on the probability that a given γ ray is emitted. This probability is a complex interplay between the initial spin distribution of the product and the level structure. To analyze this, three spin cases were calculated (each with 500000 events) for ^{238}U$(n = 1.75\,{\rm MeV}, f)$ using CGMF. The spin cases had an average spin over all fragments of $\langle J \rangle = 8.22, 9.94, 11.8\,\hbar$, which were chosen to span a reasonable range of prompt γ-ray multiplicities:

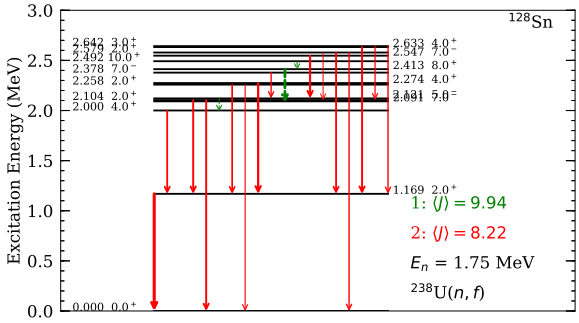

Fig. 2: Example emission scheme for ^{128}Sn produced in $^{238}\mathrm{U}(n = 1.75\,\mathrm{MeV}, f)$ fission. The arrows indicate transitions, where the colors (dashing) indicate which of two spin cases, $\langle J\rangle = 8.22\,\hbar$ (red solid) or $\langle J\rangle = 9.94\,\hbar$ (green dashed), had a larger transition probability. The thickness of the arrow indicates the magnitude of this probability difference. We note that ^{128}Sn has a $2.091\,\mathrm{MeV}$ isomer with a halflife of $6.5\,\mathrm{s}$.

$\bar{\nu}_\gamma = 7.4, 8.4, 9.5\,\gamma$/fission. Larger $\langle J\rangle$ leads to higher γ-ray multiplicities as the nuclei emit more γ rays (typically E1 transitions in the continuum) to remove the excess spin, as shown in Ref. [22].

For each spin case, the transition scheme of specific fission products was analyzed. In Fig. 2, we plot the comparison of the ^{128}Sn emission scheme for $\langle J\rangle = 8.22\,\hbar$ (red, solid) and $\langle J\rangle = 9.94\,\hbar$ (green, dashed). Normalizing by the number of events producing ^{128}Sn, we compared the probability to emit 18 discrete transitions in each spin case. Transitions are colored according to which spin case showed a higher probability for a given transition. The arrow size corresponds to the magnitude of the probability difference between the two spin cases. For example, the $10^+ \rightarrow 8^+$ and $7^- \rightarrow 7^-$ transitions are more probable in the high-spin case, hence they are colored green in Fig. 2. However, the ground-state band $2^+ \rightarrow 0^+$ transition is red and large, suggesting it heavily favors low-spin cases. This is caused by the $6.5\,\mathrm{s}$ isomer at $U = 2.091\,\mathrm{MeV}$, which acts as a roadblock for subsequent transitions.

From the above discussion, it is clear that corrections, which can be estimated [23], must be used to relate the fission product yields to the intensity of γ-ray transitions. However, these corrections will depend on the spin distribution of the product and the timing window as well. We determine the corrections associated with the nuclear level structure using `CGMF` via

$$\eta(A_p, Z_p, \epsilon_\gamma) = \frac{Y(\epsilon_\gamma; A_p, Z_p)}{Y(A_p, Z_p)}, \tag{1}$$

where the probability to generate the product with mass A_p and charge Z_p after prompt neutron emission is $Y(A_p, Z_p)$. The probability to emit a γ ray of energy ϵ_γ *and* the product (A_p,Z_p) is $Y(\epsilon_\gamma; A_p, Z_p)$.

Figure 3 shows level correction factors for the ground-state band $2^+ \rightarrow 0^+$ transition of 19 even-even fission products using Eq. 1 and `CGMF`. The different curves correspond to the different spin cases. We note that the assumption that the ground-state band $2^+ \rightarrow 0^+$ transition is emitted every time the specified product is generated in fission would correspond to unity. These level corrections, as well as corrections for the use of a multiplicity cut, energy resolution, and timing window, are critical factors in γ-ray spectroscopy.

Overall, we find that the majority of studied $2^+ \rightarrow 0^+$ transitions would require corrections on the order of $10 - 20\%$ when correlating the fission product yields to the intensity of discrete γ-ray lines. Some nuclei, ^{128,132}Sn and ^{150}Ce, had much more severe corrections, primarily due to long-lived isomers and sparse level spacings. The derived correction factors depend on the discrete level data [16], as `CGMF` cannot predict level information. Thus, the calculation is only as reliable as the input data. We note that each fission reaction is unique, so the level corrections presented here are only applicable to $^{238}\mathrm{U}(n = 1.75\,\mathrm{MeV}, f)$. However, this process demonstrates that `CGMF` could determine similar level corrections for other fission reactions, allowing for more accurate results from γ-ray spectroscopic

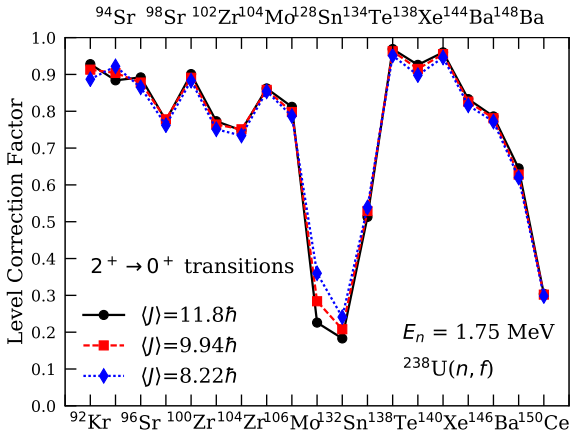

Fig. 3: Level correction factors (see text), which represent the percent of fission events producing the specified product and the ground-state band $2^+ \rightarrow 0^+$ transition, for 19 even-even fission products. Calculation for three spin cases of $^{238}\mathrm{U}(n = 1.75\,\mathrm{MeV}, f)$ are shown.

studies. In particular, we intend to demonstrate how these corrections and data from γ-ray detector arrays [24–26] could help infer fission product yields in a future work. This process has already been applied in Ref. [11] to provide a possible cause for some of the discrepancies observed in $^{238}\mathrm{U}(n, f)$ yields [10].

4 Summary

We have used a Monte Carlo Hauser-Feshbach model, `CGMF`, to simulate fission events and draw connections between the fission yields and the prompt fission γ-ray spectrum (PFGS). Focusing on the high-energy part of the PFGS, we found that the slope between $2 - 6\,\mathrm{MeV}$ is correlated with the production of fission products near doubly-magic ^{132}Sn, where the level spacing and, hence, average γ-ray energies are larger. After analyzing the low-energy discrete peaks in the PFGS, we found that the peak intensities are a complex interplay between the fission yields, the nuclear level structure, and the spin distribution. This was illustrated in the specific case of $^{238}\mathrm{U}(E_n = 1.75\,\mathrm{MeV}, f)$ and we proceeded to determine the level corrections for a variety of even-even fission products, over a range of spin cases. These corrections show that particular fission products are susceptible to large errors if their nuclear level structures are not accounted for properly. Therefore, it may be necessary to incorporate spin-dependent calculations of the level corrections into γ-ray spectroscopy studies of fission product yields.

Acknowledgements

This work was performed under the auspices of the US Department of Energy by Lawrence Livermore National Security, LLC under contract DE-AC52-07NA27344 and by Los Alamos National Security, LLC under contract DE-AC52-06NA25396. Partial funding is gratefully acknowledged from the U.S. DOE/NNSA Office of Defense Nuclear Nonproliferation Research and Development.

References

[1] A. Chyzh, C. Y. Wu, E. Kwan, R. A. Henderson, T. A. Bredeweg, R. C. Haight, A. C. Hayes-Sterbenz, H. Y. Lee, J. M. O'Donnell, J. L. Ullmann, Phys. Rev. C 90 (2014) 014602. doi:10.1103/PhysRevC.90.014602.

[2] A. Gatera, T. Belgya, W. Geerts, A. Göök, F.-J. Hambsch, M. Lebois, B. Maróti, A. Moens, A. Oberstedt, S. Oberstedt, F. Postelt, L. Qi, L. Szentmiklósi, G. Sibbens, D. Vanleeuw, M. Vidali, F. Zeiser, Phys. Rev. C 95 (2017) 064609. doi:10.1103/PhysRevC.95.064609.

[3] A. Chyzh, P. Jaffke, C. Wu, R. Henderson, P. Talou, I. Stetcu, J. Henderson, M. Buckner, S. Sheets, R. Hughes, B. Wang, J. Ullmann, S. Mosby, T. Bredeweg, A. Hayes-Sterbenz, J. O'Donnell, Physics Letters B 782 (2018) 652 – 656. doi:https://doi.org/10.1016/j.physletb.2018.06.006.

[4] B. Becker, P. Talou, T. Kawano, Y. Danon, I. Stetcu, Phys. Rev. C 87 (2013) 014617. doi:10.1103/PhysRevC.87.014617.

[5] O. Litaize, O. Serot, L. Berge, The European Physical Journal A 51 (12) (2015) 177. doi:10.1140/epja/i2015-15177-9.

[6] P. Talou, T. Kawano, I. Stetcu, J. P. Lestone, E. McKigney, M. B. Chadwick, Phys. Rev. C 94 (2016) 064613. doi:10.1103/PhysRevC.94.064613.

[7] G. Rimpault, D. Bernard, D. Blanchet, C. Vaglio-Gaudard, S. Ravaux, A. Santamarina, Physics Procedia 31 (2012) 3 – 12, gAMMA-1 Emission of Prompt Gamma-Rays in Fission and Related Topics. doi:https://doi.org/10.1016/j.phpro.2012.04.002.

[8] Nuclear data high priority request list of the nea (req. id: H.3, h4), http://www.oecd-nea.org/dbdata/hprl/hprlview.pl?ID=421 (2006).

[9] I. Stetcu, P. Talou, T. Kawano, M. Jandel, Phys. Rev. C 88 (2013) 044603. doi:10.1103/PhysRevC.88.044603.

[10] Wilson, J. N. and Lebois, M. and Qi, L. and Amador-Celdran, P. and Bleuel, D. and Briz, J. A. and Carroll, R. and Catford, W. and De Witte, H. and Doherty, D. T. and Eloirdi, R. and Georgiev, G. and Gottardo, A. and Goasduff, A. and Hadyńska-Klęk, K. and Hauschild, K. and Hess, H. and Ingeberg, V. and Konstantinopoulos, T. and Ljungvall, J. and Lopez-Martens, A. and Lorusso, G. and Lozeva, R. and Lutter, R. and Marini, P. and Matea, I. and Materna, T. and Mathieu, L. and Oberstedt, A. and Oberstedt, S. and Panebianco, S. and Podolyák, Zs. and Porta, A. and Regan, P. H. and Reiter, P. and Rezynkina, K. and Rose, S. J. and Sahin, E. and Seidlitz, M. and Serot, O. and Shearman, R. and Siebeck, B. and Siem, S. and Smith, A. G. and Tveten, G. M. and Verney, D. and Warr, N. and Zeiser, F. and Zielinska, M., Phys. Rev. Lett. 118 22 (2017) 222501. doi:10.1103/PhysRevLett.118.222501.

[11] N. Fotiades, P. Casoli, P. Jaffke, M. Devlin, R. Nelson, T. Granier, P. Talou, T. Ethvignot, submitted to Phys.Rev.C (2018).

[12] W. Hauser, H. Feshbach, Phys. Rev. 87 (1952) 366–373. doi:10.1103/PhysRev.87.366.

[13] P. Jaffke, P. Möller, P. Talou, A. J. Sierk, Phys. Rev. C 97 (2018) 034608. doi:10.1103/PhysRevC.97.034608.

[14] A. Koning, J. Delaroche, Nuclear Physics A 713 (3) (2003) 231 – 310. doi:https://doi.org/10.1016/S0375-9474(02)01321-0.

[15] J. Kopecky, M. Uhl, Phys. Rev. C 41 (1990) 1941–1955. doi:10.1103/PhysRevC.41.1941.

[16] R. Capote, M. Herman, P. Obložinský, P. Young, S. Goriely, T. Belgya, A. Ignatyuk, A. Koning, S. Hilaire, V. Plujko, M. Avrigeanu, O. Bersillon, M. Chadwick, T. Fukahori, Z. Ge, Y. Han, S. Kailas, J. Kopecky, V. Maslov, G. Reffo, M. Sin, E. Soukhovitskii, P. Talou, Nuclear Data Sheets 110 (12) (2009) 3107 – 3214, special Issue on Nuclear Reaction Data. doi:https://doi.org/10.1016/j.nds.2009.10.004.

[17] A. Gilbert, A. G. W. Cameron, Canadian Journal of Physics 43 (8) (1965) 1446–1496. arXiv:https://doi.org/10.1139/p65-139, doi:10.1139/p65-139.

[18] C. Wagemans, E. Allaert, A. Deruytter, R. Barthélémy, P. Schillebeeckx, Phys. Rev. C 30 (1984) 218–223. doi:10.1103/PhysRevC.30.218.

[19] P. Schillebeeckx, C. Wagemans, A. Deruytter, R. Barthélémy, Nuclear Physics A 545 (3) (1992) 623 – 645. doi:https://doi.org/10.1016/0375-9474(92)90296-V.

[20] K. Nishio, Y. Nakagome, I. Kanno, I. Kimura, Journal of Nuclear Science and Technology 32 (5) (1995) 404–414. arXiv:https://doi.org/10.1080/18811248.1995.9731725,

doi:10.1080/18811248.1995.9731725.

[21] V. V. Verbinski, H. Weber, R. E. Sund, Phys. Rev. C 7 (1973) 1173–1185. doi:10.1103/PhysRevC.7.1173.

[22] I. Stetcu, P. Talou, T. Kawano, M. Jandel, Phys. Rev. C 90 (2014) 024617. doi:10.1103/PhysRevC.90.024617.

[23] P. Casoli, Etude de la production de fragments dans la fission induite par neutrons sur l'uranium-238, Ph.D. thesis, Université de Bordeaux (2003).

[24] I.-Y. Lee, Nuclear Physics A 520 (1990) c641 – c655. doi:https://doi.org/10.1016/0375-9474(90)91181-P.

[25] W. Urban, J. Durell, W. Phillips, A. Smith, M. Jones, I. Ahmad, A. Barnett, M. Bentaleb, S. Dorning, M. Leddy, E. Lubkiewicz, L. Morss, T. Rzaca-Urban, R. Sareen, N. Schulz, B. Varley, Zeitschrift für Physik A Hadrons and Nuclei 358 (2) (1997) 145–151. doi:10.1007/s002180050291.

[26] W. Younes, J. A. Becker, L. A. Bernstein, P. E. Garrett, C. A. McGrath, D. P. McNabb, G. D. Johns, R. O. Nelson, W. S. Wilburn, AIP Conference Proceedings 529 (1) (2000) 192–199. arXiv:https://aip.scitation.org/doi/pdf/10.1063/1.1361378, doi:10.1063/1.1361378.

A systematic TDDFT data for nuclear fission analysis - Tin isotopes

Takashi Nishikawa[1,2]*, Yoritaka Iwata*[2]*, and Satoshi Chiba*[2]
[1]Nuclear Engineering Ltd, Osaka 550-0001, Japan
[2]Tokyo Institute of Technology, Tokyo 152-8550, Japan

Abstract
Dissipation of nuclear many-body systems is studied by means of TDDFT+ Langevin model. Much attention is paid to the energy dependence of the friction coefficient, identifying the thermodynamic property of nuclear medium for given nucleon numbers, neutron-richness, and energies. In this article, following the preceding work showing a systematics on $Z = 92$ to 100 nuclei, macroscopic friction coefficients for $Z = 50$ nuclei are derived from a microscopic framework. The comparison between $Z = 92$ and $Z = 50$ cases clarifies the similarity and the difference of fissions between heavy and medium mass nuclei. It is not only the completion of a systematic theoretical database, but also pinning down the dissipative features of the r-process nuclei. In addition, the knowledge about the obtained fission probability and fission fragment yields is expected to be useful for both nuclear synthesis and nuclear engineering.

1 Introduction

Nuclear friction arises from the dissipation effect. Indeed, the microscopic dissipation in quantum dynamics leads to the macroscopic friction effect to be found in the collective dynamics. Needless to say, the dissipation is a concept to be associated with the time-reversal symmetry breaking. That is, the sufficient understanding of nuclear dissipation is expected to be useful for clarifying not only the breaking mechanism of time reversal symmetry, but also the origin of friction-like effect in the sub-atomic collective dynamics.

In this article, following the preceding work [1] showing the systematics on $Z = 92$ region (Uranium, Plutonium isotopes and so on), the dissipation in many-nucleon systems is studied by the collective friction effects. A systematics of friction coefficients for Tin isotopes (in the following, we call "Sn isotopes") is presented. As distinct from $Z = 92$ region, the investigation on $Z = 50$ region clarifies that the energy dependence itself is complicated.

2 Proposed method

The analysis of quasi-fission events is made based on the TDDFT+Langevin model being introduced in [1] after our preparatory works on nuclear fission [2–5], where the terminology "TDDFT" stands for the time-dependent density functional theory. The TDDFT+Langevin model, at the present stage, consists of three steps:

(i) calculate collision dynamics by the TDDFT to obtain the microscopic wave function,
(ii) using the wave function, the averaged friction coefficient is calculated,
(iii) using the friction coefficient, the fission fragment yields are calculated by the Langevin model,

where Sky3D [6] is employed for the TDDFT calculations, and fission dynamics is stochastically calculated by by 4D Langevin code [8].

By hybridizing the TDDFT and the Langevin calculations, the total amount of dissipation during the reaction is calculated as the averaged friction coefficient in macroscopic dynamics. The averaged friction coefficient means that the friction (function of energy and time) is averaged for time. This treatment

is practically reasonable in terms of providing a coefficient to the Langevin calculations and obtaining dissipation effect comparable to experiments, because only the time-averaged value can be measured in experiments. The outline of the above three steps is explained in the following (for details, see Ref. [1]).

(i) TDDFT calculation

For the TDDFT calculations, we employ three different effective nuclear interactions: SV-bas [9], SLy4 [10], and SkM* [11]. We carried out the TDDFT calculations of symmetric quasi-fission processes

$$ {}^{A}Z + {}^{A}Z \;\rightarrow\; {}^{2A}2Z \;\rightarrow\; {}^{A}Z + {}^{A}Z \,, \tag{1} $$

where A and Z are a mass number and a proton number respectively. In particular, Z is fixed to $Z = 50$ in this research, and several excitation energies for each choice of A are examined. Here the energy E is taken as the initial energy of the collision, and E/A is from 3 MeV to 10 MeV. The value of A is 100, 104, 108, $\cdots$ 132. Consequently, the TDDFT wave function including all the information about microscopic collision dynamics is obtained. The distance $R(t)$ between the center-of-mass of two colliding nuclei is extracted from the TDDFT wave function. For the details of $R(t)$, see Ref. [12]. It is remarkable that the collective distance $R(t)$ is affected by the microscopic quantum effect such as the shell effect.

(ii) Friction coefficient

By substituting $R(t)$ into the macroscopic equation of motion describing nuclear dynamics,

$$ \mu\ddot{R}(t) + \frac{dV(R(t),E)}{dR} + \gamma(R(t),E)\dot{R}(t) = 0 \,, \tag{2} $$

the master equation for the collective motion for a given energy E is obtained, where the reduced mass μ is a constant, and the potential V can disappear by adjusting the initial time t_i and final time t_f to satisfy $V(R(t_i),E) = V(R(t_f),E)$. Note that $V(R(t),E)$ includes both the nuclear and the Coulomb interactions. Though the determination scheme is not exactly the same, the combination of the TDDFT and Eq. (2) has already been studied in Refs. [13, 14]. Consequently, for an input $R(t)$, the friction coefficient γ for the collective dynamics is obtained as an output, where the dissipation effect included in the TDDFT is known as the quantum one-body dissipation. The averaged friction coefficient $\overline{\gamma}(E) = \int_{t_i}^{t_f} \gamma(R(t),E)\{\dot{R}(t)\}^2 dt / \int_{t_i}^{t_f} \{\dot{R}(t)\}^2 dt$ is obtained by

$$ \overline{\gamma}(E) = \frac{\{\frac{1}{2}\mu\dot{R}^2(t_i) + V(t_i)\} - \{\frac{1}{2}\mu\dot{R}^2(t_f) + V(t_f)\}}{\int_{t_i}^{t_f}\{\dot{R}(t)\}^2 dt} \,, \tag{3} $$

where $\overline{\gamma}(E)$ is averaged for time t. t_i and t_f are usually taken as the initial and the final time of reaction. Again, this treatment is practically reasonable in terms of introducing a coefficient to the Langevin calculations and obtaining comparable theoretical results to experiments. Note that $\overline{\gamma}(E)$ values at extraordinary energies, which are too low or too high to be treated by the TDDFT, are also obtained using the extrapolation method being explained in Ref. [1].

(iii) Langevin calculation

Fission dynamics is obtained by the Langevin model equations:

$$ \begin{aligned} \frac{dq_\mu}{dt} &= m_{ij}^{-1} p_j, \\ \frac{dq_\mu}{dt} &= -\frac{dV}{dq_\mu} - \frac{1}{2}\frac{d}{dq_\mu} m_{ij}^{-1} q_i q_j - \gamma_{ij} m_{ij}^{-1} p_j - g_{ij} R_j, \end{aligned} \tag{4} $$

where a part of γ_{ij}, more precisely γ_{11}, is replaced with $\overline{\gamma}(E)$, and the values obtained by the Wall-and-Window formula [7] are employed for the other components. Indices i, j $(1 \le i, j \le 4)$ mean collective

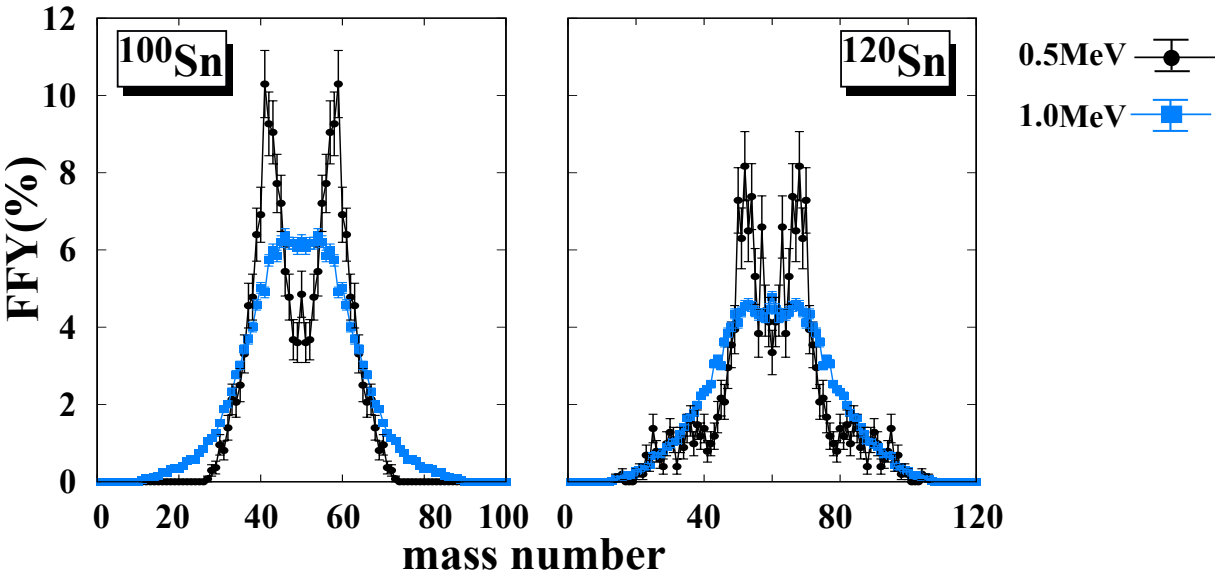

Fig. 1: (Color online) Fission fragment yield (FFY) calculated by the TDDFT+Langevin model (SV-bas). The FFYs at 0.5 MeV and 1 MeV per nucleon are shown for ^{100}Sn and ^{120}Sn. The corresponding fission probability is 0.006 % for 0.5 MeV, and 2.61 % for 1.0 MeV in case of ^{100}Sn, and 0.004 % for 0.5 MeV, and 2.67 % for 1.0 MeV in case of ^{120}Sn.

Table 1: The friction coefficient $\overline{\gamma}(E)$ of unit $\hbar$ is calculated for Sn isotopes (Z=50) using three effective nuclear interactions (SV-bas, SLy4, and SkM*). The energy is $E = 20$ MeV (E/A ∼0.17 MeV) being calculated by the extrapolation method. In the column "Average", the averaged values for those three interactions are shown.

N	SV-bas	SLy4	SkM*	Average
54	52.0	41.0	50.9	48.0
58	52.6	44.8	43.9	47.1
62	55.1	47.3	45.2	49.2
66	57.7	49.9	52.1	53.2
70	60.7	52.0	53.8	55.5
74	63.7	53.9	57.4	58.3
78	67.6	57.6	57.4	60.9
82	61.1	54.3	56.0	57.1

coordinate. Detailed explanation is shown in Ref [8]. Although the stochastic aspect of the dynamics is introduced in the Langevin model, its dynamics accounts only for the nucleus degrees of freedom. The Langevin calculations enable us to incorporate the stochastic aspect of reaction dynamics resulting in both fission and fusion dynamics.

As a result, the refined friction coefficients for $^{2A}2Z$ are obtained in an energy dependent manner, and they are employed in the Langevin calculation. The coefficient is refined in terms of including the microscopic quantum effect obtained by a less phenomenological and time-dependent theoretical framework.

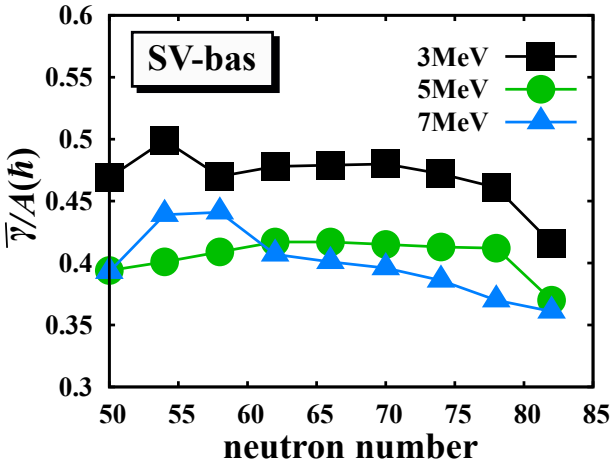

Fig. 2: (Color online) Energy and mass dependence of friction coefficient $\overline{\gamma}$ per nucleon, where A denotes the mass number. The amplitude of $\overline{\gamma}$ stands for the amount of dissipated energy at a given excitation energy.

3 Result

Figure 1 shows the fission fragment yield (FFY) for ^{100}Sn and ^{120}Sn. The transitions from symmetric fission to asymmetric fission are well described. In this case, the mass number is too small for low-energy fission events including spontaneous fission to take place, while collision-fissions such as fusion-fission and quasi-fission appear by giving a sufficient high energy. In this case, we found no corresponding experimental fission data to compare, so that the calculation is carried out as the prediction for future research in the context of figuring out the role of collision-fission events in nuclear synthesis, as well as for the completion of the theoretical $\overline{\gamma}$ database. By comparing low and high energy cases, the energy dependence is remarkable in which asymmetric fissions are favored for lower energies and symmetric fissions are favored for higher energies. The shell effect is seen in the mass yield $A = N + Z = 40$ or 48. $A = 40$ nuclei are more produced in the fission of ^{100}Sn, while $A = 48$ nuclei are mainly obtained in the fission of ^{120}Sn. For the higher energies, fission probabilities are calculated to be around 3% for both ^{100}Sn and ^{120}Sn. Fission events with quite small fission probability are calculated based on the microscopic TDDFT dynamics. The present prediction is worth believing by accounting for the agreement between the TDDFT+Langevin result and the experimental FFY in Uranium and Plutonium isotopes [1].

The coefficient $\overline{\gamma}$ at the energy closed to the Coulomb barrier is shown in Table 1. Fission at or around the barrier energy is useful to analyze the low-energy fission events such as quasi-fission, photo-fission, neutron-induced fission and so on.

Energy and mass dependence of $\overline{\gamma}$ can be found in Fig. 2. As a trend, the amplitude of $\overline{\gamma}$ becomes smaller for higher energies. Such a trend is reasonable, because the shorter duration time in higher energy collisions should lead to the smaller amount of dissipated energy in reaction processes. As a more weak dependence, the value of $\overline{\gamma}$ becomes smaller for more neutron-rich cases. However, Note that the neutron number dependence is not definitely monotonous. Although some local extremal values can be found in Fig. 2: e.g., maximum at $N = 54$ and $E/A = 3$ MeV, their origins are not easy to be identified, because many factors such as shell effect and/or pauli effect may contribute in certain complicated manners. The detail investigation on the energy and mass dependence of $\overline{\gamma}(E)$ is a future problem in which the different properties of effective nuclear interaction should be investigated more carefully. Consequently, for Sn isotopes, the energy dependence ($\sim$0.1 $\hbar$ difference in $\overline{\gamma}/A$) is more prominent than the neutron-richness or mass dependence ($\sim$0.05 $\hbar$ difference in $\overline{\gamma}/A$). With respect to the total amount of dissipated energy during the fission process, the most dissipative isotope can be different depending on the energy. In

Table 2: The friction coefficient $\overline{\gamma}(E)$ of unit $\hbar$ calculated for Sn isotopes (Z=50) using three effective nuclear interactions (SV-bas, SLy4, and SkM*). The energy is taken for 3 MeV, 5 MeV and 7 MeV per nucleon. In the column "Average", the averaged values for those three interactions are shown.

a) $E/A = 3$ MeV

N	SV-bas	SLy4	SkM*	Average
50	46.9	43.0	49.0	46.3
54	51.9	44.2	50.5	48.8
58	50.7	47.8	50.8	49.8
62	53.6	48.3	52.1	51.3
66	55.6	49.2	53.4	52.7
70	57.6	50.3	55.5	54.5
74	58.5	51.1	56.2	55.3
78	59.0	51.9	57.1	56.0
82	54.9	48.8	53.3	52.4

b) $E/A = 5$ MeV

N	SV-bas	SLy4	SkM*	Average
50	39.4	32.7	36.4	36.1
54	41.7	35.3	39.5	38.8
58	44.2	37.4	41.7	41.1
62	46.8	39.0	43.7	43.1
66	48.3	40.2	44.9	44.5
70	49.8	41.3	45.9	45.7
74	51.2	41.7	46.7	46.5
78	52.7	40.2	46.3	46.4
82	48.8	37.1	43.1	43.0

c) $E/A = 7$ MeV

N	SV-bas	SLy4	SkM*	Average
50	39.3	30.0	35.1	34.8
54	45.6	30.8	39.6	38.7
58	47.6	31.9	38.0	39.2
62	45.6	33.7	39.2	39.5
66	46.6	34.4	40.1	40.4
70	47.5	34.6	40.8	41.0
74	47.8	33.1	40.0	40.3
78	47.4	31.6	38.4	39.1
82	47.7	30.9	37.8	38.8

fact, ^{128}Sn ($N = 78$) is the most dissipative for low energies up to $E/A = 6.0$ MeV (SV-bas), while isotopes with smaller neutron numbers are rather dissipative for higher energies; ^{124}Sn ($N = 74$), ^{120}Sn ($N = 70$), and ^{116}Sn ($N = 66$) are the most dissipative nuclei for $E/A = 7.0, 8.0$ and 9.0 MeV, respectively. This fact implies that the neutron-richness contributes to the dissipation (leading to fission) rather prominently for higher energies. Accordingly, the energy and mass dependences of $\overline{\gamma}$ are shown. It will provide us a clue to discover the origin of quantum one-body dissipation.

4 Summary

The friction coefficients utilizable to the Langevin calculations have been obtained based on the TDDFT framework. In a more microscopic point of view, possible dissipation for a given excitation energy is systematically obtained for Sn isotopes. Since the low-energy heavy-ion reactions ($\sim E/A < 10$MeV) have known to be well described by the TDDFT(for a review, see [15]), the reliability of proposed method is expected to be sufficiently high.

The obtained coefficient has been used in the TDDFT+Langevin model calculation. It is the first time attempt to carry out the TDDFT+Langevin model calculations for medium-mass nuclei. Even based on the quantum and less-phenomenological input, it will open-up a new way to study the stability and the related stochastic dynamics of medium and heavy mass nuclei. The proposed method requires only a system of light-weight calculations, so that it is advantageous to make up a large-scale theoretical database.

In terms of the future utility in nuclear engineering, the obtained coefficients are summarized in Table 2. Table 2 shows the calculated coefficient $\overline{\gamma}$ for Sn isotopes ($Z = 50$). The $\overline{\gamma}$ values depend more prominently on the energy than on neutron-richness. The smaller $\overline{\gamma}$ is calculated for a heavier case ($N = 82$), where such a trend can be found for $Z = 92$ region. According to the preceding result [1], $\overline{\gamma}$ values distribute from 110 to 120 for the uranium isotopes ($N = 142$ to 150). It also tells us another aspect of the mass dependence; i.e., Z dependence. Table 2 provides a part of theoretical database of systematic friction coefficients.

Sn isotopes are regarded as the fission product of U and Pu isotopes. From this point of view, calculating the FFY of Sn is the product of the secondary fission. Asymmetric fission producing $A = 40$ or 48 nucleus occurs for low energy, while symmetric fission producing $A = 50 \sim 60$ occurs for high energy. Because the secondary fission can occur when the energy in the field of nuclear synthesis or nuclear reactor is sufficiently high, the FFYs of Sn isotopes constrain a possible scenario of nuclear synthesis, as well as a possible control of nuclear reactors.

Acknowledgement

Numerical computation was carried out at a workstation system at Tokyo Institute of Technology (AEGIS system). This work was supported by JSPS KAKENHI Grant No. 17K05440. One of the authors (Y. I.) is grateful to Prof. Dr. Hans Feldmeier for presenting an essential idea at the preparatory stage of this research.

References

[1] T. Nishikawa, Y. Iwata, and S. Chiba, in preparation.

[2] T. Nishikawa, Y. Iwata, and S. Chiba, to appear in JAEA-Conf (2018).

[3] Y. Iwata and S. Heinz, Exotic Nuclei, EXON-2012, World Scientific, 153 (2013).

[4] Y. Iwata and S. Heinz, CERN Proceedings 2012 - 002, 241 (2013).

[5] Y. Iwata, JAEA-Conf 2015-003, INDC(JPN)-201, 93 (2015).

[6] J. A. Maruhn, P.-G. Reinhard *et al.*, Comput. Phys. Commun. **185** 2195 (2014).

[7] T. Dossing and J. Randrup, Nucl. Phys. A **475** 557-568 (1987),

[8] M. D. Usang, F. A. Ivanyuk, C. Ishizuka, and S. Chiba, Phys. Rev. C **94** 044602 (2016).

[9] P. Klüpfel, P.-G. Reinhard, J. Bürvenich, and J. A. Maruhn, Phys. Rev. C **79** 034310 (2009).

[10] E. Chabanat, P. Bonche, P. Haensel, J. Meyer, and F. Schaeffer, Nucl. Phys. **A 635**, 231 (1998).

[11] J. Bartel, P. Quentin, M. Brack, C. Guet, and H.B. Hakansson, Nucl. Phys. **A 386**, 79 (1982).

[12] Y. Iwata, H. Feldmeier, and J. A. Maruhn, AIP Conf. Proc. 1377, 365 (2011).

[13] K. Washiyama and D. Lacroix, Phys. Rev. C **78** 024610 (2008).

[14] K. Washiyama, D. Lacroix, and S. Ayik, Phys. Rev. **C 79** 024609 (2009).
[15] C. Simenel, and A. S. Umar, Prog. Part. Nucl. Phys. **103**, Nov. 2018, 19 (2018).

Fission Product Yield Calculation by Hauser-Feshbach Statistical Decay and Beta Decay

Shin Okumura[1]*, Toshihiko Kawano*[2]*, Patrick Jaffke*[2]*, Patrick Talou*[2]*, Tadashi Yoshida*[1]*, Satoshi Chiba*[1]
[1] Laboratory for Advanced Nuclear Energy, Tokyo Institute of Technology, 2-12-1 Ookayama, Meguro-ku, Tokyo 152-8550, Japan
[2] Theoretical Division, Los Alamos National Laboratory, Los Alamos, NM 87545, USA

Abstract

We demonstrate calculations of the prompt neutron emission, the independent and cumulative fission product yield (FPY), decay heat, and delayed neutron yield of ^{235}U(n,f) starting from a set of the primary fission fragment distribution. We employ the recently developed Hauser-Feshbach fragment decay code, HF^{3}D, to calculate the prompt neutron multiplicity and the independent FPY. The β-decay chain of each nuclide in the independent FPY is tracked to obtain the cumulative FPY. The decay heat and delayed neutron yield are calculated by the summation calculation method. Comparisons of the fission and β-decay observables calculated in this work, experimental data, and the evaluated nuclear data libraries provide an important insight for improvements of evaluation of the nuclear data.

1 Introduction

The nuclear fission and decay process of the fission fragment constitute of many different physical phenomena. Due to its complexity, accurate predictions of fission observables by theoretical calculations still remain difficult. At least three processes need to be taken into account for the neutron induced fission of fissile nuclides such as ^{235}U. (1) The formation of compound nucleus, the change of its shape to the saddle-point, and the scission are defined as the process before the scission. (2) After the scission, complementary primary fission fragments are fully accelerated by the Coulomb repulsion and they are highly excited. The fission fragment, which can be characterized by its charge (Z), mass (A), excitation energy (E_x), spin (J), and parity (Π), are then de-excites by emitting the prompt neutrons and photons to reach their ground-state or long-lived isomeric states. (3) The post particle emitted fission fragments, also called fission products (FP), then decay by β-decay leading further delayed neutron and photon emissions.

Due to the very short timescale of the nuclear fission, it makes the direct experimental observation difficult, and very limited experimental information is accessible for (1) to (2). Hence the present evaluation of nuclear data is compiled by combining available experimental data and some phonomenological models, e.g., Los Alamos model (LAM) for prompt fission neutron spectrum [1], Wahl systematics for independent fission product yield (FPY) [2], to supplement scarce experimental data. In addition, such FPY and the other observables are evaluated separately and there are not consistent with each other [3]. There is no certain models and codes that allow us to calculate all of the fission observables simultaneously and consitently from the process (1) through (3). In particular, energy dependence of fission observables has not been well modelled.

In this study, we demonstrate the incident neutron energy dependent calculations of the decay processes of the fission fragment from (2) through (3) starting with the primary fission fragment distribution of ^{235}U(n,f) that characterized by $Y(A, Z, E_{ex}, J, \Pi)$. We discuss the calculated independent and cumulative FPY, decay heats, delayed neutron yields, and their energy dependence compared with the experimental and evaluated nuclear data libraries. We limit our calculation to ^{235}U(n,f) and the incident neutron energy up to 5 MeV, which is the multi-chance fission threshold.

2 Methods

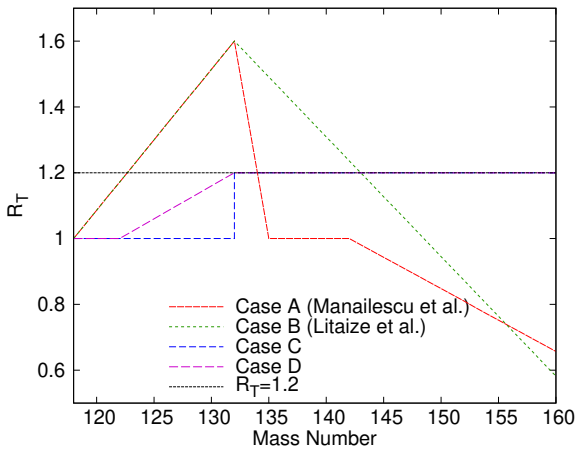

Fig. 1: Variations of the anisothermal parameter R_T as a function of the heavy fragment mass.

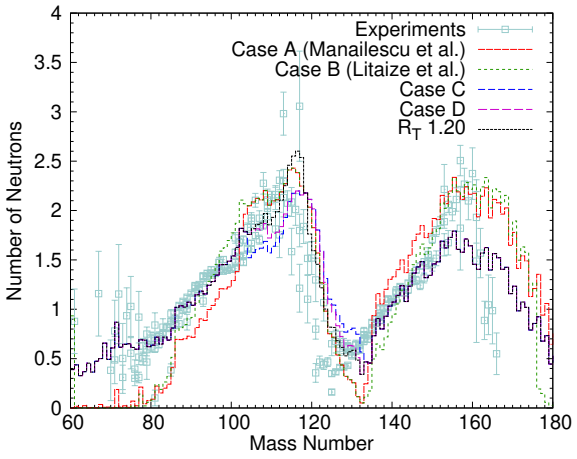

Fig. 2: Comparison of prompt neutron multiplicities of five R_T models.

2.1 Hauser-Feshbach approach

For the de-excitation process of the fission fragments described as (2) in the previous section, a straightforward approach is to apply the Hauser-Feshbach theory to the statistical decay of primary fission fragment pairs. However, the Hauser-Feshbach calculatiion requires many input model parameters. The fission fragment distribtuions are the key ingredients in prompt neutron emission calculations. In order to perform such calculations, one needs to integrate all of the distributions characterizing each of the primary fission fragment. Such integrations have been done by the sampling through Monte Carlo. However, if their distributions have extremely small probability such as FPY, which varies in the order of magnitude typically from 10^{-15} to 10^{-2}, they never samples such cases in a reasonable computation time.

Instead of performing the integration over all probabilities by Monte Carlo sampling, we developed the Hauser-Feshbach Fission Fragment Decay (HF^{3}D) model to calculate various fission observables, i.e., prompt neutron multiplicity ($\overline{\nu}$), independent FPY, and isomeric ratio, simultaneously [4]. The HF^{3}D model performs a numerical integration over the whole ranges of the primary fission fragment yield, their initial excitation energy, spin and parity distributions. In this model, the neutron multiplicities $\overline{\nu}_{l,h}^{(k)}$ are given by integrating the neutron evaporation spectrum $\phi_{l,h}^{(k)}$ from the light or heavy fragment in the center-of-mass system,

$$\overline{\nu}_{l,h}^{(k)} = \int dE_x \sum_{J\Pi} \int d\epsilon \; R(J,\Pi) G(E_x) \phi_{l,h}^{(k)}(J,\Pi,E_x,\epsilon) \; , \tag{1}$$

where $R(J,\Pi)$ is the probability of nucleus having the state of spin J and parity Π, and $G(E_x)$ is the distribution of excitation energy.

2.2 Generation of fission fragment distributions

Scince the general concept of the HF^{3}D model and the generation of the fission fragment distributions have been discussed elsewhere [4], a brief description will be given here. The primary fission fragment yields are generated form the five Gaussians fitted to the experimentally available mass distributions of neutron induced fission of ^{235}U. A charge distribution for each mass is generated by the Z_p model in the Wahl systematics [2]. The total kinetic energy (TKE) as a function of primary fission fragment mass

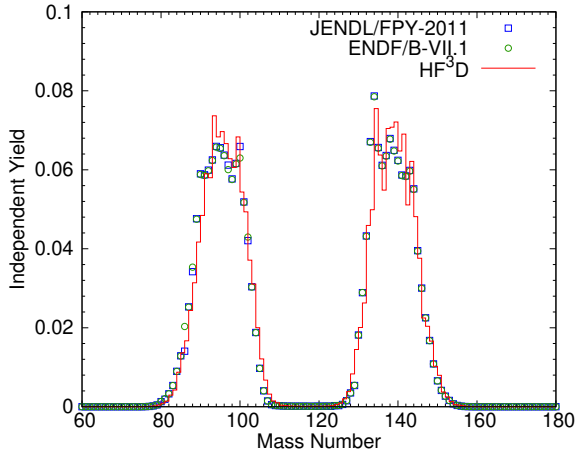

Fig. 3: The mass total of independent FPY of ^{235}U(n$_{th}$,f) calculated by the HF^{3}D model shown with JENDL/FPY-2011 and ENDF/B-VII.1.

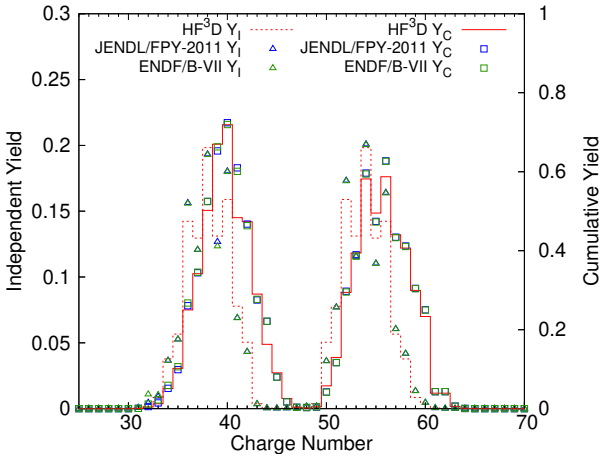

Fig. 4: The charge total of independent(Y_I) and cumulative(Y_C) FPY of ^{235}U(n$_{th}$,f) calculated by the HF^{3}D model with JENDL/FPY-2011 and ENDF/B-VII.1.

is generated based on the fitting an analytical function to the experimental data. The total excitation energy (TXE) can be calculate from TKE by taking into account the energy balance of the reaction. The incident neutron energy dependence of the fission fragment distributions is generated by interpolations of the mass distribution and Wahl's Z_p model.

2.3 Energy sharing between two primary fragments

The evaporating prompt neutrons take away large energy from the primary fission fragments. There is no complete explanations that tells us how the available TXE at a full acceleration is partitioned between two complemental fragments. In the HF^{3}D model, we calculated the energy sharing between the complemental light and heavy fragments by the anisothermal model which is defined by the ratio of effective temperature T_L and T_H of the complemental light and heavy fission fragments expressed as

$$R_T = \frac{T_L}{T_H} = \sqrt{\frac{a_H U_L}{a_L U_H}}, \tag{2}$$

where U is the excitation energy and a is the level density parameter [5]. We took an average value of R_T = 1.2 as previously proposed for ^{235}U(n$_{th}$.f), ^{239}Pu(n$_{th}$.f), and ^{252}Cf(SF) [6, 7].

There exist some different estimates of energy sharing by R_T. Figure 1 shows five cases of different R_T functions. The linear R_T dependence as a function of the heavy fragment mass have been reported for the Spontaneous fission of ^{252}Cf [8] and ^{235}U(n, f) [9] shown as the Case A and B in Figure 1, respectively. Both cases divide minimum excitation energy into the heavy fragment at A_H = 132 because the nuclei with A_H around 132 are almost spherical and the most of deformation energy should be taken by the complementary light fragments. Furthermore, based on the asumption that the symmetrically divided fission fragments should have the same temperatures, we additionally examined two other cases with R_T = 1 around symmetric region. For the case C in Figure 1, R_T = 1 for A_H < 132 and the average R_T for A_H > 132 were used. For the case D, R_T = 1 for A_H < 122, the average R_T for A_H > 132, and linear dependence between A_H = 122 and 132 were used.

2.4 Beta decay

The cumulative FPY can be calculated using the independent FPY by adopting the Bateman equation to each FPs with the decay data library, which contains the radionuclide half-lives and branching ratios.

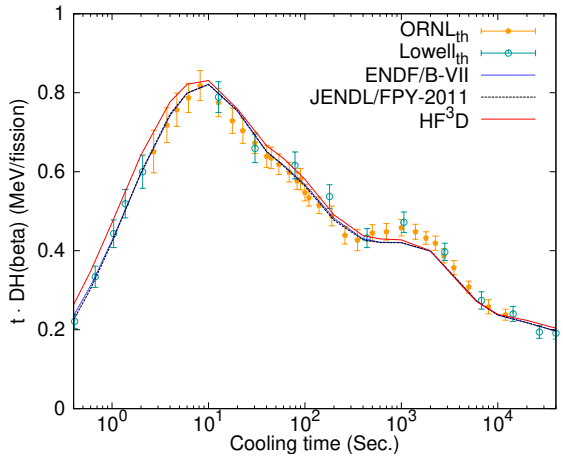

Fig. 5: Decay heat from β emission shown together with experimental data from Lowell and Oak Ridge National Laboratory.

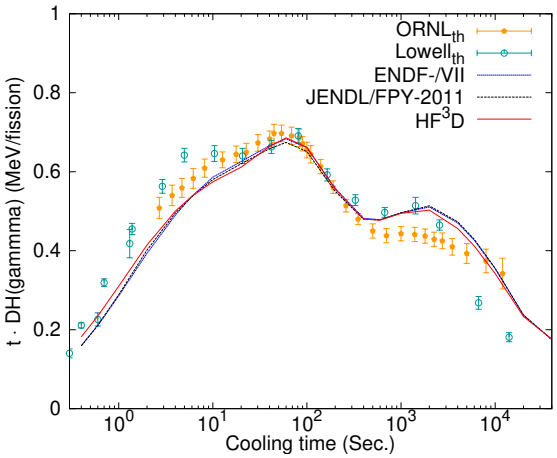

Fig. 6: Decay heat from γ emission shown together with experimental data from Lowell and Oak Ridge National Laboratory.

Suh calculations are performed using a code implemented in HF^{3}D model. The summation calculation predicts aggregate properties of the fission products such as decay heat. The decay heat and the delayed neutron calculations are the sum of the β and γ energies and neutron released from all individual β-decay nuclides [10]. The calculation requires an independent FPY as an input.

3 Results

3.1 Prompt neutron multiplicity

Figure 2 shows the calculated neutron multiplicities ($\overline{\nu}$) of ^{235}U(n$_{\rm th}$,f) as a function of the fission fragment mass for five cases compared with some experimental data [11]. The both of linear R_T functions of [8, 9] show sudden decrease in $\overline{\nu}$ at A_L < 80 and overestimate at A_H > 160. The cases C and D show similar mass dependence of $\overline{\nu}$ compared with the $R_T = 1.2$ case. By comparison with some experimental results [11], the constant $R_T = 1.2$ shows a good agreement with overall mass range. From these results, we concluded that the use of constant R_T for the whole mass range can be quite reasonable for ^{235}U(n$_{\rm th}$,f) case. The average $\overline{\nu}$ for the case R$_{\rm T}$ = 1.2 is 2.38 which is slightly lower than that of the evaluated value 2.41 in ENDF/B-VII.1.

3.2 Independent and cumulative FPY

Figure 3 illustrates the fission product mass dependence of the independent FPY for ^{235}U(n$_{\rm th}$,f). The calculation well reproduce the structures of the independent FPY, seen as peaks (A = 99 and 134) and dips (A = 98 and 136). These fine structures can be seen in both ENDF/B-VII and JENDL/FPY-2011 libraries. The peaks at A = 99 and 134 are due to the high production ratio of ^{99}Zr and ^{134}Te, respectively, and the isobar productions in the same mass. The calculated independent FPY reproduces not only the case with higher production yield region but also very low yield regions down to 10^{-15}.

The cumulative FPY was obtained by performing the β-decay calculation using the calculated independent FPY. Since the β decay and the following delayed neutron emission hardly affect the mass yield, the masses of FP are mostly governed by the independent FPY. We thus compare the charge distribution of FPY before and after β decay. As shown in Figure 4, the charge distribution of the independent FPY has quite clear even-odd effect and the mass distribution of the cumulative FPY shows the clear shift towards the heavy charge. A relatively large discrepancy appears at Z = 41 (Nb). This is mainly due to a treatment of long-lived FP in the decay chain. In our β-decay calculations, we treat

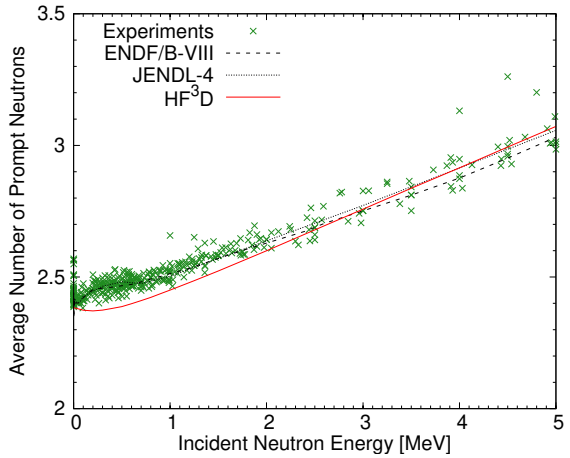

Fig. 7: Energy dependence of calculated prompt neutron multiplicity.

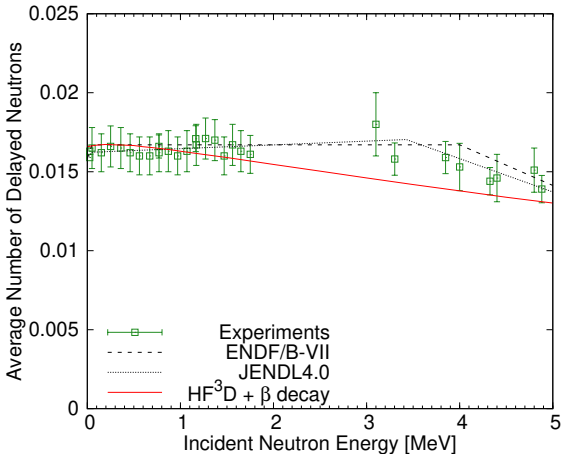

Fig. 8: Energy dependence of calculated delayed neutron yield.

the fission products with half-lives longer than 1,000 years as stable nuclides. JENDL/FPY-2011 and ENDF/B-VII treat ^{93}Zr ($T_{1/2}$ = 1.61 $\times$ 10^6 years) which is the β-decay precursor of ^{93}Nb. However, the overall appearance of the calculated cumulative FPY shows a good agreement with ENDF/B-VII and JENDL/FPY-2011 libraries.

3.3 Summation calculation

The β- and γ-energy components in the decay heat were obtained separately. Figure 5 shows the decay heat multiplied by the cooling time from the fission burst as a function of t. The calculated decay heat from the β emission agrees with the experimental data from Lowell and Oak Ridge National Laboratory [12,13]. The major differences occurred in the decay heat from the γ emissions below 10 second after the fission burst. By comparing with the cases using independent FPY of JENDL/FPY-2011 and ENDF/B-VII, ^{97g}Y is highlighted to the cause of the overestimating. In this study, any of adjustments were introduced at each calculation steps. For the better evaluation of FPY, more detailed investigation on the starting distribution and introducing some adjustments would be required.

3.4 Energy dependence of prompt and delayed neutron emissions

The number of emitted neutrons obviously play a main role for governing the fission product yields in both prompt and delayed emissions. Figure 7 shows the incident neutron energy dependence of the prompt neutron multiplicity calculated with the HF^{3}D model compared with the experimental data. Below 1 MeV, our results show an opposite tendency to experimental and evaluated data, however, the differences are still quite small. On the contrary, the number of the experimental data of the delayed neutron emission yields (ν_d) are less sufficient in particular between 1.5 and 5 MeV. Figure 8 shows the incident neutron energy dependence of ν_d compare with JENDL-4.0 and ENDF/B-VII. The HF^{3}D model calculations are approximately follow the experimental data below 5 MeV. In both evaluated libraries, ν_d slightly increase up to around 4 MeV and sharply decrease above 4 MeV. This sharp decrease is attributed to the effect of the multi-chance fission.

4 Conclusion

The independent FPY of ^{235}U(n,f) is calculated with the HF^{3}D model by applying the Hauser-Feshbach theory to the fission fragment decay. The cumulative FPY, the decay heat and delayed neutron are also calculated by the β decay calculation and the summation calculation using the calculated independent

FPY as an input. We demonstrated the calculations of the fission observables such as independent and cumulative FPY, $\overline{\nu}$, and ν_d simultaniously and consistently starting from one fission fragment distribution. These fission observables were reproduced reasonably well comparing with experimental data and evaluated nuclear data libraries.

We extended our calculation up to 5 MeV where the multi chance fission takes place. The incident energy dependence of $\overline{\nu}$ and ν_d was compared with experimental data and evaluated nuclear data libraries. Although there are some discrepancies between the calculated and experimental results, the overall predictions are quite successful. This method should be a quite powerful tool for evaluating fission observables in the future.

5 Acknowledgeents

This work was partially supported by the grant 'Development of prompt-neutron measurement in fission by surrogate reaction method and evaluation of neutron- energy spectra,' entrusted to JAEA by Ministry of Education, Culture, Sports, Science and Technology. This work was partly carried out under the auspices of the National Nuclear Security Administration of the U.S. Department of Energy at Los Alamos National Laboratory under Contract No. DE-AC52-06NA25396.

References

[1] David G. Madland and J. Rayford Nix. New calculation of prompt fission neutron spectra and average prompt neutron multiplicities. *Nuclear Science and Engineering*, 81(2):213–271, 1982.

[2] A. C. Wahl. Systematics of fission-product yields. Technical Report LA-13928, Los Alamos National Laboratory, 2002.

[3] Patrick Jaffke. Identifying inconsistencies in fission product yield evaluations with prompt neutron emission. *Nuclear Science and Engineering*, 190(3):258–270, 2018.

[4] S. Okumura, T. Kawano, P. Jaffke, P. Talou, and S. Chiba. ^{235}U(n, f) independent fission product yield and isomeric ratio calculated with the statistical Hauser-Feshbach theory. *Journal of Nuclear Science and Technology*, 0(0):1–15, 2018.

[5] T. Ohsawa, T. Horiguchi, and H. Hayashi. Multimodal analysis of prompt neutron spectra for ^{237}Np(n,f). *Nuclear Physics A*, 653(1):17 – 26, 1999.

[6] P. Talou, T. Kawano, and L. Bonneau. Prompt fission neutrons as probes to nuclear configurations at scission. *AIP Conference Proceedings*, 1005(1):198–201, 2008.

[7] P. Talou. Advanced modeling of prompt fission neutrons. *AIP Conference Proceedings*, 1175(1):261–268, 2009.

[8] O. Litaize and O. Serot. Investigation of phenomenological models for the monte carlo simulation of the prompt fission neutron and γ emission. *Phys. Rev. C*, 82:054616, Nov 2010.

[9] C. Manailescu, A. Tudora, F.-J. Hambsch, C. Morariu, and S. Oberstedt. Possible reference method of total excitation energy partition between complementary fission fragments. *Nuclear Physics A*, 867(1):12 – 40, 2011.

[10] K. Oyamatsu, H. Takeuchi, M. Sagisaka, and J. Katakura. New method for calculating aggregate fission product decay heat with full use of macroscopic-measurement data. *Journal of Nuclear Science and Technology*, 38(7):477–487, 2001.

[11] K. Nishio, Y. Nakagome, H. Yamamoto, and I. Kimura. Multiplicity and energy of neutrons from 235U(nth,f) fission fragments. *Nuclear Physics A*, 632(4):540 – 558, 1998.

[12] J.K. Dickens, T.A. Love, J.W. McConnell, and R.W. Peelle. Fission-product energy release for times following thermal-neutron fission of ^{235}U between 2 and 14000 s. *Nuclear Science and Engineering*, 74(2):106–129, 1980.

[13] S. Li. Beta decay heat following ^{235}U, ^{238}U and ^{239}Pu neutron fission. *Ph.D. thesis*, 1997.

Description of fission: first comparison between microscopic and macroscopic-microscopic Potential Energy Surfaces

M. Verriere[1], T. Kawano[1], M.R. Mumpower[1], P. Talou[1] and N. Schunck[2]
[1] Los Alamos National Laboratory, Los Alamos, NM 87545, USA
[2] Lawrence Livermore National Laboratory, Livermore, CA 94551, USA

Abstract
The description of the fission process is challenging and has two modern interpretations: on one hand, the microscopic approaches and on the other hand, the macroscopic-microscopic approaches. From the perspective of macroscopic-microscopic approaches, the nucleus is treated as a macroscopic system in a first place, and microscopic corrections are then added. From the perspective of microscopic approaches, the focus is on the direct resolution of the quantum A-body problem with a 2-body interaction between the nucleons as the only ingredient. In this contribution, we compare these two approaches for the first time by analyzing the differences in both formalism as well as by a comparison of the different valleys in the potential energy surfaces (PES), with a focus on the ^{240}Pu.

1 Introduction

The first theoretical description of the fission process was established in 1939 by L. Meitner and O.R. Frisch [1] using an essentially classical approach, the Liquid-Drop-Model (LDM) [2]. This model has been improved since then by adding microscopic effects in the smooth part of the binding energy (e.g. the asymmetric term to take into account the Pauli exclusion principle, the pairing term, etc). However, some microscopic correlations were missing (shell effect, pairing). Today, these correlations are added in a second step, mostly using the Strutinsky approach [3].

Microscopic models for the description of fission appeared in the eighties [4]. In this case, the nucleus is directly considered as a microscopic system with A nucleons interacting with each other. The Hartree-Fock-Bogoliubov method (HFB) is part of this class of models and assumes that the nucleus can be approximated by a set of independent quasi-particles.

In the first part of this paper, we discuss the formalism of the Finite-Range Liquid-Drop-Model (FRLDM) [5], a macroscopic-microscopic approach. In the second part, we describe the microscopic models and more specifically the HFB case. In the third part, we compare both approaches.

2 Macroscopic-microscopic approach

In these approaches, we assume that the total binding energy $E(\varrho)$ for a given shape ϱ of the nucleus can be written as a sum of two components:

$$E(\varrho) = E_{\text{mac}}(\varrho) + \Delta E_{\text{mic}}(\varrho). \tag{1}$$

The first term, $E_{\text{mac}}(\varrho)$, corresponds to the macroscopic part of the energy. In FRLDM, this term is obtained by assuming that the nucleus is an incompressible drop of a charged liquid. The shape ϱ is parametrized using the 3-Quadratic-Surface (3QS) [6]. In this parametrization, the shape is axial and defined by part along the z-axis:

$$\varrho^2(z) = \begin{cases} a_1^2 - \frac{a_1^2}{c_1^2}(z-l_1)^2 & , \quad l_1 - c_1 \leq z \leq z_1 \\ a_2^2 - \frac{a_2^2}{c_2^2}(z-l_2)^2 & , \quad z_2 \leq z \leq l_2 + c_2 \\ a_3^2 - \frac{a_3^2}{c_3^2}(z-l_3)^2 & , \quad z_1 < z < z_2 \end{cases}. \tag{2}$$

In this expression, z_1 and z_2 correspond to the junctions of the left/middle and middle/right bodies respectively, and $a_{1...3}$, $c_{1...3}$ and $l_{1...3}$ are the nine parameters describing the shape of the nucleus. However, by enforcing continuity and derivability at the junctions, we end up with the seven following parameters:

$$u = \sqrt{\frac{a_1^2 + a_2^2}{2}} \tag{3}$$

$$\alpha_1 = \frac{l_1 + l_2}{2u} \quad \alpha_2 = \frac{a_1^2 - a_2^2}{u^2} \quad \alpha_3 = \frac{a_1^2}{c_1^2} - \frac{a_2^2}{c_2^2} \tag{4}$$

$$\sigma_1 = \frac{l_2 - l_1}{u} \quad \sigma_2 = \frac{a_3^2}{c_3^2} \quad \sigma_3 = \frac{1}{2}\left(\frac{a_1^2}{c_1^2} + \frac{a_2^2}{c_2^2}\right). \tag{5}$$

The first parameter, u, is set such as the volume of the shape is equal to $\frac{4}{3}\pi A r_0^3$ and the second one, α_1, is set such as the center of mass of the shape is at the origin. The two next parameters α_2 and α_3 represent the asymmetry between the left and right bodies. The three last ones describe the distance between the center of mass of the left and right bodies (σ_1), and the curvature of the 3 bodies (σ_2 and σ_3). The calculation of the macroscopic energy is then as illustrated on FIG. 1(a).

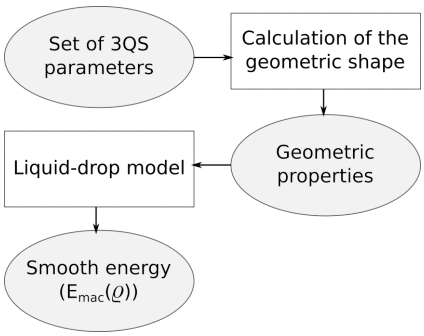

(a) Calculation of the macroscopic energy $E_{\text{mac}}(\varrho)$.

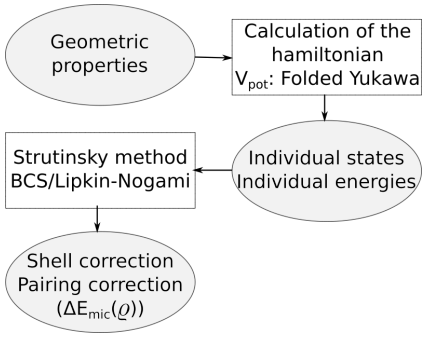

(b) Calculation of the microscopic energy correction $\Delta E_{\text{mic}}(\varrho)$.

Fig. 1: Illustration of the steps to calculate a total binding energy with FRLDM

However, some microscopic effects cannot be completely included by only using the Liquid-Drop-Model approach, such as the shell and pairing effects, and the microscopic correction $\Delta E_{\text{mic}}(\varrho)$ is added to the macroscopic energy to take these effects into account. To calculate $\Delta E_{\text{mic}}(\varrho)$, a shape-dependent 1-body potential $V_{\text{pot}}(\varrho)$ is considered. In our case, $V_{\text{pot}}(\varrho)$ is defined as:

$$V_{\text{pot}}(\varrho) = V_{\text{Yuk.}}(\varrho) + V_{\text{Coul.}}(\varrho) + V_{\text{S.O.}}(\varrho), \tag{6}$$

where $V_{\text{Yuk.}}(\varrho)$ is a folded Yukawa potential, $V_{\text{Coul.}}(\varrho)$ is the Coulomb part and $V_{\text{S.O.}}(\varrho)$ is the spin-orbit term. The Schrödinger equation associated with A independent nucleons in this potential is then solved in a truncated axial harmonic oscillator basis to obtain the individual particle states and the associated individual energies. The Strutinsky method [3] is used to extract the shell correction. The pairing correction is obtained with the Lipkin-Nogami method [7], using the individual energies previously calculated.

3 Microscopic approach

The Hartree-Fock-Bogoliubov (HFB) method allows the description of a deformed nucleus by assuming the expression of the many-body quantum state $|\text{HFB}(\vec{q})\rangle$ as a Slater determinant of quasi-particle [8, 9]. The vector $\vec{q}$ is a set of constrains associated with the axes of the PES (for example, $\vec{q} = (q_{20}, q_{30})$). The Hamiltonian $\hat{H}$ is assumed to be:

$$\hat{H} = \hat{T} + \hat{V}, \tag{7}$$

where $\hat{T}$ is the kinetic operator and $\hat{V}$ is, in our case, an effective 2-body interaction (e.g. Skyrme [10,11] or Gogny [12,13]). The starting point of the HFB method is the minimization of the total binding energy $E(\vec{q}) = \langle \text{HFB}(\vec{q})|\hat{H}|\text{HFB}(\vec{q})\rangle$:

$$\delta E(\vec{q}) = 0. \tag{8}$$

This expression leads to the HFB equations:

$$[\mathcal{H}(\vec{q}), \mathcal{R}(\vec{q})] = 0, \tag{9}$$

where $\mathcal{H}(\vec{q})$ is the HFB hamiltonian matrix and $\mathcal{R}(\vec{q})$ is the generalized density matrix, associated with the constrains $\vec{q}$ and defined as:

$$\mathcal{H}(\vec{q}) = \begin{pmatrix} h(\vec{q}) + \lambda(\vec{q}) & \Delta(\vec{q}) \\ -\Delta^\star(\vec{q}) & -h^\star(\vec{q}) + \lambda(\vec{q}) \end{pmatrix} - \sum_k \mu_k(\vec{q}) \begin{pmatrix} \mathcal{Q}_k(\vec{q}) & 0 \\ 0 & -\mathcal{Q}_k^\star(\vec{q}) \end{pmatrix} \tag{10}$$

$$\mathcal{R}(\vec{q}) = \begin{pmatrix} \rho(\vec{q}) & \kappa(\vec{q}) \\ -\kappa^\star(\vec{q}) & 1 - \rho^\star(\vec{q}) \end{pmatrix}, \tag{11}$$

where $h(\vec{q})$ is a 1-body hamiltonian, $\Delta(\vec{q})$ is the pairing field, $\lambda(\vec{q})$ is a diagonal matrix with the chemical potentials for the protons and the neutrons, $\mu_k(\vec{q})$ is the Lagrange parameter associated with a constrain on a one-body operator $\hat{O}_k$ (for example, $\hat{O}_0 = \hat{Q}_{20}$ and $\hat{O}_1 = \hat{Q}_{30}$), $\rho(\vec{q})$ is the 1-body density matrix and $\kappa(\vec{q})$ is the pairing tensor.

The equation (9) is solved iteratively. One possible scheme of resolution is the following:

1. choose an initial density and pairing tensor for a given set of constrains $\vec{q}$;
2. calculation of the HFB hamiltonian $\mathcal{H}(\vec{q})$;
3. diagonalization of $\mathcal{H}(\vec{q})$;
4. calculation of the new density and pairing tensor from the eigenvectors of $\mathcal{H}(\vec{q})$;
5. loop to the step 2 up to convergence.

4 Comparison

In this section, we propose to compare in a first part both theoretical formalism, and in a second part to take a look at the potential energy surfaces of ^{240}Pu.

4.1 Comparison of the approaches

The calculation of microscopic PES involves the use of a 2-body interaction, with approximately 15 parameters. Each HFB states requires 10 minutes of calculation and a microscopic PES with two collective coordinates (q_{20} and q_{30}) contains around 10000 states. Consequently, a full 2-D PES requires at least 1500h.cpu of calculation. The HFB method minimizes the total binding energy. Consequently, the generated microscopic PES can contain discontinuities. A discontinuity occurs when two states of the PES are associated with infinitely close collective coordinates but drastically different density matrices and pairing tensors [14]. Several methods have been developed to limit the impact of the discontinuities [14,15], but increase the total calculation time.

The calculation of macroscopic-microscopic PES involves more parameters than the microscopic ones (≈ 25) but is very fast (< 1s/state). It is therefore possible to include more degree of freedom. The parametrization presented in Section 2, for example, contains 5 degrees of freedom. Finally, the approach does not minimize the total binding energy and therefore the full PES does not contain discontinuities.

4.2 Comparison of the ^{240}Pu PES

The degrees of freedom in both approaches are completely different. Consequently, we focus here on the existence of fission valleys in both PES.

A microscopic two-dimensional PES for ^{240}Pu obtained with the Gogny D1S interaction is presented in FIG. 2. The right limit of the PES is due a discontinuity due to the scission of the nucleus. The potential energy surface presents two valleys: a deep asymmetric valley and a smaller symmetric one, disconnected from the rest of the potential energy surface due to a discontinuity and therefore hardly accessible.

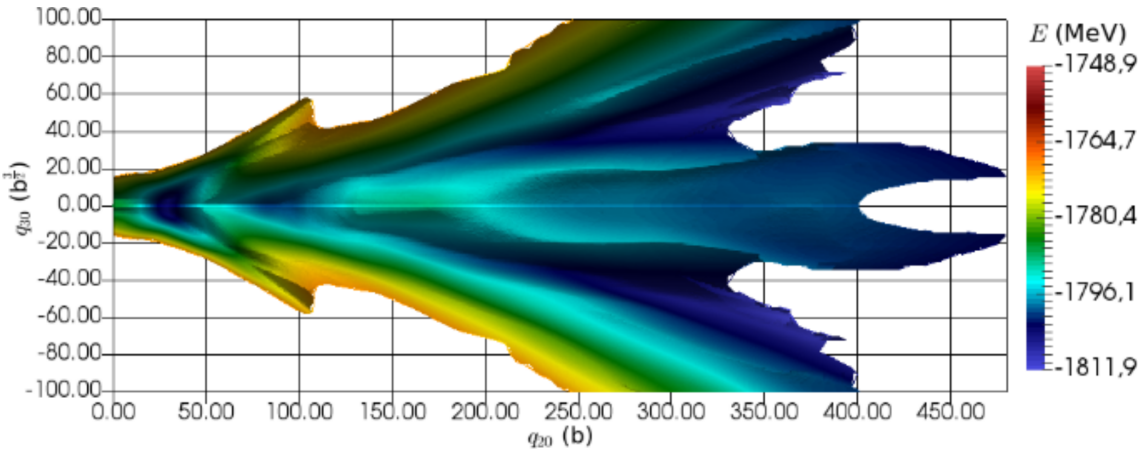

Fig. 2: Microscopic PES obtained for ^{240}Pu with two degrees of freedom: the elongation (q_{20}) and the asymmetry (q_{30}).

The macroscopic-microscopic PES for ^{240}Pu obtained with FRLDM is depicted in FIG. 3. A same row corresponds to a same value of σ_3 and a same column corresponds to a same value of σ_2. The x-axis corresponds to the only asymmetric parameter α_3 and the y-axis corresponds to σ_1. The fragments appear on the left column. The potential energy surface presents here also an asymmetric valley. One the middle row, the two slices on the left show the asymmetric valley.

In both potential energy surfaces, we see an asymmetric valley of fission, which corresponds to the available experimental data. A 4-dimensional calculation of a microscopic potential energy surface with the same degrees of freedom as the macroscopic-microscopic one will allow a deeper analysis. It is challenging due to the calculation time of the microscopic states using HFB: the biggest number of freedom used in microscopic PES for fission up to now is 3 [16].

5 Conclusion

On one hand, the microscopic approach for the construction of potential energy surfaces allows the inclusion of more microscopic correlations but is very time consuming. On the other hand, the macroscopic-microscopic approach offers the possibility to include more collective degrees of freedom.

Both approaches use very different degree of freedom and a full comparison of the corresponding potential energy surface is therefore not direct. However, both potential energy surfaces predict the existence of an asymmetric valley, in agreement with experimental data.

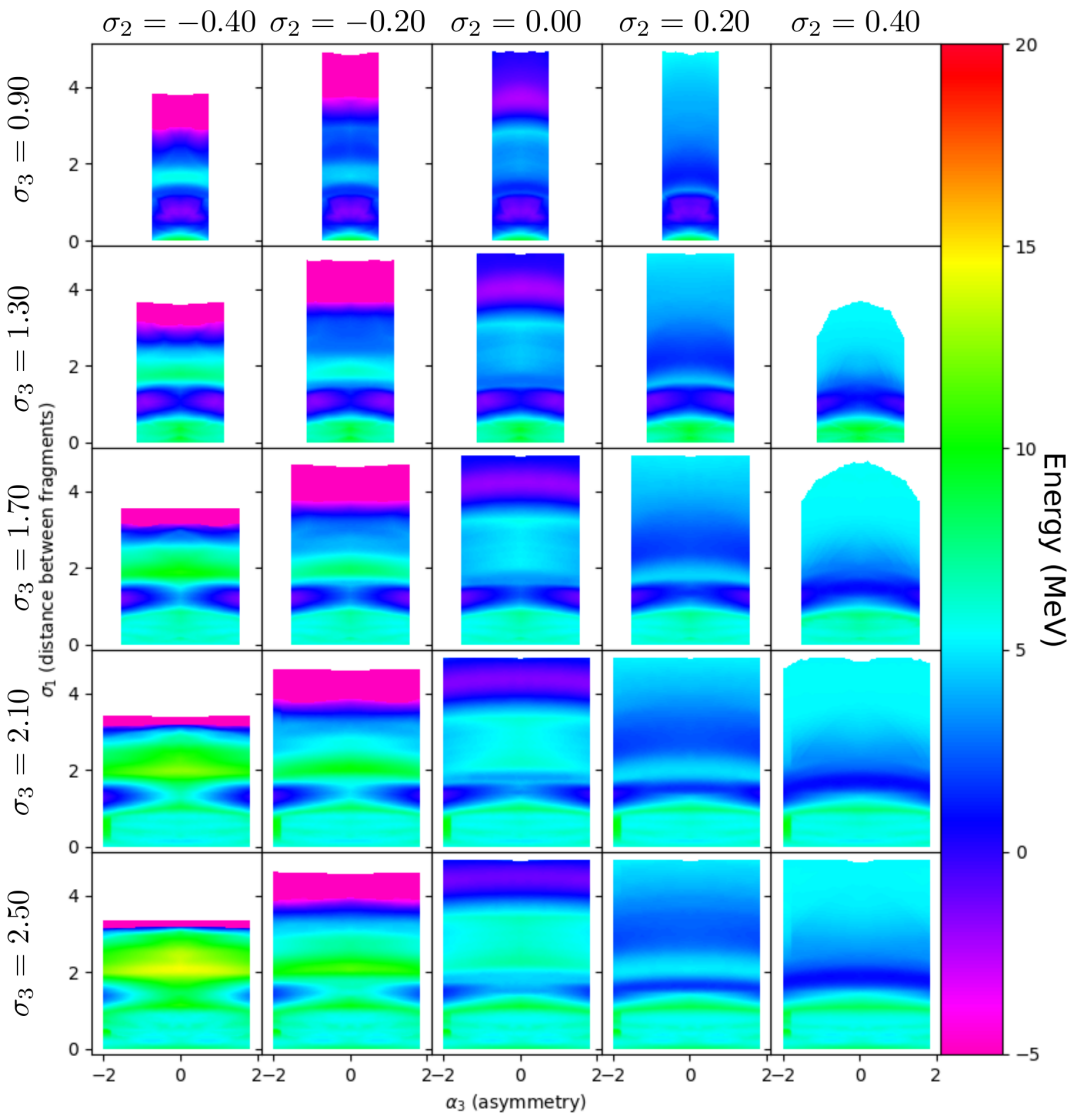

Fig. 3: Macroscopic-microscopic PES obtained for ^{240}Pu with four degrees of freedom using the 3QS parametrization and a minimization along α_2.

References

[1] Lise Meitner and O.R. Frisch, Disintegration of Uranium by Neutrons: a New Type of Nuclear Reaction, Nature Vol. 143, p. 239 (1939)

[2] G. Gamow, Proc. R. Soc. Lond. A 1930 126 632-644

[3] V.M. Strutinsky, Shell effects in nuclear masses and deformation energies, Nuclear Physics A, Volume 95, Issue 2, 1967, Pages 420-442

[4] J.F. Berger, M. Girod, and D. Gogny. "Self-consistent microscopic description of fission the scission mechanism." Dynamics of Nuclear Fission and Related Collective Phenomena. Springer, Berlin, Heidelberg, 1982. 82-93.

[5] P. Möller, A.J. Sierk, T. Ichikawa, H. Sagawa, Nuclear ground-state masses and deformations: FRDM(2012), Atomic Data and Nuclear Data Tables, Volumes 109-110, 2016, Pages 1-204

[6] J.R. Nix, Further studies in the liquid-drop theory on nuclear fission, Nuclear Physics A, Volume 130, Issue 2, 1969, Pages 241-292

[7] Y. Nogami, Improved Superconductivity Approximation for the Pairing Interaction in Nuclei Phys. Rev. 134, B313 (1964)

[8] H. Goutte, J. F. Berger, P. Casoli, and D. Gogny Phys. Rev. C 71, 024316 (2005).

[9] N. Schunck, D. Duke, H. Carr, and A. Knoll Phys. Rev. C 90, 054305 (2014).

[10] J. Bartel, P. Quentin, M. Brack, C. Guet, H.-B. HÃěkansson, Towards a better parametrisation of Skyrme-like effective forces: A critical study of the SkM force, Nuclear Physics A, Volume 386, Issue 1, 1982.

[11] T.H.R. Skyrme, The effective nuclear potential, Nuclear Physics, Volume 9, Issue 4, 1958, Pages 615-634.

[12] J.F. Berger, M. Girod, D. Gogny, Microscopic analysis of collective dynamics in low energy fission, Nuclear Physics A, Volume 428, 1984, Pages 23-36.

[13] D. Gogny, P. Pires, R. De Tourreil, A smooth realistic local nucleon-nucleon force suitable for nuclear Hartree-Fock calculations, Physics Letters B, Volume 32, Issue 7, 1970, Pages 591-595.

[14] N. Dubray, D. Regnier, Numerical search of discontinuities in self-consistent potential energy surfaces, Computer Physics Communications, Volume 183, Issue 10, 2012, Pages 2035-2041

[15] M. Verriere, Description de la dynamique de la fission dans le formalisme de la méthode de la coordonnée génératrice dépendante du temps. Physique Numérique [physics.comp-ph]. Université Paris-Saclay, 2017.

[16] D. Regnier et al., EPJ Web of Conferences. Vol. 146. EDP Sciences, 2017.

Aggregate Decay Behavior of Fission Products in Nuclear Reactors

T.Yoshida[1]*, T.Tachibana*[2]*, S.Okumura*[1]*, S.Chiba*[1]
[1]Tokyo Institute of Technology, Japan
[2]Waseda University, Japan

Abstract
There exist a lot of important quantities which have their origin in aggregate behavior of unstable fission products (FP) in nuclear reactors. Decay heat is a typical example of importance. These quantities are calculated by summing up all the contributions coming from each unstable nucleus accumulated during reactor operation by using of FP decay data libraries. In their infancy, however, they were suffered from so-called the *pandemonium* problem. For decades, the difficulty caused by pandemonium problem has been circumvented by introduction of a β-decay theory. In recent years, the total absorption gamma-ray spectroscopy (TAGS) is saving the situation remarkably even though leaving some open problems.

1 Introduction

In nuclear engineering, there exist a lot of quantities of crucial importance which have their origin in aggregate behavior of fission products (FP) in reactor cores. They are the reactor decay heat, the delayed γ-ray spectrum, the delayed neutron fractions and their spectra among others. The flux and the spectrum of the reactor antineutrino also belong to this category which are attracting interest from neutrino physicists recent years. As these quantities generally depends on the details of the reactor operation history and the time lapse after the reactor shutdown, one has to calculate them using these conditions as inputs. The most typical way of calculation is the so-called summation method which sums up all the contributions from decaying FP nuclides existing in the reactor core.

Summation calculations require a data library on the decay properties of almost a thousand of FPs which consist of the average β- and γ-ray energies, their energy spectra, the β-delayed particle $(n, e, \bar{\nu_e})$ emission probabilities and their spectra *et al.* depending on what quantity one wants to calculate, along with exact information on each β-decay chain in common. Most of these nuclide-wise quantities, however, are known to be suffering from the $pandemonium$ problem [1], and the history and the future of overcoming this problem will be detailed in the following sections.

2 Pandemonium problem in nuclear decay schemes

The effect of the pandemonium problem on the reactor decay heat is illustrated in Fig. 1. This is an highly simplified toy-model of β-decay schemes. Real decay schemes are widely used and available in the form of books/CD-ROM [2], journals [3] or internet data-basis [4]. Assume that a parent nucleus having Q_β-value of 6 MeV feeds the two excited levels at 2 and 4 MeV by 50% each in its daughter which will be de-excited emitting γ-rays. It may happen that the feed to 4 MeV level is missed in constructing the decay scheme as in the right-hand side of Fig. 1. This missing leads to remarkable overestimation of the average β-ray energy E_β and underestimation of E_γ both by 33% in this case.

By using a computer simulation, Hardy *et al.* warned this kind of missing is inevitable in decay schemes of highly Q_β-valued unstable nuclides which are constructed from hundreds of discrete high-resolution γ-ray energy and intensity data from experiments [1]. Reconstruction of a complex decay scheme can be a very difficult task like a extremely complicated jigsaw puzzle. In addition, completeness of the γ-ray data is not expected especially when the parent is a short-lived, high Q_β-valued nuclide. Figure2 shows an example of a decay scheme of such a nuclide, ^{106}Tc [5]. In this case, the β-feeding

to levels above 3930 keV seems to be missed up to 6549 keV(=Q_β). Being calculated as a weighted sum of E_β and E_γ, this kind of feed (or level) missing results in over- and underestimation of β- and γ-ray components of reactor decay heat, respectively. This was revealed when extensive FP decay data libraries for decay-heat calculation were completed and tested in Japan, Europe and the US in the end of 1970's.

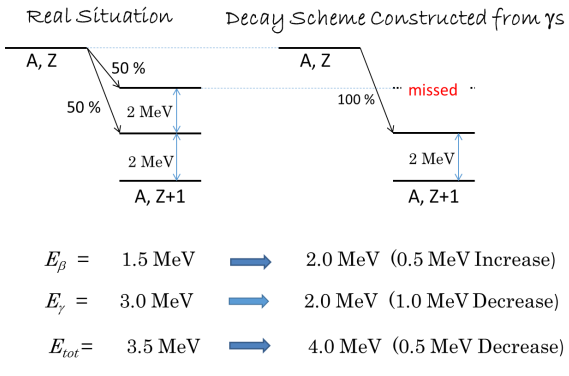

Fig. 1: Extremely simplified decay-scheme toy model with β-feedings followed by γ-transitions

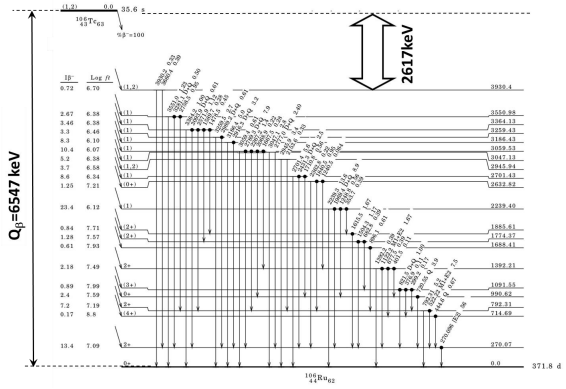

Fig. 2: An example of complex decay scheme of a fisson product nuclide with a high Q_β-value

3 Brief history of pandemonium problem

Comparing their decay-heat calculations with sample irradiation experiments, they found big discrepancies, a serious overestimation in the β-ray and underestimation in the γ-ray component, contrary to their optimistic expectations to their new libraries in the late 1970's. After a year of discussion they came to a conclusion that this disagreement comes from the pandemonium problem. In parallel at the same period, one of the present authors demonstrated that the gross theory of β-decay [6–8] works remarkably well against the pandemonium problem [9]. Here in addition, let us check the pandemonium effect on the delayed γ-ray spectrum, or the γ-ray component of the decay heat. Figure 3 shows the γ-ray spectrum 2.7 sec after a fission burst in ^{235}U. The dashed curve is calculated from high-resolution γ-ray based decay schemes and the solid from the gross theory [10]. Comparison with the measured spectrum by Dickens *et al.* [11] indicates the pandemonium effect (red arrow) reaches more than a factor 2 at most and that the gross-theory result is essentially pandemonium free.

The mean β- and the γ-ray energies had been adopted for most of short-lived FPs in the Japanese evaluated nuclear data library JENDL and in its US counterpart ENDF/B-IV for decades of years until recently when they are gradually being replaced by data from the total absorption gamma-ray spectroscopy (TAGS) on which we will describe hereafter especially in the next section. Anyway, adoption of the gross-theory mean energies is the reason why both JENDL and ENDF/B-IV reproduced the direct decay-heat measurements much better than the European evaluated nuclear data data files, JEF and JEFF, which intentionally exclude theoretical predictions. Because of this policy, however, the European files indicate us the seriousness and persistence of the pandemonium effect in conventional decay schemes. As we see in Fig.4 the underestimation caused by the pandemonium effect is becoming more and more along with the passage of years. This seems to come from the increase of available high resolution γ-based decay schemes toward more neutron rich exotic FPs.

Even though we could circumvent the pandemonium problem by introduction of the gross theory especially for the decay heat and related quantities, experimental decay data for FPs is indispensable for wide range of applications. Construction of decay schemes has its own limitation especially for highly Q_β-valued, short-lived nuclides. The best and only way available now seems to be TAGS. The

first extensive TAGS measurements were performed by Idaho group in 1990's [12]. From the viewpoint of usefulness of the TAGS data, Working Party on International Nuclear Data Evaluation Cooperation of OECD/Nuclear Energy Agency started a research coordination of TAGS physicists and data users in 2006 [13] and this activity was then handed over to a series of Consultants' Meeting of IAEA/Nuclear Data Section. Discussions there led to first important results for technetium and molybdenum isotopes by Valencia group [14], which remarkably improved the summation calculation of plutonium decay heat. The IAEA meeting extended its scope to reactor neutrino spectra [15] and Valencia, Oak Ridge [16], Nantes [17] groups responded to this with fruitful TAGS data.

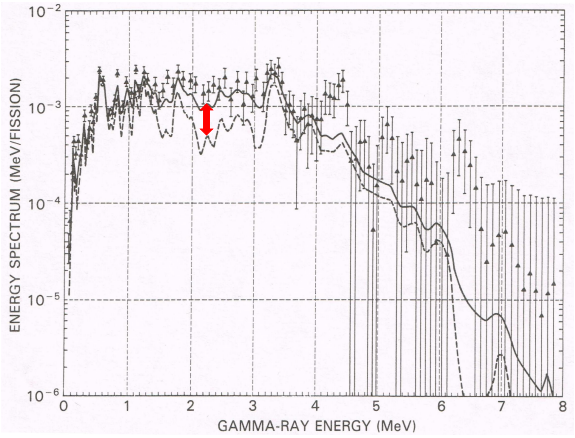

Fig. 3: Measured and calculated delayed γ-ray energy spectra

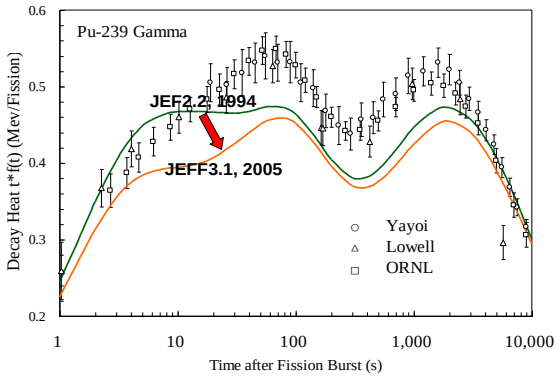

Fig. 4: Effect of the pandemonium problem on the decay heat after a burst fission in ^{235}U sample. The vertical axis is multiplied by the cooling just for concise display

4 Total absorption gamma-ray spectroscopy

The idea of TAGS is to detect the total energy of the γ-ray emitted just after a single β-transition to a certain excited level. In the case of the simplified decay model of Fig.1, a transition from the parent (A,Z) to the 4 MeV level in its daughter (A,Z+1) results in a single 4 MeV photon or two 2 MeV photons. In both cases, the total energy released in the form of γ-ray is 4 MeV. On the contrary, a transition to the 2 MeV level results in a energy release of 2MeV. TAGS uses a large scintillation detector within which all the photons deposit their energy and the data acquisition system gets the signal proportional to the total energy released as photons which is equal, ideally at least, to the excitation energy of the fed level. Though the principle is rather simple but its real execution is quite difficult and requires a complicated data analysis.

As is schematically shown on the left-hand side of Fig.5 TAGS gives us the β-strength function or the β-transition rate per small energy-bin almost up to Q_β above the ground state, the energetic ceiling. It does not, however, provide any information about the level structure or the γ-branching ratios which are very important components of the conventional decay schemes. In order to constitute the best possible β-decay diagram, the TAGS data (pandemonium free) and the current high-resolution scheme, have to be combined at a certain appropriate energy above which level missing becomes sizable as is illustrated on the left-hand side of Fig.5. Then the continuum-to-continuum (bin-to-bin) and the continuum-to-discrete (bin-to-level) γ-transition rates must be calculated and be added into the diagram. It may needs a reliable Hauser-Feshbach type calculation.

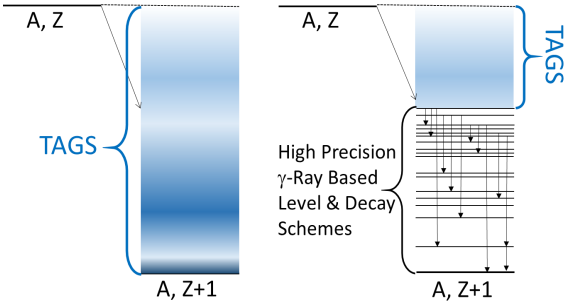

Fig. 5: TAGS data, the conventional decay schemes obtained from high resolution γ-ray data and their integration

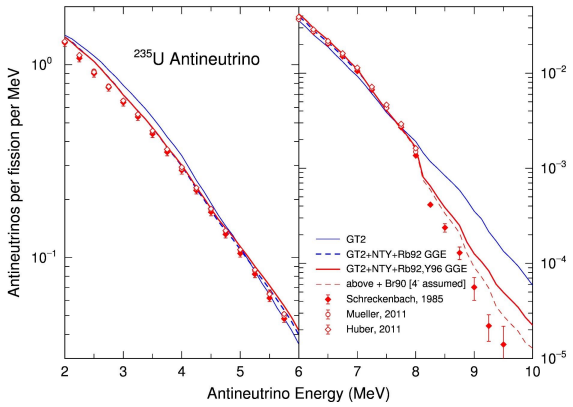

Fig. 6: Antineutrino energy spectrum ^{235} sample under neutron irradiation at ILL high flux reactor

5 Antineutrino as another example

The gross theory of β-decay played an important role to overcome the pandemonium problem. In practice it is widely used to predict the decay behavior of nuclides far off the stability line even now. As an example we introduce here the case of reactor antineutrino $\bar{\nu}_e$. The curves shown in Fig.6 were obtained from the $\bar{\nu}_e$ spectrum of each contributing FP nuclide with the summation method. All the spectra of about 500 FPs were calculated based on the improved version of the gross theory [18, 19], GT2. The NTY treatment applied here was introduced by Nakata *et al.* [20] for odd-odd decaying nuclides. GGE stands for the fact that the grand-to-grand transition rate was enhanced in order to reflect a peculiar behavior of ^{92}Rb and ^{96}Y. The three series of experimental data here are all based on the same electron spectrum measured by Schreckenbach *et al.* [21] by three different authors including themselves. The overall agreement between fully theoretical calculation with the experimental data is fairly good.

6 Concluding remarks

For decades, the difficulty caused by pandemonium problem has been circumvented by introduction of a β-decay theory. In recent years, the TAGS data is becoming available year by year saving the situation remarkably. The TAGS data (pandemonium free) and the current high-resolution decay-scheme should be integrated into a better description of β- and γ-decay property of FPs for application purposes with the help of some reliable statistical γ-decay theory.

References

[1] Hardy, J.C., Carraz, L.C., Jonson, B., and Hansen, P.G., Phys. Lett. B, **71** (1977) 307

[2] Firestone, R.B. and Shirley, V.S., ed. *Table of Isotopes*, (John Wiley & Sons. Inc.,)

[3] Nuclear Data Sheets, (Elsevier Inc.)

[4] National Nuclear Data Center, *NuDat, a Interactive Chart of Nuclides*, available at the URL `http://www.nndc.bnl.gov/nudat2/`.

[5] De Frenne, D. and Negret, A., Nucl. Data Sheets, **109** (2008) 943

[6] Takahashi, K. and Yamada, M., Prog. Theor. Phys., **41** (1969) 1470

[7] Koyama S., Takahashi, K. and Yamada, M., Prog. Theor. Phys., **44** (1970) 663

[8] Takahashi, K., Prog. Theor. Phys., **45** (1971) 1466

[9] Yoshida, T. and Nakasima, R., J. Nucl. Sci. Technol, **18** (1981) 393

[10] Yoshida, T. and Katakura, J., Nucl. Sci. Eng, **93** (1986) 193

[11] Dickens, J.K., Love, T.A., McConnell, J.W., and Peelle, R.W., Nucl. Sci. Eng, **74** (1980) 106

[12] Greenwood, R.G., Helmer, M.H., Putnam M.H. and Watts, K.D., Nucl. Instr. Methods in Nuclear Research, **A390** (1997) 95

[13] Yoshida, T. and Nichols, A.L., NEA/WPEC-25 (2007)

[14] Algora, A., Jordan, D., Tain, J.L., Rubio, B., Agramunt, J. *et al.* Phys. Rev. Lett., **105** (2010) 202501

[15] Dimitriou, P. and Nichols, A.L., INDC(NDS)-0676, (2015)

[16] Rasco, B.C., Wolinska-Cichocka, M., Fijalkowsksa, A., Rykaczewski, K.P., Karny, R.K. *te al.* Phys. Rev. Lett., **117** (2016) 092501 and references therein

[17] Zakari-Issoufou, A.A., Fallot, M., Porta, A., Algora, A., Tain, J.L. *et al.* Phys. Rev. Lett., **115** (2015) 102503

[18] Kondoh, T., Tachibana, T. and Yamada, M., Progr. Theor. Phys., **74** (1985) 708

[19] Tachibana, T., Yamada, M. and Yoshida, Y., Progr. Theor. Phys., **84** (1990) 641

[20] Nakata, H., Tachibana, T. and Yamada, M., Nucl. Phys. A, **594** (1995) 27

[21] Schreckenbach, K., Colvin, G., Gelletly, W. and Von Feilitzsch, Phys. Lett. B, **160** (1985) 160

Dependence of the prompt fission γ-ray spectrum on the entrance channel of compound nucleus: spontaneous vs neutron-induced fission

C.Y. Wu[1], A. Chyzh[2], P. Jaffke[3], R.A. Henderson[1], P. Talou[3], I. Stetcu[3], J. Henderson[1], M.Q. Buckner[1], S.A. Sheets[1], R. Hughes[1], B. Wang[1], J.L. Ullmann[4], S. Mosby[4], T.A. Bredeweg[5], A.C. Hayes-Sterbenz[3], and J.M. O'Donnell[4]

[1] Lawrence Livermore National Laboratory, Livermore, California 94550, USA
[2] North Carolina State University, Raleigh, North Carolina 27695, USA
[3] Theoretical Division, Los Alamos National Laboratory, Los Alamos, New Mexico 87545, USA
[4] Physics Division, Los Alamos National Laboratory, Los Alamos, New Mexico 87545, USA
[5] Chemistry Division, Los Alamos National Laboratory, Los Alamos, New Mexico 87545, USA

Abstract

Prompt γ-ray spectra were measured for neutron-induced fission of ^{239,241}Pu with incident neutron energy from thermal to about 100 keV and spontaneous fission of ^{240,242}Pu using the Detector for Advanced Neutron Capture Experiments (DANCE) array in coincidence with the detection of fission fragments by a parallel-plate avalanche counter. The unfolded prompt fission γ-ray spectra can be reproduced reasonably well by Monte Carlo Hauser-Feschbach statistical model for neutron-induced fission channel but not for the spontaneous fission channel. However, this entrance-channel dependence of the prompt fission γ-ray emission can be described qualitatively by the model due to the very different fission-fragment mass distributions and a lower average fragment spin for spontaneous fission. A supportive evidence is provided by the unfolded 2-D spectrum of total γ-ray energy vs multiplicity where the γ-ray multiplicity distribution has a tail extended to higher multiplicity for neutron-induced fission channel.

1 Introduction

The prompt energy released in the nuclear fission is dominated by the kinetic energy of the fission fragments and then followed by the prompt neutron and γ-ray emission from the fission fragments. In the past, most model and experimental efforts were devoted to the kinematic energy of fission fragments and the neutron emission. Little attention was paid to the γ-ray emission until recently. A single γ-ray detector was used for most measurements made in 1970's and their results were summarized in Refs. [1]. Recent years have seen an increased interest in the prompt γ-ray emission in fission [2-14] because the data are important for fission modeling and applications in nuclear industries. For example, new prompt fission γ-ray data at thermal neutron energy and above for ^{235}U and ^{239}Pu, required for the precise modeling of γ-ray heating in reactor cores, were categorized as high-priority by the Nuclear Energy Agency under the Organization for Economic Cooperation and Development [15].

Most measurements for the prompt γ-ray emission in fission were made using one or a few γ-ray detectors for the neutron-induced fission of U and Pu isotopes as well as ^{252}Cf(sf) and ^{240,242}Pu(sf). More recently, a new class of fast scintillators, such as cerium-doped-$LaBr_3$, $CeBr_3$, and $LaBr_3$ detectors, was used by Billnert *et al*. [4], Oberstedt *et al*. [7,10,12,13], and Gatera *et al*. 14]. Lately, a new generation of measurements has emerged for the prompt γ-ray emission in fission that uses highly segmented 4π γ-ray calorimeters, such as the Heidelberg-Darmstadt Crystal Ball [16] and the Detector for Advanced Neutron Capture Experiments (DANCE) array [17,18].

Measurements of the prompt fission γ-ray emission for the cases mentioned above were made for either the neutron-induced fission at a given incident neutron energy or the spontaneous fission. No report was made for the impact of compound nucleus entrance channel on prompt fission γ-ray emission except for

a recent study of ^{240,242}Pu, where the spontaneous fission was measured for γ-ray energy up to 4 MeV [13]. The comparison with thermal neutron-induced fission ^{241}Pu(n_{th},f) indicates no or little dependence on the entrance channel of the ^{242}Pu* compound nucleus. Furthermore, there are known cases where the prompt fission γ-ray spectra were measured using fast neutrons with energy up to 20 MeV for ^{235}U(n,f) and ^{238}U(n,f) [19.20] and no obvious dependence on the incident neutron energy was found. However, the measurement given in Refs. [21,22] showed that the prompt γ-ray spectrum for neutron-induced fission of ^{238}U after the third-chance fission is different from those with lower incident neutron energy that can be described adequately by model calculations [23].

In this work, we present a new study of the dependence of prompt fission γ-ray emission on the entrance channels of ^{240,242}Pu* compound nuclei. There are two distinct entrance channels for their fission. One is spontaneous fission and has an entrance channel of zero intrinsic excitation energy and spin 0^+. The second channel is neutron-induced fission of ^{239,241}Pu with the incident neutron energy from thermal to 100 keV. They have the entrance channel of ≈ 6.3 MeV intrinsic excitation energy with spin of 0 or 1 for ^{239}Pu(n,f) and ≈ 6.5 MeV intrinsic excitation energy with spin of 2 or 3 for ^{241}Pu(n,f). The prompt fission γ-ray emission for both fission channels of both compound nuclei was measured using the DANCE array in coincidence with the detection of fission fragments by a compact parallel-plate avalanche counter (PPAC) [24], designed specifically for DANCE. The description of experiments and data analysis as well as the discussion of results will be presented in the sections below. Some of the results have been published [25].

2 Experiments and data analysis

Measurements of the prompt γ-ray spectrum of ^{239,241}Pu(n,f) and of ^{240,242}Pu(sf) were performed at the Lujan Neutron Scattering Center at LANL/LANSCE. For neutron-induced fission experiments, PPACs with either ^{239}Pu or ^{241}Pu targets were assembled at LLNL and bombarded by neutrons with energies from thermal up to several hundred keV. Neutrons were produced first by bombarding a tungsten target with an 800 MeV proton beam at a repetition rate of 20 Hz and then moderated by water. The prompt γ rays emitted in fission were detected by the DANCE array in coincidence with the detection of fission fragments by PPACs. A total of over 10^6 fission events with at least one γ ray detected by DANCE were collected for both isotopes. These results were published earlier [5,9]. For the spontaneous fission, PPACs with a total mass of about 642 μg of ^{242}Pu enriched to 99.93 % or about 769 μg of ^{240}Pu enriched to 98.86 % were assembled at LLNL and used for the fission-fragment detection in coincidence with the detection of the prompt γ rays by DANCE. A total of about 10^5 fission events with at least one γ ray detected by DANCE were collected for both targets.

In the offline analysis using the code FARE [26], a valid fission event required a coincidence between the detection of a fission fragment by the PPAC and the detection of γ rays by DANCE with an 8-10 ns time window on their time difference spectrum. A time resolution better than 2 ns was achieved for all fission reactions studied. Three physical quantities were inferred from the coincident γ rays detected by DANCE: (1) the total prompt fission γ-ray energy $E_{\gamma,tot}$ spectrum defined as the sum of energy of all detected γ rays; (2) the total prompt fission γ-ray multiplicity M_γ spectrum determined according to the number of clusters, grouped adjacent detectors triggered; (Note that this counting method for M_γ avoids double counting due to the Compton scattering, is largely independent of the γ-ray energies E_γ, and is closer to the simulated results using γ-ray calibration sources [3,27,28] (3) the prompt fission γ-ray energy E_γ spectrum determined by excluding any γ ray with adjacent crystals triggered to avoid the summing effect. Details of this analysis have been described in our earlier publications [3,5,9].

Corrections must be made to the measured spectra to obtain the actual physical ones that can be compared to model calculations. This can be accomplished by unfolding the measured spectra using the detector response matrices. For unfolding one-dimensional spectra such as E_γ, the iterative Bayesian [29,30,31] and the singular-value decomposition (SVD) [32] methods are available. The detector

response matrices are simulated using the GEANT4 [33] geometrical model including both DANCE and PPAC [3,5,9]. To make sure the simulated detector response matrices have sufficient coverage of the phase space beyond the measured one, we use the E_γ spectrum in the range 0.1-12 MeV for the response matrix in the unfolding.

For unfolding 2-D spectra such as $E_{\gamma,tot}$ vs M_γ, the iterative Bayesian method is adopted. The value of M_γ up to 25 and $E_{\gamma,tot}$ up to 40 MeV are included to have sufficient coverage of the phase space beyond the measured one, The $E_{\gamma,tot}$ has a bin size of 200 keV and an energy threshold of 150 keV. So, the response matrix has a size of 200 × 25. For any given grid point ($E_{\gamma,tot}$, M_γ) in the response matrix, a two-dimensional DANCE response matrix of a size of 200 × 25 is generated with a given assembly of no more than 20,000 samples. Note that the DANCE response to the total prompt γ-ray is relatively insensitive to the content of γ rays for a given sample since the γ-ray detection efficiency (84 to 88%) and the peak-to-total ratio (~ 55%) remain nearly constant for the γ-ray energy ranging from 150 keV to 10 MeV [3,27,28]. Each sample has a matching number of γ rays to M_γ, selected randomly according to the unfolded E_γ distributions in Refs. [3,5] and this work with the condition on the total γ-ray energy that is equal to $E_{\gamma,tot} \pm 100$ keV. This simulation is repeated for all the grid points within the lower and upper bound of $E_{\gamma,tot}$ for a given M_γ, established by this random sampling technique.

3 Results and discussions

The unfolded E_γ spectra obtained by using the iterative Bayesian method, for ^{240}Pu(sf) as well as ^{239}Pu(n,f) are shown in Fig. 1(a), and the spectra for ^{242}Pu(sf) and ^{241}Pu(n,f) are shown in Fig. 1(b). A very similar trend is observed for fission of both compound nuclei; that is the E_γ spectrum for the spontaneous fission is harder than that of the neutron-induced fission for γ-ray energies above 2 MeV. The difference in yield is nearly a factor of 2 for γ-ray energy near 6 MeV. In general, the systematic uncertainty is about 10 % for the unfolding with simulated detector responses, which is an order of magnitude smaller than the observed difference in yield and has no impact on the conclusion.

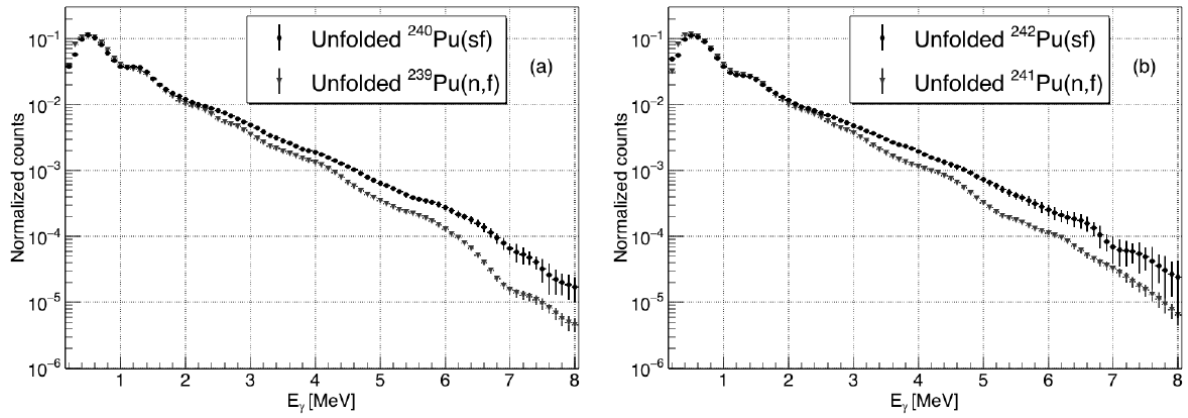

Fig. 1 Comparison of unfolded E_γ spectrum between ^{240}Pu(sf) (black) and ^{239}Pu(n,f) (red) is shown in (a) and between ^{242}Pu(sf) (black) and ^{241}Pu(n,f) (red) shown in (b). All spectra are self-normalized to one.

We have used the CGMF code [8] to model the de-excitation of fission fragments through a Monte Carlo implementation of the statistical Hauser-Feshbach theory [34]. Both the prompt γ-ray observables as well as prompt neutron observables are calculated. These include the average prompt neutron multiplicity $\langle\nu\rangle$, its dependence on fragment mass $\langle\nu\rangle(A)$, and the distribution $P(\nu)$, as well as the average prompt γ-ray multiplicity $\langle M_\gamma\rangle$ and prompt fission γ-ray energy E_γ spectrum (PFGS). The prompt neutron observables for ^{239,241}Pu(n,f) and ^{240,242}Pu(sf) are used to constrain the CGMF calculations. Details of the parameters used in the calculation and their sensitivities to the observables,

such as the total kinetic energy, fission-fragment mass and angular momentum distribution are described in Ref. [25] and elsewhere in this proceeding by P. Jaffke *et al*..

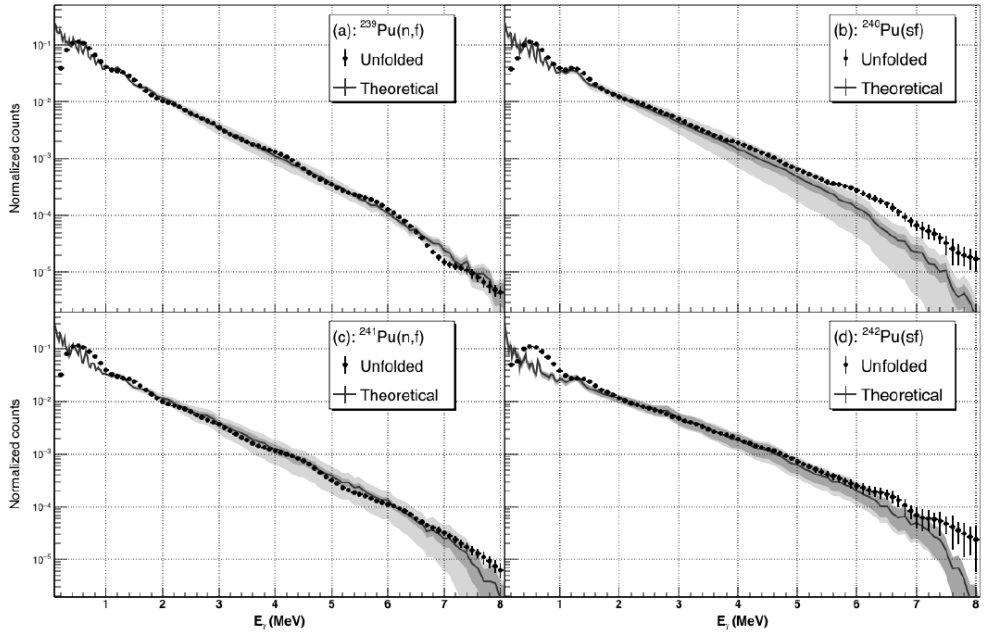

Fig. 2 Comparison of the unfolded (points) and calculated (lines and bands) prompt fission γ-ray spectrum (PFGS) for ^{239}Pu(n,f) (a), ^{240}Pu(sf) (b), ^{241}Pu(n,f) (c), and ^{242}Pu(sf) (d). The calculated central values (lines) use the nominal total kinetic energy of the fragments $\langle TKE \rangle_{exp}$ and the light (dark) bands are the ± 0.5 MeV (± 1.0 MeV) uncertainties. Unfolded spectra are self-normalized to one. To account for a lack of experimental sensitivity below 1 MeV, calculated data were normalized to experimental data in the $1 \leq E_\gamma \leq 5$ MeV range.

Plotted in Fig. 2 are the comparisons between the unfolded results from DANCE and the CGMF calculations. The lighter and darker bands indicate the calculated spectra when we vary $\langle TKE \rangle_{exp}$ by ± 0.5 MeV and ± 1.0 MeV. We can see that the measured ^{239}Pu(n,f) PFGS is reproduced nicely by the calculations, even up to $E_\gamma \sim 7$ MeV. The ^{240}Pu(sf) PFGS is reasonably well reproduced, but the slope is too steep. The ^{241}Pu(n,f) calculation is slightly harder than the measured result, indicating that a lower $\langle TKE \rangle$ than the used $\langle TKE \rangle_{exp}$ could produce a better fit and a higher $\langle M_\gamma \rangle$ as well, in agreement with Refs. [9,10]. The ^{242}Pu(sf) PFGS can reproduce the unfolded data reasonably well, but the large $\langle TKE \rangle_{exp}$ we have used generates a very small $\langle M_\gamma \rangle \sim 4.2$ γ/fission, far below the values in Refs. [1,13]. For both ^{240}Pu* and ^{242}Pu*, neutron-induced fission required a larger average angular momentum carried by the fission fragments to achieve good agreement with $\langle \nu \rangle$. Overall, the neutron-induced fission reactions are in better agreement than spontaneous fission. This is further supported by the observation of unfolded 2-D spectrum of $E_{\gamma,tot}$ vs M_γ for ^{242}Pu* compound nucleus, shown in Fig 3, where the M_γ distribution has a tail stretched to higher multiplicity for neutron-induced fission channel.

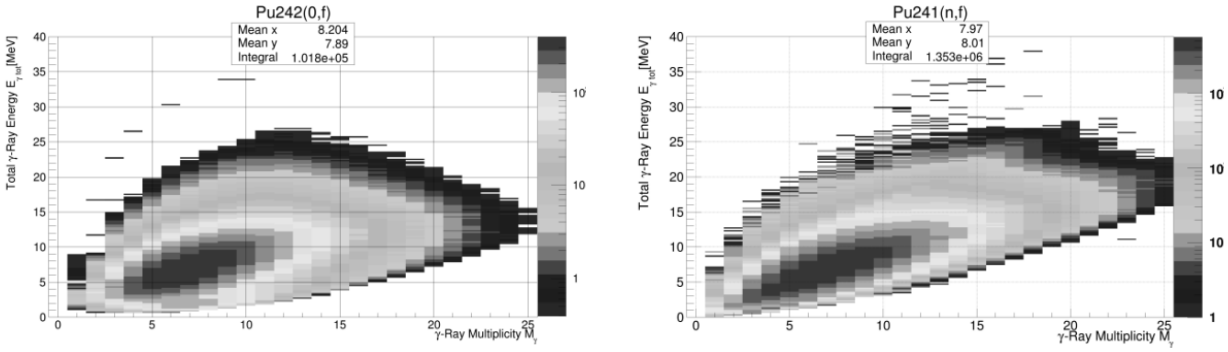

Fig. 3 Comparison of the unfolded 2-D spectrum of the total γ-ray energy ($E_{\gamma,tot}$) vs multiplicity (M_γ) between spontaneous (L) and neutron-induced (R) fission of ^{242}Pu*. The M_γ multiplicity has a long tail toward higher multiplicity for neutron-induced fission channel.

4 Summary

In summary, the prompt γ-ray spectra of ^{240,242}Pu(sf) and ^{239,241}Pu(n,f) with the incident neutron energy range from thermal to ~ 100 keV were measured using the DANCE array in coincidence with the detection of fission fragments using a PPAC. This offers an opportunity to study the dependence of prompt fission γ-ray emission on the entrance channel for the formation of the compound nucleus. It was carried out by comparing the unfolded experimental spectra and the ones calculated using the CGMF code, a Monte Carlo Hauser-Feshbach statistical model. The experimental results with DANCE observed a relative hardening in both the ^{240}Pu* and ^{242}Pu* compound systems. The observed differences in the E_γ spectrum between the spontaneous and neutron-induced fission were qualitatively confirmed by the model calculations and interpreted as due to the difference in the fission-fragment mass distributions and fragment spin distributions. The mass distributions for spontaneous fission peak near A ~ 133 and has a narrower variance, where the average γ-ray energies are known to increase. A portion of the observed hardening of the E_γ spectrum relative to the neutron-induced reaction for the ^{242}Pu* and ^{240}Pu* compound system can be attributed to this change in mass distributions. A decrease in the average angular momentum carried by fission fragments for the spontaneous fission reactions could account for most of the observed differences in the prompt γ-ray spectra. Additional evidence to support this explanation is provided by the unfolded 2-D spectrum of $E_{\gamma,tot}$ vs M_γ where the γ-ray multiplicity shows a tail extended to higher multiplicity for neutron-induced fission channel.

Acknowledgement

This work benefited from the use of the LANSCE accelerator facility as was performed under the auspices of the US Department of Energy by Lawrence Livermore National Security, LLC under contract DE-AC52-07NA27344 and by Los Alamos National Security, LLC under contract DE-AC52-06NA25396. Funding also is acknowledged from the U.S. DOE/NNSA Office of Defense Nuclear Nonproliferation Research and Development and DOE/SC Office of Nuclear Physics. All isotopes used in the measurements were obtained from Oak Ridge National Laboratory.

References

[1] T.E. Valentine, Annals of Nuclear Energy 28, 191 (2001).
[2] A. Hotzel *et al.*, Z Phys. A356 (1996) 299.
[3] A. Chyzh, C.Y. Wu, E. Kwan, R.A. Henderson, J.M. Gostic, T.A. Bredeweg, R.C. Haight, A.C. Hayes-Sterbenz, M. Jandel, J.M. O'Donnell *et al.*, Phys. Rev. C 85 (2012) 021601(R).
[4] R. Billnert, F.-J. Hambsch, A. Oberstedt, and S. Oberstedt, Phys. Rev. C 87 (2013) 024601.
[5] A. Chyzh, C.Y. Wu, E. Kwan, R.A. Henderson, J.M. Gostic, T.A. Bredeweg, A. Couture, R.C. Haight, A.C. Hayes-Sterbenz, M. Jandel *et al.*, Phys. Rev C 87 (2013) 034620.

[6] J.L. Ullmann, E.M. Bond, T.A. Bredeweg, A. Couture, R.V. Haight, M. Jandel, T. Kawano, H.Y. Lee, J.M. O'Donnell, A.C. Hayes *at el*., Phys. Rev. C 87 (2013) 044607.
[7] A. Oberstedt *et al*., Phys. Rev. C 87 (2013) 051602(R).
[8] B. Becker, P. Talou, T. Kawano, Y. Danon, and I. Stetcu, Phys. Rev. C 87 (2013) 014617.
[9] A. Chyzh, C.Y. Wu, E. Kwan, R.A. Henderson, T.A. Bredeweg, R.C. Haight, A.C. Hayes-Sterbenz, H.Y. Lee, J.M. O'Donnell, and J.L. Ullmann, Phys. Rev C 90 (2014) 014602.
[10] A. Oberstedt *et al*., Phys. Rev. C 90 (2014) 024618.
[11] I. Stetcu, P. Talou, T. Kawano, and M. Jandel, Phys. Rev. C 90 (2014) 024617.
[12] A. Oberstedt, R. Billnert, F.-J. Hambsch, and S. Oberstedt, Phys. Rev. C 92 (2015) 014618.
[13] S. Oberstedt, A. Oberstedt, A. Gatera, A. Gook, F.-J. Hambsch, and A. Moens, G. Sibbens, D. Vanleeuw, and M. Vidali, Phys. Rev. C 93 (2016) 054603.
[14] A. Gatera et al., Phys. Rev. C 95 (2017) 064609.
[15] Nuclear Data High Priority Request List of the NEA (Req. ID: H.3, H4).
[16] V. Metag *et al*., in *Proceedings of the Symposium on Detectors in heavy-ion Reactions, Berlin 1982*, edited by V. Oertzen, Lect. Notes Phys. 178 (Springer, Berlin, 1983) p. 163.
[17] M. Heil, R. Reifarth, M. M. Fowler, R. C. Haight, F. Kappeler, R. S. Rundberg, E. H. Seabury, J. L. Ullmann, and K. Wisshak, Nucl. Instrum. Methods in Phys. Res. A 459 (2001) 229.
[18] R. Reifarth *et al*., IEEE Transactions on Nuclear Science 53 (2006) 880.
[19] E. Kwan *et al*., Nucl. Instrum. Methods Phys. Res. A 688 (2012) 55.
[20] M. Lebois *et al*., Phys. Rev. C 92 (2015) 034618.
[21] J.M. Laborie, G. Belier, and J. Taieb, Phys. Proc. 31 (2012) 13.
[22] J.M. Laborie, G. Belier, J. Taieb, A. Oberstedt, S. Oberstedt, Eur. Phys. Jour. Web of Conferences 146 (2017), 04032.
[23] A. Oberstedt, R. Billnert, and S. Oberstedt, Phys. Rev. C 96 (2017) 034612.
[24] C.Y. Wu, A. Chyzh, E. Kwan, R. Henderson, J. Gostic, D. Carter, T. Bredeweg, A. Couture, M. Jandel, J. Ullmann, Nucl. Instrum. Methods Phys. Res. A 694 (2012) 78.
[25] A. Chyzh, P. Jaffke, C.Y. Wu, R.A. Henderson, P. Talou, I. Stetcu, J. Henderson, M.Q. Buckner, S.A. Sheets, R. Hughes, B. Wang, J.L. Ullmann, S. Mosby, T.A. Bredeweg, A.C. Hayes-Sterbenz, and J.M. O'Donnell, Phys. Lett. B 782 (2018) 652.
[26] M. Jandel, T.A. Bredeweg, A. Couture, J.M. O'Donnel, and J.L. Ullmann, Los Alamos National Laboratory, LA-UR-12-21171 (2012).
[27] R. Reifarth *et al*., Los Alamos National Laboratory, LA-UR-01-4185 (2001).
[28] R. Reifarth *et al*., Los Alamos National Laboratory, LA-UR-03-5560 (2003).
[29] G. D'Agostini, Nucl. Instrum. Methods Phys. Res. A362, 487 (1995).
[30] G. D'Agostini, arXiv: 1010.0612 (2010).
[31] T.J. Adye, arXiv: 1105.1160 (2011).
[32] A. Hocker and V. Kartvelishvili, Nucl. Instrum. Methods Phys. Res. A 372, 469 (1996).
[33] S. Agostinelli *et al*., Nucl. Instrum. Methods Phys. Res. A 506 (2003) 550.
[34] W. Hauser and H. Feshbach, Physical Review 87, 2 (1952).

Real time description of fission

I. Stetcu[1]*, A. Bulgac*[2]*, S. Jin*[2]*, K. J. Roche*[2,3]*, and N. Schunck*[4]
[1]Los Alamos National Laboratory, Los Alamos, New Mexico, 87545, USA
[2]University of Washington, Seattle, Washington 98195-1560, USA
[3]Pacific Northwest National Laboratory, Richland, WA 99352, USA, USA
[4]Lawrence Livermore National Laboratory, Livermore, California 94551, USA

Abstract
Using the time-dependent superfluid local density approximation, the dynamics of fission is investigated in real time from just beyond the saddle to fully separated fragments. Simulations produced in this fully microscopic framework can help to assess the validity of the current approaches to fission, and to obtain estimate of fission observables. In this contribution, we concentrate on general aspects of fission dynamics.

1 Introduction

The microscopic description of nuclear fission remains a goal of nuclear theory even almost 80 years after its discovery. Recent developments, both in theoretical modeling and computational power, give us hope that progress can be finally made towards a microscopic theory of nuclear fission [1]. Even if the complete microscopic description remains a computationally demanding task, the information that can be provided by current calculations can be extremely useful to guide and constraint more phenomenological approaches. First, a microscopic model that describes the real-time dynamics of the fissioning system can justify or rule out some of the approximations. Second, the microscopic approach can be used to obtain trends, e.g., with increasing excitation energy of the fissioning system, or even to compute observables that cannot be otherwise calculated in phenomenological approaches or that can be hindered by the limitations of the method. For example, in all phenomenological approaches, the full separation of the fragments cannot be modeled. While this approximation can have little impact on the mass numbers of the fission fragments, the same approximation can be of concern when the total kinetic energy (TKE) or the total excitation energy (TXE) of the fission fragments are computed, if these can be even computed in these approaches. Moreover, most phenomenological models implicitly built in the approximation that no neutrons are emitted at scission or during the acceleration of the fission fragments. Given that one cannot distinguish experimentally between neutrons emitted from the fission fragments after full acceleration, and neutrons emitted earlier in the process, only a microscopic theory able to follow in real time the evolution of the system to fully separated fission fragments can answer such questions.

Our approach to nuclear fission is the time-dependent superfluid local density approximation (TDSLDA). This is an extension of the superfluid local density approximation (SLDA) introduced in 2002 as an alternative to the density functional theory (DFT) framework for superfluid systems of Oliveira, Gross, and Kohn [2], approach that lacked the local character and would be prohibitive to implement even on exascale computers. TDSLDA has becoome a very successful theoretical model. It reproduced correctly, and often predicted before experimental data became available, a large number of phenomena and properties such as the ground state energy, pairing gap, collective modes, quantized vortices, see QMC and experimental studies discussed in Refs. [3–6]. In nuclear physics, TDSLDA was used to study the excitation of collective modes in deformed open shell nuclei, in particular triaxial nuclei, without any restrictions [7]. In the case of relativistic Coulomb excitation of Uranium [8] the external field created by another impinging Uranium nucleus is so strong that nonlinear and non-adiabatic effects are very important, and cannot be captured by a traditional QRPA approach. The TDSLA incorporates the effects of the continuum, the dynamics of the pairing field, and the numerical solution is implemented with controlled approximations and with negligible numerical corrections [9, 10].

Within the TDSLDA we have investigated in a series of papers [11, 12] the fission of a ^{240}Pu nucleus, following the dynamics of the process in real time from the outer saddle to scission and beyond. In our investigations, the fragments are well separated, which allows us to estimate quantities like the TKE or TXE and investigate the emission of neutrons at scission and from the fragments before full acceleration. We have shown that many collective degrees of freedom are excited in fission dynamics, on the way from saddle-to-scission, not only 2 or even 5, as used in other models [13, 14], and that the one-body dissipation plays an important role in the dynamics [12]. We will discuss in this contribution some of the characteristics of the fission dynamics and discuss further developments of the method. The ultimate goal of the theoretical effort is to produce reliable description and/or trends of fission observables that can be used as input in applications.

2 Theoretical Framework

(TD)SLDA is formally equivalent to (TD)HFB or (TD) Bogoliubov-de Gennes mean-field approaches by design and it is a very complex mathematical problem. In various studies over the years we solved up to 500,000 or more complex-valued, nonlinear, coupled TD partial differential equations (PDEs) on large 3D spatial lattices for up to $400,000$ of time steps, with very high numerical accuracy. This feat has only been feasible by using some of the largest supercomputers in the world with highly-optimized computer codes [15].

In TDSLDA, one assumes that the system is described by a single generalized Slater determinant, or HFB vacuum, composed of quasi-particle wavefunctions from the start to the finish of the simulations. The evolution of the wavefunctions is described by the time-dependent Schrödinger equation,

$$i\hbar\frac{\partial}{\partial t}\begin{pmatrix} u_{k\uparrow} \\ u_{k\downarrow} \\ v_{k\uparrow} \\ v_{k\downarrow} \end{pmatrix} = \begin{pmatrix} h_{\uparrow\uparrow} & h_{\uparrow\downarrow} & 0 & \Delta \\ h_{\downarrow\uparrow} & h_{\downarrow\downarrow} & -\Delta & 0 \\ 0 & -\Delta^* & -h^*_{\uparrow\uparrow} & -h^*_{\uparrow\downarrow} \\ \Delta^* & 0 & -h^*_{\downarrow\uparrow} & -h^*_{\downarrow\downarrow} \end{pmatrix} \begin{pmatrix} u_{k\uparrow} \\ u_{k\downarrow} \\ v_{k\uparrow} \\ v_{k\downarrow} \end{pmatrix}, \tag{1}$$

where we have suppressed the spatial $\boldsymbol{r}$ and time coordinate t and k labels the quasiparticle wavefunctions (qpwfs) $[u_{k\sigma}(\boldsymbol{r},t), v_{k\sigma}(\boldsymbol{r},t)]$, where $\sigma =\uparrow,\downarrow$. The single particle Hamiltonian $h_{\sigma,\sigma'}(\boldsymbol{r},t)$, and the pairing field $\Delta(\boldsymbol{r},t)$ are functionals of various neutron and proton densities, which are determined by the quasiparticle wavefunctions, see Ref. [10] for details. As input to the calculations we use Skyrme-type functionals, which ensure that the equations remain local and consistent with the Kohn-Sham philosophy. The TDSLDA equations (1) are discretized and solved on rectangular lattices. The size of the discretized Hamiltonian in Eq. (1) is $4N_xN_yN_z \times 4N_xN_yN_z$, where $N_x,\ N_y,\ N_z$ are the number of lattice points in the corresponding spatial directions. Each qpwf has 4 components and thus one has to solve $16N_xN_yN_z$ partial differential equations (PDEs), where each function is defined on $N_xN_yN_z$ lattice points. Over the years, we have developed a highly efficient code which takes advantage of the GPU accelerators and which provide an enormous speedup with respect to a CPU-only code. On Titan a GPU code, a single trajectory from saddle to scission (10^3 to 10^4 fm/c) can be finished within 12 hours using $1,000$ GPUs with a time step $\Delta t = 0.03$ fm/c.

The main ingredient necessary in fission simulations, which also makes the numerical calculations much more complex than in other approaches, is the pairing field in Eq. (1). It was well understood long time ago that without including pairing correlations a nucleus will not fission at low energies in a microscopic dynamic approach [16–18]. In calculations performed in the time-dependent Hartree-Fock (TDHF) model, fission was obtained only by introducing unrealistically large pairing gaps [19]. In other more recent simulations like [20–23], the system fissioned only at high energy, or if the initial state was far along the fission path so that the two fragments were already formed.

Only one-body (current) densities are included in TDSLDA. Hence, while the system is described by a single generalized Slater determinant throughout the simulations, we observe the separation between the fission fragments by looking at the density profile. As noted in Ref. [11], the dynamics involves a

large number of degrees of freedom, and can take a long time, although the duration of the process depends very strongly on the nuclear energy density functional (NEDF) used in the calculation. The results obtained in TDSLDA are consistent [11] with expectations that the light fragment emerges deformed, while the heavy fragment is close to spherical shape, as it is expected to be close to a closed shell configuration. Fission quantities such as the fission fragment masses, charges, kinetic and excitation energies etc., are calculated after separation, by dividing the simulation box in two.

3 Selected features of the fission dynamics

The initial state in TDSLDA simulation is located beyond the fission barrier, but close to the saddle point. If the initial state were placed in the ground-state potential well, even at an energy above the fission barrier, it would take a very long time to evolve toward a scission configuration, making the simulation impossible because numerical errors accumulate after a large number of time steps. Thus, a first valid question is how sensitive to the choice of the initial state our results are. In addition, the choice of the NEDF used as input in the calculations can influence the results. In Ref. [11], the choice was to use the generic Skyrme SLy4 parameterization for the NEDF, which is not considered one of the appropriate parameterizations by fission practitioners, since it provides a very poor description of the potential energy surfaces, in particular of the fission barriers. For our latest investigation presented in Ref. [12], we have used two more realistic NEDFs to calculate several trajectories, starting from different points on the potential energy surface. In the left hand panel of Fig. 1, we show several trajectories in the (Q_{20}, Q_{30}) space for the SKM* NEDF. The initial states have an average excitation energy of 8.3 MeV, with a standard deviation of 3 MeV, not including the symmetric trajectory (starting around $Q_{30} \approx 0$).

Most of the trajectories shown in Fig. 1 produce fission fragments with very similar properties $\langle N_l \rangle = 61.8(9)$ and $\langle Z_l \rangle = 40.9(5)$, TKE$\rangle = 174.5(2.5)$ MeV and $\langle$TXE$\rangle = 31.5(3.8)$ MeV. These results are significantly different from the result that ends in the symmetric region, where TKE is much lower (149 MeV). One trajectory ends up in a local minimum and in the absence of fluctuations, it will take a long time for the system to fission. Although the initial conditions are all located on different points of the energy surface, the corresponding trajectories leading to asymmetric fission produce fragments with very similar properties, since the mean field by definition provides an average path toward fission. Fluctuations missing from the mean field are expected to play an important role to reach a good agreement of the simulations with experimental data on fission mass and TKE yields. Surprisingly, only a relatively narrow ensemble of initial conditions was considered in the TDHF+BCS calculations of Tanimura et. al. [24] resulted in distributions with widths comparable with experimental data. The simulations presented in this contribution and previously [12] do not support their findings.

One particularly important feature of fission dynamics is illustrated in the left-hand side of Fig 1, where we plot the collective flow energy as a function of time. The collective flow energy is defined as

$$E_{\text{coll.flow}} = \int d^3\vec{r} \frac{\vec{j}^2(\vec{r},t)}{2M_N\rho(\vec{r},t)}, \tag{2}$$

where $\vec{j}(\vec{r},t) = \frac{i\hbar}{2}\sum_k \left(v_k(\vec{r},t)^*\vec{\nabla}v_k(\vec{r},t) - v_k(\vec{r},t)\vec{\nabla}v_k^*(\vec{r},t)\right)$ is the current density, and $\rho(\vec{r},t) = \sum_k |v_k(\vec{r},t)|^2$ is the particle number density. For a point-like particle, this is simply the kinetic energy, and thus, from the classical point of view, if the particle is on an incline, one expects that the collective energy flow would increase quickly in time. Instead, we observe that the collective energy remains small (around 1 MeV) and almost constant, and it increases drastically only after scission, when the Coulomb repulsion takes over. This is in contrast with adiabatic approaches, where one expects a full conversion of the collective energy potential surface into a collective flow energy of about 15 to 20 MeV from saddle to scission. Hence, these results are consistent with the hypothesis of overdamped collective motion, as assumed in the work by Randrup et. al. [25]. The motion is strongly dissipative due to the strong one-body dissipation.

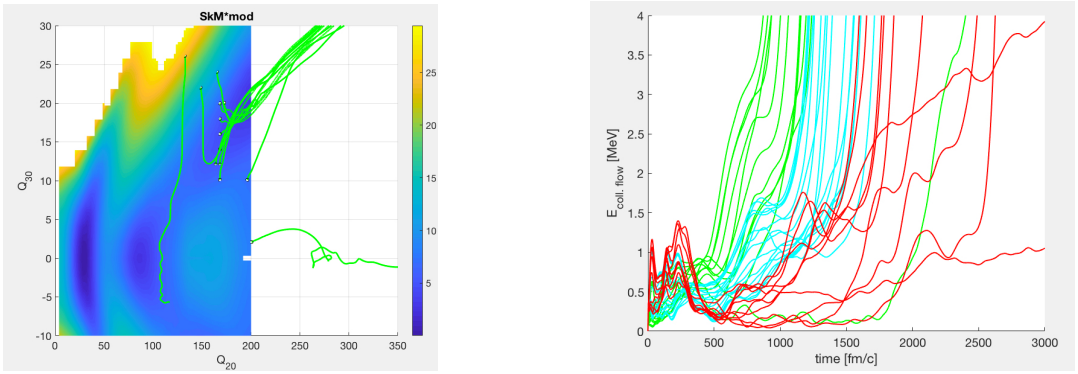

Fig. 1: Left: sample of trajectories from starting different points to fission configurations. Right: the collective flow energy remains very low during fission trajectories, up to the scission point.

It is well accepted today that these prompt neutron and gamma emission (that is, neutron or gammas emitted before any β decay toward stability) and angular and/or energetic correlations between them can offer information regarding the fission process [26]. For example, the average neutrons emitted as a function of mass can give indirect information regarding the energy sharing between fragments, since the most efficient way to de-excite above the neutron separation energy is by neutron emission. Hence, the higher the excitation energy the more neutrons on average are emitted from the fragments. In addition, it was observed that when the incident energy of the neutron inducing fission increases, the number of neutrons emitted from the heavy fragments increases, while the average number of neutrons emitted from the light fragment remains the same (see Fig. 6 in Ref. [27]). This is an experimental indication that the extra excitation energy goes mostly into the heavy fragment. No other microscopic models available today can predict this behavior. Only TDSLDA, where fragments can be fully separated and thus the excitation energy extracted, has the potential to make reliable predictions, for example by setting initial conditions at finite temperature.

State-of-the-art phenomenological models that simulate the prompt neutron and gamma emissions [28–30] rely on the assumption that the prompt particle emission takes place only after the particles are fully accelerated. Moreover, since the neutron emission is very fast, the mass yields are always measured after the neutron emission. Hence, corrections have to be applied in order to obtain information regarding quantities before neutron emission, which are used as input in simulations. From this point of view, additional corrections both for theory and experiment could be required if the number of neutrons emitted at scission and/or during the acceleration of the fission fragments is significant as suggested by some phenomenological models [31]. Our investigation suggests that the average number of neutron emitted from scission to full acceleration can reach more than 0.4, almost independent of the trajectory [12]. However, more simulations in bigger boxes are necessary in order to eliminate any possible numerical artifacts.

4 Outlook

We have presented evidence that the TDSLDA can be a very effective tool in answering qualitative and quantitative questions regarding the dynamics of the fission process. Our simulations suggest that the one-body dissipation is strong, which leads to an overdamped dynamics. As a consequence, the trajectories follow predominantly the direction of the steepest descent and it is expected that the fluctuations left out in the mean field would play an important role in describing the widths of the distributions observed experimentally. Recently, we have formulated the framework to include such fluctuations and dissipation within the time-dependent DFT [32]. While for testing purposes the theoretical modes was initially implemented in a simpler hydrodynamic approach that does not include pairing or shell effects,

it is straightforward to extend the same framework in TDSLDA. In fact, we have already presented in Ref. [32] a couple of TDSLDA trajectories including fluctuations and dissipation. While TDSLDA is significantly more demanding computationally than any other theoretical models for fission, a reasonable number of trajectories can be run with today's computing capabilities in order to obtain a reasonable distributions.

In this contribution, the discussion was limited to a few aspects of fission dynamics, including the evidence for emission of neutrons during acceleration. However, because it can follow the dynamics of the fissioning system until full separation, TDSLDA has the unique ability to provide information on all fission observables, eventually as a function of the excitation energy of the fissioning nucleus. In this framework, one can study the excitation energy sharing mechanism between the two fragments, and, with some modification, the average spin of the fission fragments before neutron emission. This work is already planned and will be investigated as soon as computational resources become available.

Acknowledgment. Work for this contribution was supported by the U.S. Department of Energy through different programs (Nuclear Physics, SciDAC, Office of Science, ASC, and SSAA).

References

[1] N. Schunck and L. M. Robledo, "Microscopic theory of nuclear fission: a review," *Reports on Progress in Physics*, vol. 79, no. 11, p. 116301, 2016.

[2] L. N. Oliveira, E. K. U. Gross, and W. Kohn, "Density-functional theory for superconductors," *Phys. Rev. Lett.*, vol. 60, pp. 2430–2433, June 1988.

[3] A. Bulgac, "Time-dependent density functional theory and the real-time dynamics of Fermi superfluids," *Annu. Rev. Nucl. Part. Sci.*, vol. 63, pp. 97–121, 2013.

[4] A. Bulgac, M. M. Forbes, M. M. Kelley, K. J. Roche, and G. Wlazłowski, "Quantized superfluid vortex rings in the unitary Fermi gas," *Phys. Rev. Lett.*, vol. 112, p. 025301, Jan. 2014.

[5] G. Wlazłowski, W. Quan, and A. Bulgac, "Perfect-fluid behavior of a dilute fermi gas near unitary," *Phys. Rev. A*, vol. 92, p. 063628, Dec 2015.

[6] A. Bulgac, Y.-L. Luo, and K. J. Roche, "Quantum Shock Waves and Domain Walls in the Real-Time Dynamics of a Superfluid Unitary Fermi Gas," *Phys. Rev. Lett.*, vol. 108, p. 150401, Apr. 2012.

[7] I. Stetcu, A. Bulgac, P. Magierski, and K. J. Roche, "Isovector giant dipole resonance from the 3d time-dependent density functional theory for superfluid nuclei," *Phys. Rev. C*, vol. 84, p. 051309(R), Nov. 2011.

[8] I. Stetcu, C. Bertulani, A. Bulgac, P. Magierski, and K. J. Roche, "Relativistic Coulomb excitation within Time Dependent Superfluid Local Density Approximation," *Phys. Rev. Lett.*, vol. 114, p. 012701, Jan. 2014.

[9] A. Bulgac and M. M. Forbes, "Use of the discrete variable representation basis in nuclear physics," *Phys. Rev. C*, vol. 87, p. 051301(R), May 2013.

[10] S. Jin, A. Bulgac, K. Roche, and G. Wlazłowski, "Coordinate-space solver for superfluid many-fermion systems with the shifted conjugate-orthogonal conjugate-gradient method," *Phys. Rev. C*, vol. 95, p. 044302, Apr 2017.

[11] A. Bulgac, P. Magierski, K. J. Roche, and I. Stetcu, "Induced fission of ^{240}Pu within a real-time microscopic framework," *Phys. Rev. Lett.*, vol. 116, p. 122504, Mar 2016.

[12] A. Bulgac, S. Jin, K. Roche, N. Schunck, and I. Stetcu, "Fission Dynamics." arXiv:1806.00694, 2018.

[13] P. Moller, D. G. Madland, A. J. Sierk, and A. Iwamoto, "Nuclear fission modes and fragment mass asymmetries in a five-dimensional deformation space," *Nature*, vol. 409, pp. 785–790, 02 2001.

[14] A. J. Sierk, "Langevin model of low-energy fission," *Phys. Rev. C*, vol. 96, p. 034603, Sep 2017.

[15] A. Bulgac and K. J. Roche, "Time-dependent density functional theory applied to superfluid nuclei," *Journal of Physics: Conference Series*, vol. 125, no. 1, p. 012064, 2008.

[16] G. F. Bertsch, F. Barranco, and R. A. Broglia, "Windsurfing the Fermi sea: Proceedings of the international conference and symposium on unified concepts of many-body problems held at the state university of new york, stony brook, september 4-6, 1986 in honor of gerry brown's 60th birthday," in *Windsurfing the Fermi Sea: Proceedings of the International Conference and Symposium on Unified Concepts of Many-Body Problems held at the State University of New York, Stony Brook, September 4-6, 1986 in honor of Gerry Brown's 60th birthday* (T. T. S. Kuo and J. Speth, eds.), (Amsterdam), p. 33, North-Holland, 1987.

[17] F. Barranco, R. A. Broglia, and G. F. Bertsch, "Exotic radioactivity as a superfluid tunneling phenomenon," *Phys. Rev. Lett.*, vol. 60, pp. 507–510, Feb. 1988.

[18] G. F. Bertsch and A. Bulgac, "Comment on "spontaneous fission: A kinetic approach"," *Phys. Rev. Lett.*, vol. 79, pp. 3539–3539, Nov 1997.

[19] J. W. Negele, S. E. Koonin, P. Möller, J. R. Nix, and A. J. Sierk, "Dynamics of induced fission," *Phys. Rev. C*, vol. 17, pp. 1098–1115, Mar. 1978.

[20] Y. Tanimura, D. Lacroix, and G. Scamps, "Collective aspects deduced from time-dependent microscopic mean-field with pairing: Application to the fission process," *Phys. Rev. C*, vol. 92, p. 034601, Sep 2015.

[21] Y. Hashimoto and G. Scamps, "Gauge angle dependence in time-dependent Hartree-Fock-Bogoliubov calculations of ^{20}O $+^{20}$ O head-on collisions with the Gogny interaction," *Phys. Rev. C*, vol. 94, p. 014610, Jul 2016.

[22] P. Goddard, P. Stevenson, and A. Rios, "Fission dynamics within time-dependent Hartree-Fock: Deformation-induced fission," *Phys. Rev. C*, vol. 92, p. 054610, Nov 2015.

[23] P. Goddard, P. Stevenson, and A. Rios, "Fission dynamics within time-dependent Hartree-Fock. II. Boost-induced fission," *Phys. Rev. C*, vol. 93, p. 014620, Jan 2016.

[24] Y. Tanimura, D. Lacroix, and S. Ayik, "Microscopic phase-space exploration modeling of $^{258}\mathrm{Fm}$ spontaneous fission," *Phys. Rev. Lett.*, vol. 118, p. 152501, Apr 2017.

[25] J. Randrup, P. Möller, and A. J. Sierk, "Fission-fragment mass distributions from strongly damped shape evolution," *Phys. Rev. C*, vol. 84, p. 034613, Sep 2011.

[26] P. Talou, R. Vogt, J. Randrup, M. E. Rising, S. A. Pozzi, J. Verbeke, M. T. Andrews, S. D. Clarke, P. Jaffke, M. Jandel, T. Kawano, M. J. Marcath, K. Meierbachtol, L. Nakae, G. Rusev, A. Sood, I. Stetcu, and C. Walker, "Correlated prompt fission data in transport simulations," *The European Physical Journal A*, vol. 54, p. 9, Jan 2018.

[27] A. A. Naqvi, F. Käppeler, F. Dickmann, and R. Müller, "Fission fragment properties in fast-neutron-induced fission of $^{237}\mathrm{Np}$," *Phys. Rev. C*, vol. 34, pp. 218–225, Jul 1986.

[28] R. Vogt, J. Randrup, D. A. Brown, M. A. Descalle, and W. E. Ormand, "Event-by-event evaluation of the prompt fission neutron spectrum from ^{239}Pu(n, f)," *Phys. Rev. C*, vol. 85, p. 024608, Feb 2012.

[29] B. Becker, P. Talou, T. Kawano, Y. Danon, and I. Stetcu, "Monte carlo hauser-feshbach predictions of prompt fission γ rays: Application to $n_{\mathrm{th}} + ^{235}$U, $n_{\mathrm{th}} + ^{239}$Pu, and ^{252}Cf (sf)," *Phys. Rev. C*, vol. 87, p. 014617, Jan 2013.

[30] K.-H. Schmidt, B. Jurado, C. Amouroux, and C. Schmitt, "General description of fission observables: GEF model code," *Nuclear Data Sheets*, vol. 131, pp. 107 – 221, 2016.

[31] N. Carjan and M. Rizea, "Similarities between calculated scission-neutron properties and experimental data on prompt fission neutrons," *Physics Letters B*, vol. 747, pp. 178 – 181, 2015.

[32] A. Bulgac, S. Jin, and I. Stetcu, "Unitary evolution with fluctuations and dissipation." arXiv:1805.08908, May 2018.

Microscopic optical potential derived from NN chiral potentials

Carlotta Giusti[1]*, Matteo Vorabbi*[2]*, Paolo Finelli*[3]
[1]Dipartimento di Fisica, Università degli Studi di Pavia and INFN, Sezione di Pavia, Via A. Bassi 6, I-27100 Pavia, Italy,
[2]TRIUMF, 4004 Wesbrook Mall, Vancouver, British Columbia, V6T 2A3, Canada,
[3]Dipartimento di Fisica e Astronomia, Università degli Studi di Bologna and INFN, Sezione di Bologna, Via Irnerio 46, I-40126 Bologna, Italy

Abstract
A microscopic optical potential is derived from NN chiral potentials at fourth (N^3LO) and fifth (N^4LO) order, with the purpose to check the convergence and to assess the theoretical errors associated with the truncation of the chiral expansion in the construction of an optical potential. The numerical predictions of our optical potential are compared with those of a successful phenomenological optical potential and with available empirical data for elastic proton scattering on different isotopic chains and for incident proton energies in the range $156 \leq E \leq 333$ MeV.

1 Introduction

The optical potential (OP) provides a suitable tool to describe elastic nucleon-nucleus (NA) scattering. Its use can be extended to inelastic scattering and to perform calculations for a wide variety of nuclear reactions. Many of these calculations make use of phenomenological OPs, that are obtained assuming an analytical form and a dependence on a number of adjustable parameters for the real and imaginary parts (the OP is complex) that characterize the shape of the nuclear density distribution and that vary with the nucleon energy and the nuclear mass number (the OP is energy dependent and can depend on the nuclear mass number A). The values of the parameters are determined through a fit to elastic pA scattering data. Alternatively and more fundamentally, the OP can be obtained from a microscopic calculation, which, in principle, requires the solution of the full many-body nuclear problem for the incident nucleon and the A nucleons of the target and that, therefore, represents a very hard and challenging task. When A is a sizable number the task is beyond present capabilities and several approximations are needed to reduce the complexity of the original problem. In general, we do not expect that a theoretical OP, which is the results of several approximations, will be able to describe elastic NA scattering data better than a phenomenological OP whose parameters have been determined through a fit to empirical data, in particular if we consider data included in the database used for the fitting procedure, but it might have a greater predictive power when applied to situations for which experimental data are not yet available.

In Refs. [1–3] we derived a microscopic OP for elastic pA scattering from NN chiral potentials up to fourth (N^3LO) and fifth (N^4LO) order in the chiral perturbative expansion. The first purposes of our work were to study the domain of applicability of microscopic two-body chiral potentials, to check the convergence, and to assess the theoretical errors associated with the truncation of the chiral expansion in the construction of an OP. The theoretical framework that has been used to obtain the OP is based on the Watson multiple scattering theory [4], which was originally developed by Kerman, McManus, and Thaler (KMT) [5]. In the calculations we adopted several approximations, with the idea to start from a relatively simple model that, in subsequent steps, can then be improved .

The contribution is organized as follows: In Section 2 we briefly outline the theoretical framework used to calculate our microscopic OP. In Section 3 we discuss the performances of our OP in comparison with data for elastic pA scattering data on different nuclei and isotopic chains. Our results are compared with those of the successful phenomenological OP of Refs. [6,7]. Our conclusions are drawn in Section 4.

2 Theoretical framework

Proton elastic scattering off a target nucleus with A nucleons can be formulated in the momentum space by the full Lippmann-Schwinger (LS) equation

$$T = V\,(1 + G_0(E)T)\ , \tag{1}$$

where V represents the external interaction which, if we assume only two-body forces, is given by the sum over all the target nucleons of two-body potentials describing the interaction of each target nucleon with the incident proton, and $G_0(E)$ is the free Green's function for the $(A+1)$-nucleon system.

As a standard procedure, Eq. (1) is separated into a set of two coupled integral equations: the first one for the T matrix

$$T = U\,(1 + G_0(E)PT) \tag{2}$$

and the second one for the OP U

$$U = V\,(1 + G_0(E)QU)\ . \tag{3}$$

A consistent framework to compute U and T is provided by the spectator expansion, that is based on the KMT [5] multiple scattering theory. We retain only the first-order term, corresponding to the single-scattering approximation, where only one target-nucleon interacts with the projectile. In addition, we adopt the impulse approximation, where nuclear binding forces on the interacting target nucleon are neglected [1]

After some manipulations, the OP is obtained in the so-called optimum factorization approximation as the product of the free NN t matrix and the nuclear matter densities

$$U(\boldsymbol{q},\boldsymbol{K};\omega) = \frac{A-1}{A}\,\eta(\boldsymbol{q},\boldsymbol{K}) \sum_{N=n,p} t_{pN}\,(\boldsymbol{q},\boldsymbol{K},\omega)\ \rho_N(q)\,, \tag{4}$$

where $\boldsymbol{q}$ and $\boldsymbol{K}$ are the momentum transfer and the total momentum, respectively, in the NA reference frame, t_{pN} represents the proton-proton (*pp*) and proton-neutron (*pn*) t matrix, ρ_N represents the neutron and proton profile density, and $\eta(\boldsymbol{q},\boldsymbol{K})$ is the Møller factor, that imposes the Lorentz invariance of the flux when we pass from the NA to the NN frame in which the t matrices are evaluated. Through the dependence of η and t_{pN} upon $\boldsymbol{K}$, the factorized OP in Eq. (4) exhibits nonlocality and off-shell effects [1].

Two basic ingredients are required to calculate the OP: the NN potential and the neutron and proton densities of the target nucleus. For the neutron and proton densities we use a relativistic mean-field (RMF) description [8], which has been quite successful in the description of ground state and excited state properties of finite nuclei, in particular in a density dependent meson exchange (DDME) version, where the couplings between mesonic and baryonic fields are assumed as functions of the density itself [9]. For the NN interaction we have used in Ref. [1] two different versions of chiral potentials at fourth order ($\mathrm{N^3LO}$) in the chiral expansion, developed by Entem and Machleidt (EM) [10] and Epelbaum, Glöckle, and Meißner (EGM) [11], and in Ref. [2] the more recent NN potentials at fifth order ($\mathrm{N^4LO}$) presented by Epelbaum, Krebs, and Meißner (EKM) [12] and Entem, Machleidt, and Nosyk (EMN) [13].

3 Results

3.1 Optical potentials derived from NN chiral potentials at $\mathrm{N^3LO}$ and at $\mathrm{N^4LO}$

As a first step, microsopic OPs have been derived from two different versions of chiral potentials at $\mathrm{N^3LO}$ [10, 11], that use different regularization prescriptions to treat divergent terms. In general, the integral in the Lippmann-Schwinger (LS) equation is divergent and needs to be regularized. A usual procedure is to multiply the NN potential entering the LS equation by a regulator function f^{Λ}. Both EM and EGM present results with three values of the cutoff parameter Λ (450, 500, 600 MeV for EM

and 450, 550, 600 MeV for EGM), and treat differently the short-range part of the two-pion exchange contribution, that has unphysically strong attraction: EM adopt a dimensional regularization and EGM a spectral function regularization which introduces an additional cutoff $\tilde{\Lambda}$ and give the following cutoff combinations: $\{\Lambda, \tilde{\Lambda}\} = \{450, 500\}, \{450, 700\}, \{550, 600\}, \{600, 600\}, \{600, 700\}$. The sensitivity of the results to the choice of the cutoff parameters and the order-by-order convergence of the chiral perturbation theory (ChPT) expansion have been investigated comparing the results produced by the different chiral potentials with available experimental data for the NN scattering amplitudes (*pp* and *pn* Wolfenstein amplitudes a and c) and for the observables (differential cross section $d\sigma/d\Omega$, analyzing power A_y, and spin rotation Q) of elastic proton scattering off ^{16}O [1].

Concerning the order-by-order convergence, the results show that it is mandatory to use chiral potentials at N^{3}LO: NN potentials at lower orders produce results in clear disagreement with the experimental NN scattering amplitudes and with the observables of elastic pA scattering [1].

All the NN potentials at N^{3}LO are able to reproduce the experimental amplitudes at 100 MeV, with the only exception of the real part of the c_{pp} amplitude, that is anyhow extremely small. The agreement becomes, as expected, worse upon increasing the energy and at 200 MeV the set of potentials with lower cutoffs fail to reproduce empirical data [1].

The observables for elastic proton scattering on ^{16}O computed with the different NN potentials at N^{3}LO at 100 MeV and 200 MeV are displayed in Fig. 1 and compared with the empirical data. All sets of

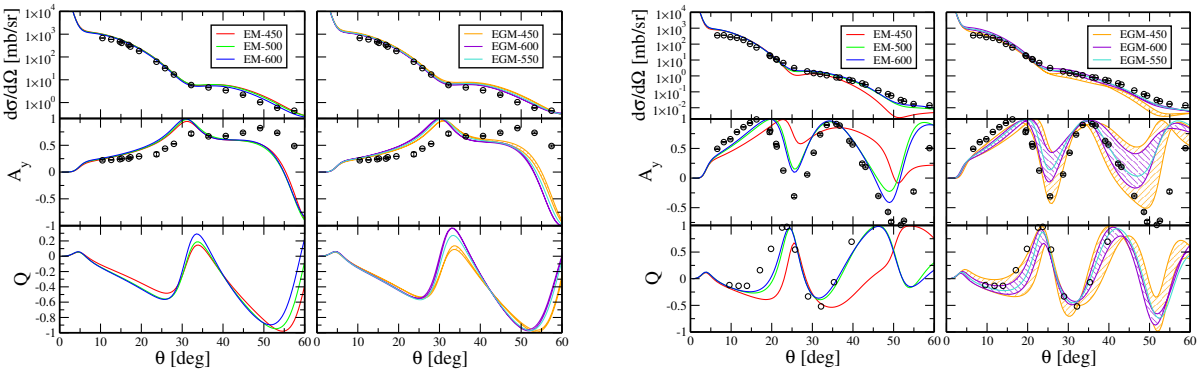

Fig. 1: Scattering observables (differential cross section $d\sigma/d\Omega$, analyzing power A_y, and spin rotation Q) as a function of the center-of-mass scattering angle θ for elastic proton scattering on ^{16}O computed at a laboratory energy of 100 MeV (left figure) and 200 MeV (right figure). The results obtained with the EM [10] and EGM [11] NN chiral potentials at N^{3}LO are denoted in the figures by the value of the LS cutoff. Data are taken from [14,15].

potentials give close results, with the exception of A_y above 50 degrees, where all potentials overestimate the experimental data up to the maximum and then display an unrealistic downward trend, and Q around the maximum at 30 degrees. In particular, the experimental cross section is well reproduced by all potentials in the minimum region, between 30 and 35 degrees. Polarization observables, which are more sensitive to the differences in the potentials and to the approximations of the model, are usually more difficult to reproduce. At 200 MeV EM and EGM potentials with the lower cutoffs ($\Lambda = 450$ MeV) give results in clear disagreement with empirical data, which are well described by the potentials with higher cutoffs.

As a next step, a microscopic OP has been derived, within the same theoretical framework and adopting the same approximations, from the more recent NN potentials at fifth order (N^{4}LO) presented by Epelbaum, Krebs, and Meißner (EKM) [12] and Entem, Machleidt, and Nosyk (EMN) [13]. Our aims were to check the convergence of the ChPT expansion, to assess the theoretical errors associated with the truncation of the expansion and the sensitivity of the results to the choice of the NN potential and to the adopted regularization prescription.

Numerical results have been presented in comparison with empirical data for the *pp* and *np*

Wolfenstein amplitudes and scattering observables of elastic proton scattering off ^{16}O, ^{12}C, and ^{40}Ca nuclei at an incident proton energy of 200 MeV [2]. The results indicate that the order-by-order convergence pattern is clear and that robust convergence has been reached at N^{4}LO. We do not expect large contributions from the higher-order extension in the NN sector. The agreement of the theoretical results with experimental data is comparable, neither better nor worse, than the agreement obtained with chiral potentials at N^{3}LO. A better agreement would require a better model for the OP, a model where the approximations adopted in the present calculations of the OP are reduced.

3.2 Microscopic and phenomenological optical potentials

Although obtained assuming several approximations, our OP is the result of a microscopic calculation that does not contain phenomenological inputs. In contrast, phenomenological OPs are based on the use of some free parameters, specifying the well and the geometry of the system, that are determined by a fitting procedure over a set of available experimental data of elastic pA scattering. The phenomenological approach provides OPs able to give an excellent description of data in many regions of the nuclear chart and for energy ranges where data are available, but which may lack predictive power when applied to situations where experimental data are not yet available. We have seen that our OP gives a reasonable description of elastic pA scattering data without the need of introducing free parameters fitted to empirical data. Being the result of a model and not of a fitting procedure, a microscopic OP should have more theoretical content and might have a more general predictive power than a phenomenological OP, but the approximations which are needed to reduce the complexity of the original many-body problem might give a poorer agreement with available empirical data. In order to investigate and clarify this issue, it can be useful to compare the performances of our microscopic OP and of a successful phenomenological OP in the description of elastic proton scattering data on nuclei of some isotopic chains. For the comparison we have considered the phenomenological OP of Refs. [6, 7] (KD). A systematic investigation has been performed and presented in Ref. [3] for several proton energies around and above 200 MeV, with the aim to test the upper energy limit of applicability of our OP before the chiral expansion scheme breaks down.

The nonrelativistic phenomenological KD potential [6] is a so-called "global" OP, which means that the free adjustable parameters are fitted for a wide range of nuclei ($24 \leq A \leq 249$) and of incident energies (1 keV $\leq E \leq$ 200 MeV) with some parametric dependence of the coefficients in terms of the target mass number A and of the incident energy E. Recently, an extension of the OP up to 1 GeV has been proposed [7], with the aim to test at which energy the validity of the predictions of the nonrelativistic OP fails. Above 200 MeV an approach based on the Dirac equation would probably be a more consistent choice, but, since we are interested in testing the limit of applicability of our (nonrelativistic) microscopic OP, we have employed such an extension for our present purposes. All the calculations have been performed by ECIS-06 [16] as a subroutine in the TALYS software [7, 17].

The microscopic OP adopted for the comparison has been derived from the two different versions of the NN chiral potentials at N^{4}LO, EKM [12] and EMN [13], which have significant differences in the the renormalization procedures. The strategy followed for the EKM potentials [12] consists in a coordinate space regularization for the long-range contributions $V_{\rm long}(\boldsymbol{r})$, by the introduction of $f\left(\frac{r}{R}\right) = \left(1-\exp\left(-\frac{r^2}{R^2}\right)\right)^n$, and a conventional momentum space regularization for the contact (short-range) terms, with a cutoff $\Lambda = 2R^{-1}$. Five choices of R are available: $0.8, 0.9, 1.0, 1.1$, and 1.2 fm, leading to five different potentials.

A slightly more conventional approach was pursued for the EMN potentials [13]. A spectral function regularization, with a cutoff $\tilde{\Lambda} \simeq 700$ MeV, was employed to regularize the loop contributions and a conventional regulator function, with $\Lambda = 450, 500$, and 550 MeV, to deal with divergences in the LS equation.

If we want to test the predictive power of our microscopic OP in comparison with available experimental data it can be useful to show the uncertainties produced by chiral potentials with different values

of the regularization parameters. For this purpose, all calculations have been performed with three of the EKM potentials, corresponding to $R = 0.8, 0.9$, and 1.0 fm, and with two of the EMN potentials, corresponding to $\Lambda = 500$ and 550 MeV. Since we want to compare results at energies around and above 200 MeV, and on the basis of the results of Ref. [2], we have excluded the EKM potentials with $R = 1.1$ and 1.2 fm and the EMN potential with $\Lambda = 450$. In the following Figs. 2, 3, and 4 the bands give the differences produced by changing R for EKM (red bands) and Λ for EMN (green bands).

Calculations have been performed with the phenomenological and microscopic OPs for proton energies between 156 and 333 MeV, for which experimental data are available. The energy range considered was chosen on the basis of the assumptions and approximations adopted in the derivation of the theoretical OP. In particular, the impulse approximation does not allow us to use our microscopic OP with enough confidence at much lower energies, where we can expect that the phenomenological KD potential is able to give a better agreement with the experimental data. The upper energy limit is determined by the fact that the EKM and EMN chiral potentials are able to describe NN scattering observables up to 300 MeV [12, 13].

The ratios of the differential cross sections to the Rutherford cross sections for elastic proton scattering off nichel and lead isotopes are shown in Figs. 2 and 3, respectively. The results calculated with the microscopic and phenomenological OPs are compared with the experimental data taken from Refs. [14, 15].

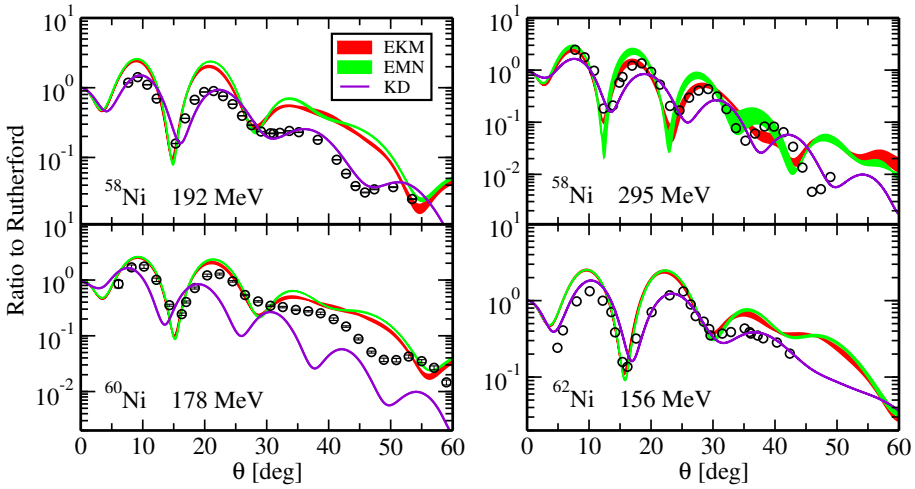

Fig. 2: Ratio of the differential cross section to the Rutherford cross section as a function of the center-of-mass scattering angle θ for elastic proton scattering on Ni isotopes: ^{58}Ni at $E = 192$ and 295 MeV, ^{60}Ni at $E = 178$ MeV, and ^{62}Ni at $E = 156$ MeV. In the calculations the microscopic OPs derived from the EKM [12] (red band) and EMN [13] (green band) NN chiral potentials at N^{4}LO and with the phenomenological global OP of Ref. [7] (KD, violet line). The meaning of the bands is explained in the text. Experimental data from Ref. [14, 15].

For nichel isotopes, in Fig. 2, ^{58}Ni up to 200 MeV and ^{60}Ni up to 65 MeV are included in the experimental database used to generate the KD potential. The phenomenological OP gives an excellent description of ^{58}Ni data at 192 MeV but a much worse agreement at the higher energy of 295 MeV, where it is able to describe only the overall behavior of the experimental cross section. The EKM and EMN results provide a better and reasonable description of the data at 295 MeV, up to $\theta \sim 40°$, while at 192 MeV they give a rough description of the shape of the experimental cross section but the size is somewhat overestimated. KD gives only a poor description of the data for ^{60}Ni at 178 MeV and a very good agreement for ^{62}Ni at 156 MeV. The microscopic OP gives a better and reasonable agreement with the ^{60}Ni data, over all the angular distribution, while for ^{62}Ni the results are a bit larger than

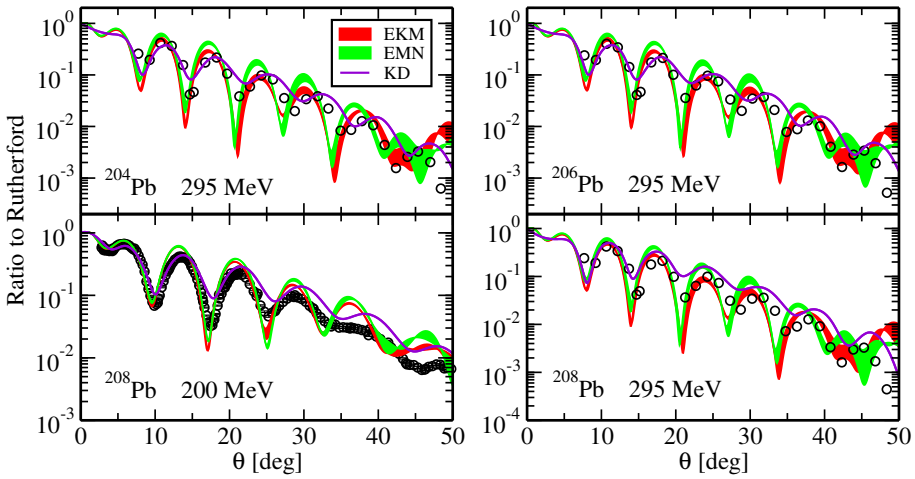

Fig. 3: The same as in Fig. 2 for Pb isotopes: ^{208}Pb at $E = 200$ MeV and ^{204,206,208}Pb at $E = 295$ MeV. Experimental data from Ref. [14, 15].

those of the KD potential. The EKM and EMN results are always very close to each other and the bands, representing the theoretical uncertainties produced by chiral potentials with different values of the regularization parameters, are generally narrow.

For lead isotopes, in Fig. 3, ^{208}Pb at 200 MeV is included in the experimental database used to generate the KD potential and here KD gives indeed a very good description of empirical data, better than the microscopic OP. On the other hand, the microscopic OP provides a better description of data for ^{204,206,208}Pb at 295 MeV, in particular when the EMN chiral potential is adopted in the calculations. For all the three isotopes considered the EKM and EMN results practically overlap for $\theta \leq 20^{\circ}$, where they are also very close to the KD result, then they start to separate and the EMN result is a bit larger than the EKM one and in better agreement with data. The uncertainty bands, that are generally narrow, in this case become larger increasing the scattering angle, when also the agreement with data declines.

The results shown in Figs. 2 and 3 indicate that our microscopic OP has a comparable and in some cases even better predictive power than the KD potential in the description of the cross sections for the isotopic chains and energy range here considered. KD is able to give a better and excellent description of data in specific situations, in particular, in the case of nuclei included in the experimental database used to generate the original KD potential and at the lower energies considered. For energies above 200 MeV our microscopic OP gives, in general, a better agreement with experimental data. This conclusion is confirmed by the results shown in Fig. 4, where the ratios of the differential cross sections to the Rutherford cross sections are displayed for elastic proton scattering off ^{16}O and ^{40,42,44,48}Ca at $E = 318$ MeV and ^{58}Ni at $E = 333$ MeV in comparison with the data taken from Refs. [14, 15]. The differences between the phenomenological and microscopic OPs increase with increasing scattering angle and proton energy. For ^{58}Ni at 333 MeV both EKM and EMN give a much better and very good description of data. In the other cases KD is able to describe data only at the lowest angles. The EKM and EMN results are in general very close to each other, the width of the uncertainty bands increases at larger scattering angles, but the uncertainties are not crucial for the comparison with data.

4 Conclusions

We have obtained a new microscopic optical potential for elastic pA scattering. Our optical potential has been derived as the first-order term within the spectator expansion of the nonrelativistic multiple scattering theory. In the interaction between the projectile and the target nucleon, we have adopted the

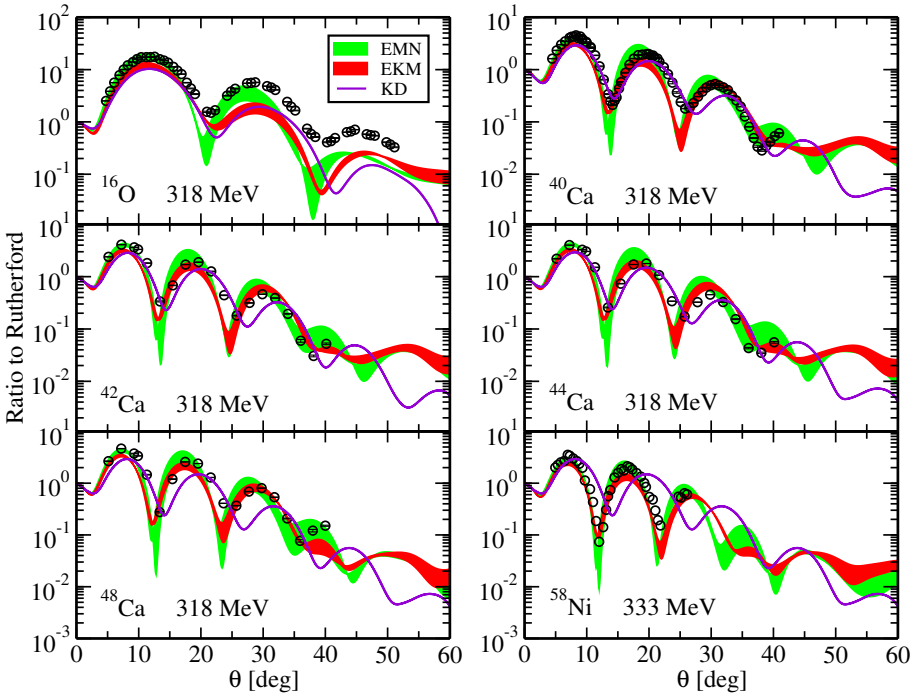

Fig. 4: The same as in Fig. 2 for ^{16}O and ^{40,42,44,48}Ca at $E = 318$ MeV and ^{58}Ni at $E = 333$ MeV. Experimental data from Ref. [14, 15].

impulse approximation and we have neglected medium effects. As a further simplification, we have adopted the optimum factorization approximation, where the optical potential is given in a factorized form by the product of the free NN t matrix and the nuclear density. This form conserves the off-shell and nonlocal nature of the optical potential.

The calculation of the optical potential requires two basic ingredients: the nuclear density and the NN interaction. The nuclear density has been obtained within a relativistic mean-field description by using a density dependent meson exchange model, where the couplings between mesonic and baryonic fields are assumed as functions of the density itself. For the NN interaction we have used different versions of chiral potentials at fourth (N^{3}LO) and fifth (N^{4}LO) order in the chiral expansion, which differ in the regularization prescriptions to treat divergent terms.

The first aims of our work were to study the domain of applicability of microscopic two-body chiral potentials in the construction of an optical potential, to check the convergence of the perturbative expansion, assessing theoretical errors associated with the truncation of the ChPT expansion, and to compare the results produced by the different NN chiral potentials, and their different regularization prescriptions, on elastic pA scattering observables.

Our work shows that building an optical potential within chiral perturbation theory is a promising approach for describing elastic pA scattering. The order-by-order convergence pattern is clear and robust convergence has been reached at N^{4}LO.

The performances of our microscopic optical potential have been studied in comparison with those of the successful phenomenological KD optical potential in the description of elastic proton scattering data on some isotopic chains at energies around and above 200 MeV. The agreement of our results with empirical data is comparable with the predictions given by the phenomenological potential, in particular for energies above 200 MeV.

A better agreement with empirical data would require an improved model for the microscopic

optical potential. As possible improvements we mention: 1) To go beyond the optimum factorization approximation and calculate the full-folding integral. This has already been done for light nuclei, in combination with non-local densities obtained consistently from the same chiral interactions used for the calculation of the NN t matrix [18]); 2) To go beyond the impulse approximation and take into account nuclear-medium effects; 3) To include three-body forces. Work is under way to improve the model in these directions.

References

[1] M. Vorabbi, P. Finelli, and C. Giusti, *Phys. Rev.*, **C93** (2016) 034619.

[2] M. Vorabbi, P. Finelli, and C. Giusti, *Phys. Rev.*, **C96** (2017) 044001.

[3] M. Vorabbi, P. Finelli, and C. Giusti, arXiv:1806.01037.

[4] K.M. Watson, *Phys. Rev.*, **89** (1953) 575.

[5] A. K. Kerman, H. McManus, and R. M. Thaler, *Ann. Phys. (NY)* **8** (1959) 55.

[6] A. J. Koning and J. P. Delaroche, *Nucl. Phys.* **A713** (2003) 231.

[7] A. J. Koning, S. Hilaire, and M.C. Duijvestijn, *Proc. of the International Conference on Nuclear Data for Science and Technology, April 22-27, 2007, Nice, France* (2008) 211.

[8] T. Nikšić *et al.*, *Computer Physics Communications* **185** (2014) 1808.

[9] T. Nikšić *et al.*, *Phys. Rev.*, **C66** (2002) 024306.

[10] D. R. Entem and R. Machleidt, *Phys. Rev.* **C68** (2003) 041001.

[11] E. Epelbaum, W. Glöckle, and U.-G. Meißner, *Nucl. Phys.* **A747** (2005) 362.

[12] E. Epelbaum, H. Krebs, and U.-G. Meißner *Eur. Phys. J* **A51** (2015) 53; *Phys. Rev. Lett.* **115** (2015) 122301 (2015).

[13] D. R. Entem, R. Machleidt, and Y. Nosyk, *Phys. Rev.* **C96** (2017) 024004.

[14] **http://www.physics.umd.edu/enp/jjkelly/datatables.htm**.

[15] **http://www.nndc.bnl.gov/exfor/exfor.htm**.

[16] J. Raynal, "Notes on ecis94" (1994).

[17] **www.talys.eu/fileadmin/talys/user/docs/talys1.8.pdf**.

[18] M. Gennari, M. Vorabbi, A. Calci, and P. Navratil, *Phys. Rev.*, **C97** (2018) 034619.

What pions can tell us about the neutron skin of nuclei

Christoph Hartnack[1]*, Arnaud Le Fèvre*[2]*, Yvonne Leifels*[2] *and Jörg Aichelin*[1,3]
[1] SUBATECH, UMR 6457, IMT Atlantique, IN2P3/CNRS, Université de Nantes,
4 rue Alfred Kastler, 44 307 Nantes, France
[2] GSI Helmholtzzentrum für Schwerionenforschung GmbH,
Planckstraße 1, 64291 Darmstadt, Germany
[3] Frankfurt Institute for Advanced Studies, Ruth Moufang Str. 1, 60438 Frankfurt, Germany

Abstract
We use the Isospin Quantum Molecular Dynamics approach to analyse the isospin ratios of pion production in collisions of heavy ions at incident energies below 2 AGeV. It is found that the comparison of the centrality dependence at different energies allows to gain information on the neutron skin of the nuclei, but also on other ingredients like the nuclear equation of state of asymmetric matter.

1 Introduction

One of the main interests of the study of relativistic heavy ion collisions is the investigation of the properties of nuclear matter at extreme densities and excitation energies. These investigations include the production of secondary particles, the properties of particles in a (dense) nuclear medium, the compression and repulsion of dense nuclear matter, its equilibration during the reaction and its decay into fragments and single particles. The most prominent secondary particle is the pion, a pseudoscalar meson which due to its very small mass can already be produced in heavy ion collisions of a few hundred AMeV of incident energies in the laboratory frame. This article will focus on the production of that particle in an energy range of several hundred AMeV to a few AGeV. For our calculations we use the IQMD approach [1], a microscopic transport model calculating heavy ion collisions on an event-by-event basis. We will first describe the production of pions in IQMD and the initialisation of protons and neutrons. In the next step we will discuss the rescattering of pions in nuclear matter and its effect on the isospin ratio to finally study the effect of the neutron skin and of the nuclear equation of state of asymmetric matter on these ratios.

1.1 Pion production in IQMD

The philosophy of IQMD follows the idea used by many other microscopic transport models [2–4] to decompose the interaction of nucleons into a long-range part described by local central force two-body potentials and a short-range part described by stochastic collisions. The long-range term leads to nuclear potentials, which become important for the stability of the nucleus and also touch topics like the nuclear equation of state [5]. We will shortly summarize the important part of the collision term and refer for a detailed description of both parts and their application in IQMD on [6]. Inside IQMD particles are described by Gaussian wave packages in coordinate and momentum space. Two particles collide if their minimum distance d, i.e. the minimum relative distance of the centroids of the Gaussians during their motion, in their CM frame fulfills the requirement:

$$d \leq d_0 = \sqrt{\frac{\sigma_{\rm tot}}{\pi}}, \qquad \sigma_{\rm tot} = \sigma(\sqrt{s},\ \text{type}). \tag{1}$$

where the cross section is assumed to be the free cross section of the regarded collision type ($N-N$, $N-\Delta$, ...). The cross sections for elastic and inelastic collisions are obtained by a table lookup using experimentally measured cross sections (when available) or derived from available cross sections using symmetry assumptions and detailed balance.

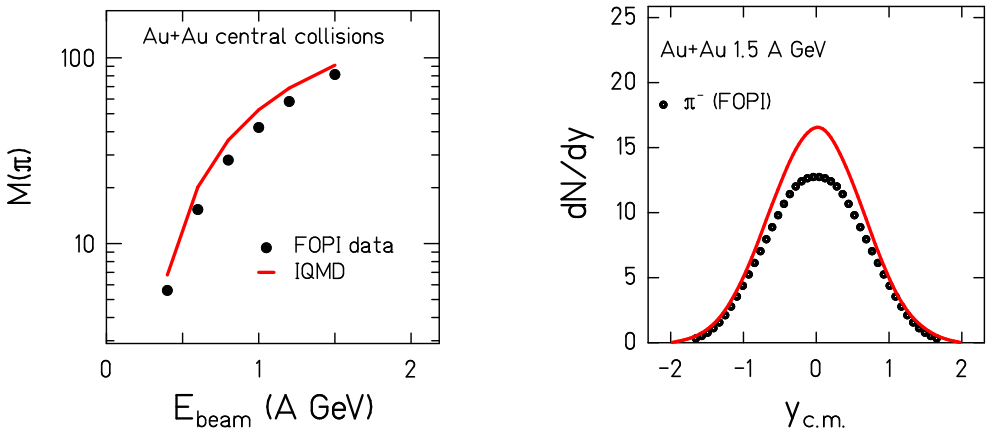

Fig. 1: Comparison between IQMD calculations and FOPI results on the absolute pion number as function of the incident energy (left) and of the rapidity distribution of π^- in collisions of Au+Au at 1.5 AGeV (right). (from [9])

The pion production in IQMD is done via the Δ-channel, where deltas can be produced in nucleon-nucleon (NN) collisions and be reabsorbed in $N\Delta$ collisions. The Δ decays and produces a free pion, which can be reabsorbed in collisions with a nucleon and form a Δ again:

$$NN \leftrightarrow N\Delta \qquad \Delta \leftrightarrow N\pi \tag{2}$$

These reactions have to comply with detailed balance and isospin effects have to be taken into account by the use of Clebsch-Gordon coefficients. For more details see [7].

The production of pions in IQMD has successfully been tested by various comparisons with experimental measurements performed by the FOPI collaboration at GSI [8]. Giving an example taken from [9], figure 1 compares the excitation function of the total pion yield in Au+Au collisions measured by FOPI to IQMD calculations (left hand side). For this purpose, the events calculated by IQMD have undergone the same analysis procedures as the experimental data. The multiplicities calculated by IQMD are slightly higher than those obtained by FOPI but the excitation functions show nicely the same behavior. Figure 1 compares on the right hand side the rapidity distributions of negative pions in central collisions. As already stated before, IQMD shows slightly larger absolute pion yields, therefore it is not astonishing that the absolute numbers of the rapidity distribution are also higher than the experimental points. However, the structure of the distribution is quite similar. The distribution is peaked at midrapidity underlining that most of the pions are produced by first collisions or in collisions of the stopped participant matter. Afterwards they will undergo rescattering and we will come to that point later on.

1.2 Density profiles of protons and neutrons

In standard IQMD calculations the centroids of the Gaussians are distributed inside a sphere in the rest frame of the nucleus according to

$$(\vec{r}_i - \vec{r}_{CM})^2 \leq R_A^2 \qquad R_A = R_0 \cdot A^{1/3} \tag{3}$$

where $\vec{r}_i$ and $\vec{r}_{CM}$ are the position vectors of particle i and of the center-of-mass of the nucleus, respectively, and $A = Z + N$ is the number of nucleons of the nucleus. The radius parameter is chosen as $R_0 = 1.12$ fm. This initialization, which we will call "R_P=R_N ", assures the same rms radius for protons and neutrons even for heavy isospin-asymmetric systems. Consequently, in the whole nucleus the neutrons have systematically a higher density than the protons. It should be noted that most other

microscopic models with the exception of [10] use a similar procedure yielding the same rms radius for protons and neutrons. If we want to assume the same density of protons and neutrons at least in the centre of the nucleus we have to allow protons and neutrons to have different rms radii, which can be obtained by the distribution of the centroids of the Gaussians according to

$$R_P = R_0 \cdot (2Z)^{1/3} \qquad R_N = R_0 \cdot (2N)^{1/3} \tag{4}$$

with R_P and R_N denoting the radii for protons and neutrons. We will call this initialisation "R_P<R_N ". However, R_P<R_N yields a difference of the rms radii of protons and neutrons of around 0.5 fm in a system like ^{197}Au.

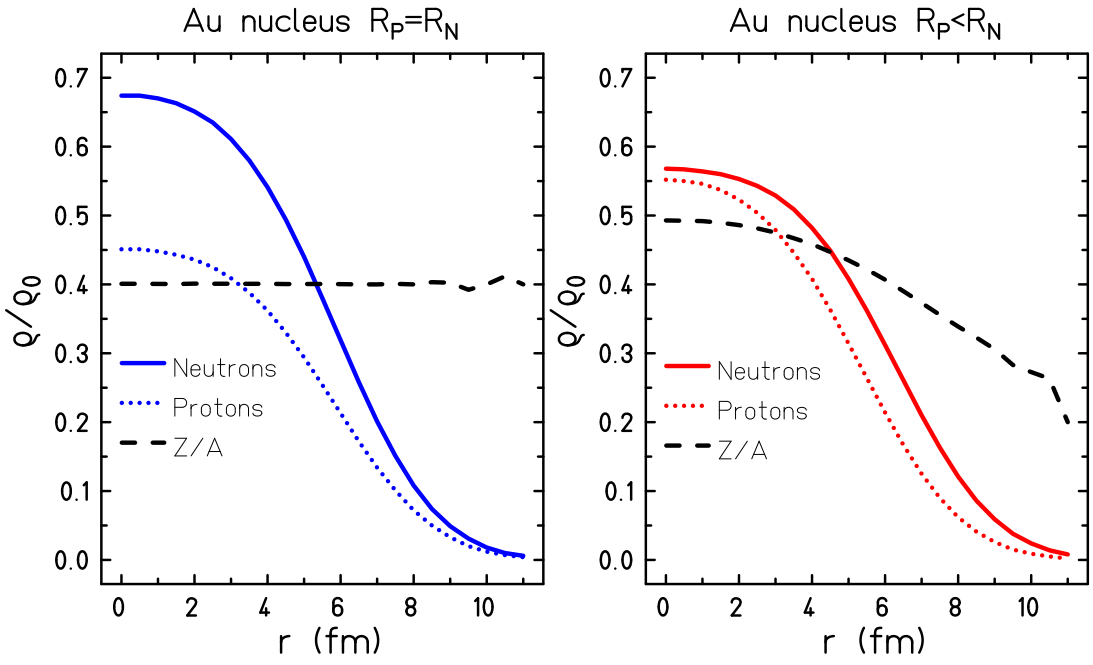

Fig. 2: Profiles of proton and neutron densities and for the charge ration $Z/A(r)$ for initialisations assuming R_P=R_N (left) and R_P<R_N (right).

Figure 2 shows the density profiles of protons (dotted lines) and neutrons (full lines) in a ^{197}Au nucleus using both initialisations R_P=R_N (left hand side) and R_P<R_N (right hand side). While for the first one the charge density $Z/A(R)$ (dashed line) remains constant over the whole nucleus, that ratio varies strongly for R_P<R_N . It should be noted that the rescattering cross sections of π^- with neutrons are higher than those with protons - and analogously those of π^+ with protons are higher than those with neutrons, therefore this difference will have an effect on the isospin ratios as we will see later on.

2 Dynamics of pion production and the importance of rescattering

Let us first focus on the collisions of Au(400 AMeV)+Au. This system has gained a lot of interest, since the experiment shows a strong enhancement of the ratio π^-/π^+ [8] which could not be completely explained by microscopic calculations and thus yielded a lot of speculations about its relation to the nuclear equation of state of asymmetric nuclear matter [11, 12].

Figure 3 shows the time evolution of a central collision of that system using both initialisations, R_P=R_N (blue lines) and R_P<R_N (red lines). The left hand side presents on the top the total nucleon density reached in the central point of the collisions. We see identical curves for both initialisations, reaching a maximum of $2.5\rho_0$ at a time of about 12 fm/c. On the bottom (still left hand side) we see that the isospin-integrated absolute numbers of free pions (dashed lines), deltas (dotted lines) and of their

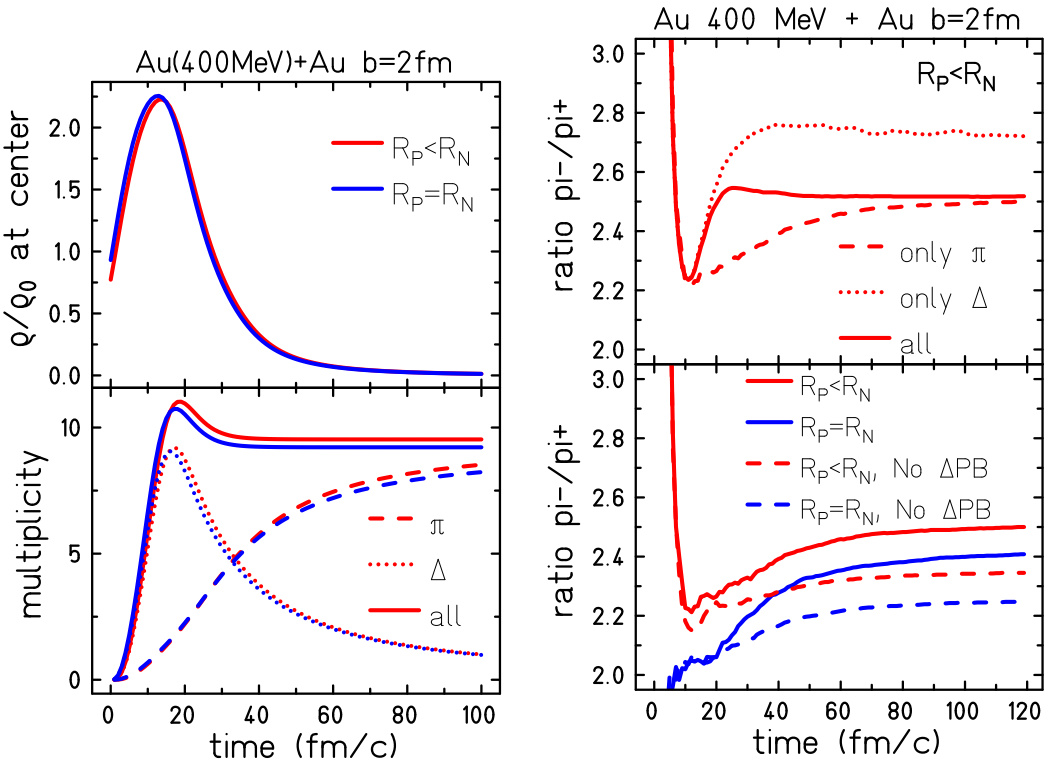

Fig. 3: Time evolution of a collision of Au(400 AMeV)+Au. Left: central density (top) and yields of deltas and pion (bottom), right: ratios π^-/π^+ assumed from deltas and free pions (top) and the for different assumptions on the initialisation and Pauli blocking in the delta decay.

sum (full lines) are also quite identical for both initialisations. The final total pion yields seems thus not to be affected by one or the other choice of the initialisation. The total pion numbers (full lines) rise up quite quickly during the compression stage to obtain its maximum at the moment of maximum compression but reaches its final value in the beginning of the expansion phase. We also see that the free pions (dashed lines) come out quite late, while in the high density stage most of the pions are "hidden" in the deltas (dotted lines). This is due to the huge reabsorption cross section $\pi N \rightarrow \Delta$.

On the right hand side we now study the time evolution of the isospin ratio π^-/π^+: on the top we distinguish that ratio by determining it by only counting the free pions (dashed line), taking only the deltas and applying the Clebsch-Gordon coefficients for the decay (dotted lines) or combining both calculations (full line). We see that the final value is determined quite early when taking the combined calculations, while the free pions smoothly converge to that value and the deltas always compile higher values. This may be interpreted such, as negative pions seem to "stay longer" in the delta, which may be a hint for higher rescattering and perhaps Pauli blocking in neutron rich matter. We will return to that point later.

The bottom part shows the influence of the initialisations on the ratio obtained from the free pions: the initialisation with R_P<R_N (red lines) systematically yields higher values than that with R_P=R_N (blue lines). This may be explained by the effect that neutron rich matter acts differently on π^- and π^+: while for π^- rescattering will lead to an intermediate Δ^- which decays only by $\Delta^- \rightarrow n\pi^-$ - and thus does not influence the π^- yield, a rescattering of a π^+ - yielding a Δ^+ - will reproduce a π^+ with a probability of only one third and thus penalises the π^+ yield. This effect is enhanced when the Pauli blocking of the delta decay is activated (full lines): the high density of neutrons will add a penalty to the the $\Delta^+ \rightarrow n\pi^+$ channel and reduce the π^+ yield even more with respect to calculations without Pauli blocking (dashed lines). The Pauli blocking also acts on the channel $\Delta^- \rightarrow n\pi^-$, but since there is

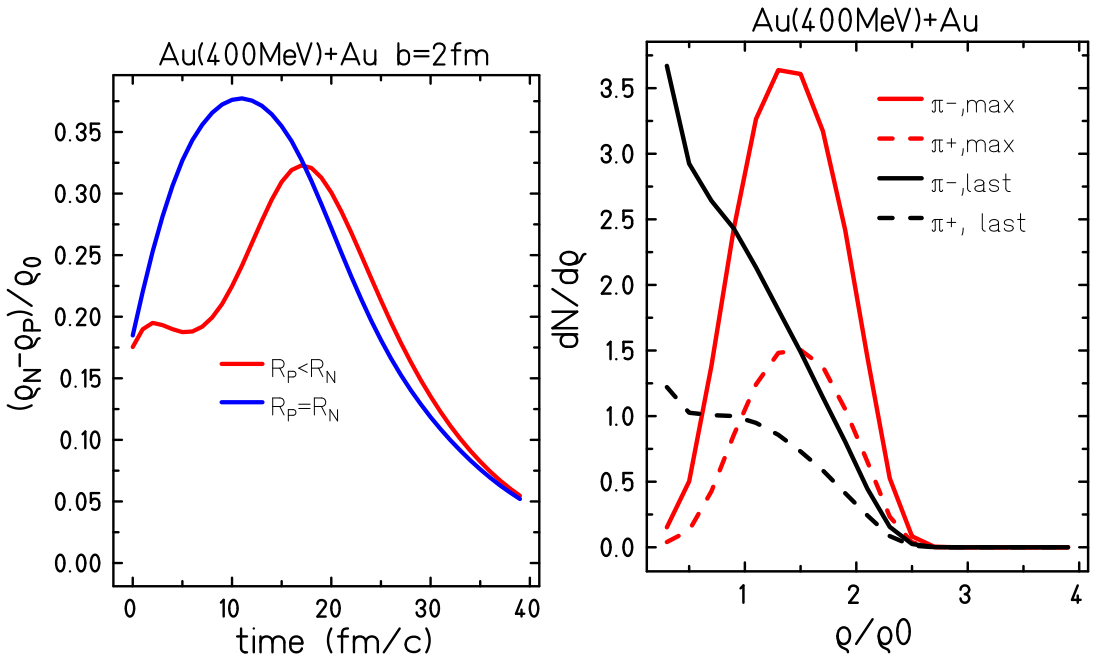

Fig. 4: Left: Time evolution of the density difference between neutrons and protons, right: distribution of maximum density and of freeze-out density of pions

no concurrent channel, this will only delay the decay of the delta, as we have seen this on the top graph. This could also explain the effect, why in the top part of Fig. 3 the ratio obtained from the deltas only than the ratio obtained from the free pions.

Another significant difference are the values of the ratios at very early times: while the calculation using R_P=R_N (blue line) starts with low values nearby 2 which smoothly rise, the calculation using R_P<R_N starts with very high values above 3 which rapidly fall down to rise smoothly again. This corresponds to the fact, the the very first deltas are created at the moment when the nuclei start to touch each other. At this time they feel the $Z/A(R = R_A)$ which is always around 0.4 for R_P=R_N but much lower for R_P<R_N as seen in figure 2. Here we see already an indication, that later on the study of very peripheral collisions might be quite interesting. The rise of the ratio after about 20 fm/c - common for both initialisations - is due to rescattering as explained before.

In order to test this assumption, we will inspect the rescattering of pions in more detail. Figure 4 analyses the time evolution of the central density in a different way: instead of summing up the densities for protons and neutrons (as done in fig.3) the difference $(\rho_n - \rho_p)/\rho_0$ is compared for the initialisation with R_P=R_N (blue line) and R_P<R_N (red line). We see that while in R_P=R_N the compression of matter with neutron excess ($Z/A(R) \approx 0.4$ everywhere) causes quite significant density differences, the nearly isospin-equilibrated center of the nuclei ($Z/A(R = 0) \approx 0.5$ yield much weaker values, which only enhance at late times, after the maximum compression had been reached. In the expansion stage both simulations reach similar values. From this finding we may assume that effects at the high density stage, e.g. the effects of asymmetry dependent potentials (like the equation of state of asymmetric matter) should be even weaker with R_P<R_N ! This would give a paradoxal result: the higher neutron densities obtained with R_P=R_N should lead to even a higher π^-/π^+ ratio, if the high density stage is decisive for the pion yields. The right hand side explains this paradoxal situation: here the maximum density (red lines) seen by a π^- (full line) and a π^+ (dashed line) is compared to the freeze-out density (black lines), i.e. the density of the last delta decay. While the pions are initiated in the compression phase and thus "felt" the high densities (with a maximum of the distribution nearby $1.5\rho_0$), the density signal from the last interaction (black lines) peak at lowest densities: the pions will only "memorize" low densities seen

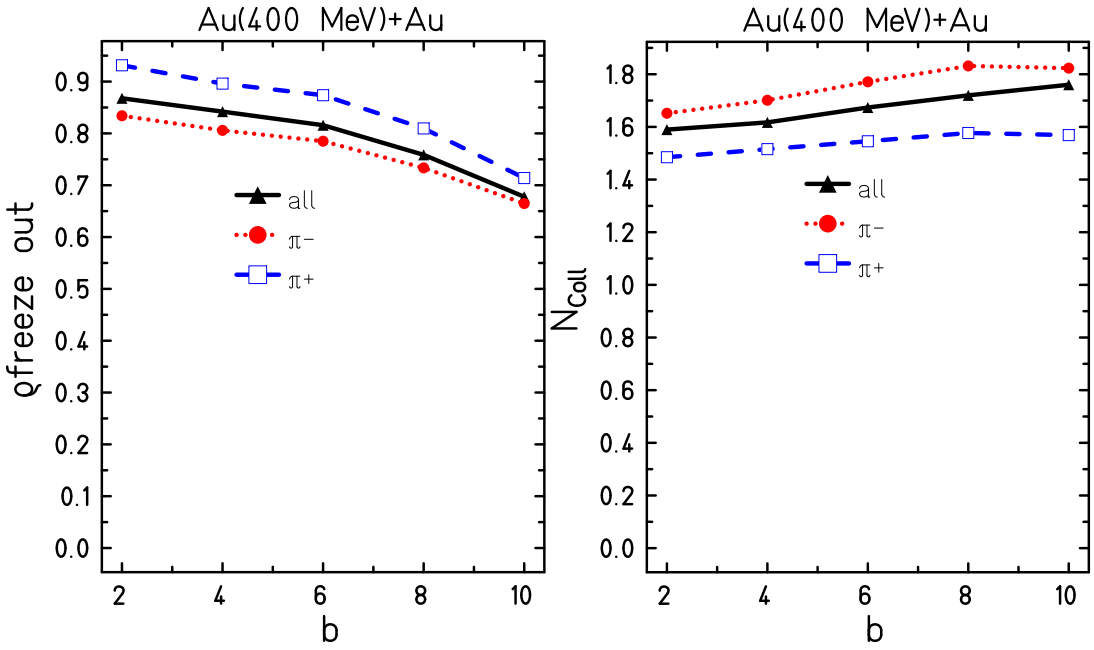

Fig. 5: Impact parameter dependence of π^- and π^+ freeze-out density (left) and number of collisions (right) in reactions of Au+Au at 400 AMeV

at the freeze-out.

This is nicely shown in figure 5 which describes on the left hand side the centrality dependence of the mean freeze-out density of π^- (red dotted line) and π^+ (blue dashed line): Both types freeze-out at densities below ρ_0. However, π^- systematically freeze-out at lower densities than π^+ which supports the idea of a late freeze-out in the expanding matter. Additional analysis show indeed that the freeze-out time of π^- is later than that of π^+. In this context it should be reminded, that the rescattering cross sections of π^- in neutron rich matter is higher than that of π^+. The right hand side supports this by presenting the mean number of collisions the pions have undergone: π^- show higher rescattering numbers than π^+ and values nearly up to 2 are obtained. Thus the idea of the importance of the neutron skin on the π^-/π^+ ratio seems to be coherent.

3 Centrality dependence of the isospin ratio

As shown in the precedent section the isospin ratio of pions in central collisions is influenced by the description of the neutron skin of the nucleus as well of the Pauli blocking in the delta decay. This seem to add an ingredient to other propositions [11–14] mainly addressing the nuclear equation of state of asymmetric matter and therefore that effect should be discussed as well. A very common description is to scale the density dependence of the asymmetry potential with an exponent γ. The (classical) linear dependence thus corresponds to $\gamma = 1$, a soft asy-eos to $\gamma < 1$ and a hard one to $\gamma > 1$.

Figure 6 presents on the left hand side the effects of the initialisations R_P<R_N (red full line) and R_P=R_N (blue dashed line) as well of the neglection of the Pauli blocking in the delta decay (black dotted line). For central collisions this effect has already discussed previously: the effect of rescattering in neutron rich matter penalises the π^+ - especially in case of R_P<R_N , where $Z/A(R)$ is quite low in the outer part, which is the region where the last rescattering happens. Since no penalty applies to the π^- this enhances the π^-/π^+ ratio. The Pauli blocking in the delta decay strengthens this penalty on the π^+ and thus enhances the ratio with respect to a calculation without Pauli blocking of the delta decay (black dotted line). However, a significant rise of the ratio can be seen for R_P<R_N when going to peripheral collisions. Here a strongly neutron rich environment is found even in the first initial collisions.

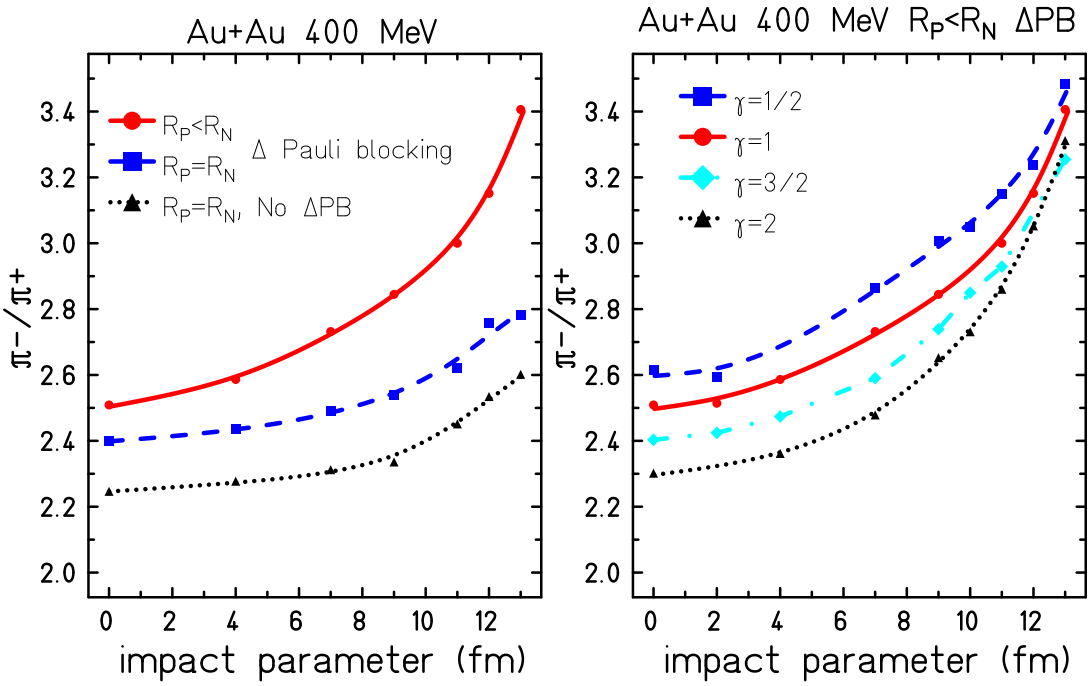

Fig. 6: Impact parameter dependence of the ratio π^-/π^+ in collisions of Au(400 AMeV)+Au. Left: influence of neutron skin and delta Pauli blocking right: influence of the equation of state of asymmetric matter.

We already indicated this when discussing the early time behavior of the ratio in figure 3.

The effect of the equation of state of asymmetric matter (right hand side, the initialisation R_P<R_N is used) shows on the contrary a rather moderate influence at peripheral collisions but a significant effect for central collisions. Here a softer asy-eos (blue dashed line) enhances the π^-/π^+ ratio with respect to a hard one (black dotted line). This can be interpreted such a way, that a strong (hard) asymmetry potential tries to dilute regions with strong neutron enrichment and thus reduces the effects described above. For peripheral collisions less compression is reached and the effects become smaller. This gives us a first indication that the analysis of the centrality dependence may play a very important role for disentangling the different effects.

The effect of the neutron skin on the centrality dependence increases even at higher incident energies, as it can be depicted from figure 7 presenting the same analysis but for Au(1200 AMeV)+Au. While the effect of the neutron skin becomes very prominent, the influence of the Pauli blocking in the delta decay and the effects of the equation of state of asymmetric matter vanish completely. Here we get a very good handle to test the neutron skin from π^-/π^+ ratios at high energies: from comparison of central and very peripheral collisions we may estimate the thickness of the neutron skin. A more detailed investigation of that procedure is presented in [15], where more refined parametrisations of the neutron skin are studied and applied to different nuclei like ^{48}Ca or ^{208}Pb. Once the question of the neutron skin is fixed, one may attack the other effects at low energies.

4 Conclusion

In this articles the influence of the neutron skin on the isospin ratio of pions π^-/π^+ has been discussed. It has been shown that due to rescattering a neutron skin is able to enhance this ratio in collisions of Au (400 AMeV)+Au. This enhancement becomes very significant at very peripheral collisions and gets even more prominent when going up in the incident energy. The effects of the equation of state of asymmetric matter only show up at low incident energy and dominate in central collisions. Therefore, a procedure of disentangling the effects can be proposed by measuring the full impact parameter dependence of π^-/π^+

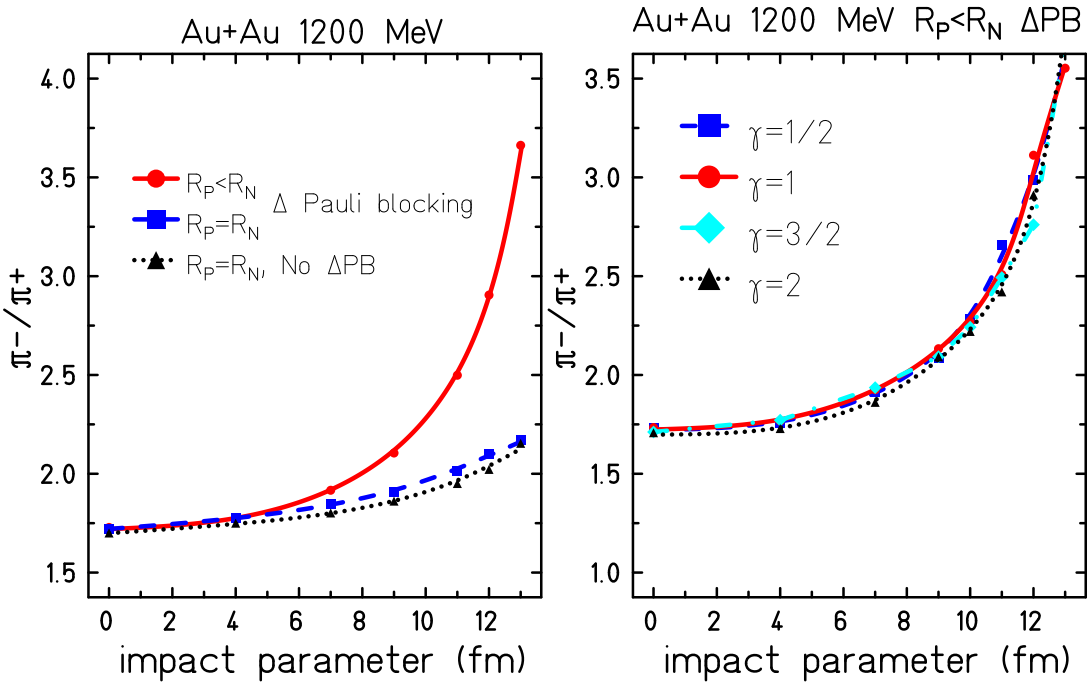

Fig. 7: Impact parameter dependence of the ratio π^-/π^+ in collisions of Au(400 AMeV)+Au. Left: influence of neutron skin and delta Pauli blocking right: influence of the equation of state of asymmetric matter.

at low and at high incident energies. From the comparison of high precision data to simulation one may thus reveal better information on the neutron skin and get another handle to attack the nuclear equation of state of asymmetric matter.

References

[1] C. Hartnack *et al.*, Nucl. Phys. A **495**, 303C (1989).

[2] H. Stöcker and W. Greiner. Phys. Reports **137**, 277 (1986).

[3] W. Cassing, V. Metag, U. Mosel and K. Niita. Phys. Reports **188**, 361 (1990).

[4] J. Aichelin. Phys. Reports **202**, 233 (1991).

[5] A. Le Fèvre, Y. Leifels, W. Reisdorf, J. Aichelin, C. Hartnack Nucl.Phys. **A945** 112 (2016)

[6] C. Hartnack, R. K. Puri, J. Aichelin, J. Konopka, S. A. Bass, H. Stoecker and W. Greiner Eur. Phys. J. A **1**, 151 (1998)

[7] S. A. Bass, C. Hartnack, H. Stoecker and W. Greiner, Phys. Rev. C **51**, 3343 (1995)

[8] W. Reisdorf *et al.* [FOPI Collaboration], Nucl. Phys. A **781**, 459 (2007)

[9] C. Hartnack, H. Oeschler, Y. Leifels, E. L. Bratkovskaya and J. Aichelin, Phys. Rept. **510** (2012) 119

[10] G. F. Wei, B. A. Li, J. Xu and L. W. Chen, Phys. Rev. C **90** (2014) no.1, 014610

[11] Z. Xiao, B. A. Li, L. W. Chen, G. C. Yong and M. Zhang, Phys. Rev. Lett. **102**, 062502 (2009)

[12] Z. Q. Feng and G. M. Jin, Phys. Lett. B **683**, 140 (2010)

[13] J. Hong and P. Danielewicz, Phys. Rev. C **90**, no. 2, 024605 (2014)

[14] M. D. Cozma, Phys. Lett. B **753**, 166 (2016)

[15] C. Hartnack, A. Le Fèvre, Y. Leifels, J. Aichelin Arxiv 1808.09868

Production of strange particles and hypernuclei in spallation reactions from the coupling of intranuclear cascade and de-excitation models

J. Hirtz[*1,2], *J.-C. David*[1], *J.L Rodriguez Sanchez*[1,3,4], *A. Boudard*[1], *J. Cugnon*[5], *S. Leray*[1], *I. Leya*[2], *D. Mancusi*[6] *and G. Schnabel*[1]

[1] IRFU, CEA, Université Paris-Saclay, F-91191, Gif-sur-Yvette, France
[2] Space Research and Planetary Sciences, Physics Institute, University of Bern, 3012 Bern, Switzerland
[3] Universidad de Santiago de Compostela, E-15782 Santiago de Compostela, Spain
[4] GSI-Helmholtzzentrum für Schwerionenforschung GmbH, D-64291 Darmstadt, Germany
[5] AGO department, University of Liège, allée du 6 août 17, bât. B5, B-4000 Liège 1, Belgium
[6] Den-Service d'étude des réacteurs et de mathématiques appliquées (SERMA), CEA, Université Paris-Saclay, F-91191, Gif-sur-Yvette, France

Abstract

Motivated by a renewed interest in hypernucleus studies, the strangeness degree of freedom was implemented in the intranuclear cascade model INCL. This model takes care of the first stage of reactions between a nucleon (or a light cluster) and a nucleus at energies from a few tens of MeV up to a few GeV. After emission of fast particles, a hot remnant nucleus is produced and another model, combined to INCL, handles the de-excitation (the ABLA model in our case). The main ingredients will be discussed and results will be compared to experimental data. The experimental kaon spectra for different target elements and at different energies agree reasonable well with the model predictions. The main remaining discrepancies are analysed and will be explained.

1 Introduction

On the one hand, there is a renew of interest about strangeness physics with new experiments, either in progress or planned, in several worldwide facilities (JPARC, MAMI, JLab, GSI, FAIR, ...). These experiments plan to produce numerous strange particles and notably hypernuclei, which are the best laboratory to study YN and YY interactions. Obviously the light hypernuclei have been studied more extensively than the heaviest ones, but still some questions remain. As examples, we can cite in particular the ${}^{3}_{\Lambda}H$ lifetime, which is shorter than the lifetime of the free Λ, and the Charge Symmetry Breaking observed in the Λ binding energy of the two mirror nuclei ${}^{4}_{\Lambda}H$ and ${}^{4}_{\Lambda}He$ [1]. However, the heavier hypernuclei are also interesting objects to study. They are ideal to study the behaviour of hyperons in nuclear matter and, beyond, to get information on the role of the Λ particles in neutron stars.

On the other hand, there is a nuclear reaction code, called INCL (Liège IntraNuclear Cascade), which treats spallation reactions between light particles and atomic nuclei with incident energies from $\sim 100\ MeV$ up to a few GeV. More precisely, this code handles the first stage of the reaction, leading to an excited nuclear remnant. The de-excitation is usually treated by ABLA, a code often combined to INCL to simulate the entire reaction. INCL, combined to ABLA, is known as a reliable code-combination in the non-strange sector for energies up to 2-3 GeV [2] and, after 2010 with implementation of the multiple pion emission, up to 15 GeV [3].

The renewed interest in strange particle studies and the strong bases of INCL were the motivations to add K's, Λ and Σ's as participant particles in INCL. Most important reactions involving these particles are also included. The de-excitation code ABLA was also upgraded to treat hypernuclei de-excitation

*Corresponding author: jason.hirtz@cea.fr

with evaporation of Λ's and fission of hypernuclei (hyper-fission). Below we give first the ingredients required to perform the calculations and, second, we compare the results obtained to experimental data and to predictions from other model codes. We conclude this paper by summarizing the benchmarking of the code on strange particle emission and on hypernucleus production, with possible improvements.

2 Ingredients

An intranuclear cascade can be summarised to a series of collisions between hadrons. Therefore main ingredients to simulate these collisions are the elementary cross sections (production, scattering, absorption), the final state characteristics of outgoing particles (charges, momenta), the nuclear potential felt by all particles and, possibly, their lifetimes and decay modes. Obviously, other aspects, like Pauli blocking, must be taken into account. It must be stressed that in INCL the resonances are not considered as participant particles (except the $\Delta(1232)$); only their decay products play a role. The reason is threefold. First, the half-lives are short compared to the time between two interactions, second, some resonances overlap and, third, the needed information (cross sections, etc.) are not well known, requiring additional hypotheses.

2.1 Cross sections

Adding the four (anti)Kaons (K^+, K^0, K^-, $\overline{K}^0$), the Λ and the three Σ (Σ^+, Σ^0, Σ^-), calls for hundreds of channels, when isospin is considered. We list below the reactions (isospin not take into account) implemented in INCL. The implementation was done in two steps (Table 1 and Table 2). The second step turned out to be necessary after implementation of the first step.

This short report is not the place to explain all details of how each reaction cross section was determined. This is described in a paper accepted for publication [4]. Here we only draw the attention to the difficulties to obtain all necessary information. As example, the first set, defined in Table 1, includes 382 isospin channels, and therefore as many cross section parametrizations. Only 17% of them were experimentally measured, sometimes very partially. Considering isospin symmetry at the initial and final states, an extra 18% is obtained from relations between known and unknown cross sections. Still relying on isospin symmetry, but working with leading order Feynman diagrams, used within a hadron exchange model, 37% of the cross sections is determined by ratios between known and unknown cross sections. The remaining cross sections are based on models or hypotheses, namely, assuming similarities when a hyperon (kaon) replaces a nucleon (pion). Obviously, the more hypotheses are assumed, less reliable are the reaction cross sections and benchmarking is the only way to know a posteriori the reliability of our model.

NN	$\rightarrow$	$N\Lambda K$	πN	$\rightarrow$	ΛK	$N\overline{K}$	$\rightarrow$	$N\overline{K}$	NK	$\rightarrow$	NK
	$\rightarrow$	$N\Sigma K$		$\rightarrow$	ΣK		$\rightarrow$	$\Lambda\pi$		$\rightarrow$	$NK\pi$
	$\rightarrow$	$N\Lambda K\pi$		$\rightarrow$	$\Lambda K\pi$		$\rightarrow$	$\Sigma\pi$		$\rightarrow$	$NK\pi\pi$
	$\rightarrow$	$N\Sigma K\pi$		$\rightarrow$	$\Sigma K\pi$		$\rightarrow$	$N\overline{K}\pi$	$N\Lambda$	$\rightarrow$	$N\Lambda$
	$\rightarrow$	$N\Lambda K\pi\pi$		$\rightarrow$	$\Lambda K\pi\pi$		$\rightarrow$	$\Lambda\pi\pi$		$\rightarrow$	$N\Sigma$
	$\rightarrow$	$N\Sigma K\pi\pi$		$\rightarrow$	$\Lambda\pi\pi$		$\rightarrow$	$\Sigma\pi\pi$	$N\Sigma$	$\rightarrow$	$N\Lambda$
	$\rightarrow$	$NNK\overline{K}$		$\rightarrow$	$NK\overline{K}$		$\rightarrow$	$N\overline{K}\pi\pi$		$\rightarrow$	$N\Sigma$

Table 1: First set of reactions involving strangeness considered in INCL.

2.2 Final state characteristics

Once a reaction between two hadrons in the nucleus is chosen, charges and momenta of the particles in the final state must be defined. Concerning the charges, Clebsch-Gordan coefficients are used as far as possible if two or more particles are involved. When the number of particles increases, additional models

ΔN	$\rightarrow$	$N\Lambda K$	NN	$\rightarrow$	$K+X$
	$\rightarrow$	$N\Sigma K$			
	$\rightarrow$	$\Delta\Lambda K$	πN	$\rightarrow$	$K+X$
	$\rightarrow$	$\Delta\Sigma K$			
	$\rightarrow$	$NNK\overline{K}$			

Table 2: First set of reactions involving strangeness considered in INCL.

are sometimes needed to remove ambiguities. The reader will find more details in [4]. Otherwise, as in the case of the inclusive reactions listed in the second column of Table 2, results of other codes are used to determine the number and type of particles emitted. Momenta are taken from double differential cross sections, in case measurements exist, or by assuming isotropy or considering phase-space distribution. Here again, the reliability of our approach may differ from channel to channel.

2.3 Average nuclear potentials and decays

While the potential is quite well known for the Λ, the K^+ potential is known to be slightly repulsive and the K^- potential strongly attractive. For Σ's the potential seems to be repulsive, but this is still under debate. For K^0 and $\overline{K}^0$, the same potentials as for K^+ and K^-, respectively, were assumed, but corrected to Coulomb force. The values used in this study are: V_Λ = $-28\ MeV$, V_Σ = 16 MeV, V_K^+ = 25 MeV, V_K^- = $-60\ MeV$, V_K^0 = 15 MeV, $V_{\overline{K}^0}$ = $-50\ MeV$. The latest value implemented in INCL for V_Λ is actually mass dependent. However, the results presented here were performed with the value of $-28\ MeV$, which is very close to the new $V_\Lambda(A)$ for the light and medium mass nuclei except for the figures on hypernuclei de-excitation. Note that, the potential plays a role mainly at low energies.

With half-lives around 10^{-8}-10^{-10} s, none strange particle decays during the cascade, except the Σ^0 (10^{-20} s). The latter point plays a role for Λ and Λ-hypernucleus production rates. After the cascade, the Σ^0 can obviously decay and the K^0 and $\overline{K}^0$ mix to create propagation eigenstate K_s^0 and K_L^0.

3 Results

Comparisons to experimental data and other models are the only way to test the reliability of a model and to try to understand remaining deficiencies. Most of the measured data in this domain are related to the K^+ production. However, some other experimental data exist and were used to benchmark this first version of INCL considering strangeness. Below, figures showing the production of K^+, K^-, K^0, Λ and hypernucleus are shown and analysed.

3.1 K^+ production

Most of the time, K^+ production is well described by INCL. As an example are given two plots (fig. 1) displaying the invariant production cross sections for various angles measured by the KaoS collaboration [5] for different configurations. Either for the left panel with Kaon production near threshold on a light nucleus (carbon) or for the right panel with Kaon production at higher energy on a heavy nucleus (gold), the results of INCL match very well experimental data. Comparison with calculations from the Bertini model [6] implemented in the transport code Geant4 like INCL shows that the INCL model is more than competitive. The difference between both models at low momenta is due to the different K^+ potential values used.

The fig. 2 depicts the production of K^+ with proton projectile from sub-threshold region, with collective effect needed, up to 2.91 GeV on four targets from Be ($Z = 4$) up to Ta ($Z = 73$) is analysed to study the role of the Δ-induced Kaon production by allowing it or not. In the experiment, K^+'s are detected in a very specific phase-space. However, the conclusions are pretty clear. First,

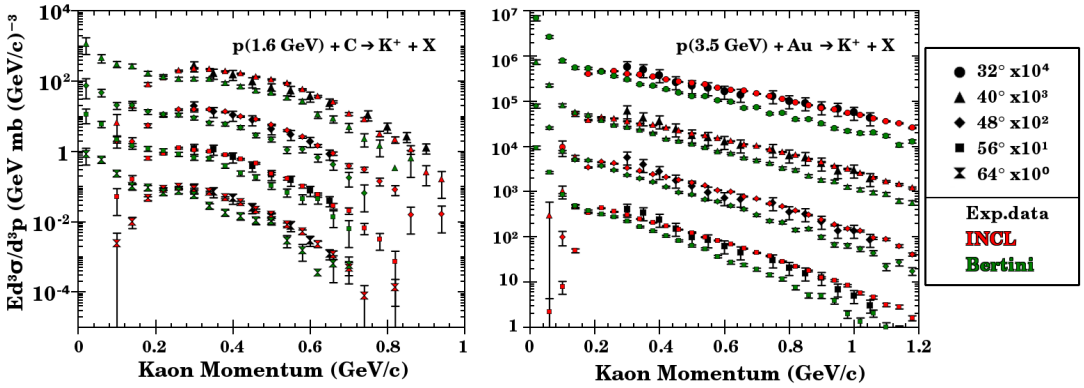

Fig. 1: K^+ invariant production cross sections in $p(1.6\ GeV) + C$ (left) and $p(3.5\ GeV) + Au$ (right) reactions. Experimental data [5] (black) are compared to Bertini [6] (green) and INCL (red)

Δ's play an important role in K^+ production, especially below threshold ($\sim$ 2.1 GeV) and, second, reproduce relatively well ITEP experimental data [7]. Going deeper in the analysis, we can see that INCL slightly overestimates the production with increasing proton energy. This is probably related to the parametrizations used for the Δ-induced Kaon production Ref. [8], where the authors already observed overestimations in some cross section parametrization beyond $\sqrt{s} - \sqrt{s_0} = 200\ MeV$. This is a potential topic to improve.

INCL can also handle heavier projectiles than protons. In fig. 3 are plotted the results obtained for the reaction 2.1 GeV/A in ^{2}H+^{208}Pb. The conclusions are the same as for fig. 1, i.e., INCL matches well the LBL data [9]. Experimental data at lower momenta would help to test the K^+ potential.

With fig. 4, the momentum spectrum is tested in the forward direction. It can be seen the three models plotted, INCL, LAQGSM, and Bertini, fit relatively well experimental data at low momenta. At higher momenta, INCL and LAQGSM reproduce the ANKE data [10] while Bertini underestimates them. Beyond the experimental data, all models have different shapes. Extrapolations from fig. 2 suggest INCL overestimate the real cross section by a factor of roughly 30% for K^+ momentum of 1.28 GeV/c for the configuration of fig. 4. This would be compatible with Bertini's values. Δ-induced kaon production in INCL is probably, here again, overestimated. The same type of data in the entire momentum range

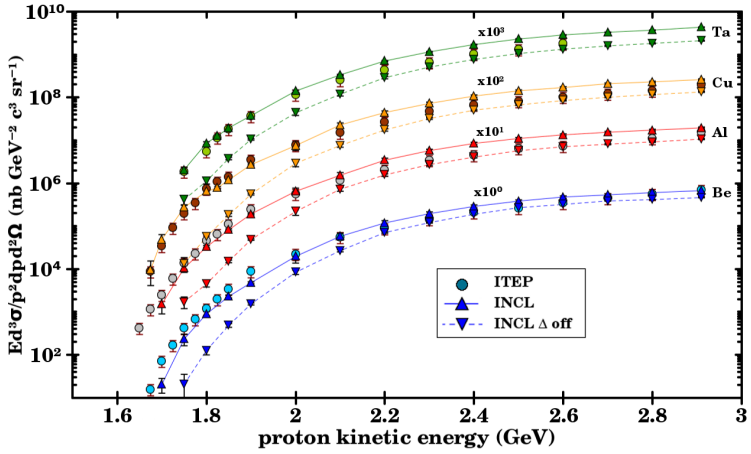

Fig. 2: K^+ production invariant cross section for $p_{K^+} = 1.280 \pm 0.014\ GeV/c$ at $\theta = 10.5°$. Exp. data [7] (circles) are compared to INCL with (up oriented triangles) and without (down oriented triangles) Δ-induced strange production .

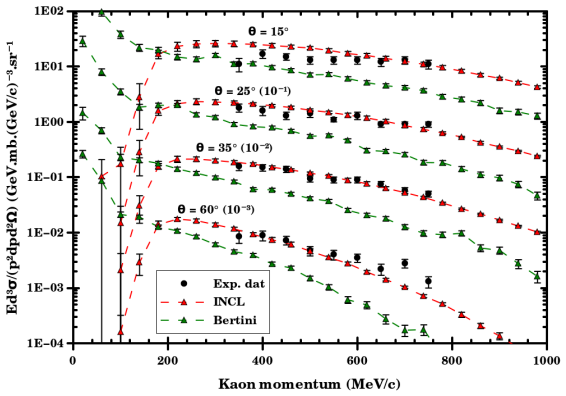

Fig. 3: Kaon production invariant cross section at 2.1 GeV/A in ^{2}H+^{208}Pb collisions. Experimental data [9] (black) are compared to the Bertini cascade model [6] (green) and INCL (red).

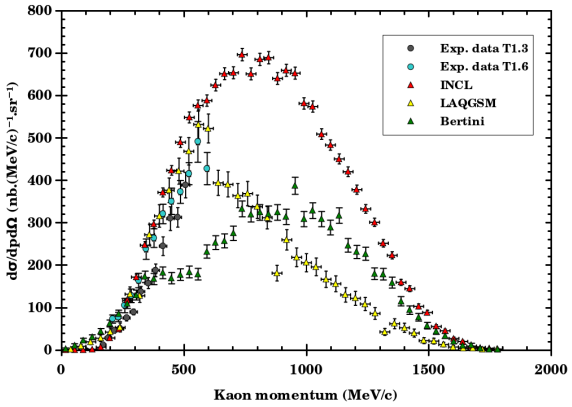

Fig. 4: Forward K^+ spectrum in $p(2.3\ GeV) +^{12} C$ collision. Experimental data [10] (circles) are compared to INCL (red), LaQGSM [11] (yellow) and the Bertini cascade model [6] (green).

would help to better understand the mechanisms involved.

Most of experiment on strangeness production are carried out with projectile energies between 1.5 and 3.5 GeV. However, INCL is designed to do calculation up to 15 GeV. Fig. 5 allows tests for the highest energies with a projectile momentum of 14.6 GeV/c ($T \simeq 13.7\ GeV$). The rapidity spectra for the four targets exhibit good simulation of INCL at high energies. However, an underestimation at high rapidity for the heaviest targets could be observed.

While fig. 5 deals with high energies, fig. 6 tests the lowest energies with the far sub-threshold K^+ production. The threshold for the K^+ production in proton-proton collision is around 1580 MeV. Here, energies are much below, which imply strong collective effects. The first observation, which can be done, is the overestimation by a factor 4 of the experimental data. However, we observed also the slops are relatively well reproduced. Drawing a conclusion from this figure is extremely hard because of the complexity of the sub-threshold K^+ production processes.

In addition to the physical analysis, fig. 6 was a good opportunity to test a novelty in INCL: the biasing. Production rates of strange particles are much lower than those of *non-strange* particles, resulting in a dramatical increase of computation time. However, this has been mitigated by introducing

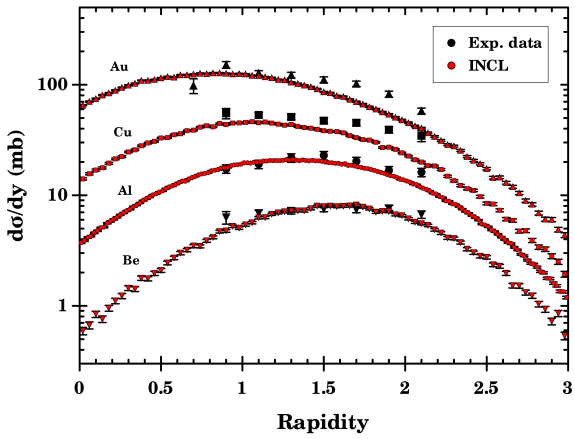

Fig. 5: K^+ rapidity spectrum in $p(14.6\ GeV/c) + A$ collision. The experimental data are from [12].

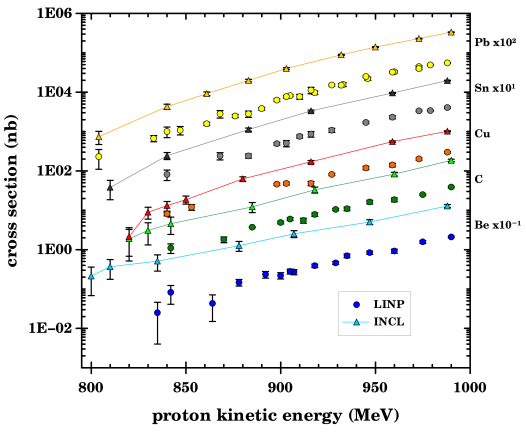

Fig. 6: Subthreshold K^+ production cross section in $p + A$ collision. Experimental data from [13]

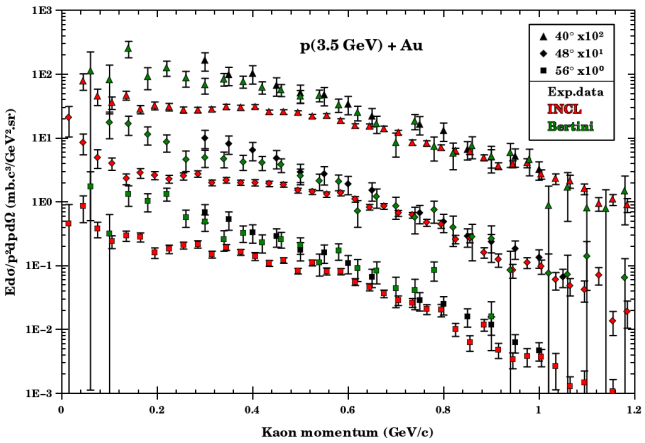

Fig. 7: K^- invariant cross section in $p(3.5\ GeV) + Au$ collision. Experimental data [5] (black) are compared to Bertini (green) and INCL (red).

a biasing process in INCL. Calculation times needed to obtain good statistics for strange particles are now reasonable. Here, the conditions are excellent. As a result, the biasing reduced by a factor between 1000 and 2000 the time needed to get this figure.

3.2 K^- production

The conclusions for the K^- differ from the conclusions above for the K^+. The spectra on fig. 7 are well reproduced except for low momenta. In this region the Bertini code gives better results, what seems to indicate that in INCL some production channels are missing, especially the $YN \rightarrow \overline{K}NN$. This corroborates the state made in Ref. [5], arguing that the role of strangeness exchange reactions was important in K^- production.

3.3 Neutral kaon production

AntiKaon production is marginal compared to Kaon production. Therefore, physics associated to neutral kaons in experiments are dominated by the K^0 production, which is strongly correlated to K^+ production. Considering this, results as good as for K^+ are expected. However, comparisons with experimental data show significant discrepancies.

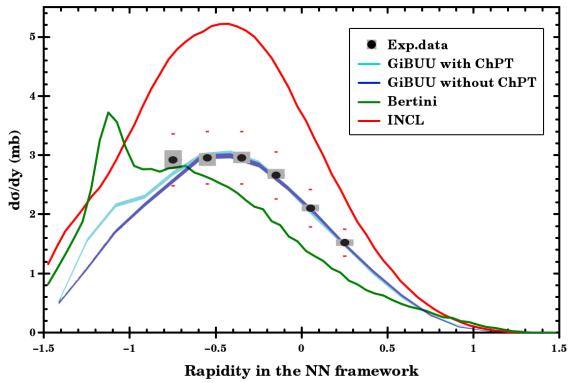

Fig. 8: K^0_s rapidity distribution in $p(3.5\ GeV) + Nb$ collisions. HADES data [14] (black) are compared to GiBUU (blue), Bertini (green), and INCL (red).

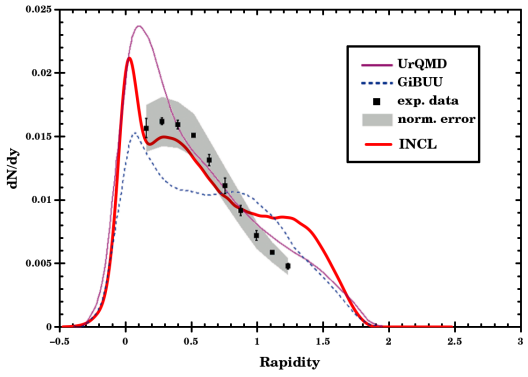

Fig. 9: Λ rapidity in $p(3.5\ GeV) + Nb$ collisions. HADES data [16] (black) are compared to UrQMD (purple), GiBUU (blue), and INCL (red).

On fig. 8, the shape of INCL is good but the calculation overestimates experimental data [14] by roughly 40%. As for K^+ production, Δ-induced production could be an explanation, but another reason can be put forward: the total reaction cross section $\sigma_{tot}^{p\ Nb}$ measured by HADES is $848 \pm 127\ mb$, while INCL calculates a value of $1048\ mb$. A measurement of the total reaction cross section for the same system at a lower energy ($1.2\ GeV$ instead of $3.5\ GeV$) gave $1063 \pm 40\ mb$ [15]. Therefore, a part of the overestimation is probably due to the normalization.

3.4 Λ production

The production of hypernuclei is strongly connected to the production of Λ, since most of the observed hypernuclei are involving a Λ. Therefore, before studying the hypernucleus production, we tested our model for the Λ production. Once again, experimental data are very scarce and we can only show one diagram. We compared the INCL results to the HADES rapidity spectrum for the reaction $p(3.5GeV) + Nb$ (fig. 9), as well as to some other models. INCL matches rather well the HADES data [16], except for rapidities larger than 0.8. The bump seen with INCL around $y = 1.3$, but not with the HADES data, also exists for the GiBUU model [17], but at lower rapidities. The UrQMD model [18] does not exhibit such a behaviour and is close to HADES, but misses strongly the two data points at low rapidity. The shape of the rapidity spectrum beyond 0.8 is possibly due to the low transverse momenta, but a careful study must be carried out to understand the differences between experimental data and model predictions.

3.5 Hypernucleus production

While single strange particle production is dominated by the intranuclear cascade and can be described by INCL alone, hypernucleus production is strongly dependent on both processes, the intranuclear cascade and the de-excitation. Comparisons with experimental data require so a combination of INCL and ABLA.

Here, two types of plots are displayed. The fig. 10 shows the isobaric production of hypernuclei by π^+-induced reactions (${}^A X(\pi^+, K^+)^A_\Lambda X$) as a function of the mass target. It can be seen INCL-ABLA fits very well the KEK experimental data [20]. Initially, INCL-ABLA underestimated the KEK data for the two heaviest nuclei. This led us to consider an Λ potential dependant on the nucleus mass [19]. The thus updated INCL model produces a perfect fit of the measurements. Another conclusion is the crucial role played by the de-excitation code, reducing the production rate by more than one order of magnitude compared to the rate at the end of the cascade. This latter result gives the probability that the

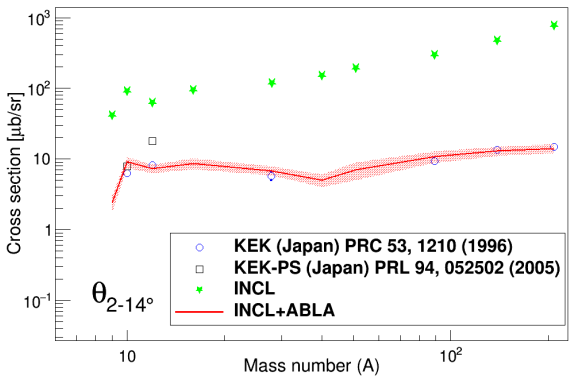

Fig. 10: Hypernucleus production cross section in function of the mass target for ${}^A X(\pi^+, K^+)^A_\Lambda X$ reactions, with incident energies of 1.06 and 1.048 GeV/c. Experimental data are from [20](circles) and [21] (squares). Are plotted INCL hyper-remnant production (green stars) and INCL-ABLA result (red line)

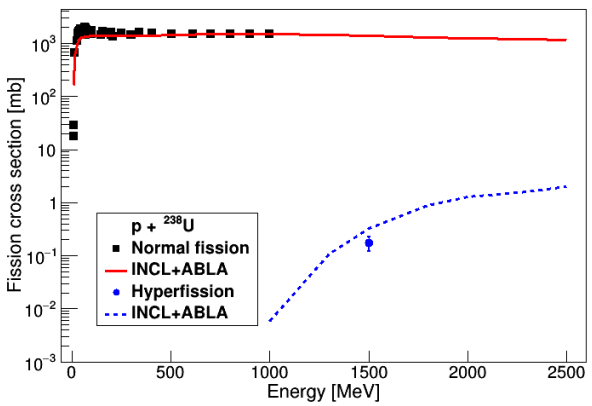

Fig. 11: Fission and hyper-fission cross sections in function of the proton projectile energy in p+U. *Normal* fission [22] and hyper-fission [23] experimental data are compared to INCL-ABLA results (red line and dotted-blue line respectively).

Λ particle does not evaporate and the ABLA code, upgraded on purpose, describes well the de-excitation of hypernuclei.

In fig. 11, the fission of hypernuclei is tested. At the end of the intranuclear cascade, if the target is heavy enough, the remnant can undergo fission. This remnant can be a hypernucleus or not. For *normal* nuclei, we know that the combination INCL-ABLA gives good results, as shown in fig. 11. With the implementation of hyper-fission in ABLA, in particular by taking into account hyper-energy in the fission barrier height, we conclude that ABLA is able to calculate a hyper-fission cross section very close to the rare experimental data.

4 Conclusion

The strange particles K^+, K^-, $\overline{K}^0$, K^-, Λ, Σ^+, Σ^0 and Σ^- are implemented into the intranuclear cascade code INCL. Since the de-excitation code ABLA is usually combined to INCL for a full simulation of spallation reactions, ABLA has also been upgraded by adding Λ evaporation and hyper-fission. Results obtained by the codes, and especially INCL, are very encouraging. Main mechanisms are incorporated and now it is time for improvements. Δ-induced strangeness production is probably overestimated when energy goes up and some strangeness exchange reactions must be added, like $\Lambda N \rightarrow \overline{K}NN$, to better reproduce antiKaon production. Other aspects must also be studied, like the momentum distribution of the emitted particles. However, the lack of experimental data to get better elementary ingredients and to benchmark carefully our model makes the task difficult.

References

[1] C. Rappold, T.R.Sait et al., Physics Letters B 728, 543-548 (2014)

[2] S. Leray et *al.*, J. Korean Phys. Soc. 59, 791-796 (2011) IAEA Benchmark of Spallation Models

[3] S. Pedoux and J. Cugnon, Nucl. Phys. A 866, 16-36 (2011)

[4] J. Hirtz, J.C. David et al., arXiv:1805.01655 [nucl-th] (2018)

[5] W. Scheinast et al., PRL 96, 072301 (2006)

[6] D.H. Wright, M.H. Kelsey, NIM in Physics Research A 804, 175-188 (2015)

[7] A.V. Akindinov et al., JETP Letters, Vol. 72, 100 (2000)

[8] K. Tsushima, A. Sibirtsev, A. W. Thomas, and G. Q. Li, Phys. Rev. C 59, 369 (2000), Erratum.

[9] S. Schnetzer, R. M. Lombard et al., Phys. Rev. C 40, 640 (1990), Erratum

[10] Büscher, M., Koptev, V., Nekipelov, M. et al., Eur. Phys. J. A 22, 301 (2004)

[11] N.V. Mokhov, K.K. Gudima, S.I. Striganov., arXiv:1409.1086 [nucl-ex] (2014)

[12] T. Abbott et al. (E-802 Collaboration), Phys. Rev. D 45, 3906 (1992).

[13] V.P. Koptev et al., Zh. Eksp. Teor. Fiz. 94,1-14 (1988).

[14] HADES Collaboration, Phys. Rev. C 90, 054906 (2014)

[15] C.-M. Herbach et al., Nucl. Instr. Meth. A 562, 729 (2006)

[16] HADES Collaboration, Eur. Phys. J. A 50, 81 (2014)

[17] O. Buss and all. Physics Reports 512, 1-124 (2012)

[18] S. A. Bass et al., arXiv:nucl-th/9803035v2

[19] J. L. Rodríguez-Sánchez, J.-C. David, J. Hirtz, J. Cugnon, and S. Leray Phys. Rev. C 98, 021602 (2018)

[20] T. Hasegawa and al., Phys. Rev. C 53, 1210 (1996)

[21] P. K. Saha et al. Phys. Rev. Lett. 94, 052502 (2005)

[22] IAEA EXFOR data base, https://www-nds.iaea.org/exfor/exfor.htm

[23] P. Kulessa et al., Physics Letters B 427, 403-408 (1998)

Charged-current quasielastic (anti)neutrino cross sections on ^{12}C with realistic spectral functions including meson-exchange contributions

M.V. Ivanov[1], A.N. Antonov[1], G.D. Megias[2], J.A. Caballero[2], M.B. Barbaro[3], J.E. Amaro[4], I. Ruiz Simo[4], T.W. Donnelly[5], and J.M. Udías[6]

[1]Institute for Nuclear Research and Nuclear Energy, Bulgarian Academy of Sciences, 1784 Sofia, Bulgaria
[2]Departamento de Física Atómica, Molecular y Nuclear, Universidad de Sevilla, 41080 Sevilla, Spain
[3]Dipartimento di Fisica, Università di Torino and INFN, Sezione di Torino, 10125 Torino, Italy
[4]Departamento de Física Atómica, Molecular y Nuclear, and Instituto de Física Teórica y Computacional Carlos I, Universidad de Granada, Granada 18071, Spain
[5]Center for Theoretical Physics, Laboratory for Nuclear Science and Department of Physics, Massachusetts Institute of Technology, Cambridge, Massachusetts 02139, USA
[6]Grupo de Física Nuclear, Departamento de Estructura de la Materia, Física Aplicada y Electrónica and UPARCOS, Universidad Complutense de Madrid, CEI Moncloa, 28040 Madrid, Spain

Abstract

We present a detailed study of charged-current quasielastic (anti)neutrino scattering cross sections on a ^{12}C target obtained using a spectral function that gives a scaling function in accordance with the electron scattering data. The spectral function accounts for the nucleon-nucleon (*NN*) correlations, it has a realistic energy dependence and natural orbitals (NO's) from the Jastrow correlation method are used in its construction. The results are compared with those when *NN* correlations are not included, namely when harmonic-oscillator single-particle wave functions are used instead of NO's. A comparison of the results with recent experiments, as well as to results from the superscaling approach is done. The contribution of two-particle two-hole meson-exchange currents on neutrino–nucleus interactions is also considered within a fully relativistic Fermi gas. The results show a good agreement with the experimental data.

1 Introduction

The study of charged-current mediated quasi-elastic (CCQE) neutrino-nucleus scattering in the GeV region is a powerful tool for hadronic and nuclear studies. We note that although in the tradition of neutrino experiments the term 'elastic', either charged-current elastic or neutral-current elastic is used for neutrino scattering off free nucleons as well as on nucleons bound on nuclei, in this work we will refer to the latter case with the more precise denomination of quasi-elastic (QE). Recently, the MiniBooNE [1,2] collaboration has produced high-quality data, using a mostly carbon target, for a number of selected channels, in particular, for the Quasi-Elastic (QE) one, that is, where no pions are detected in the final state. The treatment of nuclear effects represents one of the main sources of systematic uncertainty in the experimental determination of neutrino oscillation parameters. In particular, the CCQE MiniBooNE results [1, 2] have stimulated many theoretical studies devoted to explaining the apparent discrepancies between data and most theoretical predictions based on the impulse approximation (IA). Based on results from different groups, the inclusion of effects beyond IA, such as multinucleon excitations, mainly two-particle two-hole meson-exchange current (2p-2h MEC) contributions, has allowed one to explain these data without including any effective parameter (such as the axial mass M_A) [3–7].

The aim of the present paper is to continue our work from Ref. [8] using the results obtained in Ref. [9] for a realistic spectral function $S(p, \mathcal{E})$ instead of the phenomenological superscaling approximation (SuSA) approach. The spectral function from our previous work [8] will be applied to analysis

of CCQE (anti)neutrino cross sections on a ^{12}C target measured by the MiniBooNE [1, 2] experiment. The new aspect of the present calculation concerns the treatment of 2p-2h excitations. In this work we include the fully relativistic weak (with vector and axial components) charged meson-exchange currents, in both longitudinal and transverse channels. These have been evaluated in [10–12] from an exact microscopic calculation, where the two-body current is the sum of seagull, pion-in-flight, pion-pole, and Δ-pole operators and the basis wave functions are noninteracting Dirac spinors.

2 General Formalism

2.1 Expression for the cross sections

The CC (anti)neutrino-nucleus inclusive cross section in the target laboratory frame can be written in the form (see [13, 14] for details)

$$\left[\frac{d^2\sigma}{d\Omega dk'}\right]_\chi = \sigma_0 \mathcal{F}_\chi^2, \tag{1}$$

where $\chi = +$ for neutrino-induced reactions (in the QE case, $\nu_\ell + n \to \ell^- + p$, where $\ell = e, \mu, \tau$) and $\chi = -$ for antineutrino-induced reactions (in the QE case, $\overline{\nu}_\ell + p \to \ell^+ + n$). The function $\mathcal{F}_\chi^2$ in Eq. (1) depends on the nuclear structure and is presented as a generalized Rosenbluth decomposition [13] containing leptonic kinematical factors, V_K, and five nuclear response functions, R_K, namely VV and AA charge-charge (CC), charge-longitudinal (CL), longitudinal-longitudinal (LL) and transverse (T) contributions, and VA transverse (T') contributions, where $V(A)$ denotes vector(axial-vector) current matrix elements. These are specific components of the nuclear tensor $W^{\mu\nu}$ in the QE region and can be expressed in terms of the superscaling function $f(\psi)$ (see [13] for explicit expressions).

2.2 Models: HO+FSI, NO+FSI, and SuSAv2

In the MiniBooNE experiment the interaction of the neutrino occurs with nucleons bound in nuclei. The analyses of such processes within different methods involve various effects such as nucleon-nucleon (*NN*) correlations, the final state interactions (FSI), possible modifications of the nucleon properties inside the nuclear medium and others. These effects, however, cannot be presently accounted for in an unambiguous and precise way, and what is very important, in most cases they are highly model-dependent. A possible way to avoid the model-dependencies is to use the nuclear response to other leptonic probes, such as electrons, under similar conditions to the neutrino experiments. The SuSA approach follows this general trend. The analyses of superscaling phenomena observed in electron scattering on nuclei have led to the use of the scaling function directly extracted from (e, e') data to predict (anti)neutrino-nucleus cross sections [13], just avoiding the usage of a particular nuclear structure model. A "superscaling function" $f(\psi)$ has been extracted from the data by factoring out the single-nucleon content of the double-differential cross section and plotting the remaining nuclear response versus a scaling variable $\psi(q, \omega)$ (q and ω being the momentum transfer and transferred energy, respectively). For high enough values of the momentum transfer (roughly $q > 400$ MeV/c) the explicit dependence of $f(\psi)$ on q is very weak at transferred energies below the quasielastic peak (scaling of the first kind). Scaling of second kind (*i.e.* no dependence of $f(\psi)$ on the mass number A) turns out to be excellent in the same region. The term "superscaling" means the occurrence of both first and second types of scaling.

In this work we consider three different theoretical calculations. Two of them, denoted as HO (harmonic oscillator) and NO (natural orbitals), make use of a spectral function $S(p, \mathcal{E})$, p being the momentum of the bound nucleon and $\mathcal{E}$ the excitation energy of the residual nucleus, coinciding with the missing energy E_m up to a constant offset [15]. The area of analyses of the scaling function, the spectral function, and their connection (see, *e.g.*, Refs. [9, 16]) provides insight into the validity of the mean-field approximation (MFA) and the role of the *NN* correlations, as well as into the effects of FSI. Though in the MFA it is possible, in principle, to obtain the contributions of different shells to $S(p, \mathcal{E})$ and $n(p)$ for each single-particle state, owing to the residual interactions the hole states are not eigenstates of the

residual nucleus but are mixtures of several single-particle states. The latter leads to the spreading of the shell structure and requires studies of the spectral function using theoretical methods going beyond the MFA to describe successfully the relevant experiments. In Ref. [9] a realistic spectral function $S(p, \mathcal{E})$ has been constructed that is in agreement with the scaling function $f(\psi)$ obtained from the (e, e') data. For this purpose effects beyond MFA have been considered. The procedure included (i) the account for effects of a finite energy spread and (ii) the account for *NN* correlation effects considering single-particle momentum distributions $n_i(p)$ [that are components of $S(p, \mathcal{E})$] beyond the MFA, such as those related to the usage of natural orbitals (NO's) [17] for the single-particle wave functions and occupation numbers within methods in which short-range *NN* correlations are included. For the latter the Jastrow correlation method [18] has been considered. Also, in Ref. [9] FSI were accounted for using complex optical potential that has given a spectral function $S(p, \mathcal{E})$, leading to asymmetric scaling function in accordance with the experimental analysis, thus showing the essential role of the FSI in the description of electron scattering reactions.

In Fig. 1 of Ref. [8] the results for the superscaling function $f(\psi)$ within the HO+FSI and NO+FSI models are presented. Accounting for FSI leads to a redistribution of the strength, with lower values of the scaling function at the maximum and an asymmetric shape around the peak position, *viz.,* when $\psi = 0$. Also, we see that the asymmetry in the superscaling function gets larger by using the Lorentzian function for the energy dependence of the spectral function than by using the Gaussian function [8, 9]. The two spectral function models, including FSI, clearly give a much more realistic representation of the data than the relativistic Fermi gas.

The third model, SuSAv2, that is an improved version of the superscaling prescription, called SuSAv2 [19], has been developed by incorporating relativistic mean field (RMF) effects [20–22] in the longitudinal and transverse nuclear responses, as well as in the isovector and isoscalar channels. This is of great interest in order to describe CC neutrino reactions that are purely isovector. Note that in this approach the enhancement of the transverse nuclear response emerges naturally from the RMF theory as a genuine relativistic effect.

The detailed description of the SuSAv2 model can be found in [7, 19, 23]. Here we just mention that it has been validated against all existing (e, e') data sets on ^{12}C, yielding excellent agreement over the full range of kinematics spanned by experiments, except for the very low energy and momentum transfers, where all approaches based on impulse approximation (IA) are bound to fail. Furthermore, the success of the model depends on the inclusion of effects associated with two-body electroweak currents, which will be briefly discussed in the next Section.

2.3 2p-2h MEC contributions

Ingredients beyond the impulse approximation (IA), namely 2p-2h MEC effects, are essential in order to explain the neutrino-nucleus cross sections of interest for neutrino oscillation experiments [4–7, 24, 25]. In particular, 2p-2h MEC effects produce an important contribution in the "dip" region between the QE and Δ peaks, giving rise to a significant enhancement of the impulse approximation responses in the case of inclusive electron- and neutrino-nucleus scattering processes. In this work we make use of the 2p-2h MEC model developed in [11], which is an extension to the weak sector of the seminal papers [26–28] for the electromagnetic case. The calculation is entirely based on the RFG model, and it incorporates the explicit evaluation of the five response function involved in inclusive neutrino scattering. The MEC model includes one-pion-exchange diagrams derived from the weak pion production model of [29]. This is at variance with the various scaling approaches that are largely based on electron scattering phenomenology, although also inspired in some cases by the RMF predictions.

Following previous works [7, 23, 30, 31], here we make use of a general parametrization of the MEC responses that significantly reduces the computational time. Its functional form for the cases of ^{12}C and ^{16}O is given in [7, 23, 32], and its validity has been clearly substantiated by comparing its predictions with the complete relativistic calculation.

3 Analysis of results

In this section we show the predictions of the two spectral function approaches previously described, HO and NO, both including FSI and 2p–2h MEC. We compare the results with data from MiniBooNE experiment. The neutrino and antineutrino mean energies corresponding to MiniBooNE experiment are around 0.8 and 0.7 GeV [1, 2]. Our study is restricted to the QE-like regime where the impulse approximation in addition to the effects linked to the 2p-2h MEC play the major role. We follow closely the general analysis presented in [7] for the case of the superscaling approach. Hence, for reference, we compare our new theoretical predictions with the results corresponding to the SuSAv2-MEC model.

In Figs. 1 and 2 we show the double differential cross section averaged over the neutrino and antineutrino energy flux against the kinetic energy of the final muon. The data are taken from the MiniBooNE Collaboration [1, 2]. We represent a large variety of kinematical situations where each panel refers to results averaged over a particular muon angular bin.

We compare the data with the results obtained within the HO+FSI, NO+FSI, and SuSAv2 approaches, all of them including 2p–2h MEC, that are also presented separately. As already shown in [7], notice the relevant role played by 2p-2h MEC contributions, of the order of $\sim$20-25% of the total response at the maximum. In the neutrino case (Fig. 1) this relative strength is almost independent of the scattering angle, except for the most forward bin, $0.9 < \cos\theta_\mu < 1$, where the MEC contribution is $\sim$15%; this angular bin, however, largely corresponds to very low excitation energies ($\omega < 50$ MeV) and in this case completely different modeling, appropriate for the near-threshold regime, should be used. In the antineutrino case (Figs. 2) the 2p-2h relative strength gets larger for backward scattering angles ($\cos\theta_\mu < -0.2$). This is due to the fact that the antineutrino cross section involves a destructive interference between the T and T' channels and is therefore more sensitive to nuclear effects.

Theoretical predictions including both the QE and the 2p-2h MEC contributions are in good accord with the data in most of the kinematical situations explored. Only at scattering angles approaching 90° and above does one see a hint of a difference, although in these situations only a small number of data points with large uncertainties exist.

With regard to the comparison between the different models, we observe that HO+FSI and NO+FSI

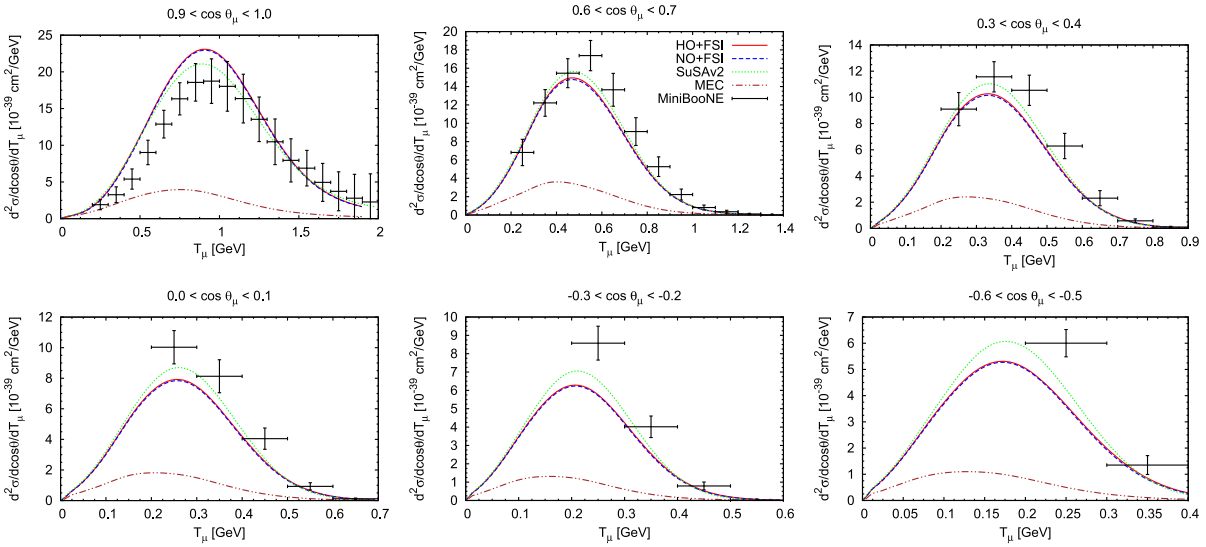

Fig. 1: (Color online) MiniBooNE flux-folded double differential cross section per target neutron for the ν_μ CCQE process on ^{12}C displayed versus the μ^- kinetic energy T_μ for various bins of $\cos\theta_\mu$ obtained within the SuSAv2, HO+FSI, and NO+FSI approaches including MEC. 2p–2h MEC results are also shown separately. The data are from [1].

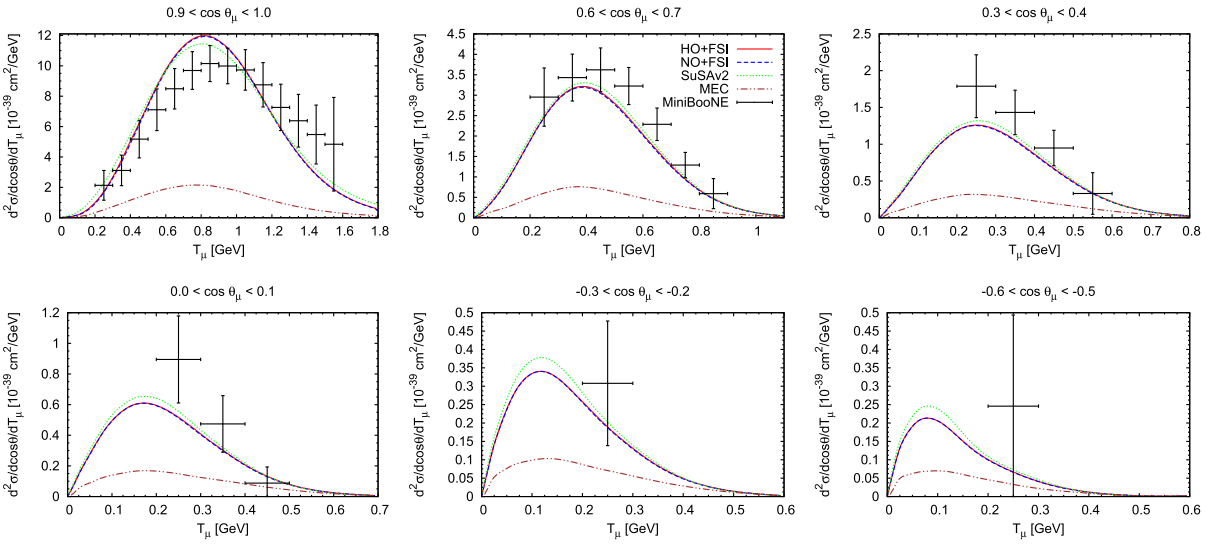

Fig. 2: (Color online) As for Fig. 1, but now for the $\overline{\nu}_\mu$ CCQE process on ^{12}C. The data are from [2].

provide almost identical responses in all kinematical situations for neutrinos and antineutrinos: the inclusive cross section is not sensitive to the details of the spectral function. Compared with SuSAv2, some differences emerge whose magnitude depends on the scattering angle region explored. Whereas the SuSAv2 prediction is slightly smaller than the SF+FSI one at very forward kinematics (very small energy and momentum transfers), the reverse tends to occur as θ_μ gets larger. Notice that at the most backward kinematics for neutrinos, the SuSAv2 results exceed by $\sim$15% those of the SF+FSI model at the maximum. Similar comments also apply to antineutrinos (Fig. 2).

4 Conclusions

This work extends our previous studies of CCQE neutrino-nucleus scattering processes that are of interest for (anti)neutrino oscillation experiments. Here we focus on models based on the use of two spectral functions, one of them including *NN* short-range correlations through the Jastrow method and, for a comparison, another without them. Effects of final-state interactions are also incorporated by using an optical potential. These calculations, based on the impulse approximation, are complemented with the contributions given by two-body weak MEC, giving rise to 2p-2h excitations. These new predictions are compared with the systematic analysis presented in [7] based on the SuSAv2-MEC approach. We find that the spectral function based models (HO+FSI, NO+FSI) lead to results that are very close to the SuSAv2-MEC predictions. Only at the most forward and most backward angles do the differences become larger, being at most of the order of $\sim 10\% - 12\%$. This is in contrast with the contribution ascribed to the 2p-2h MEC effects that can be even larger than $\sim 30\% - 35\%$ compared with the pure QE responses. This proves without ambiguity the essential role played by 2p-2h MEC in providing a successful description of (anti)neutrino-nucleus scattering data for different experiments and a very wide range of kinematical situations.

An interesting outcome of the present study is that the results obtained with the NO spectral function, which accounts for *NN* short-range Jastrow correlations, are very close to those obtained with the uncorrelated HO spectral function, thus indicating that the role played by this type of correlations is very minor for the observables analyzed in this study. The results in this work can be seen as a test of the reliability of the present spectral function based models. They compare extremely well with the SuSAv2 approach, based on the phenomenology of electron scattering data, although they fail in reproducing (anti)neutrino scattering data unless ingredients beyond the impulse approximation are incorporated.

Acknowledgements

This work was partially supported by the Bulgarian National Science Fund under Contracts Nos. DFNI-T02/19, DFNI-E02/6, and DNTS/Russia 01/3, by the Russian Foundation for Basic Research grant No. 17-52-18057-bolg-a, by the Spanish Ministerio de Economia y Competitividad and ERDF (European Regional Development Fund) under contracts FIS2014-59386-P, FIS2014-53448-C2-1, FIS2017-88410-P, FIS2017-85053-C2-1-P, FPA2015-65035-P, by the Junta de Andalucia (grants No. FQM-225, FQM160), by the INFN under project MANYBODY, by the University of Turin under contract BARM-RILO-17, and part (TWD) by the U.S. Department of Energy under cooperative agreement DE-FC02-94ER40818. GDM acknowledges support from a Junta de Andalucia fellowship (FQM7632, Proyectos de Excelencia 2011). MBB acknowledges support from the “Emilie du Châtelet" programme of the P2IO LabEx (ANR-10-LABX-0038).

References

[1] A. A. Aguilar-Arevalo *et al.* (MiniBooNE Collaboration), *Phys. Rev. D* **81** (2010) 092005.
[2] A. A. Aguilar-Arevalo *et al.* (MiniBooNE Collaboration), *Phys. Rev. D* **88** (2013) 032001.
[3] M. Martini, M. Ericson, G. Chanfray, and J. Marteau, *Phys. Rev. C* **80** (2009) 065501.
[4] J. E. Amaro *et al.*, *Phys. Lett. B* **696** (2011) 151.
[5] J. Nieves, I. Ruiz Simo, and M. J. Vicente Vacas, *Physics Letters B* **707** (2012) 72.
[6] O. Lalakulich, K. Gallmeister, and U. Mosel, *Phys. Rev. C* **86** (2012) 014614.
[7] G. D. Megias *et al.*, *Phys. Rev. D* **94** (2016) 093004.
[8] M. V. Ivanov *et al.*, *Phys. Rev. C* **89** (2014) 014607.
[9] A. N. Antonov *et al.*, *Phys. Rev. C* **83** (2011) 045504.
[10] I. R. Simo *et al.*, *Phys. Rev. D* **90** (2014) 033012.
[11] I. Ruiz Simo *et al.*, *J. Phys.* **G44** (2017) 065105.
[12] I. R. Simo *et al.*, *Phys. Rev. C* **94** (2016) 054610.
[13] J. E. Amaro *et al.*, *Phys. Rev. C* **71** (2005) 015501.
[14] D. B. Day *et al.*, *Annu. Rev. Nucl. Part. Sci.* **40** (1990) 357.
[15] M. Barbaro *et al.*, *Nuclear Physics A* **643** (1998) 137.
[16] J. A. Caballero *et al.*, *Phys. Rev. C* **81** (2010) 055502.
[17] P.-O. Löwdin, *Phys. Rev.* **97** (1955) 1474.
[18] M. V. Stoitsov, A. N. Antonov, and S. S. Dimitrova, *Phys. Rev. C* **48** (1993) 74.
[19] R. González-Jiménez *et al.*, *Phys. Rev. C* **90** (2014) 035501.
[20] J. A. Caballero *et al.*, *Phys. Rev. Lett.* **95** (2005) 252502.
[21] J. A. Caballero, *Phys. Rev. C* **74** (2006) 015502.
[22] J. Caballero *et al.*, *Physics Letters B* **653** (2007) 366.
[23] G. D. Megias *et al.*, *Phys. Rev. D* **94** (2016) 013012.
[24] T. Katori and M. Martini, *Journal of Physics G: Nuclear and Particle Physics* **45** (2018) 013001.
[25] L. Alvarez-Ruso *et al.*, *Prog. Part. Nucl. Phys.* **100** (2018) 1.
[26] J. W. Van Orden and T. W. Donnelly, *Annals Phys.* **131** (1981) 451.
[27] A. De Pace *et al.*, *Nucl. Phys.* **A726** (2003) 303.
[28] J. E. Amaro *et al.*, *Phys. Rev. C* **82** (2010) 044601.
[29] E. Hernández, J. Nieves, and M. Valverde, *Phys. Rev. D* **76** (2007) 033005.
[30] G. D. Megias *et al.*, *Phys. Rev. D* **91** (2015) 073004.
[31] M. V. Ivanov *et al.*, *Journal of Physics G: Nuclear and Particle Physics* **43** (2016) 045101.
[32] G. D. Megias *et al.*, (2017) `arXiv:1711.00771 [nucl-th]`.

Challenges in double charge exchange measurements for neutrino physics

D.Torresi[1], C. Agodi[1], J. Bellone[1,2], D. Bonanno[3], V. Branchina[2,3], S. Brasolin[4], G. Brischetto[1,2], O. Brunasso[4], S. Burrello[1,12], S. Calabrese[1,2], L. Calabretta[1], D. Calvo[4], V. Capirossi[4,5], F. Cappuzzello[1,2], D. Carbone[1], M. Cavallaro[1], I. Ciraldo[1,2] M. Colonna[1], G. D'Agostino[1,2], F. Delaunay[5,6], N. Deshmukh[1], J. Ferretti[7], P. Finocchiaro[1], M. Fisichella[4], A. Foti[3], G. Gallo[1,2], H. Garcia-Tecocoatzi[7,8], A. Hacisalihoglu[9], F. Iazzi[4,5], G. Lanzalone[1,10], F. La Via[11], J.A. Lay[12], F. Longhitano[3], D. Lo Presti[2,3], P. Mereu[4], L. Pandola[1], F. Pinna[4,5], S. Reito[3], D. Rifugiato[1], A. D. Russo[1], G. Russo[2,3], E. Santopinto[7], O. Sgouros[1], V. Soukeras[1], A. Spatafora[1,2], S. Tudisco[1], R.I.M. Vsevolodovna[7,8], T. Borello-Lewin[13], P.N. de Faria[14], J.L. Ferreira[14], R. Linares[14], J. Lubian[14], N. Medina[13], D.R. Mendes[14], M. Moralles[15], J. R. B. Oliveira[13], M.R.D. Rodrigues[13], R.B.B. Santos[16], M.A.G. da Silveira[16] , V.A.B. Zagatto[14], A. Pakou[17], G. Souliotis[18], L. Acosta[19], P. Amador[20], R. Bijker[21], D. Belmont[21], E.R. Chávez Lomelí[21], R. Espejel[21], A. Flores[21], B. Ggongora[21], A. Huerta[21], D. Marin-Lambarri[21], S. Martínez[21], J. Mas C. Ordoñez[21], G. Reza[21], S. Sandoval[21], H. Vargas[21], G. Vega[21], H. Lenske[22], I. Boztosun[23], H. Djapo[23], S. Firat[23], S. Hazar[23], Y. Kucuk[23], S.O. Solakci[23], A. Yildirin[23], N. Auerbach[24] H. Petrascu[25], J. Kotila[26], G. De Geronimo[27], N. Pietralla[28], P. Ries[28], V. Werner[28], J. Barea[29], R. Chen[30], J. Ma[30], J.S. Wang[30], Y.Y. Yang[30], N. Deshmukh[31]
For the NUMEN collaboration
[1] Istituto Nazionale di Fisica Nucleare, Laboratori Nazionali del Sud , Italy
[2]Dipartimento di Fisica e Astronomia, Università di Catania, Italy
[3]Istituto Nazionale di Fisica Nucleare, Sezione di Catania, Italy
[4]Istituto Nazionale di Fisica Nucleare, Sezione di Torino, Italy
[5]DISAT, Politecnico di Torino, Italy
[6]LPC Caen, Normandie Université, ENSICAEN, UNICAEN, CNRS/INP3, France
[7]Istituto Nazionale di Fisica Nucleare, Sezione di Genova, Italy
[8]Dipartimento di Fisica, Università di Genova, Italy
[9]Institute of Natural Sciences, Karadeniz Teknik University, Turkey
[10]Università degli Studi di Enna "Kore", Italy
[11]CNR-IMM, Sezione di Catania, Italy
[12]Departamento de FAMN, University of Seville, Spain
[13]Universidade de Sao Paulo, Brazil
[14]Universidade Federal Fluminense, Brazil
[15]Instituto de Pesquisas Energeticas e Nucleares IPEN/CNEN, Brazil
[16]Centro Universitario FEI Sao Bernardo do Brazil, Brazil
[17]Department of Physics, University of Ioannina, Greece
[18]Department of Chemistry, National and Kapodistrian University of Athens, Greece
[19]Instituto de Fìsica, Universidad Nacional Autónoma de México, Mexico
[20]Instituto Nacional de Investigaciones Nucleares, México
[21]Instituto de Ciencias Nucleares, Universidad Nacional Autónoma de México, Mexico
[22]Department of Physics, University of Giessen, Germany
[23]Department of Physics, Akdeniz University, Turkey
[24]School of Physics and Astronomy, Tel Aviv University, Israel
[25]IFIN-HH, Romania
[26]University of Jyväskylä, Finland
[27]Stony Brook University, USA
[28]Institut fur Kernphysik, Technische Universitat Darmstadt, Germany
[29]Universidad de Conception, Chile
[30]Institute of Modern Physics, Chinese Academy of Sciences, Lanzhou, China
[31]Nuclear Physics Division, Saha Institute of Nuclear Physics, India

Abstract
The neutrinoless double beta ($0\nu\beta\beta$) decay, if observed, has important implications on particle physics, cosmology and fundamental physics. In particular it can give access to the effective neutrino mass. In order to extract such information from the $0\nu\beta\beta$-decay half-life measurement, the knowledge of the Nuclear Matrix Elements (NME) is of utmost importance. In this context the NUMEN and the NURE projects aim to extract information on the NME by measuring the Double Charge Exchange (DCE) reaction cross section in selected systems of interest for the $0\nu\beta\beta$-decay. The experimental difficulties that have to be faced are the measurements at very forward-angle, the very low cross section of the process to be measured, the requirement of a high energy resolution and, eventually, the unambiguous identification of the DCE reaction from other competing processes. The large-acceptance spectrometer MAGNEX, present at INFN-LNS, Catania fulfills all the requirement above mentioned.

1 Introduction

About ninety year after the existence of neutrino has been hypothesized, the study of the property of this particle is still of crucial importance in the landscape of particle physics, cosmology and fundamental physics. In particular one of the most studied process involving neutrino particles is the $0\nu\beta\beta$-decay since, if observed, it will represent a gate through physics beyond the standard model. In fact it will sign the Majorana or Dirac character of the neutrino, it will establish if the leptonic number is conserved or not, and could give access to the neutrino effective mass.
The $0\nu\beta\beta$-decay rate can be written as product of three factors:

$$T_{0\nu}^{-1/2} = G_{0\nu}|M_{0\nu}|^2 f(m_i, U_{ei}, \xi_i)$$

where $G_{0\nu}$ is the phase space factor, $|M_{0\nu}|^2$ are the Nuclear Matrix Elements (NME) and $f(m_i, U_{ei}, \xi_i)$ is a function containing the effective mass of the neutrino that include all the physics beyond the standard model.
The issues related to such process can be separated in two classes. The first is related to the particle physics that include the function $f(m_i, U_{ei}, \xi_i)$ the second instead is related to the nuclear physics represented by the NME. In fact the $0\nu\beta\beta$-decay is, first of all, a nuclear process that occurs inside the nuclear medium. Assuming that the decay rate is known, to have access to the function $f(m_i, U_{ei}, \xi_i)$ that contains the effective mass and the physics beyond the standard model, an accurate and reliable knowledge of the NME is mandatory.
Nowadays the knowledge of the NME is mainly based on theoretical calculations that use different models as QRPA, Interacting Shell Model, IBM, Energy Density Functional Method and others [1–4]. Significant discrepancies are presently reported in literature among the different models, moreover the lack of any constrains coming from experimental data represents a major problem to extract reliable neutrino effective mass.

In order to get experimentally-driven quantitative information on NMEs the NUMEN and the NURE [5–8] projects propose to use heavy-ion induced Double Charge Exchange reactions (DCE). In DCE reactions two charge units are transfered leaving the mass number of the involved nuclei unaltered. The two processes are mediated by different interactions: the strong interaction for the DCE and the weak interaction for the $0\nu\beta\beta$-decay. Anyway there are important and strong similarity, in fact:

i the initial and the final nuclear state of the two processes are the same,
ii the operators describing the two processes are a mix of Fermi, Gamow Teller and rank-two tensor components,

iii a large momentum is available in the intermediate channel.

iv they take place in the same nuclear medium.

The use of DCE reactions with the aim to obtain information on the NMEs useful for the double-β decay was investigated some decades ago. These early studies of heavy-ion induced DCE reaction was inconclusive mainly due to the lack of data at very forward angles (zero degrees) and to low statistics in the energy and angular distribution. The main limitation can be identified on the very low cross section of the DCE process [9, 10]. Furthermore additional complication in the interpretation of the data arose from the possible contribution of multinucleon transfer to the same final state of the DCE process. Today such limitations can be overcome by modern high-resolution and large-acceptance spectrometers, as the MAGNEX spectrometer [11] at INFN-LNS, Catania, a relevant instrument in the research of heavy-ion physics [12–14].

In order to study the feasibility of the proposal a pilot experiment have been performed at INFN-LNS, to measure the cross section for the reaction ^{40}Ca(^{18}O,^{18}Ne)^{40}Ar at 270 MeV and at 0° [15]. The key tools that allowed to overcome the above-mentioned limitations were the high resolution ^{18}O beam delivered by the Superconducting Cyclotron (SC) and the large-acceptance MAGNEX spectrometer. The pilot experiment demonstrates that it is possible to measure the DCE at very forward angle (zero degree) with an high energy resolution that allow to identify the transition to the ground state and the excited states, and it it is possible to measure the other reaction mechanism competing with the DCE. Therefore high resolution and statistically significant experimental data can be measured for DCE processes and they can provide useful information for the determination of the NME for the $0\nu\beta\beta$ decay.
Even thought the DCE reaction ^{40}Ca(^{18}O,^{18}Ne)^{40}Ar have been successfully measured, the final aim of the project is to measure the cross section for DCE reaction for systems where the target nucleus is a $0\nu\beta\beta$-decay candidate nucleus. To move toward such hot cases a number of experimental difficulties must be overcome:

i The Q-value of the DCE reactions on nuclei of interest is usually more negative than in the case of the ^{40}Ca explored in [15]. This could strongly reduce the cross section at zero degree.

ii The (^{18}O,^{20} Ne) reaction, used in the pilot experiment, is particularly favorable since has a large value of the B(GT) strengths. Anyway such reaction emulate the $\beta^+\beta^+$-decay. The most of the hot cases are of the $\beta^-\beta^-$ kind, to investigate such reactions the available reaction (^{20}Ne,^{20}O) or (^{12}C,^{12}Be) have smaller B(GT), so an further reduction of the yield is expected.

iii In same case, like for the ^{130}Xe on ^{136}Xe nuclei, a gas target is required. Since gas target are usually thinner than solid target such target will suffer an additional yield reduction.

iv For same system the energy resolution of the spectrometer is not enough to disentangle the ground state from the first excited state in the final recoiling nucleus. Therefore for such cases the measurement of gamma rays is required that implies a lower yield due to the typically low efficiency of gamma detection.

In order to obtain measurements with a significant statistics the beam intensity must be substantially increased. This requires an upgrade of the experimental set-up able to work with a beam current higher of two or three orders of magnitude compared to the present value. Such upgrade requires deep changes for the accelerator, the detection system and for the target assembly.

Concerning the beam, the project requires mainly beams of carbon, oxygen and neon with intensity up to 10^{14} pps delivered to the MAGNEX spectrometer. The required energies for these beams are in the

range 15-70 AMeV, which corresponds to a beam power in the range 1-10 kW to be compared with the present maximum power of about 100 W. To overcome the present limit, a stripper induced extraction, for ions with A<40, was proposed. Calculations demonstrate that such method is able to provide the required beam power [16, 17].

The main issues concerning the target are related to production of thin and very uniform target and the high heat dissipated by the beam on the target itself. The demand of a good energy resolution ($\sim$ 1/1000) requires that the targets must be thin and uniform. On the other hand, the large beam current together with the small thickness require that the generated heat inside the target be efficiently dissipated to avoid target damages. A cryogenic radiation-tolerant target system have been designed. It is based on the deposition of the target material on a thin layer of pyrolytic graphite that ensures a large heat transfer from the central region to the surrounding cold frame, thanks to the high thermal conductivity of the graphite [18, 19].

For the detection system the main upgrade foreseen are:
a) Replacement of the present focal-plane detector gas tracker.
In fact the present FPD has an intrinsic limitation in the incident-ion bearable rate of few kHz, mainly due to the fact that the multiplication is done by mean of long wires. For this reason a new gas tracker based on micro patterned technology, like GEM or THGEM is under development. This require that the electron multiplication region and the segmented readout board of the FPD tracker will be radically re-designed, at the same time new full-custom front-end and read-out electronics will be also designed [20].
b) Replacement of the silicon detector wall.
The existing stopping wall of silicon detectors is made of 50×70 mm^2, 1 mm thick silicon pad detectors and needs to be replaced in view of the higher detection rate. The new stopping wall must fulfill the requirement of energy resolution better than 1% to keep the same performances for the particle identification; a good time resolution better than 1-2 ns in order to guarantee an accurate measurement of the drift time in the gas chamber used to reconstruct the vertical track of the ejectiles; an a high granularity(modules of 1 cm^2 are in progress in SiCILIA project [21]) is required in order to limit pile-up events; the detector should be thick enough to stop the ions in a wide dynamical range of incident energies (from 10 up to 60 MeV/A) [22, 23].
c) Design of a γ-ray detectors array.
For some target ion, especially at higher energies, the energy resolution is not enough to separate the ground from the first excited state of the reaction products. An array of gamma detector (GNUMEN), with a large solid angle, will be developed with the aim to allow the discrimination of different energy states [24].

Finally the NUMEN project include inside it a theory program [25, 26]. Such theoretical developments aim at reaching a full description of the DCE reaction cross section, including also competing channels that may lead to the same final outcome, and at investigating the possible analogies with double beta decay.

1.1 Acknowledgements

This project has received funding from the European Research Council (ERC) under the European Union's Horizon 2020 research and innovation programme (grant agreement No 714625).

References

[1] Vergados J D, Eijire H and Simkovic F 2012 *Rep. Prog. Phys* **75** 106301.
[2] Vogel P 2012 *Jour. of Phys. G: Nucl. and Part. Phys.* **39** 124002.
[3] Engel J and Menendez K, (2017) *Rep. Prog. Phys.* **80** 046301.
[4] Dell'Oro S, Marcocci S, Viel M and Vissani F 2016 *Adv High Energy Phys.* **2016** 2162659.

[5] Agodi C et al. 2015 *Nucl. Part. Phys. Proc.* **265** 28.
[6] Cappuzzello F et al. 2018 *Eur. Phys. J. A* **54** 72.
[7] Cavallaro M. et al. 2017 *Proceedings of Science* **302** 15.
[8] Cappuzzello F et al. 2015 *J. Phys.: Conf. Ser.* **630** 12018.
[9] Blomgren J et al. 1995 *Phys. Lett.* **B 362** 34.
[10] Drake D M et al. 1980 *Phys. Rev. Lett.* **45** 1765.
[11] Cappuzzello F, Agodi C, Carbone D, Cavallaro M, 2016 *Eur. Phys. J. A* **52** 167.
[12] Carbone et al, Phys. Rev. C 95 (2017) 034603.
[13] Cavallaro M et al., Phys Rev C 93 (2016) 064323.
[14] Cappuzzello F et al, Nature Comm 6,(2015) 6743.
[15] Cappuzzello F et al., *Eur. Phys. J.* **A 51**, 145 (2015).
[16] L. Calabretta et al., *Modern Physics Letters* **A 32**, 17 (2017).
[17] S. Russo, et al. 2017 Journal of Physics: Conference Series **1056** 012051.
[18] F. Pinna et al. 2017, Journal of Physics: Conference Series **1056** 012046.
[19] F. Iazzi et al. 2017, WIT Transactions on Engineering Sciences, **116** 206.
[20] D. Lo Presti et al. 2017 Journal of Physics: Conference Series **1056** 012034.
[21] S. Tudisco et al. , Sensors 2018, 18(7), 2289;
[22] A. Muoio, et al., *Eur. Phys. J. Web of Conferences Volume:* **117** 10006 (2016).
[23] D. Carbone et al., Results in Physics 6 (2016) 863.
[24] J. R. B. Oliveira et al. 2017 Journal of Physics: Conference Series **1056** 012040.
[25] H. Lenske, J. Bellone, M. Colonna, J.H. Lay, Phys. Rev C 98 (2018) 044620.
[26] E. Santopinto, H. Garcia-Tecocoatzi, R.I. Magana-Vsevolodovna and J. Ferretti. Phys. Rev C (2018) accepted

Demand for TRU nuclide cross-sections from the view point of TRU production and radiotoxicity

R. Kimura, K. Yoshioka, K. Hiraiwa, S. Sakurai, S. Wada and T. Sugita
Toshiba Energy Systems & Solutions, Kawasaki, Japan

Abstract
The environmental load reduction of nuclear energy is required in Japan, from the view point of public acceptance. Here, the long-term radiotoxicity of radioactive wastes is dominated by trans-uranium (TRU) nuclides. We evaluated the effects of differences between the nuclear data libraries of heavy-metal-nuclide cross-section on the radiotoxicity of LWR spent fuels. In this study, the MVP-BURN code and the JENDL-4.0u nuclear data library were used as a burn-up calculation code and a reference nuclear data library, moreover, only a heavy metal cross section of interest was replaced to JEFF-3.2 or ENDF/B-VII.1 to evaluate the effect of difference between libraries for each nuclides. The calculation results revealed that the productions of Pu-238, Am-241 and Cm-244 with JEFF-3.2 were 8% larger than those with JENDL-4.0u and ENDF/B-VII.1. The thermal energy capture reaction of Pu-238 and 1.356eV resonance capture reaction of Am-243 have a large impact on the radiotoxicity of Pu-238 and Cm-244, consequently, these cross sections should be improved.

1 Introduction

The environmental load reduction of nuclear energy is required in Japan, from the view point of public acceptance due to the increase of safety demand to the nuclear energy utilization. This environmental load is mainly caused by the mass and radiotoxicity of radioactive wastes. Especially, long-term radiotoxicity (>100 years) of the radioactive waste is dominated by trans-uranium (TRU) nuclides [1]. Additionally, most of the TRU nuclides, which are large part of environmental loads, are generated from light water reactors. Therefore, the evaluation of TRU nuclide production in the light water reactors is important to estimate the environmental load of nuclear energy [2-4].

As well known, the amount of TRU nuclide is evaluated through burn-up calculations. Here, the burn-up chain of actinides is shown in Fig. 1. This figure also shows high-radiotoxicity nuclides and major ancestor nuclides among these TRU nuclides, and besides, the radiotoxicity of the TRU nuclides is deduced by radioactivity, type of decay, decay energy and biological-effect of radiation. As shown in this figure, high-radiotoxicity nuclides have some of major ancestor nuclides.

For these reason, the evaluation of high-radiotoxicity nuclide production require many actinide cross-section data from a nuclear data library. However, also as well known, these cross section data have a different value between libraries due to its uncertainty of experimental data.

Fig. 2 shows the difference of a neutron capture cross section for ^{238}Pu between ENDF/B-VII.1, JENDL-4.0u and JEFF-3.2 [5-7]. As shown in this figure,the neutron cross section is different in a range from thermal to epi-thermal energy region. From this result, it would be considered that other nuclide cross section data also have a difference between libraries. Ultimately, these differences should be improved in the future. However, measurements for all nuclides in same time are not realistic

option. Therefore, the priority of measurement should be given by the effect of nuclide cross section on TRU nuclide production in burn-up chain from the view point of environmental load reduction.

For these backgrounds, we investigated cross section difference effects between libraries on high-radiotoxicity nuclides; furthermore, we made the requirement for cross section to improve the precision of burn-up calculation on high-radiotoxicity nuclides production.

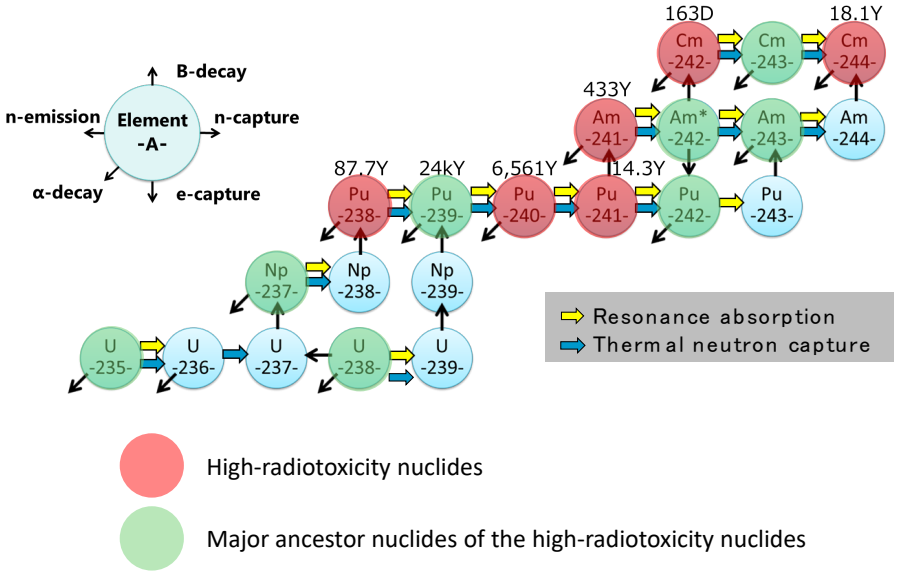

Fig. 1 Burn-up chain of the Actinides

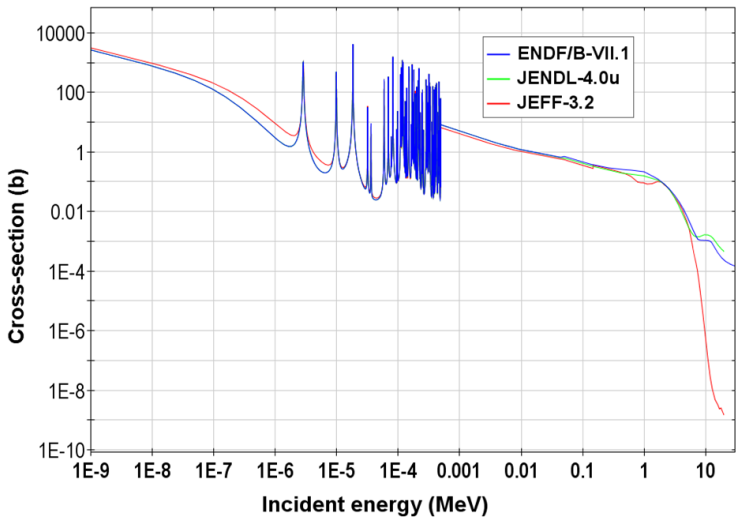

Fig. 2 Neutron capture cross section difference of ^{238}Pu between ENDF/B-VII.1, JENDL-4.0u and JEFF-3.2

2 Calculation method of the effect of nuclear data libraries

The diagram of nuclide cross section data replacement method is shown in Fig. 3. In this study, JENDL-4.0u was used as a reference nuclear data library; furthermore, the cross section data of nuclides were replaced by ENDF/B-VII.1 or JEFF-3.2 one by one to evaluate the effect of the cross section on TRU nuclide production.

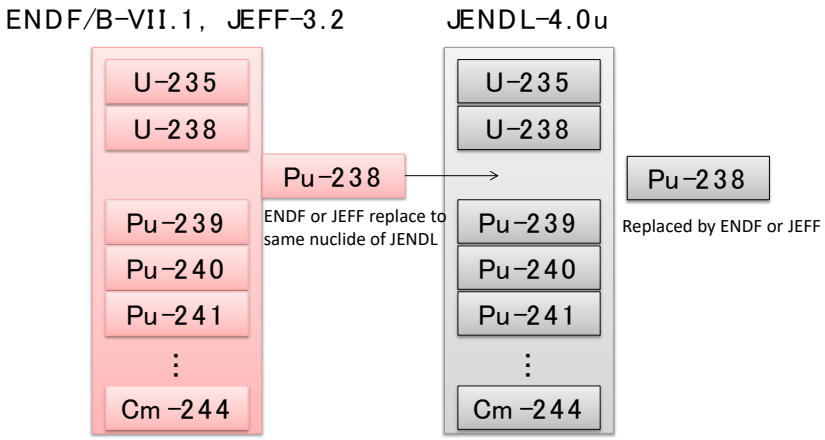

Fig.:3 Replacement method of nuclide cross section data

The 9x9A type BWR fuel assembly was utilized in the present study. The cross section of this fuel assembly is shown in Fig. 4. Additionally, calculation condition is shown in Table 1. The MVP-BURN code was used as a Monte-Carlo burn-up calculation code [8], additionally; the burnup calculation of the 9x9A type BWR fuel assembly was conducted by MVP-BURN with a typical burn-up condition as shown in Table 1, the number density of each nuclides were evaluated at the burnup of 45GWd/t.

Table 1: Calculation Condition

Item	Condition
CODE	MVP-BURN
Nuclear Data Libraries	JENDL-4.0u(Ref) ENDF/B-VII.1 JEFF-3.2
Power Density	50 kW/L
Fuel pellet diameter	0.956 cm
Pin pitch	1.438 cm
Cladding thickness	0.071 cm
U-235 Enrichment	3.84 wt%
Burn-up	45 GWd/t

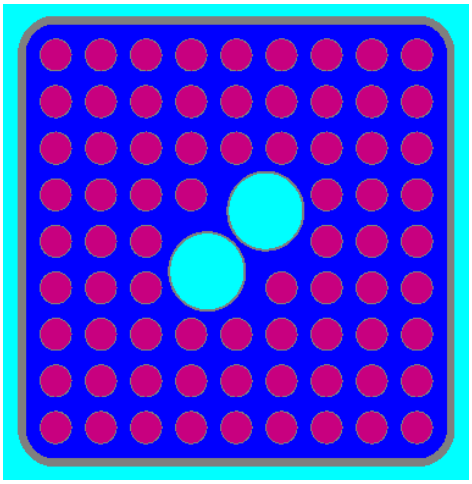

Fig. 4: Cross section image of the 9x9A type BWR fuel assembly

In the present study, number density ratio at the discharge burnup NR_{ij} was defined as equation (1)

$$NR_{ij} = \frac{N_{ij,ENDF}}{N_{i,JENDL}} \quad or \quad \frac{N_{ij,JEFF}}{N_{i,JENDL}} \tag{1}$$

Here, $N_{ij,JENDL}$ is the number density of a nuclide i at the discharge burnup calculated withJENDL-4.0u, $N_{ij,ENDF}$ and $N_{ij,JEFF}$ are discharged number density of nuclide i calculated with the cross section of nuclide j replaced by ENDF or JEFF. We evaluated this NR_{ij} for all nuclides in Table 2.

Table 2: Evaluated nuclides

Element	Nuclide
U	^{235}U, ^{238}U
Np	^{237}Np
Pu	^{238}Pu, ^{239}Pu, ^{240}Pu, ^{241}Pu, ^{242}Pu
Am	^{241}Am, ^{242g}Am, ^{242m}Am, ^{243}Am
Cm	^{242}Cm, ^{243}Cm, ^{244}Cm

3 Results and discussion

3.1 Results of the number density ratio and cause of the difference

The NR_{ij} results of ENDF/B-VII.1 and JEFF-3.2 are shown in Fig. 5 and Fig. 6. NR_{ij} results replacing JENDL-4.0u with ENDF/B-VII.1 shows the maximum difference of 2 %. In case that Minor Actinide (MA) cross sections were replaced, the maximum difference of NR_{ij} was smaller than 0.5 %. Because, ENDF/B-VII.1 have used the same cross sections data as JENDL-4.0u. While, the differences of some NR_{ij} values from 1.0 in JEFF-3.2 were larger than 8 %. Especially, effect of the ^{238}Pu, ^{241}Am and ^{243}Am cross sections had a large impact on the NR_{ij} values.

Fig. 5: NR_{ij} results of each nuclide based on the ENDF/B-VII.1

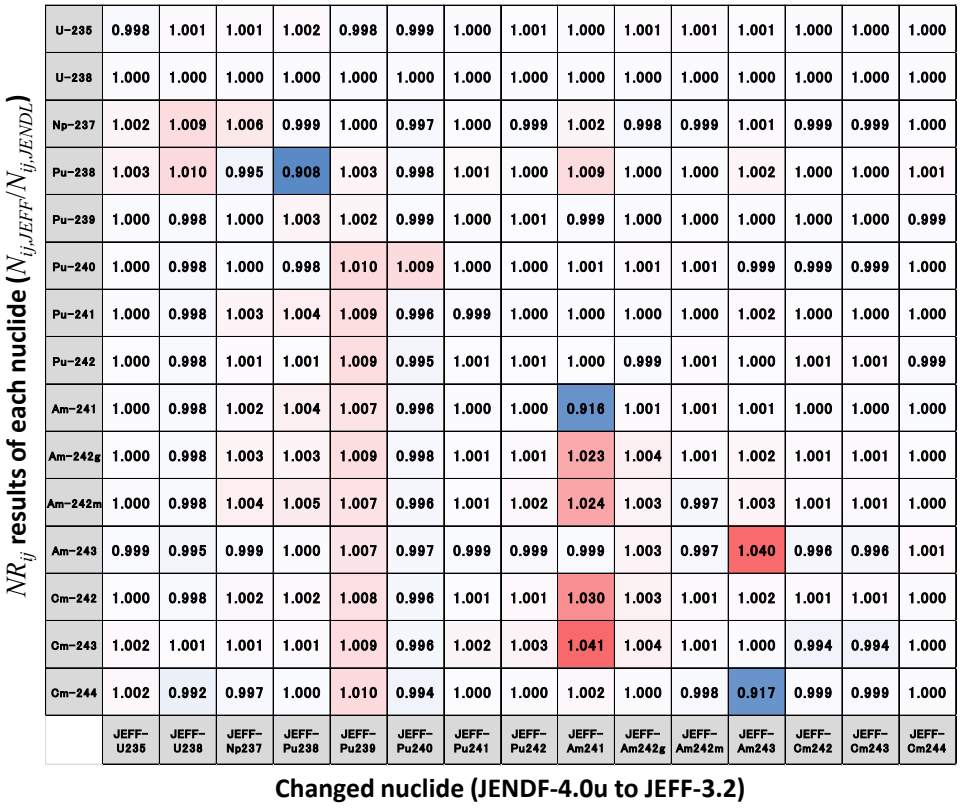

Fig. 6: NR_{ij} results of each nuclide based on the JEFF-3.2

Accordingly, the different of reaction rate and major cross sections are shown in Fig. 7 to Fig. 9 to realize important energy region in each nuclides. Here, the different of the reaction rate Dif_R is defined as equation (2).

$$Dif_R = (\text{Reaction rate by JEFF-3.2 or ENDF-B/VII.1}) - (\text{Reaction rate by JENDL-4.0u}) \quad (2)$$

Firstly, Fig. 7 (a) shows the Dif_R of ^{238}Pu. As shown in this figure, the difference of capture reaction rate replacing JENDL-4.0u with JEFF-3.2 was dominated by thermal region. This difference came from capture cross section difference in the thermal energy region between these nuclear data libraries as shown in Fig. 7 (b).

Secondly, Fig. 8 (a) and (b) show the Dif_R and capture cross section of ^{241}Am. Here, capture cross section was drawn in liner scale to make it easier to understand. As shown in both figures, capture reaction rate difference between JEFF-3.2 and JENDL-4.0u was dominated by resonance region.

Finally, Fig. 9 (a), (b) and (c) show the Dif_R and capture cross section of ^{243}Am. As shown Fig. 9 (a), reaction rate difference was dominated by almost one resonance cross section. The capture cross sections of each library in 0.1-10 eV are drawn in Fig. 9 (b), additionally, resonance cross sections at 1.356 eV are shown in Fig. 9 (c). It was confirmed that the resonance cross section of ^{243}Am at 1.356 eV had a difference larger than 2000 b among theese libraries. In addition, measurement values between these libraries were compared in Fig. 10. As shown in this figure, the latest evaluated libraries do not support measurement value, but TENDL-2015 supported the measurement value. For these results, resonance cross section at 1.356 eV of ^{243}Am could have a large uncertainty.

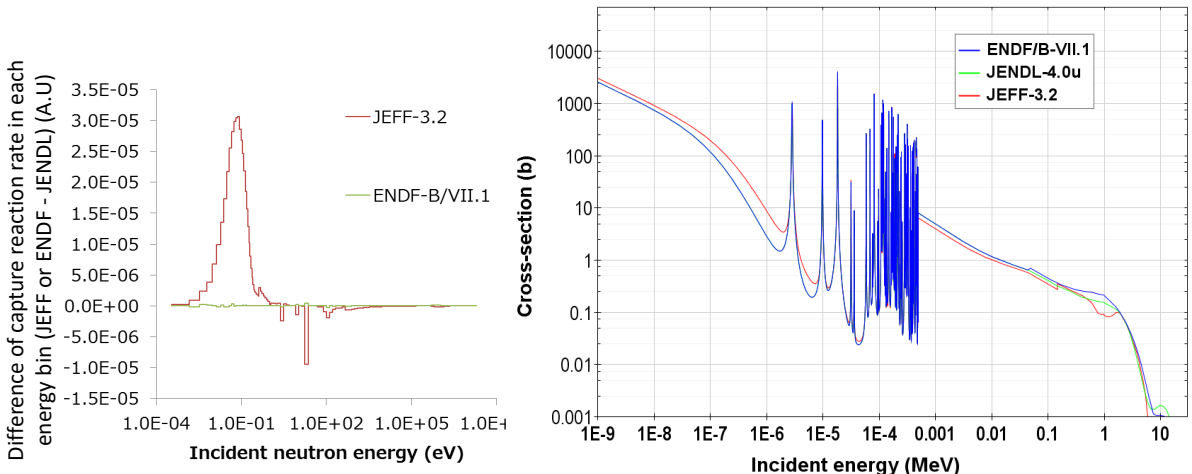

Fig. 7: Reaction rate and capture cross section difference of ^{238}Pu between JENDL-4.0, ENDF/B-VII.1 and JEFF-3.2

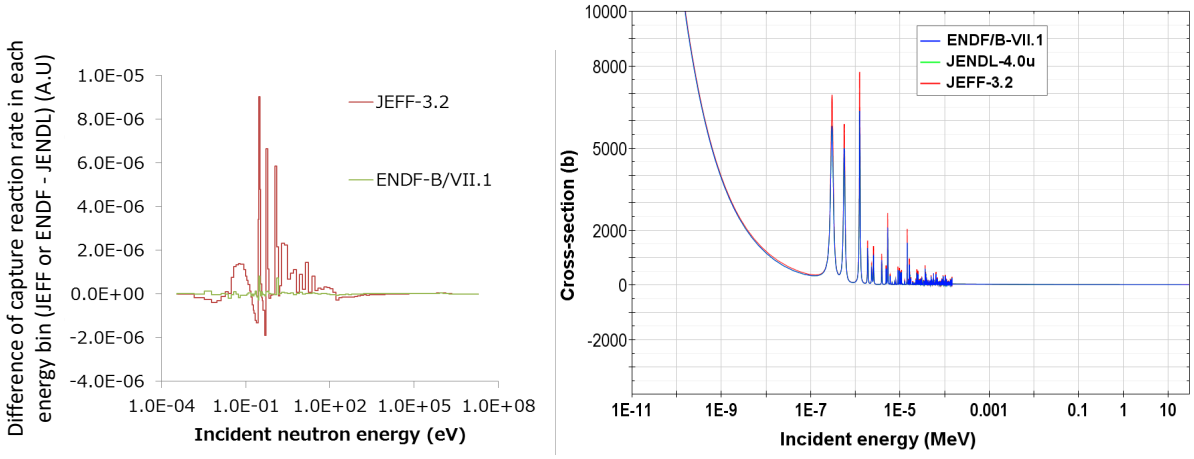

(a) Difference of ^{241}Am capture reaction rate in each energy bin

(b) Comparison of ^{241}Am capture cross section

Fig. 8: Reaction rate and capture cross section difference of ^{241}Am between JENDL-4.0, ENDF/B-VII.1 and JEFF-3.2

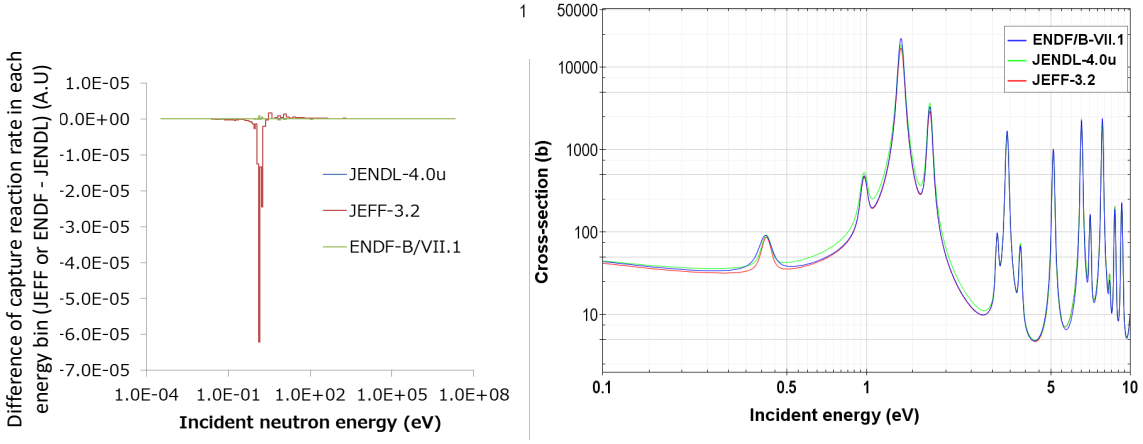

(a) Difference of ^{243}Am capture reaction rate in each energy bin

(b) Comparison of ^{243}Am capture cross section

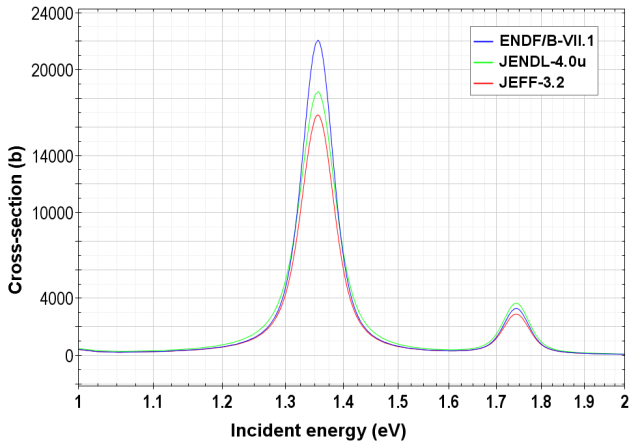

(c) Comparison of ^{243}Am resonance capture cross section at 1.356eV

Fig.9: Reaction rate and capture cross section difference of ^{243}Am between JENDL-4.0, ENDF/B-VII.1 and JEFF-3.2

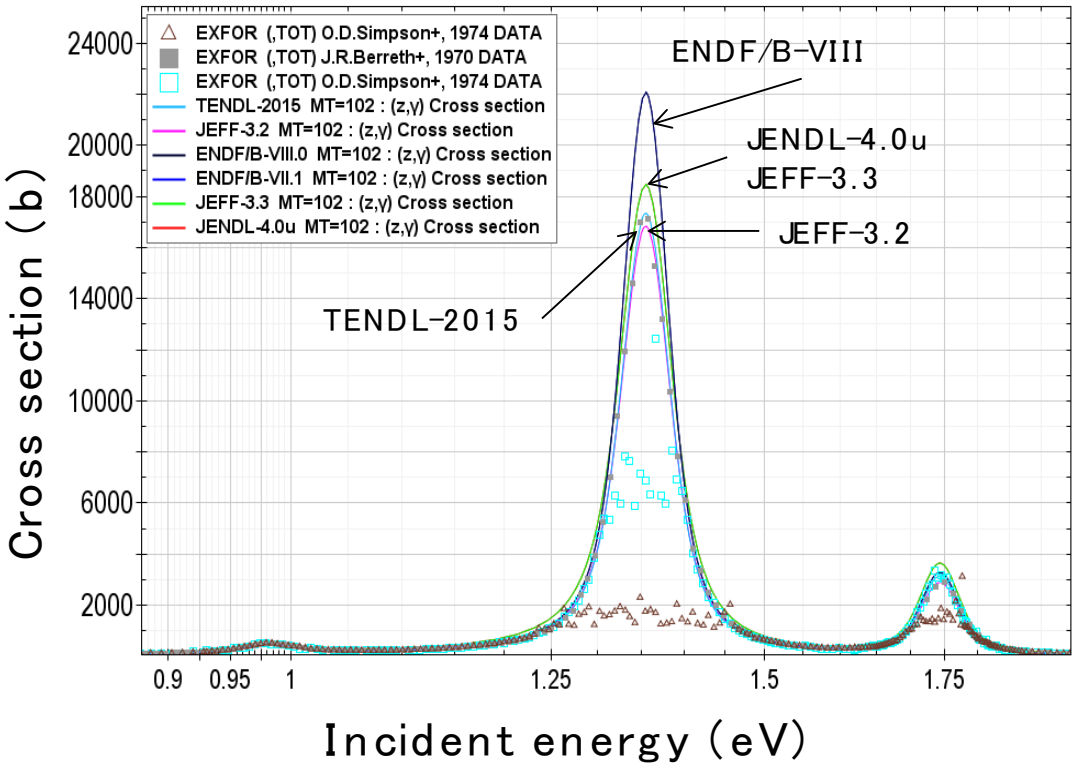

Fig.10: Measured value and libraries data of ^{243}Am total cross section [9-13]

3.2 Prioritization of requirement for nuclear data improvement

The important nuclide cross sections to estimate actinides discharged number density were realized in section 3.1. However, importance classifying of these cross sections were required for efficient nuclear data improvement. Hence, requirements for nuclear data improvement were prioritized in this section.

The relative composition of nuclides causing radiotoxicity in the UO_2 and MOX fuel are shown in Fig. 11. As shown in this figure, ^{238}Pu, ^{241}Pu and ^{244}Cm had a large composition at a discharged spent fuel. On the other hand, ^{238}Pu, ^{241}Am and ^{243}Am had a large sensitivity for actinides discharged number density as mentioned in section 3.1. Here, all actinide cross sections is insensitive to ^{241}Pu number density as shown in Fig. 5 and Fig. 6. Additionally, post irradiation experiment (PIE) data of ^{241}Pu number density shows good agreement with calculated result [14]. Therefore, ^{241}Pu was excluded from prioritization target.

Table 3 shows the prioritization results. In the results, first priority was ^{238}Pu capture cross section in thermal energy region. Because, the radiotoxicity of ^{238}Pu had a large weight in UO_2 and MOX spent fuel. Additionally, the latest libraries (JEFF-3.3, it use the same data as JENDL-4.0u (July, 2013)) do not consider the latest experiment data as shown in Fig. 12. Consequently, the cross section of ^{238}Pu would be better to be improved as first priority from view point of radiotoxicity evaluation.

The second priority was ^{243}Am capture cross section. The capture reaction of ^{243}Am produces ^{244}Cm which had a large radiotoxicity as shown in Fig. 11. Especially, the radiotoxicity of ^{244}Cm is important during 100 years after discharge due to half-life of ^{244}Cm (18.1 y). Additionally, ^{243}Am cross section had the same problem of ^{238}Pu cross section; the latest library data (JENDL-4.0u) do not consider latest experiment data as shown in Fig. 14 [19] (2014).

Finally, third priority was ^{241}Am. The radiotoxicity of ^{241}Am was not so high. However, radiotoxicity of ^{241}Am was important to design of radioactive waste disposal site. Because, the half-life of ^{241}Am (432.6 y) is longer than ^{238}Pu (87.7 y) and ^{244}Cm (18.1 y), therefore, ^{241}Am had long-term environmental load.

Table 3: Prioritization results of improve requirement for the nuclear data

Priority	nuclides	Energy range	Reason and *comment*
1	**Pu-238**	**1meV~1.0eV**	**1.Large weight of radiotoxicity in UO2 and MOX spent fuel** 2.***Latest libraries not considered latest experiment results***
2	**Am-243**	**Resonance of 1.356eV and 1.744 eV**	**1.radiotoxicity of Cm-244 from Am-243 have large impact during 100y from discharge** 2.***Latest libraries not considered latest experiment results***
3	**Am-241**	**0.1~100eV**	**1.Large impact for long term (Am-241) and short term (Cm-242) radiotoxicity.** 2.***Large differences were exist between libraries and experiment results***

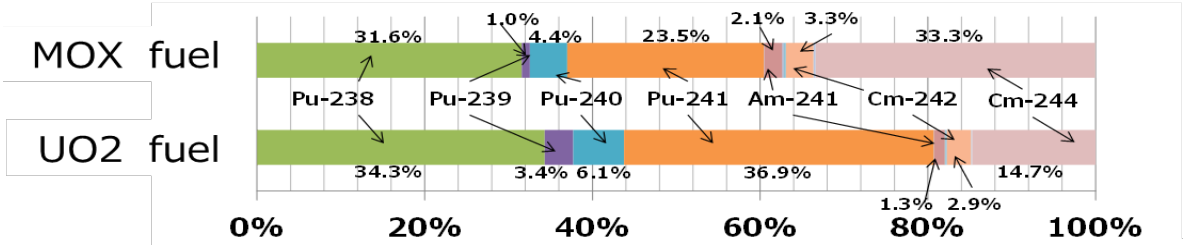

Fig. 11: Relative radiotoxicity composition in the discharged spent fuel

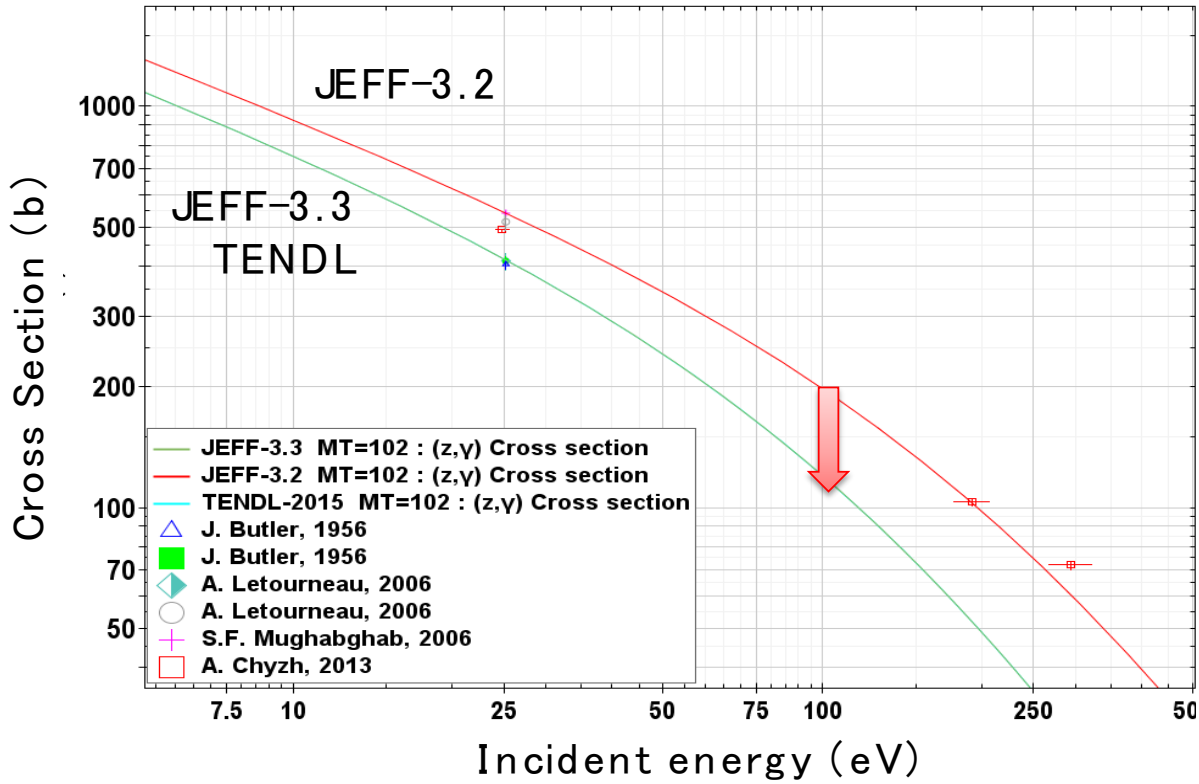

Fig. 12: Comparison of ^{238}Pu neutron capture cross section data of libraries and experiment data [15-18]

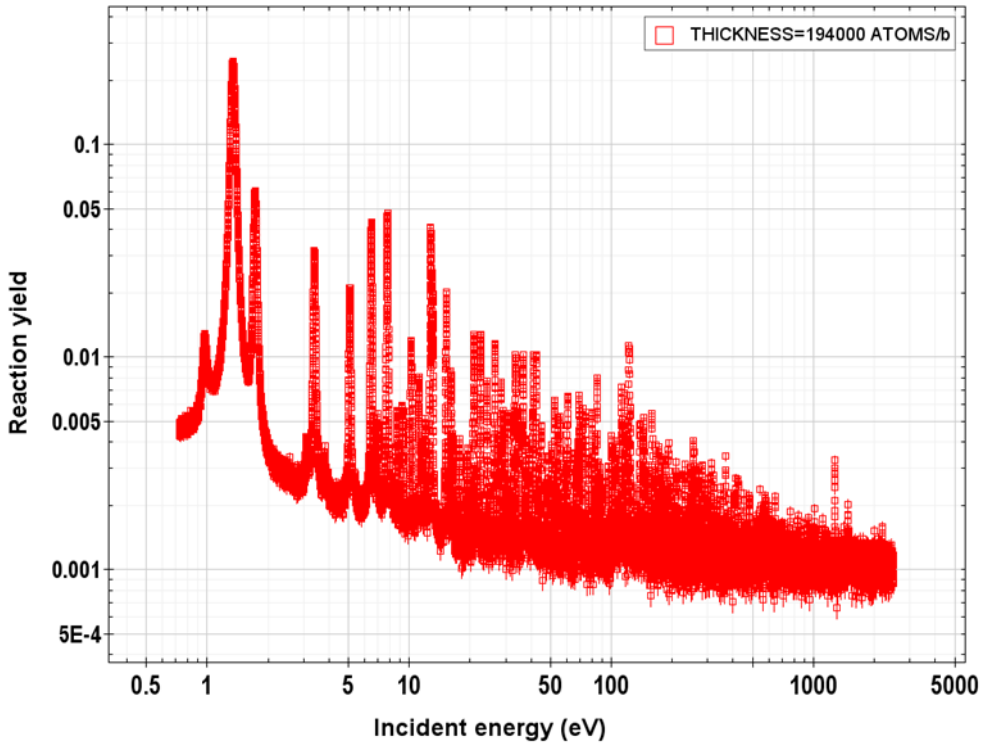

Fig. 14: Experiment data of ^{243}Am capture reaction measured by E. Mendoza et. Al. [19]

4 Conclusion

The cross section sensitivity for the discharged number density of actinide nuclides were demonstrated, furthermore, requirements for the nuclear data were prioritized. For the present study, the priorities of the cross section improvement of ^{238}Pu, ^{243}Am and ^{241}Am were summarized as shown in Table 3.

Moreover, the latest libraries of these nuclides uses some common data, namely, important nuclear data for environmental load estimation were shared between libraries. Therefore, if these nuclear data have a serious error, it would lead systematic error in different libraries. Additionally, the latest nuclear data libraries of ^{238}Pu, ^{243}Am and ^{241}Am have large difference from the latest experiment data. Hence, these nuclides still have room to improve theoretically and experimentally.

Especially, ^{238}Pu, ^{243}Am and ^{241}Am have a large impact to estimate radiotoxicity, decay heat, the volume of radioactive waste and the area of final disposal site. Therefore, improvement in the accuracy of these cross section are important for the utilization of nuclear energy, additionally, these nuclides cross section improvement are clearly important for the future of nuclear industry.

Acknowledgement

This study is being performed under the contract with Ministry of Education, Culture, Sports, Science and Technology (MEXT) “MEXT nuclear system research and development Program”

References

[1] K. Nakahara, JAEA-Data/Code2010-012 (2010)

[2] K. Hiraiwa et al., Study on Minimization of LWR Spent Nuclear Fuel 1) Outline of the Studies , 2015 Fall meeting of AESJ (2015)

[3] S. Sakurai et al., Study on Minimization of LWR Spent Nuclear Fuel 2) Optimization for combination of Higher Moderation and Higher Burnup, 2015 Fall meeting of AESJ (2015)

[4] R. Kimura et al., Study on Minimization of LWR Spent Nuclear Fuel 3) Low Solf-shielding Fuel and the Nuclear Characteristics of the fuel, 2015 Fall meeting of AESJ (2015)

[5] K. Shibata, *et. al. J. Nucl. Sci. Technol*. **48**(1), 1-30 (2011)

[6] M. B. Chadwick, et al., Nuclear Data Sheet, **112**(12), 2887-2996 (2011)

[7] The JEFF team, , http://www.oecd-nea.org/dbdata/jeff, (2014)

[8] K. Okumura, *et. al. J. Nucl. Sci. Technol*. **37**(1), 128-138 (2000)

[9] D. A. Brown, et al., Nuclear Data Sheets, **148**, 1-142 (2018)

[10] The JEFF team, , http://www.oecd-nea.org/dbdata/jeff/jeff33, (2017)

[11] A. J. Koning, et al., TENDL-2015 (2016)

[12] O. D. Shimpson, *et al, Nucl. Sci. Technol*, **55**, 273 (1974)

[13] J. R. Berreth and F. B. Simpson, Idaho Nuclear Corp. Reports, 1407, **66** (1970)

[14] Y. Nakahara, K. Suyama and T. Suzaki, JAERI-Tech 2000-071 (2000)

[15] J. Butler, *et al., Canadian Journal of Chemistry*, **34**, 253 (1956)

[16] A. Chyzh, *et al., Physical Review Part C Nuclear Physics*, **88**, 044607 (2013)

[17] A. Letourneau, et al., *Workshop Nucl.Data Meas., Theo.&Appl.,* Budapest,2009, page 81 (2009)
[18] S. F. Mughabghab, Atlas of Neutron Resonance (2006)
[19] E. Mendoza, et al., *Physical Review Part C Nuclear Physics*, **90**, 034608 (2014)

Nuclear Astrophysics at n_TOF facility, CERN

G. Tagliente[1], O. Aberle[2], V. Alcayne[9], J. Andrzejewski[7], L. Audouin[17], V. Babiano-Suarez[4], M. Bacak[2,20,10], M. Barbagallo[2,1], V. Bécares[9], Th. Benedikt[6], S. Bennett[18], E. Berthoumieux[10], J. Billowes[18], D. Bosnar[19], A. Brown[21], M. Busso[22,23], M. Caamaño[5], L. Caballero-Ontanaya[4], F. Calviño[24], M. Calviani[2], D. Cano-Ott[9], A. Casanovas[24], F. Cerutti[2], E. Chiaveri[2,18], N. Colonna[1], G. Cortés[24], M. A. Cortés-Giraldo[3], L. Cosentino[25], S. Cristallo[22,26], L. A. Damone[1,27], P. J. Davies[18], M. Dietz[28], C. Domingo-Pardo[4], R. Dressler[12], Q. Ducasse[29], E. Dupont[10], I. Durán[5], Z. Eleme[30], B. Fernández-Domínguez[5], A. Ferrari[2], P. Finocchiaro[25], V. Furman[31], K. Göbel[6], A. Gawlik[7], S. Gilardoni[2], I. F. Gonçalves[8], E. González-Romero[9], C. Guerrero[3], F. Gunsing[10], S. Heinitz[12], J. Heyse[32], D. G. Jenkins[21], A. Junghans[11], F. Käppeler[33], Y. Kadi[2], A. Kimura[34], I. Knapova[35], M. Kokkoris[16], Y. Kopatch[31], M. Krtička[35], D. Kurtulgil[6], I. Ladarescu[4], C. Lederer-Woods[28], S. J. Lonsdale[28], D. Macina[2], A. Manna[36,37], T. Martínez[9], A. Masi[2], C. Massimi[36,37], P. Mastinu[38], M. Mastromarco[2], E. A. Maugeri[12], A. Mazzone[1,39], E. Mendoza[9], A. Mengoni[13], V. Michalopoulou[2,16], P. M. Milazzo[40], F. Mingrone[2], J. Moreno-Soto[10],A. Musumarra[25,41], A. Negret[14], F. Ogállar[15], A. Oprea[14], N. Patronis[30], A. Pavlik[42], J. Perkowski[7], L. Persanti[22,26], C. Petrone[14], E. Pirovano[29], I. Porras[15], J. Praena[15], J. M. Quesada[3], D. Ramos-Doval[17], T. Rauscher[43,44], R. Reifarth[6], D. Rochman[12], M. Sabaté-Gilarte[3,2], A. Saxena[45], P. Schillebeeckx[32], D. Schumann[12], A. Sekhar[18], S. Simone[25], A. G. Smith[18], N. V. Sosnin[18], P. Sprung[12], A. Stamatopoulos[16], J. L. Tain[4], A. Tarifeño-Saldivia[24], L. Tassan-Got[2,16,17], A. Tsinganis[2], J. Ulrich[12], S. Urlass[11,2], S. Valenta[35], G. Vannini[36,37], V. Variale[1], P. Vaz[8], A. Ventura[36], D. Vescovi[22], V. Vlachoudis[2], R. Vlastou[16], A. Wallner[46], P. J. Woods[28], T. Wright[18], P. Žugec[19] and the n_TOF Collaboration

[1]Istituto Nazionale di Fisica Nucleare, Sezione di Bari, Italy, [2]European Organization for Nuclear Research (CERN), Switzerland [3]Universidad de Sevilla, Spain, [4]Instituto de Física Corpuscular, CSIC - Universidad de Valencia, Spain, [5]University of Santiago de Compostela, Spain, [6]Goethe University Frankfurt, Germany, [7]University of Lodz, Poland, [8]Instituto Superior Técnico, Lisbon, Portugal, [9]Centro de Investigaciones Energéticas Medioambientales y Tecnológicas (CIEMAT), Spain, [10]CEA Irfu, Université Paris-Saclay, F-91191 Gif-sur-Yvette, France, [11]Helmholtz-Zentrum Dresden-Rossendorf, Germany, [12]Paul Scherrer Institut (PSI), Villingen, Switzerland, [13]Agenzia nazionale per le nuove tecnologie (ENEA), Bologna, Italy, [14]Horia Hulubei National Institute of Physics and Nuclear Engineering, Romania, [15]University of Granada, Spain, [16]National Technical University of Athens, Greece, [17]Institut de Physique Nucléaire, CNRS-IN2P3, Univ. Paris-Sud, Université Paris-Saclay, F-91406 Orsay Cedex, France, [18]University of Manchester, United Kingdom, [19]Department of Physics, Faculty of Science, University of Zagreb, Zagreb, Croatia, [20]Technische Universität Wien, Austria, [21]University of York, United Kingdom, [22]Istituto Nazionale di Fisica Nucleare, Sezione di Perugia, Italy, [23]Dipartimento di Fisica e Geologia, Università di Perugia, Italy, [24]Universitat Politècnica de Catalunya, Spain, [25]INFN Laboratori Nazionali del Sud, Catania, Italy, [26]Istituto Nazionale di Astrofisica - Osservatorio Astronomico di Teramo, Italy, [27]Dipartimento di Fisica, Università degli Studi di Bari, Italy, [28]School of Physics and Astronomy, University of Edinburgh, United Kingdom, [29]Physikalisch-Technische Bundesanstalt (PTB), Bundesallee 100, 38116 Braunschweig, Germany, [30]University of Ioannina, Greece, [31]Joint Institute for Nuclear Research (JINR), Dubna, Russia, [32]European Commission, Joint Research Centre, Geel, Retieseweg 111, B-2440 Geel, Belgium, [33]Karlsruhe Institute of Technology, Campus North, IKP, 76021 Karlsruhe, Germany, [34]Japan Atomic Energy Agency (JAEA), Tokai-mura, Japan, [35]Charles University, Prague, Czech Republic, [36]Istituto Nazionale di Fisica Nucleare, Sezione di Bologna, Italy, [37]Dipartimento di Fisica e Astronomia, Università di Bologna, Italy, [38]Istituto Nazionale di Fisica Nucleare, Sezione di Legnaro, Italy, [39]Consiglio Nazionale delle Ricerche, Bari, Italy, [40]Istituto Nazionale di Fisica Nucleare, Sezione di Trieste, Italy, [41]Dipartimento di Fisica e Astronomia, Università di Catania, Italy, [42]University of

Vienna, Faculty of Physics, Vienna, Austria, [43]Department of Physics, University of Basel, Switzerland, [44]Centre for Astrophysics Research, University of Hertfordshire, United Kingdom, [45]Bhabha Atomic Research Centre (BARC), India, [46]Australian National University, Canberra, Australia

Abstract
CERN's neutron time-of-flight facility n_TOF has produced a considerable amount of experimental data since it has become fully operational with the start of its scientific measurement programme in 2001. The innovative features of the facility, in the two experimental areas, (flight paths 20 m and 185 m), allow for an accurate determination of the neutron cross section for radioactive samples or for isotopes with small neutron capture cross section, of interest for Nuclear Astrophysics. An outline of the experimental nuclear astrophysical data activities at n_TOF will be presented.

1 Introduction

Neutron-induced cross sections play a fundamental role in Nuclear Astrophysics, being nuclear physics a key ingredient in stellar nucleosynthesis of heavy elements [1], as well as in light element production in Big Bang Nucleosynthesis [2]. In stars, neutron capture reactions are responsible for the production of the majority of elements heavier than Fe, with two processes contributing more or less equally to the overall abundance pattern: the s- and the r-process. The r-process, associated to explosive stellar scenario, is characterized by very high neutron densities, higher than 10^{20} cm^{-3}. In this process the reaction flow is driven towards the neutron rich side, since neutron captures are faster than radioactive decays. In the s-process, which involves low neutron densities and mostly stable isotopes, progressively heavier elements are produced starting from the Fe seed nuclei, by neutron captures and subsequent β-decays. An interesting case occurs when an unstable nucleus with a relatively long half-life is produced in the process, as it can either decay or undergo a further neutron capture reaction, thus generating a branching in the s-process path. The competition between neutron capture and β-decay depends on the capture cross section, on the stellar half-life of the branching isotope and, most importantly, on the stellar thermodynamic conditions, in particular the neutron density and stellar temperature. As a consequence, the study of the branching points can shed some light on the stellar environment in which the s-process takes place, provided that accurate nuclear data on capture cross section and decay half-life are available. Apart from heavy elements, neutron capture cross sections are needed to clarify one of the most intriguing and long-lasting problems in Big Bang Nucleosynthesis (BBN), i.e. the gross overestimate in BBN models of the primordial abundance of Lithium. Although neutron-induced reactions of relevance for Nuclear Astrophysics are being studied since many decades at neutron facilities worldwide, some open issues in stellar and primordial nucleosynthesis still remain to be addressed in order to reach a more comprehensive understanding of the elemental abundance distribution and of the galactic chemical evolution. To this end, an intense experimental program is undergoing at the neutron facility n_TOF (CERN) since almost two decades, in order to reduce the uncertainty on neutron capture and (n, charged particle) cross sections for some key isotopes, and ultimately improve the reliability of astrophysical models.

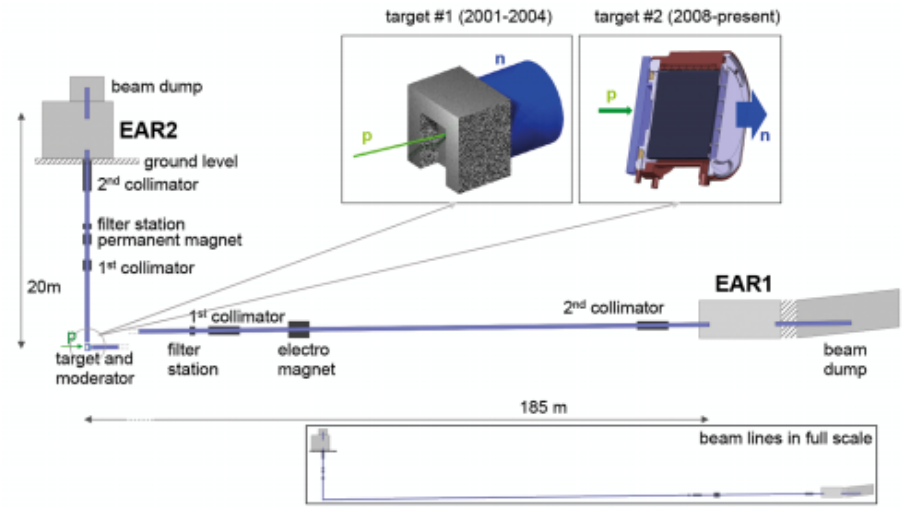

Figure 1 Sketch of the n TOF facility with its two neutron beam lines (drawn in blue) ending in the experimental areas EAR1 and EAR2. The neutron source, on the left lower part of the drawing, is a lead spallation target on which the proton beam (in green) impinges. In the direction of EAR1 a separate neutron moderator is located. The two different targets that have been used up to now are shown in the top insets (surrounding cooling water omitted, see text).

2 The n_TOF facility

The neutron time-of-flight facility n TOF was constructed following an idea proposed by Rubbia et al. [3] and has become fully operational in 2001. The facility is based on the 6 ns wide, 20 GeV pulsed proton beam from CERN's Proton Synchrotron (PS) with typically 7×10^{12} protons per pulse, impinging on a lead spallation target, yielding about 300 neutrons per incident proton. A layer of water around the spallation target moderates the initially fast neutrons down to a white spectrum of neutrons covering the full range of energies between meV and GeV. The neutron bunches are spaced by multiples of 1.2 s, a characteristic of the operation cycle of the PS. This allows measurements to be made over long times of flight, reaching to low neutron energies, as low as 10 meV, without any overlap into the next neutron cycle. The large energy range that can be measured at once is one of the key characteristics of the facility. Another important feature of n_TOF is the very high number of neutrons per proton burst, also called instantaneous neutron flux. In case of cross section measurements on radioactive samples in the neutron beam, as the case of branching points, this results in a favourable ratio between the number of signals due to neutron-induced reactions and those due to radioactive decay events contributing to the background. At present two beam lines are in operation, one in the horizontal direction and the other one on the vertical of the spallation target. A schematic drawing of the facility is shown in Fig. 1. The two insets depict the two spallation targets used up to now. The neutron flux in the two experimental areas, in units of lethargy, is shown in Figure 2.

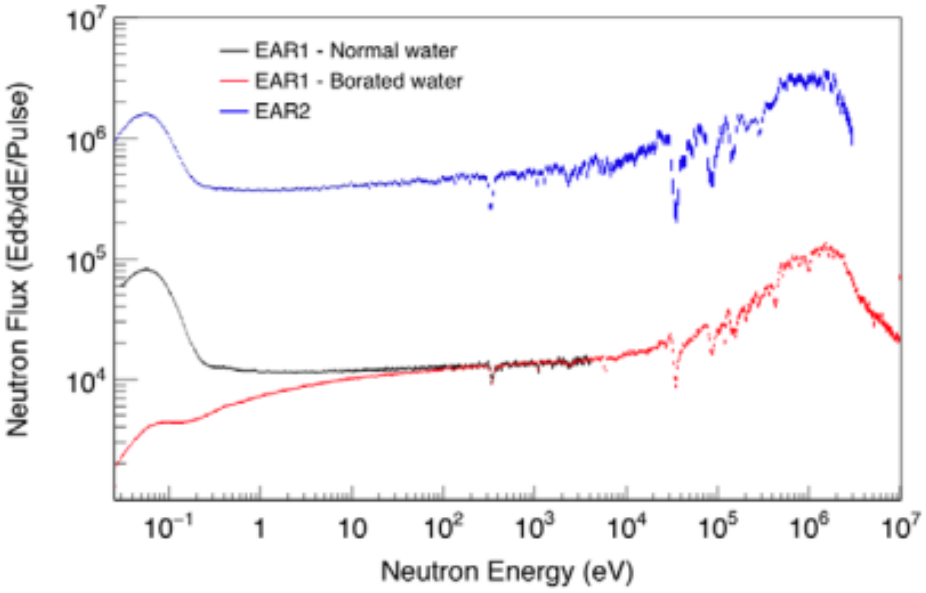

Figure 2 n_TOF neutron flux at EAR1 with normal (black) and borated (red) water as moderator compared with neutron flux at EAR2 (blue)

The strong suppression of the thermal neutron peak in EAR1 is due to the use of ^{10}B-loaded moderator, whose main purpose is to suppress the γ-background related to neutron capture in water. The shorter flight distance of about a factor 10 also results in a 10 times shorter time interval for a same energy region. Therefore, the combination of the higher flux and the shorter time interval results in an increase of the signal to noise ratio of a factor 250 (flux expressed in neutrons/ns/pulse) for radioactive samples, at cost of lower energy resolution.

3 Measurements at the n_TOF facility and their implications

The experimental program of the n_TOF Collaboration in the field of Nuclear Astrophysics has mostly regarded neutron capture cross sections. Since the start of operation, in 2001, a large number of capture reactions have been measured, in EAR1, on a variety of subjects, from neutron magic nuclei, acting as bottleneck for the reaction flow of the s-process, to branching point isotopes, from light nuclei acting as neutron poison, to end-point nuclei, and, finally, to isotopes of special interest, such as those involved in the Os/Re nuclear cosmochronometer. In all cases, a considerable reduction of the uncertainty on the neutron capture cross section has been obtained, thanks to the peculiar features of the n_TOF facilty, in particular the high instantaneous neutron intensity and the high resolution. With the construction of the second experimental area, new lines of research have become accessible, in particular on reactions leading to light charged particle emission. In the following, a few indicative results recently obtained on some of the abovementioned classes of reactions are described more in details.

3.1 Neutron capture cross section of branching point isotopes

The branching points are radioactive isotopes of relatively short half-life for which a competition exists between neutron capture and β-decay. The neutron capture cross sections of these isotopes are

poorly known, manly due to the difficulties in producing samples of sufficient mass and adequate purity, as well as due in handling and measuring samples of very high activity. For these reasons, before 2001 very few measurements existed for these isotopes, at a time-of-flight facility, despite the fact that they could provide very important information on the thermodynamical conditions of the stellar site in which s-process occurs.

In the following a description of the most recent measurements carried out in the two experimental areas is reported.

3.1.1 ^{171}Tm(n,γ), ^{147}Pm(n,γ) and ^{204}Tl(n,γ) measurements

The isotopes ^{171}Tm, ^{147}Pm and the ^{204}Tl are important s-process branching points [1]. The unstable isotope ^{171}Tm (half-life 1.92 years) represents a branching in the s-process path that is independent of stellar temperature and therefore suited to constrain explicitly the s-process neutron density in low mass AGB stars. Being Tm a rare earth element, the relative abundances of stable the isotopes are known with high accuracy.

The isotope ^{204}Tl (half life 3.8 years) decays in ^{204}Pb, which produces ^{205}Pb when undergoing neutron capture. The fact that both isotopes ^{204,205}Pb are screened from the r-process by the stable isotopes ^{204}Hg and ^{205}Tl, makes ^{204}Tl particularly interesting, indeed, its capture cross section is of crucial importance for understanding the nucleosynthesis of heavy elements in AGB stars, but it can also be used to provide chronometric information about the time span between the last s-process nucleosynthesis events that modified the composition of the proto-solar nebula and the formation of solar system solid bodies [4].

The ^{147}Pm isotope is a branching point in the mass region A=147-148, that is the Nd-Pm-Sm region. A detailed analysis of this branching is important for modeling the AGB star evolution and to put accurate constraints on the interplay between metallicity and initial stellar mass, mixing processes or hot bottom burning effects [5].

All these isotopes are radioactive and with a relatively short half-life. As a consequence of the natural activity of the sample, the measurement of the neutron capture cross section requires a very large instantaneous neutron flux. Another big challenge is to find a sufficient amount of material with adequate purity.

The samples were all produced at the Institute Laue Langevin ILL (Grenoble, France) high flux reactor, by irradiating for several weeks under the thermal neutron beam the stable progenitors with thermal neutrons.

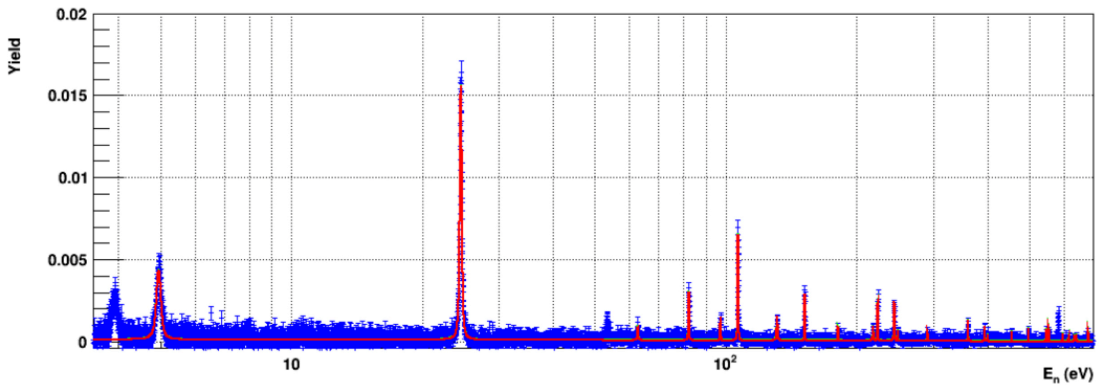

Figure 3 Experimental capture yield of the ^{171}Tm(n,γ) measurement [6]

The measurements were performed both in EAR1 and EAR2 with C_6D_6 liquid scintillator detectors. The data analysis is currently in progress [6,7], Fig 2 reports the preliminary results of the ^{171}Tm(n,γ). When the analysis will be completed it will provide for the first time experimental information on the capture cross section of these isotopes

3.2 Neutron capture cross section of neutron magic nuclei

The nuclei with a magic number of neutrons (N=50, 82 and 126), whose nuclear configuration makes them particularly stable, have very small cross sections and they act as bottlenecks in the s-process path and build up a large abundances. This nuclear feature explains the three peaks in the isotopic solar abundance distribution. A precise and accurate knowledge of the neutron capture cross section for these isotopes is fundamental for modelling the star evolution.

3.2.1 ^{88}Sr(n,γ), ^{89}Y(n,γ) and ^{140}Ce(n,γ) measurements

The Solar System abundances of Sr, Y and Zr are relatively high, forming the first peak in the isotopic abundances of the solar system. These elements are mostly synthesized by the s-process in Asymptotic Giant Branch (AGB) stars (their production in massive stars is limited to a few per cent of the total solar abundance [8]). Their abundances hence define the "ls" (light-s) s-process index routinely used to compare theoretical models to observations. The existence of this first peak is due to ^{88}Sr, ^{89}Y, and ^{90}Zr, all having a magic number of neutrons (N=50), which implies that their neutron-capture cross sections are lower than those of neighbouring nuclei. As a result, they act as bottlenecks on the neutron-capture path, constraining the value of the total neutron flux necessary to proceed to the production of heavier elements up to the second s-process peak, corresponding to the next bottleneck at Ba, La, Ce, with neutron magic number of 82 (defining the heavy-s "hs" index).

The region at N = 50 and N = 82 has been already investigated at n_TOF facility, studying the neutron capture cross section of ^{90}Zr(n,γ) [9] and ^{138}La(n,γ) [10], recently the cross section of the ^{88}Sr(n,γ), ^{89}Y(n,γ) and ^{140}Ce(n,γ) reactions has been measured. The neutron cross sections of these isotopes do not only influence the abundance of neighbouring isotopes, but the whole s-process abundance distribution.

The measurements were performed both in EAR1 with C_6D_6 liquid scintillator detectors, the new results will provide new inputs to accurately model the synthesis of heavier elements.

3.3 Measurement of (n,cp) reactions

The very high instantaneous neutron intensity in the second experimental area at n_TOF has also made feasible to measure (n, charged particle) reactions of low cross section and/or for isotopes of short-half life and/or with samples of extremely small mass. Two isotopes of high relevance in astrophysics reactions have been investigated so far at n_TOF: ^{7}Be and ^{26}Al. Neutron-induced reactions on ^{7}Be ($t_{1/2}$=53.2 days) are of interest for Big Bang Nucleosynthesis, more specifically for the so-called “Cosmological Lithium problem” [2]. Two reactions were measured on this isotope at n_TOF: the ^{7}Be(n,α)^{4}He and the ^{7}Be(n,p)^{7}Li reactions. Combined with the characteristics of the EAR2 neutron beam, the world-class expertise in sample preparation and detector development has led the n_TOF collaboration to collect high quality results on both reactions [11-12]. Other successful measurements recently performed at n_TOF regard the ^{26}Al(n,p) and ^{26}Al(n,α) reactions [13]. Precise satellite observations of this cosmic γ-ray emitter, whose relatively short lifetime (1 My) provides evidence of ongoing nucleosynthesis in our galaxy, offer the opportunity to improve calculations of the production and destruction rates of some key astrophysical reaction. However, the poor knowledge of the (n, cp) reactions on ^{26}Al, responsible for its destruction, are at present the major source of uncertainty in predicting the amount of ^{26}Al ejected into the interstellar medium by Wolf-Rayet stars in the stellar wind or following the supernova explosion. The challenge in this case is related to the availability of a sufficient amount of ^{26}Al, and to the need of identifying the emitted particles. At n_TOF, a sample of

10 μg mass, produced at Los Alamos National Laboratory (USA) [14] was irradiated under the high-flux neutron beam of the second experimental area, with the reaction product detected in a position-sensitive solid state telescope. While the analysis is still in progress, preliminary results indicate that the n_TOF measurement might provide accurate new data on the important $n+^{26}Al$ reaction cross sections.

4 Conclusions

Since 2001 the n_TOF facility at CERN has been providing valuable data on neutron capture reactions of interest for Nuclear Astrophysics, as well as for energy and medical applications. The unique features of high flux and resolution have allowed in many cases to reduce the uncertainties on cross sections of various isotopes involved in s-process nucleosynthesis. In particular, high accuracy data have been collected on radioactive nuclides around branching points, on bottleneck magic nuclei, or on isotopes available only in small amount, of the order of a few milligrams. The construction of a second experimental area at a shorter flight path has opened the way to even more challenging measurements of (n,γ) and (n,charged particle) reaction on isotopes of short half-life, low cross section and limited amounts (possibly down to a few micrograms). All this is expected to lead in the near future to exciting new results and significant advancements towards the refinement of models of stellar nucleosynthesis.

References

[1] F. Käppeler et al., Rev. Mod. Phys 83(2011),157
[2] R.H. Cyburt et al., Phys Rev. D. 69(2004), 123519
[3] C. Rubbia et al., Tech. Rep. CERN/LHC/98-02 CERN(1998)
[4] K. Yokoi, K. Takahashi and M. Amould, Astronomy and Astropysics 145(1985) 339
[5] F. Herwig, Anny. Rev. Astron. Astrophys. 43, (2005) 435
[6] C. Guerrero et al., Jap. Phys. Soc. Conference proceeding, 14(2016), 010903
[7] C. Guerrero et al., Eur. Phys. J. web of conference, 146(2017), 01007
[8] C. Travaglio et al., Ap. J. **601**, (2004), 864
[9] G.Tagliente *et al.*, Phys. Rev. C**77**, (2008), 035802
[10] R. Terlizzi et al., Phys. Rev. C 75, (2007), 035807
[11] M. Barbagallo et al., Phys. Lett. 117(2016), 0152701
[12] L.A. Damone et al., Phys. Lett. 117(2018), 0152701
[13] C. Ledere et al., CERN-INTC-20154-0066INTC-P-406
[14] C. Ingelbrecht et al., Nucl. Instr. Meth. A 480(2002), 114

(n,cp) reactions study at the n_TOF facility at CERN: results for the Cosmological Lithium problem.

M. Barbagallo[1,2], O. Aberle[1], V. Alcayne[3], J. Andrzejewski[4], L. Audouin[5], V. Bécares[3], V. Babiano-Suarez[6], M. Bacak[1,7,8], Th. Benedikt[9], S. Bennett[10], E. Berthoumieux[8], J. Billowes[10], D. Bosnar[11], A. Brown[12], M. Busso[2,13,14], M. Caamaño[15], L. Caballero-Ontanaya[6], F. Calviño[16], M. Calviani[1], D. Cano-Ott[3], A. Casanovas[16], F. Cerutti[1], E. Chiaveri[1,10], N. Colonna[2], G. Cortés[16], M. A. Cortés-Giraldo[17], L. Cosentino[18], S. Cristallo[2,13,19], L. A. Damone[2,20], P. J. Davies[10], M. Dietz[21], C. Domingo-Pardo[6], R. Dressler[22], Q. Ducasse[23], E. Dupont[8], I. Durán[15], Z. Eleme[24], B. Fernández-Domínguez[15], A. Ferrari[1], P. Finocchiaro[18], V. Furman[25], K. Göbel[9], A. Gawlik[4], S. Gilardoni[1], I. F. Gonçalves[26], E. González-Romero[3], C. Guerrero[17], F. Gunsing[8], S. Heinitz[22], J. Heyse[27], D. G. Jenkins[12], A. Junghans[28], F. Käppeler[29], Y. Kadi[1], A. Kimura[30], I. Knapova[31], M. Kokkoris[32], Y. Kopatch[25], M. Krtička[31], D. Kurtulgil[9], I. Ladarescu[6], C. Lederer-Woods[21], S. J. Lonsdale[21], D. Macina[1], A. Manna[33,34], T. Martínez[3], A. Masi[1], C. Massimi[33,34], P. Mastinu[35], M. Mastromarco[1], E. A. Maugeri[22], A. Mazzone[2,36], E. Mendoza[3], A. Mengoni[37], V. Michalopoulou[1,32], P. M. Milazzo[38], F. Mingrone[1], J. Moreno-Soto[8], A. Musumarra[18,39], A. Negret[40], F. Ogállar[41], A. Oprea[40], N. Patronis[24], A. Pavlik[42], J. Perkowski[4], L. Persanti[2,13,19], C. Petrone[40], E. Pirovano[23], I. Porras[41], J. Praena[41], J. M. Quesada[17], D. Ramos-Doval[5], T. Rauscher[43,44], R. Reifarth[9], D. Rochman[22], M. Sabaté-Gilarte[17,1], A. Saxena[45], P. Schillebeeckx[27], D. Schumann[22], A. Sekhar[10], A. G. Smith[10] , N. V. Sosnin[10], P. Sprung[22], A. Stamatopoulos[32], G. Tagliente[2], J. L. Tain[6], A. Tarifeño-Saldivia[16], L. Tassan-Got[1,32,5], A. Tsinganis[1], J. Ulrich[22], S. Urlass[28,1], S. Valenta[31], G. Vannini[33,34], V. Variale[2], P. Vaz[26], A. Ventura[33], D. Vescovi[2,13], V. Vlachoudis[1], R. Vlastou[32], A. Wallner[46], P. J. Woods[21], T. Wright[10], P. Žugec[11] and the n_TOF Collaboration

[1]European Organization for Nuclear Research (CERN), Switzerland
[2]Istituto Nazionale di Fisica Nucleare, Sezione di Bari, Italy
[3]Centro de Investigaciones Energéticas Medioambientales y Tecnológicas (CIEMAT), Spain
[4]University of Lodz, Poland
[5]Institut de Physique Nucléaire, CNRS-IN2P3, Univ. Paris-Sud, Université Paris-Saclay, F-91406 Orsay Cedex, France
[6]Instituto de Física Corpuscular, CSIC - Universidad de Valencia, Spain
[7]Technische Universität Wien, Austria
[8]CEA Irfu, Université Paris-Saclay, F-91191 Gif-sur-Yvette, France
[9]Goethe University Frankfurt, Germany
[10]University of Manchester, United Kingdom
[11]Department of Physics, Faculty of Science, University of Zagreb, Zagreb, Croatia
[12]University of York, United Kingdom
[13]Istituto Nazionale di Fisica Nucleare, Sezione di Perugia, Italy
[14]Dipartimento di Fisica e Geologia, Università di Perugia, Italy
[15]University of Santiago de Compostela, Spain
[16]Universitat Politècnica de Catalunya, Spain
[17]Universidad de Sevilla, Spain
[18]INFN Laboratori Nazionali del Sud, Catania, Italy
[19]Istituto Nazionale di Astrofisica - Osservatorio Astronomico di Teramo, Italy
[20]Dipartimento di Fisica, Università degli Studi di Bari, Italy
[21]School of Physics and Astronomy, University of Edinburgh, United Kingdom
[22]Paul Scherrer Institut (PSI), Villingen, Switzerland
[23]Physikalisch-Technische Bundesanstalt (PTB), Bundesallee 100, 38116 Braunschweig, Germany
[24]University of Ioannina, Greece
[25]Joint Institute for Nuclear Research (JINR), Dubna, Russia
[26]Instituto Superior Técnico, Lisbon, Portugal

[27]European Commission, Joint Research Centre, Geel, Retieseweg 111, B-2440 Geel, Belgium
[28]Helmholtz-Zentrum Dresden-Rossendorf, Germany
[29]Karlsruhe Institute of Technology, Campus North, IKP, 76021 Karlsruhe, Germany
[30]Japan Atomic Energy Agency (JAEA), Tokai-mura, Japan
[31]Charles University, Prague, Czech Republic
[32]National Technical University of Athens, Greece
[33]Istituto Nazionale di Fisica Nucleare, Sezione di Bologna, Italy
[34]Dipartimento di Fisica e Astronomia, Università di Bologna, Italy
[35]Istituto Nazionale di Fisica Nucleare, Sezione di Legnaro, Italy
[36]Consiglio Nazionale delle Ricerche, Bari, Italy
[37]Agenzia nazionale per le nuove tecnologie (ENEA), Bologna, Italy
[38]Istituto Nazionale di Fisica Nucleare, Sezione di Trieste, Italy
[39]Dipartimento di Fisica e Astronomia, Università di Catania, Italy
[40]Horia Hulubei National Institute of Physics and Nuclear Engineering, Romania
[41]University of Granada, Spain
[42]University of Vienna, Faculty of Physics, Vienna, Austria
[43]Department of Physics, University of Basel, Switzerland
[44]Centre for Astrophysics Research, University of Hertfordshire, United Kingdom
[45]Bhabha Atomic Research Centre (BARC), India
[46]Australian National University, Canberra, Australia

Abstract
The Big Bang Nucleosynthesis describes the production of the lightest nuclides from deuterium to Li at the early stages of the Universe. While a general good agreement is found for most of the isotopes involved in the synthesis, a serious discrepancy between the predicted abundance of ^{7}Li and the related experimental observations is still present. This discrepancy has been referred since several decades as Cosmological Lithium Problem. In one last attempt to find nuclear solutions to this longstanding conundrum, the ^{7}Be(n,α)^{4}He and ^{7}Be(n,p)^{7}Li reactions, that affect predominantly the production of ^{7}Li via the destruction of his parent nucleus ^{7}Be, have been studied. Here we present the ^{7}Be(n,α)^{4}He and ^{7}Be(n,p)^{7}Li reaction cross-section measurements performed at the high-resolution n_TOF facility using the time-of-flight technique and high purity samples. The result of the experiments definitely rules out neutron induced reactions as a solution to the puzzle, thus indicating that explanations have to be sought out in other Physics scenarios.

1 Cosmological Lithium Problem and Nuclear Physics

Big Bang Nucleosynthesis (BBN) is one of the cornerstones for Big Bang Theory and at the same time it represents one of the few reliable links to the first seconds of the Universe having consequences directly observable nowadays. BBN theory yields precise predictions for the abundancies of primeval light elements and since its first formulation and following developments [1-2] it has been based on the firmly established physics background of Standard Model. While the predictions of BBN for D and ^{4}He are in agreement with the primordial abundancies inferred by experimental observations at high red-shift or in metal poor stars [3], a serious discrepancy is observed for ^{7}Li, where a mismatch of a factor from two to three is observed between predictions. This discrepancy is now referred to as the Cosmological Lithium Problem (CLiP). In order to solve this longstanding puzzle, a plethora of

solutions has been put forward, ranging from solutions in the fields of Astrophysics, Nuclear Physics, non Standard Cosmology and new physics beyond Standard Model.

In standard BBN, the nuclear reactions chain begins when the temperature in the Universe has dropped down below 1 MeV allowing to reach the equilibrium between protons and neutrons. Subsequently, with temperature continuously decreasing, 16 well established main reactions drive the formation of stable light nuclei up to mass number A=8. In this scenario, 97% of ^{7}Li is produced via electron capture beta decay of primordial ^{7}Be ($t_{1/2}$=52.3d), consequently the abundance of ^{7}Li is intrinsically determined by the production and destruction of his father nucleus ^{7}Be. As a matter of fact a nuclear solution to the Cosmological Lithium Problem is related to this isotope. ^{7}Be is produced essentially via ^{3}He(α,γ)^{7}Be reaction that has been extensively studied and is accurately known [4-5], leaving no room for possible modifications in thermonuclear rate for ^{7}Be production. On the other hand, while charged particle induced reactions responsible for ^{7}Be destruction have been measured and the related significant contributions have been ruled out [6-9], data on reactions induced by neutrons have been so far scarce and incomplete, affecting the reliability of BBN calculations at the energy window of interest for the CLiP, i.e. 20-120 keV (or equivalently 0.23 T_9 - 1.4 T_9).

According to BBN theory ^{7}Be is destroyed via (n,α) and (n,p) channels, accounting respectively for 2.5% and 97% to its destruction rate. The lack of experimental data for these reactions is essentially due to the intrinsic difficulty of the measurement, related to the extremely high specific activity of ^{7}Be (13 GBq/μg). Concerning ^{7}Be(n,α)^{4}He reaction, only one direct measurement performed at thermal energy (0.025 eV) was available in literature [10]. Therefore in BBN calculations data have been extrapolated to the relevant energy window assuming typically an uncertainty of a factor 10. On the other hand, previous data for ^{7}Be(n,p)^{7}Li reaction cross-section extend on a wider range, from thermal energy up to 13.5 keV [11], leaving nevertheless the BBN energy window uncovered.

2 n_TOF program on Cosmological Lithium Problem

In order to address this lack of data, the time-of-flight measurements of the ^{7}Be(n,α)^{4}He and ^{7}Be(n,p)^{7}Li reaction cross-sections have been performed at the newly built second experimental area (EAR2) of the n_TOF facility at CERN. The main features of the n_TOF neutron beam at the EAR2 measurement station are the wide neutron energy spectrum, spanning from 2 meV to 100 MeV, the high intensity of $>10^{7}$ neutrons/pulse at the sample position, the low repetition rate, of less than 0.8 Hz, and the good energy resolution ($10^{-3} \leq \Delta E/E \leq 10^{-2}$ in the energy range of interest for these measurements) [12]. All these features make EAR2 ideal for measurements on isotopes only available in very small amounts, with short half-lives, or both, as is the case for ^{7}Be.

2.1 The ^{7}Be(n,α)^{4}He cross-section measurement and its implication for CLiP

The measurement of ^{7}Be(n,α) ^{4}He cross-section has been performed by means of a detection system capable of detecting in coincidence the two alpha particles emitted back-to-back in the reaction, whose Q-value is about 19 MeV. The detection system used consisted of two sandwiches of 140 μm thickness and 3x3 cm^2 active area silicon detectors placed directly in the neutron beam. Each sandwich of silicons hosted in the middle part a sample with the ^{7}Be deposit, providing a high coverage of solid angle [14]. The samples were produced by means of two different techniques, namely molecular plating and vaporization, at the Paul Scherrer Institut (PSI) [13]: starting from a solution of $Be(NO_3)_2$, a total amount of ~40 GBq of ^{7}Be was deposited on two thin backings, respectively 5 μm aluminum and 0.6 μm stretched polyethilene foil. Such thin backings permitted the high-energy alpha particles emitted in the reaction to reach the active area. The combination of the coincidence and time-of-flight techniques allowed to distinguish clearly the α-particles from the background due to the high activity of the samples

and to competing reactions, as shown in Fig. 1 where coincidences matrices for correlated detectors (i.e. detectors hosting the ^{7}Be samples) and uncorrelated ones are reported.

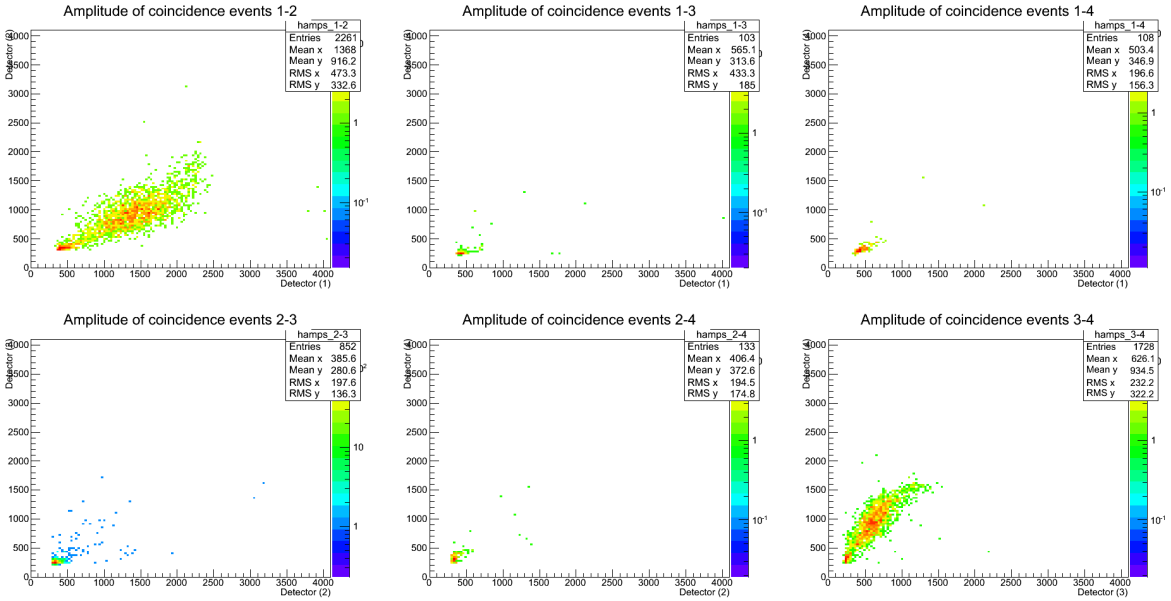

Fig. 1: Scatter plot for signal amplitudes in all possible pairs of detectors of the stack. Top left and bottom right plot refer to pairs hosting the ^{7}Be sample, while the remaining panels show coincidence events for uncorrelated pairs of detectors

The cross-section of the ^{7}Be(n,α)^{4}He reaction has been then determined in the energy range from 10 meV to 10 keV and while at thermal energy it has been found in agreement with the previous measurement, it has indicated that at higher energy a substantial revision is needed. The n_TOF results combined with ENDF/B-VII.1 evaluation lead to a change of the ^{7}Be destruction rate due do this reaction, hinting nevertheless to a minor role of this channel in BBN and leaving therefore Cosmological Lithium Problem unsolved [15]. At a later time a second independent measurement performed at the Osaka Research Center for Nuclear Physics (RCNP) confirmed this conclusion, finally ruling out the possibility that the so far poorly known ^{7}Be(n,α)^{4}He channel could account for a significant ^{7}Be depletion [16].

2.2 The ^{7}Be(n,p)^{7}Li cross-section measurement and its implication for CLiP

The ^{7}Be(n,p)^{7}Li reaction is featured by a relatively small Q-value, equal to 1.64 MeV, with low energy protons emitted with about 1.02 MeV and 1.40 MeV, according to the state in which the residual ^{7}Li nucleus is left. Therefore, together with the availability of a sufficiently intense neutron beam, also strong constraints on the level of purity of the sample are set. The combination of the measurement capabilities on the n_TOF and ISOLDE [17] facilities at CERN allowed to perform the accurate measurement of the ^{7}Be(n,p)^{7}Li reaction cross-section from 0.025 eV to 325 keV neutron energy, hence fully covering for the first time in a direct measurement the energy range of interest for Big Bang Nucleosynthesis. In particular, a high purity ^{7}Be sample was produced by ISOL technique at ISOLDE and shortly after exposed to the pulsed wide spectrum neutron beam at the n_TOF facility. The ^{7}Be target preparation was carried out in two steps: 200 GBq of ^{7}Be were extracted from the cooling water of the SINQ spallation source at the Paul Scherrer Institute (PSI) [18] and deposited onto a suitable support in the form of a ^{7}Be $(NO_3)_2$ colloid [19]. Afterward the solution was used to produce at ISOLDE

a ^{7}Be beam that was implanted on a thin aluminium backing, resulting in a 1.1 GBq activity sample with a purity of about 99% (the remaining 1% was due to ^{7}Li contamination) [18].

At n_TOF the measurement of the ^{7}Be(n,p)^{7}Li cross-section relied on the detection and identification by means of a silicon telescope of the protons emitted in the reaction. The telescope consisted of two silicon strip detectors of 300 μm and 20 μm thickness and 5x5 cm^{2} wide active area divided in 16+16 strips. Thanks to the high purity of the sample and the telescope technique, in combination with the time-of-flight measurement at the high intensity pulsed neutron beam, the contributions of any source of background associated to the activity of the sample or to reactions induced on the sample backing could be heavily suppressed [19]. The n_TOF results of this measurement show that ^{7}Be(n,p)^{7}Li cross-section is higher than previously recognized at low energy, by ~40%, but consistent with current evaluations above 50 keV [20].

This new result, in combination with the n_TOF result on the ^{7}Be(n,α)^{4}He cross-section, has been used to calculate new BBN reaction rates and it has been found that it leads to, at most, a 10% decrease in the lithium production relative to previous estimations. Such a change does not have a significant impact on the Cosmological Lithium Problem, left therefore still unsolved.

3 Conclusions

The Cosmological Lithium Problem is one of the most important unresolved problems in Nuclear Astrophysics. The large discrepancy between the abundance of primordial ^{7}Li predicted by the standard theory of Big Bang Nucleosynthesis and the value deduced from the observation of galactic halo dwarf stars. A few neutron-induced reactions are important in the processes leading to the formation of the first nuclides at the very beginning of our universe, amongst these, the (n,p) and (n,α) reactions on ^{7}Be play a key role in the determination of the abundance of primordial lithium. Taking advantage of the new high intensity flux neutron beam line of the n_TOF facility at CERN the measurements of the ^{7}Be(n,α)^{4}He and ^{7}Be(n,p)^{7}Li reaction cross-sections have been performed, in order to provide for the first time data in the neutron energy range of interest for Nuclear Astrophysics. The two n_TOF measurements finally rule out neutron-induced reactions, and possibly nuclear physics, as a potential explanation of the CLiP, leaving all alternative physics and astronomical scenarios still open.

References

[1] Alpher R. A., Bethe H. A. and Gamow G., 1948, Phys. Rev., 73, 803.

[2] R.V. Wagoner et al., Astrophys. J. 148, 3 (1967).

[3] B. D. Fields, *Ann.* Rev. *Nuc.* Par. *Sci*, 61, 47-68 (2011)

[4] F. Confortola et al., Phys Rev. C 75 (2007) 065803

[5] L. Canton and L.G. Levchuk, Nucl. Phys. A 808 (2008) 192

[6] C. Angulo et al., Astroph. J. 630, L105 (2005)

[7] P. O. Malley et al., Phys Rev. C 84, (2011) 042801

[8] O.S. Kirsebom and B. Davis, Phys. Rev. C 84, (2011) 058801

[9] C. Broggini, L. Canton, G. Fiorentini and F.L. Vilante, J. Cosmol. Astrop. 06 (2012) 30
[10] P. Bassi et al., Il Nuovo Cimento XXVIII, 1049 (1963)
[11] P. E. Koehler et al., Phys Rev. C 37, (1988) 917
[12] M. Sabate-Gilarte et al., Eur. Phys. J. A 53, 210 (2017)
[13] E. Maugeri et al., Journal of Instrumentation, 12 P02016 (2017).
[14] L. Cosentino et al., Nucl. Instrum. Methods Phys. Res., Sect. A 830, 197 (2016)
[15] M. Barbagallo et al., Phys. Rev. Lett. 117(2016), 0152701
[16] T. Kawabata et al., Phys Rev. Lett. 118 (2017), 052701
[17] M. J. G. Borge and B. Jonson, J. Phys. G 44, 044011 (2017).
[18] E. Maugeri et al., Nucl. Instrum. Methods Phys. Res., Sect. A 889, 138 (2018)
[19] M. Barbagallo et al., Nucl. Instrum. Methods Phys. Res., Sect. A 887, 27 (2018)
[20] L. Damone et al., Phys. Rev. Lett. 121 (2018), 042701

Nuclear astrophysics at Gran Sasso Laboratory: the LUNA experiment

Francesca Cavanna for the LUNA collaboration
Istituto Nazionale di Fisica Nucleare sezione di Genova, Genoa, Italy

Abstract
Nuclear processes are responsible for energy generation that makes stars shine, and for the synthesis of the elements in stars and also play a decisive role in explaining the chemical composition of the interstellar medium. Thermonuclear fusion reactions convert protons into heavier elements from He to Fe. Deep underground in the Gran Sasso Laboratory the key reactions of the proton-proton chain, the carbon-nitrogen-oxygen cycle and the neon sodium cycle have been studied down to the energies of astrophysical interest. The latest results are reviewed, together with future developments of underground nuclear astrophysics.

1 Introduction

Thermonuclear reactions most likely proceed at energies below the Coulomb barrier height. Therefore the cross-sections are extremely small and very difficult to be measured. In the laboratory, the rate of the reactions, characterized by a typical energy release of a few MeV, is very low and one should adopt all the possible techniques to achieve the point.

A possible solution to reach the low energies of interest for astrophysics is to install an accelerator facility in a laboratory deep underground reducing the natural and cosmic background. The Laboratory for Underground Nuclear Astrophysics (LUNA) is located at Gran Sasso National Laboratories, Italy, where the 1400 meters of rocks dominating the laboratory guarantee a reduction of six orders of magnitude in the cosmic muon flux and a reduction of three orders of magnitude in the neutron flux.

Several experimental campaigns have been accomplished in the past; in particular reactions of hydrogen burning [1] e.g. ^{22}Ne(p,γ)^{23}Na [2–5], ^{17}O(p,α)^{14}N [6] and ^{23}Na(p,γ)^{24}Mg [7] were deeply studied and outstanding results were achieved. Also few reactions of Big Bang Nucleosynthesis were measured as the ^{2}H(α,γ)^{6}Li [8] and ^{2}H(p,γ)^{3}He reactions. This paper focuses on ^{17}O(p,α)^{14}N and ^{2}H(p,γ)^{3}He cross section measurements and on the future program.

2 LUNA experimental setup

The first accelerator installed underground was a compact 50 kV machine (now dismissed) and, in a second phase, a commercial 400 kV accelerator. Both machines had/have high beam current, long term stability and precise control of the beam energy. The first feature maximizes the reaction rate, the second is demanded by the long time typically needed for a cross-section measurement, and the third is important because of the exponential energy dependence of the cross-section.

The 400 kV accelerator (LUNA400), presently in operation, is an electrostatic accelerator produced by High Voltage Engineering Europe. It is embedded in a 2 m^3 steel tank filled with a gas mixture of N_2 (75%) and CO_2 (25%) at a total pressure of 20 bar. The High Voltage is provided by an Inline-Cockcroft-Walton power supply; it is stabilized by a RC-filter at the HV power supply output and by an active feedback loop based on a chain of resistors. This is a key feature, as the cross sections to be measured depend exponentially on the beam energy. Using a proton beam, it has been shown that the long-term energy stability remains within 2 eV [9].

The beam is provided by a radio frequency ion source from the excitation of a gas that forms an ion plasma with charge e+ confined by an axial magnetic field. The source is mounted directly on the

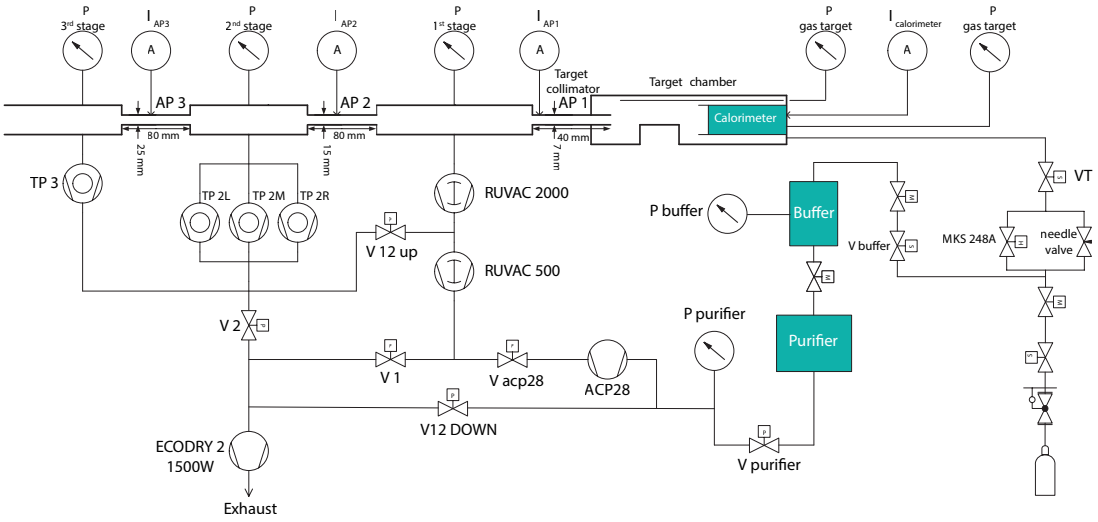

Fig. 1: Schematic lay-out of the LUNA windowless gas target setup.

accelerator tube and the ions are extracted by a voltage applied to an electrode inside the tube itself. The source is able to produce ion beams up to 1 mA intensity for hydrogen at 75% purity and up to 0.5 mA for helium. The machine has been calibrated in energy, through the non-resonant radiative capture reaction ^{12}C(p,γ)^{13}N [9]. The calibration has been checked several times by the well known resonances of (p,γ) captures on ^{23}Na, ^{25}Mg and ^{26}Mg. The uncertainty on the beam energy is equal to 100 eV statistical and 300 eV systematic. The energy spread of the accelerator is smaller than 0.1 keV, and the long term energy stability is better than 5 eV/h.

The ions can be sent into one of two beam lines, thereby allowing the installation of two different target setups, i.e. solid and gas target. In the first case, the proton beam is guided and focused to the target station using an highly stable analysing magnet and a copper pipe extending to 2 mm from the target. The pipe is cooled to liquid nitrogen temperature and serves as a cold trap to prevent carbon buildup.

Instead, in case of the windowless gas target the setup is more complex and includes, besides the several magnets, vacuum pumps, necessary to maintain a pressure of 10^{-7} mbar inside the accelerating tube (Fig. 1). Before reaching the gas target, the beam passes through: a Faraday cup, used to monitor the proton beam current, a safety gate valve which automatically closes when the pressure, on the gas target side, exceeds 10^{-4} mbar and three water-cooled apertures (Fig. 1) with decreasing diameter and hence increasing impedance which collimate the beam into the target chamber. Typical pressures in the second and third pumping stages are in the 10^{-6} - 10^{-7} mbar range, with the gas pressure maintained at 1 mbar in the target chamber. When isotopically enriched or rare gases are used, the exhaust from the Roots pumps cannot be discarded but must instead be recycled. The gas coming out from the first and the second stages can be compressed by a dry forepump, sent to a purifier which removes oxygen and nitrogen contaminations and finally stocked in a buffer.

3 The ^{17}O(p,α)^{14}N reaction

The $^{17}O(p,\alpha)^{14}N$ reaction (Q_{val}=1.2 MeV) plays a key role in several astrophysical scenarios, in particular in AGB stars [10–12]. Models predict that massive AGB stars should produce significant amounts of cosmic dust, and yet no pre-solar grain appears to match the HBB signature expected from these stars [13]. The most obvious candidates, Group II grains, have ^{17}O/^{16}O ratios that are a factor of two lower than expected. For this reason is crucial the measurement of the $^{17}O(p,\alpha)^{14}N$ cross section.

At energies of astrophysical interest its reaction rate is dominated [15] by a narrow and isolated resonance at E_p=70 keV. This resonance has been studied several times in the past, using both direct and

indirect methods, as summarised in ref. [16]. However, the picture painted in the literature is still not completely satisfying. The uncertainty in the resonance strength is not negligible (≈20%). Furthermore, published strength values obtained with direct measurements have all been retracted or reanalysed [16]. An experimental campaign aimed at measuring the E_p=70 keV resonance in $^{17}O(p,\alpha)^{14}N$ was recently completed at the underground LUNA accelerator by a thick-target setup. Solid Ta_2O_5 targets, 95% enriched in ^{17}O and roughly 5 keV thick for 200 keV protons, were used [17]. Protons were accelerated at a typical beam intensity of 100 μA and alpha particles produced by the reaction at E_{alpha}= 1 MeV were detected with an array of eight silicon detectors mounted in an hemi-spherical configuration. A small lead shielding was mounted around the setup to further suppress the natural background. Aluminised mylar foils, nominally 2.4 μm thick, were mounted in front of each detector to shield the intense flux of elastically scattered protons [18]. As a result, the energy of the alpha particle at the silicon detector was around 250 keV, making the measurement extremely challenging. Nevertheless, the signal at the E_p=70 keV resonance was detected at a five sigma confidence level and tuned out to be about 3 times higher than the previous literature value [19]. This achievement has strong consequences in a number of astrophysical scenarios [14] and gives ligth to the long-standing issue in the identification of the over mentioned pre-solar grains [13] produced in massive AGB stars.

4 The ^{2}H(p,γ)^{3}He reaction

Nuclear physics plays a role in the very early life of the Universe: between 3 and 20 minutes after the Big Bang, a few light isotopes of H, He, Li and Be are formed through a net of reactions. This is known as Big Bang Nucleosynthesis and its importance is not just limited to the formation of the primordial material giving origin, about 10^9 y later, to the first pro-stars. Actually, the rate of the BBN reactions and the final abundances of the involved isotopes are strictly related to fundamental quantities like the barion density of the Universe. The barion to photon density is the sole free parameter to describe, according the Lambda Cold Dark Matter model (ΛCDM [21]), the Universe evolution. From the Cosmic Microwave background measured by the PLANK satellite [20] and the cross section of the BBN reactions, the abundances of the primordial isotopes can be calculated and compared with astronomical observations. This open the possibility to infer, from the accurate determination of the nuclear cross section, information widely beyond the limit of nuclear astrophysics. Among the relevant process for BBN nucleosynthesis there's the ^{2}H(p,γ)^{3}He currently under study at LUNA.

The primordial abundance of deuterium, $(D:H)_{obs}$, is presently known with good accuracy, $(D:H)_{obs}$= (2.527 $\pm$ 0.030) 10^{-5} [22], while the corresponding $(D:H)_{BBN}$ obtained from the BBN calculations, $(D:H)_{BBN}$ = (2.58 $\pm$ 0.04) 10^{-5} [23], is affected by the insufficient knowledge of S_{12} in the relevant energy interval. Only a single dataset of S_{12} is available in the relevant energy range [24] and, according to the Authors, it is affected by a systematic error of 9%. The situation is even worst when considering a 20% discrepancy of that data with the theoretical previsions [25]. For all these reasons an experimental effort to measure the cross section with 3-5% accuracy is needed.
The ^{2}H(p,γ)^{3}He experiment at LUNA consists of two main phases characterized by different setups. The former is a windowless gas target filled with deuterium surrounded by a 4π BGO detector [26]. The data taking as well as the analysis of this phase have been concluded and the results will be published as soon as also the second phase will be over. The set up of this latter phase consists of a 137% HPGe detector in close geometry with the interaction chamber. With this setup the angular distribution can be inferred by exploiting the high energy resolution of the detector and the Doppler effect responsible for the broad energy distribution of the detected gamma rays coming from different directions inside the extended gas target. The ^{2}H(p,γ)^{3}He photons have an energy of about 5.5 MeV, far away from the energy of the commonly used radioactive sources. Thus, for determining the setup efficiency a different technique based on the well-known resonant reactions ^{14}N(p,γ)^{15}O and on ^{60}Co radioactive decay has been used. In order to reduce the systematic error due to the summing correction, the set-up efficiency

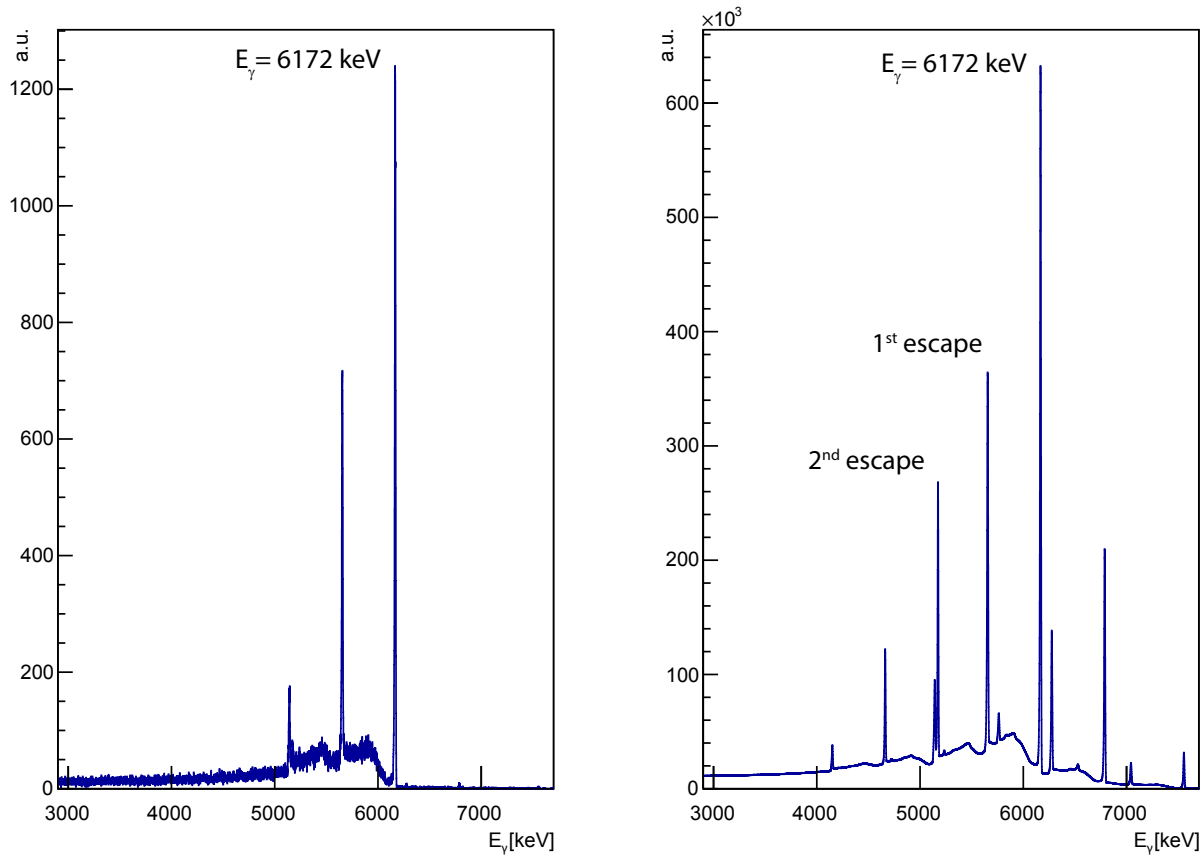

Fig. 2: ^{14}N(p,γ)^{15}O resonance spectra: left the one acquired in coincidence configuration, right the one acquired in inclusive configuration.

has been measured exploiting the coincidence between two γ-rays emitted in cascade (from source as well as from reaction) and detected by two different germanium detectors, the main detector (Ge1) and a second one used as the acquisition trigger (Ge2). Whenever Ge2 detects an event 1, it enables Ge1 that can thus detect photon 2 emitted in cascade: the ratio of the observed photons with respect to the number of triggers provides the Ge1 efficiency. In case of ^{60}Co, for each radioactive decay process, two photons, 1 = 1.17 MeV and 2 = 1.33 MeV, are produced. In the case of the resonant capture, several decay branches are able to provide two photons in cascade of energies up to 6.7 MeV, even higher than the ^{2}H(p,γ)^{3}He reaction. This method allows fixing precisely the detector energy response (fig. 2).
To measure the cross section an energy scan in the energy range of interest (30 keV $<$ E$_{cm}$ $<$ 300keV) with 30-50 keV steps was done; two runs were performed for each energy: one with deuterium gas inside the scattering chamber, the other with ^{4}He in order to evaluate the beam induced background contribution and the eventual deuterium implantation. The data taking has been completed, the analysis is ongoing.

5 The future of LUNA: LUNA MV

While the most relevant nuclear processes involved in the H-burning phase are now known with a quite satisfactory level of accuracy (missing tiles and/or refinements in the above discussed mosaic will be likely fixed at the existing facilities in the next fore coming years), the picture for the successive evolutionary phases is still far to be completed. When the hydrogen in the star core has been spent, the

gravitational contraction starts again and the temperature in the core reaches values high enough to allow fusion reactions between the hydrogen ashes, i.e. the He nuclei. In such conditions, the 3-alpha process is the mechanism to fill the mass gap between Helium and Carbon. This way the stellar core gets populated in He and ^{12}C which, in the following phases, are involved in key reactions as the ^{12}C(α,γ)^{16}O and the ^{12}C+^{12}C. The first process competes with the 3-alpha during the He-burning step while the fusion of two ^{12}C nuclei is possible only in stars with a mass great enough to produce core temperatures greater than hundreds of million Kelvin (typically more than 7 Solar masses). The astrophysical energies for such processes range, according to the peculiar stellar environment, from hundreds to a few thousands of keV and their study at an accelerator facility needs intense ion beams in the MeV range.

The LUNA MV project has conceived to approach these particular sub-frames of the stellar evolution mosaic: it is based on a new 3.5 MV single-ended accelerator to be installed under the Gran Sasso mountain. The accelerator will be devoted to the study of those key reactions of helium and carbon burning that determine and shape both the evolution of massive stars towards their final fate and the nucleosynthesis of most of the elements in the Universe. In particular, the ^{12}C(α,γ)^{16}O and ^{12}C+^{12}C reactions are the most ambitious goals of the project [27, 28]. The first reaction competes with the triple-alpha during the He burning. Both release a comparable amount of energy (about 7 MeV), but the He consumption of the ^{12}C+alpha is only 1/3 of that of the 3-alpha. Therefore, a change of the ^{12}C+alpha reaction directly affects the He burning lifetime. Furthermore, it determines the C:O ratio left at the end of the He burning. This is a fundamental quantity affecting, for instance, white dwarf cooling timescale and the outcomes of both type Ia and core-collapse supernovae. The ^{12}C+^{12}C reaction is the trigger of C burning. The temperature at which C burning takes place depends on its rate: the larger the rate, the lower the C-burning temperature. Since the temperature controls the nucleosynthesis processes, reliable estimations of all the yields produced by C burning, for example the weak component of the s process which produce the elements between Fe and Sr, require the precise knowledge of the ^{12}C+^{12}C rate. The ^{12}C+^{12}C rate also determines the lower stellar mass limit for C ignition. This limit separates the progenitors of white dwarfs, nova and type Ia supernovae, from those of core-collapse supernovae, neutron stars, and stellar mass black holes.

In an underground environment, there is a clear advantage for experiments looking at neutron emission too. For instance, the neutron flux at LNGS is about 3 orders of magnitude lower than at a surface laboratory, just because of the reduced flux of neutrons from cosmic-ray muons. Background neutrons in LNGS and in other underground laboratories are therefore originated from (α,n) reactions on light elements (A $\pm$ 12–28). The alpha particles are emitted by radioactive decays in the rock, mainly those belonging to the ^{238}U family. As a consequence, the list of the outstanding reactions which can be addressed with MV accelerator includes the "neutron sources" as pointed out for the first time in the famous BBFH article in 1957 [29]. Neutron-captures (slow or rapid, i.e., the s or r process, respectively) were early recognized as the most important mechanism to produce the elements heavier than iron. Several reactions can produce neutrons, among them ^{13}C(α,n)^{16}O and ^{22}Ne(α,n)^{25}Mg represent the most favored candidates [27, 28]. This is because they operate from relatively low temperatures typical of He burning (100 - 300 MK) and because ^{13}C and ^{22}Ne are relatively abundant nuclei in stellar interiors. The ^{13}C(α,n)^{16}O reaction, with a Q-value of about 2.22 MeV, operates in the He-burning shell of low-mass (less than 4 solar masses) AGB stars and it is the neutron source reaction that allows the creation of the bulk of the s-process elements such as Sr, Zr and the light rare earth elements. The Gamow peak in AGB stars lies around 190 keV while low energy data with a suitable accuracy are available in literature down to about 300 keV [30]. In view of new experimental studies, the presence of a broad resonance at E_{cm} $\approx$ 800 keV definitively makes necessary an α beam up to 1 MeV to reconstruct a full excitation curve. However, an exploratory experiment with a nominal sensitivity of a few event per day, which should be enough to touch the upper edge of the Gamow window, is planned at the LUNA400 facility and the data taking should be completed within the year 2018. The ^{22}Ne(α,n)^{25}Mg reaction, with a negative Q-value and a reaction threshold at E_α = 560 keV, operates in the He-burning shell of high-mass (more than 4

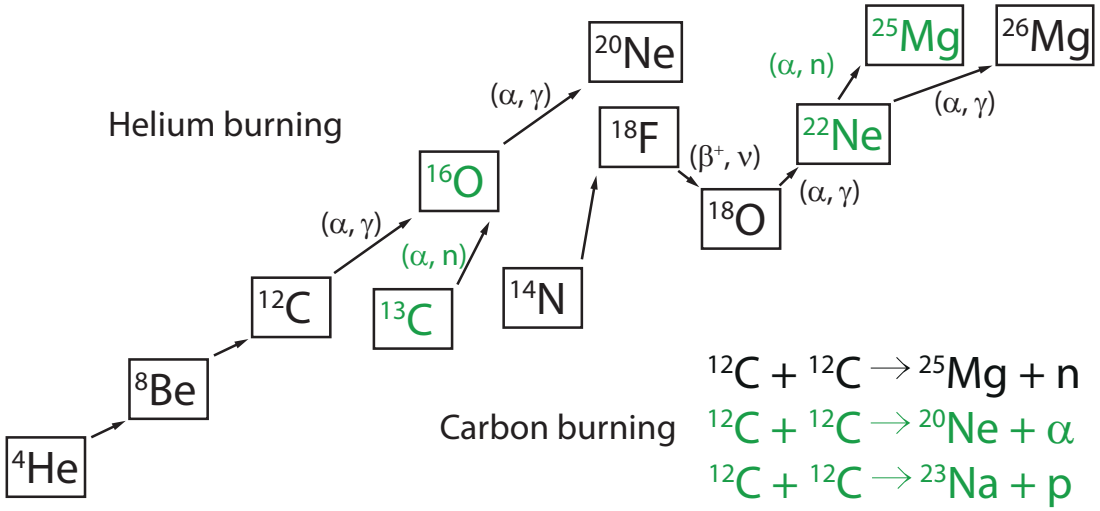

Fig. 3: The network of reactions of the helium and carbon burning phases. In green the processes which are part of the LUNA scientific program.

solar masses) AGB stars and during the core-He burning and the shell-C burning of massive stars (more than 10 solar masses). Last experimental studies date back to the year 2001 [31] and produced cross section values down to a minimum energy of 825 keV and upper limits at the lower energies. The last evaluation of the reaction rate is due to Longland and coworkers [32] who re-analyzed all the available data adopting however several assumptions and new, accurate experiments pushing the limit of direct measurements at the lowest energies, are definitively necessary.

The LUNA-MV facility will be installed at the beginning of the year 2019 in the north side of Hall B, one of the three big experimental areas of the underground Gran Sasso laboratory and will consist of an accelerator room with concrete walls and a further building hosting the control room and technical facilities including the cooling system, the electric power center, the monitors to guarantee the respect of the radiation levels. The concrete walls and ceiling (thickness of 80 cm) of the accelerator room will serve as neutron shielding. Considering the worst case scenario for the operation of the LUNA-MV facility of a maximum neutron production rate of R_n = 2 10^3 s^{-1} with an energy E_n = 5.6 MeV, the simulations determined a mean value for the neutron flux outside the accelerator room, Φ_n, of about $\Phi_n^{max} \sim 1.4$ 10^{-7} cm^{-2} s^{-1}. The Φ_n^{max} values is about a factor 5 lower than Φ_{n-LNGS} = 3 10^{-6} cm^{-2} s^{-1}, the reference neutron background at LNGS [33] (sum of the thermal, epi-thermal and fast components).

The LUNA-MV accelerator [28] is an Inline Cockcroft Walton accelerator currently under construction at High Voltage Engineering Europe (HVEE). The machine will cover a Terminal Voltage (TV) range from 0.2 to 3.5 MV and will deliver ion beams of H^+, $^4He^+$, $^{12}C^+$ and $^{12}C^{++}$ in the energy range from 0.35 to 7 MeV. A key feature to perform experiments on reactions important in astrophysics scenarios is the intensity of the beam delivered to the target. Such intensity will be particularly high with LUNA-MV. Following the deployment at LNGS, a six months installation and commissioning phase will start and first data taking for physics experiments are envisaged to start at LUNA-MV during the year 2020. A summary of the reactions which will be measured in the first five years of data taking is reported in fig. 3.

Since the year 2017, LUNA is no more the sole underground facility for nuclear astrophysics studies. New underground facilities are now in operation in USA-SD (CASPAR: Compact Accelerator System for Performing Astrophysical Research, at Homestake mine; accelerated species p and He; maximum beam energy = 1 MeV) and in China (JUNA: Jinping Underground Nuclear Astrophysics laboratory; accelerated species p and He; maximum beam energy = 0.4 MeV, beam intensity around

10 mA). The possibility to install a MV accelerator in presently considered at the Canfranc underground laboratory too. As for the past LUNA activity, the underground deployment of the next experiments will be not enough to guarantee significant steps forward. The development of new solid and/or gas target set-ups which have to be resilient to alpha and carbon beams with delivered power of a few kW, and of high-efficiency detectors with large angular coverage and high granularity, will be fundamental as well.

References

[1] A. Boeltzig *et al.*, *Eur. Phys. J. A* **52**, 75 (2016)
[2] F. Cavanna *et al.*, *Eur. Phys. J. A* **50**, 179 (2014)
[3] F. Cavanna *et al.*, *Phys. Rev. Lett.* **115** 252501 (2015)
[4] R. Depalo *et al.*, *Phys. Rev. C* **94** 055804 (2016)
[5] A. Slemer *et al. MNRAS* **465** 4817-4837 (2017)
[6] C.G. Bruno *et al.*, *Physical Review Letters* **117**, 142502 (2016)
[7] A. Boeltzig *et al.*, *Journal of Physics G: Nuclear and Particle Physics*, **45**, 025203 (2018)
[8] D. Trezzi *et al.*, *Astroparticle Physics* **89**, 57 (2017)
[9] A. Formicola *et al.*, *Nucl. Inst. Meth. A* **507**, 609-616, (2013)
[10] K.M. Nollett *et al.*, *Astrophys. J.* **582**, 1036 (2003)
[11] M. Lugaro *et al.*, *Astronomy & Astrophysics* **461**, 657 (2007)
[12] S. Palmerini *et al.*, *Astroph. J.* **764**, 128 (2013)
[13] M. Lugaro *et al.*, *Nature Astronomy* **1**, 0027 (2017)
[14] O. Straniero *et al.*, *Astronomy & Astrophysics* **598**, A128 (2017)
[15] M.Q. Buckner *et al.*, *Phys. Rev. C* **91**, 015812 (2015)
[16] M.L. Sergi *et al.*, *Phys. Rev. C* **91**, 065803 (2015)
[17] A. Caciolli *et al.*, *Eur. Phys. J. A 48*, 144 (2012)
[18] C.G. Bruno *et al.*, *Eur. Phys. J. A* **51**, 94 (2015)
[19] C.G. Bruno *et al.*, *Physical Review Letters* **117**, 142502 (2016)
[20] Plank Collaboration *et al.*, *Astronomy & Astrophysics* **594**, A13 (2016)
[21] V. Canuto *et al.*, *Phys. Rev. D* **16**, 1643-1663, (1977)
[22] R.J. Cooke *et al.*, *Astroph. J.*, **885**, 102 (2018)
[23] R.H. Cyburt *et al.*, *Rev. Mod. Phys.*, **88**, 015004 (2016)
[24] L. Ma *et al.*, *Phys. Rev. C* **55**, 588 (1997)
[25] L. E. Marcucci *et al.*, Phys. Rev. Lett. **116**, 102501 (2016)
[26] F. Ferraro *et al.*, *The Eur. Phys. J. A*, **54**(3), 44 (2018)
[27] M. Aliotta *et al.*, *The Eur. Phys. J. A*, **52**, 76 (2016)
[28] Prati P. *et al.*, *INFN/17-19/LNGS*, (2018)
[29] Burbidge E. M. *et al.*, *Reviews of Modern Physics* **29**, 547-650 (1957)
[30] Heil M. *et al.*, *Phys. Rev. C*, **78**, 025803 (2008)
[31] Jaeger M. *et al.*, *Phys. Rev. Lett.*, **87**, 202501 (2001)
[32] Longland R. *et al.*, *Phys. Rev. C*, **85** 065809 (2012)
[33] Wulandari H. *et al.*, *Astropart. Phys.*, **22**, 313-322 (2004)

The Study of the ^{22}Ne(α,γ)^{26}Mg Reaction at LUNA

D. Piatti for LUNA collaboration
University of Padova and INFN of Padova, Padova, Italy

Abstract
The ^{22}Ne(α,γ)^{26}Mg reaction is the competitor of the ^{22}Ne(α,n)^{25}Mg reaction, an effective neutron source for element synthesis through s-process. Currently the ratio between the rates of these two reactions is affected by high uncertainty because of the wide range of values proposed for the ^{22}Ne(α,γ)^{26}Mg 395 keV resonance strength (10^{-15} - 10^{-9} eV). The present study represents the first direct measurement. This was performed at the ultra-low background LUNA laboratory where an high efficiency detector was installed at the gas target beamline of LUNA 400kV accelerator. The Ne gas, 99% enriched in ^{22}Ne, was irradiated with a 399.9 keV α-beam. No significant signal was detected in the ^{22}Ne(α,γ)^{26}Mg region of interest, thus an upper limit for the 395 keV resonance strength was estimated.

1 Astrophysical Motivation

The ^{22}Ne(α,γ)^{26}Mg reaction is mainly involved in two stellar scenarios. First it competes with the ^{22}Ne(α,n)^{25}Mg reaction which is an efficient source of neutrons for s-process in low-mass asymptotic giant branch (AGB) stars [1], and in massive stars (with initial mass $M_i > 8$ $M_\odot$) [2]. Then it was recently found that the uncertainty of the ^{22}Ne(α,γ)^{26}Mg reaction rate affects the nucleosynthesis of isotopes between ^{26}Mg and ^{31}P in intermediate-mass AGB stars [3].
Currently the ^{22}Ne(α,γ)^{26}Mg reaction rate is affected by high uncertainty, whose main source is the wide range of values proposed for the $E_\alpha = 395$ keV resonance strength, see tab. 1. All the values reported in literature were derived from indirect measurements. The poorly constrained 395 keV resonance strength affects also the ratio between the ^{22}Ne(α,γ)^{26}Mg and the ^{22}Ne(α,n)^{25}Mg reaction rate, in particular for $0.25 \leq T \leq 0.5$ of interest for the s-process in low-mass AGB stars and in massive stars. From the description above is evident that a direct measurement, even if it results in an upper limit would greatly clarify the role of this resonance.

Table 1: Values for the strength of $E_\alpha = 395$ keV resonance reported in literature.

Reference	Lower Limit [eV]	$\omega\gamma$ [eV]	Upper Limit [eV]
Giesen et al. 1993 [4]	$1.4 \cdot 10^{-14}$	$1.7 \cdot 10^{-13}$	$1.6 \cdot 10^{-12}$
Giesen et al. corrected	-	$4.7 \cdot 10^{-13}$	-
NACRE 1999 [5]	-	$1.4 \cdot 10^{-13}$	$1.3 \cdot 10^{-12}$
Iliadis et al. 2010 [6]	-	-	$3.6 \cdot 10^{-9}$
Longland et al. 2012 [7]	-	-	$8.7 \cdot 10^{-15}$
STARLIB 2013 [8]	-	-	$3.6 \cdot 10^{-9}$

2 Experimental Setup

The ^{22}Ne(α,γ)^{26}Mg 395 keV resonance was investigated at Laboratory for Underground Nuclear Astrophysics (LUNA), located under 1400 m of Gran Sasso rock (Italy). The rock coverage guarantees an unprecedented reduction of the cosmic rays background [9].

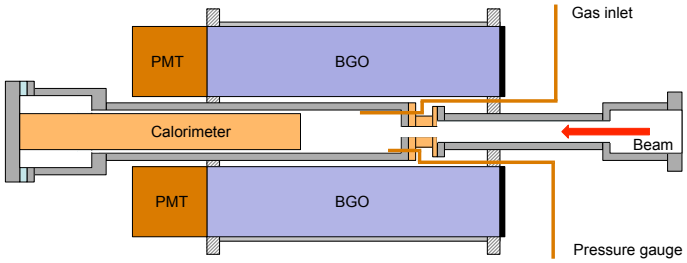

Fig. 1: BGO detector with target chamber

The high intensity beam provided by the LUNA400kV accelerator can be switched between two different beamlines: the gas target and the solid target. The current measurement was performed exploiting the gas target beamline combined with an high efficiency detection system, the same employed for the second campaign on ^{22}Ne(p,γ)^{23}Na reaction [10].
The high intensity He^+ beam was delivered to a devoted scattering chamber through three differential pumping stages. At the entrance of the scattering chamber no window were installed in order to prevent the beam energy loss and straggling as well as the possible beam induced reactions taking place in the entrance foil.
The neon gas, 99.99% pure and 99.99% enriched in ^{22}Ne, was kept at a pressure of 1 mbar. The gas target pumping system worked in recirculation mode, the target gas was pumped to a purifier and then it re-entered in the scattering chamber through a devoted pipeline. The scattering chamber was partially occupied by the calorimeter on which the beam stopped, see fig. 1 [10].
The calorimeter was used to measure the beam intensity run by run. It consists mainly of two parts: the hot side and the cold side. A chiller provided the circulation of a refrigerating liquid, at T = -5 C°, which kept the cold side at a temperature of about (7 ± 0.1)°C. The hot side was kept at the constant temperature of (70 ± 0.2)° by eight heating resistors. When the beam deposited its energy on the calorimeter it heated up the hot side. Consequently the temperature sensor of the Pt100, installed on the calorimeter, regulated the power supply of the resistors in order to keep the temperature constant. From the difference in the power supply required to keep the hot side at a constant temperature without, W_0, and with the beam, W_{run}, it was possible to evaluate the beam intensity:

$$I = \frac{W_0 - W_{run}}{E_\alpha - \Delta E} q\,, \tag{1}$$

where $(W_0 - W_{run})$ is the power provided by the beam, W_{beam}. E_α is the energy of the beam entering the scattering chamber. ΔE is the beam energy loss inside the target along the path to the calorimeter.
The calibration of the calorimeter was performed in vacuum for two temperatures of the cooling liquid ($T = -5°$ and $T = -20°$). The current measured by the calorimeter was compared with the one measured by the scattering chamber, which works as a Faraday Cup in vacuum. The calibration result is reported in fig. 2, the best fit function was found to be [10]:

$$W_{elec} = (0.936 \pm 0.002) \cdot W_{calo} + (-0.67 \pm 0.13)\, Watt\,. \tag{2}$$

The energy loss is a fundamental quantity in beam intensity calculation, see eq. (1), thus a precise knowledge of the gas density along the beam path, $\rho(z)$, is required.
According to the ideal gas law, the density can be derived directly from the pressure and temperature profiles. A new scattering chamber identical to the one used during the experiment except for seven additional KF25 flanges welded on its side, which allowed to put in place the baratrons and the Pt 100 for the pressure and temperature measurement, see fig. 3. The pressure profile was studied in 0.5 mbar steps from a target pressure of 0.5 mbar to 5 mbar along the chamber in the last collimator. As reference pressure a gauge connected to the center of the chamber, as during the experiment, was used, see

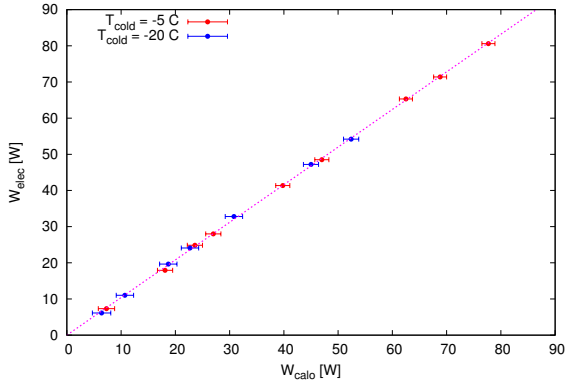

Fig. 2: Calibration of the calorimeter. On the x-axis the beam power measured with the calorimeter and on the y-axis the beam power as read by the scattering chamber. The calibration was performed at two different temperature of the cooling liquid, here referred as T_{cold}.

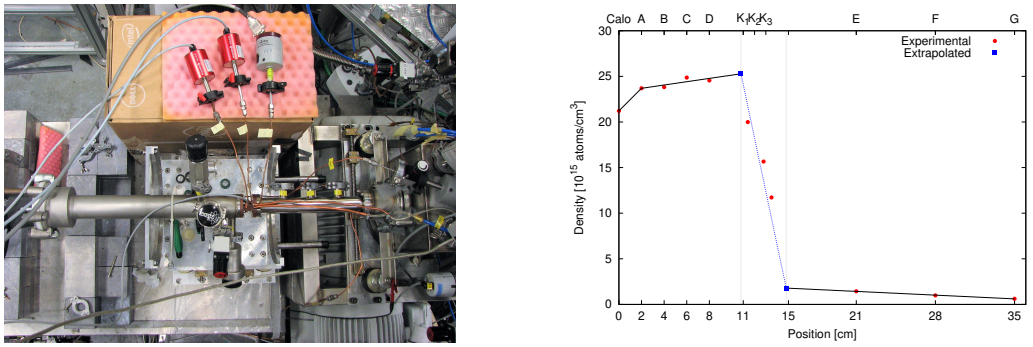

Fig. 3: On the left the *flute* chamber seen from the top. The different tools used to measure the pressure and the temperature are visible.On the right the gas density profile along the beam axis (beam from the right).

fig. 1. The temperature was measured only inside the chamber but additional Pt100 were located in the experimental hall and on the calorimeter. Combining the pressure profile and the temperature profile the density profile of the target was obtained, fig. 3. The density increases with decreasing of the temperature from the calorimeter to the collimator, inside which the density drops and then it decreases slowly in the remaining beamline.

Taking into account the uncertainties from the pressure and temperature measurements and the extrapolation in the collimator, a total uncertainty of 1.3% was found for the integrated gas thickness [10].

The scattering chamber and the calorimeter were located inside the borehole of the detector, see fig. 1 which consists of six optically independent BGO crystals, 28 cm long and 7 cm thick. Each crystal is read out by one photomultiplier (PMT) and it had a devoted digital acquisition chain and independent power supply. An homemade software program created the addback spectrum, which contains the sum of the coincident signals in two or more crystals. Indeed the BGO detector, thanks to its high efficiency and its solid angle, could detect multiple radiation emitted in the same nuclear decay. Events laying in a 3.5 μs wide window were considered coincident by the program and their energies are summed and recorded in the addback spectrum. The BGO efficiency was studied during the second campaign of the ^{22}Ne(p,γ)^{23}Na reaction study combining two methods: an experimental approach and Monte Carlo simulations. Geant3 and Geant4 codes were used to simulate the setup design and to derive the detection efficiency. The codes were tested and validated on a wide range of energies (from 0.5 MeV up to 7.6 MeV) using the efficiency measurements performed with four pointlike sources (^{7}Be, ^{60}Co, ^{88}Y and

t_m days	Charge [C]	Target Gas	Target Pressure [mbar]	E_α [keV]	Aim
49	-	-	-	-	Laboratory background
0.5	13.5	Ar	0.468	399.9	Beam induced background
21.2	430	^{22}Ne	1	399.9	395 keV resonance

Table 2: Time of measurement (t_m) and collected charge for each experiment task.

^{137}Cs and exploiting the well known resonance at $E_p = 278$ keV in the ^{14}N(p,γ)^{15}O reaction [11]. Once the codes were validated, the simulation of the ^{22}Ne(α,γ)^{26}Mg was performed assuming a single transition to the ground state for the 395 keV resonance. The efficiency was found to be of the 60% in the ^{22}Ne(α,γ)^{26}Mg region of interest. The uncertainty to the validation of the simulations has been assumed to be 4% [10].

3 Results and Discussion

The measurement time was allocated, following some experimental issues encountered during the measurement, as described in table 2.

The beam induced background was studied delivering the 399.9 keV α-beam to 0.468 mbar of Ar gas in the target chamber. The pressure was calculated in order to match the same enrgy loss as in 1 mbar of ^{22}Ne. The argon gas is expected to be not reactive to the ion beam at this energy. This feature allows to identify contaminants in the target chamber which can be source of background for the experiment. Because of some experimental issues and delays the data acquired were insufficient for the purpose, see table 2.

The study of the 395 keV resonance was performed impinging an high intensity α-beam (I$> 200\,\mu$A), accelerated up to 399.9 keV, on 1 mbar of enriched ^{22}Ne target gas. The energy of the beam and the pressure of the target gas were chosen in order to have the beam at the resonance energy exactly at the location of the maximum detection efficiency, the middle of the chamber. 49 day of background were acquired with the same setup in the same geometry with the beam off. All the data acquired for the laboratory background and the ^{22}Ne(α,γ)^{26}Mg reaction are plotted as sum of all the corresponding addback spectra in fig. 4.

The expected gamma-ray energy is E$_\gamma = Q + E_\alpha^{c.m.} = (10614 + 334)$ keV$= 10950$ keV, the region of interest (R.O.I.) centered at this energy exploited in the analysis is shown in fig. 4. Because there were no evident peaks in the identified region of interest, see fig. 4, the analysis had to proceed through a precise comparison with the laboratory background in order to understand the origin of the counts in the region of interest.

In the current case it was found that the net count in the region of interest was lower than the critical limit which takes into account the statistical uncertainty of the background. Thus no significant signal was detected and an upper limit for the 395 keV resonance strength was estimated. Because of the missing information on the beam induced background, two approaches were used to calculate the upper limit. First the net count found was treated as beam induced background count, while the second approach was to not take into account the beam induced background. The two results are located between the result reported in [6, 8] and the result in [5]. The two values obtained for the 395 keV resonance strength were used to calculate its contribution to the ^{22}Ne(α,γ)^{26}Mg reaction rate. The ^{22}Ne$+\alpha$ reactions rate ratios obtained by LUNA with the two methods previously described do not differ significantly between each other in the temperatures range of interest for He burning (0.25 - 0.5 GK). Indeed the maximum discrepancy is of about a factor 2 at T≤ 0.25 GK.

Comparing LUNA results with those reported in literature there is a good agreement at T>0.5. On the other hand in the He burning temperature range the LUNA reaction rate ratios lay between those sug-

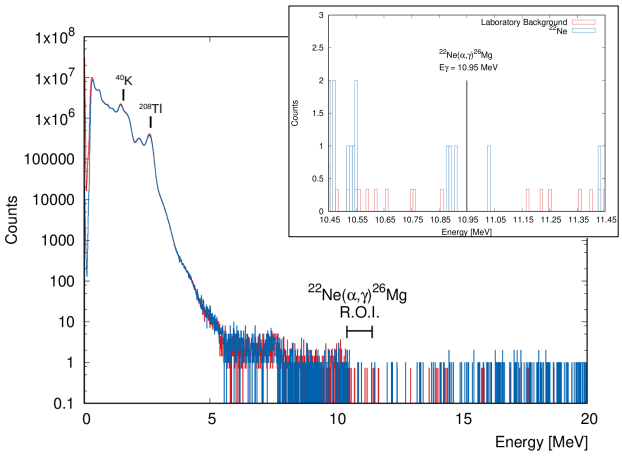

Fig. 4: In red the sum of all the addback spectra acquired to investigate the laboratory background. In blue the same for the study of ^{22}Ne(α, γ)^{26}Mg reaction. A zoom of the region of interest (R.O.I) for the 395 keV resonance is also reported.

gested by NACRE and Iliadis. In the new scenario the neutron production starts to be effective at T $>$ 0.31 GK with great impact on the predicted s-nuclei production in low-mass AGB stars and in massive stars. The new cross-over temperature is in disagreement with all the previous ratios proposed in literature. As a matter of fact the (α,n) channel dominates at T corresponding to the He burning for both NACRE and Longland, while Iliadis suggested the neutron production to be effective at T $>$ 0.4 GK. The discrepancy between LUNA results and NACRE and Longland reaction rate ratios increases for T $\leq$ 0.25 0.25 GK at which the ^{22}Ne(α,γ)^{26}Mg reaction dominates and the reaction rate ratio is more sensitive to the contribution of the 395 keV resonance. The LUNA result at low temperatures is expected to affect the predicted nucleosyinthesis in intermediate-mass AGB stars at T $\leq$ 2.5 GK.
Some problems were encountered and identified during the present study data acquisition and analysis. A new campaign of the ^{22}Ne(α,γ)^{26}Mg reaction is actually ongoing at LUNA, for which some solution were designed in order to avoid the problems encountered during the previous experiment. The expected impact of the new campaign on the previous results is either to measure the resonance or to reduce the upper limit found in the current study by one order of magnitude. This would definitely make the contribution of the 395 keV resonance to the ^{22}Ne(α,γ)^{26}Mg reaction rate negligible and it would fix the role of the ^{22}Ne(α,n)^{25}Mg reaction as neutron source for the s-process. In addition, it would better constrain both the AGB star and massive star model parameters and their impact on the chemical evolution of galaxies.

Acknowledgements

The work at LUNA is carried out in the framework of the LUNA collaboration see [10] for an author list.

References

[1] F. Herwig, Evolution of Asymptotic Giant Branch Stars, Annual Review of Astronomy and Astrophysics, vol. 43, p. 435, (2005).

[2] R. G. Couch, A. B. Schmiedekamp, and W. D. Arnett, S-PROCESS Nucleosynthesis in Massive Stars: Core Helium Burning, The Astrophysical Journal, vol. 190, p. 95, (1974).

[3] A. I. Karakas *et al.*, The Un- certainties in the ^{22}Ne+α-Capture Reaction Rates and the Production of the Heavy Magnesium Isotopes in Asymptotic Giant Branch Stars of Intermediate Mass, The Astrophysical Journal, vol. 643, p. 471, (2006).

[4] U. Giesen *et al.*, The astrophysical implications of low-energy resonances in ^{22}Ne + α, Nuclear Physics A, vol. 561, p. 95, (1993)

[5] C. Angulo *et al.*, A compilation of charged-particle induced thermonuclear reaction rates, Nuclear Physics A, vol. 656, p. 3, (1999).

[6] C. Iliadis *et al.*,Charged-particle thermonuclear reaction rates: II. Tables and graphs of re- action rates and probability density functions, Nuclear Physics A, vol. 841, p. 31, (2010).

[7] R. Longland *et al.*, Photoexcitation of astrophysically important states in Mg26, Physical Review C, vol. 80, p. 055803, (2009)

[8] A. L. Sallaska *et al.*, STARLIB: A Next-generation Reaction-rate Library for Nuclear Astrophysics, The Astrophysical Journal Supplement Series, vol. 207, p. 18, (2013).

[9] C. Broggini *et al.* , LUNA: Status and prospects, Progress in Particle and Nuclear Physics, vol. 98, p. 55, (2018).

[10] F. Ferraro, M. P. Takács, D. Piatti, and V. Mossa *et al.*, A high-efficiency gas target setup for underground experiments, and redetermination of the branching ratio of the 189.5 keV ^{22}Ne(p,γ)^{23}Na resonance, European Physical Journal A, vol. 54, p. 44, (2018).

[11] M. Marta *et al.*, Resonance strengths in the ^{14}N(p,γ)^{15}O and ^{15}N(p,$\alpha\gamma$)^{12}C reactions, Physical Review C, vol. 81, p. 055807, (2010).

Major Accelerator Facilities for Nuclear Physics in Asia Pacific

Kazuhiro Tanaka
(kazuhiro.tanaka@kek.jp),
Chair of Asian Nuclear Physics Association (ANPhA).
Institute of Particle and Nuclear Studies (IPNS) and
Particle and Nuclear Physics Division, J-PARC Centre,
High Energy Accelerator Research Organization (KEK),
Oho 1-1, Tsukuba-shi, Ibaraki-ken, 305-0801 JAPAN.

Abstract
Asian Nuclear Physics Association (ANPhA) is the central organization representing nuclear physics in Asia Pacific. ANPhA is now preparing a list of accelerator facilities applicable for nuclear physics experiments in Asia Pacific. Among them, characteristics of the world class "Major" accelerator facilities were briefly summarized in Varenna2018 in comparing to similar facilities in Europe and North America.

1 Introduction to ANPhA

Asian Nuclear Physics Association (ANPhA) [1] was established in 2009 in Beijing, where representatives of the first four member countries of ANPhA gathered together in a founding meeting. ANPhA is the central organization representing nuclear physics in Asia Pacific and consist of eleven member countries and regions, i.e. Australia, China, Hong Kong, India, Japan, Kazakhstan, Korea, Mongolia, Myanmar, Taiwan, and Vietnam.

The basic objectives of ANPhA are;

1. To strengthen "Collaboration" among Asian nuclear research scientists through the promotion of nuclear physics and its transdisciplinary and applications,
2. To promote "Education" in Asian nuclear science through mutual exchange and coordination,
3. To "coordinate" among Asian nuclear scientists by actively utilizing existing research facilities,
4. To "discuss future planning" of nuclear science facilities and instrumentation in Asia.

In 2015, ANPhA decided to play a role as the Division of Nuclear Physics (DNP) of Association of Asia Pacific Physics Societies (AAPPS). AAPPS approved our proposal in 2016, and AAPPS-DNP was established. Now ANPhA chair is the chair of AAPPS-DNP. Practically, ANPhA (=AAPPS-DNP) is an organization to discuss and pursuit issues in Asian nuclear physics community at present.

Participating countries or regions in ANPhA will appoint several (1 to 4) Board members for ANPhA. Board members elect one chairperson and several vice chairpersons by mutual election. The chairperson will also appoint a secretary from Board members. The Chairperson, Vice Chairperson, and Secretary constitute an Executive Officer team, and handle daily affairs.

ANPhA Board members meet together once a year at some appropriate place in one of ANPhA member countries or regions and exchange information of the status of nuclear physics in each country/region and have discussions on our future collaborations. This kind of meeting is organized in conjugation with ANPhA symposium on "Status of Nuclear Physics in Asia Pacific". The most recent (13th) ANPhA Board meeting was held in Beijing, China in September 14th in 2018. Next Board Meeting will be held in Korea in the fall in 2019.

As the chair of AAPPS-DNP, ANPhA chair attends the extended Council meeting of AAPPS.

Another important activity of ANPhA is to organizing DNP-AAPPS (=ANPhA) awards for young Scientists [2] for ANPhA supported scientific meetings.

2 ANPhA White Paper

Nuclear physics is a typical accelerator-based science. However, in contrast to elementary particle physics, which is another field of science based on accelerators, nuclear physics requires to prepare a variety of accelerators to tackle the various problems involved. In other words, one needs a distributed approach and efforts, i.e. different accelerator types and energies, in order to find answers to the nuclear physics problems existing in our universe. The development of accelerator-based research facility always involves big construction work. It is also expensive and requires very large amount of money. Today we can understand that it is very difficult to prepare all kinds of accelerators necessary for the nuclear physics research in one country. Then it is becoming a common to advance research through international collaboration, i.e. international division of labor.

Even in Asia Pacific region, many advanced accelerator facilities have been constructed. Some of them are really world class facilities. ANPhA is now preparing a list of accelerator facilities applicable for nuclear physics experiments existing in Asia Pacific. The list is so called ANPhA White Paper [3]. This White Paper, the catalog of accelerators in Asia Pacific, is the most basic material for us to consider today's international collaboration within present accelerator facilities, and to establish the long range plan of the construction of accelerator facilities for our future activities of nuclear physics in Asia Pacific. Such international scheme of collaboration is originally global. Then the ANPhA White Paper can be important inputs for European and American colleagues of nuclear physics.

It should be noted that accelerator facilities originally prepared for nuclear physics research have many applications of science, such as material science, life science, medicine, and especially education and training of young students. Therefore ANPhA White Paper can be a good guide line for researchers in neighboring research field to expand their research to accelerator based science using near-by facilities.

Now 28 accelerator facilities for nuclear physics in Asia Pacific are listed in the ANPhA White Paper. Data will be updated frequently and the latest update was done in August 2018. Critical analysis of the present data will be made for future facility planning and for possible future international collaboration.

Data are now temporarily open on the KEK Indico system;

https://kds.kek.jp/indico/category/1706/

Notes for KEK Indico users, please find the username and password at the first page you opened (Most users) or "click for the password" on the page which you can find after closing the popup window to login (Google Chrome users).

3 Major Accelerator Facilities in Asia Pacific

Major facilities in Asia Pacific region are mainly locating in China (Heavy Ion Research Facility in Lanzhou (HIRFL), Beijing Tandem Accelerator National Laboratory (BTANL)), India (Variable Energy Cyclotron Centre (VECC)), Korea (RISP/RAON), and Japan (RIBF at RIKEN, J-PARC, and ELPH/LIPS). Most of them (HIRFL, BTANL, VECC, RISP/RAON and RIBF) are medium energy heavy-ion accelerator facilities and are competing to European and American Facilities such as SPIRAL2, HIE-ISOLDE and ARIEL-II. In addition, future extension plans of these Asian facilities are really aiming far beyond the wave front of the research of this field of nuclear physics. In this

meaning, Asian research facilities are keeping world best positions in medium energy heavy-ion physics. Hadron physics facility in Asia Pacific (J-PARC) is also world leading facility. ELPH/LIPS facilities can provide world competitive photon beams for nuclear and hadron physics.

However, there are no high energy heavy-ion accelerators and colliders (such as ALICE in LHC in CERN, RHIC in BNL in USA, and NICA in DUBNA in Russia) in Asia Pacific region. In other word, we concentrated our research resources to medium energy heavy-ion physics and chosen to promote high energy heavy-ion physics at abroad (outside Asia). This strategy seems successful at present. However we have to check our strategy of this field of nuclear physics for our future research activities in Asia Pacific. For example, I'm wondering that too much concentration might be happening in medium energy heavy-ion accelerator facilities in Asia Pacific region. This concentration is happening also in Europe and America. Should we be much more careful on our investment for our future activities in nuclear physics, which should have much wider spectrum, I think?

Some of our "Major Facility status and future plans" are introduced in the following Chapters.

4 Chinese Facilities

Construction of accelerator facilities in China is in very much strategic and clever way. They constructed ordinal experimental facility based on the tandem electrostatic accelerator in 1986 in Beijing and construction of the experimental facility based on Split Sector Cyclotron (SSC) followed it in 1988 in Lanzhou.

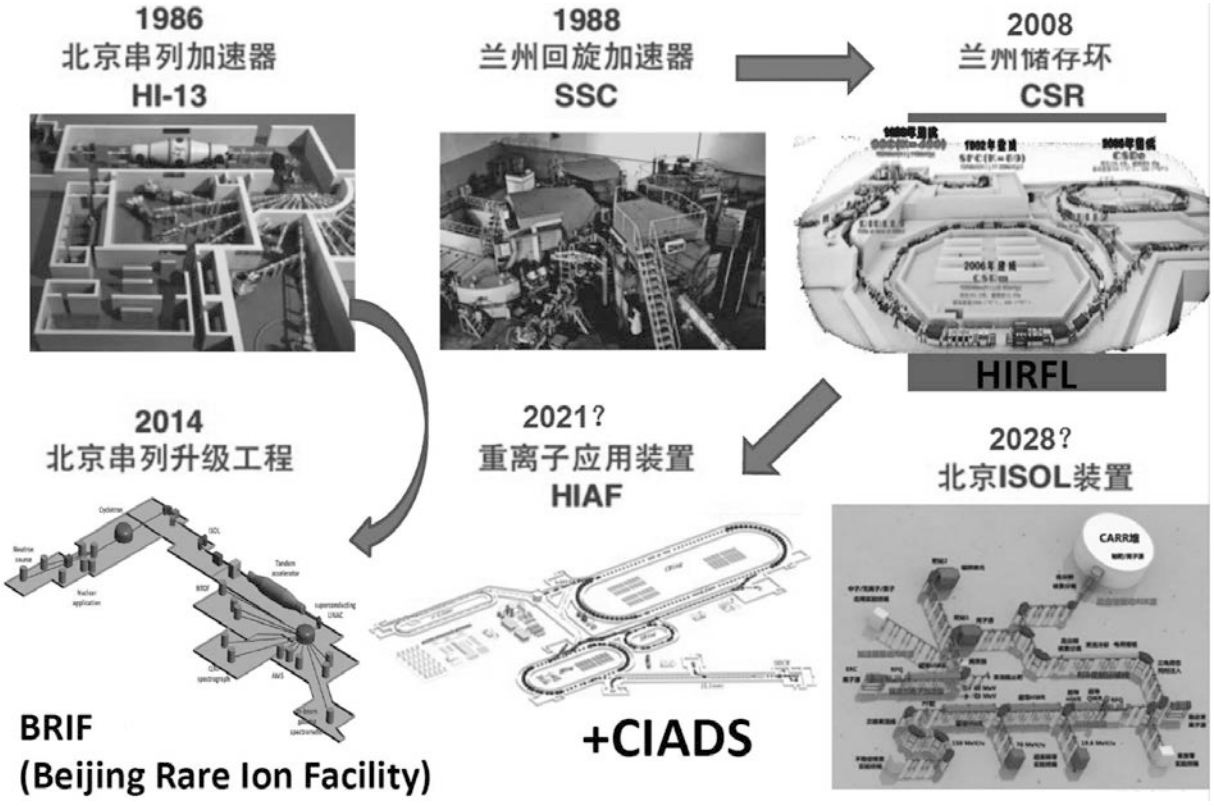

Fig. 1: Chinese accelerator facilities for nuclear physics.

After the successful operation of both facilities for approximately 20 years as "normal" beam facilities,

accumulator rings were constructed in SSC facility in 2008 and SSC was used as the injector to rings. “Unstable” nuclear beams produced through projectile fragmentation from stable (normal) nuclear beams obtained from SSC were accumulated in rings and extracted for experiments after energy boosted and beam quality improved in the rings. For Beijing facility they added small cyclotron to produce “unstable” nuclear beams by using target ion source. Proton beam obtained from small cyclotron irradiated the target material which was heated up by beam power as well as electrical heater. Unstable nuclei produce in the target material through nuclear reactions were thus evaporated from the surface of the target material and collected for the re-acceleration by the tandem electrostatic accelerator. Then the tandem facility and SSC facility were well converted to the most modern “unstable” nuclear beam facilities.

Their next steps are the construction of very High Intensity Accelerator Facility (HIAF) for the production of unstable nuclear beams based on the projectile fragmentation, which is the natural extension from Lanzhou’s SSC facility but constructed in the other place, i.e. Huizhou city, and the SUPER ISOL facility based on the combination of nuclear reactor and linear accelerator in Beijing, i.e. Beijing ISOL.

5 Korean Facility

The major accelerator facility under construction in Korea is RAON (Rare isotope Accelerator complex for ON-line experiments) of RISP (Rare Isotope Science Project) hosted by IBS (Institute of Basic Science). This is the first big scientific project in Korea concerning to the construction of the world class accelerator complex. Location of RAON is Sindong area in Daejeon city, which is almost the central part of South Korea and almost 2-3 hours travel by KTX fast train from both Seoul and/or Pusan. The ground breaking for accelerators and experimental buildings was done on Feb. 13th in 2017.

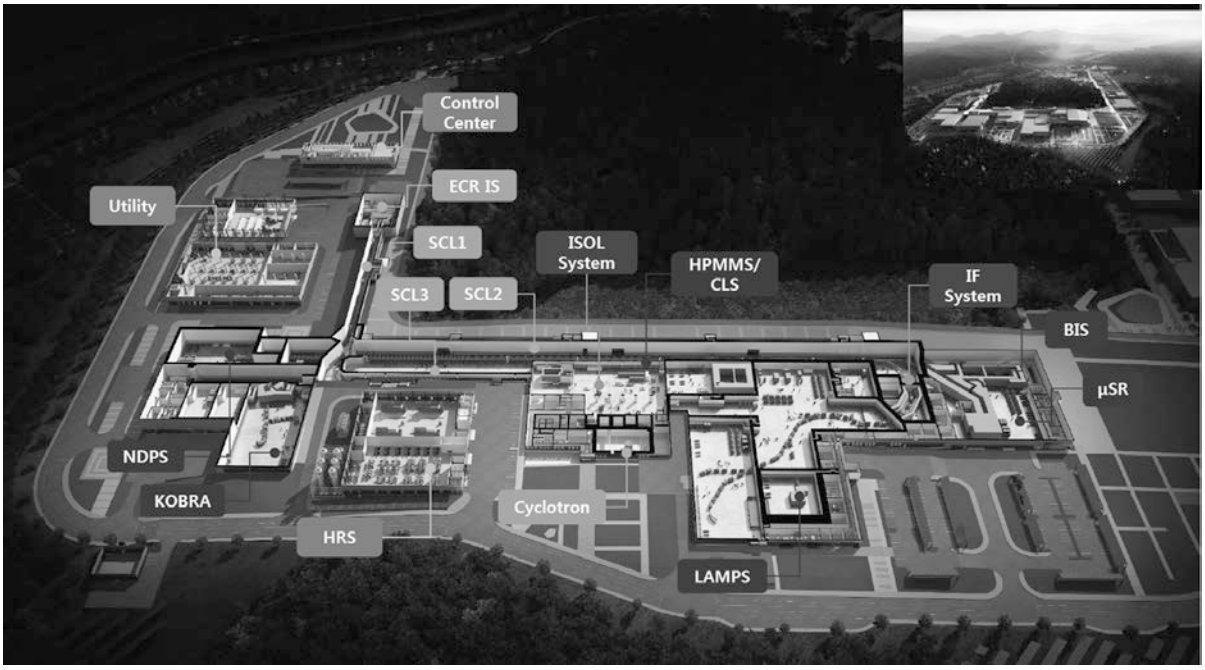

Fig. 2: RAON accelerator complex of RISP of IBS in Korea.

RAON accelerator consists of three superconducting linear accelerators. Combining three linacs,

acceleration of normal heavy-ion beams and unstable nuclear beams extracted from target ion source to sufficiently high energies to projectile fragmentation. As results RAON can provide much higher intensity unstable nuclear beams for experiments than any other facilities in the world. For the target ion sources, high intensity proton cyclotrons are introduced as drivers.

R&D of superconducting accelerator devices have already started and test cryo-module of acceleration cavity showed sufficiently high field gradient with less heat load than expected, i.e ready for mass production. Operation test of ISOL target ion sources has started at hot-cell mockup. Remote maintenance scheme of the target ion source will be tested there.

6 Japanese Facilities

There are several large scale accelerators in Japan as shown in Figure 3. Among them following 3 research complexes were endorsed by Japanese Nuclear Physics Executive Committee in 2016 as main middle term (~5 years) important future plans of nuclear physics in Japan. These are;

- J-PARC (KEK)
  - Hadron/nuclear physics with hadron beams
    - -> Hadron Hall extension.
  - Fundamental Physics and Particle physics with muons
    - -> mu-e conversion (COMET), g-2.
- RIBF (RIKEN)
  - RIBF upgrade for intensity x30
    - -> Expand neutron-rich heavy element productions to trans-uranium.
    - -> Production of superheavy z=119 element and beyond.
- ELPH (Tohoku Univ.) and LEPS@SPring-8 (RCNP, Osaka Univ.),
  - Hadron physics with GeV electron and photon beams
    - -> Detector/Beam upgrades.

In addition to them, two research fields were selected as important subjects for Japanese nuclear physics;

- High energy heavy-ion collision (LHC, RHIC, J-PARC)
  - QGP properties, QCD phase diagram, High density nuclear matter.
    - -> ALICE upgrade, s-PHENIX/STAR upgrade, J-PARC-HI R&D.
- Nuclear theory
  - Hadrons via lattice QCD, nuclear structure via Monte Carlo shell model, etc.
    - 9 projects with K-computer and beyond.

J-PARC in KEK and RIBF in RIKEN are main two-top facilities of Japanese nuclear physics community. Then extension of Hadron Experimental Hall and 30 times intensity upgrade of RIBF are two-main big future plans in Japan.

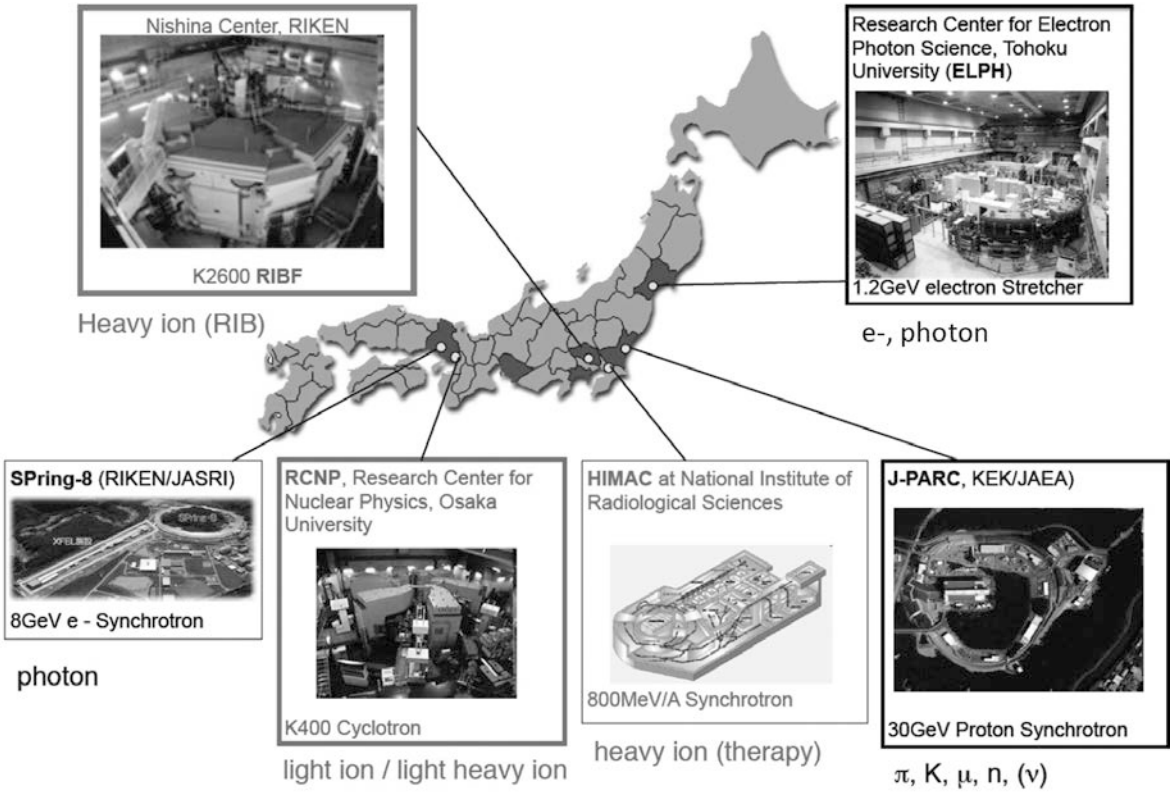

Fig. 3: Large scale accelerator complexes located in Japan.

Schematic layout of RIKEN-RIBF is shown in Figure 4. RIKEN-RIBF consists of several types of ring cyclotrons connected in cascade and one big superconducting ring cyclotron, SRC. Unstable nuclear beams are produced by projectile fragmentation (PF) and a large solid angle PF separator, the BigRIPS, is in operation. Upgrade for 30 times higher intensity is mainly performed by upgrading injector LINAC and by the modification of SRC and BigRIPS in order to accept higher intensity primary nuclear beams. High intensity unstable nuclear beam thus produced will be used for the search of new superheavy elements such as Z=119, 120 and beyond. This upgrade project is named as “Landing to Stable Island”.

J-PARC (Japan Proton Accelerator Research Complex) is the brand-new and the most advanced accelerator facility in Japan. J-PARC consists of three accelerators, i.e. 400 MeV Linac, 3 GeV Rapid Cycle Synchrotron (RCS) and 50 GeV-PS (Main Ring, MR). The bird eye view of J-PARC is shown in Fig. 5. The most important characteristic of J-PARC is its high design beam power, which is 1MW for RCS and 0.75MW for MR. RCS provides its intense proton beam to neutron spallation source (n) and pulsed muon source (μ) prepared in Materials and Life Science Facility (MLSF). Some fraction of the beam extracted from RCS is injected to MR and accelerated up to 30 GeV. Two extractions from MR were constructed. One is the fast extraction for Neutrino Beam Facility (ν) for long baseline neutrino oscillation experiment, T2K, and the other is the slow extraction for counter experiments in Hadron Experimental Facility (Hd). Four experimental facilities (n, μ, ν and Hd) could provide their characteristic intense secondary beams for experimental users.

The highest proton beam energy of MR is now only 30 GeV instead of its design energy of 50 GeV. It is mainly because of the budget problem for preparing power supplies of MR magnets.

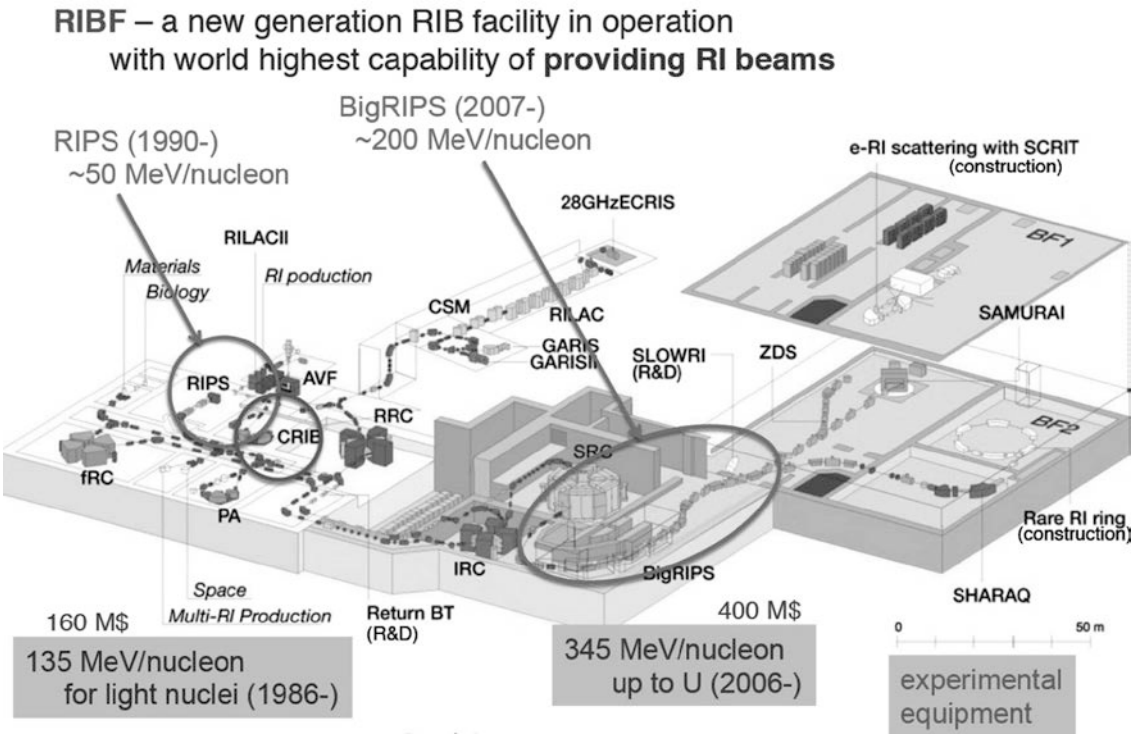

Fig. 4: Schematic layout of RIBF-RIKEN accelerator complex.

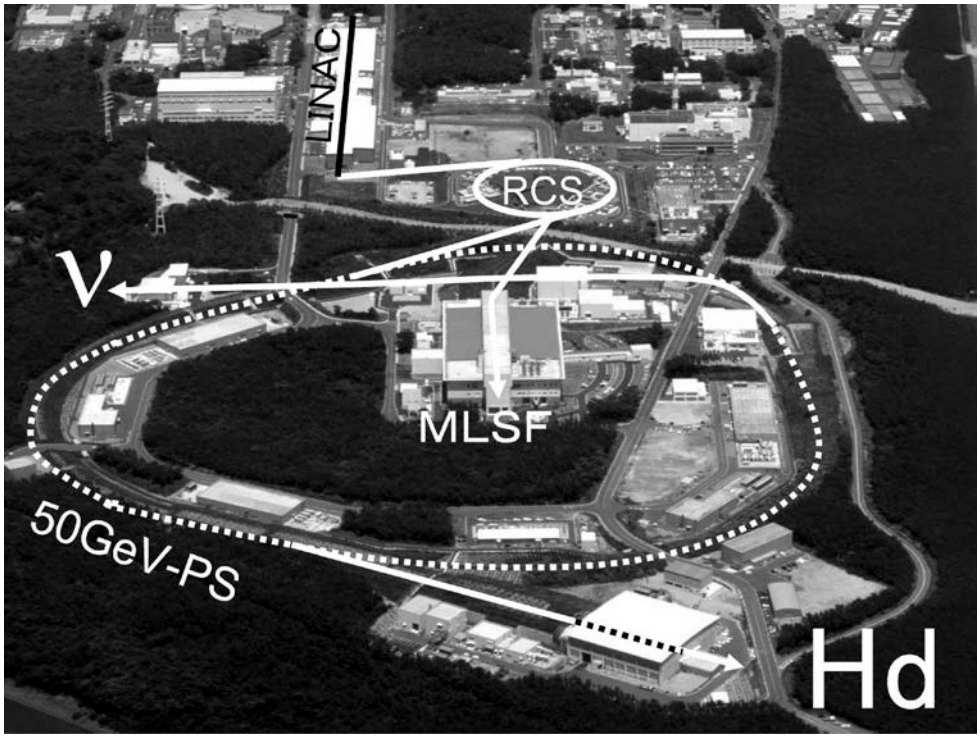

Fig. 5: J-PARC site at Tokai campus of JAEA.

Major future project of J-PARC for nuclear physics is the extension of the Hadron Hall three times as shown in Figure 6.

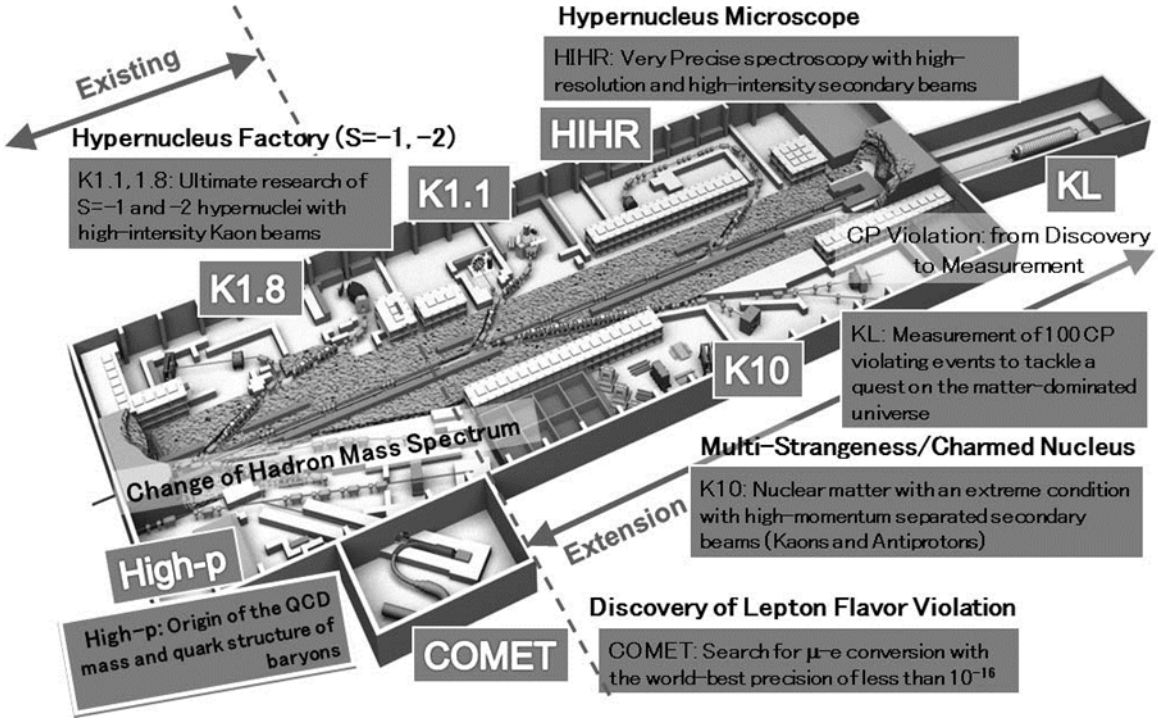

Fig. 6: Drawing of the extension of Hadron Experimental hall. Two new target stations are constructed and four new secondary beam lines are connected to these two targets. Very forward angle neutral kaon beam line, KL, high momentum separated kaon/antiproton beam line, K10, very high resolution dispersion matching beam line, HIHR, and very low energy separated kaon beam line, K1.1, are now under consideration. High-p beam line with COMET branch is now under construction at present Hadron Experimental hall.

Acknowledgement

The author would like to express his sincere thanks to Board members of Asian Nuclear Physics Association (ANPhA), who prepared the data for ANPhA White Paper.

References

[1] ANPhA: http://ribf.riken.jp/ANPhA/

[2] Kazuhiro Tanaka, “The First Year of the ANPhA (AAPPS-DNP) Awards for Young Scientists”, AAPPS Bulletin, Vol. 28, No. 1, pp. 43-45.

[3] ANPhA White Paper: https://kds.kek.jp/indico/category/1706/

Notes for KEK Indico users, please find the username and password at the first page you opened (Most users) or “click for the password” on the page which you can find after closing the popup window to login (Google Chrome users).

Neutrino, wine and fraudulent business practices

Michael S. Pravikoff[*]*, Philippe Hubert and Hervé Guegan*
CENBG (CNRS/IN2P3 & University of Bordeaux), 19 chemin du Solarium, CS 10120, F-33175 Gradignan cedex, France

Abstract
The search for the neutrino and its properties, to find if it is a Dirac or Majorana particle, has kept physicists and engineers busy for a long time. The Neutrino Ettore Majorana Observatory (NEMO) experiment and its latest demonstrator, SuperNEMO, demanded the development of high-purity low-background γ-ray detectors to select radioactive-free components for the demonstrator. A spin-off of these detectors is inter-disciplinary measurements, and it led to the establishment of a reference curve to date wines. In turn, this proved to be an effective method to fight against wine counterfeiters.

1 Introduction

Over the last few decades, demand for fine wines has soared tremendously. Especially some particular vintages, notably from famous wine areas, lead to stupendous market prices, be it between private collectors as well as through wine merchants and/or auction houses. The love of wine was not and is still not the main factor in this uprising business: wine has become or maybe always was a financial asset. No surprise that this lured many people to try to make huge and easy profit by forging counterfeited bottles of the most prestigious - and expensive - "Grands Crus". But for old or very old fine wines, experts are at loss because of the complexity of a wine, the lack of traceability and so on. By measuring the minute quantity of radioactivity contained in the wine without opening the bottle, a method has been developed to counteract counterfeiters in most cases. And the origin of this method lies in the study of the neutrino...

2 The Neutrino Ettore Majorana Observatory (NEMO) experiment and PRISNA (Plateforme Régionale Interdisciplinaire de Spectrométrie Nucléaire en Aquitaine)

In a typical double beta decay, two neutrons in the nucleus are converted to protons, and two electrons and two electron antineutrinos are emitted. This is the $2\beta2\nu$ process. The Neutrino Ettore Majorana Observatory (NEMO) experiment, which is running in the Modane Underground Laboratory (LSM aka Laboratoire Souterrain de Modane), located in the Traforo del Frejus between Italy and France, is looking for a very rare process of the natural radioactivity, called the neutrinoless double beta decay, in which a nucleus emits two electrons simultaneously and no neutrino. The expected half-life being so large ($> 10^{26}$ years), few counts per year are expected, which implies that all the background components must be reduced by few orders of magnitude. Cosmic rays, external γ-rays, natural β emitters, neutrons and radon are a nuisance and have to be suppressed or dampened. Fig. 1 shows the challenge of detecting the $2\beta0\nu$ signal.

The SuperNEMO detector (6 m long, 2 m wide, 4 m high) is partly built out of materials containing no measurable radioactive isotopes such as U, Th, Ra and their progeny. In Fig. 2 we see the assembly of the different parts of the demonstrator: a source foil sandwiched between tracker (to reconstruct the electron trajectories) and calorimeter (to record the energy) walls. Since most of the natural radioactive isotopes are γ-emitters, to select and control the radio-purity of all materials, we had to develop ultra-low background γ-ray spectrometers on the basis of HPGe (High Purity Germanium) crystals. Four

[*]pravikof@cenbg.in2p3.fr

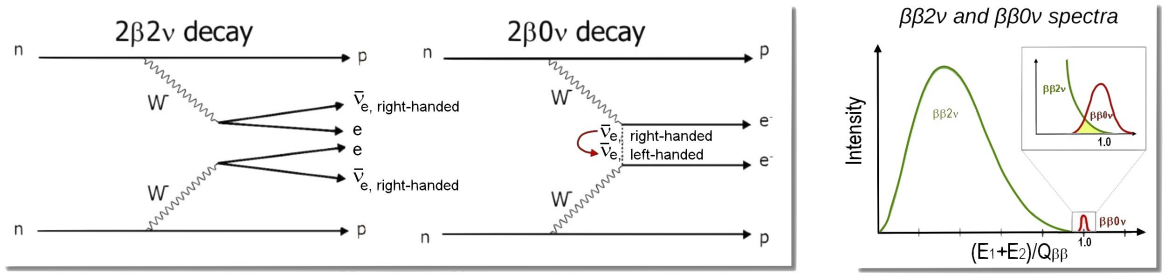

Fig. 1: Double Beta Decay with or without neutrino emission. [left] The two double-beta decay modes. [right] The aim is to measure the tiny $2\beta0\nu$ signal despite the overlap due to the most common $2\beta2\nu$ process.

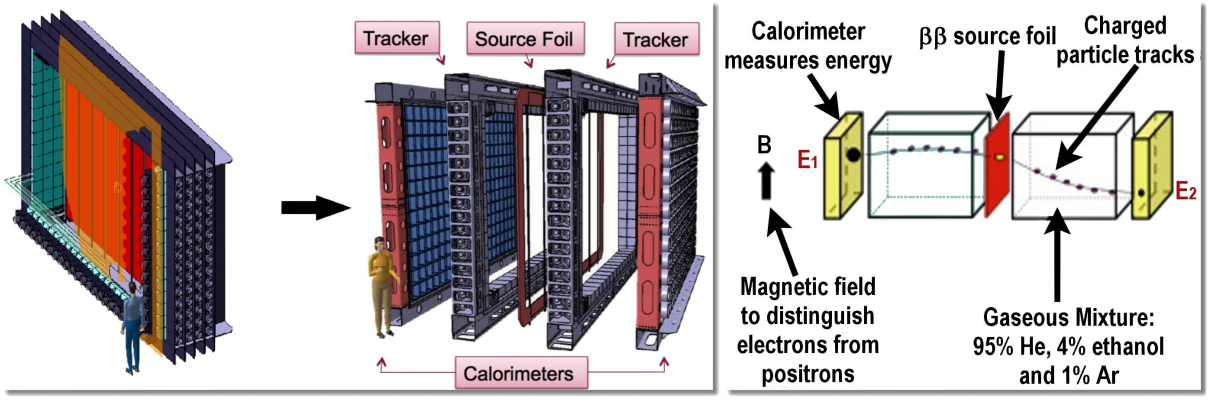

Fig. 2: SuperNEMO demonstrator. [left] From left to right, calorimeter, tracker, 2β source foil, tracker, calorimeter. [right] Schematic principle of the particle identification.

such spectrometers are hosted in the low-background environment PRISNA platform at our Institute in Bordeaux (Fig. 3). Their aim is to make a selection of the materials which, when validated, are measured for a final test by two similar detectors we have in the Modane Underground Laboratory.

3 From the neutrino to wine dating

Dating a wine through its radioactivity is an old idea. In 1954, Nobel Prize W.F. Libby proved one could date wines thanks to their Tritium content [1]. In the 1970s, P. Martinière et al. did the same with ^{14}C. And in 2001, the Centre d'Etudes Nucléaires de Bordeaux-Gradignan (CENBG), because of its expertise in very weak radioactivity measurements for the neutrino research, teamed with the French State local Agency for Consumer Protection (now Service Commun des Laboratoires). The initial goal was to infer if there was some possibility of dating wines in the frame of fraud fighting [2].

Our expertise in measuring low-background γ-ray emission, several orders of magnitude lower than natural radioactivity, is already applied to several inter-disciplinary research domains: characterisation of the geographic origin of edible foods (cocoa, plums, salt flowers, etc.), dating animal bones mostly in a fraud-fighting approach together with the French Bureau of Consumer Protection [3], inquiring the role of natural radioactivity in the set-on of neurodegenerative diseases [4]. But thanks to media, our best research program known to the public is dating wine by measuring its radioactivity, and the subsequent fraud affairs. Two approaches have been investigated, both involving γ-ray measurement of ^{137}Cs and ^{210}Pb resp. The former is a formidable answer to the challenge of dating a wine without opening the bottle. The latter, a destructive method, can be used in a few undetermined cases.

Fig. 3: PRISNA facility [left] and its protection against muons and related interactions [right]

Fig. 4: γ-ray measurement. [left] Bottle laying flat on a Ge detector. [right] 2 bottles shown against the Germanium detector just for illustration purpose.

3.1 Low background gamma-ray spectrometry

Most of the radioactive nuclei found in Nature, whether natural occurring ones like ^{40}K, Uranium and Thorium natural radioactive families, or anthropogenous ones like ^{137}Cs, are γ emitters. To detect and measure very weak activity levels, the detectors cryostats are made of the lowest radioactive possible materials. They are enclosed in lead shielding, the innermost part being made of archaeological lead, i.e. at least a few centuries-old lead, which is free of ^{210}Pb ($T_{1/2}$ = 22.2 y). Borated polyethylene is added to prevent neutrons reaching the Ge crystal. Plastic scintillators are placed on top of the spectrometers to veto to cosmic radiation which may interfere with the data taking by reacting with the matter surrounding the detectors. To further decrease those parasitic events, the spectrometers are installed in a special facility called PRISNA (Plate-forme Régionale Interdisciplinaire de Spectrométrie Nucléaire en Aquitaine) (Fig. 3), a building devoted to the measurement of very low radioactive samples with dampened outside radioactive background. Its specificity lies in the fact that it lays under 2.5 m of concrete and dirt (6 m water equivalent), that the walls, the roof and the floor inside the 70 m^2 are covered by radon-stopping foils. The climate environment control is set to have a residual radon content in the air equal or lower to the one outside the building.

Depending on the sample and the looked-after γ-ray isotope, sensitivity can reach values as low

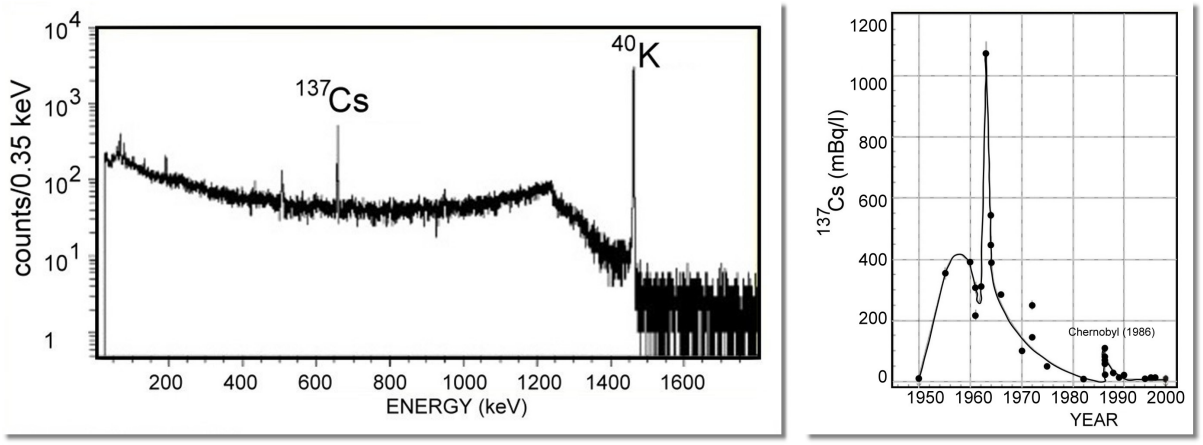

Fig. 5: Vintage spectrum and dating curve as measured by P. Hubert et al. in 2001. The γ-ray spectrum on the left shows the presence of ^{40}K and ^{137}Cs in the wine. On the Cs-137 Activity vs Year, all points are normalised to activities on Jan. 1st, 2000. Therefore, the maximum value in the 1960's was at that time a little more than twice the plotted value.

as 20 mBq/kg.

3.2 Wine data taking

^{137}Cs, with a half-life of 30 years is a man-made isotope. Its main origin comes from the numerous above ground atom bomb tests during the 1950's and 1960's with still some contributions in the the 1970's. The Chernobyl (1986) and Fukushima (2011) incidents have their share. The released activities were spread worldwide, then deposited on earth. The amount of subsequent ^{137}Cs radioactivity found at ground level is an almost perfect remembrance of the amount released, and it is different for each year since the early 1950's. When making wine, grapevines collect the activity coming from the fall-outs, and after bottling, each year harvest "records" that particular vintage radioactivity. We established therefore a reference curve ^{137}Cs activity vs vintage". Until our study, with pre-existing γ spectrometers, the limit of detection was not low enough to infer the existence of such a curve or even to detect whatsoever.

In a first attempt in 2001, 29 Bordeaux wines spanning the years 1950 to 1998 were burned to ashes at 500°C. The ashes were put in plastic boxes on top of the Germanium detectors. In Fig. 5 we see on the left side the corresponding spectrum with two main γ lines at Eγ = 661 keV (^{137}Cs) and Eγ = 1461 keV (^{40}K). The ^{137}Cs activity values are plotted as a function of the vintage year on the right-hand side of Fig. 5. It revealed a strong dependence of the activity and the year the wine was made and bottled. Note that in this representation, P. Hubert et al decided to normalise all values to Jan. 1st, 2000, taking into account the half-life of ^{137}Cs (30.1 y). This means that the maximum activity recorded for a 1964 wine was a little bit more than double the value shown on the plot.

This was a remarkable result, but it meant destroying the bottle content, which is hardly the best authentication method for valuable wines. The idea was then to let the bottle untouched and to measure it directly. Fig. 4 shows the two possibilities of doing so. On the right, a bottle (0.75 l) and a magnum (1.5 l) are shown together to emphasise the fact that different bottle sizes can be examined. By lowering the floor shielding, one can measure even Imperial bottles (6 l). For the real experiment, only one bottle is measured at a time. Another possible setup is to lay horizontally the bottle on top of the detector. This method has the advantage that the bottle and the wine remain intact. A drawback are that the glass itself, although not thick enough to stop the γ-ray of ^{137}Cs, is radioactive: ^{40}K and U/Th/Ra which induce a rise in the background of the spectrum. Another fact is that, because of geometry reasons, the detection efficiency is de facto lower than with a small vessel containing ashes.

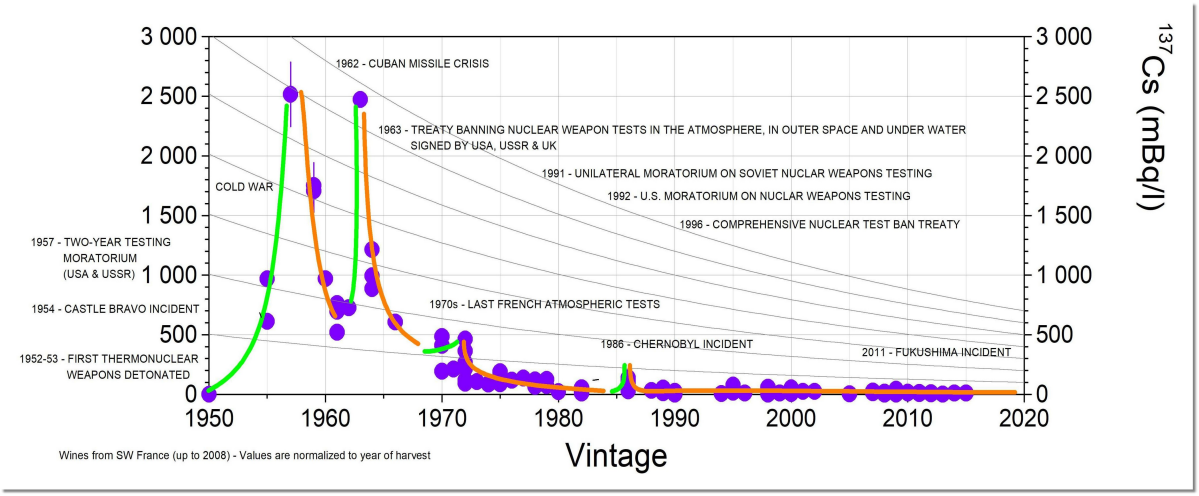

Fig. 6: Cs-137 content in wines from years 1950 to 2016. All activity values are for the corresponding vintage year. Green and orange lines are line-guides for the respective growth and decay tendencies. Comments on the figure report to above-ground tests, incidents and relevant political events.

Wines from 1929 to nowadays have been since measured this way. The latest, updated, curve is shown in Fig. 6. To stay away from normalising the data points at a given date, all reported and plotted values are now given for the respective vintages. Abacus curves allow one to take into account ^{137}Cs decay along the passing years. Relevant political events and incidents like the Castle Bravo and the Chernobyl ones are indicated on the plot. The rise and fall of the curve is a very good remembrance of those events. Fig. 6 is for the Northern Hemisphere. Just a couple of bottles from the Southern Hemisphere has been measured, but there is some renewed interest in doing the same work notably for Australia(e.g. for wines from the Barossa Valley) where fall-outs were a result of British tests above ground in the 1950s.

In 1986, the Chernobyl incident lead to a surge of the radioactivity levels. The closest the wine region was from Chernobyl, the greater was the increase. Fig. 6 is mainly based on SW France wines, and the "Chernobyl" peak is somewhat small. But we have measured French wines from Alsace and Corsica, two French regions several hundred miles east of Bordeaux with values of the order of 1 Bq/l instead of 0.1 Bq/l.

In 2011, the Fukushima incident released radioactive elements in the environment. The "cloud" crossed the Pacific Ocean all the way to Northern California. The nuclides deposition on the Weast Coast was minute. Nonetheless it was interesting to see if we could measure any variation of the ^{137}Cs level in California wines at that time. First measurements with unopened bottles were not conclusive and could only give limits of detection. But returning to the ash-producing methods allowed to see some increase of ^{137}Cs content for wines from 2011 and 2012. This is very preliminary and needs further investigation to confirm or not these findings [5].

3.3 Limits of the ^{137}Cs dating method

In some cases, dating a wine by the measurement of the ^{137}Cs content is out-of-reach. One cannot date this way young wines and wines from before the time of nuclear tests above the ground. For pre-1950 wine, there should be no ^{137}Cs in the wine and therefore no way to date it. For the recent wines, one can check if the alleged vintage year is compatible with the radioactivity content. In both cases one needs added tests, using other radionuclides like ^{210}Pb, ^{14}C, Tritium or even ^{90}Sr.

Fig. 7: [left] 1787-1789 "Thomas Jefferson bottles" (fake, measured at the LSM). [middle] Series of 1900 Château Lafitte bottles which had various levels of ^{137}Cs activity. [right] A magnum bottle of 1945 Mouton-Rothschild being investigated.

4 A Tool to Fight Counterfeited Wines

Since a wine dating from the pre-atomic era cannot contain ^{137}Cs, finding traces of this radioisotope in a bottle of wine assumed to be from before the 1950s has only one explanation: the wine has been tampered and younger or much younger wine has been poured in the bottle. This is being used to fight counterfeiters who brought to the market alleged vintage wines which are fake ones. These crooks have been very efficient have been on the market for the last 30 years, while famous rare wines reached astronomical prices in prestigious auction sales as well as through wine outlets. We have worked with several investigators, private and public, and testimonied as experts at the New York Court of Justice. To state a few cases, one involved the four so-called "Thomas Jefferson" bottles (Fig. 7). The complete story is to be found at Ref. [6]. Others cases stemmed from the sudden profusion of fine 1945 Mouton Rothschild bottles and magnums, as well as from other vineyards, on auction sales worldwide.

In Fig. 8 we see some examples of γ-ray spectra of fine wines. In all cases, since the bottles are untouched, the spectra combine the measured radioactivities of bot the glass of the bottle and the wine. Therefore, at 665 keV one always have a lline due to ^{214}Bi which is contained in the glass. On the left side, two bottles of 1942 Petrus wine: ^{137}Cs is present in one case, not in the other. Clearly the former is a counterfeited wine. Underneath, a 1964 Fronsac red wine exhibits a large ^{137}Cs line as expected and it is used as a reference bottle. On the right part of Fig. 8, four bottles of red Mouton wine from the 19$^{\text{th}}$ Century (from 1853 to 1896) have been tampered with...

Since 2009, we have service-delivery activities performed at PRISNA by a Technical Unit (PRISNA Prestations) which benefits from technology transfers from our proof-of-concept studies, and has a wide panel of public and private clients. This has allowed to clean up the market and to encourage the actors in this domain to engage a quality approach including traceability. PRISNA Prestations is equipped with its own high-purity low-background Germanium detector and can deliver results in the frame of several European legal accreditations.

5 A last word

The amount of radiation present in all the wine tested is too small to harm a person's health. For more details on the original work which lead to ^{137}Cs dating method, please refer to [7, 8].

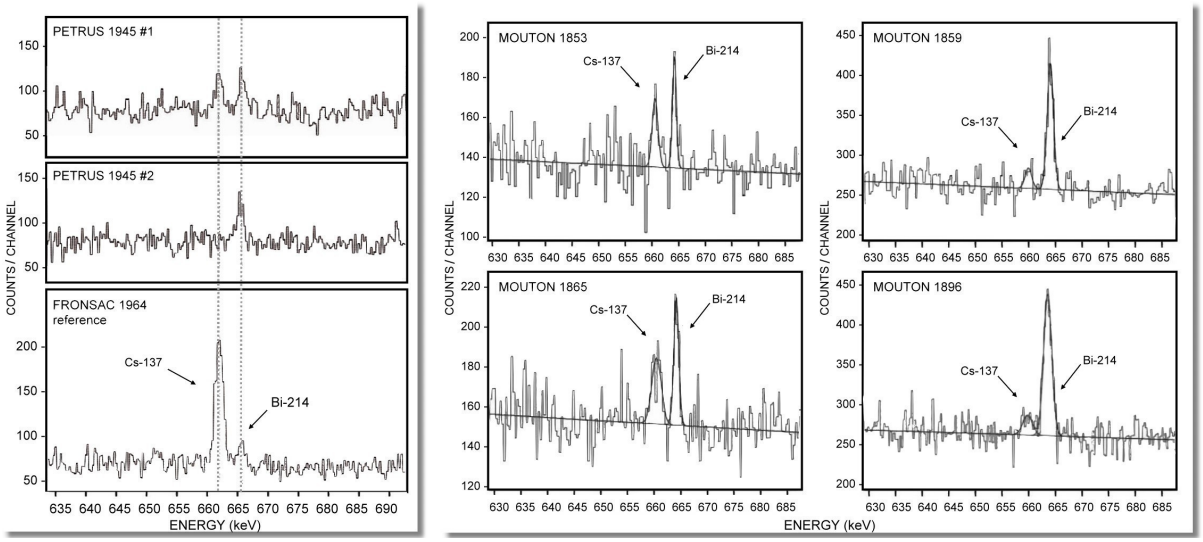

Fig. 8: [left] Two Petrus 1945 bottles from the same year: one is fake, one is genuine. The Fronsac 1964 bottle is used as a reference. [right] A series of 19th Century Mouton bottles, wines dating between 50 and 100 years before man-made ^{137}Cs appeared on Earth! These are fake wines. As usual, ^{214}Bi is always present and stems from the glass of the bottle.

Acknowledgments

The authors wish to acknowledge the work of the the staff of Canberra with whom we developed the γ-ray detectors. Many thanks to the Conseil Interprofessionnel des Vins de Bordeaux (CIVB) for their support. We are grateful to Christine Marquet of the CENBG neutrino group, spokesperson of the SuperNEMO International Collaboration, for the information about the SuperNEMO demonstrator.

References

[1] S. Kaufman and W.F. Libby. The Natural Distribution of Tritium. Phys. Rev. 93, 1337-1344 (1954)

[2] P. Hubert, F. Hubert, H. Ohsumi, J. Gaye, B. Médina et J.-M. Jouanneau. Application de l'analyse par spectrométrie gamma bas bruit de fond à la datation des vins d'origine française. Ann. Fals. Exp. Chim., 957, 357-368 (2001)

[3] M. S. Pravikoff, P. Hubert, H. Guégan. Natural Radioactivity Measurements Applied to the Dating and Authentication of Edible Meat. arXiv:1806.10455 [physics.pop-ph] (2018)

[4] M. S. Pravikoff, C. Marquet, P. Hubert. Environmental Lead-210 gamma-ray measurements in brain tumors. arXiv:1806.09539 [physics.med-ph] (2018)

[5] M. S. Pravikoff and P. Hubert. Dating of wines with Cesium-137: Fukushima's imprint. arXiv:1807.04340 [physics.pop-ph] (2018)

[6] Davia Nelson and Nikki Silva. How Atomic Particles Helped Solve A Wine Fraud Mystery. https://www.npr.org/sections/thesalt/2014/06/03/318241738/how-atomic-particles-became-the-smoking-gun-in-wine-fraud-mystery (2014)

[7] P. Hubert, F. Hubert et V. Raffestin-Tort. La datation des vins : une application des mesures des très faibles radioactivités. Le Bup (1) n°862, Vol.98, pp. 281-394 (2004)

[8] P. Hubert, F. Perrot, J. Gaye, B. Médina, M. S. Pravikoff. Radioactivity measurements applied to the dating and authentication of old wines. Comptes Rendus Physique, Elsevier Masson, 10, 622-629 (2009)

Perspectives on Neutron Capture Therapy of Cancer

I. Porras, J. Praena, F. Arias de Saavedra, M.P. Sabariego, M. Pedrosa, F. Ogállar, P. Torres-Sánchez
Department of Atomic, Molecular and Nuclear Physics, University of Granada, Granada, Spain.
C. Ruiz-Ruiz, M.J. Ruiz-Magaña.
Department of Molecular Biology III and Inmunology, University of Granada, Granada, Spain.

Abstract
Boron Neutron Capture Therapy (BNCT), which is a promising experimental form of radiotherapy, is facing a new era with renewed projects and under very active research. In this paper, some advances that are expected in the near future for this therapy are reviewed.

1 Introduction

Neutron Capture Therapy is an experimental form of radiotherapy which has the unique feature of delivering the radiation dose selectively at cellular level. It is based upon the induction of a nuclear reaction inside the target cell which produces charged particles delivering a huge amount of energy locally. Neutrons are used for their ability of inducing these reactions. The only isotope used as target in all clinical trials has been ^{10}B, because of its large cross section in the low energy range and because most of the energy of the reaction is delivered in the form of charged particles:

$$n + {}^{10}\mathrm{B} \rightarrow {}^{7}\mathrm{Li} + \alpha + 2.79\ \mathrm{MeV}\ . \qquad (1)$$

In 96% of the captures, the nucleus ^{7}Li is left in its first excited state and the emission of a 478 keV gamma ray follows. The resulting alpha particle and recoil nucleus are particles of a high linear energy transfer and therefore a higher biological effectiveness than conventional radiotherapy. Furthermore the products of the reaction have a very short range (a few micrometres), so they usually deliver all their kinetic energy inside the target cell, as the typical cell dimension is of 10 μm, not affecting the surrounding cells. For these features this isotope has been used, giving name to this therapy as Boron Neutron Capture Therapy (BNCT).

Therefore, this therapy requires a compound which selectively delivers boron atoms to the tumour cells in order to kill them sparing the nearby healthy ones. The compound should be non-toxic at the quantities required and present a selective uptake by the tumours with respect to the surrounding healthy tissue. These features had been empirically found to be fulfilled by a borated amino acid, *boron phenylalanine* (BPA) for different malignancies. With these features, BNCT is especially suited for the treatment of disseminated tumours in critical organs, or for local recurrences already treated with radiation, having reached the dose limit of conventional radiation. Precisely these cancers are among those of worst prognosis, and conventional therapies are not effective for their treatment.

The first idea of a BNCT dates back to 1936 when Gordon L. Locher, just a few years after the discovery of the neutron [1], hypothesized that, if boron could be concentrated on tumour, and this volume would be exposed to thermal neutrons, the tumour would absorb more dose than the surrounding healthy tissue. The first BNCT clinical trials were done for brain tumors in the 50's by W.H. Sweet [2] from the Massachusetts General Hospital and collaborators from the Massachusetts Institute of Technology (MIT) and Brookhaven National Laboratory (BNL) using a thermal beam from a research reactor at BNL with several boron compounds [3]. Although they were not as successful as

desired, addressed to the insufficient selectivity of the compounds used, they opened a research field for which great advances could be expected (see a captivating dedication in Ref. [4]). Then, H. Hatanaka, who participated in these studies as a Fulbright Scholar, developed in Japan a strong BNCT programme [5] introducing a new compound, sodium borocaptate ($Na_2B_{12}H_{11}SH$, called BSH) recently synthesized by A.H. Soloway and coworkers [6]. A strong limitation of those early clinical trials was the poor penetrability of thermal neutrons, which required the use of intraoperative techniques for reaching deep seated tumors. A major advance in the field happened some years later when the group of Y. Mishima introduced a more selective compound, the previously mentioned BPA [7], and more energetic neutron beams, in the epithermal (up to 10 keV) range were achieved from the research reactors [8]. This allowed delivering the neutrons, thermalized inside the body, to deeper regions while delivering less radiation dose at the surface.

Since then, in the 1990, new clinical trials started of what can be called “modern BNCT” in different countries, specially Japan, USA, Finland, the Netherlands, Sweden, Argentina, Italy, the Czech Republic and Taiwan (see reviews of clinical trials in Ref. [9] and in the bibliography). They have been applied for cancers of bad prognosis. Most of the protocols have been focused on brain tumours such as Glioblastoma Multiforme (GBM) [10-24], and recurrent head and neck cancers [25-29]. In addition to this, trials for malignant melanoma have been performed [30], for the treatment of multiple metastases in the liver by extracorporeal irradiation [31] and very recently trials for lung cancer have started [32].

In all of these clinical trials the neutron beam came from research reactors, because they were the only possibility of delivering a neutron flux of the intensity required (at least 10^9 neutrons/s cm^2). The clinical results have been quite promising. In the NUPPEC report of 2014 [33], a statistical study of different clinical trials shows a 5-year survival rate of more than 10% after BNCT for the GBM, much higher than conventional therapies for which is of a few percent. Even larger is the survival reported for the head and neck cancers, in which for many cases a complete response after BNCT follows. The adverse effects are usually of a low grade, which remit within a few days, while the symptoms of the disease itself, often very severe, are reduced drastically [27].

In spite of these promising results of BNCT, there is a line of active research throughout the world for improvements. This field is a paradigm of interdisciplinary research, where physicists, engineers, biologists, chemists, pharmacologists and of course medical scientists (oncologists, surgeons and other specialists) work in close connection in a problem which has different facets. There are possible avenues for improvement in most of these aspects. The aim of this talk is to present some of the research problems actually being under study and development for the improvement and expansion of this promising therapy, and it will be more focused on those related to physics.

2 Perspectives for the future of BNCT

Along these lines, some problems of active research which may contribute to the improvement of BNCT and its widespread presence as an option for cancer therapy will be presented.

2.1 Accelerator-based neutron sources (ABNS)

In spite of the promising outcome of the therapy, and because of the few cases treated (in the order of just a thousand, including all clinical trials in- and out-protocols) BNCT requires more experimentation (ideally randomized clinical trials) for becoming an actual option widely accepted. A strong limitation in the widespread of these clinical trials comes from the neutron source. Up to now, only research reactors had been used for the clinical trials. These are relatively scarce nuclear facilities, old and far from the hospitals. Some of the facilities used for the clinical trials are now closed. It is difficult that new initiatives of this kind come out from private or even public sources, because of their cost and other drawbacks, just for an experimental therapy. However, the advancements in the

technology of high intensity, compact particle accelerators have opened the way to in-hospital BNCT facilities which will allow to an increased number of trials.

Table 1: Projects of Accelerator-based BNCT facilities worldwide. Updated from Ref. [34]

Institute	Accelerator	Beam energy	Intensity	Reaction	Max. n energy	Ref
Kyoto Univ, Japan (in clinical trials)	Cyclotron	30 MeV	1 mA	^{9}Be(p,n)	28 MeV	[35]
Helsinki Univ. CH, Finland	Electrostatic (Hyperion)	2.6 MeV	30 mA	^{7}Li(p,n)	0.89 MeV	[36]
Budker Institute, Novosibirsk, Russia	Vacuum insulated Tandem	2 MeV	2 mA	^{7}Li(p,n)	0.23 MeV	[37]
IPPE Obninsk, Russia	Cascade generator KG-2.5	2.3 MeV	3 mA	^{7}Li(p,n)	0.57 MeV	[38]
Birmingham Univ., UK	Electrostatic (Dynamitron)	2.8 MeV	1 mA	^{7}Li(p,n)	1.1 MeV	[39]
Tsukuba Univ., Japan	RFQ-DTL [a]	8 MeV	10 mA	^{9}Be(p,n)	6.1 MeV	[40]
CNEA Bs. As., Argentina	Tandem Electrost. Quadrupole	1.4 MeV 2.5 MeV	30 mA 30 mA	^{9}Be(d,n) ^{7}Li(p,n)	5.7 MeV 0.79 MeV	[41]
INFN, Italia	RFQ [a]	5 MeV	50 mA	^{9}Be(p,n)	3.1 MeV	[42]
SOREQ, Israel	RFQ-DTL [a]	4 MeV	2 mA	^{7}Li(p,n)	2.3 MeV	[43]
LBNL, USA	Electrostatic Quadrupole	2.5 MeV	50 mA	^{7}Li(p,n)	0.79 MeV	[44]
NCC, Japan	RFQ [a]	2.5 MeV	20 mA	^{7}Li(p,n)	0.79 MeV	[45]
Nagoya Univ., Japan	Electrostatic (Dynamitron)	2.8 MeV	15 mA	^{7}Li(p,n)	1.1 MeV	[46]

[a] RFQ stands for Radio Frequency Quadrupole and DTL for Drift Tube Linac.

In Table 1 a list of projects ongoing or just finished is displayed. The only one which has already started clinical trials is C-BENS at the Kyoto University Research Reactor Institute (KURRI). The most popular reaction is ^{7}Li(p,n), because of the rapidly increasing of the cross section from the threshold at 1.880 MeV and the relatively low energy of the neutrons obtained, which require less moderation for reaching the epithermal range.

2.1.1 The optimal neutron energy for BNCT

Keeping into mind that the most suitable energy for BNCT may depend on the depth and size of the tumour, we will study which is the best range of energies in order to deliver to the tumour as much dose as possible in the widest range and higher than the maximum dose delivered to normal tissue. The advantage of BNCT is that there are two different depth dose distribution for the tumour and the normal cells, assuming that they uptake the boron compound differently. In Figure 1, left panel, we illustrate, by means of a Monte Carlo simulation, the depth dose profile in a standard ICRU 4-component tissue phantom, of a 10 keV monoenergetic neutron source of 10^{10} n/s cm^{2}, for both tumour and normal cells, assuming typical concentrations of boron of 35 ppm for the former and 10 ppm for the latter.

As a matter of fact, this physical dose is not the quantity to be used for quantifying the BNCT treatment, it is the so-called biological or weighted dose instead, which is believed to represent the

dose from conventional radiation (photons) producing the same biological effect. As the dose in BNCT is delivered by a mixed radiation field (mixture of different secondary particles which have different values of the LET), the dose is decomposed in individual contributions which must be weighted differently according with their biological effectiveness. The following formula is used to estimate this weighted dose:

$$D_W = w_f D_f + w_t D_t + w_B D_B + w_\gamma D_\gamma \ . \tag{2}$$

The values of D_W, when the individual dose terms are in Gy (J/kg), are expressed as Gy-Eq. The different terms are: D_f, the so-called fast dose, which includes contributions from neutrons above 0.5 eV and it is dominated by the recoiling nuclei in elastic scattering (mostly hydrogen, for which the cross section is larger); D_t, the thermal dose, denotes the local dose contribution from neutrons below 0.5 eV excluding boron captures and it is dominated by the protons emitted in the capture reaction by nitrogen (sometimes it is called nitrogen dose); D_B, is the dose delivered by the heavy charged particles from the reactions with boron, and the gamma dose D_γ includes the contribution of all secondary photons (mainly 2.224 MeV photons from hydrogen captures). These four contributions are illustrated separately in Figure 1 for an example case of 10 keV neutrons. The values commonly used for the weighting factors in BNCT clinical trials are $w_f = w_t = 3.2$, $w_B = 1.3$ (normal tissue) and 3.8 (tumour), and $w_\gamma = 1$ [13], and they reflect the differences between the biological effectiveness of the different mechanisms of interaction.

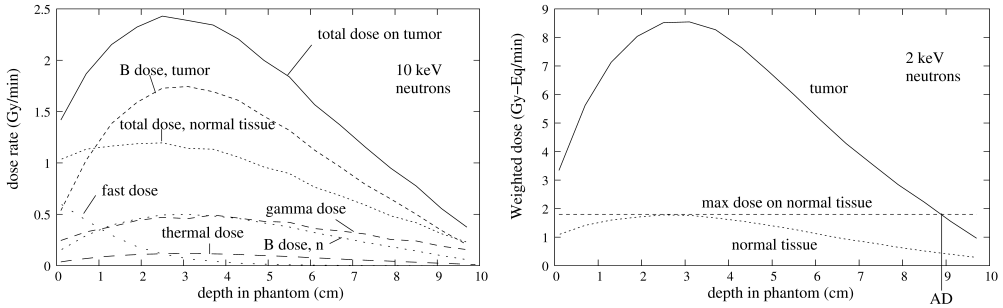

Fig. 1: (left) Dose components as a function of depth for 10 keV neutrons, (right) weight dose total dose at tumour and normal tissue as a function of depth for 2 keV neutrons.

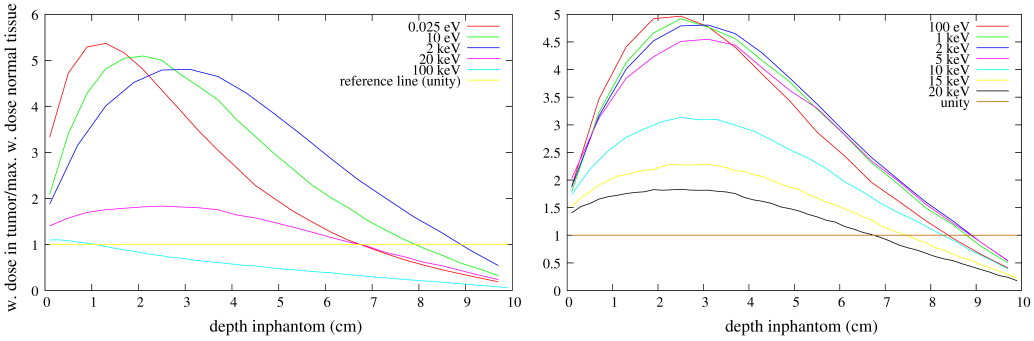

Fig. 2: Ratio between the weighted dose at tumour and the maximum dose in normal tissue as a function of depth, (left) for some energies in a wide range, and (right) for energies in a shorter epithermal range.

Therefore for estimating the optimal energies we evaluate the values of the weighted dose for different monoenergetic beams, which are also illustrated in Figure 1 (right panel) for the energy of 2 keV, where we observe that up to near 9 cm (called advantage depth, AD) the dose on tumour exceeds the maximum dose in healthy tissue. This is the optimal energy as it is illustrated in Figure 2, where plots of the ratio between the weighted dose at tumour and the maximum dose in healthy tissue are

displayed for different neutron energies. It is interesting to note that for neutrons between 100 eV and 15 keV there is a region in which the dose delivered to the tumour is more than twice the maximum dose delivered to the normal tissue. Above these, the dose in normal tissue at the surface increases rapidly, and below, the beam penetrability becomes too low. Nevertheless, for superficial tumours a thermal beam is quite adequate.

The accelerator-based neutron source may in principle provide beams which require less moderation than the beams from reactors, which contain neutrons up to several MeV. However, what is called a beam shape assembly is required in order to obtain a flux mainly in the epithermal range. Different materials as MgF_2, Al, LiF, AlF, D_2O, BeO, MgO, Al_2O_3, Teflon® or Fluental® or combinations of them have been proposed for this purpose [47-50].

2.1.2 Other considerations

The development of these facilities will probably lead to a new era for BNCT. It is worth mentioning that the list of planned facilities is larger than the list of facilities used for clinical trials since 1950 up to now, suggesting a future expansion of BNCT.

The possibility of performing other applications with the high current accelerators required by BNCT may further stimulate the development of new facilities, as e.g. medical isotope production in the same site. F. Arias de Saavedra et al. [51] calculated that with an accelerator of this kind isotopes for PET as ^{11}C, ^{13}N and ^{15}O can be produced in comparable quantities to those obtained from current cyclotrons. These isotopes, due to their short life, have to be produced in the same place to be used.

2.2 New compounds and isotopes

2.2.1 Boron nanoparticles for BNCT

The outcome of a BNCT treatment depends critically on the selective uptake of boron atoms by the tumour cells. Therefore, active research is being done toward the development of new boron carriers which may increase the boron tumour uptake (see the recent review in Ref. [52]). Specially, BNCT can benefit from the strong activity that is being carried out in the synthesis of nanoparticles for tumour targeting. Nanoparticles of the size of tens of nanometres can carry many atoms to the tumour cell, and are very promising for this purpose by means of the so-called *Enhanced Permeation and Retention effect*. The tumour vasculature, which is not as structured as that of healthy tissue due to its rapid growth, presents fenestrations in which nanostructures of tens of nanometres can enter, and they are retained because the lymphatic drainage is also compromised [53]. Also, nanoparticles can be designed for active targeting, i.e. can be functionalized by specific ligands such as monoclonal antibodies that can attach antigens overexpressed by the tumour cells (see the review of H. Nakamura in the book of the bibliography). A major breakthrough of BNCT can be expected from the development of these new agents.

2.2.2 Other isotopes for BNCT

The study of other isotopes of elements that may react with neutrons and could be selectively uploaded in tumours may help synergistically to BNCT because an additional dose would be produced at the tumour with the same neutron field, i.e. keeping the dose in healthy tissue low.

2.2.2.1 ^{33}S as a cooperative capturer for BNCT

With this aim, an isotope of sulphur, ^{33}S, was studied recently as a potential target for neutron capture therapy [54-57], the reason being the much stronger biological role that sulphur compounds present respect to boron ones. Sulphur is an essential component of life cells, and it has been observed much enhanced sulphur levels in a wide range of tumour types, reaching concentrations of a part per

thousand, which can be addressed to an enhanced synthesis of glutathione, essential for cell growth, by the tumour cells. This suggests the feasibility of incorporating ^{33}S-enriched compounds selectively to the tumour cells via the essential sulphur-containing amino acids. ^{33}S has the feature of capturing neutron via the (n,α) reaction with no gamma emission, and the Q-value (3.5 MeV) is larger than the one for the boron reaction. Only data at the resonance region was available for this isotope, and an important resonance in the epithermal range (at 13.5 keV) motivated the studies mentioned. However, discrepancies between experimental data for this resonance and the lack of data below 10 keV motivated two 7measurements led by J. Praena and M. Sabaté-Gilarte at the two experimental areas of n_TOF (CERN) [58-60]. These were the first experiments of a (n,α) reaction at this facility and were challenging measurements that were performed successfully with a new method of sample production [61] and the use of in-beam gaseous Micromegas detectors. From these studies it is concluded that for a beam of the resonance energy, ^{33}S can be a cooperative capturer of boron for neutron capture therapy, enhancing the tumour dose at small depths [62].

2.2.2.2 Gd-NCT

Since the 80's, they have been studies of gadolinium compounds for neutron capture therapy [63]. The reason is that the isotope ^{157}Gd has the highest thermal neutron capture cross section of the stable isotopes (259000 b.). Although the reaction is the radiative capture (n,γ), which means that most of the energy is released by gamma emission, which delivers dose non-locally, it has been observed from in vitro studies a strong killing effect in tumour cells, caused by the short-range Auger and internal conversion electrons emitted [64]. For this interest, among others, the neutron capture reaction of ^{157}Gd has been recently measured by C. Massimi, M. Mastromarco and coworkers at n_TOF [65].

As the ratio between tumour and normal tissue has been estimated to be below those of BNCT with BPA [66], the future of GdNCT, both by itself or in combination with BNCT, may come from successful DNA-bound Gd compounds that may fully exploit the strong damage of Auger electrons in the nanometre range.

2.3 Reducing uncertainties in treatment planning

In a BNCT clinical trial performed in Helsinki, it was studied the survival of patients separated on two cohorts which received a slightly different dose in the planning tumour volume [20]. The survival was much higher in those receiving a higher dose. The dose in BNCT is delivered with a large safe margin with respect to the maximum tolerable dose for the healthy tissue, which has important uncertainties. Reducing these uncertainties may allow to increase the irradiation time and to improve substantially the efficacy of the treatments. The International Commission on Radiation Units (ICRU) recommend for all kinds of radiotherapy keeping the uncertainties of every step of the planning below 5%. In the case of neutrons, the nature of the procedure and the complexity of the interactions make this a challenging goal. We will talk about some research towards reducing those sources of uncertainty more related to nuclear facilities, skipping others that can be important such as the boron concentration in the tumour and the different surrounding organs in patients, which are not related to physics.

2.3.1 Nuclear data for BNCT

With respect to the neutron interactions, there are nuclear data which are required with accuracy for the Monte Carlo simulations performed for the treatment planning. In Figure 3, we illustrate the partial contributions to the dose delivered to brain by epithermal neutrons for the main contributing individual neutron interactions. Apart from the aforementioned capture reaction from ^{14}N, it is worth to note the role of ^{35}Cl, which is present in 0.3% in brain and may account for more than 10% of the dose on healthy tissue. Neutron cross sections for the reactions with both isotopes are not well known, and the scarce data present strong discrepancies. For this reason, the n_TOF collaboration at CERN performed recently measurements of the cross sections for the reaction ^{14}N(n,p) and ^{35}Cl(n,p) simultaneously at

EAR-2 with Micromegas and DSSSD detectors (see proposal in [67]), and for the ^{35}Cl(n,γ) at EAR-1 with liquid C_6D_6 scintillators [68], which are currently being analysed. They will provide data for more accurate Monte Carlo of the dose delivered in healthy tissue, which is the limiting factor in radiotherapy.

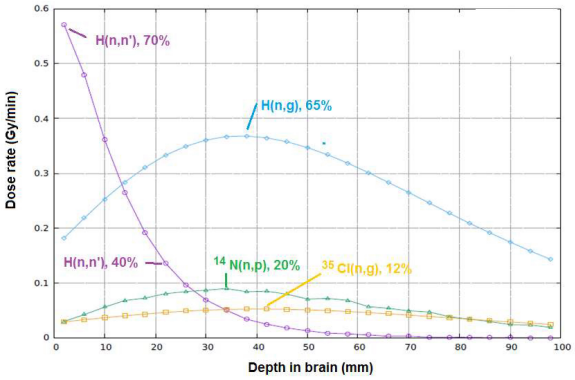

Fig. 3: Plot of the main components of the dose by individual neutron interactions as a function of depth. At some points it is displayed the percentage of the total dose due to that particular process.

2.3.2 Radiobiology of BNCT

A major source of uncertainty in BNCT treatment planning is the radiobiological data. As it has been mentioned, weighting factors are used for comparing the different dose components by means of their biological effect and in order to predict the effect of the total dose itself (both at the tumour and at the surrounding organs). This must be done by estimating the corresponding dose from conventional radiation, where there is a lot of clinical experience, producing the same effect. The use of Eq. (2) with the factors given below has arisen some debate. First, the values of the weighting factors themselves comes from a relative scarce set of radiobiological measurements, where the contamination from photons on the neutron beam is usually very large and makes difficult the determination of the pure neutron effect. Second, the effect of thermal and fast neutrons was difficult to separate from each other, and they were assumed to be equal for the beams from research reactors, but this could not be the case for different spectra as those expected from ABNS. Third, the biological effect of the photon dose is not linear with the dose, what is assumed implicitly in Eq. (2). This effect is better described by means of the linear-quadratic (LQ) model, which should at least be taken into account for this component and for the reference photon irradiation dose to be compared with. In this way, it has been proposed to estimate the effect of a BNCT treatment via the photon isoeffective dose [69]. The simplest way to take this into account in first approximation leads to a different equation to substitute Eq. (2), i.e.

$$D_0 + \frac{D_0^2}{\alpha/\beta} = w_f^* D_f + w_t^* D_t + w_B^* D_B + w_\gamma^* \left(D_\gamma + \frac{D_\gamma^2}{\alpha/\beta} \right), \qquad (3)$$

where D_0 , which is the quantity to be obtained, denotes the photon iso-effective dose, the α/β ratio is a well known tissue-dependent radiobiological parameter of conventional radiotherapy, and the w^* are new weighting factors that have to be determined from radiobiology experiments. The thermal factor w_t^* is a key factor because it is universal, while the w_f^* will depend on the spectra to be used in the BNCT treatment and should be determined for each facility. Our group has recently started a series of radiobiological measurements for determining this factor for different cell lines (both from tumours and healthy tissue) at the cold neutron PF1b line of the Institute Laue-Langevin (ILL, Grenoble, France) [70]. This is a perfect line for the absence of gamma contamination, which allows observing the pure neutron cell damage. The presence of culture medium (which contains hydrogen) in the target of cells produces indirect gamma and has to be minimized, but it can be enlarged to perform

simultaneous measurements of the gamma weighting factor, as it is produced by the same gamma rays. Also the boron weighting factor can be obtained from the irradiation of cells previously treated with boron and new boron compounds are being studied by the direct observation of cell survival after irradiation and compared to BPA. Finally, a measurement of the fast dose weighting factor from an ABNS has been the subject of a dedicated measurement at a neutron source from a lithium target at 1912 KeV from the TANDEM accelerator in the Centro Nacional de Aceleradores (CNA, Seville, Spain). These data, which are in the analysis phase, will bring more light to the relative uncertain estimations of the biological dose.

2.3.3 Treatment Planning Systems for BNCT

As BNCT has been an experimental therapy, there are no commercial treatment planning computer systems available. Dose calculations of neutrons in tissue are very complicated and all the clinical trials have been performed according to estimations performed by means of Monte Carlo simulations. The main codes employed have been NCTplan [71], JCDS [72], SERA [73], and THORplan [74]. Most of the codes were designed for the treatment of brain tumours with research reactors and make use of old cross section data. It is of great interest the development of new dose calculation planning systems adapted to import directly medical image data from the most recent techniques and to make use of updated cross section data. It is very important to realize that neutron dosimetry depends crucially not only on the concentration of different elements (and their isotopic percentages), in spite that they have similar Z value, but also on the cross section data in the low energy range.

There has been recently a strong progress in the development of interfaces for Monte Carlo simulation codes for other medical physics applications, mainly for proton and heavy ion therapies. Adapting those interfaces to the peculiarities of BNCT is an objective which will lead to better treatments. As mentioned, in BNCT, there are different dose components which have to be weighted differently in order to determine the photon isoeffective dose. The resulting interface should be able to, from DICOM medical images, construct by means of voxels or predefined bodies the geometry of the patient and perform fast calculations of isodose curves, depth-dose functions and dose-volume histograms. Special caution must be paid to the compositions of the different tissues, to which the neutron dose is very sensitive. Neutron spectra and directions can be incorporated via the phase space distribution, but for the ABNS it can be studied also incorporating the neutron production to the simulation code via MC calculations from the original proton or deuteron beam, incorporating the beam shape assembly of the neutron source in the geometry of the simulations.

3 Concluding remarks

BNCT is a promising therapy for tumours of very bad prognosis which is under active research from their different multidisciplinary aspects. The construction of in-hospital facilities will bring BNCT closer to the medical practice and will increase the clinical experience. The continuous incorporation of the results of BNCT basic research in the new clinical trials will probably lead to an improved therapy option against some of the worst types of cancer.

Acknowledgements

The author wishes to thank the sponsors of the research: Spanish Government, Regional Government of Andalucía, the Spanish Association Against Cancer (AECC) and the Spanish ACS Foundation, and the organizers of this conference for the kind invitation to participate in it.

References

[1] G.L. Locher, *Am. J. Roentgenol. Radium Ther.* **36** (1936) 1.

[2] W.H. Sweet, *N. Engl. J. Med.* **245** (1951) 875.

[3] L.E. Farr *et al., Am. J. Roentegenol.* **71** (1954) 279.

[4] R.F. Barth and A.H. Soloway*, Int. J. Radiat. Oncol. Biol. Phys.* **28** (1994) 1057.

[5] H. Hatanaka, *J. Neurol.* **209** (1975) 81.

[6] A.H. Soloway, H. Hatanaka and M.A. Davis, *J. Medicinal Chem.* **10** (1967) 714.

[7] Y. Mishima *et al., Strahlenther Onkol.* **165** (1989) 251.

[8] International Atomic Energy Agency, IAEA-TECDOC-1223 (2001).

[9] R.F. Barth, *et al., Radiat. Oncol.* **7** (2012) 146.

[10] M. Chadha *et al., Int. J. Radiat. Oncol. Biol. Phys.* **40** (1998) 829.

[11] W. Sauerwein and A. Zurlo, *Eur J Cancer.* **38** (2002) S31.

[12] V. Dbaly *et al*., *Cesaslov Neurol Neurochir.* **66** (2002) 60.

[13] H. Joensuu *et al., J. Neuro-Oncol.* **62** (2003) 123.

[14] T. Yamamoto *et al., Appl. Radiat. Isot.* **61** (2004) 1089.

[15] S-I. Miyatake *et al., J. Neurosurg.* **103** (2005) 1000.

[16] S. Kawabata *et al., J. Radiat. Res. (Tokyo)* **50** (2009) 51.

[17] S-I. Miyatake *et al., J. Neuro-Oncol.* **91** (2009) 199.

[18] Y. Nakagawa *et al., Appl. Radiat. Isot.* **67** (2009) S27.

[19] S. Kawabata *et al., Appl. Radiat. Isot.* **69** (2011) 1796.

[20] L. Kankaanranta *et al., Int. J. Radiat. Oncol. Biol. Phys.* **80** (2011) 369.

[21] K. Nakai *et al., Appl. Radiat. Isot.* **69** (2011) 1790.

[22] T. Yamamoto *et al., Appl. Radiat. Isot.* **69** (2011) 1817.

[23] H. Aiyama *et al.*, *Appl. Radiat. Isot.* **69** (2011) 1819.

[24] S-I. Miyatake *et al., Neuro Oncol.* **15** (2013) 650.

[25] I. Kato *et al., Appl. Radiat. Isot*. **61** (2004) 1069,

[26] I. Kato *et al., Appl. Radiat. Isot.* **67** (2009) S37.

[27] L. Kankaanranta *et al*., *Int. J. Radiat. Oncol. Biol. Phys.* **82** (2012) e67.

[28] L. Kankaanranta *et al.*, *Radiother Oncol.* **99** (2011) 98.

[29] L.W. Wang *et al., Appl. Radiat. Isot.* **69** (2011) 1803.

[30] P.R. Menéndez *et al*., *Appl. Radiat. Isot.* **67** (2009) S50.

[31] A. Zonta *et al*., *Appl. Radiat. Isot*. **67** (2009). S67.

[32] M. Suzuki *et al.*, *Int. Canc. Conf. J.* **1** (2012) 235.

[33] Nuclear Physics European Collaboration Committee (NUPECC), *Nuclear Physics for Medicine Report,* 2014. http://www.nupecc.org/pub/npmed2014.pdf

[34] A.J. Kreiner et al., *Rep. Pract. Oncol. Radiother.* **21** (2016) 95.

[35] H. Tanaka et al., *Appl. Radiat. Isot.* **69** (2011) 1642.

[36] Yle News, https://yle.fi/uutiset/osasto/news/finland_to_debut_new_high-powered_reactor_for_cancer_treatment/10061298

[37] V. Aleynik et al., *Appl. Radiat. Isot.* **69** (2011) 1639.

[38] O.E. Kononov et al., *Appl. Radiat. Isot.* **61** (2004) 1009.

[39] S. Green et al., *Radiother. Oncol.* **102** (2012) S164.

[40] H. Kumada et al., *Appl. Radiat. Isot.* **88** (2014) 211.

[41] A.J. Kreiner et al., *Appl. Radiat. Isot.* **88**, (2014) 185.
[42] C. Ceballos et al., *Appl. Radiat. Isot.* **69** (2011) 1660.
[43] S. Halfon et al., *Appl. Radiat. Isot.* **69** (2011) 1654.
[44] B.A. Ludewigt et al., Development of an accelerator-based BNCT facility at the Berkeley Lab, University of North Texas Libraries (1998), digital.library.unt.edu/ark:/67531/metadc720376/
[45] Home page of CICS, Inc. http://www.cics.jp/nct/category_1.html
[46] Y. Kiyanagi, *Phys. Procedia* **26** (2012) 223.
[47] D.L. Bleuel et al., *Med. Phys.* **25** (1998) 1725.
[48] B.F. Bayanov et al., *Nucl. Instr. and Meth. in Phys. Res. A* **413** (1998) 397.
[49] D.A. Minsky, *Appl. Radiat. Isot.* **69** (2011) 1668.
[50] E. Musacchio González and G. Martín Hernández, *Nucl. Instr. and Meth. in Phys. Res. A* **865** (2017) 148.
[51] F. Arias de Saavedra et al., *Nucl. Instr. and Meth. in Phys. Res. A* **887** (2018) 50.
[52] R.F. Barth et al., *Cancer Commun (Lond).* **38** (2018) 35.
[53] H. Maeda et al., *J Control Rel*ease **65** (2000) Mar 271.
[54] I. Porras, *Phys. Med. Biol.* **53** (2008) L1.
[55] I. Porras, *Appl. Radiat. Isot.* **69** (2011) 1838.
[56] J. Praena et al., *Appl. Radiat. Isot.* **88** (2014) 203.
[57] I. Porras et al., *Nucl. Data Sheets* **120** (2014) 246.
[58] J. Praena et al., *Phys. Rev. C* **97** (2018) 064603.
[59] M. Sabaté-Gilarte et al., *Rep. Pract. Oncol. Radiother.* **21** (2016) 113.
[60] M. Sabaté-Gilarte et al., *Radiat. Prot. Dosim.* **180** (2017) 342.
[61] J. Praena et al., *Nucl. Instr. and Meth. in Phys. Res. A* **890** (2018) 142.
[62] M. Sabaté-Gilarte, Ph.D. Thesis, Univ. of Seville, 2017. http://hdl.handle.net/11441/61303
[63] R.F. Martin et al. *Int. J. Radiat. Biol.* **54** (1988) 205.
[64] B.H. Laster et al. *Acta Oncol.* **35** (1996) 917
[65] M. Mastromarco et al., 2018. https://arxiv.org/pdf/1805.04149
[66] J.T. Goorley, Ph.D. Thesis, MIT, 2002. http://hdl.handle.net/1721.1/30001
[67] J. Praena et al., CERN-INTC-2017-039 (2017).
[68] I. Porras et al., CERN-INTC-2018-010 (2018).
[69] S.J. Gonzalez and G.A. Santa Cruz, *Radiat. Res.* **178** (2012) 609.
[70] M. Pedrosa et al., ILL Experimental Report 3-07-369 (2017).
[71] R. Zamenhof et al., *Int. J. Radiat. Oncol. Biol. Phys.* **35** (1996) 383.
[72] H. Kumada et al., *Phys. Med. Biol.* **49** (2004) 3353.
[73] D.W. Nigg et al., *Trans. Am. Nuc. Soc.* **80** (1999) 66.
[74] T.-Y. Lin and Y.-W.H. Liu, *Appl. Radiat. Isot.* **69** (2011) 1878.

Bibliography

W.A. Sauerwein, A. Wittig, R. Moss and Y. Nakagawa (eds.), *Neutron capture therapy: principles and applications.* (Springer, Berlin, 2012).

The FOOT FragmentatiOn Of Target Experiment

M.Marafini and Others:

(10) Alexandrov Andrey; (11) Alpat Behcet; (11) Ambrosi Giovanni; (28,17) Argirò Stefano; (8) Battistoni Giuseppe; (2,21) Bisogni Maria Giuseppina; (2,21) Belcari Nicola; (4,20) Biondi Silvia; (4) Bruni Graziano; (2,21) Camarlinghi Niccolò; (2,21) Carra Pietro; (17) Cerello Piergiorgio; (2,21) Ciarrocchi Esther; (7) Clozza Alberto; (15,16) Colombi Sofia; (10,19) De Lellis Giovanni; (2,21) Del Guerra Alberto; (26,12) De Simoni Micol; (10,19) Di Crescenzo Antonia; (17,5) Donetti Marco; (8,23) Dong Yunsheng; (15) Durante Marco; (8) Embriaco Alessia; (3) Emde Max; (12,26) Faccini Riccardo; (28,17) Ferrero Veronica; (12,26) Ferroni Fernando; (11,24) Fiandrini Emanuele; (14) Finck Christian; (5,21) Fiorina Elisa; (22,12) Fischetti Marta; (2,21) Francesconi Marco; (4,20) Franchini Matteo; (21) Galli Luca; (4,20,1) Garbini Marco; (31) Gentile Valerio; (17) Giraudo Giuseppe; (3) Hetzel Ronja; (15) Hild Sebastian; (11) Ionica Maria; (11,24) Kanxheri Keida; (21) Kraan Aafke Christine; (5) Lante Valeria; (10,19) Lauria Adele; (15,16) La Tessa Chiara; (17,30) Lopez Torres Ernesto; (1,12) Marafini Michela; (8) Mattei Ilaria [1]; (4) Mengarelli Alberto; (26,12,1) Mirabelli Riccardo; (10,19) Montesi Maria Cristina; (13,27) Morone Maria Cristina; (21) Morrocchi Matteo; (21) Muraro Silvia; (13,27) Narici Livio; (29) Pastore Alessandra; (17) Pastrone Nadia; (17) Pennazio Francesco; (11,25) Placidi Pisana; (5) Pullia Marco; (17,18) Ramello Luciano; (20) Ridolfi Riccardo; (2,21) Rosso Valeria; (15) Rovituso Marta; (7) Sanelli Claudio; (22,7,1) Sarti Alessio; (4,20) Sartorelli Gabriella; (9) Sato Osamu; (5) Savazzi Simone; (22,12) Schiavi Angelo; (6) Schuy Christoph; (15) Scifoni Emanuele; (22,12, 1) Sciubba Adalberto; (4) Selvi Marco; (11) Servoli Leonello; (11,24) Silvestre Gianluigi; (17,18) Sitta Mario; (4) Spighi Roberto; (7) Spiriti Eleuterio; (21,2) Sportelli Giancarlo; (3) Stahl Achim; (7) Tomassini Sandro; (15,16) Tommasino Francesco; (26,12,1) Traini Giacomo; (10) Valeri Tioukov; (8,23) Valle Serena Marta; (14) Vanstalle Marie; (4,20) Villa Mauro; (6) Weber Ulrich; (4,20) Zoccoli Antonio; (22,12,1) Patera Vincenzo

1 Museo Storico della Fisica e Centro Studi e Ricerche Enrico Fermi, Rome, Italy
2 University of Pisa, Department of Physics, Pisa, Italy
3 Rheinisch-Westfälische Technische Hochschule (RWTH) University, Aachen, Germany
4 Istituto Nazionale di Fisica Nucleare (INFN), Section of Bologna, Bologna, Italy
5 Centro Nazionale di Adroterapia Oncologica (CNAO), Pavia, Italy
6 Gesellschaft für Schwerionenforschung (GSI), Darmstadt, Germany
7 Istituto Nazionale di Fisica Nucleare (INFN), Laboratori Nazionali di Frascati, Frascati, Italy
8 Istituto Nazionale di Fisica Nucleare (INFN), Section of Milano, Milano, Italy
9 Nagoya University, Department of Physics, Nagoya, Japan
10 Istituto Nazionale di Fisica Nucleare (INFN), Section of Napoli, Napoli, Italy
11 Istituto Nazionale di Fisica Nucleare (INFN), Section of Perugia, Perugia, Italy
12 Istituto Nazionale di Fisica Nucleare (INFN), Section of Roma 1, Rome, Italy
13 University of Rome Tor Vergata, Department of Physics, Rome, Italy
14 Université de Strasbourg, CNRS, IPHC UMR 7871, F-67000 Strasbourg, France
15 Trento Institute for Fundamental Physics and Applications (TIFPA-INFN), Trento, Italy
16 University of Trento, Department of Physics, Trento, Italy
17 Istituto Nazionale di Fisica Nucleare (INFN), Section of Torino, Torino, Italy
18 University of Piemonte Orientale, Department of Science and Technological Innovation, Al, Italy
19 University of Napoli, Department of Physics "E. Pancini", Napoli, Italy
20 University of Bologna, Department of Physics and Astronomy, Bologna, Italy
21 Istituto Nazionale di Fisica Nucleare (INFN), Section of Pisa, Pisa, Italy

[1] corresponding author ilaria.mattei@mi.infn.it

22 University of Rome La Sapienza, Department of Scienze di Base e Applicate per l'Ingegneria, Italy
23 University of Milano, Department of Physics, Milano, Italy
24 University of Perugia, Department of Physics and Geology, Perugia, Italy
25 University of Perugia, Department of Engineering, Perugia, Italy
26 University of Roma La Sapienza, Department of Physics, Rome, Italy
27 Istituto Nazionale di Fisica Nucleare (INFN), Section of Rome 2, Rome, Italy
28 University of Torino, Department of Physics, Torino, Italy
29 Istituto Nazionale di Fisica Nucleare (INFN), Section of Bari, Bari, Italy
30 CEADEN, Havana, Cuba
31 Gran Sasso Science Institute, L'Aquila, Italy
32 Currently employed at Derga Consulting Srl, Bolzano, Italy

Abstract

In proton-therapy clinical practice a constant RBE equal to 1.1 is adopted, regardless of the demonstrated RBE variations, which depends on physical and biological parameters. Among other mechanisms, nuclear interactions might influence the proton-RBE due to secondary heavier particles produced by target fragmentation that can significantly contribute to the total dose: an unwanted and undetermined increase of normal tissues complications probability may occur. The FOOT experiment is designed to study these processes. Target (^{16}O,^{12}C) fragmentation induced by $150 - 250\ MeV$ proton beam will be studied via inverse kinematic approach, where ^{16}O and ^{12}C therapeutic beams, with the same kinetic energy per nucleon of the proton, collide on graphite and hydrocarbons target to provide the cross section on Hydrogen (to explore also the projectile fragmentation). The detector design, the performances and expected resolution results obtained form Monte Carlo study, based on the FLUKA code will be presented.

Introduction

Particle Therapy (PT) uses protons and light ions beams for the treatment of deep-seated solid tumours. Due to the features of energy deposition of charged particles a small amount of dose is released to the healthy tissue in the beam entrance region, while the maximum of the dose is released to the tumour at the end of the beam range, in the Bragg peak region. Nowadays the efficacy of particle therapy is well established [1, 2] and the national social security services are increasingly heading towards the coverage of medical expenses related to PT treatments (e.g. Italy [3]). Many new centres are under construction: in Europe 11 new centres are expected to be running in $2017 - 2019$ and in the next few years Europe is going to host about 30% of the world PT centres. About 80% of the particle therapy centres (about 70 centres in operation, from ptcog.ch, 4/2017) exploit proton beams.

Despite the large advantage of particle therapy treatments in sparing dose to the healthy tissues, nuclear interactions between beam and patients induce fragmentation both of projectile and target and must be carefully taken into account. The projectile fragmentation contributes mainly to the dose release after the Bragg Peak while the target fragmentation, characterised by particles that have on average a small velocity, changes the radiation Relative Biological Effectiveness (RBE), along its path inside the body. In the current clinical practice, when planning patient treatments, the proton RBE is assumed to be constant and equal to 1.1. There are, however, grown and solid evidences [4] that a non-constant effectiveness should be used to account for the ion slowing down and secondary target fragments production. The authors of [4] suggest that about 10% of the biological effect induced in the entrance channel of the beam in the patient might be associated with target fragments. At the same time, due to the slowing down of primary protons energy, this contribution is reduced to about 2% when approaching the Bragg

peak.

A more accurate description of the RBE in the entrance region would allow for a better definition of the peak-to-entrance RBE ratio, which largely characterises the therapeutic advantage of proton therapy. The deposition of dose associated with target fragmentation, even though low if considered in absolute terms, could be relevant concerning the risk assessment for secondary cancer induction. This is true in particular considering the high LET associated with those fragments [4].

Those aspects impact not only in medical application (proton/particle therapy), but also for the space research: astronauts are exposed to galactic cosmic rays, consisting of accelerated charged particles in the range from protons to iron ions, thus the knowledge of the released dose associated to the high LET fragments is crucial to their healthy. The measurement of the effective flux and spectra of the fragments produced by target fragmentation represents an experimental challenge due to the very short range of the produced particles. This issue will be addressed by the FOOT experiment [5].

1 FragmentatiOn Of Target

When performing the target fragmentation measurements, one has to account for the extremely small range of the secondary products, immediately re-absorbed in the target itself. By pursuing an **inverse kinematic** approach is it possibile to gain experimental access to the secondary production cross sections. Obviously, this requires fragment direction and incoming projectile particle four-momentum to be well measured in the laboratory frame to obtain the correct energy in the patient frame. The inverse kinematic approach lead to the use of Carbon ion (and hopefully Oxygen) beams on H target, however a pure H target is a very challenging and expensive. The FOOT strategy is to use double layers of pure C (Graphite) and C_bH_a (Plastic Scintillators) targets. The cross sections on C and H are therefore evaluated exploiting the relation:

$$\frac{d\sigma}{dE_{kin}}(H) = \frac{1}{a} \cdot [\frac{d\sigma}{dE_{kin}}(C_bH_a) - b \cdot \frac{d\sigma}{dE_{kin}}(C)] \tag{1}$$

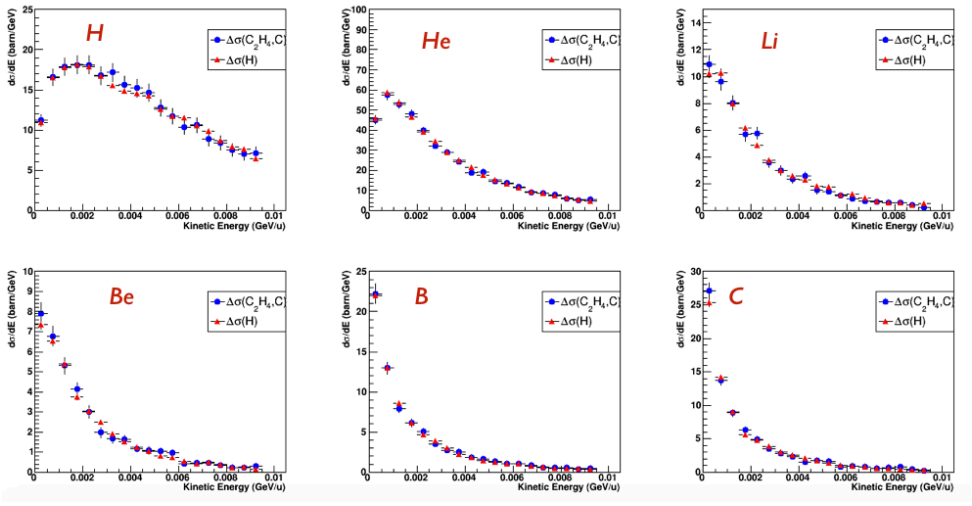

Fig. 1: FLUKA proton fragmentation via inverse kinematic. Check of the validity of the target cross sections combination method.

To check the validity of the cross sections measured with the method of combination of targets we evaluated from the simulation data both the cross section on hydrogen target and the cross section obtained from the difference method. The Fig. 1 shows the energy differential cross-section of ^{12}C beam (200 MeV/u) on hydrogen target obtained in inverse kinematics for different produced fragments.

The estimations performed with the $\Delta\sigma(C_2H_4,C)$ and $\sigma(H)$ methods are reported as blue dots and red triangles, respectively and confirm the validity of the method. Similarly, with C_bH_a, PMMA (C_5H_8O2) and C targets it is possible to measure the cross sections on C, O and H.

1.1 FOOT Detector

The FOOT detector has been optimised to study the forward target fragment production ($Z \geq 3$ contained within a cone of 10^o) with plastic scintillators detectors, trackers and a calorimeter able to stop the heavier fragments produced, in order to provide:

- the charge Z and mass A fragments identification;
- the fragments energy spectra;
- the different fragments production cross sections.

A dedicated emulsion chamber apparatus will characterise the light fragment production scattered at larger angles (see section1.3).

The forward detector includes a magnetic spectrometer for the momentum determination based on silicon pixel and strip detector, a plastic scintillator for the deposit energy and the ToF and a calorimeter for the kinetic energy measurement necessary for the particle identification (Figure 2. The detector has been designed to measure precisely the production cross sections of the fragments. FOOT results will impact on the biological dose evaluation. The radiobiology goal is to improve the NTCP (Normal Tissue Complication Probability) model precision using data from p+C and p+O collisions in the energy range of $[200; 400\ MeV/n]$. The FOOT goal is to obtain a $d\sigma/dE$ and $d\sigma/d\theta$ with a 5% precision, for all the fragments in inverse and direct kinematics with p, C, O, He beams in the $[200 - 400]\ MeV/n$ energy range. In order to reach the needed resolutions on cross sections the detector has been designed to achieve the following experimental resolutions:

- $\Delta p/p \sim 4\%$
- ToF $\sim 70\ ps$
- $\Delta(dE)/dE \sim 3 - 10\%$ depending of Z
- $\Delta Ekin/Ekin \sim 1.5\%$

The experiment is being planned as a *table-top* experiment in order to cope with the small dimensions of the experimental halls of the CNAO and HIT treatment centres and GSI, where the data taking is foreseen in the next years. The experimental setup is shown in Figure 2.

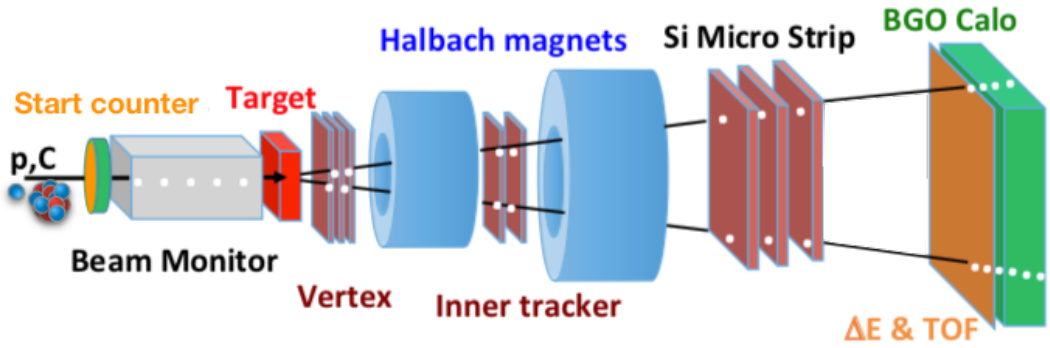

Fig. 2: The FOOT experimental setup is shown in this scratch.

A work of data-model verification will be done in synergy with the MC community and the correlation between the measured cross section and the biological uncertainty will be calculated. More details

on the different detectors can be found in [5] and on the experiment website[2].

1.2 Expected Performances

In order to evaluate the detector performance, thus the resolution on charge and mass of the fragments, a Monte Carlo Study has been realised. The full experimental setup has been simulated in FLUKA [6].

The fragments energy loss (dE/dx) is related to their charge by the well know equation (2):

$$-\frac{dE}{dx} = (\frac{\rho \cdot Z}{A})_{target} \frac{4\pi N_A m_e c^2}{M_U} (\frac{e^2}{4\pi\epsilon_0 m_e c^2})^2 (\frac{z^2}{\beta^2}) [ln(\frac{2m_e c^2 \beta^2}{I \cdot (1-\beta^2)}) - \beta^2]. \quad (2)$$

1.2.1 Fragment Charge

In FOOT the energy loss is therefore measured with thin plastic scintillators, exploiting ToF information to measure the β of the fragments it is possible to reconstruct their charge.

Table 1: True and reconstructed Z values of the selected fragments obtained for a 200 MeV ^{16}O ion beam impinging on a 2 mm thick C_2H_4 targets.

Frag.	^{7}Li	^{9}Be	^{11}B	^{12}C	^{14}N
Z	3	4	5	6	7
Z_{rec}	3.03 ± 0.08	4.05 ± 0.09	5.06 ± 0.10	6.09 ± 0.12	7.11 ± 0.14

The reconstructed Z values are presented along with their resolutions in Tab. 1 for some selected fragments (^{7}Li, ^{9}Be, ^{11}B, ^{12}C and ^{14}N); these values were obtained applying a ΔE resolution parametrised as a function on the deposited energy.

1.2.2 Fragment Mass

The fragments mass A can be retrieved by coupling two of the three measured quantities E_k, ToF and p for each fragment, exploiting equations 3.

$$\begin{aligned} A_1 &= \frac{m}{U} = \frac{p}{U\beta\gamma} \\ A_2 &= \frac{m}{U} = \frac{E_{kin}}{U(\gamma-1)} \\ A_3 &= \frac{m}{U} = \frac{p^2 - E_{kin}^2}{2\,U E_{kin}} \end{aligned} \quad (3)$$

Moreover, to improve the resolution, a global fit with the Augmented Lagrangian Method (ALM [7]) using E_k and ToF and p simultaneously has been implemented; as an example, in the left (right) panel of Fig. 3 it is reported the Helium mass with the ALM method (with a χ^2 cut).

The achievable resolutions on mass determination for the fragments ^{7}Li, ^{9}Be, ^{11}B, ^{12}C and ^{14}N are reported in Tab. 2.

The values and the plots of Fig. 3 are obtained assuming the following resolutions: $dp/p = 4\%$, $ToF = 70\ (140)\ ps$ for heavy (light) fragments and $dE_{kin}/E_{kin} = 1.5\%$.

[2] $https://web.infn.it/f00t/index.php/it$

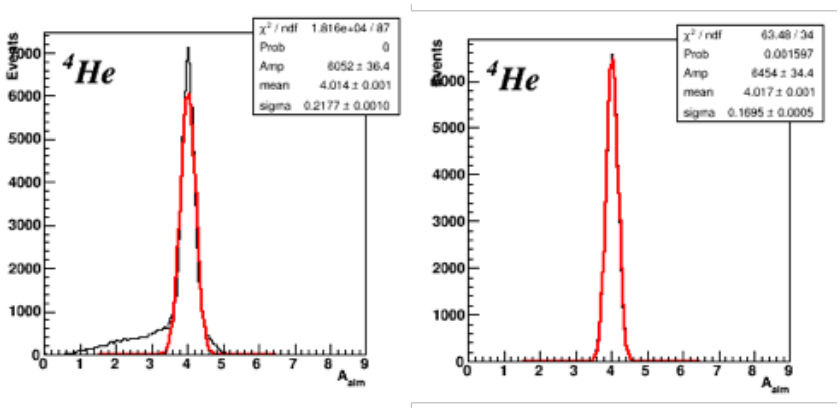

Fig. 3: As an example of the mass reconstruction method (a global fit obtained with the Augmented Lagrangian Method (ALM)) is shown for the ^4He fragment (left). A tail for neutron emission in the calorimeter detector is present. An appropriated cut on χ^2 removes the tail (right).

Table 2: True and reconstructed A values of the selected fragments obtained for a 200 MeV ^{16}O ion beam impinging on a 2 mm thick C_2H_4 targets.

Frag.	^{7}Li	^{9}Be	^{11}B	^{12}C	^{14}N
A	7	9	11	12	14
A_{χ^2}	7.00 ± 0.31	8.99 ± 0.34	10.99 ± 0.44	11.99 ± 0.43	14.00 ± 0.48
A_{alm}	7.00 ± 0.31	8.98 ± 0.33	10.98 ± 0.44	11.98 ± 0.43	13.99 ± 0.48

1.3 Emulsion spectrometer

Complementary light fragments ($Z \leq 3$) measurements will be achieved by means of an emulsion chamber [8]. This dedicated setup is shown in Figure. 4. In this setup both target and detector are

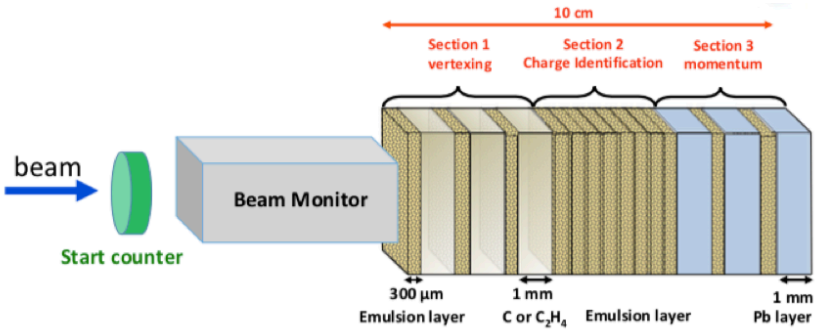

Fig. 4: Scheme of the emulsion spectrometer detector.

integrated in a very compact setup allowing for a very accurate reconstruction of the interactions inside the target, with a sub-micrometric resolution. It will provide measurements of fragments emitted in a cone with semi-aperture up to 70^o, which are mainly protons, deuterons, tritons, Helium and Lithium ions. The pre-target region of the electronic setup will be employed to monitor the incoming primary beam, while the emulsion chamber will act both as target and fragments detector: in the first section target layers (C or C_2H_4) are alternated with emulsion films to reconstruct the interaction vertex, the second one will be made only by emulsion films to provide charge reconstruction, while in the last one the emulsion films are interleaved with Lead layers to measure fragments energy and momentum. The fragments charge will be assessed with an expected efficiency better than 99%.

2 Timeschedule

The construction of different part of the detectors is already started and some preliminary results show the effective feasibility of the experiment. A calorimeter prototype made of 145 BGO crystal has already been tested with different particles (H, He and C) in a large energy range in HIT experimental room. The energy resolution has been measured to be about $1 - 2\%$. The full calorimeter exploits the $24\ cm$ long BGO crystal of L3 [3] and will be available in about an year. Its new readout system is under optimisation. Preliminary and very encouraging measurement with the ToF detector, bars of plastic scintillators instrumented with SiPM readout with a dedicated electronic system, has been performed with protons and carbon ions. A time resolution of $100 - 180\ ps$ and $\sim 50\ ps$ respectively for p and C ions has been obtained. The energy resolution on dE/dx measurement with the ToF detectors is about $5 - 12\%$ for protons and about the 7% for carbon ions.
The construction of the start detector is also started: $250\ \mu m$ plastic scintillator read out by 48 SiPM $(12/\text{side})$ readout by the same ToF detector system.
FOOT experiment is advancing as expected: data taking will start in 2019 with the emulsions setup and in 2020 the full setup will be operational.

Conclusions

The FOOT experiment is the dedicated to the characterisation of the target fragmentation production cross sections. This will improve the modelling of the true RBE of protons, thus PT treatment quality. To this aim an inverse kinematics strategy will be exploited and two experimental setups, one for light and an other one for heavy fragments, are currently under development. A full detectors MonteCarlo FLUKA simulations has been developed in order to optimise the experimental setups and to evaluate the expected performances of the FOOT experiment. Besides target fragmentation, the experiment will also provide projectile cross sections measurements which are crucial in ion therapy. In addition, by considering the application to the radio-protection framework, the operation of FOOT at higher energies would allows to achieve important contributions to the planning of long duration and far from earth space missions. A resolution of about 2% and $3 - 4\%$ is obtained for the charge Z and number of mass A determination respectively.

References

[1] Loeffer J S and Durante M *Charged particle therapy-optimization, challenges and future directions* Nat. Rev. Clin. Oncol. 10 411-24, 2013

[2] Durante M and Paganetti H *Nuclear physics in particle therapy: a review* Rep. Prog. Phys. 79 096702, 2016

[3] *Definizione e aggiornamento dei livelli essenziali di assistenza (LEA)* Novembre 2016 - Atti del Governo n. 351 http://www.senato.it/service/PDF/PDFServer/BGT/00994183.pdf

[4] F. Tommasino and M. Durante *Proton Radiobiology* Cancers, 7(1), (2015) 353-381 doi:10.3390/cancers7010353

[5] A. Alexandrov et al., *The FOOT (Fragmentation Of Target) Experiment* PoS (Bormio 2017) 023 https://pandora.infn.it/public/1e5288, A. Alexandrov et al., *FOOT Conceptual Design Report* https://pandora.infn.it/public/912bb8

[6] Ferrari A. et al., *INFN-TC-05-1* CERN 2005-10; SLAC-R-773L.

[7] Hestenes M. R J. Optimiz. Theory App.4 1969 5.

[8] De Lellis G. et al. in Fabjan C. W. and Schopper H. *Elementary Particles: Detectors for Particles and Radiation*, Vol. 21B, Springer (2011).

[3] https://home.cern/about/experiments/l3

A radiobiological database produced by the BIANCA model to predict the biological effectiveness of hadrontherapy beams

M.P. Carante, J.J. Tello Cajiao and F. Ballarini
National Institute of Nuclear Physics (INFN), Section of Pavia, Pavia, Italy
University of Pavia, Physics Department, Pavia, Italy
Universidade Estadual de Campinas, Campinas, Brasil

Abstract
The BIANCA biophysical model was used to simulate cell survival curves by protons, He- and C-ions over a wide LET range and for several doses. Each simulated curve was then fitted by a linear-quadratic exponential function of the form $S(D)=\exp(-\alpha D-\beta D^2)$. This allowed to produce an almost continuous set of α and β values as a function of LET for each ion type. The same procedure was repeated for chromosome aberration dose-response curves, using the following fitting function: $A(D)=\alpha_A D+\beta_A D^2$. In the context of hadrontherapy, the tables of α and β (as well as α_A and β_A) were read by the FLUKA radiation transport code, which provides the necessary information about particle type, LET and absorbed dose, thus allowing fast computing of biological outputs in every position of a therapeutic dose profile. Some examples of the variation of the two considered biological quantities, i.e. probability of cell survival and chromosome aberrations, along Spread Out Bragg Peaks in water are reported as preliminary results.

1 Introduction

The main rationale for the use of charged particles in cancer therapy relies in their physical properties: when traversing a material, they deposit most of their energy at the end of their path, in the so-called Bragg peak. By using several beams with different initial energies, it is possible to shape a "Spread Out Bragg Peak" (SOBP), thus delivering most of the physical dose in the tumour region, while minimizing the dose in the surrounding healthy tissues [1]. Nevertheless, also the ion biological effectiveness plays an important role in this context: the higher Relative Biological Effectiveness (RBE, defined as the ratio between a photon dose and the ion dose necessary to induce the same effect) is the main advantage in the use of ions heavier than protons (e.g. carbon ions) [2]. However, it is well-known that, in general, RBE is not constant along a flat SOBP, but it tends to increase with increasing depth. Therefore, it is fundamental to use a tool (e.g. a biophysical model) able to quantify the RBE, in principle in each position and for each physical and biological configuration.

Currently, in clinical practice the variability of RBE is ignored in the case of protons, for which a constant RBE of 1.1 is usually assumed. Nevertheless, it would be important to quantify the consequences of the well-known increase of RBE in the last few millimetres of proton SOBPs, as well as the "shift" of the biological peak beyond the physical dose fall-off [3]; this may be critical, especially for mono-directional irradiations, when an organ at risk is present beyond the tumour. On the other hand, the variability of RBE is usually taken into account for carbon ions; two biophysical models are currently coupled with the Treatment Planning Systems (TPS) used in hadrontherapy centres worldwide. In particular, the Local Effect Model (LEM) is used in Europe (Germany, Italy and Austria) [4], whereas the Microdosimetric Kinetic Model (MKM) is applied in Japan [5].

In clinical practice, the physical dose distribution for the treatments is provided by the TPSs, which are typically fast-performing analytical algorithms; these tools needs to adopt some

simplifications in the physical processes of radiation transport in matter, and may suffer some limitations in presence of severe tissue heterogeneities. On the other hand, time-consuming Monte Carlo (MC) transport codes, like GEANT4, PHITS and FLUKA, are more accurate and are considered a good benchmark to support and validate the clinical activity. In particular, the FLUKA code has already been coupled with both the LEM [6] and the MKM (7) models, and it is used for treatment plan verification and re-calculation.

Following an approach similar to those adopted by Mairani et al and by Magro et al, in this work an interface between FLUKA [8,9] and the BIANCA (BIophysical ANalysis of Cell death and chromosome Aberrations) biophysical model [10-12] is presented. Tables of biological effectiveness for many different physical configurations were produced by BIANCA and read offline by FLUKA, which can thus provide a three-dimensional biological output based on BIANCA, in addition to those based on LEM and MKM. A procedure was also developed to easily build-up SOBPs with FLUKA, and some preliminary quantifications of the biological-effectiveness variability along these profiles are presented. This biological effectiveness is provided in terms of both cell death and chromosome aberrations: the latter, being useful in the evaluation of healthy tissue damage, represents a peculiar feature with respect to the already cited LEM and MKM.

2 Methods

The core of the present work consisted of the production of tables of biological effectiveness by the BIANCA biophysical model, which will be described in this Section illustrating its assumptions, adjustable parameters and simulation steps. The reading of the produced tables by the FLUKA code will be also described. Eventually, the tool developed to build up SOBPs with FLUKA will be illustrated step-by-step: this tool is fundamental in order to easily investigate the biological effectiveness variations along realistic dose profiles.

2.1 The BIANCA model

The last version of the BIANCA II model, which is described in detail in [13], was adopted for the present study. The model, which is implemented as a Monte-Carlo code and assumes a pivotal role for DNA cluster damage, is based on the following assumptions: i) ionizing radiation can induce DNA “Cluster Lesions” (CLs), where a CL is defined as a critical DNA damage that produces two independent chromosome fragments; ii) distance-dependent fragment mis-rejoining or un-rejoining give rise to chromosome aberrations; iii) certain aberrations (dicentrics, rings and large deletions) lead to cell death.

An attempt to provide a characterization of the nature of a CL was reported in [14,15], where it was suggested that a cluster of Double Strand Breaks at the kilobase-pair scale might be a good candidate as a CL. However, since the question is still controversial, CLs are not defined a priori, and their yield is the first adjustable parameter of the model. Its value mainly depends on radiation quality (i.e. particle type and energy), but it is also modulated by the target cell features.

Concerning the second assumption, a distance-dependent probability of rejoining between two chromosome fragments was adopted: this probability is assumed to have the shape of a step function, with threshold distance d equal to the average distance between two adjacent chromosome territories, like in previous works [e.g. 15]. In particular, fragments with initial distance smaller than d may undergo rejoining, while fragments with initial distance greater than d will never undergo rejoining. Moreover, a fragment un-rejoining probability, called f, is adopted in BIANCA II: each chromosome fragment has a probability f to remain un-rejoined even if there are possible partners within a distance d. The value of f is the second, and last, adjustable parameter of the model: it is assumed to be cell-line dependent but independent of radiation quality, as explained in [12]. Although not relevant for the present work, it is worth mentioning that in recent works, specific for the study of chromosome aberrations, a negative exponential function for fragment rejoining has also been tested [16,17].

The BIANCA model can be used to perform virtual experiments of chromosome aberration [18] and cell death for cells exposed in vitro to ionizing radiations. Focusing on charged particles, the starting physical information are the Linear Energy Transfer (LET) in keV/µm and the absorbed dose (*D*) in Gy, from which it is possible to calculate the average number of ions (*N*) traversing a cell nucleus:

$$N = \frac{D \cdot S}{0.16 \cdot LET} \ , \tag{1}$$

where *S* is the nucleus cross-sectional area in µm^2. For each cell irradiation, i.e. each run, an actual number of traversals is extracted from a Poisson distribution with mean value *N*. Starting from a mean number of CLs per track, an actual number of CLs for each track is then extracted from a Poisson distribution. For (low-energy) protons and He-ions these CLs are uniformly distributed along the segments representing the tracks of the primary ions, whereas for heavier ions some CLs are "shifted" radially to model the effects of the so-called "delta rays". Further details on this issue can be found in [10]. When the positions of all CLs inside the cell nucleus are known, the hit chromosomes and chromosome-arms are identified, the chromosome-fragment rejoining process is simulated, the different aberration types are scored and the cell is labelled as survived if there is no lethal aberration. The procedure is repeated for many cells, till the relative error on the surviving fraction is smaller than 5%.

2.2 SOBP production with FLUKA

In order to easily investigate the variations of biological effectiveness along realistic dose profiles, an approach aimed to the fast production of SOBPs, presented in [19,20], was refined, extended and applied in the present work. The approach is based on the analytical computation of the initial energies and weights of the different monoenergetic Bragg peaks that are summed up to shape the SOBP.

The starting information is the longitudinal extension of the tumour region, that is the SOBP plateau, identified by a minimum and a maximum range (R_{min} and R_{max}, respectively). The SOBP is then divided into *n* equal intervals, with ranges:

$$r_k = R_{min} + (R_{max} - R_{min}) \cdot \frac{k}{n} \ , \tag{2}$$

with *k=0,1,...,n*. Now, the main assumption of this approach is that the relationship between the energy *E* of a beam and its range, *R*, can be described by a power-law of this type:

$$R = \alpha E^{p_0} \ , \tag{3}$$

where α and p_0 are free parameters. Therefore, the initial energy of the monoenergetic beam of range r_k is given by:

$$e_k = \left(\frac{r_k}{\alpha}\right)^{\frac{1}{p_0}} \ . \tag{4}$$

The normalized weights to be assigned to the different monoenergetic beams are thus given by

$$w_k = \begin{cases} 1 - \left(1 - \frac{1}{2n}\right)^{1-1/p} \\ \left[1 - \frac{1}{n}\left(k - \frac{1}{2}\right)\right]^{1-1/p} - \left[1 - \frac{1}{n}\left(k + \frac{1}{2}\right)\right]^{1-1/p} \\ \left(\frac{1}{2n}\right)^{1-1/p} \end{cases} . \tag{5}$$

where *p* is a parameter that needs to be adjusted in order to produce a flat SOBP. The procedure to obtain Equation 5 is described in [19].

In the present work, the relationship of Equation 3 was verified for protons, helium and carbon ions independently, and the corresponding parameters were derived. In particular, a wide set of experimental data on ion ranges as a function of their initial energy was taken from [21] and we fit these data with Equation 3. For protons we considered the energy range from 1 keV to 200 MeV, for He ions from 1 keV to 1000 MeV and for C ions from 1 keV to 5000 MeV. The α and p_0 parameters that allowed to obtain the best fits are reported in Table 1.

Table 1: Fitting parameters of Equation 3 for three different ions

Ion type	**α**	**p_0**
Protons	0.002365	1.758
Helium ions	0.0002432	1.733
Carbon ions	0.00001949	1.671

At this stage, a routine was implemented in the FLUKA code, in order to produce many pristine Bragg peaks with the desired initial energies and the correct weights: it is thus easy to produce SOBPs at arbitrary depths and with arbitrary extensions, for the three considered ion types. In each voxel of a 3D dose profile, the information about the particle types, their energy and the corresponding absorbed dose, are thus available; in the next session, the procedure to associate the biological effectiveness computed by BIANCA to these information will be described. The FLUKA development version fluka2017.2 was adopted for the present work.

3 Results and discussion

The main goal of the present work was the development of an interface between FLUKA and BIANCA: in the next Sections the production of tables of biological effectiveness by the BIANCA model will be described, as well as the way FLUKA can read and interpret these tables. Furthermore, some preliminary examples of SOBPs calculated by FLUKA will be reported; in particular, the differences between the physical dose and the biological effectiveness calculated by the FLUKA/BIANCA interface will be investigated.

3.1 Tables of biological effectiveness

In [13] a systematic comparison between BIANCA simulations and proton, helium and carbon ion data over a wide energy range was performed for two cell lines of different radiosensitivity (V79 cells, which are rather radioresistant and are widely used to characterize hadrontherapy beams, and AG01522 cells, which can be considered as representative of normal cells). By analysing the input parameters used to obtain the best agreement with the experimental cell survival curves, a well-defined dependence of the CL yield per unit path length on the LET was found: the mean number of CLs/μm was fitted by a linear-quadratic function of the form $Y(L) = a \cdot L + b \cdot L^2$, where Y is the CL yield expressed in CL/μm, L is the LET in keV/μm, and a and b are fitting parameters. This relationship was found to hold independently for the three considered ion types till the overkilling region, i.e. around 150 keV/μm for carbon ions. In order to describe the trend over the whole LET range, a function of the form $Y(L) = c \cdot \mathrm{arctg}(a \cdot L + b \cdot L^2)$ was found to work better.

In the present work, focusing on V79 cells, the fitting functions for the three ions (as reported in [13]) were used to establish a one-to-one correspondence between the CL input parameter and the LET; this allows to perform simulations for an arbitrary LET value, by using as input parameter the CL yield

provided by the fit, even at those LET values for which experimental data are not available. This approach was used to perform many simulations of cell survival over a wide LET range: for protons 12 curves were simulated from 2.5 to 30.0 keV/µm, with LET steps of 2.5 keV/µm each; for helium ions 18 curves from 5 to 90 keV/µm, with LET steps of 5 keV/µm each; for carbon ions 15 curves from 10 to 150 keV/µm, with LET steps of 10 keV/µm each, and 14 curves from 175 to 500 keV/µm, with LET steps of 25 keV/µm each.

For each curve, the BIANCA simulations of cell surviving fraction were performed at doses of 0.5, 1.0, 1.5, 2.0, 2.5 and 3.0 Gy. Each simulated dose-response curve thus consisted of 6 points, each one with its statistical uncertainty; each set was then fitted by a function of the form

$$S(D) = e^{-(\alpha D + \beta D^2)} \ , \tag{6}$$

where S is the surviving fraction, D is the dose, and α and β are two fitting parameters. Tables of α and β parameters as a function of LET were thus obtained for protons, helium ions and carbon ions. These values are graphically reported in Figure 1 and 2.

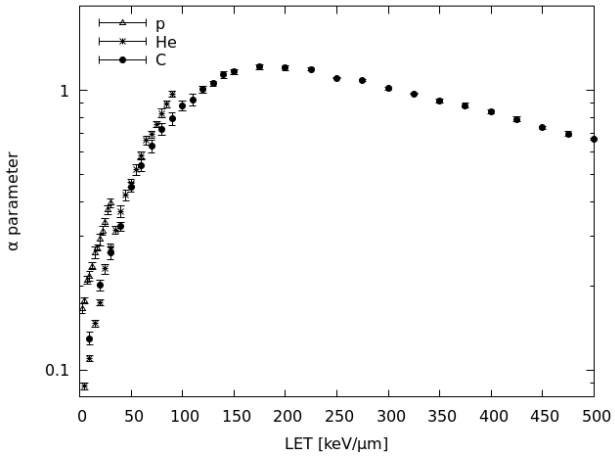

Fig. 1: α parameters as a function of LET, for protons, helium ions and carbon ions

In the context of hadrontherapy, in each voxel of a three-dimensional SOBP, produced as described in Section 2.2, FLUKA can read the tables produced by BIANCA and associate a α and β couple to each particle, which has a well-defined LET, traversing the voxel itself; the routine performing this procedure was written by Alfredo Ferrari and Andrea Mairani. Since in general a number N of particles traverse each voxel, the approach to mixed fields already presented in [6] was adopted: dose-averaged α and β parameters are calculated as

$$\bar{\alpha} = \frac{\sum_{i=1}^{N} \alpha_i D_i}{D}; \ \bar{\beta} = \left(\frac{\sum_{i=1}^{N} \sqrt{\beta_i} D_i}{D} \right)^2 , \tag{7}$$

where D_i is the dose deposited by the i-th particle, a_i and b_i are its associated parameters, and D is the total dose deposited in the considered voxel. It is thus possible to associate a cell survival level to each voxel (by putting the parameters of Equation 7 into Equation 6) and to calculate quantities like cell death probability and RBE along the whole dose profile of arbitrary SOBPs.

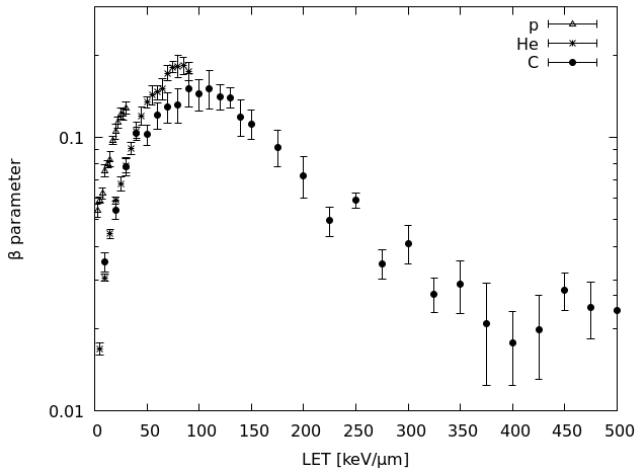

Fig. 2: β parameters as a function of LET, for protons, helium ions and carbon ions

The whole procedure was then repeated for a specific type of chromosome aberrations, called dicentrics: since their yield is similar to that of reciprocal translocations, which in turn can be responsible of the development of secondary cancers, the dicentric yield is generally regarded as an indicator of normal tissue damage. The simulated curves of dicentrics as a function of dose were fitted by a function of the form: $A(D) = \alpha_A \cdot D + \beta_A \cdot D^2$. Tables of α_A and β_A values for dicentrics as a function of LET were thus produced and the approach to mixed fields was applied also for chromosome aberrations.

3.2 Biological effectiveness along SOPBs

In Figure 3 a proton SOBP calculated by FLUKA following the approach described in Section 2.2 is shown; the extension of the SOBP is of 5 cm and its maximum depth is 15 cm. In addition to the physical dose, the figure reports the fraction of inactivated cells (cell death) and the yield of dicentrics per cell; all these quantities are normalized to the proximal point of the SOBP, in order to highlight the variation of the biological quantities with depth. The longitudinal profiles shown in Figure 3 are the result of a radial integration of the quantities obtained in all the voxels which have the same depth (or z coordinate).

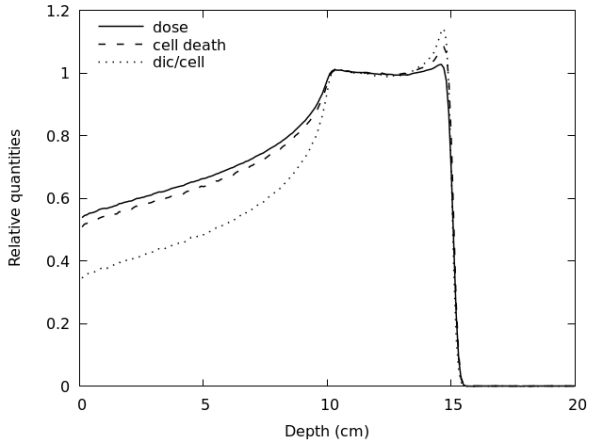

Fig. 3: proton SOBP at a depth of 10-15 cm: physical dose (calculated by FLUKA), fraction of inactivated cells and yield of dicentrics (calculated by BIANCA)

Thanks to the tools developed in the present work, it is easy to produce SOBPs at different depths and with different extensions. Another example is presented in Figure 4, where a proton SOBP with depth between 2 and 3 cm is presented. Both in this case and in the previous one it is possible to observe

an increase in the two considered biological quantities (especially for chromosome aberrations) along the SOBP, which is commonly ignored in proton clinical practice. Moreover, this increase seems to be slightly more pronounced for the SOBP at smaller depth.

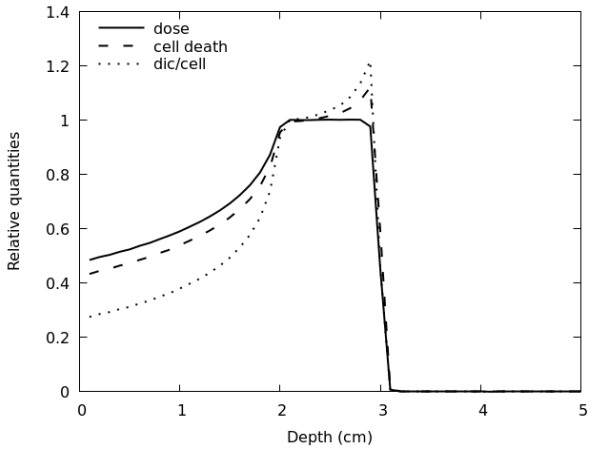

Fig. 4: proton SOBP at a depth of 2-3 cm: physical dose (calculated by FLUKA), fraction of inactivated cells and yield of dicentrics (calculated by BIANCA)

The new tool can also produce SOBPs for other primary ions (He and C ions at the moment). Since in the last few years a renewed interest in helium ion treatments has grown [22], in Figure 5 the physical dose of a helium-ion longitudinal profile is shown, along with the fraction of inactivated cells; the SOBP plateau is positioned between 2 and 3 cm, like in the previous example. For He-ions, the increase in the biological effectiveness is much sharper than in the case of protons: this variability should not be ignored in clinics and a modulation of the physical dose with depth, like in the case of C ions, would be required, as already suggested by others, e.g. [23].

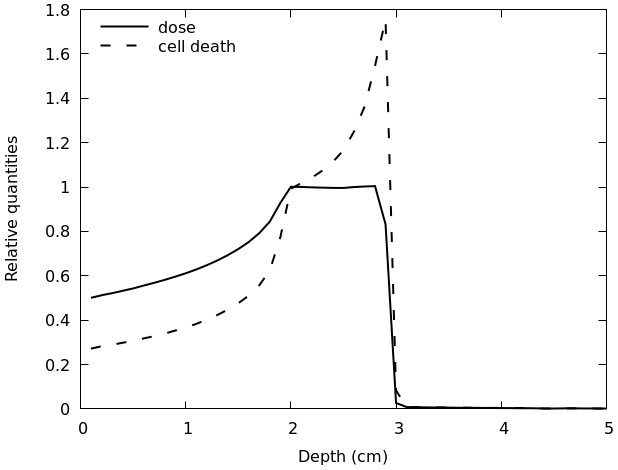

Fig. 5: helium SOBP at a depth of 2-3 cm: physical dose (calculated by FLUKA) and fraction of inactivated cells (calculated by BIANCA)

4 Conclusions

In the present work, the approach adopted to interface the FLUKA radiation transport code with the BIANCA biophysical model was described. Thanks to this new tool, levels of biological damage were predicted along some hadrontherapy SOBPs calculated by FLUKA. FLUKA has already been coupled

to other biophysical models, including LEM and MKM [24]. The interface to BIANCA will allow to easily calculate and predict the biological effectiveness along SOBPs of varying depth and longitudinal extension, for several primary ions and for cell lines of different radiosensitivity. Furthermore, unlike LEM and MKM, thanks to BIANCA it will be possible to calculate the yields of chromosome aberrations in addition to levels of cell death, thus providing a quantification of the probability of healthy tissue damage.

Acknowledgement

This work was partially supported by the National Institute of Nuclear Physics (INFN) and in particular by the MC-INFN/FLUKA project. The authors are also thankful to A. Ferrari, A. Mairani and G. Aricò for useful discussions and program sharing.

References

[1] U. Amaldi and G. Kraft, *Rep. Prog. Phys.* **68** (2005) 1861.

[2] W.K Weyrather and G. Kraft, *Radiother. Oncol.* **73** (2004) S161.

[3] L.E. Gerweck and S.V. Kozin, *Radiother. Oncol.* **50** (1999) 135.

[4] M. Krämer and M. Scholz, *Phys. Med. Biol.* **45** (2000) 3319.

[5] T. Inaniwa *et al*., *Phys. Med. Biol.* **60** (2015) 3271.

[6] A Mairani *et al., Phys. Med. Biol.* **55** (2010) 4273.

[7] G Magro *et al., Phys. Med. Biol.* **62** (2017) 3814.

[8] A. Ferrari *et al.*, CERN-2005-010, SLAC-R-773, INFN-TC-05-11 (2005).

[9] G. Battistoni et al., *Front. Oncol*. **6** (2016) 116.

[10] F. Ballarini *et al,. Radiat. Environ. Biophys*. **53** (2014) 525.

[11] F. Ballarini and M.P. Carante, *Radiat. Phys. Chem.* **128** (2016) 18.

[12] M.P. Carante and F. Ballarini, *Front. Oncol.* **6** (2016) 76.

[13] M.P. Carante *et al., Phys. Med. Biol.* **63** (2018) 075007.

[14] F. Ballarini *et al., Rad. Prot. Dosim.* **166** (2015) 75.

[15] M.P. Carante *et al., Radiat. Environ: Biophys*. **54** (2015) 305.

[16] J.J. Tello Cajiao *et al., DNA Rep.* **58** (2017) 38.

[17] J.J. Tello Cajiao *et al., DNA Rep.* **64** (2018) 45.

[18] A. Testa *et al., Radiat. Res.* **189** (2018) 597

[19] T. Bortfeld and W. Schlegel, *Phys. Med. Biol.* **41** (1996) 1331.

[20] D. Jette and W. Chen, Phys. Med. Biol. **56** (2011) N131.

[21] Report 90, Journal of the ICRU, **14** (2014).

[22] M. Krämer *et al., Med. Phys.* **43** (2016) 1995.

[23] T. Tessonier *et al., Radiat. Oncol.* **13** (2018) 2.

[24] M.P Carante and F. Ballarini, *AIMS Biophys.* **4** (2017) 465.

Developments of the nuclear reaction and fragmentation models in FLUKA for ion collisions at therapeutic energies

G. Aricò[1], A. Ferrari[1], F. Horst[2, 3], A. Mairani[4, 5], C.A. Reidel[2, 6], C. Schuy[2], U. Weber [2]
[1] CERN, Geneva, Switzerland
[2] GSI, Darmstadt, Germany
[3] THM, Giessen, Germany
[4] HIT, Heidelberg, Germany
[5] CNAO, Pavia, Italy
[6] University of Strasbourg, France

Abstract
Protons and carbon ions have been used for decades in several institutes worldwide for cancer treatments. The treatment planning systems rely on accurate modeling of the nuclear reaction and fragmentation processes that occur inside the patient's tissues. The accuracy of FLUKA in the field of proton and carbon ion therapy has been extensively validated. Helium ions are considered as a viable alternative to protons and carbon ions as they are featured by intermediate physical and biological properties. However, as the interest on helium ions is growing again only recently, and therefore some refinements on the FLUKA physics models for helium ions are still needed, prior to the deployment of FLUKA for helium ion therapy. In this work, nuclear reactions of primary helium ions were investigated in the therapeutic energy range and in elements of interest for hadron therapy (carbon and oxygen). Based on recent experimental measurements performed at the Heidelberg Ion-Beam Therapy center by the Space Radiation physics sub-group of the Biophysics Department at GSI (Germany), the nuclear reaction cross section models implemented in FLUKA were refined. This allowed the achievement of more accurate dose calculations.

1 Background

Ionizing radiation is exploited in radiotherapy to damage malignant cells' DNA and therefore to cause tumor death. In radiotherapy the absorbed dose D is defined as the energy deposited per unit of mass by ionizing radiation and is measured in gray (Gy). The main goal of radiotherapy is to deliver high dose to the tumor, such to completely destroy it, whereas the dose delivered to healthy tissues has to be minimized as much as possible. Unlike photons, the depth-dose profile of light ions is characterized by an initial low plateau and a so called Bragg peak at the end of the particle range. The Bragg peak is due to the increasing energy loss, dE, in the unit path, dx, with decreasing particle velocity, as described by the Bethe-Bloch equation.
As a result of the physical characteristics of ions, especially in the case of deep-seated tumors, hadron therapy offers an improved dose conformation to the tumor and a better sparing of the surrounding healthy tissues in comparison to conventional radiotherapy [1]. Furthermore, carbon ions possess a higher biological effectiveness, which makes them particularly suitable for treating radio-resistant tumors.
Protons and carbon ions have been implemented for radiotherapy treatments for decades worldwide. In addition, helium ions are planned to be used in the near future at the Heidelberg Ion-Beam Therapy center (HIT) in Germany [2, 3]. In comparison to protons, helium ions shows a reduced lateral beam spread. With respect to carbon ions, helium ions have a much lower linear energy trasnfer and therefore, a less pronounced biological effectiveness, which might be particularly beneficial in the case of pediatric

patients. Nevertheless, in the case of ions heavier than protons, the quality of biological dose calculations in hadron therapy strongly depends on the ability to predict secondary fragments produced as a consequence of non-elastic nuclear reactions that occur in the patient's tissues. The resulting fragments have broader lateral distributions and most have longer paths than the primary particles, as range scales with A/Z^2. Therefore, they can reach and damage healthy tissues surrounding the tumor. For accurate calculations of the dose and relative biological effectiveness (RBE), the secondary fragments produced, as well as their physical and biological properties, have to be correctly predicted. Commercial treatment planning systems (TPS) used in clinics are supported by Monte Carlo particle transport and interaction codes, which are able to model non-elastic nuclear reactions and fragment production very accurately. For instance, the FLUKA code [4, 5], developed by an INFN-CERN collaboration, is used at HIT (Heidelberg, Germany), MIT (Marburg, Germany) and CNAO (Pavia, Italy) to provide all the basic inputs to the TPS and to validate the TPS's dose calculations, especially in complex scenarios [6].
Our research aims at improving the physics models embedded in FLUKA for helium ions, in order to calculate the dose delivered during radiotherapy treatments more accurately.

2 Method

2.1 Nuclear reaction cross sections in FLUKA

Nucleus-nucleus reaction cross sections are calculated in FLUKA based on a cross-section parametrization, developed by NASA, and whose original expression is [7]:

$$\sigma_R = \pi r_0^2 (A_p^{1/3} + A_t^{1/3} + \delta_E)^2 (1 - R_C B / E_{cm}) X_m \tag{1}$$

where r_0 = 1.1 fm, A_p and A_t are the mass number of the projectile and target, respectively, δ_E is an energy dependent parameter which includes the effects of Pauli blocking and transparency, R_C is a Coulomb multiplier, needed to make the formalism for light, medium and heavy systems unique, B is the energy-dependent Coulomb interaction barrier, E_{cm} is the colliding system center of mass energy, X_m is a low-energy multiplier that accounts for the strength of the optical model interaction and differs from the unity only in case of light systems. In [7] δ_E was expressed in terms of a factor D that depends on the density of the colliding system. In particular, for alpha-nucleus collisions, the proposed best values for D was:

$$D_{Tripathi} = 2.77 - 8.0 \cdot 10^{-3} \cdot A_t + 1.8 \cdot 10^{-5} \cdot A_t^2 - \frac{0.8}{1 + e^{\frac{250 - E}{75}}} \tag{2}$$

However, to increase the agreement with experimental data at low energies, some refinement in the original Tripathi model is needed. For instance, in [8] the following value for D was proposed:

$$D_{Tripathi}^{optimized} = 2.2 - 8.0 \cdot 10^{-3} \cdot A_t + 1.8 \cdot 10^{-5} \cdot A_t^2 - \frac{0.3}{1 + e^{\frac{120 - E}{50}}} \tag{3}$$

Concerning FLUKA, the theoretical expression from [7] was empirically modified [9], based on experimental data available in literature (e.g. [10, 11]). New measurements in the therapeutic energy range [8, 12] have allowed further refinements of the FLUKA model for nuclear reaction cross sections of helium ions in graphite and oxygen, as discussed in section 3.1.

2.2 Dose calculations in FLUKA

Continuous ionizing energy losses of charge particles are modeled in FLUKA based on a continuous slowing down approach on the basis of the Bethe-Bloch equation. However, in addition to the energy loss due to inelastic collisions with atomic electrons, nuclear interactions with material nuclei have to be considered, as they influence the beam fluence, and therefore the dose delivered during radiotherapy treatments. The probability of nuclear interactions are sampled in FLUKA on an event-by-event basis. The probability, P, that a particle travels a path length x without undergoing a nuclear reaction is:

$$P(x) = e^{-\frac{xN_A\rho\sigma_R}{A_t}} \quad (4)$$

where σ_R is the total nuclear reaction cross section. However, in many experiments (e.g. [8, 12]) only mass- and charge-changing cross sections, i.e. variations in the mass number or atomic number of the projectile, could be measured, whereas for dose calculations, the *total* nuclear reaction cross section is needed. The difference between total and mass-changing cross section arises as some primary helium ions may undergo a non-elastic reaction in the target without undergoing fragmentation. The amount of such events was estimated in FLUKA at different energies in the therapeutic energy range (50-250 MeV/u). Based on these results, an energy dependent normalization factor was calculated. Applying the normalization factor to the fragmentation cross sections shown in Figure 1, the total nuclear reaction cross section was obtained. The total cross section values were finally used to calculate the dose delivered from helium ion beams, at different therapeutic initial energies, as a function of depth in water. Experimental data measured at HIT [13] were compared with the FLUKA predictions.

3 Results and Discussion

3.1 Nuclear reaction cross sections in FLUKA

Especially at low energies the lack of experimental data for light and medium systems makes benchmarking of the nuclear reaction models in FLUKA and validation of the FLUKA predictions a challenging task. As example, Figures 1 a) and c) show the fragmentation cross sections for ^{4}He+^{12}C and ^{4}He+^{16}O collisions that were implemented in the FLUKA development version 2017.1. Comparisons with recently acquired experimental data on fragmentation cross sections of ^{4}He on ^{12}C [8] showed that a refinement of the fragmentation cross section curve in FLUKA was required in the therapeutic energy range. Subsequent measurements of ^{4}He ion collisions in ^{16}O also confirmed those findings [12]. The new fragmentation cross section curves, which have been implemented in the FLUKA development version starting from 2018, are shown in Figure 1 b) and d).

3.2 Dose calculations in FLUKA

Dose calculations were performed using the FLUKA development version 2017.1 (which contains the old cross section curves, shown on the left in Figure 1) and 2018.0 (which contains the new cross section curves, shown on the right in Figure 1). For both versions the normalization factor needed to obtain the total nuclear reaction cross section from the fragmentation cross sections was considered (see section 2.2). As example, table 1 lists the percentage of primary helium ions that, according to predicitions of the FLUKA models, interact in the target without breaking up for some representative energy, both for carbon and oxygen targets.

Table 1: Percentage of primary helium ions calculated with FLUKA that interact in the target without breaking up, for 5 initial beam energies in the therapeutic energy range.

Beam energy	Target material	
(MeV/u)	Carbon	Oxygen
50	14.7%	11.0%
100	11.5%	8.0%
150	7.8%	7.6%
200	5.7%	4.9%
250	4.6%	4.2%

Figure 2 shows the dose calculated in water using the FLUKA development versions 2017.1 and 2018.0, for two initial beam energies, 100 and 190 MeV/u. Simulations are compared with experimental data

[13], and the results are normalized to the integrated area under the simulated curves. In the case of the FLUKA development version 2018.0, less primary ions reach the Bragg peak, due to the increased nuclear reaction cross section values, and consequently higher probability that the primary ions undergo a nuclear reaction, in the more recent FLUKA development version (see Figure 1 and Eq. 4). As a result, a stronger degradation of the Bragg peak and therefore a significant improvement on the dose calculation was achieved, especially for more energetic beams. For example, for the cases shown in Figure 2, the maximum difference between experimental and simulated data at the peak was reduced from 3% to 0.5% for the less energetic beam, and from 8% to 1.6% in the more energetic beam.
The residual differences are not a critical issue, as they are mitigated when the so-called spread-out Bragg peak is used in the clinical practice, i.e. hundreds or even thousands of single pencil beams are combined together in order to cover the entire tumor in depth. Consequently, the differences between experiments and simulations, as far as dose calculations are concerned, are sufficiently small with respect to the clinical requirements.

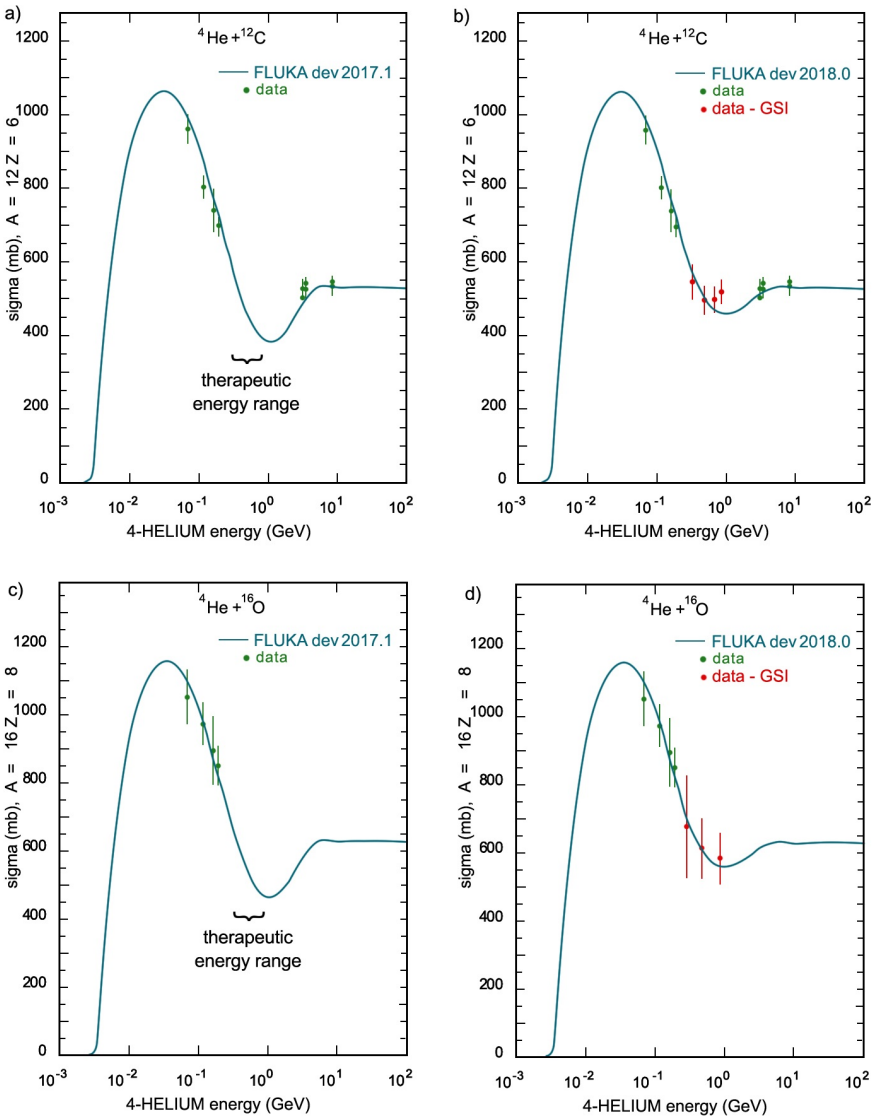

Fig. 1: Fragmentation cross section curves for ^{4}He+^{12}C (*top*) and ^{4}He+^{16}O (*bottom*) collisions implemented in the previous FLUKA development version, 2017.1 (*left*) and in the new FLUKA development version, 2018.0 (*right*), compared with experimental measurements [8, 10, 11]

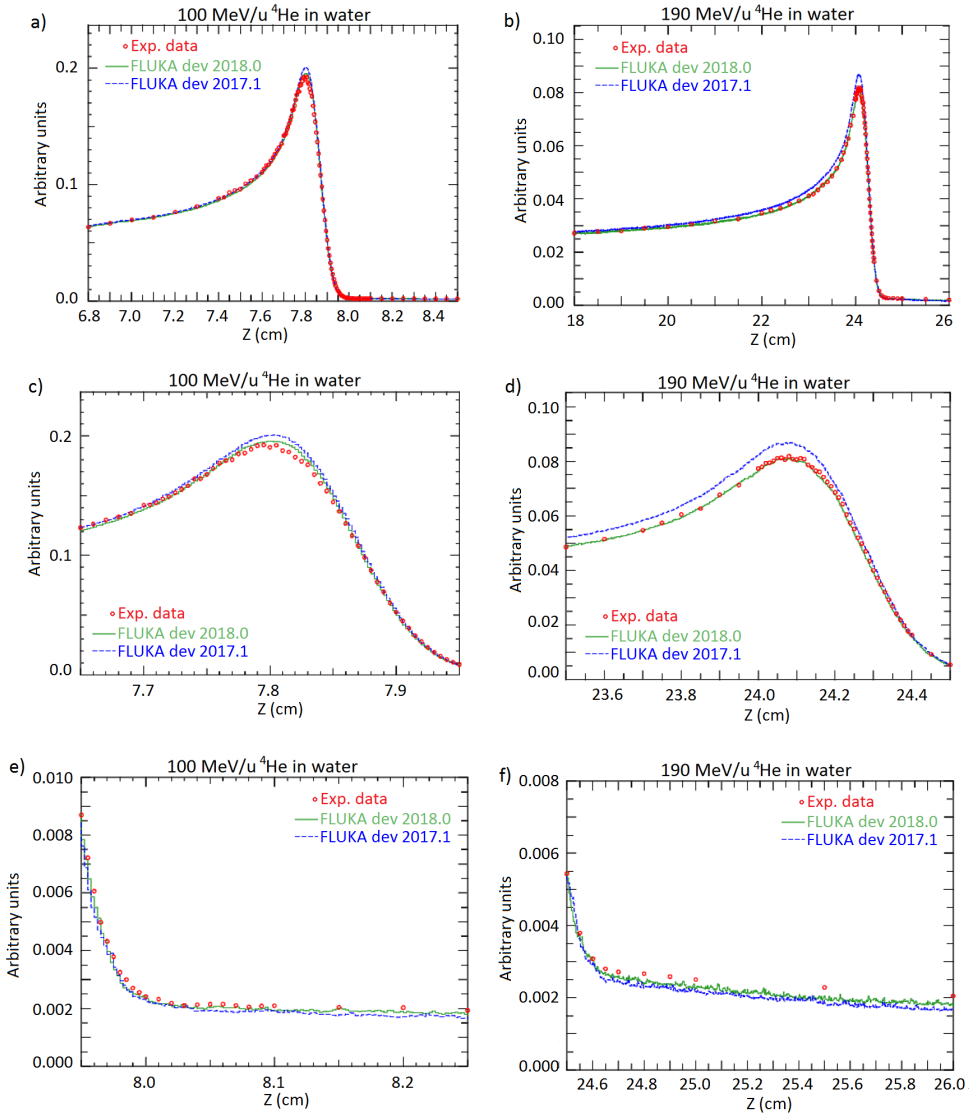

Fig. 2: Experimental dose measurements (*red dots*) [13] acquired with helium ion beams at 100 MeV/u (*left*) and 190 MeV/u (*right*) are compared with FLUKA predictions, using two different development versions, 2017.1 (*dashed, blue line*) and 2018.0 (*solid, green line*). The top row shows a broader range of depth values in water, whereas the middle row and bottom row are, respectively, a zoom of the peak and fragmentation tail.

4 Conclusions and Outlook

In view of the employment of helium ions for radiotherapy at HIT in the close future, refinements and improvements of the physics models embedded in the FLUKA code were required. In this work, the fragmentation cross section curves implemented in FLUKA for ^{4}He+^{12}C and ^{4}He+^{16}O collisions were benchmarked against new experimental data in the therapeutic energy range. The previous models used in the FLUKA development version 2017.1 were adapted such to increase the agreement with experimental measurements (see Figure 1). Validation of the new cross section curves was performed by comparing experimental data and FLUKA simulations of dose delivered in water by helium ion beams. Depth-dose profiles obtained with two initial beam energies, 100 and 190 MeV/u, were investigated and shown in this article as examples (see Figure 2). It was found that using the refined nuclear reaction cross section curve, a better agreement with the experimental data was achieved. Therefore, the new nuclear reaction

cross section parametrization has been implemented in the FLUKA development version starting from 2018.These improvements were needed prior to the clinical use of FLUKA for helium ion therapy.
This work can be extended at energies above those used for hadron therapy and for projectile and target materials heavier than carbon. Enhancement of the accuracy of the nuclear reaction cross section models could be beneficial also for other FLUKA applications, like heavy ion collisions and space radiation research.

Acknowledgements

GA wants to thank the European Union's Horizon 2020 research and innovation programme under the Marie Sklodowska-Curie grant agreement No 675265 OMA fo the funding. The authors wish to thank the Heidelberg Ion-Beam Therapy center for the beam time and the GSI target laboratory for the support regarding the targets.

Bibliography

References

[1] O. Jäkel, Medical physics aspects for particle therapy, *Radiat Prot Dosimetry* **137**(1-2) (2009) 156-166

[2] A. Mairani *et al.*, Biologically optimized helium ion plans: calculation approach and its in vitro validation, *Phys. Med. Biol.* **61** (2016) 4283-4299

[3] T. Tessonnier *et al.*, Helium ions at the Heidelberg ion beam therapy center: comparison between FLUKA Monte Carlo code predictions and dosimetric measurements, *Phys. Med. Biol.* **62** (2017) 6784-6803

[4] A. Ferrari *et al.*, FLUKA: a multi-particle transport code, CERN-2005-10, INFN/TC-05/11, SLAC-R-773

[5] T.T. Böhlen *et al.*, The FLUKA Code: Developments and Challenges for High Energy and Medical Applocations, Nuclear Data Sheets 120 (2014) 211-214

[6] G. Battistoni *et al.*, The FLUKA Code: An Accurate Simulation Tool for Particle Therapy, *Front. Oncol.* 6: 116 (2016)

[7] R.K. Tripathi, F.A. Cucinotta and J.W. Wilson, Universal parametrization of absorption cross sections III - light systems, *Nucl. Instr. Meth.* **B** 155 (1999) 349-356

[8] F. Horst *et al.*, Measurement of charge- and mass-changing cross sections for 4He+12C collisions in the energy range 80–220 MeV/u for applications in ion beam therapy, *Phys. Rev. C 96*, (2017) 024624

[9] V. Andersen *et al.*, The FLUKA code for space applications: recent developments, *Advances in Space Research* **34** (2004) 1302–1310

[10] I .Tanihata *et al.*, Measurements of interaction cross sections and radii of He isotopes, *Phys. Lett.* **160** (1985) 380

[11] A. Ingemarsson *et al.*, New results for reaction cross sections of intermediate energy α-particles on targets from ^{9}Be to ^{208}Pb, *Nucl. Phys.* **A** 676 (2000) 3

[12] F. Horst *et al.*, Measurement of 4He charge- and mass-changing cross sections on H, C, O, and Si targets in the energy range 70-220 MeV/u for radiation transport calculations in ion-beam therapy, accepted in Phys. Rev. C

[13] T. Tessonier *et al.*, Experimental dosimetric comparison of 1H, 4He, 12C and 16O scanned ion beams, *Phys. Med. Biol.* **62**10 (2017) 3958-3982

MONET code: evaluation of the dose in Hadrontherapy

A. Embriaco[1], *A.Fontana*[2], *A. Rotondi*[2,3]
[1] INFN, Sezione di Milano , Milano, Italy
[2] INFN, Sezione di Pavia , Pavia, Italy
[3] Dipartimento di Fisica, Università di Pavia - Pavia, Italy

Abstract
The energy deposition of Helium ion beams in a water target was investigated with the development of a new model. The model, called MONET (MOdel of ioN dosE for Therapy), evaluates the 3D energy deposition distribution for protons in a water phantom. In this work, the code is extended to calculate the energy distribution of Helium ions and renamed MONETα. The code evaluates the lateral and longitudinal terms starting from first principles and has been validated with FLUKA, which is currently used in many hadrontherapy centers and is continuously validated with experimental data. The MONET code accounts for all the physical effects of the interaction of Helium ions with water and is based on well known and validated theories. The advantage of our model are the physical foundation, the small number of parameters, the fast calculation time and the accuracy.

1 Introduction

In particle therapy, the most commonly used particles are protons and carbon ions. Recently, Helium beams have been rediscovered as a good compromise between protons and ^{12}C ions [1].
From a physical and biological point of view, ^{4}He ions seem to fill the gap between protons and ^{12}C [2]. The most important advantages of ^{4}He beams are a reduction of multiple Coulomb scattering and energy straggling compared to protons and less projectile fragmentation than Carbon ions.
The necessary step for the application of ^{4}He ions in cancer therapy is the development of new algorithms for TPS or extensions of existing versions. In this work, the extension of MONET code for the evaluation of deposited energy in case of ^{4}He ions (MONETα) and the comparison with the Monte Carlo (MC) simulation are shown.

2 MONETα code

MONET (Model of ioN dosE for Therapy) is a code for the computation of the 3D dose distribution for protons and Helium ions in water [3]. MONET was born for the dose evaluation for proton beam in water, but it is extended in case of Helium beam (MONETα).
In the code, the input variables are the energy and the beam shape. The first step is the evaluation of lateral distribution taking into account the Multiple Coulomb scattering and the nuclear interaction. Afterwards, starting from the 1D lateral profile the model reconstruct the 2D radial distribution. The last step is the calculation of energy deposition and the scale of the 2D lateral distribution at this value.
MONET code is able to evaluate a 3D dose distribution, with only four free parameters for the nuclear interaction.
All results of MONET code are compared with the FLUKA MC code, this is supported by the fact that FLUKA has been validated with experimental data of ^{4}He ions, acquired at the HIT center [4].

2.1 Lateral profile

The shape of lateral profile come from the combination of multiple Coulomb scattering and the nuclear interactions. In the MONET code, the implementation of multiple Coulomb scattering is based on the

well known and validated Molière's theory. To take into account also the nuclear interaction, we have added to Molière distribution the Cauchy-Lorentz function, that describes the nuclear tail of distribution. The lateral distribution is given by [5]:

$$f_x(x) = W_p f_M(x) + (1 - W_p)\frac{t(x)}{\int t(u)du} \tag{1}$$

The Cauchy-Lorentz distribution is:

$$t(y) = \frac{1 - A\exp\left[-\frac{y^2}{2b^2\sigma^2}\right]}{\pi b\left(\frac{y^2}{b^2} + 1\right)} \tag{2}$$

where the free parameters A, b and σ have been obtained by a fit to FLUKA simulation with the nuclear interactions switched on. During the fit study, a good results has been obtained with the variance fixed ($\sigma = 1$).
The Molière distribution is weighed for the primary particle weight W_p, while the Cauchy-Lorentz distribution is multiplied for the nuclear contribution $(1 - W_p)$. For the evaluation of W_p a parametrization of attenuation curve obtained with FLUKA has been proposed in the following section.

2.1.1 Attenuation of primary particle

When large thicknesses are involved, the nuclear interactions give a contribution to the deposited energy that can be estimated as about 2% per cm of water depth for Helium beams [6]. This factor accounts for the primary particles fluence decrease and describes interactions, that also affect the tails of the lateral distribution.

With FLUKA, the decrease of fluence as a function of depth for each energy analyzed has been evaluated. The attenuation curves are fitted using an error function multiplied by a linear parametrization:

$$W_p = (\alpha z + \beta) \times \text{erf}\left(\frac{R - z}{\gamma}\right) \tag{3}$$

where z is the depth in water, R is the range and a, b and c are the free parameters.

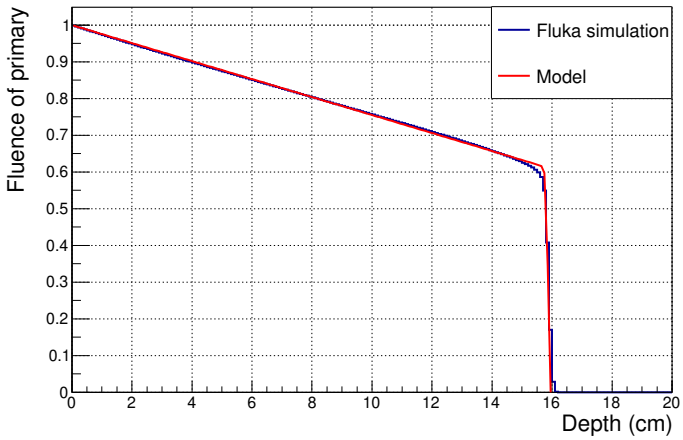

Fig. 1: The attenuation curve of 150 MeV/u ^4He ions as a function of depth: FLUKA simulation is reported in blue line and the result of fit with Eq. 3 is in red line. The best fit value of Eq. 3: $\alpha = 0.0245$, $\beta = 1$ and $\gamma = 0.1$.

The linear parametrization describes the initial part of the attenuation, while the error function represents the decrease to almost zero in the correspondence of the Bragg peak.
The fit results of the attenuation are reported in Fig.1, where the agreement between the simulation and model is good (2%) for the analyzed energies.

2.1.2 From 1D to 2D lateral distribution

The next step for the evaluation of lateral distribution is the passage from the projected lateral distribution to a 2D distribution. The projected distribution f_x and f_y are uncorrelated but not independent [7]. In the MONET code, the Papoulis theorem has been implemented, that allow, in case of cylindrical symmetry to rebuild the radial distribution starting from the projected one [8].
In Figure 2, the total lateral distribution is in good agreement with FLUKA simulation (left), while the radial distribution evaluated with Papoulis algorithm has been compared to FLUKA radial distribution (right).

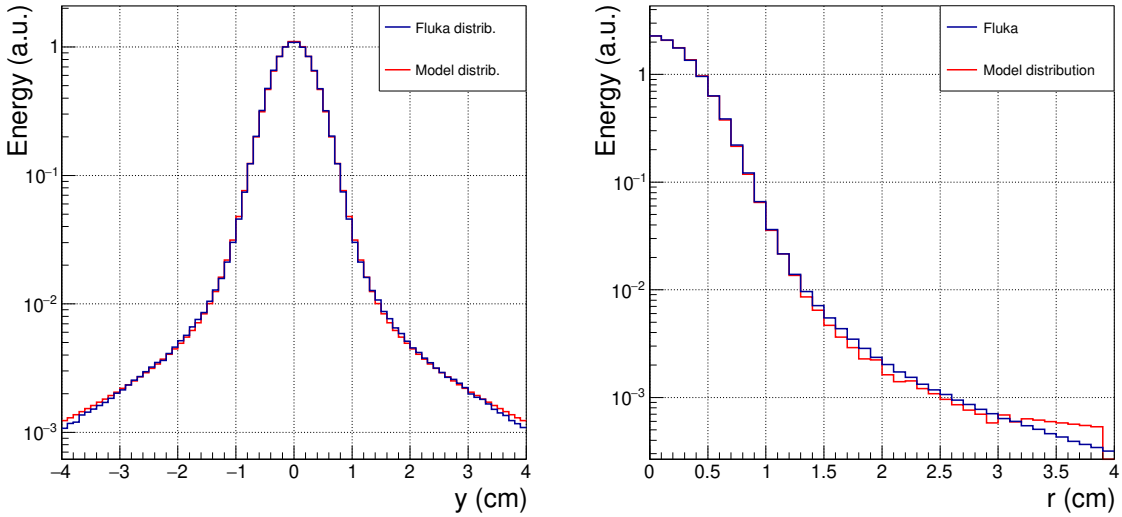

Fig. 2: Lateral (left) and radial (right) distribution for 150 MeV ^4He ions in water at a depth z=14 cm (Bragg peak at 15.9 cm).

2.2 Longitudinal profile

The second part of MONET code is the estimation of energy loss in the longitudinal profile.
The longitudinal dose profile is mainly determined by the stopping process of projectile due to inelastic collisions with the atomic electrons. In the MONET code, the average energy loss is evaluated using the following expression [3]:

$$E_k(z) = -m + \frac{F(z)}{2} + \sqrt{m^2 + \frac{F^2(z)}{4}} \tag{4}$$

where:

$$F(z) = p\beta\Big(1 - \frac{z}{R}\Big)^{k/2}, \qquad k = 1.07 \tag{5}$$

The comparison of the Eq.4 and FLUKA simulation shows a good agreement within 1%.

For a complete description of the longitudinal profile, we have also considered the statistical variations in the energy lost by the incident particle, the so called straggling. Due to the straggling, the shape

of the longitudinal profile changes specially at the end of the particle track: the Bragg peak is less sharp and the curve has a small tail at the end. A good approximation for the straggling is given by a Gaussian distribution around the mean depth $\bar{z}$. The energy deposed can be obtained by the convolution of the analytical dose (Eq. 4) with a Gaussian function [9] of standard deviation $\sigma(\bar{z})$:

$$\hat{E}_k(z) = \int_0^R E_k(\bar{z}) \frac{e^{-(z-\bar{z})^2/2\sigma^2(\bar{z})}}{\sqrt{2\pi}\sigma(\bar{z})} d\bar{z} \tag{6}$$

Since the longitudinal profile is extremely flat until the end, only the last part including the Bragg peak will be significantly affected by a convolution.
For Helium beam, the energy deposition with straggling is evaluated by a convolution with a Gaussian of $\sigma(\bar{z})$:

$$\bar{\sigma} \approx 0.012 R^s \tag{7}$$

where the s values are tuned on the FLUKA depth dose profile including straggling.

In the evaluation of the longitudinal profile, nuclear interactions play an important role by reducing the fluence of the primary particles. Due to nuclear reactions particles are removed from the electromagnetic peak and their secondaries deposit their energy upstream. To complete the longitudinal dose profile, also the nuclear contributions are included in the MONET calculation:

$$f_z(z) = W_p \hat{E}_k(z) + (1 - W_p) E_N(z) \tag{8}$$

where the first term represents the energy deposition of the primary particles and the second is the contribution of nuclear interactions. The energy deposited by the nuclear fragments $E_N(z)$ is added using a linear parametrization, according to [10]:

$$E_N(z) = a'(E)z + b'(E) \tag{9}$$

where the coefficients a' and b' are obtained by fitting the FLUKA results in the presence of the nuclear interactions. The electromagnetic and nuclear contribution are weighted for the primary particle weight and for the nuclear contribution respectively, according to Eq.3.
In case of ^4He ions, there is an important contribution to the dose beyond the Bragg peak, due to nuclear fragmentation. A study of the tail of ^4He ions in water is performed: the depth dose curves from FLUKA simulations are analyzed, focusing in the few centimeters after the peak.
The description of nuclear fragmentation tail is based on the search of practical range, following the approach of [11]. The practical range R_p is defined as the depth corresponding to the intersection point between the tangent at the inflection point of the descending part of the depth dose profile and the exponentially extrapolated fragmentation tail.

The total energy deposition for ^4He ions is given by:

$$f_z(z) = \begin{cases} W_p \hat{E}_k(z) + (1 - W_p)(a'z + b') & 0 < z < R \\ mz + q & R < z < R_p \\ \exp(p_0 + p_1 z) & z > R_p \end{cases} \tag{10}$$

where m and q are the parameter of the tangent at the inflection point and the p_0 and p_1 the parameters of the exponential fit of the tails. In Figure 3, the modelization of the fragmentation tail of ^4He is validated with FLUKA simulations and the agreement is within 3%, as indicated in the inset plot.

3 Results

The MONET code is able to evaluate the total dose profile in a 3D mesh with only four free parameters, by calculating at each depth the longitudinal deposited energy and by distributing it laterally on the

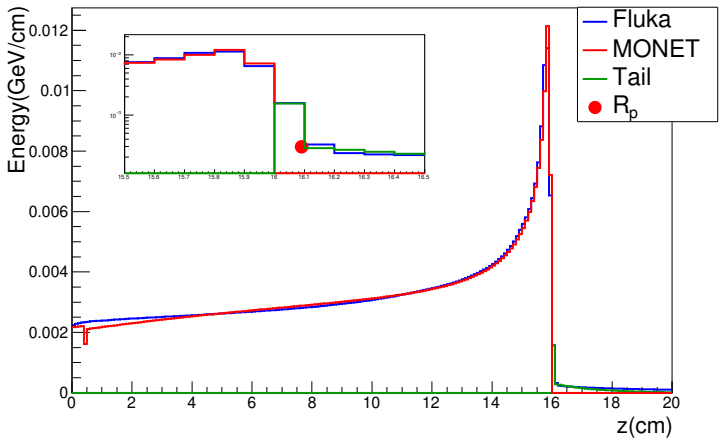

Fig. 3: Bragg curves including nuclear contributions of ^4He ions calculated with MONETα compared with FLUKA simulations for 150 MeV/u. The bullet point represent the practical range R_p. In the inset plot, a zoom of fragmentation tail is reported in logarithmic scale.

transverse plane. Therefore, the dose is the product between the longitudinal energy deposition and the radial probability distribution in the transverse plane.
To assess the accuracy of MONET code, the dose distribution of a single beam with Gaussian profile is

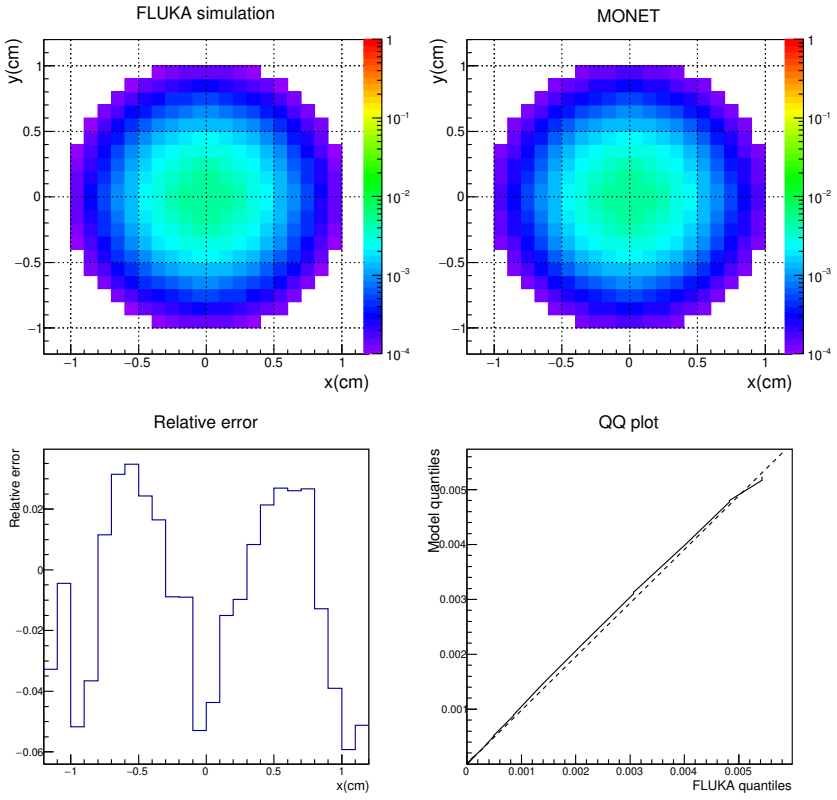

Fig. 4: The energy deposition of 4 He beam of 150 MeV/u at 14 cm in water phantom (Bragg peak at 15.9 cm).

evaluated in a 3D mesh with a voxels of 1mm dimension: the results are obtained by selecting transverse plane at fixed depths.

In Fig.4, the comparison between FLUKA and MONETα profile for ^4He ions of 150 MeV/u at 14 cm water depth is shown. The relative error is evaluated in a central cross section and is about 4%. The quantile-quantile (QQ) plot is also reported in order to compare the quantiles of the model and MC distribution. The QQ plot is a 45° line in case of perfect match and in our case this is well verified.

In addition to the accuracy, another advantage of MONET approach is the fast calculation time. Indicatively, for each depth the calculation time is $\sim$ 2 seconds for the single beam, competitive if compared to the simulation time ($\sim$ hours for 10^7 primaries).

4 Conclusions

The possibility to describe the energy deposition for ^4He beams with the MONET approach has been investigated. The dose deposition for different therapeutic energies has been analyzed, comparing the distributions obtained with the model using the FLUKA code.
The results obtained demonstrate the possibility to extend the MONET code to the case of ^4He ions, making MONETα a possible new tool for the evaluation of the energy deposition for applications to Treatment Planning Systems (TPS).
A possible development of this study is the creation of dose database of interest for the clinical use and an online/in-room fast dose evaluation tool.

References

[1] Francesco Tommasino, Emanuele Scifoni, and Marco Durante. New ions for therapy. *International Journal of Particle Therapy*, 2(3):428–438, 2015.

[2] M Rovituso, C Schuy, U Weber, S Brons, MA Cortés-Giraldo, C La Tessa, E Piasetzky, D Izraeli, D Schardt, M Toppi, et al. Fragmentation of 120 and 200 MeV/u ^4He ions in water and pmma targets. *Physics in Medicine and Biology*, 62(4):1310, 2017.

[3] A. Embriaco, V.E. Bellinzona, A. Fontana, and A. Rotondi. An accurate model for the computation of the dose of protons in water. *Physica Medica*, 38:66 – 75, 2017.

[4] T. Tessonnier, A. Mairani, S. Brons, T. Haberer, J. Debus, and K. Parodi. Experimental dosimetric comparison of 1h, 4he, 12c and 16o scanned ion beams. *Physics in Medicine and Biology*, 62(10):3958, 2017.

[5] E V Bellinzona, M Ciocca, A Embriaco, A Ferrari, A Fontana, A Mairani, K Parodi, A Rotondi, P Sala, and T Tessonnier. A model for the accurate computation of the lateral scattering of protons in water. *Physics in Medicine & Biology*, 61(4):N102, 2016.

[6] A. Embriaco, V.E. Bellinzona, A. Fontana, and A. Rotondi. On the lateral dose profile of 4he beams in water. *Physica Medica*, 40:51 – 58, 2017.

[7] R. Frühwirth and M. Regler. On the quantitative modelling of core and tails of multiple scattering by gaussian mixtures. *Nuc. Instr. Meth. Phys. Res. A*, 456(3):369–89, 2001.

[8] A. Papoulis. Joint densities with circular symmetry (corresp.). *IEEE Trans. on Inf. Theo.*, 14(1):164–65, 1968.

[9] T. Bortfeld. An analytical approximation of the bragg curve for therapeutic proton beams. *Medical Physics*, 24(12):2024–33, 1997.

[10] A. Carlsson, P. Andreo, and A. Brahme. Monte carlo and analytical calculation of proton pencil beams for computerized treatment plan optimization. *Phys. Med. Bio.*, 42(6):1033, 1997.

[11] J. Kempe and A. Brahme. Energy-range relation and mean energy variation in therapeutic particle beams. *Medical Physics*, 35(1):159–70, 2008.

Diagnostic (^{99}Mo/^{99m}Tc) and Therapeutic (^{67}Cu) Radioisotopes Produced by Neutrons from C,Be(*d*,*n*)

Y. Nagai[1], K. Hashimoto[1], M. Kawabata[1,3], K. Tsukada[1,2], Y. Hatsukawa[1], F. Minato[2], Y. Sugo[1], H. Saeki[1,3], and Si Motoishi[1,3]

1. National Institutes for Quantum and Radiological Science and Technology, Ibaraki, Japan
2. Japan Atomic Energy Agency, Ibaraki, Japan
3 Chiyoda Technol Corporation, Ibaraki, Japan

Abstract

New production routes to produce ^{99}Mo and ^{67}Cu by the ^{100}Mo(*n*,2*n*)^{99}Mo and the ^{68}Zn(*n*,*n'p*+*d*)^{67}Cu reactions using accelerator neutrons are discussed. A thermoschromatographic system was developed to separate high quality ^{99m}Tc from ^{99}Mo of low specific activity with high efficiency. The pharmaceutical quality of ^{99m}Tc pertechnetate solution obtained from ^{99}Mo met the United States Pharmacopeia requirements. The calculated ^{99}Mo yield from a 100 – 150 g $^{100}MoO_3$ sample indicates that about 50% of the demand for ^{99}Mo in Japan can be met with a single accelerator capable of 40 MeV, 2 mA deuteron beams for an irradiation time of 24 h. The radionuclide purity of ^{67}Cu is quite high. The measured biodistribution of $^{67}CuCl_2$ in colorectal tumor-bearing mice showed a high uptake of ^{67}Cu in the tumor, which suggests that $^{67}CuCl_2$ can be a potential radionuclide agent for cancer radiotherapy.

Keywords

medical radioisotope, accelerator neutrons, neutron induced reaction, PET, SPECT, immunotherapy

1 Introduction

More than 80% of all diagnostic procedures in the world are carried out every year using ^{99m}Tc ($T_{1/2}$ = 6 h) separated from ^{99}Mo ($T_{1/2}$ = 66 h). Currently, most ^{99}Mo is produced by the fission reaction of enriched ^{235}U in about nine research reactors around the world [1]. However, an unscheduled shutdown of some of the reactors in 2008–2009 caused a shortage of ^{99}Mo worldwide. The shortage of ^{99}Mo due to the incident has triggered widespread discussions on the medium- and long-term supplies of ^{99}Mo. In fact, a variety of alternative methods to produce ^{99}Mo and/or ^{99m}Tc in reactors and accelerators have been proposed [2]. Nagai and Hatsukawa proposed a new route of producing ^{99}Mo via the ^{100}Mo(*n*,2*n*)^{99}Mo (hereafter, (*n*,2*n*)^{99}Mo) reaction using accelerator neutrons produced by the C(*d*,*n*) reaction using deuteron beams [3]. The neutron source for (for example) 40 MeV deuterons provides a continuous spectrum from thermal energy to about 40 MeV with a most probable energy of 14 MeV and a peak at forward angles with respect to the deuteron beam direction [4].

Noninvasive radionuclide therapy is playing an important role in the treatment of various cancers. Among various radionuclides useful for diagnostic imaging and in targeted radionuclide therapy (hereafter, theragnostic radionuclide), Cu radionuclides are known to have unique potentials [5,6]. ^{64}Cu ($T_{1/2}$ = 13 h) is used for PET imaging and ^{67}Cu ($T_{1/2}$ = 62 h) is considered to be a promising theragnostic radionuclide [3]. ^{67}Cu emits the 91, 93 and 185 keV γ-rays suitable for SPECT imaging, and β-rays with a mean energy of 0.141 MeV to kill targeted cancer cells. Owing to the low availability of ^{67}Cu, however, there have been few medical studies with the use of ^{67}Cu. Currently, the ^{68}Zn(*p*,2*p*)^{67}Cu reaction is used to produce ^{67}Cu, but the production of ^{67}Cu is about 3.7 GBq per month worldwide [7], which might be too low for the study of medical applications. A new route

was proposed by Kin et al. to produce a significant amount of ^{67}Cu by the ^{68}Zn(n,$n'p$+d)^{67}Cu reaction by using accelerator neutrons mentioned above [8].

We report the experimental procedure and the results for producing ^{99}Mo/^{99m}Tc and ^{67}Cu by using accelerator neurons from the Be,C(d,n) reaction with a deuteron energy of 40 and 50 MeV.

2. Production of ^{99}Mo/^{99m}Tc

2.1 ^{99}Mo production by ^{100}Mo(n,2n)^{99}Mo

We found that accelerator neutrons have a great potential to produce a large quantity of high-quality ^{99}Mo with a minimum level of radioactive wastes without ^{235}U. The characteristic points of the ^{99}Mo production methods are as follow. The evaluated cross section of the (n,2n)^{99}Mo reaction in the neutron energy (E_n) range between 10 and 20 MeV is quite large, about 1.5 barn [9]. On the other hand, the cross sections of the (n,α), (n,$n'p$), and (n,p) reactions on ^{100}Mo, which can produce impurity radionuclides other than ^{99}Mo, are less than a few mb at E_n ~ 14 MeV. A large amount of ^{100}Mo sample (> 100 g) can be used. In addition, intense neutrons with the energy of 11 – 18 MeV, necessary to produce ^{99}Mo with good specific-activity, are available as discussed later.

2.2 ^{99}Mo yield

The cross section of the (n,2n)^{99}Mo reaction has not yet been measured using accelerator neutrons from the C(d,n) reaction at the deuteron energy of 40 MeV (E_d = 40 MeV). Note that the neutron energy and angular distributions at E_d = 40 MeV have been measured by two groups; the latest result of the neutron flux is approximately a factor of two larger than that of older one [4]. The cross section of the (n,2n)^{99}Mo reaction was measured at 8.5 ≤ E_n ≤ 20.5 MeV [10]. Note that the neutrons have a continuous energy spectrum from the thermal energy to about 40 MeV. An accurate measurement of the ^{99}Mo yield for a large mass MoO_3 sample of approximately 100 g is necessary to solve the discrepancy of the neutron flux between existing data including the evaluated cross section of the (n,2n)^{99}Mo reaction. The measurement would also provide information in considering the economic sustainability of the proposed production method by the (n,2n)^{99}Mo reaction.

We used four pellet $^{nat}MoO_3$ samples having each mass of about 26 g mass. Schematic of the experimental setup is shown in Fig. 1.

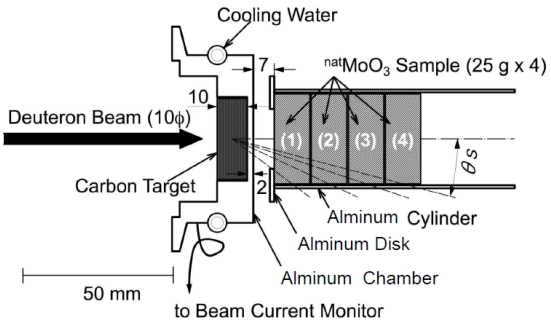

Fig. 1. Schematic of the experimental setup at the $^{nat}MoO_3$ sample position [12].

Here, θ_s indicates an opening angle between the lines connecting the outer edge of the sample to the geometric centers of the sample. This arrangement of the samples was aimed at being a rigorous test of the measurement of the energy and angular distributions of the accelerator neutrons including the

evaluated cross section. The measurement was performed by using accelerator neutrons provided by the C(*d*,*n*) reaction of 40 MeV deuterons at the Takasaki Ion Accelerators for Advanced Radiation Application of the National Institutes (TIARA) for Quantum and Radiological Science and Technology, and at Cyclotron and Radioisotope Center, Tohoku University [11,12].

The measured yield of ^{99}Mo at the end of irradiation (EOI) agrees well with the calculated one as given in Table 1. The calculated yield was obtained by using the latest data on the neutron flux and the neutron-nucleus reaction cross sections given in the fourth version of the Japanese Evaluated Nuclear Data Library (JENDL-4.0) [9].

$^{nat}MoO_3$ (g)	25.869	25.868	25.483	25.220
$^{99}Mo_{meas.}$(10^4 Bq)	3.9 ± 0.2	2.6 ± 0.1	1.7 ± 0.1	1.3 ± 0.1
$^{99}Mo_{cal.}$(10^4 Bq)	3.6 ± 0.7	2.3 ± 0.4	1.5 ± 0.3	1.0 ± 0.2

Table 1. Measured ^{99}Mo yield ($^{99}Mo_{meas.}$) at the EOI compared with the calculated yield ($^{99}Mo_{cal.}$) [12]

The agreement provides reliable evidence to determine the best conditions for obtaining the calculated maximum yield of ^{99}Mo under a given condition such as a $^{100}MoO_3$ sample mass and the distance between the carbon target and the $^{100}MoO_3$ sample. In fact, using 40 MeV, 2 mA deuterons the calculated yields of ^{99}Mo at the end of irradiation for an irradiation time of 24 h for the $^{100}MoO_3$ samples of 100 – 150 g mass would meet about 50% of the demand for ^{99}Mo in Japan [11,12].

2.2 Separation of ^{99m}Tc from the ^{99}Mo of low-specific activity

There have been two key issues in obtaining high-quality ^{99m}Tc for any alternative ^{99}Mo production method other than the fission reaction of ^{235}U. Firstly, the specific activity of alternative ^{99}Mo is so low that one cannot use a conventional ^{99}Mo/^{99m}Tc generator. The second key issue is that the pharmaceutical quality of ^{99m}Tc pertechnetate ($^{99m}TcO_4^-$) solution obtained from (n,2n)^{99}Mo has yet to satisfy the United States Pharmacopeia (USP).

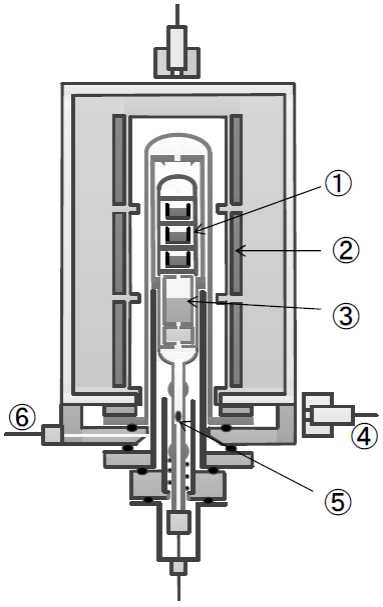

Fig. 2. Schematic of the experimental setup of the thermochromatographic separation. [13]

Among various methods to separate ^{99m}Tc from the ^{99}Mo of low-specific-activity, we employed the thermo-separation method in an electric furnace [13]. Note that the method could allow us to obtain ^{99m}Tc with a high radioactive concentration, and to reuse an irradiated enriched ^{100}Mo sample. Despite the progress so far made concerning the method, several problems to challenge remain: the separation efficiency of ^{99m}Tc is low, diminishes markedly with repeated milking tests, and decreases with an increasing mass of MoO_3 loaded into a sublimation furnace at a time [14].

The separation of ^{99m}Tc from the irradiated $^{100}MoO_3$ sample was carried out using a three-zone electric furnace which contained a quartz tube, three platinum boats to hold irradiated MoO_3 samples, and crumpled gold wire to trap vaporized ^{99m}Tc oxide as shown in Fig. 2 [13]. The maximum temperature of the furnace zone was set at around 830°C to melt the irradiated MoO_3 samples. The high separation efficiency of 95% was achieved for the 20.3 g molten MoO_3 sample [13]. It should be added that a 99% recovery of an enriched $^{100}MoO_3$ sample of over 100 g mass was achieved by using the thermochromatography apparatus [15]. Note that an enriched $^{100}MoO_3$ sample is very expensive, so recycling of the sample by recovering it with high efficiency is crucial for the economical production of $(n,2n)^{99}$Mo.

The results of the quality assessments of the $(n,2n)^{99m}TcO_4^-$ saline solution and several ^{99m}Tc-radiopharmaceuticals commonly used for the imaging of brain perfusion (^{99m}Tc-ECD), myocardial perfusion (^{99m}Tc-MIBI), and kidney (^{99m}Tc-MAG3), to ensure the safe clinical use of $(n,2n)^{99m}$Tc are summarized in Table I [16]. The quality of $^{99m}TcO_4^-$ should be noted to satisfy the United States Pharmacopeia (USP), which stipulates regulatory requirements on the radionuclide purity of ^{99m}Tc, radiochemical purity of $^{99m}TcO_4^-$, radiochemical yields of ^{99m}Tc radiopharmaceuticals, and the concentration of aluminium (Al) in the ^{99m}Tc product.

Parameter	USP	Exp. 1	Exp. 2	Exp. 3	Exp. 4
pH	4.5 to 7.5	7.23	7.16	6.66	6.58
Endotoxins	<175 EU/V	<0.03 EU/mL	>0.03 EU/mL	<0.03 EU/mL	<0.03 EU/mL
Radionuclidic purity - non fission	^{99}Mo/^{99m}Tc<0.015% Other γs/^{99m}Tc<0.05%	<0.015% <0.05%	<0.015% <0.05%	<0.015% <0.05%	<0.015% <0.05%
Aluminum	<10 ppm	<10 ppm	<10 ppm	<10 ppm	<10 ppm
Molybdenum	Not specified	-	0.138 ppm	0.020 ppm	0.034 ppm
Radiochemical purity	>95% $^{99m}TcO_4^-$	>99%	>99%	>99%	>99%

Radiochemical yield	>90%	^{99m}Tc-MIBI >95%	^{99m}Tc-ECD >95%	^{99m}Tc-MAG3 >95%	^{99m}Tc-MDP >95%

Table 2. Results of the quality control tests of the $^{99m}TcO_4^-$ saline solution and ^{99m}Tc-radiopharmaceuticals and USP specifications. [16]

3. Production of ^{67}Cu

3.1 Radionuclide purity of ^{67}Cu produced by the ^{68}Zn(n,$n'p$+d)^{67}Cu reaction

So far, many studies were performed to produce as much ^{67}Cu as possible by using reactors via the ^{67}Zn(n,p)^{67}Cu reaction and accelerators via the ^{68}Zn(p,2p)^{67}Cu, ^{68}Zn(γ,p)^{67}Cu, ^{67}Zn(n,p)^{67}Cu, ^{70}Zn(p,α)^{67}Cu, and ^{70}Zn(d,αn)^{67}Cu reactions [17].

In this study the radionuclide purity of ^{67}Cu produced by the ^{68}Zn(n,$n'p$+d)^{67}Cu reaction was investigated using an enriched ^{68}ZnO sample and neutrons from the C(d,n) reaction of 40 MeV deuterons [18]. The purity at EOI was shown to be high, thus solving the impurity problems of ^{64}Cu and ^{65}Zn which were coproduced together with ^{67}Cu by the ^{68}Zn(p,2p)^{67}Cu reaction [18].

	Beam energy (MeV)	Ratio to ^{67}Cu						
		^{64}Cu	^{66}Ga	^{67}Ga	^{69m}Zn	^{65}Zn	^{65}Ni	^{66}Ni
^{68}Zn(p,2p)^{67}Cu	100 → 20	10	~12	~2.5		~0.1		
^{70}Zn(d,αn)^{67}Cu	19.5 → 18.4	0.1	0.03	0.07	2.3			
Present Exp. ^{68}Zn(n,x)		<0.016	~0	~0	0.14	6.7×10^{-4}	2.6	$(2.4–5.0)\times10^{-3}$

Table I. Activity ratios of impurity radionuclides to ^{67}Cu produced by ^{68}Zn(p,2p)^{67}Cu, ^{70}Zn(d, αn)^{67}Cu, and ^{68}Zn(n,$n'p$+d)^{67}Cu reactions at EOI. [18]

3.2 Chemical separation of ^{67}Cu from Zn

Stable copper isotopes in the ^{68}ZnO samples were removed by chelating ion-exchange column chromatography to obtain high specific activity of ^{67}Cu. The chemical separation of ^{67}Cu from the neutron-irradiated ^{68}ZnO sample was performed to obtain highly purified ^{67}Cu to form ^{67}CuCl$_2$ (^{64}CuCl$_2$) by using a cation-exchange column, a chelating ion-exchange column, and an anion-exchange column [19]. The separation yield of ^{67}Cu was 91%.

The specific activity of ^{67}Cu was determined to be 4.5 MBq/(μg Cu) at EOI. This value is much smaller than the typical specific activity of ^{64}Cu produced by the ^{64}Ni(p,n)^{64}Cu reaction in the range of 2.4 – 11 GBq/(μg Cu) quoted from the recent study on the biodistribution of ^{64}CuCl$_2$ in rats [20]. In low-specific-activity radiopharmaceuticals, stable isotopes such as ^{63}Cu and ^{65}Cu compete with radioactive isotopes, which results in poor radiolabeling and low uptake of the tracer in tissues. Hence, it is very interesting to study the role of ^{67}CuCl$_2$ with low specific activity in the biodistribution of ^{67}Cu ions in colorectal tumor-bearing mice.

3.3 Biodistribution of ^{67}CuCl$_2$ in mice

Cu-based radiopharmaceuticals that can accumulate in cancer cells have been developed and widely used. Recently, ^{64}CuCl$_2$ has been identified as a potential agent for PET imaging and radionuclide therapy. The results suggest that Cu metabolism is also important for many cancers, and prompted us to measure the biodistribution of ^{67}CuCl$_2$ in colorectal tumor-bearing mice. The biodistribution of ^{67}CuCl$_2$ in LS180 tumor-bearing mice was determined by using ^{67}Cu of very low-specific-activity as shown in Fig. 3 [21]. It is very interesting that a high uptake of ^{67}Cu in the tumor was found, which may indicate an important role of Cu metabolism in colorectal cancer. The accumulation of ^{67}Cu in the

tumor was 7.0 ± 1.4 %ID/g at 48 h, comparable to that of ^{64}Cu, ~5 %ID/g, in spite of the differences in the cancer cell lines and in the specific activities. $^{67}CuCl_2$ can be a potential radionuclide agent for cancer radiotherapy.

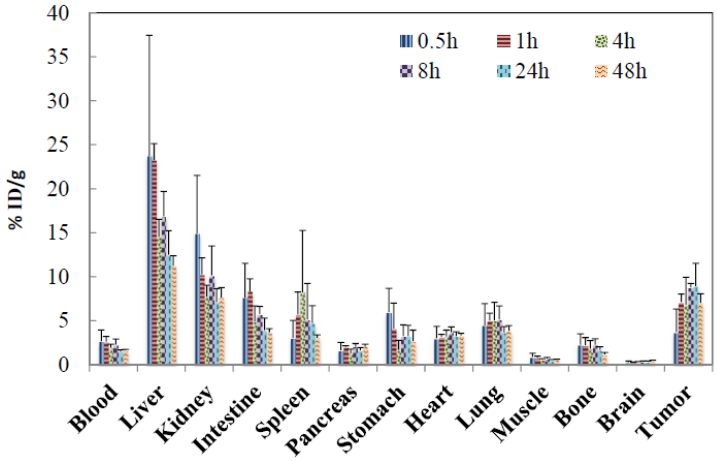

Fig. 2. Biodistribution of $^{67}CuCl_2$ in LS180 tumor-bearing mice with standard deviation. [21]

4. Production of accelerator neutrons

The intensity of neutrons having energies at $10 \leq E_n \leq 20$ MeV is the key issue for sufficiently producing ^{99}Mo by the $(n,2n)^{99}$Mo reaction. Recently significant progress has been achieved in accelerator technology to obtain intense neutrons. In fact, at SPIRAL2 located at GANIL, neutrons with an intensity of 10^{15} n/s are expected to be produced by the C(d,n) reaction using 40 MeV 5 mA deuterons [22]. A great advance has also been achieved with the development of a neutron converter, which can withstand the high power of the 40 MeV 5 mA deuteron beams [23]. On the basis of these developments, we propose to construct an AVF cyclotron with a deuteron beam intensity of 2 mA as a prototype facility, since a fixed radiofrequency cyclotron is robust in operation, compact in size, and relatively cheap compared to a linear accelerator.

5. Conclusions

A new method has been proposed for the generation of radioisotopes such as ^{99}Mo and ^{67}Cu with accelerator neutrons by deuterons (hereafter, GRAND). A prototype facility for the GRAND consists of a cyclotron to produce intense accelerator neutrons from the C(d,n) reaction with 40MeV 2mA deuteron beams. The characteristic feature of the GRAND lies in its capability to produce a wide variety of high-quality, carrier-free radioisotopes with a minimum level of radioactive waste without using uranium. The separation of high quality ^{99m}Tc from ^{99}Mo of low specific activity, which was produced by the ^{100}Mo(n,$2n$)^{99}Mo reaction, was performed by developing a thermoschromatographic system. The pharmaceutical quality of ^{99m}Tc pertechnetate solution obtained from ^{99}Mo met the United States Pharmacopeia requirements. About 50% of the demand for ^{99}Mo in Japan can be met with the prototype facility. The biodistribution of $^{67}CuCl_2$ in colorectal tumor-bearing mice was measured using ^{67}Cu of high radionuclide purity that was produced by the ^{68}Zn(n,$n'p$+d)^{67}Cu reaction and a high uptake of ^{67}Cu in the tumor was observed, which suggests that $^{67}CuCl_2$ can be a potential radionuclide agent for cancer radiotherapy. It should be mentioned that the potential of the GRAND for various medical radioisotopes coproduction provides an important indication of the economic sustainability,

demand risk mitigation and the ability to avoid creating other isotope shortage. The prototype system is compact in size, and easy to operate; therefore it could be used worldwide to produce radioisotopes for medical, research, and industrial applications.

Acknowledgement

We thank C. Konno, K. Ochiai, H. Yamabayashi, Y. Ohshima, Sa. Watanabe, N. S. Ishioka, Y. Kawauchi, N. Takeuchi, Y. Adachi, Y. Morikawa, and M. Itoh for their continuous support and useful discussions.

References

[1] The Supply of Medical Radioisotopes: Report by OECD Nuclear Energy Agency (April 2017).
[2] K. Bertsche, Proc. IPAC'10, p.121 (2010).
[3] Y. Nagai and Y. Hatsukawa, *J. Phys. Soc. Jpn.* **78**, 033201 (2009).
[4] G. Lhersonneau et al., *Nucl. Instrum. Methods Phys. Res., Sect.* A **603**, 228 (2009).
[5] I. Novak-Hofer and P. A. Schubiger, *Eur. J. Nucl. Med.* **29**, 821 (2002).
[6] Suresh C. Srivastava and Leonard F. Mausner, R. P. Baum (ed.), Therapeutic Nuclear Medicine, Medical Radiology. Radiation Oncology, Springer-Verlag Berlin Heidelberg 2013
[7] C. S. Cutler et al., *Chem. Rev.* **113**, 858 (2013).
[8] T. Kin et al., *J. Phys. Soc. Jpn.* **82**, 034201 (2013).
[9] K. Shibata et al., *J. Nucl. Sci. Technol.* **48**, 1 (2011).
[10] A. I. M. Plompen et al., *J. Nucl. Sci. Technol, Suppl*. **2**, 192 (2002).
[11] F. Minato et al., *J. Phys. Soc. Jpn.* **86**, 093201 (2017).
[12] K. Tsukada et al., *J. Phys. Soc. Jpn*. **87**, 043201 (2018).
[13] Y. Nagai et al., *J. Phys. Soc. Jpn*. **83**, 083201 (2014).
[14] R. E. Boyd: Int. *J. Appl. Radiat. Isot*. **33**, 801 (1982).
[15] M. Kawabata et al., *J. Phys. Soc. Jpn*. **86**, 053201 (2017).
[16] Y. Nagai et al., *J. Phys. Soc. Jpn*. **86**, 053202 (2017).
[17] J. Kozempel et al., *Radiochimica Acta* **100**, 419 (2012).
[18] N. Sato et al., *J. Phys. Soc. Jpn*. **83**, 073201 (2014).
[19] M. Kawabata et al., *J. Radioanal. Nucl. Chem*. **303**, 1205 (2015).
[20] J. C. Manrique-Arias et al., *Appl. Radiat. Isot*. **115**, 18 (2016).
[21] Y. Sugo et al., J. Phys. Soc. Jpn. 86, 023201 (2017).
[22] M. Fadil et al., *Nucl. Instrum. Methods Phys. Res., Sect*. B **266**, 4318 (2008).
[23] M. Avilov, et al.,: LNL-INFN (REP) 179/02 (2002).

Cyclotron-based production of the theranostic radionuclides ^{67}Cu and ^{47}Sc

G. Pupillo[1], L. Mou[1], P. Martini[1,2], M. Pasquali[1,2], J. Esposito[1], A. Duatti[2], C. Rossi Alvarez[1], H. Skliarova[1], S. Cisternino[1], A. Boschi[2], L. Canton[3], A. Fontana[4], F. Haddad[5]

[1] National Institute of Nuclear Physics, Legnaro National Laboratories (INFN-LNL), Legnaro, Italy
[2] Ferrara University and INFN section of Ferrara (INFN-FE), Ferrara, Italy
[3] National Institute of Nuclear Physics, section of Padua (INFN-PD), Padua, Italy
[4] National Institute of Nuclear Physics, section of Pavia (INFN-PV), Pavia, Italy
[5] GIP ARRONAX and SUBATECH, Nantes University, Nantes, France

Abstract
^{67}Cu and ^{47}Sc are theranostic radionuclides in the spot-light of the scientific community: the insufficient availability is limiting their use in clinical and pre-clinical studies. The aim of this work is the analysis of ^{67}Cu and ^{47}Sc production by using high-energy and high-intensity cyclotrons, by exploring promising nuclear reactions induced by proton-beams. In this work are presented the first measurement in the energy range 45-70 MeV of the ^{70}Zn(p,x)^{67}Cu, ^{64}Cu, ^{67}Ga, ^{66}Ga nuclear cross sections (outcome of the COME project), and the preliminary results of the ^{nat}V(p,x)^{47}Sc, ^{46}Sc, ^{44m}Sc, ^{44}Sc, ^{48}Sc, ^{43}Sc nuclear cross sections, investigated in the on-going PASTA project.

1 Introduction

The aim of this work is the analysis of ^{67}Cu and ^{47}Sc production by using high-energy and high-intensity cyclotrons, as the one installed at Legnaro National Laboratories of the Italian Institute of Nuclear Physics (INFN-LNL, Padua, Italy), in the framework of SPES project [1]. The SPES project is focused both on the use of Radioactive Ion Beams (RIB) and applied research in the field of nuclear medicine, through the LARAMED project – acronym of LAboratory of RAdionuclides for MEDicine. LARAMED infrastructure (beam-lines and laboratories) is currently under construction and the research activities regarding cross section measurements are carried out at the ARRONAX facility (Nantes, France) [2], where a 70 MeV cyclotron is operative. Among the radionuclides of major interest for the collaboration LARAMED-ARRONAX there are ^{67}Cu and ^{47}Sc, thanks to their great potential in theranostic applications, allowing the selection of patients with higher chance to respond to specific treatments and the application of individually customized dosimetry. The worldwide increasing interest on this topic is well-represented by the recent Coordinated Research Project (CRP), promoted by the International Atomic Energy Agency (IAEA), focused on "*^{67}Cu, ^{186}Re and ^{47}Sc as Emerging Theranostic Radionuclides*" [3]. The interest on ^{67}Cu- and ^{47}Sc-labelled radiopharmaceuticals stands on their physical characteristics (Table 1): the β^- particles of low-medium energy are useful to deliver cytotoxic dose to small-medium sized tumours while the emitted γ-rays are suitable for SPECT or SPECT/CT cameras; moreover, the relatively long half-life of ^{67}Cu and ^{47}Sc (about 2.6 d and 3.3 d respectively) permits to follow the slow biodistribution of monoclonal antibodies and specific molecular vectors, such as peptides, allowing their use also in radioimmunotherapy. The long half-life allows also centralizing the production, limiting the investment to be done. Finally, β^+ counterparts such as ^{64}Cu and ^{44}Sc exist and may also allow the theranostic approach to be used with PET imaging.

Nowadays, the insufficient availability of ^{67}Cu and ^{47}Sc is limiting their use in clinical and pre-clinical studies. The aim of this work is to study unexplored nuclear reactions to find out possible production routes for these emerging radionuclides. In view of an optimized production, the co-production of

contaminant radionuclides, especially the isotopic impurities that cannot be chemically separated from the desired product and affect the RadioNuclidic Purity (RNP), is a key-point. For this reason, experiments are designed in order to measure not only the nuclear cross section of the radionuclide of interest (*e.g.* ^{67}Cu and ^{47}Sc), but also the production of isotopic contaminants (*e.g.* ^{64}Cu and ^{46}Sc) and other impurities (*e.g.* ^{67}Ga and ^{51}Cr) that may affect the radiochemical procedure aimed at the radionuclide extraction and purification.

Table 1: Nuclear data of interest extracted from NuDat database [4]

Radionuclide	*Half-life*	*γ-ray Energy (Intensity)*	*β⁻ Mean Energy (Intensity)*
^{67}Cu	61.83 h (*12*)	184.577 keV (48.7% *3*)	141 keV (100% *6*)
^{47}Sc	3.3492 d (*6*)	159.381 keV (68.3% *4*)	162.0 keV (100% *8*)

The COME project is focused on the first measurement of the ^{70}Zn(p,x)^{67}Cu nuclear reaction in the energy range 45-70 MeV, complementing the existing data up to 35 MeV [5-7]. Experimental evaluation of the ^{70}Zn(p,x)^{64}Cu, ^{70}Zn(p,4n)^{67}Ga and ^{70}Zn(p,5n)^{66}Ga reactions are also presented for the first time and compared with theoretical estimations provided by the TALYS code [8].

The PASTA project is focused on the production of ^{47}Sc by using proton beams (up to 70 MeV) and enriched metal targets of ^{48}Ti, ^{49}Ti, ^{50}Ti and ^{nat}V metal targets. Considering the high cost of the enriched metal powders, the collaboration with experts in nuclear codes such as EMPIRE, FLUKA and TALYS [9, 10, 8], is essential to compare the different nuclear reactions and identify the most promising energy region for ^{47}Sc production. In fact, no experimental data are available for the ^{49}Ti(p,x)^{47}Sc reaction, while only few measurements were performed with the ^{48}Ti and ^{50}Ti targets in oxide form [11, 5, 7]. Among the radionuclidic impurities of ^{47}Sc co-produced during the irradiation, ^{46}Sc (83.79 d) causes the major concern since it is the only radioisotope with a longer half-life than ^{47}Sc. For this reason, a cooling time after irradiation may only decrease the ^{47}Sc/^{46}Sc activity ratio: it is thus crucial to minimize as much as possible the ^{46}Sc production by carefully selecting the target material and the energy range. Aiming at this goal, the different nuclear codes were employed to estimate the cross sections to produce ^{47}Sc and ^{46}Sc by using the different target of interest (^{48}Ti, ^{49}Ti and ^{50}Ti).

2 Materials and Methods

Irradiation runs have been performed at the ARRONAX facility by using the proton beam with tunable energy 35-70 MeV and the stacked-foils method. Considering the use of enriched expensive materials, a dedicated target holder (Ø 11 mm), a graphite collimator (Ø 9 mm) and a plastic support have been designed and realized at the INFN-LNL workshop and used to precisely define the beam size on target during these irradiation runs. The duration of a typical run was 1.5 h with a constant current of about 100 nA, monitored during the bombardment by using an instrumented beam dump.

2.1 COME project

A typical stacked-foils arrangement was made of two identical patterns composed by an enriched ^{70}Zn target foil followed by a ^{nat}Al monitor foil. Enriched ^{70}Zn (> 95%) foils were realized by lamination at INFN-LNL Target Laboratory, starting from enriched metal powders, purchased by Trace Science International and Chemotrade. The ^{nat}Al foil is used to measure the effective beam flux by considering

the reference reaction $^{nat}Al(p,x)^{24}Na$ recommended by IAEA [12] but also as catcher of possible recoil atoms from the target foil. Aluminium foils (0.5–1.0 mm thick) were in-between the two patterns to decrease the proton beam energy. An additional enriched ^{63}Cu (99.7%) thin metal foil is added at the end of the target arrangement to assure the production of the ^{61}Cu radionuclide, that is used as a tracer isotope of copper-elements in the separation process. In fact, the proton-irradiation of enriched ^{70}Zn produces a variety of radionuclides including ^{67}Ga (half-life 3.2617 d), that is of concern because it has a similar half-life of ^{67}Cu (about 2.6 d) and it decays to ^{67}Zn, as ^{67}Cu, thus emitting the same γ-lines [4]. Similarly to the previous with ^{68}Zn targets [13], also in this work we applied a radiochemical process aimed at the Cu/Ga separation to get an accurate measurement of ^{67}Cu and ^{67}Ga activity values by γ-spectroscopy. In view of the future need of reusing the enriched ^{70}Zn material through a dedicated recovery process, the chemical procedure is developed in order to separate also Cu and Zn elements. The efficiency of the chemical process is monitored for each irradiation run by using the tracer radionuclides ^{61}Cu, ^{66}Ga and ^{69m}Zn, respectively for copper, gallium and zinc elements. The chemical separation process (Figure 1), developed starting from the process described by [14], lasted approximately 4 hours and it is based on the following steps:

(a) removal of Ga isotopes by passing the radioactive target solution through a cation exchange resin AG50W-X4 hydrogen form, 100-200 mesh purchased from BioRad, Hercules (CA) USA, previously packed and conditioned in a glass column for chromatography: diameter 1.2 cm, height 20 cm;

(b) evaporation of the resulting solution to adjust the HCl concentration by a dedicated evaporation system, designed with acid fumes collection and neutralization;

(c) purification of Cu isotopes from zinc bulk by anion exchange resin AG1-X8 chloride form, 100-200 mesh purchased by BioRad, Hercules (CA) USA, previously packed and conditioned in a glass column for chromatography: diameter 1.2 cm, height 20 cm.

From the three final solutions named *xCu*, *xGa* and *xZn* (containing the three separate elements of interest Cu, Ga and Zn), three homogeneous aliquots of 5 ml each have been taken and analyzed by γ-spectrometry for the activity determination. The yield of chemical processing has been monitored for all target foils, by measuring the activity of the tracer radionuclides before and after the radiochemical procedure. All samples have been measured with the same high-purity germanium (HPGe) detector (10% relative efficiency, FWHM 1.0 keV at 122 keV, Canberra GC1020), previously calibrated with 5 ml reference liquid source (purchased to Cerca-Lea, France).

Fig. 1: Schematic description of the radiochemical process (left) and pictures of the key-steps of the radiochemical separation (right).

2.2 PASTA project

Generally, the accuracy of a cross section measurement is strongly related to the number of target atoms irradiated by the incident particles, making the characterization of the target a crucial issue. For this reason, metallic targets are more desirable than the oxide ones, whose accurate thickness and density are more difficult to measure. Since highly pure metal ^{nat}V foils are available commercially, the $^{nat}V(p,x)^{47}Sc$ reaction was measured first. On the contrary, enriched metal Ti-foils are not manufactured: these isotopes are usually available only in the oxide form while only few suppliers worldwide provide such materials in the metal powder form. Among the Ti-isotopes (abundance ^{48}Ti 73.72%, ^{49}Ti 5.41% and

^{50}Ti 5.18%), the priority was given to ^{48}Ti thanks to the achievable maximum enrichment and relatively low price. The enriched ^{48}Ti metal targets were realized by using the High energy VIbrational Powders Plating (HIVIPP) method [15], to homogeneously (>90%) [16] deposit the titanium powder on an aluminium support, as one of the deliverables of the *E_PLATE* project. Enriched ^{48}Ti metal targets were irradiated at the ARRONAX facility by using the stacked-foils technique (Figure 2); data analysis is on-going.

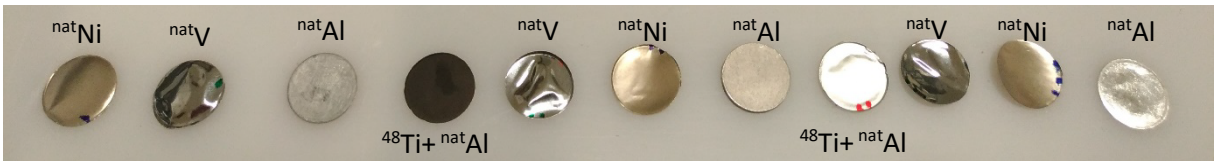

Fig. 2: Photograph of the stacked-foils target typically used in the PASTA project.

In order to optimize future irradiation runs on enriched ^{49}Ti and ^{50}Ti targets, the nuclear codes TALYS [8], EMPIRE [9], and FLUKA [10] were employed to estimate the trend of the nuclear reactions of interest, in particular the production of ^{47}Sc and ^{46}Sc. EMPIRE is a nuclear reaction code designed in a modular array and contains a variety of nuclear models designed for calculations over a broad range of energies, targets and incident particles. Likewise, TALYS is a modular computer code for the analysis and prediction of nuclear reactions. Specifically, it simulates nuclear reactions that involve neutrons, photons, protons, deuterons, tritons, ^{3}He and alpha-particles, in the 1 keV - 200 MeV energy range and for target nuclides of mass 12 and heavier. The last nuclear reaction code we take into consideration, FLUKA, is a general purpose Monte Carlo code for modeling particle transport and interaction with matter. The main application of FLUKA is devoted to high-energy physics, but over the last years it has been widely employed also in medical physics applications in a lower energy regime, such as proton therapy and production of PET radioisotopes. The FLUKA model at low energies, PEANUT (Pre-Equilibrium Approach to Nuclear Thermalization), can be used to calculate the production of residual nuclei (and, thus, radionuclides); in many cases the results are already validated with experimental data. Residual nuclei in FLUKA emerge directly from the inelastic hadronic interaction models and can be calculated for arbitrary projectile-target configurations, including nucleus-nucleus interactions, and energies.

3 Results and discussion

3.1 COME project

Figures 3-7 reports the experimental data compared with theoretical results obtained by using TALYS nuclear code: *Talys 1.*9 refers to the default set of parameters [8], *Talys* 1.9* refers to a new set of models proposed by [17] to run the TALYS code. In all cases, the results obtained in different irradiation runs show a regular trend of the ^{70}Zn(p,x)^{67}Cu, ^{64}Cu, ^{66}Ga, ^{67}Ga cross sections. No literature data are available for the energy range investigated in this work (45-70 MeV): when available, even if at lower energies, previous measurements are reported [5-7]; in case of the ^{70}Zn(p,α)^{67}Cu reaction (Figure 3), the recommended cross section by IAEA up to 40 MeV is also shown [18].

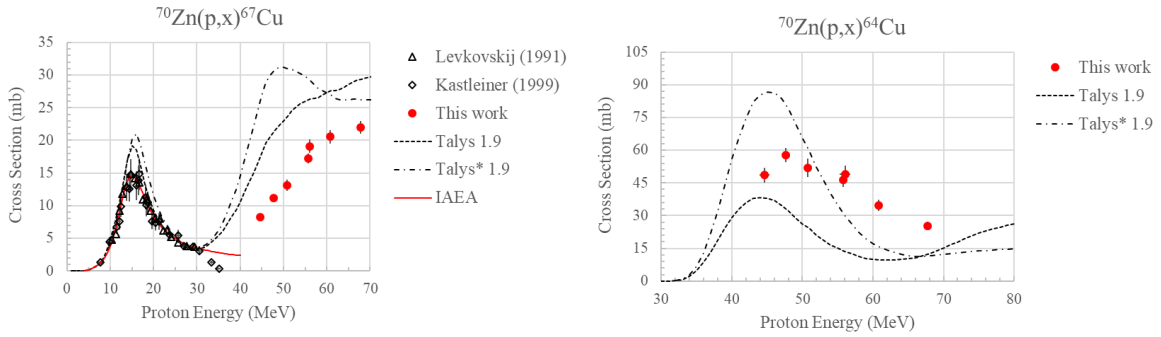

Fig. 3: Results obtained for the $^{70}Zn(p,x)^{67}Cu,^{64}Cu$ nuclear reactions; when available, previous measurements and IAEA recommended cross section are reported.

Experimental data of the $^{70}Zn(p,x)^{67}Cu$ nuclear reaction are reported in Figure 3 (left): in the investigated energy range (45-70 MeV) the cross section shows a regular increasing trend, that is properly described, even if overestimated, by the TALYS 1.9 code with default parameters. Figure 3 (right) reports the experimental data of the $^{70}Zn(p,x)^{64}Cu$ nuclear reaction, compared with TALYS estimations: both set of parameters do not properly describe the trend of measured values. Although the cross section values for ^{64}Cu production are always higher than those of ^{67}Cu, it has to be noted that the trend is decreasing for $E_P > 48$ MeV, whereas the $^{70}Zn(p,x)^{67}Cu$ reaction is increasing. The production of ^{64}Cu is of particular interest, because it is the only copper radionuclide that may affect the RNP of ^{67}Cu-labelled radiopharmaceuticals.

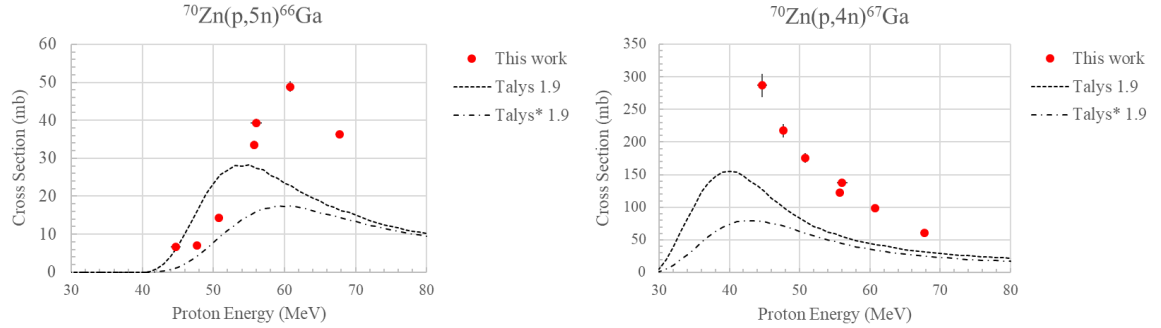

Fig. 4: Results obtained for the $^{70}Zn(p,x)^{66}Ga,^{67}Ga$ nuclear reactions.

The measurement of the cross section of the $^{70}Zn(p,5n)^{66}Ga$ and $^{70}Zn(p,4n)^{67}Ga$ nuclear reactions are shown in Figure 4 and compared with estimations by TALYS code. As in case of ^{64}Cu, theoretical estimations do not properly describe the trend of experimental data. The $^{70}Zn(p,5n)^{66}Ga$ reaction has a 50 mb peak at about 61 MeV, while the $^{70}Zn(p,4n)^{67}Ga$ reaction seems to have a peak at low energy ($E_P < 45$ MeV), whose value is not predictable without new dedicated irradiation runs at lower proton energies.

Figure 5 shows the new experimental data (red dots) with relative fit (red dashed line) obtained in this work for the nuclear reaction $^{70}Zn(p,x)^{67}Cu$, compared with the recommended cross section by IAEA of the $^{70}Zn(p,\alpha)^{67}Cu$ (red line) and $^{68}Zn(p,2p)^{67}Cu$ (blue line) reactions [18]. It is important to note that the cross section at 70 MeV on ^{70}Zn targets (about 22 mb) is double than the one on ^{68}Zn targets (about 11 mb). For this reason, the ^{67}Cu thick target yield in the energy range 45-70 MeV on 100% enriched ^{70}Zn is 39 MBq/µAh, nearly double than the one on fully enriched ^{68}Zn targets, i.e. 23 MBq/µAh. In order to estimate reasonable ^{67}Cu yield at EOB, a 62 hours irradiation run (equivalent to one ^{67}Cu half-life) is

considered for both target materials: in case of ^{70}Zn the resulting ^{67}Cu activity is 1753 MBq/μA, i.e. 74% higher than the one with ^{68}Zn targets, that is equivalent to 1007 MBq/μA.

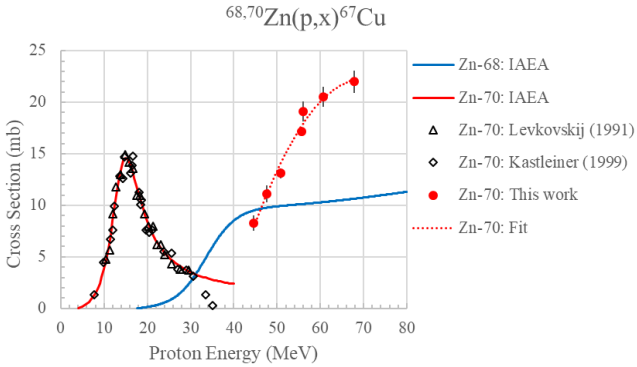

Fig. 5: Comparison of the nuclear reactions to produce ^{67}Cu by using enriched ^{70}Zn and ^{68}Zn target.

3.2 PASTA project

Data analysis on ^{48}Ti targets is still in progress. Preliminary results obtained of the ^{nat}V(p,x)^{47}Sc, ^{46}Sc, ^{44m}Sc, ^{44}Sc, ^{48}Sc, ^{43}Sc are shown in Figures 6-7 (red dots) and compared with previous measurements [7]. In case of ^{43}Sc, the interference with the γ-ray at 373 keV emitted by ^{43}K was corrected; in case of ^{48}Sc, the nuclear cross section is calculated by considering the γ-rays at 175 keV and 1037 keV, in order to avoid the interference with ^{48}V at the 938 keV and 1312 keV γ-lines [4].

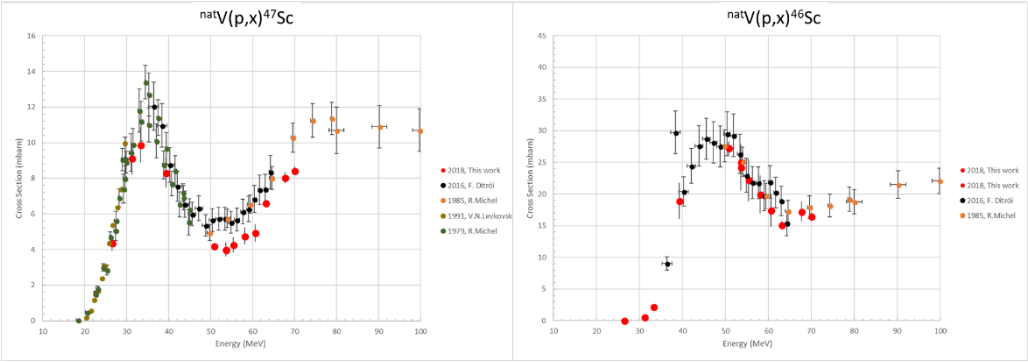

Fig. 6: Preliminary results obtained for the ^{nat}V(p,x)^{47}Sc, ^{46}Sc nuclear reactions, compared with literature data [7].

In case of ^{47}Sc our experimental values are lower than the previous one in the energy range 50-60 MeV (discrepancy < 35%). On the contrary, in case of ^{46}Sc there is a good agreement with literature data in the entire energy range investigated (Figure 7); our measurements are the first near the threshold energy (E_{THR} = 17.6 MeV [4]), describing the initial trend of this cross section.

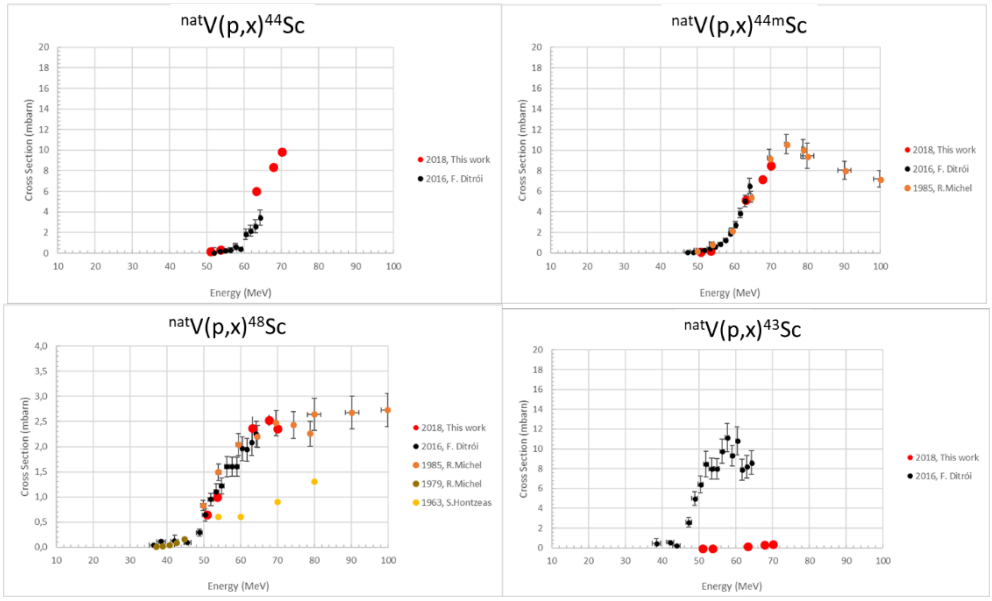

Fig. 7: Preliminary results obtained for the $^{nat}V(p,x)^{44m}Sc$, ^{44}Sc, ^{48}Sc, ^{43}Sc nuclear reactions, compared with literature data [7].

3.2.1 Theoretical estimations of the $^{47}Sc/^{46}Sc$ cross sections in case of ^{49}Ti and ^{50}Ti targets

Figure 8 reports the ratio of $^{47}Sc/^{46}Sc$ cross sections in case of ^{49}Ti and ^{50}Ti targets: results from FLUKA are plotted with a blue line, TALYS with a red line and EMPIRE with a brown line. It can be noted that all the nuclear codes indicate that for ^{49}Ti targets the most interesting energy region is 25-40 MeV, while in case of ^{50}Ti targets the best energy interval is 40-70 MeV. Considering the estimated value of $^{47}Sc/^{46}Sc$ cross sections ratio, *i.e.* 8-26 and 3.5-4.2 for ^{49}Ti and ^{50}Ti targets respectively, it results that the reaction on ^{49}Ti target provides a more favorable ^{47}Sc production in comparison with the one on ^{50}Ti targets.

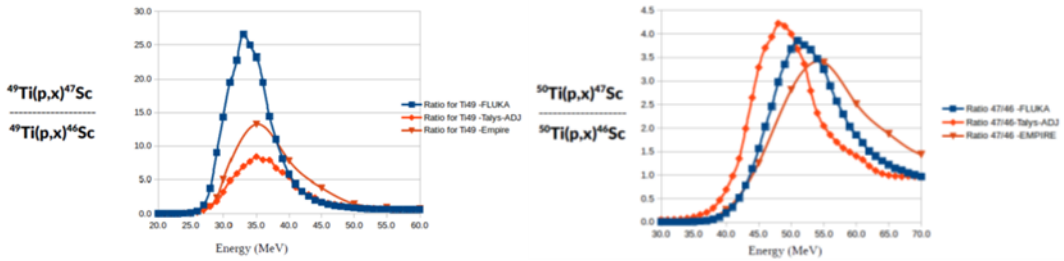

Fig. 8: Estimations of the $^{47}Sc/^{46}Sc$ cross section ratio in case of ^{49}Ti (left) and ^{50}Ti targets (right) performed by using FLUKA (blue line), TALYS (red line) and EMPIRE (brown line) codes.

4 Conclusion

This work describes the results obtained by COME and PASTA projects, performed in collaboration with the ARRONAX facility. The first cross section measurement of the $^{70}Zn(p,x)^{67}Cu$, ^{64}Cu, ^{66}Ga, ^{67}Ga reactions in the energy range 45-70 MeV, by using highly enriched ^{70}Zn metal targets and a dedicated

radiochemical procedure to separate Cu/Ga/Zn elements is presented. Results obtained in the COME project show that in the energy range 45-70 MeV the ^{67}Cu yield with ^{70}Zn targets is 74% higher than the yield obtained by using ^{68}Zn with same irradiation parameters. Preliminary results of the PASTA project, *i.e.* experimental data of the ^{nat}V(p,x)^{47}Sc, ^{46}Sc, ^{44m}Sc, ^{44}Sc, ^{48}Sc, ^{43}Sc nuclear reactions and theoretical estimations of ^{47}Sc/^{46}Sc ratio in case of ^{49}Ti and ^{50}Ti targets, are reported.

Acknowledgement

This work was funded by INFN with the research project *COME – COpper MEasurement* (CSN3 Dotazioni LNL, 2016) and *PASTA – Production with Accelerator of Sc-47 for Theranostic Applications* (CSN5 Bando N. 18203, 2017-2018). It is developed in the framework of the CRP by IAEA (No. F22053) on "*Therapeutic Radiopharmaceuticals Labelled with New Emerging Radionuclides (^{67}Cu, ^{186}Re, ^{47}Sc)*". It has been also, in part, supported by a grant from the French National Agency for Research called "*Investissements d'Avenir*", Equipex Arronax-Plus (ANR-11-EQPX-0004) and Labex IRON (ANR-11-LABX-18-01).

References

[1] M. Maggiore et al., *Mod Phys Lett A* (2017) 32 (17) 1740010.

[2] F. Haddad et al., *Eur J Nucl Med Mol Imaging* (2008) 35:1377–1387.

[3] IAEA CRP No. F22053, http://cra.iaea.org/cra/explore-crps/all-active-by-programme.html

[4] National Nuclear Data Center (NNDC) Database 2.6, http://www.nndc.bnl.gov/nudat2/.

[5] V.N. Levkovskij, Middle mass nuclides (A=40-100) activation cross sections by medium energy (E=10-50 MeV) protons and α-particles (experiment and systematics). Moscow: Inter-Vesti (1991).

[6] S. Kastleiner et al., *Radiochim Acta* (1999) 84:107-110.

[7] EXFOR Database, https://www-nds.iaea.org/exfor/exfor.htm

[8] A.J. Koning et al., *EDP Sciences* (2008) p. 211-214.

[9] M. Herman et al., *Nucl. Data Sheets* (2007) 108:2655-2715.

[10] T.T. Boehlen et al., *Nucl. Data Sheets* (2014) 120:211-214.

[11] E. Gadioli et al., *Z. Phys. A – Atoms and Nuclei* (1981) 301:289-300.

[12] IAEA Monitor Reactions 2017, https://www-nds.iaea.org/medical/monitor_reactions .html

[13] G. Pupillo et al., *Nucl Instrum Methods Phys Res, Sect B* (2018) 415:41-47.

[14] D.G. Medvedev et al., *Appl Radiat Isot* (2012) 70:423–429.

[15] I. Sugai et al., *Nucl. Instr. and Meth. A* 397 (1997) 81-90.

[16] I. Sugai et al., *Nucl. Instr. and Meth. A* 613 (2010) 407–411.

[17] C. Duchemin et al., *Phys Med Biol* (2015) 60:931-946.

[18] IAEA website on Emerging Isotopes, https://www-nds.iaea.org/radionuclides/emerging.html

Challenges in the modeling of nuclear reactions for theranostic applications

Fontana A.[1]*, Calzaferri S.*[1,2]*, Canton L.*[3]*, Esposito J.*[4]*, Mou L.*[4]*, Pupillo G.*[4]*, Rossi Alvarez C.*[4]
[1]INFN - Sezione di Pavia, Italy
[2]Dipartimento di Fisica, Università di Pavia, Italy
[3]INFN - Sezione di Padova, Italy
[4]INFN - Laboratori Nazionali di Legnaro, Italy

Abstract
We present the results obtained for a selection of nuclear reactions of interest for the INFN SPES/LARAMED initiative, focusing on the study of cross sections for the production of theranostic ^{47}Sc from Ti and V targets with state-of-art nuclear codes (Talys, Empire and Fluka). Radioisotope production for theranostics (i.e. their combined use for therapy and diagnostics) is currently a topic of great interest and a set of new, emerging isotopes has been identified to be used with existing clinical scanners or as therapeutic agents in alternative to the standard isotopes. Three new promising isotopes were recently recommended by IAEA: ^{67}Cu, ^{47}Sc and ^{186}Re. These isotopes can be produced at cyclotrons by means of nuclear reactions induced by charged particles: however these processes produce the desired nuclide together with other contaminants, and require further purification of the samples before their medical use. High-purity production is a difficult task and poses restrictions to the irradiation conditions in order to optimize the reactions yield.

1 Introduction

The physics of nuclear reactions is a well studied subject [1, 2] and, at the energies of interest for the production of radionuclides (below 100 MeV), it relies on well known models developed since the first studies on nuclei. In general there are three mechanisms: the compound nucleus formation and decay, the direct reaction and the pre-equilibrium reaction. They are not mutually exclusive and their contribution to a process depends, among other factors, on the nuclei involved and on the energy of the beam.

These models depend on free parameters that can be varied to improve the agreement with experimental data and that can be ascribed to three different aspects: the optical potential parametrization [3], the nuclear level density [4] and the pre-equilibrium description [4]. Optical potential parameters have been extensively studied in the past with different values suggested for the various nuclei and three approaches are followed: a best-fit solution with parameters optimized for a single nucleus and a single energy, a local solution valid for a single nucleus and an energy interval and a global and general solution that can be applied to many nuclei in an energy interval [3]. Also for the nuclear level density different models can be used, from the simple Fermi gas to the more advanced microscopic approaches: different data tables have been fitted to provide improved parametrizations, as those recently suggested for the Talys code as improvement of the default parametrization in the context of radioisotope production [4]. Finally on pre-equilibrium reactions, despite the exciton theory has been introduced about 50 years ago [5], there is still room for improvements, for example by considering the effect of light complex particles [6] or the effects of a quantum mechanical description of the process.

To describe these complex mechanisms different computational tools are available: in this work we have used the analytical codes Talys (version 1.9) [7], Empire (version 3.2) [8] and the montecarlo code Fluka (development version 2018.0) [9]. None of these codes can be used as an universal "best-choice tool", and it is foreseen that different results will be produced by them: a big effort, both from

theoretical and from experimental groups, is currently ongoing to collect more detailed and accurate data on nuclear reactions relevant to radioisotopes production and to allow improvements in their theoretical description.

This is the rationale of our study and in this work we will present a selection of results obtained with the mentioned tools for the theranostic isotope ^{47}Sc in the context of the PASTA (Production with Accelerator of ^{47}Sc for Theranostic Applications) collaboration.

2 New routes for ^{47}Sc

The PASTA project was recently financed by INFN to measure the production cross section of ^{47}Sc with low-energy protons at cyclotrons starting from enriched Ti (^{48}Ti, ^{49}Ti, ^{50}Ti) and natural V targets. The isotope ^{47}Sc offers interesting properties for theranostic applications due to its radioactive decays, summarized in Table 1, with only the isotope ^{46}Sc as major contaminant with long half-life (Table 2).

Isotope	$T_{1/2}$	Principal γ energy	β^- average energy
^{47}Sc	3.35 d	159 keV	162 keV

Table 1: Main properties of ^{47}Sc relevant for theranostics applications: the emitted γs are used for imaging, while the βs for therapy.

Contaminant	^{43}Sc	^{44g}Sc	^{44m}Sc	^{46}Sc	^{48}Sc	^{49}Sc
Half-life	3.89 h	3.92 h	2.44 d	83.82 d	43.67 h	57.2 m

Table 2: Half-lives of the main contaminants produced together with ^{47}Sc.

This project is part of a series of measurements that are preliminary to the beginning of activities of the SPES (Selective Production of Exotic Species) initiative at the INFN-LNL National Laboratories of Legnaro (Padova, Italy), where a new high-energy and high-intensity cyclotron has been installed and is currently under commissioning. The machine consists of a dual beam proton cyclotron (E = 35-70 MeV) that is foreseen to deliver beams both for fundamental nuclear physics research and for applied physics, for example in the LARAMED project (LAboratory for the Production of RAdioisotopes for MEDicine). In particular, the research goals of the latter will focus on the production of radioisotopes for medicine by performing new accurate measurements of production cross sections of different isotopes and their contaminants and the first irradiations are expected to start in 2020: in preparation for these activities, a collaboration between LNL and the ARRONAX (Accelerator for Research in Radiochemistry and Oncology at Nantes Atlantic) facility (Nantes, France) has been formed to allow the first measurements [10] by using the 70 MeV multi-particle cyclotron available there (see contribution by G. Pupillo at this conference on the INFN projects COME - COpper MEasurement - and PASTA).

Theoretical and computational support is essential for these experimental activities, both to propose new production routes and to interpret the experimental data. The optimal conditions for the production of a given isotope depend on various factors, like the irradiation conditions, the target properties, the beam type and energy and the nuclear reaction cross section: preliminary calculations are required to identify the best reaction channels and the optimal energy windows that maximize the desired isotope yield, minimizing at the same time the contaminants. An extensive study for the production of Scandium isotopes from Vanadium target in the energy range 37-65 MeV has been recently performed [11], with the conclusion that theoretical values of the excitation functions available in the TENDL (2014 and 2015) library generally underestimate experimental data and that in some case the code Empire gives better results. However, in this work and in all the literature that refers to the TENDL library, a generic and not optimized set of parameters for the theoretical models underlying the Talys code has been used: in the present paper we show that, with a better selection of the models and by using also the Empire

and Fluka codes, it is possible to improve the agreement of the models with experimental data [4] and to obtain more accurate predictions, providing also an estimate of the attainable theoretical uncertainties.

3 Low-energy options for ^{50}Ti and ^{51}V

The production of ^{47}Sc with protons at cyclotrons starting from enriched Ti (^{48}Ti, ^{49}Ti, ^{50}Ti) and natural Ti and V targets is challenging, in particular for the possible production at low-energy with high-purity. Models give different predictions and, in some cases, data are very old or missing and this suggests the need for a thorough investigation of these reactions.

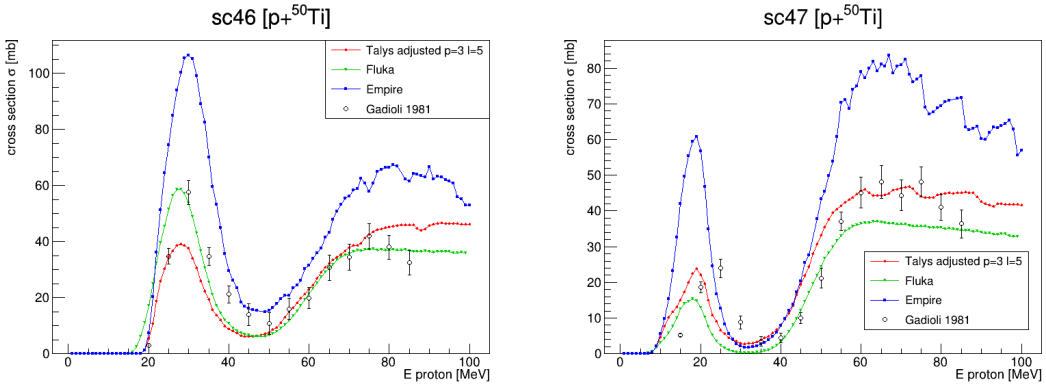

Fig. 1: Cross section for the reactions ^{50}Ti(p,x)^{46}Sc and ^{50}Ti(p,x)^{47}Sc.

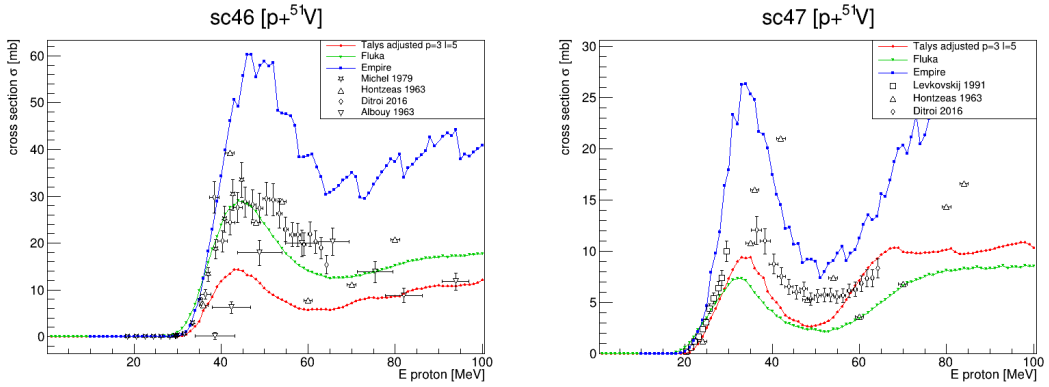

Fig. 2: Cross section for the reactions ^{51}V(p,x)^{46}Sc and ^{51}V(p,x)^{47}Sc.

Looking at the cross sections evaluated with the three programs (Figs. 1 and 2) for the targets ^{50}Ti and ^{51}V in the energy range from threshold to 100 MeV, we identify in the curve three regions that can be used to compare the different models:

- the threshold: the onset of the cross section at the threshold is reproduced with good agreement by the codes, even if in some case the differences can be dramatic (see the case of ^{43}Sc in the following). The behaviour in this region is very important, since the interplay of the thresholds of the contaminant isotopes with respect to ^{47}Sc will determine the degree of purity when the production is at low-energy (the ideal situation beeing to have the lowest threshold for ^{47}Sc that could be the only product).
- the evaporative bump: the height of the low-energy bump, due mainly to evaporative processes, determines the final activity of the produced isotope, for given irradiation conditions. In this region

a great variability is shown by the models and often data are well reproduced after an optimization of the parametrization.

– the pre-equilibrium rise: the high-energy behaviour is sensitive to both the nuclear levels density model and the pre-equilibrium parametrization adopted and also in this region the agreement with data is not always good.

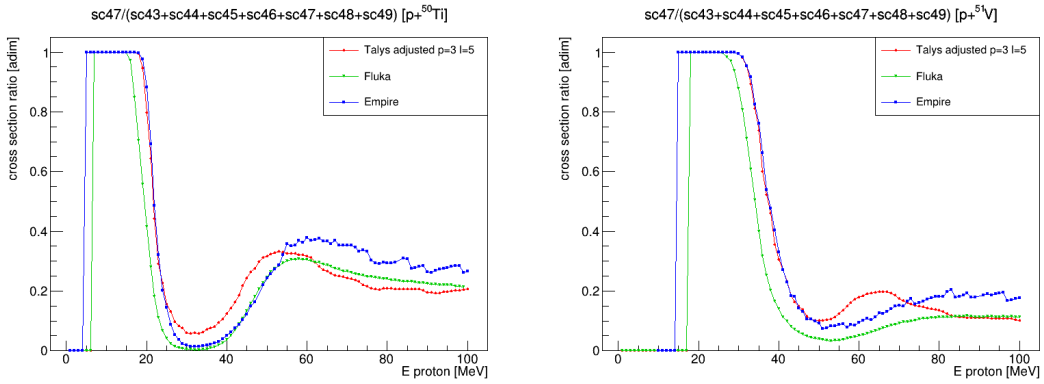

Fig. 3: Prediction of the ratio of the production rates for ^{50}Ti(p,x)^{47}Sc and ^{51}V(p,x)^{47}Sc with respect to all the other Scandium contaminants.

The variation range of the different codes provides an uncertainty band that can be useful for the comparison with data. In Figs. 1 and 2 we see that for the case of ^{46}Sc and ^{47}Sc different predictions are given by the models and that the agreement with experimental data is not always satisfactory. Nevertheless, for the case of ^{50}Ti and ^{51}V targets, an interesting situation emerges from this study: due to the interplay of the various thresholds a low-energy window can be identified in which only ^{47}Sc is produced (albeit with low absolute value of the cross section, around 10 mb) in the energy intervals 5-20 MeV in case of ^{50}Ti and 18-30 MeV in case of ^{51}V (Fig. 3). The latter target is more interesting due to the extremely high isotopic abundance of the isotope (99.75 %), making it possible to use natural V for the targets, less expensive than the enriched ^{50}Ti. Also the presence of minima in the cross sections can be exploited: as in the case shown of ^{50}Ti, the overlap of the ^{46}Sc minimum with the ^{47}Sc pre-equilibrium rise (where the absolute values of the cross sections are comparable, around 20-30 mb) gives a clear advantage for high-purity production. These results open the way to a potentially new low-energy production of high-purity ^{47}Sc at commercially available hospital cyclotrons [12] and deserve to be confirmed experimentally.

The other isotopes of Ti that we have analyzed (^{48}Ti and ^{49}Ti) do not show a favorable ratio for a high-purity production of ^{47}Sc according to the models and are not further investigated in this paper.

4 Studies on ^{nat}Ti

The case of ^{nat}Ti deserves attention, given the easy availability of the material for target production and the rich experimental dataset present in the literature. In this case the cross sections of ^{46}Sc and ^{47}Sc have similar absolute values (Fig. 4), but present a less articulated profile: therefore it is not possible to identify a high-purity energy window, since considering only ^{46}Sc as contaminant the maximum purity that can be obtained is $\approx 80\%$, while considering all scandium contaminants is $\approx 30\%$. Therefore ^{47}Sc, if produced via this route, will need to be purified from the contaminants after production by chemical separation and perhaps other techniques (like isotopic online separation with a mass spectrometer) are more convenient.

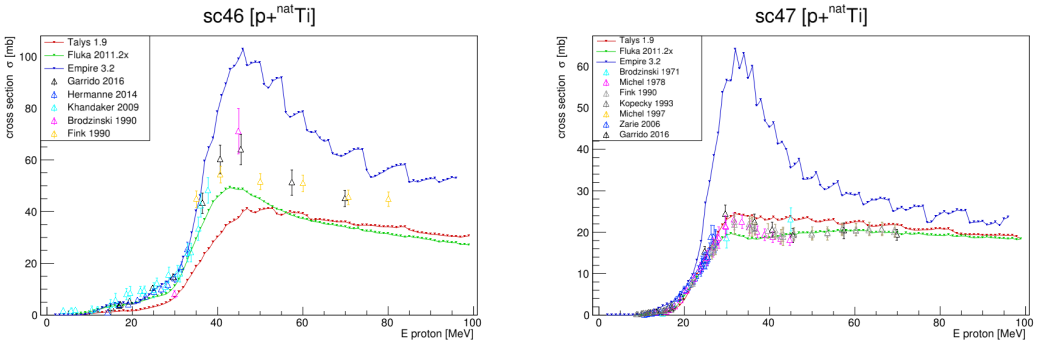

Fig. 4: Cross section for the reactions ^{nat}Ti(p,x)^{46}Sc and ^{nat}Ti(p,x)^{47}Sc.

5 The case of ^{43}Sc from ^{51}V

As an example of the difficulties that can be encountered in these studies, we show the cross section of ^{43}Sc produced from ^{51}V (Fig. 5): in this case the data depart significantly from all models predictions at low-energy and the behaviour at the threshold is not confirmed by the most recent published data [11], while there is an agreement with other data: among these there are those collected by the PASTA collaboration in LNL (see Pupillo et al. at this conference) and not yet published. This disagreement could be due to the misinterpretation of the gamma emission used to measure the production cross section of ^{43}Sc: this nuclide emits indeed a gamma ray with energy 372.9 keV, very close to the energy 372.76 keV of the gamma ray emitted by ^{43}K that is also produced in the same reaction and the two signals should be disentagled. The analysis is in progress to verify which of the models is the most reliable and preliminary results from the PASTA group should be available soon.

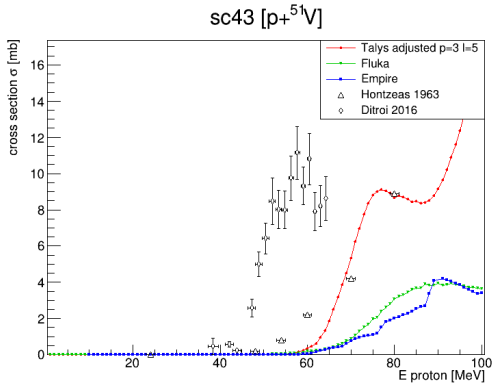

Fig. 5: Cross section for the reaction ^{51}V(p,x)^{43}Sc.

6 Outlook

In this work we have theoretically investigated new ways to produce the theranostic isotope ^{47}Sc at cyclotrons and we have found that it could be produced with high-purity by irradiating ^{50}Ti and ^{51}V targets with protons. In particular the low natural abundance of ^{50}V (0.25%) allows the production of ^{47}Sc from the irradiation of ^{nat}V targets: this option is new and could be explored at low-energy in addition to the routes proposed in a recent study [12].

These results are confirmed by all models and also by recent data from PASTA: this is promising for the possible application to the production of ^{47}Sc as innovative theranostic radiopharmaceutical and could be extended also to other isotopes. To assess this possibility, however, it is necessary to evaluate the production rates and to calculate the final activities expected for specific irradiation conditions and

for a given target: by knowing the isotopic and radionuclidic purities of the ^{47}Sc samples as a function of time it is possible to confirm the results obtained here and this will be the subject of further studies.

References

[1] P. E. Hodgson, E. Gadioli, E. Gadioli Erba, *Introductory Nuclear Physics*, Oxford science publications, 1997.

[2] C. A. Bertulani, *Nuclear reactions*, Wiley Encyclopedia of Physics, ISBN-13: 978-3-527-40691-3 - Wiley-VCH, Berlin, 2009.

[3] A.J. Koning, J.P. Delaroche, *Local and global nucleon optical models from 1 keV to 200 MeV*, , Nucl. Phys. A 713 (2003) 231.

[4] C. Duchemin et al., *Production of medical isotopes from a thorium target irradiated by light charged particles up to 70 MeV*, Phys. Med. Biol. 60 (2015) 931

[5] J. J. Griffin, *Statistical Model of Intermediate Structure*, Phys. Rev. Lett., 17 (1966) 478.

[6] C. Kalbach, *The Griffin Model, Complex Particles and Direct Nuclear Reactions*, Z. Physik A 283 (1977) 401-411

[7] A. Koning et al., *TALYS:A nuclear reaction program*, User Manual (2015)

[8] M. Herman et al, *EMPIRE: Nuclear Reaction Model Code System for Data Evaluation*, Nucl. Data Sheets, 108 (2007) 2655-2715.

[9] T.T. Böhlen et al., *The FLUKA Code: Developments and Challenges for High Energy and Medical Applications*, Nuclear Data Sheets 120 (2014) 211-214

[10] G. Pupillo et al., *New production cross sections for the theranostic radionuclide ^{67}Cu*, NIM B 415 (2018) 41.

[11] F. Ditrói et al., *Activation cross-sections of proton induced reactions on vanadium in the 37-65 MeV energy range*, NIM B 381 (2016) 16.

[12] Synowiecki M.A. et al., *Production of novel diagnostic radionuclides in small medical cyclotrons*, EJNMMI Radiopharmacy and Chemistry 3 (2018) 346

Production of innovative radionuclides for therapy and diagnostics: nuclear data measurements and comparisons with TALYS code

A. Guertin[1], E. Nigron[1], M. Sitarz[2,3], C. Duchemin[1], F. Haddad[1,2], V. Métivier[1]*
1 Subatech laboratory, CNRS/IN2P3, IMT Atlantique, Université de Nantes, Nantes, France
2 GIP ARRONAX, Saint-Herblain, France
3 University of Warsaw, Warszawa, Poland
* now at CERN, HSE-RP group, Geneva, Switzerland

Abstract
Nuclear medicine is a specialty that uses radioactive nuclei for therapy or diagnostic of diseases such as different types of cancer. The aim of this paper is to give the status of nuclear data collected for medical isotopes production and to present the large set of experimental data collected by the PRISMA team of the Subatech laboratory using the protons, deuterons and alpha particles delivered by the ARRONAX cyclotron from few MeV up to 70 MeV and covering a wide range of target masses. Using these data, we will also show that constrains can be put on simulation tools such as the TALYS code (version 1.9) and compare with TENDL-2015, the TALYS-based evaluated nuclear data library. A better overall agreement with our experimental data could be obtained with a different combination of models already included in the code.

1 Introduction

Our research activities are focused on radionuclide production mainly for medical applications, either for therapy or diagnosis. This work is carried out in close collaboration with the GIP ARRONAX that possesses a high energy and high intensity multi-particle cyclotron [1]. In this frame, production cross sections and thick target yields were measured for alpha emitters, such as the U-230/Th-226, Th-227/Ra-223 and Ac-225/Bi-213 generators [2]; for photon, Tc-99m [2], and positon, Sc-44g [3], emitters for diagnosis; for electron emitters Re-186g [4], Tb-155 [5] and Sn-117m [6] for therapeutic applications. From the irradiated materials, new experimental production cross section data of interest for medical applications and monitor reactions have been extracted which allow to expand our knowledge on these excitation functions, to confirm the existing trends and to give additional values on a wider energy range. These experiments were conducted at the ARRONAX facility using the stacked-foil technique.

This data set only represents a small part of the data needed in the field studying the production of innovative radionuclides for medical applications. In order to get answers quickly without the need of new experiments, it is interesting to use theoretical models. The TALYS code gather together several of such models for each step of a nuclear interaction. A systematic comparison of our results with the output of the TENDL-2015 nuclear data library and TALYS code (version 1.9) has been done. In this latter case, several combinations of models have been tested in order to better reproduce the available data.

2 Experimental set-up and production cross section calculation

The production cross section data are obtained using the stacked-foil method [2, 7], which consists of the irradiation of a set of thin foils, grouped as patterns. Each pattern contains a target to produce the

isotopes of interest. Each target is followed by a monitor foil to have information on the beam intensity thanks to the use of a reference reaction recommended by the International Atomic Energy Agency [8]. A degrader foil is placed after each monitor foil to change the incident beam energy from one target foil to the next one. Each foil in the stack is weighed before irradiation using an accurate scale (± 10-5 g) and scanned to precisely determine its area. The thickness is deduced from these values, assuming that it is homogeneous over the whole surface. In this work, we used thin target and monitor foils of a few tens of micrometres thick and degrader foils of few hundreds of micrometres thick. All foils were purchased from the Good Fellow© company.

These foils were irradiated by proton (up to 70 MeV), deuteron (up to 34 MeV) or alpha particle (68 MeV) beams provided by the ARRONAX cyclotron. It delivers these beams with an energy uncertainty of ± 0.50 MeV, ± 0.25 MeV and ± 0.61 MeV, respectively for p, d or alpha particle, as specified by the cyclotron provider using simulations. The beam line is under vacuum and closed using a 75 µm thick kapton foil. The stacks were located about 6.8 cm downstream in air. The energy through each foil has been determined in the middle of the thickness of the foil using the SRIM software [9]. Energy losses in the kapton foil and air have been taken into account in our analysis. All along the stack, depending on the number of foils, the energy uncertainty increases up to ± 2.0 MeV due to the energy straggling. Irradiations were usually carried out for half an hour, with beams of mean intensity between 100 and 150 nA for proton, between 50 and 140 nA for deuteron and between 140 and 200 nA particles for alpha beam. The recommended production cross section values [8] of the Ti-nat(d, x)V-48 (all energies), Cu-nat(p,x)Co-56, Zn-62 (> 50 MeV), Ti-nat(p,x)V-48 (< 20 MeV), Ni-nat(p,x)Ni-57 (20-50 MeV), Cu-nat(α,x)Ga-67 (up to 50 MeV) and Al-27(α,x)Na-22 (from 50 MeV to 70 MeV) reactions were used to get information on the beam intensity, depending on the investigated energy range.

The activity measurements in each foil were performed using a high purity germanium detector from Canberra (France) with low-background lead and copper shielding. The first measurements started the day after the irradiation (after a minimum of 15 hours cooling time) during one hour, for all target and monitor foils. Our data are then limited to γ emitter radionuclides with a half-life higher than few hours. A second series of measurements was performed one week after End Of Beam, during a minimum of 24 hours (one day) and up to 60 hours. Third measurements were devoted to long half-life radionuclides and also waiting for the decay of some radionuclides. Gamma spectra were recorded in a suitable geometry calibrated in energy and efficiency with standard Co-57, Co-60 and Eu-152 gamma sources from LEA-CERCA (France). The full widths at half maxima were 1.04 keV at 122 keV (Co-57 γ ray) and 1.97 keV at 1332 keV (Co-60 γ ray). The samples were placed at a distance of 19 cm from the detector, which is suited to reduce the dead time and the effect of sum peaks. The dead time during the counting was always kept below 10%.

The production cross section values are calculated using the well-known activation formula, defined as a relative equation in which the knowledge of the beam current is no longer necessary thanks to the recommended reactions. The uncertainty is expressed as a propagation error calculation (see [6] for more details).

3 The TALYS code and TENDL data library

In this article, all the experimental production cross section values are compared with the version 1.9 of the TALYS code released in December, 2017 [10]. TALYS is a nuclear reaction program which simulates reactions induced by light particles, neutrons, photons, protons, deuterons, tritons, ^{3}He- and alpha-particles, on target nuclides of mass 12 and heavier. It incorporates theoretical models to predict observables including production cross section values as a function of the incident particle energy (up to 1 GeV). A combination of models that best describes the whole set of available data for all projectiles, targets and incident energies have been defined by the authors and put as default in the

code. In this way, a calculation can be performed with minimum information in the input file: the type of projectile and its incident energy, the target type and its mass. The results of this combination of models are referenced in Fig. 1 to 4 as TALYS 1.9 Default.

TENDL is a TALYS-based Evaluated Nuclear Data Library using both default and adjusted TALYS calculations and data from other sources [10, 11]. Our experimental production cross section values have been compared with the 8th TENDL release: TENDL-2015. It provides evaluated data for seven types of incident particles (n, p, d, t, He-3, alpha-particle, gamma) and for all the isotopes living more than 1 second (~ 2800 isotopes), up to 200 MeV. Since there are some differences between experimental data and the results of the TALYS code using default models and the TENDL-2015 library, we have defined a combination of models, already included in the TALYS code, which better describes the production cross sections, for a variety of projectiles, incident energies and target masses. The description of the optical, pre-equilibrium and level density models have been found to have a great influence on the calculated production cross section values. When proton, deuteron and alpha particle are used as projectile, better results are in general obtained using the optical model described, respectively by [12], [13] and [14]. And for these three projectiles, when a pre-equilibrium model based on the exciton model including numerical transition rates with optical model for collision probabilities [15, 16] and a model for the microscopic level density from Hilaire's combinatorial tables [17] is used. The results of this combination of models are plotted in Fig. 1 to 4 as TALYS 1.9 Adj. Parametrizations of the models have not been changed. They are used as they are implemented in TALYS. Level density or optical model parameters haven't been tuned.

4 Results and discussion

TALYS version 1.9 results have been obtained using the default models (labelled Default) and using the combination of models (labelled Adj.) described in the section 3. In Fig. 1 to 4, the full circles correspond to our experimental values, the other geometrical symbols to literature data, the full lines to TALYS Default and the dash lines to TALYS Adj. calculations. Four reactions, extracted from previous published articles, are presented. They cover proton, deuteron, alpha particle beams and a wide range of masses. All the experimental production cross section values are compared with the version 1.9 of the TALYS code released in December, 2017 [10].

4.1 Th-226 production from the Th-232(p,3n)Pa-230 reaction

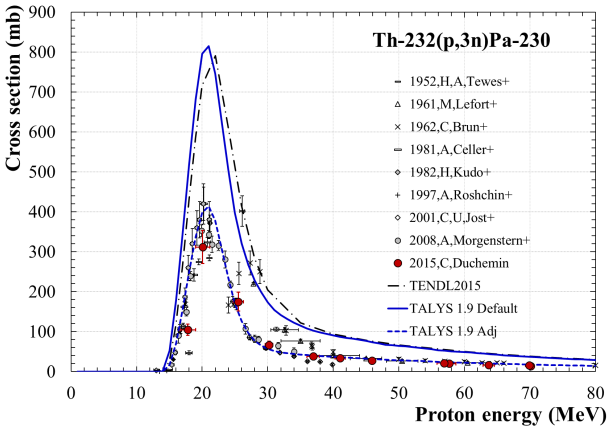

Fig. 1: Th-232(p,3n)Pa-230 cross section

Th-226 is a promising radionuclide for α RIT in leukaemia treatment. Th-226, with a half-life of 31 minutes, can be produced from the α decay of U-230, which has a half-life of 21 days, thanks to a

generator system U-230/Th-226. We studied the U-230 production using the Th-232(p,3n)Pa-230(β-)U-230 reaction. Our set of data for the Th-232(p,3n)Pa-230 reaction is plotted in Fig. 1.

There is a good agreement with our experimental data and those available in the literature. The TALYS code version 1.9 with default models and the TENDL-2015 library values, plotted with a dashed-pointed line, are not able to reproduce the production cross section amplitude even if the shape is in good agreement with our experimental data. The TALYS 1.9 Adj. results are in perfect agreement with these experimental data. As TEDL-2015 and TALYS 1.9 Default curves exhibit roughly the same shape and amplitude, TENDL-2015 will not be plotted on the following figures.

4.2 Re-186g production from natural tungsten

Re-186g, with a half-life of 3.7 days, is a β- emitter used in clinical trials for the palliation of painful bone metastases resulting from prostate and breast cancer. It emits a 137 keV gamma ray, suited for SPECT imaging. The Fig. 2 shows that our experimental production cross section values are in agreement with the literature. The TALYS 1.9 Default calculation is far from the cross section amplitude. The TALYS 1.9 Adj. values are in better agreement but still underestimate the maximum of the cross section by 20%.

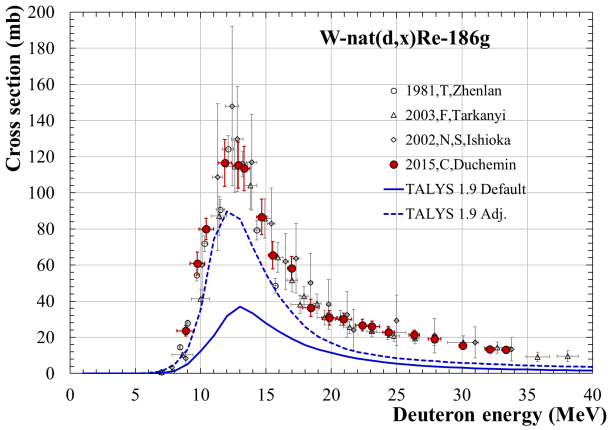

Fig. 2: W-nat(d,x)Re-186g cross section

4.3 Sn-117m production from natural cadmium

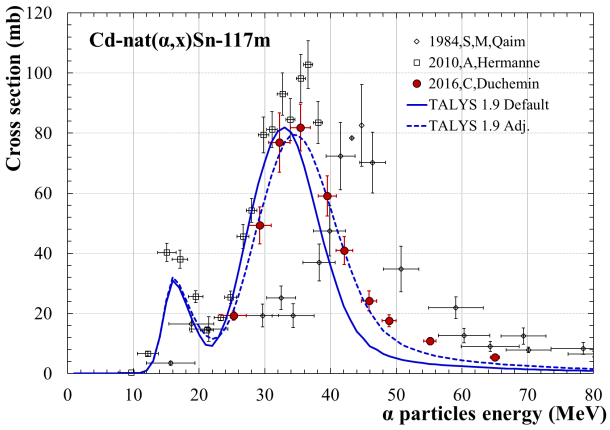

Fig. 3: Cd-nat(α,x)Sn-117m cross section

Sn-117m is a conversion and Auger electron emitter, with a half-life of 13.6 days, useful for the palliation of painful bone metastases. Moreover, imaging can be achieved with its 158 keV gamma line. Our experimental production cross section values are in agreement with the values of Hermanne et al., published in 2010 (see Fig. 3). However, the Qaim and Döhler values show a shift in energy, roughly 10 MeV higher, for the location of the cross section's maximum. The points have been degraded rather far from the initial beam energy, which could explain the shift by energy straggling through the foils.

The TALYS 1.9 Default models give the good shape but results are slightly underestimated and shifted in energy (3 MeV lower). TALYS 1.9 Adj. models are in good agreement with the general behaviour of the experimental data. This combination allows reproducing the shape, the position of the maximum and the amplitude below 45 MeV.

4.4 Tb-115 production from natural gadolinium

Several terbium isotopes are suited for diagnosis or therapy in nuclear medicine. Tb-155 is of interest for SPECT imaging and/or Auger therapy. Tb-155 has a half-life of 5.32 days. It decays by electron capture process to Gd-155 (stable) by emitting Auger electrons (4.84 keV and 34.9 keV), conversion electrons (from 2 keV to 130 keV) and nine main gamma rays (from 86 keV to 367 keV).

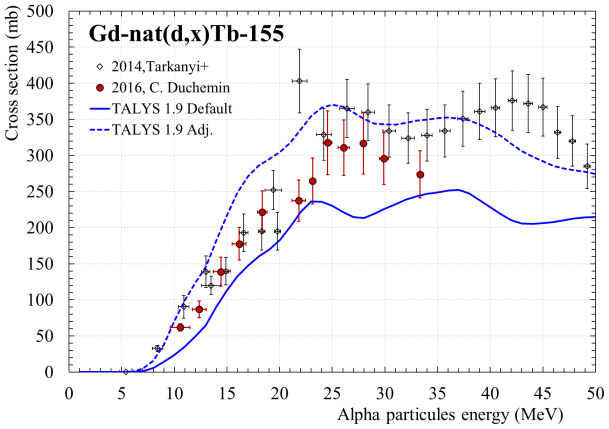

Fig. 4: Gd-nat(d,x)Tb-155 cross section

Our experimental production cross section values are plotted in Fig. 4. They are in agreement with the literature data set. The TALYS 1.9 Default models give the good shape but results are slightly underestimated. TALYS 1.9 Adj. models are in good agreement with the general behaviour of the experimental data but slightly overestimated the experimental results.

5 Conclusions

A large set of production cross section of medical radionuclides have been collected using the stacked-foil technique with proton, deuteron and alpha beams delivered by the ARRONAX cyclotron and for various materials on a wide range of masses. Some comparisons have been systematically performed with the TALYS code, version 1.9. This code has been chosen because it includes a large number of theoretical models, the possibility to combine these models to better describe the experimental data and because the authors' team is very reactive and helpful. Three main mechanisms have been investigated, which have a great impact on the studied observables in our work. They are the optical potential, the level density description and the pre-equilibrium model. A set of models have been found allowing a good description of all our collected data, which is different from the suggested

default combination of models. They can be used to get high quality data when no data are available in databases.

Acknowledgement

The ARRONAX cyclotron is a project promoted by the Regional Council of Pays de la Loire financed by local authorities, the French government and the European Union. This work has been, in part, supported by a grant from the French National Agency for Research called “Investissements d′Avenir”, Equipex Arronax-Plus No. ANR-11-EQPX-0004 and Labex No. ANR- 11-LABX-0018-01.

References

[1] F. Haddad, L. Ferrer, A. Guertin, T. Carlier, N. Michel, J. Barbet, J-F. Chatal, Eur. J. Nucl. Med. Mol. Imaging 35, 1377–1387 (2008).

[2] C. Duchemin, A. Guertin, F. Haddad, N. Michel, V. Métivier, Phys. Med. Biol. 60, 931-946 (2015).

[3] C. Duchemin, A. Guertin, F. Haddad, N. Michel, V. Métivier, Phys. Med. Biol. 60, 6847-6864 (2015).

[4] C. Duchemin, A. Guertin, F. Haddad, N. Michel, V. Métivier, Appl. Radiat. Isot. 97, 52-58 (2015).

[5] C. Duchemin, A. Guertin, F. Haddad, N. Michel, V. Métivier, Appl. Radiat. Isot. 118, 281–289 (2016).

[6] C. Duchemin, A. Guertin, F. Haddad, N. Michel, V. Métivier, Appl. Radiat. Isot. 115, 113-124 (2016).

[7] G. Blessing, W. Brautigam, H.G. Boge, N. Gad, B. Scholten, S.M. Qaim, Appl. Radiat. Isot. 955, 46–49 (1995).

[8] F. Tárkányi, S. Takács, K. Gul, A. Hermanne, M.G. Mustafa, M. Nortier, P. Oblozinsky, S.M. Qaim, B. Scholten, Yu.N. Shubin, Z. Youxiang, IAEA-TECDOC 1211, 49–152 (2001). Database available on https://www-nds.iaea. org/medical/monitor_reactions.html, updated Aug. 2017.

[9] J.F. Ziegler, M.D. Ziegler, J.P. Biersack, Nucl. Instrum. Methods Phys. Res. B 268, 1818–1823 (2010).

[10] A.J. Koning, D. Rochman, Nucl. Data Sheets 113 2841 (2012).

[11] A.J. Koning, D. Rochman, J. Kopecky, J. Ch. Sublet, E. Bauge, S. Hilaire, P. Romain, B. Morillon, H. Duarte, S. van der Marck, S. Pomp, H. Sjostrand, R. Forrest, H. Henriksson, O. Cabellos, S. Goriely, J. Leppanen, H. Leeb, A. Plompen and R. Mills, https://tendl.web.psi.ch/tendl_2015/tendl2015.html.

[12] A.J. Koning, J.P. Delaroche, Nucl. Phys. A 713 231 (2003).

[13] Y. Han, Y. Shi, Q. Shen, Phys. Review C 73 (2006).

[14] P. Demetriou, C. Grama, S. Goriely, Nucl. Phys. A 707 (1-2) 253-276 (2002).

[15] E. Gadioli, P.E. Hodgson, Oxford Univ. Press (1992).

[16] A.J. Koning and M.C. Duijvestijn, Nucl. Phys. A744 15 (2004).

[17] S. Goriely, S. Hilaire, A.J. Koning, Phys. Review C 78 (2008).

General Discussion on Medical Radionuclides

Syed M. Qaim (chair)
Forschungszentrum, Jülich, Germany

Abstract
At the end of the formal session on Medical Radionuclides, in which several invited and contributed papers were presented, a general discussion was held. Two topics were chosen: 1) New experimental facilities; 2) Feasibility of formation of a network of laboratories. This is a summary of related discussions.

1 New experimental facilities

Attention was devoted to following three aspects.

a) Security of supply of ^{99m}Tc

Due to anticipated shut down of a few nuclear research reactors in Canada (and possibly in a few other countries), which are extensively used for the production of ^{99}Mo (T½ = 66 h) via the fission process, there has been some anxiety that the supply chain of ^{99m}Tc (T½ = 6.0 h), obtained via the ^{99}Mo/^{99m}Tc generator system, may be jeopardised. Although according to a report issued in 2017 by the "High Level Committee on the Security of Supply of Medical Radioisotopes" of the Nuclear Energy Agency of the OECD, the level of supply of ^{99}Mo is estimated to be adequate till 2022, the fragility of supply chain would remain a matter of concern. A vigilant watch is necessary, particularly because worldwide about 40 million patients per year undergo diagnostic investigations using ^{99m}Tc and Single Photon Emission Computed Tomography (SPECT).

Efforts are underway to make more efficient use of existing reactors, and also to bind in the supply chain, sample irradiations even at some reactors exclusively used for research, e.g. the FRM-II at Munich. Furthermore, construction of new medium to high flux reactors is reaching completion in Australia, China (existing reactor under modification) and Korea (construction permit pending due to earthquake), and it is expected that by 2023, large quantities of ^{99}Mo will be produced at those facilities . Despite those efforts to maintain sufficiency in the supply of ^{99}Mo, it is felt that accelerator technology should receive more attention to produce ^{99}Mo/^{99m}Tc.

Canada has decided to scale up the direct production of ^{99m}Tc via the ^{100}Mo(p,2n)-reaction at a cyclotron. For this purpose a network of about 20 cyclotrons with Ep = 24 MeV is being established. There is, however, some scepticism about the amount of metallic technetium (^{99g}Tc and ^{98}Tc) present in the ^{99m}Tc produced via the (p,2n) reaction. In some other countries as well, e.g. Italy and Czech Republic, some research and development work on this process is going on.

Presently considerable attention is also being devoted to development of high-power electron accelerators. A 50 MeV e^- accelerator could deliver intense beams of neutrons or high-energy photons. They could be used to produce ^{99}Mo via the ^{98}Mo(n,γ)^{99}Mo or the ^{100}Mo(γ,n)^{99}Mo reaction.

Another approach, followed mainly in Japan, is to develop either a 14 MeV or a 40 MeV neutron source using the deuteron-tritium or the deuteron-carbon reaction, respectively. The fast neutrons could then be used to induce the ^{100}Mo(n,2n)^{99}Mo reaction. It should, however, be pointed out that the neutron and gamma induced reactions would lead to production of ^{99}Mo of low specific activity. Very strong chemical efforts would then be required to prepare suitable generator columns for separating the daughter nuclide ^{99m}Tc with the quality acceptable for medical application.

b) Supply of standard PET radionuclides

The short-lived standard positron emitters (^{11}C, ^{13}N, ^{15}O and ^{18}F) used in patient care studies via Positron Emission Tomography (PET) are generally produced at a small-sized cyclotron (Ep ~ 18 MeV, Ed ~ 9 MeV). The technology is well developed and it is expanding fast. According to a recent estimate, the number of such cyclotrons being installed in various parts of the world is reaching about 1000. Two other standard short-lived positron emitters, namely ^{68}Ga and ^{82}Rb are obtained via the generator systems ^{68}Ge/^{68}Ga and ^{82}Sr/^{82}Rb, respectively. The parent radionuclides are produced using an intermediate energy cyclotron or an accelerator delivering protons of energy 70 – 100 MeV. The number of such machines is limited but a few newer facilities are being established (see below). There seems to be no major problem with the supply of standard positron emitters.

c) Production of novel radionuclides

Among the novel radionuclides, the major interest lies on non-standard positron-emitters and low-energy highly-ionising radiation emitters, the former for studying slow metabolic processes using PET and the latter for targeted therapy. In recent years the theranostic approach has also been gaining significance. This involves the use of two radionuclides of the same element: one positron emitter for determining the quantitative uptake in an organ and the other corpuscular radiation emitter for therapy.

For production of most of the non-standard positron emitters, like ^{64}Cu, ^{86}Y, ^{89}Zr, ^{124}I, etc. the existing and planned small-sized cyclotrons mentioned above should have enough capacity, provided suitable targets of isotopically enriched materials are developed. Furthermore, a few other medium-sized multiple-particle cyclotrons are being installed in several laboratories, e.g. a 30 MeV cyclotron at Jülich, which are broadening the spectrum of production possibilities. Nonetheless, for the production of several other positron emitters, e.g. ^{52}Fe, ^{72}Se/^{72}As, ^{152}Tb, etc., protons of intermediate energy up to 120 MeV are needed.

Similar to non-standard positron emitters, some therapeutic radionuclides, like ^{103}Pd and ^{186}Re, could be produced using powerful small-sized cyclotrons. However, for the production of ^{47}Sc, ^{67}Cu, ^{225}Ac, etc. intermediate energy protons are needed. Thus the significance of intermediate energy accelerators is increasing. Several such machines exist, e.g. in Chiba, iThemba Labs, PSI Villigen, Moscow, Nantes, Legnaro, BNL, Los Alamos, TRIUMF, etc. Several others are at the planning or installation stage, e.g. in Arizona, Brazil, Korea, etc. At Forschungszentrum Jülich the extraction of a very weak intensity 120 MeV proton beam from COSY is in progress. Some exotic radionuclides are being produced at CERN in tracer quantities using the spallation process combined with on-line mass separation. Thus intermediate energy proton accelerators are expected to play increasingly important role in the production of some special novel radionuclides.

In view of the increasing demands for the theranostic pairs of radionuclides, i.e. a positron emitter and a beta emitting therapeutic radionuclide of the same element, e.g. ^{44}Sc/^{47}Sc and ^{64}Cu/^{67}Cu, the utility of (γ,p) and (n,p)+(n,np) reactions to produce the two therapeutic radionuclides (^{47}Sc and ^{67}Cu) using intense photon and fast neutron sources (as discussed above in connection with ^{99}Mo production) needs to be further investigated. It is also observed that a tendency is developing to consider ^{47}Sc and ^{67}Cu as theranostic agents on their own (i.e. without the respective paired positron-emitting counterpart). The therapy effect of beta particles is well known and, since both the radionuclides emit suitable gamma rays, organ imaging could be done by SPECT. However, in comparison to the PET imaging, SPECT is not quantitative. The dosimetry in the latter case thus lacks precision.

From the above discussion it was concluded that a large number of new facilities have been established or are being established in various parts of the world for medical radionuclide production.

2 Feasibility of formation of a network

It was agreed that concerted efforts should be directed to development of accelerator technology, which is a proven technology, to be able to assure clinical scale production of ^{99}Mo without the use of a nuclear reactor. In this connection close cooperation with nuclear chemists and/or with radiopharmaceutical companies would be called for. Furthermore, the same technology could be used also for the production of a few therapeutic radionuclides like ^{47}Sc and ^{67}Cu.

As regards cyclotrons, it was concluded that small-sized machines are abundant and are mainly used for radionuclide production for local use. There appears to be no need of coordination of those activities. On the other hand, intermediate energy cyclotrons are rather rare. Here it would be very beneficial to form a sort of network to be able to discuss problem areas with colleagues in other laboratories as well as to build up cooperative efforts, wherever possible. The feasibility of formation of such a network should be explored.

Acknowledgments

It is a pleasure to thank all the speakers of the session on medical radionuclides for their valuable contributions.